ANALYSIS OF ACOUSTIC SCATTERING LAYERS IN AND AROUND PETERMANN FJORD, NORTHWEST GREENLAND

BY

ERIN HEFFRON

Environmental Studies (B.S), Slippery Rock University, 2004

THESIS

Submitted to the University of New Hampshire

In Partial Fulfillment of

The Requirements for the Degree of

Master of Science

In

Earth Science: Ocean Mapping

May, 2022

This thesis was examined and approved in partial fulfillment of the requirements for the degree of Master of Science in Earth Science by:

Thesis Director, Larry Mayer, Professor of Earth Science and
and Ocean Engineering, and
Director, Center for Coastal and Ocean Mapping

James Pringle, Professor of Earth Sciences

Jonathan Cohen, Associate Professor of Marine Science,
School of Marine Science and Policy, University of Delaware

On April 14, 2022

Approval signatures are on file with the University of New Hampshire Graduate School

ACKNOWLEDGEMENTS

This work would not have been possible without the numerous resources and support that I have been privileged to receive. Thank you to the University of New Hampshire, the Earth Science Department, and the Center for Coastal and Ocean Mapping for accepting me as a student and researcher and to CCOM for providing the prolonged financial support that made the return to full time student researcher possible. Thank you to my advisor, Larry Mayer, for the continued support and mentorship during my time as a full time student researcher and when I decided to continue my research while contracting, and to my committee members for sharing their knowledge and being flexible with time lines: Jon Cohen for expertise on biological scatterers and migrations that were so foreign to us, and Jamie Pringle for expertise in physical oceanography.

Many thanks to the crew of the *Oden*, with special thanks to Axel Meiton for digging up info on the PAR sensor for us. Thank you to the Petermann 2015 Mapping Team, including Larry, Martin Jakobsson, Kevin Jerran, Kelly Hogan and Christian Stranne, with extra thanks to Kevin and Christian for their post-cruise data and code support. Additional thanks to Tom Weber for extensive acoustics advice and code support, as well as his former students Scott Loranger and Liz Weidner for the same. Thank you to Moe Doucet and Victoria Price-Doucet for custom code to get the EK80 data into FMMidwater, Danny Neville for Fledermaus and FMMidwater licenses, Myriax Echoview for licensing to teach myself Echoview, and Jennifer Miksis-Olds for allowing us to use her Echoview license. I would not have been able to work with the calibration

data or do any of the work examining the scattering layers without ESP3 and Yoann Ladroit, who made significant code changes and provided so much advice and support regarding fisheries acoustics. Caroline Bouchard, Céline Heuzé, Chris Cox of the BSRN Network, and Cyril Aubry of the Fortier Lab, University of Laval, provided me with unpublished data and answered questions that helped me to understand the oceanography, biological communities and radiation environment in my study area. Finally, thank you to my parents, Jo and John Heffron, for endless support over the years, and to my partner Lindsay Gee, who helped me get through this in so many ways and on so many levels.

This work was funded by the National Science Foundation Award #1417787 and NOAA grant #IDZLM0.

TABLE OF CONTENTS

LIST OF FIGURES

LIST OF TABLES

ABSTRACT

In 2015 a major international collaborative expedition took place focused on understanding the processes associated with the recent rapid decline of the Greenland Ice Sheet (GIS) and the impact that this decline could have on global sea-level rise. The Petermann Expedition collected a broad range of data designed to characterize the Petermann Glacier system, a marine-terminating glacier with a floating ice tongue that has undergone dramatic changes in the last decade. During the expedition, sonars were used to map the seafloor and the water column, generating a continuous dataset over 30 days. The water column mapping revealed extensive acoustic scattering layers, so called because the components of the layer – typically zooplankton and fish – scatter acoustic energy when concentrated in layers in the water column. The scattering layer was observed to change depth in a geospatially consistent manner and corresponded to our general, but limited understanding of the complex circulation patterns in the study area. This unexpected observation became the research question investigated in this thesis: Is the distribution of the acoustic scattering layer observed in and around Petermann Fjord a proxy for spatial and temporal changes in water mass structure and interactions? In order to answer this question, we focused on four objectives: determine the geospatial distribution of the scattering layer, determine if light influences the scattering layer depth distribution, determine if there is a consistent relationship to water column structure and circulation, and investigate the components of the scattering layer for clues as to its make-up and subsequently any potential reasoning for its distribution.

Understanding the distribution of water masses and their circulation patterns in Arctic fjords are critical to understanding the fate of floating ice shelves and the glaciers

they buttress, as the most pronounced change is occurring where ice sheets are grounded below sea level due to enhanced interaction with warming ocean waters. However, our ability to predict future sea level rise is hampered by our limited knowledge of these glacial systems, including the regional water mass distribution and circulation responsible for that enhanced ocean-ice interaction. Indeed, quantification of melting processes at marine terminating glaciers represents the largest source of uncertainty in predicting global sea level rise (Church et al., 2013). Traditional methods of oceanographic observation provide relatively sparse information at high cost, whereas acoustic records are continuous and, if the observed relationship between scattering layer depth and regional hydrography holds true, can potentially provide information about circulation, productivity, and ocean dynamics over large areas from underway platforms.

Evaluation of the scattering layer distribution focused on the continuous Simrad EK80 18 kHz split-beam echosounder sonar records (section 3.1.1.1). The top of the scattering layer was manually picked on each echogram, providing the latitude, longitude, and depth for the top of each layer (section 3.2.1) that were then plotted to show the geospatial and depth distribution. The resulting distributions (section 4.1) showed a recognizable geospatial pattern that was consistent with our understanding of the distribution of water masses. Broadly, there was a scattering layer generally present in the fjord along the coast of Greenland (eastern Hall Basin) and ringing central Hall Basin, and absent in northern Hall Basin, along the coast of Ellesmere Island (northern Nares Strait and western Hall Basin), central Hall Basin, and southern Nares Strait. The top of the scattering layer was significantly shallower in the fjord and along the coast of

Greenland, deepening in the central ring and western Hall Basin (when it was present). We evaluated whether there was a linear correlation between the scattering layer depth and the bathymetric depth and slope (sections 3.1.1.2, 3.1.1.5, 3.2.2), but no correlation was found (section 4.2.1).

The second objective was to determine whether the scattering layer distribution was influenced by light rather than water mass distribution. This analysis was undertaken because of the typical association of scattering layers with daily migrations corresponding to daily light cycles as a means of predator avoidance (section 1.3.3). Though the expedition took place in Arctic summer during the 'midnight sun' regime of 24-hour light, there was enough daily change to discern a cycle in the ship-based radiation data collected by a Photosynthetically Active Radiation (PAR) Sensor mounted on the roof of the ship's bridge (section 3.1.2.2). The relationship between light levels and scattering layer depth was examined (section 3.2.3), finding no linear correlation (section 4.2.2). A second analysis was done to see if we could discern a difference in water clarity across the study area using satellite-derived *Kd*(490) data, the diffuse attenuation coefficient for downwelling irradiance at 490 nm (section 3.1.3), and evaluate its effect on the scattering layer depth. Though available data for this region was very limited and there was some evidence of higher attenuation in the fjord where the shallower scattering layers were typically located, no correlation between scattering layer depth and *Kd*(490) values was found (section 4.2.3). Thus, neither light levels nor water clarity were responsible for the depth distribution of the scattering layer.

The third objective was to determine if there was a consistent relationship between water mass properties and scattering layer depth beyond that established by

initial observations (section 1.1). Profiles of conductivity, temperature, and depth (CTDs) were collected at 46 sites during the expedition to provide information on water mass properties and facilitate interpretation of regional circulation (section 3.1.2.1). Plots of temperature versus salinity (T-S diagrams) and temperature and salinity versus depth were generated for each CTD location, and the average depth of the scattering layer for that location was overlain on the plots (section 3.2.5). Examination of the T-S diagrams revealed a pattern in scattering layer preference for specific sections of the water column (section 4.2.4). Of the 38 profiles with an associated scattering layer, 22 had scattering layers with a preferred depth range that fell in the deeper, warmer, saltier portion of the water column associated with Atlantic Water, where salinity and temperature (and therefore density) values were steady – we called this group the 'homogeneous preference' scattering layers, in reference to the lack of change or stratification in the water column. Twelve of the profiles had scattering layers with a preferred depth range that fell in the shallower, cooler, fresher portion of the water column associated with Winter Water (or more generally, the Arctic outflow), where salinity and temperature (and therefore density) were changing relatively quickly with depth – we called this group the 'heterogenous preference' scattering layers, in reference to the changing, or stratified, water column. Four of the profiles had scattering layers that fell right at the location where the water column properties were moving from stratified to steady. This group we refer to as 'transitional' scattering layers. The homogeneous preference scattering layers were found primarily in Hall Basin and the western side of the fjord mouth, areas associated with inflow of Winter Water and Atlantic Water from the Arctic Ocean to Nares Strait. The heterogeneous preference

scattering layers were found in the fjord, an area associated with the influence of meltwater from the glacier (Petermann Glacier Water) and outflow from the glacier face through the fjord. Transitional preference layers were found primarily on eastern side of the fjord mouth, an area associated with meltwater-influenced outflow moving up along the coast of Greenland. Six of the profiles did not have an associated scattering layer, and all were found along the western edge of Nares Strait/Hall Basin, a region associated with low oxygen, cold, fast flow from the Arctic Ocean moving south through Nares Strait. These results show a clear relationship between the scattering layer depth and regional water column structure and circulation (Conclusions, Chapter 5).

The final objective was to investigate, if possible, what the scattering targets in the layers were (section 3.2.6). Target strength analysis of individual targets visible in and around the scattering layers in the EK80 data showed average target strengths of -42.04 to -44.04 dB (section 4.3.2). Estimates of volume scattering for larger sections of the scattering layer were fairly weak, -57.17 to -81.70 dB (section 4.3.2). The high individual target strengths and visual observations of single targets in the echograms (section 4.3.1) seem to indicate larger targets, with a strong possibility being *Boreogadus saida*, polar cod. The low volume scattering values and density estimates made using the volume scattering and individual targets strength values, however, do not seem to indicate that the visually dense scattering layers in the echograms were composed entirely of these fish, so we believe the scattering layers may be a mix of fish interspersed with smaller fish and zooplankton (Conclusions, Chapter 5).

All analyses described in this thesis was complicated by the fact that this was a ‘dataset of opportunity’, i.e., the objectives of this study were not at all part of the

original work plan of the expedition. Water column sonar data were collected continuously, but that collection was focused on the search for gas seeps and secondary to the many other data collection efforts taking place on the expedition. Ship radiation data were collected as a matter of course but via an uncalibrated instrument not intended for this expedition. Lack of water clarity data led to the use of remotely sensed data to attempt to estimate this parameter, and lack of biological sampling pushed us to dig into the echograms for clues as to the scattering layer components, as no ground truthing of either parameter was available. Despite these complications and imitations, we were able to extract useful information from the data and clearly demonstrate that acoustic records such as these can be used to show patterns in water mass distribution and circulation and provide clues to biological communities in this region. Optimizing water column profiling for these objectives opens up the potential of using a rapidly-acquired acoustic remote sensing technique to provide critical information on water mass distribution as a standard underway tool.

CHAPTER 1 INTRODUCTION AND BACKGROUND

1.1 The Petermann Expedition

In 2015 a major international collaborative expedition took place designed to help understand the processes associated with the recent rapid decline of the Greenland Ice Sheet (GIS) and the impact that this decline could have on global sea-level rise (Mix et al., 2022; Jakobsson et al., 2018). The Petermann Expedition was a broad-ranging experiment specifically focused on understanding the recent history of the GIS and, in particular, the attempt to understand why the floating ice tongue that represents the seaward termination of the GIS in Petermann Fjord, has retreated dramatically over the past few decades. Data collection efforts included multibeam echosounder mapping, sediment coring, ice coring, oceanography, mammal observation, boulder dating for ice-retreat timing, and subbottom profiling. The seafloor mapping and subbottom profiling were undertaken primarily to detect and map submarine glacial landforms in order to reconstruct the glacial history of the area (Jakobsson et al., 2018).

In addition to the seafloor and subbottom mapping, acoustics were used to map the water column. A team of researchers from the University of New Hampshire Center for Coastal and Ocean Mapping (UNH-CCOM) were onboard specifically to support this effort. The aim of the water column mapping was originally to identify gas bubbles in the water column, indicative of methane seeps emanating from the seafloor. Few gas seeps were found, however the team did identify an acoustic scattering layer (Figure 1) with an intriguing geospatial distribution (Figure 2). Upon initial shipboard inspection, the

scattering layer appeared to change depth or disappear completely in a pattern that seemed to mimic our limited understanding of the regional water mass circulation and interaction (Figure 3). Attempting to understand the distribution and significance of this scattering layer and whether or not it is related to regional water masses is the focus of this study. Should a correlation between the scattering layer and the water masses be established, it may provide important insight into both the biological and oceanographic processes in the region and further establish the important role that acoustic sensing can provide in understanding both the physical oceanography and biology in remote regions.

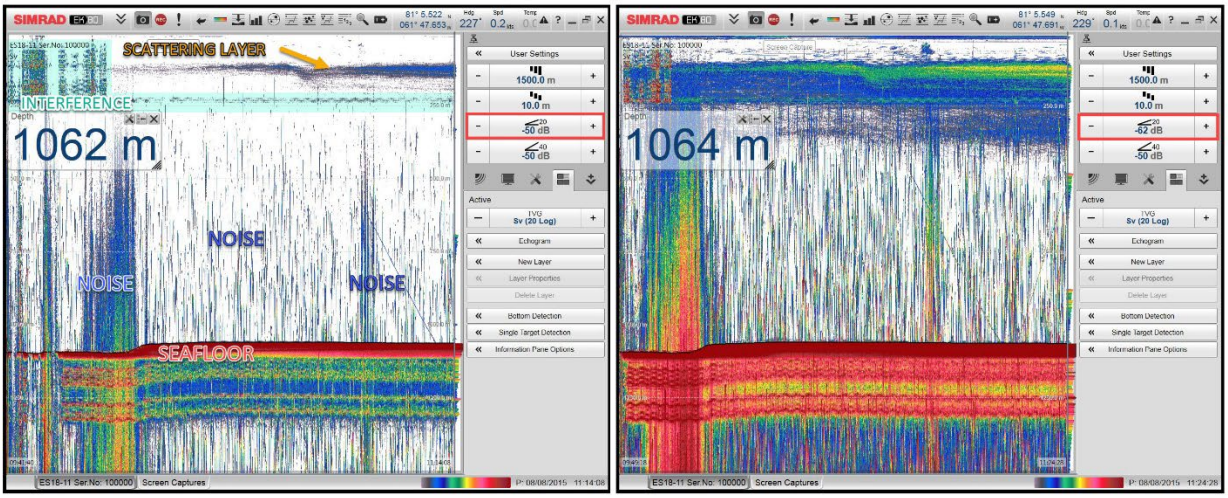

Figure 1: Screen captures of the EK80 software during the Petermann Expedition as the mapping team encountered a scattering layer. The yellow arrow on the left indicates the scattering layer. The pale blue-green box highlights some interreference that partially overlaps the scattering layer. The returns visible in the water column between the interference and the seafloor are noise (likely intermixed with some real targets, but noise is dominating). The image on the right was taken shortly after the image on the left; the large difference in appearance is due to an adjustment made to the signal threshold, as highlighted by the red box. The image on the right has a lower threshold, allowing more of the signal (and consequently, more noise and interference) to come through. This thresholding has no effect on the data being recorded, only on the data display. Screen captures courtesy of Larry Mayer and the Petermann Expedition Mapping Team, with annotation added by the author.

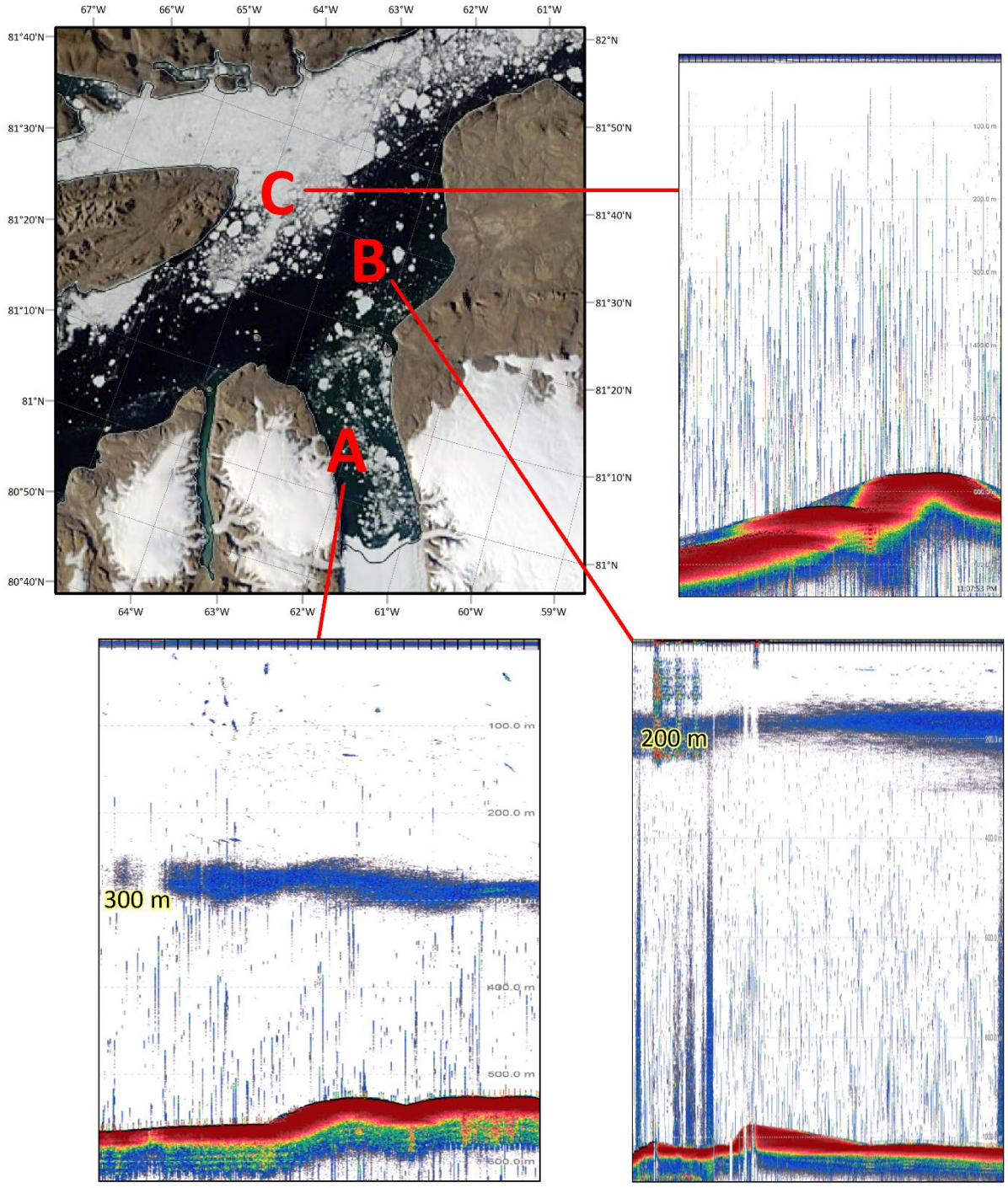

Figure 2: Changes in the scattering layer across the study area. The team found that in the fjord area (A) it was typically shallow (200 m or shallower), in the more protected parts of the basin (B) it was typically deeper (300 m or deeper), and in Nares Strait (C) it was typically absent.

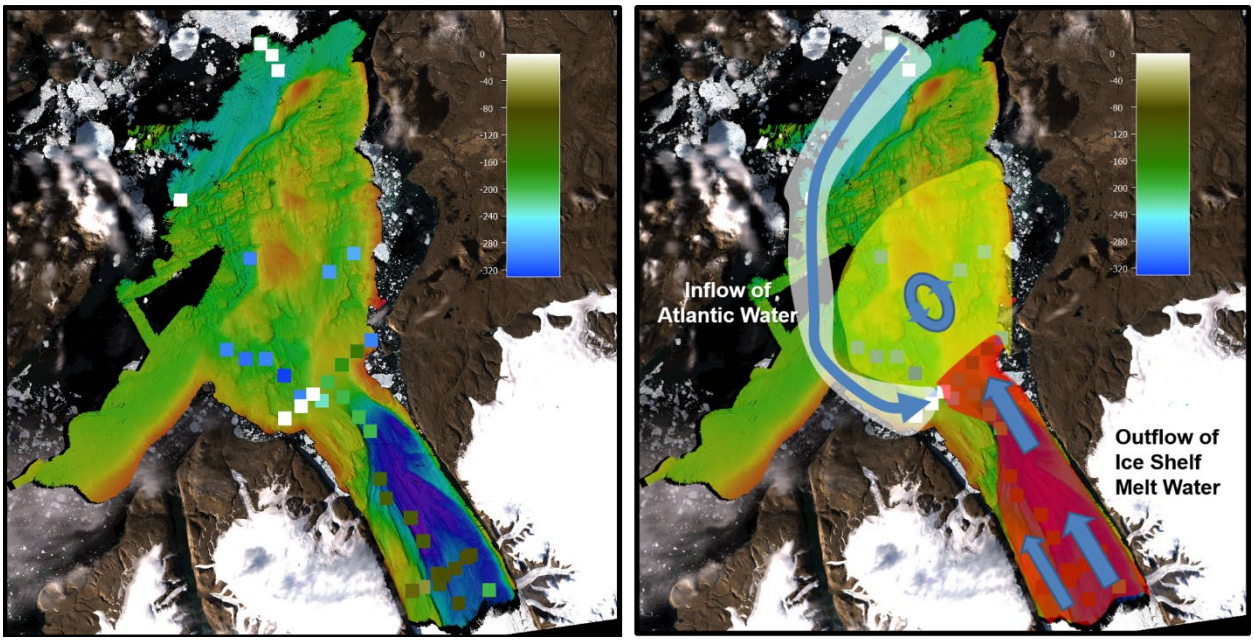

Figure 3: Results of initial onboard investigation of scattering layer depth, projection WG84 UTM 20N. The image on the left shows the results of a preliminary evaluation of scattering layer depth at CTD stations, with the color bar showing scattering layer depth. Image on right shows initial understanding of circulation of water masses in Petermann Fjord. Images courtesy of Larry Mayer.

1.1.1 Expedition Impetus: Marine Terminating Glaciers, Ice Shelves, and Sea Level Rise

The contributions of the Greenland and Antarctic ice sheets to sea level rise represent the largest source of uncertainty in global sea level projections (Church et al., 2013; van de Wal et al., 2019). Some of that uncertainty is related to ice-ocean interaction at marine terminating glaciers (Church et al., 2013) and the effect that the thinning and potential loss of floating ice shelves associated with some marine terminating glaciers will have (Benn and Evans, 2010). Mass loss from the Greenland Ice Sheet has increased rapidly in the last two decades and has contributed significantly to observed sea level rise (Straneo and Heimbach, 2013; van de Wal et al., 2019). The most pronounced changes are occurring where ice sheets are grounded well below sea level, due to enhanced interaction with warmer ocean waters (Shepard et al., 2012; Hogg et al., 2016). For the Greenland Ice Sheet, increases in warm Atlantic Water

reaching the glacier interface are likely a cause for increased submarine melting (Straneo and Heimbach, 2013; Figure 4), an important component of ice shelf mass balance and, in some cases, 18 to 20 times larger than iceberg calving and surface melting (Rignot and Steffen, 2008).

The influx of warm waters can also affect the presence or absence of floating ice shelves at the seaward extent of marine terminating glaciers (Jakobsson et al., 2018, 2020). The presence or absence of floating ice shelves at the seaward extent of marine terminating glaciers influences the dynamics of the feeder glaciers (Benn and Evans, 2010) as the ice shelves are thought to buttress up-glacier ice by providing backstress. The loss of this backstress through ice shelf loss or thinning is thought to be one trigger of rapid outlet glacier acceleration (Johnson et al., 2004).

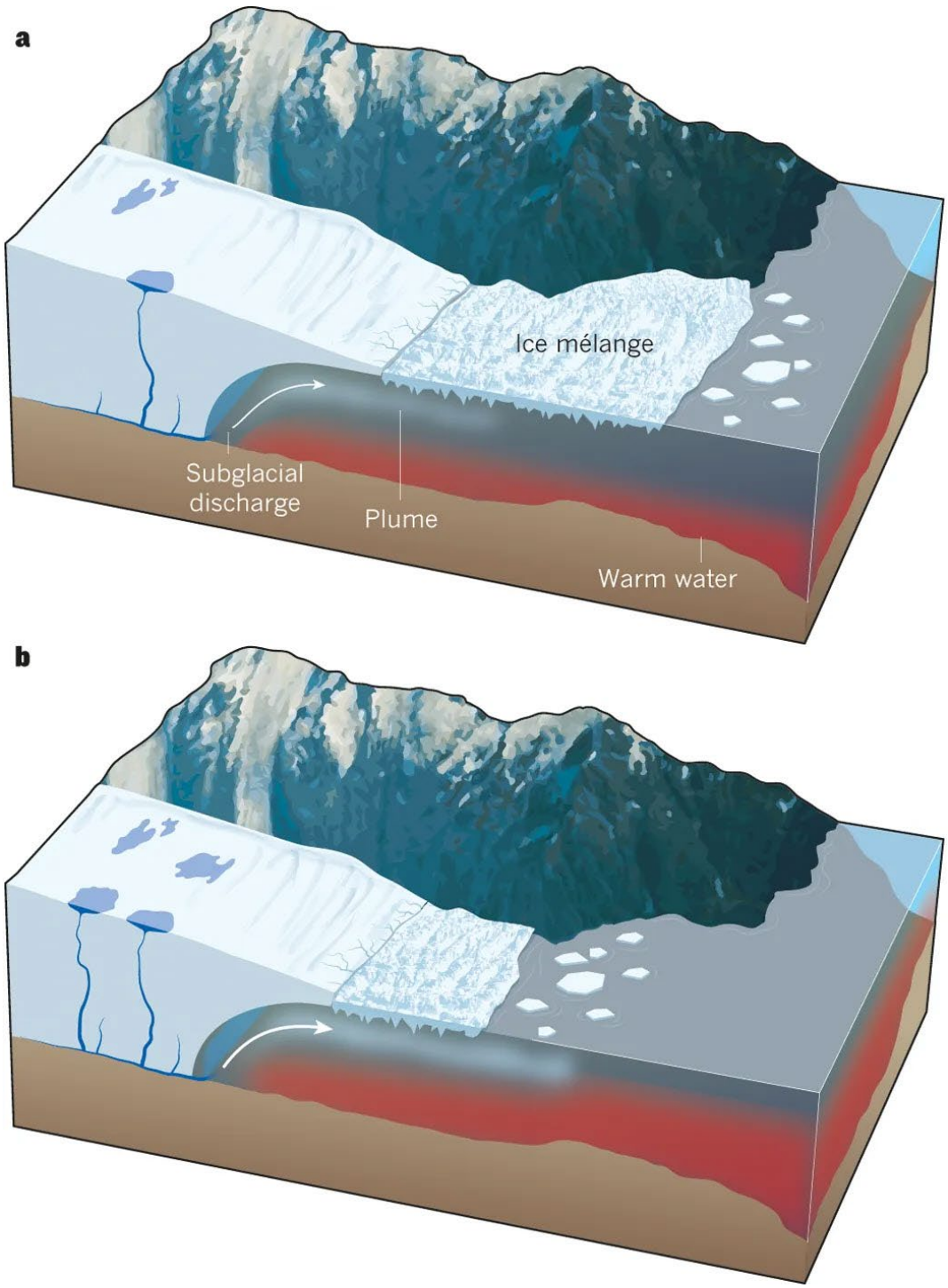

Figure 4: The effect of warming subsurface ocean waters on Greenland's outlet glaciers, from Straneo and Heimbach, 2013. Warming waters below the glacier results in increased submarine melting and the possibility of a weakened ice mélange at the marine margins of outlet glaciers, which itself may also influence glacier retreat (Amundson et al., 2010). (a) Shows pre-retreat conditions, which include relatively cold waters, limited subglacial discharge, and thick ice mélange. (b) Shows retreat conditions with warm fjord waters, increased subglacial discharge, and weakened mélange.

Increased melting from glaciers raises global sea-level and adds more fresh water to the Arctic, which in turn makes its way to the North Atlantic. Increases in freshwater to the North Atlantic can disrupt the formation of deep water (Bamber et al., 2012; Straneo and Heimbach, 2013; Münchow, 2016); the formation of deep water drives the Atlantic meridional overturning circulation, a major driver of global climate (Straneo and Heimbach, 2013). Thus, an understanding of the history and dynamics of Arctic glaciers is a key factor in understanding global climate change.

Petermann Glacier in northwest Greenland is well-suited for studying all of the above. It is a marine terminating glacier interacting with a changing ocean, grounded 400 - 600 m below sea level (Rignot and Steffen, 2008; Johnson et al., 2011; Straneo et al., 2012; Tinto et al., 2015; Münchow et al., 2016; Cai et al., 2017; Paden et al., 2019). It has a 46 km long, 20 km wide floating ice shelf extending from the grounding line that has experienced significant ice loss in the last decade (Falkner et al., 2011; Münchow et al., 2014). There has been an observed increase in the freshwater flux southward through nearby Nares Strait (Münchow, 2016), and the presence of warm Atlantic Water in the fjord, which has contributed to thinning the ice shelf from below, has been documented (Münchow et al., 2014, 2016).

1.2 Mapping the Water Column – Acoustic Water Column Data

Acoustical methods are the primary way to obtain high resolution seafloor bathymetry. An acoustic pulse is created by a transducer and travels through the water column until it encounters a boundary with a layer that has an acoustic impedance that differs from the impedance of the water in which the pulse is traveling. The acoustic

impedance is the product of the density of the material and speed of sound in that material. The strongest impedance contrast is found at the ocean surface, where water meets air; the boundary between the water and the seafloor also often creates a strong impedance contrast. When a contrast in impedance is encountered, the wave *reflects, transmits,* and *scatters*. A portion of the wave will transmit into the seafloor (where it may again reflect, scatter, or transmit at the next impedance contrast). Another portion will reflect; reflection is at the same angle as the incident wave arriving at the boundary, but in a direction away from the transducer. This *specular reflection* returns to the source (where a receiver and recorder capture the returning echo) when the wave is transmitted at normal incidence (perpendicular to the seafloor). Single beam and split-beam echosounders (here both will be abbreviated as SBES as the distinction is not important in this thesis), such as the Simrad EK80 used during the Petermann Expedition, transmit a single pulse typically at normal incidence and therefore receive the reflected pulse on the same transducers that transmitted the pulse. Multibeam Echo Sounders (MBES) such as the Kongsberg EM122 used during the Petermann Expedition also transmit a few of their beams at normal incidence and therefore receive some reflected pulses, though most of their beams are transmitted at non-normal angles resulting in reflections away from the receiver. If the boundary is rough relative to the wavelengths used, a portion of the incident wave will scatter in all directions, and some portion of that will scatter back towards the receiver no matter what the angle of incidence/reflection. This is the *backscattered energy* or *backscatter*, representing any part of the wave scattering back in the direction of the source and the receiver. We often call the interface or object that caused the signal to scatter a "*scatterer"*.

The timing of the pulse from transmit to reception is recorded by the receiver; this two-way travel time, combined with a knowledge of sound speed in the water column, allows the calculation of range of the target from the transducer. For non-normal ray paths, the sound speed profile is also used to calculate the refraction of the ray as it moves through water layers of different sound speed. Addition of offsets due to location of the instruments with respect to water level, ship motion, and tidal changes are used to convert those ranges to depths. Depth data are used to create maps of the seafloor surface (bathymetry). In addition to the two-way travel time, the receiver also records the intensity of the returned signal; this intensity value is colloquially called *"the backscatter"*. Relative intensities can provide information about the properties of the seafloor – in general, harder or rougher seafloor such as bedrock will reflect and scatter more energy than a softer or smoother seafloor, and in this way, maps of backscatter intensity can be used for broad characterization of the nature of the seafloor.

The same principles apply in the water column. An acoustic pulse travels until it encounters an impedance contrast in the water column. The *target* (the object or transition causing the impedance contrast) scatters acoustic energy in all directions; a portion of the signal is scattered back towards, and is recorded by, the receiver. In the case of targets in the water column, specifically discrete targets, it is generally assumed that there is little or no specular reflection, i.e., that all of the energy is scattered. The time difference between transmit and receive and local sound speed give the offset of the target in the water column from the transmitter, and the intensity of the backscattered signal is a function of the range to the target and the properties of the target itself. The proportion of the incident energy backscattered by the target is referred

to as the *target strength* (Simmonds and MacLennan, 2005). The target strength is based on the *backscattering cross-section*, σ_{bs},

$$\sigma_{bs} = R^2 I_{bs}/I_i$$

a measure of the ability of a target to scatter sound back to a receiver (Clay and Medwin, 1977) in units of area (typically square meters), where R is the range to the target, I_i is the intensity of the incident wave at the target, and I_{bs} is the intensity of the backscattered pulse at the receiver (Clay and Medwin, 1977; Simmonds and MacLennan, 2005). The target strength, TS, is the backscattering cross-section in decibels (re: 1 m^2),

$$TS = 10log_{10}(\sigma_{bs})$$

a more convenient expression of scattering, as the range of scatter from different targets covers many orders of magnitude. When many small targets are distributed in a portion of the water column, the signal that is returned is a combination of their individual echoes that provides a measure of the total biomass in the water column (Simmonds and MacLennan, 2005). The measure of this combined signal is the *volume backscattering coefficient*, s_V,

$$s_V = \left(\sum \sigma_{bs}\right)/V_0$$

the sum of the contributions of all the individual targets contributing to the signal over the volume, V_0 (Simmonds and MacLennan, 2005), in units of area over volume (m^2 m^{-3}). Expressed as decibels, this becomes the *volume backscattering strength*,

$$S_v = 10log(s_V)$$

in units of dB re: 1 m^{-1} (Simmonds and MacLennan, 2005).

The frequency of the sonar and the size of the intended target can be important considerations in water column backscatter. The acoustic wavelength (λ) of the sonar is determined by the frequency (f) and the sound speed (c):

$$\lambda = \frac{c}{f}$$

The backscatter response of a target will depend on its size compared to the wavelength of the signal. If the target is much smaller than the wavelength, its *frequency response* (the measured backscatter response as the frequency of the signal changes) will show a rapid increase as frequency increases. This is known as *Rayleigh scatter* (Clay and Medwin, 1977), and responses in that frequency range are said to fall within the *Rayleigh scattering region* or *Rayleigh scattering regime* for that size target (Simmonds and MacLennan, 2005; Lurton, 2010). When the target size and wavelength are similar, the scattering response will depend on the geometric structure and material properties of the target (Simmonds and MacLennan, 2005), may include one or more *resonances* (scatter where the frequency of the acoustic wave matches one of the target's natural frequencies of vibration, causing a "spike" in the response (Urick, 1983; Korneliussen, 2018)) and is dominated by interference (Lurton, 2010). Lurton (2010) refers to this as the *interferential regime*. When wavelength is much smaller than the target, the target's response will flatten and will be proportional to the size of the scatterer, which is known as *geometric scatter* (Clay and Medwin, 1977). The rapid change in the target's response in the Rayleigh scattering regime and the unpredictable

response in the interferential regime minimizes the usability of those responses for understanding the nature of the targets.

Water column backscatter has been used for detection of targets as well as to determine position, morphology, and behavior of targets (Colbo et al., 2014). Differences in intensity observed in MBES acoustical water column data has been used empirically to separate returns from fish and marine mammals (Benoit-Bird and Au, 2003) while calibrated SBES operating at multiple frequencies have successfully been used to discriminate between types of organisms in the water column (Watkins and Brierley, 2002). Further, it has recently been shown that oceanographic properties of the water column, specifically the presence of thermohaline staircases and the depth of the mixing layer, can be determined from broadband acoustic data (Stranne et al., 2017, 2018).

1.3 Biological Acoustic Scattering Layers

1.3.1 Description

Biological acoustic scattering layers are concentrations of marine organisms, particularly zooplankton and fish (Dunstan, 1979). They are so called because they “scatter” the acoustic energy from a sonar, appearing as distinguishable layers of increased intensity in the sonar records not dissimilar to the acoustic return you would get from the seafloor (though typically much weaker than the seafloor return). Scattering layers have been observed since the deployment of echosounders in the late 1940s and are found in most oceans and seas of the world (Longhurst, 1976; Dunstan, 1979). The layers may be a few meters to several tens of meters thick and can be horizontally

continuous for thousands of kilometers in some locations (Longhurst, 1976) or patchy in others (Geoffroy et al., 2017).

1.3.2 How biological acoustic scattering layers and their component organisms are studied

Acoustic observations are a primary method for studying the presence and migration behavior of the zooplankton and fish in the water column (Clay and Medwin, 1977), particularly on broader scales (i.e. the geospatial distribution of the scattering layer as a whole), and can also be used to calculate the abundance of these organisms within the scattering layer (Flagg and Smith, 1989). Groups of SBES mounted on vessels or tow-bodies, lowered from stationary vessels, or deployed as moorings and operating at different frequencies are a common method for collecting acoustic scattering layer data in order to study large fish schools, determine their composition, and estimate the size and abundances of their components (Holliday and Pieper, 1980, 1995; Pieper et al., 1990; Napp et al., 1993; Lavery et al., 2007; Geoffroy et al., 2016; Knutsen et al., 2018). Common frequencies for this work are 18, 38, 120, and 200 kHz, though frequencies well above and well below this range are also used depending on the study focus; lower frequencies (200 Hz and lower in some studies, up to 38 kHz) are used to detect fish, while higher frequencies (120 kHz, 200 kHz, and higher in some studies) are used to detect zooplankton (Holliday, 1972; Holliday and Pieper, 1980; Pieper et al., 1990; Simmonds and MacLennan, 2005; Lavery et al., 2010; Gjøsæter et al., 2017; Knutsen et al., 2018). Calibration of these systems is important for getting meaningful target strength estimates and allowing for calculation of abundance or determining individual

target character based on published target strength and frequency response data (Foote et al., 1987).

Acoustic Doppler Current Profilers (ADCPs) are also commonly used, either moored or on surface vessels or Autonomous Underwater Vehicles (AUVs), for looking at the behavior of scattering layers. Moored ADCPs have been particularly useful in providing a complete annual cycle of scattering layer behavior at a given location (Berge et al., 2014), especially in remote areas such as the Arctic. Unfortunately these instruments are generally not calibrated (Berge et al., 2014), limiting comparisons to scattering strength gained from other acoustic instruments. In some studies, MBES have been used in conjunction with multifrequency SBES arrays, with the MBES providing information on school size and morphology or scattering layer extent (Korneliussen et al., 2009).

All acoustic instruments are limited by their respective *blanking zones*, areas where no useful acoustic information is recorded, and by *acoustic deadzones*, where strong returns from boundaries prevent the detection of other nearby targets (Ona and Mitson, 1996; Simmonds and MacLennan, 2005). Near the sonar head, there can be a high level of unwanted signal due to *ringing*, when the transceiver is saturated by the transmit pulse, which limits the useful information that can be detected within a few meters of the transducer (Korneliussen, 2018); this is also referred to as *transducer ringdown*. Information is also lost above/below the depth of the transducer depending on whether it is pointing downward/upward.

The strength of the return measured by sonars can provide some information about the populations being studied, but there is often ambiguity. If an ensonified

population consists primarily of the same species and they are all of similar size, an increase in the target strength at a single frequency likely corresponds to an increase in the number of organisms (Foote, 1983; Simmonds et al., 1992; Stanton et al., 1994). Populations are often a mix of species and sizes, particularly scattering layer populations, so the relationship between target strength and biomass can rarely be assumed to be so straightforward. In a mixed population, the target strength of an organism and its contribution to the combined signal will vary depending on how “good” of a scatterer the organism in question is, which is more dependent on physical makeup of the scatterer than the size or number of organisms present (Holliday and Pieper, 1980; Stanton et al., 1994, 1996, 1998a, 1998b). A broad distinction can be made between organisms that contain inclusions of gas, and those that do not (Holliday and Pieper, 1980). Examples of organisms that contain gas inclusions are fish with swim bladders and gas-bearing zooplankton like some siphonophores. The acoustic impedance of the air in the swim bladder or siphonophore’s pneumatophore contrasts strongly with the impedance of the surrounding soft tissue and water, resulting in relatively high backscatter (Holliday, 1972; Holliday and Pieper, 1980; Stanton et al., 1994); in the case of the gas-bearing siphonophore, the backscatter is disproportionately high compared to their size (Stanton et al., 1994). When a gas inclusion is not present, the acoustic response will depend on the organism’s size, the density contrast between its tissue and the surrounding water, the speed of sound in both the water column and the organism, and the frequency of the sonar used for detection (Holliday and Pieper, 1980). This includes fish without swim bladders and zooplankton characterized as fluid-like or elastic-shelled (Stanton et al., 1994). Elastic-

shelled zooplankton such as pteropods have a semi-rigid shell whose impedance contrasts with the surrounding water, and thus are efficient scatterers for their size (Stanton et al., 1994). Fluid-like zooplankton such as euphausiids or salps have gelatinous bodies whose impedance is very similar to that of the surrounding water, and are therefore poor scatterers of sound (Stanton et al., 1994). Orientation of the organism also has a strong effect on the strength of the backscatter signal (Martin et al., 1996; Stanton et al., 1996, 1998a), as can depth, depending on frequency.

When a target is ensonified at different frequencies at the same time, information about the type of target can be gleaned from the response of the target across the frequency range and comparison of the response to theoretical scattering models based on physical makeup (Chu et al., 1992; Stanton et al., 1994, 1996; Martin et al., 1996; Simmonds and MacLennan, 2005; Lavery et al., 2007; Figure 5). For example, a fish with a swim bladder would be expected to have a higher response, and therefore higher measured target strengths at low frequencies (near the resonance frequency of the swim bladder, ~500 Hz – 2 kHz), and the response would decrease and flatten as the frequency increased and moved away from the resonance frequency (Holliday, 1972; Clay and Horne, 1994). As an example of the decrease moving away from resonance, Pedersen and Korneliussen (2009) saw a distinct decrease in frequency response between 18 and 38 kHz for two of the three target species they evaluated.

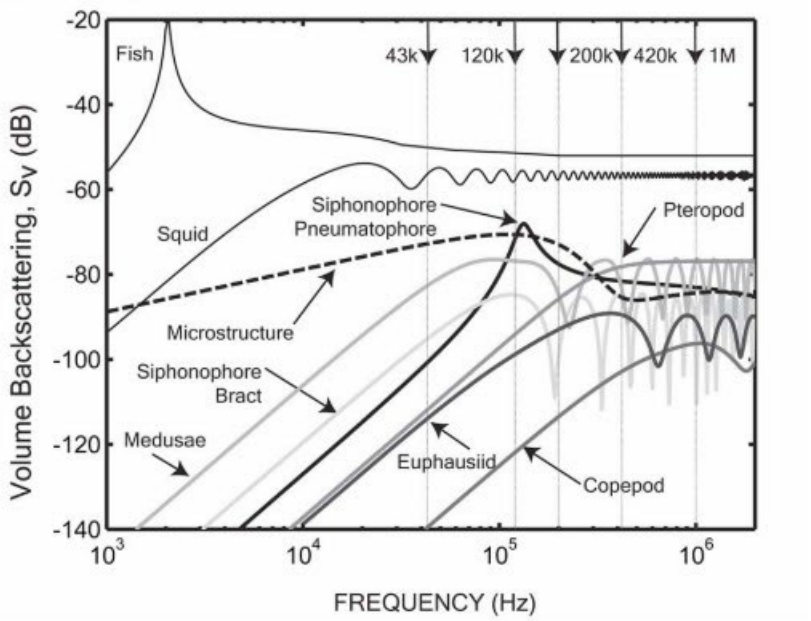

Figure 5: Modeled volume backscattering as a function for frequency for biological scatterers observed in the Gulf of Maine, assuming an abundance of one organism per cubic meter (Lavery et al., 2007).

The volume of the swim bladder (and therefore the fish as a whole) can be estimated from the resonance frequency, which requires the sonar to have a broad enough frequency range to detect the resonance (Clay and Medwin, 1977; Stanton et al., 2010). Gas-bearing zooplankton have a response similar to fish with swim bladders (Stanton et al., 1994, 1996), though the resonance frequency would be an indication of the pneumatophore size rather than the overall size of the organism. Martin et al. (1996) showed distinct echo patterns from individual zooplankton in all three scattering groups (gas-bearing, fluid-like, and elastic-shelled). If the frequency range is high enough and broad enough, the change in frequency response from sharply rising (Rayleigh regime) to flattening (geometric regime) can be used to determine the size of the zooplankton target, which may in turn help narrow down the likely biologic class it belongs to (Holliday and Pieper, 1980; Lavery et al., 2009).

Another common technique to attempt to discern organism-specific information is to look at the relative frequency response, which involves comparing the volume-backscattering coefficient (s_v) or backscattering cross section (σ_{bs}) values acquired at one frequency to s_v or σ_{bs} values at a reference frequency, typically 38 kHz, where the resulting value is a ratio of the two (Korneliussen and Ona, 2002; Pedersen and Korneliussen, 2009; Korneliussen, 2018). This approach has been used to distinguish zooplankton from fish in mixed populations, as well as distinguish different species of fish (Korneliussen and Ona, 2002; Pedersen and Korneliussen, 2009). Frequency differencing or “dB differencing” is an equivalent approach where one frequency is subtracted from the other, preferably utilizing one frequency from the Rayleigh regime and the other from the geometric regime of the intended target (Greenlaw, 1979; Madureira et al., 1993; Harris et al., 2000; Logerwell and Wilson, 2004; Webster et al., 2013; Korneliussen, 2018).

Sampling is the primary method used to validate acoustic data. Pump and net systems have been used to sample organisms in water very near the acoustic transducers (Holliday and Pieper, 1980). Nets pulled at selected depths and systems that utilizing multiple nets that open and close at particular depths are useful for understanding how the biological community changes vertically in the water column (Benoit et al., 2008; Falk-Petersen et al., 2008; Berge et al., 2014). Bottom and pelagic trawls are also used to sample fish, micronekton, and macrozooplankton, and may include multi-samplers to collect depth-stratified samples (Engås et al., 1997; Falk-Petersen et al., 2008; Korneliussen et al., 2009; Geoffroy et al., 2016; Knutsen et al., 2018). Physical sampling is not always possible or practical, so indirect sampling

methods are also employed. Video plankton recorders, plankton imaging systems, still cameras and video cameras (GoPro cameras for example) have all been utilized to capture images of organisms being studied (Benfield et al., 1996, 1998; Horne, 2000; Cowen and Guigand, 2008; McManus et al., 2008; Jacobsen and Norrbin, 2009; Cowen et al., 2013; Knutsen et al., 2018).

1.3.3 Distribution in the water column

There is much more variety in the vertical distribution of scattering layers than the horizontal distribution; this reflects the depth dependence of environmental variables (such as nutrients and light) considered to be important in determining the occurrence of the plankton that make up most of the scattering layer (Longhurst, 1976).

Scattering layers have been commonly observed to migrate vertically en-masse in the water column. The most commonly observed migration is diel vertical migration (DVM), the synchronized movement of zooplankton and fish from shallow water to deeper water and back over the course of a day (Hershey and Backus, 1962; Longhurst, 1976). It is an energetically costly undertaking, particularly for small zooplankton swimming tens to hundreds of meters over the course of a few hours in a viscous environment (Brierley, 2014). There are three general patterns of DVM. The most common form, nocturnal DVM, involves organisms congregating near the surface at night (to feed on phytoplankton, which are restricted to living in the photic zone), migrating to depth as the sun rises, and returning to the surface as the sun sets. The second form is a reverse of the first (reverse DVM), with organisms congregating at the surface during the day and moving to depth at night (Ohman et al., 1983). The third form is similar to the first – shallow at night and deep during the day – but involves an

additional descent and rise in the middle of the night; this is called twilight DVM (Cohen and Forward Jr., 2005).

Light is generally agreed to be the most important external factor driving DVM (Longhurst, 1976; Forward Jr., 1988). Organisms may be following a preferred *isolume* (constant light level), they may be triggered by an absolute change in light intensity, or it may be the light's rate of change that matters (as reviewed in Cohen and Forward Jr., 2009). In some cases, the extent of the light-driven migration is limited by barriers such as isolated bathymetric highs, the thermocline, or changes in salinity (Longhurst et al., 1984). Locally, there may be discrete layers of food-rich water – concentrations of phytoplankton within the mixed layer or thermocline that frequently coincide with density discontinuities – that are attractive enough to limit the light-driven vertical migration (Longhurst, 1976).

DVM is not constant within a species (Cohen and Forward Jr., 2009). Not all members of a species will undertake DVM, and participation in DVM may change depending on an organism's life stage (Uye et al., 1990; Hays, 1995; Cohen and Forward Jr., 2009). There may also be spatiotemporal differences for the same species, even at the same life stage (Ohman, 1990; Hays et al., 1996; Cohen and Forward Jr., 2009). It is now believed that the major cause of this changing DVM behavior within a species is due to the underlying cause of the DVM behavior itself – that it is a response to chemical cues from predators (Cohen and Forward Jr., 2009). Field studies have shown non-migrating plankton begin DVM when predatory fish are present and cease when the abundance of fish decreases (Cohen and Forward Jr., 2019).

Not all organisms migrate as group, and not all migrations are triggered by light or are undertaken for predator avoidance. As the resolution achievable with acoustic instruments has improved, it has become easier to detect thinner layers, small groups, and sometimes individual organisms. This has revealed uncoordinated, asynchronous patterns of migration in some ecosystems (Cottier et al., 2006; Brierley, 2014). Some organisms migrate at different stages of their life or spend certain seasons in specific parts of the water column; this has often been noted with some species of calanoid copepods in the Arctic (Smith and Schnack-Schiel, 1990; van Aken et al., 1991; Daase et al., 2013). Zooplankton may also migrate vertically into a certain depth of water and at a certain time in order to take advantage of currents or tides, using the water flow to achieve horizontal transport that they can't accomplish on their own (Cohen and Forward Jr., 2019).

Some species are known to distribute vertically based on age class. This behavior has been noted for polar cod, which have been observed to aggregate in different parts of the water column based on whether they are the latest crop of juveniles (age-0) or older (age-1+) (Benoit et al., 2014; Geoffroy et al., 2016).

1.3.4 Arctic Specific Observations of Scattering Layers

Scattering layers have been observed in the Arctic, but as with nearly all Arctic data, information is limited. Most studies are centered in and around Svalbard, from the southern fjords at ~76°N to the high Arctic fjords at ~80°N and the southern Arctic Ocean up to 82°10'N (Cottier et al., 2006; Søreide et al., 2008; Berge et al., 2009; Webster et al., 2013; Grenvald et al., 2016; Darnis et al., 2017; Gjøsæter et al., 2017; Ludvigsen et al., 2018). A few studies have looked at data in other regions of the Arctic

Ocean, including the Greenland Sea and Barents Sea (Fischer and Visbeck, 1993; Blachowiak-Samolyk et al., 2006), the Beaufort Sea (Benoit et al., 2010, 2014; Geoffroy et al., 2011, 2016; Parker-Stetter et al., 2011; La et al., 2015), Barrow Strait (Fortier et al., 2001), and the Central Arctic Ocean (Hunkins, 1965; Kutschale, 1969). The majority of these studies focus on zooplankton (or speculated zooplankton) abundances and migrations in relatively shallow waters less than 200 m (Hunkins, 1965; Kutschale, 1969; Fortier et al., 2001; Blachowiak-Samolyk et al., 2006; Berge et al., 2009; La et al., 2015; Grenvald et al., 2016; Darnis et al., 2017; Ludvigsen et al., 2018). A few studies extended into the mesopelagic and included observations and sampling of fish at these depths (Benoit et al., 2010, 2014; Geoffroy et al., 2011, 2016; Parker-Stetter et al., 2011; Gjøsæter et al., 2017).

Polar regions are unique in that they experience prolonged periods of polar night in the winter, when the sun does not rise above the horizon for several months, and midnight sun in the summer, when the sun does not dip below the horizon for several months. With the exception of the area just surrounding the poles themselves, polar regions do have a period in between these two extremes when there is a distinct daily sunrise and sunset. This unique light environment, and the limited data available in polar regions, particularly in winter months, has led to sometimes conflicting observations of DVM. Fischer and Visbeck (1993) did not detect clear DVM in the Greenland Sea from November to January, while others have observed reduced but continuous DVM (Berge et al., 2009) or small ‘not-quite-DVM’ migrations in the winter months (Grenvald et al., 2016). Others have observed scattering layer depth increases related to the full moon (Webster et al., 2013), and even distinct small scale vertical

migration in response to lights on the research vessel and to the headlamps used by scientists on a small vessel with other lights extinguised (Ludvigsen et al., 2018). Observations under midnight sun conditions are also conflicting. Several researchers have concluded that DVM at this time is absent or weak, though variaiblity in vertical depth could still be observed and was attributed to habitat changes, random patchiness, or unsynchronized vertical migration of individuals (Longhurst, 1976; Blachowiak-Samolyk et al., 2006; Cottier et al., 2006). La et al. (2015) found a scattering layer distribution that was well correlated with salinity, nutrient, and chlorophyll *a* levels associated with Pacific Summer Water (PSW), but with no apparent diel migration during the period of the study (summer 24-hour light regime). Other reports show distinct DVM even under 24-hr sunlight (Fortier et al., 2001). Gjøsæter et al. (2017) observed consistant smaller amplitude DVM in a 210 – 510 m-deep scattering layer from late summer midnight sun conditions through autumn sunrise-sunset conditions. Several studies noted a return to discernable patterns of DVM in the spring and autumn, when light has a more distinct light-dark cycle (Falk-Petersen et al., 2008; Benoit et al., 2010; Grenvald et al., 2016; Darnis et al., 2017). Migrations that were more seasonal in nature, such as a progressive deepening of a layer as light levels increased or as organisms matured (ontogenic migration), were also noted (Geoffroy et al., 2011, 2016; Benoit et al., 2014).

1.4 Study Summary and Significance

This study examines the distribution of scattering layers recorded in the EK80 data collected as a data set of opportunity during the Petermann Expedition of 2015 both inside Petermann Fjord and in Hall Basin just outside the fjord. It provides

evidence that the scattering layers did not appear to respond to daily changes in light levels, but that their distribution was related to temperature, salinity, and regional circulation patterns. This relationship to circulation, temperature, and salinity indicates that the scattering layer can potentially be used as a proxy for the presence/absence of water masses in the water column and patterns of regional circulation. It has recently been shown that oceanographic properties of the water column, specifically the presence of thermohaline staircases and the depth of the mixing layer, can be determined from acoustic data (Stranne et al., 2017, 2018). Oceanographic applications of acoustic data have been shown to be viable, and this study builds on that, demonstrating the potentially applicability of using acoustics to study water mass interaction and circulation on a regional scale. Additionally, the geographic region and duration of observations are significant in and of themselves, due to the limited amount of information available in the Arctic. The primary limitation of the study is the opportunistic nature of the data – the expedition did not expect to encounter an interesting biological phenomenon, thus the survey was not outfitted or designed to study biology. This led to sub-optimal data in terms of sonar frequencies and acquisition procedures, as well as a complete lack of biological sampling.

CHAPTER 2 REGIONAL SETTING

2.1 Geographic Location

The Swedish Icebreaker (IB) *Oden* departed Thule Air Base, Greenland on July 28, 2015, and returned on September 1, 2015 (Figure 6). After departing Thule, the ship entered Nares Strait via Smith Sound. Nares Strait separates Ellesmere Island, Canada from Greenland and connects the Lincoln Sea and greater Arctic Ocean in the north to Baffin Bay in the south. The *Oden* arrived at the primary study area of Hall Basin and Petermann Fjord (Figure 7) on August 2, 2015. Hall Basin is distinguished by a widening of Nares Strait from approximately 81°10'N to 81°45'N, between the entrances to Petermann and Archer Fjords. The ship remained in this study area until August 28, 2015. This study focuses on data collected during that 27-day period.

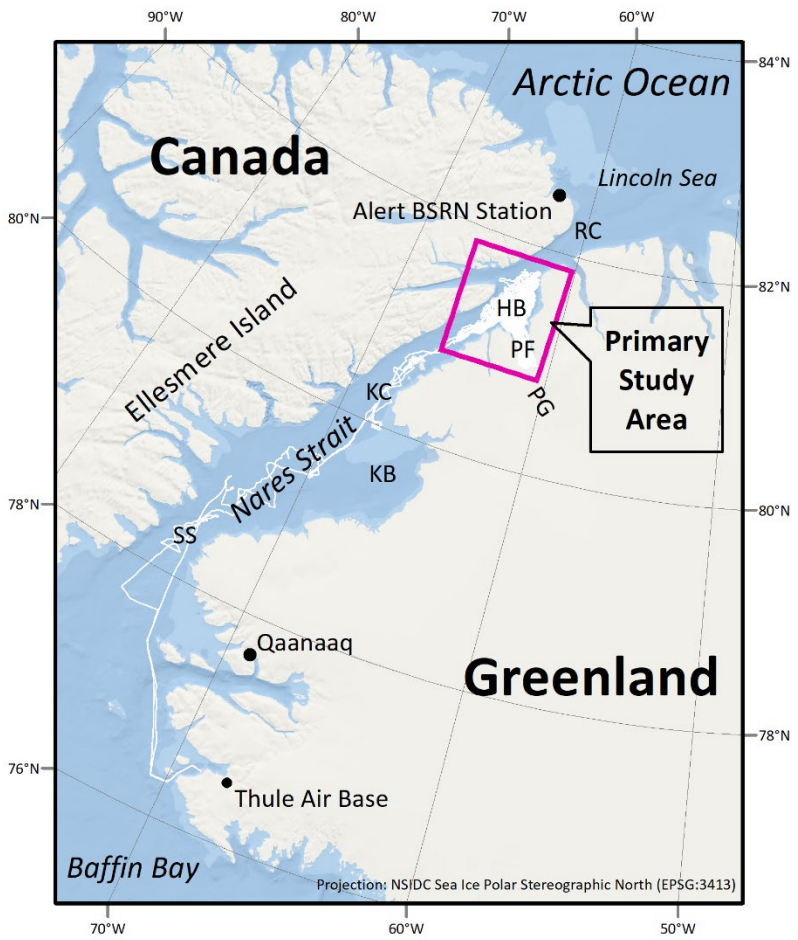

Figure 6: Regional setting. The vessel track for the IB Oden is shown as a white line. The two letter abbreviations indicate parts of Nares Strait (SS = Smith Sound, KB = Kennedy Basin, KC = Kennedy Channel, HB = Hall Basin, RC = Robeson Channel) and the Petermann System (PF = Petermann Fjord, PG = Petermann Glacier). Note that the projection is NSIDC Sea Ice Polar Stereographic North (EPSG:3413) and longitudinal meridians should be used as an indication of north.

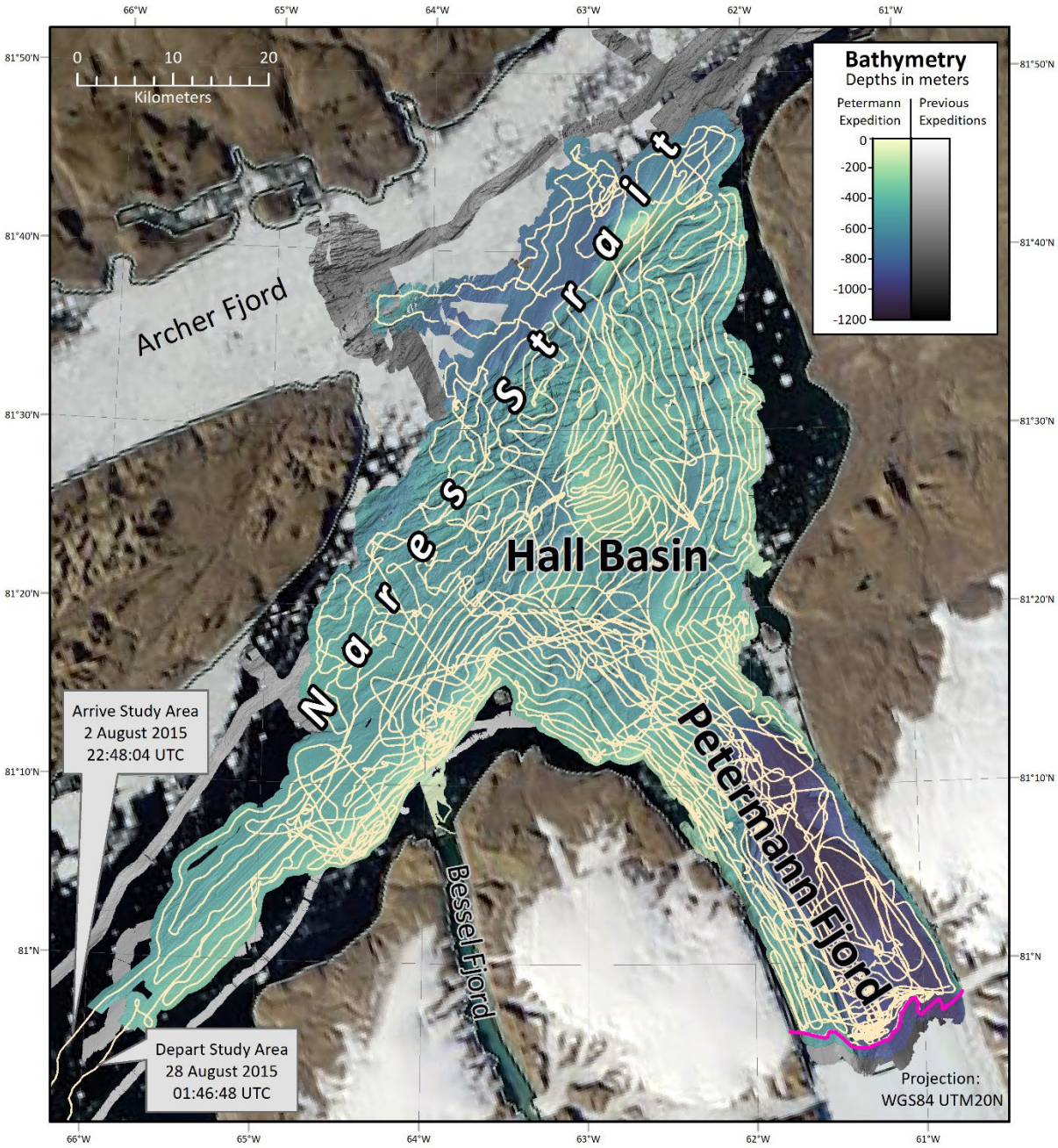

Figure 7: Primary study area. The cream-colored line is the Oden ship track. The seafloor bathymetry data underlaying the ship track that was collected during the Petermann Expedition has a pale yellow to blue colormap, while bathymetry data collected during previous unrelated expeditions (Rolling Deck to Repository (R2R), 2003; University of New Brunswick (UNB) Ocean Mapping Group, 2013) has a greyscale colormap. The magenta line is the August 2015 ice shelf margin. Imagery of the ice shelf does not continue to the magenta line because the imagery was masked based on the bathymetry, which extended beneath the ice shelf.

During the expedition, the region was in a continuous light regime (midnight sun).

Apparent sunrise for 81.5°N, 63°W (approximately the center of the study area)

occurred on April 9, 2015, and sunset on September 5, 2015. However, there was enough change in light levels during the course of each day to create a distinct diel pattern in the regional Baseline Radiation Network (BSRN; Driemel et al., 2018) and ship-based radiation observations (Figure 8).

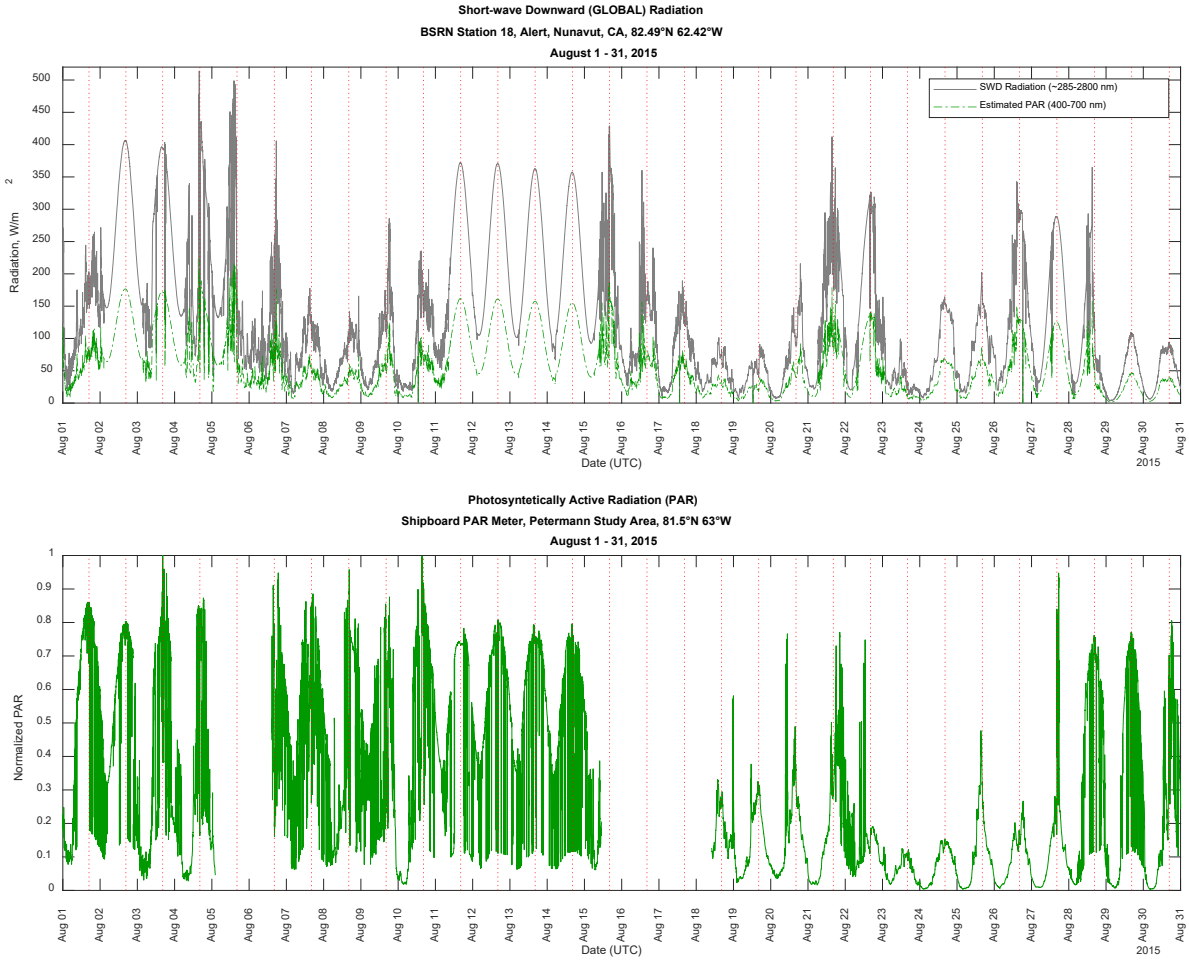

Figure 8: Top, BSRN data for Station #18, Alert Nunavut Canada; the location of the station is shown in Figure 6. The grey line shows the short-wave downward (SWD) radiation in watts m^{-2}, the green line shows photosynthetically active radiation (PAR), estimated as 44% of SWD (Moon, 1940). Bottom, normalized PAR data as collected by the shipboard PAR sensor in the study location. Red vertical lines in each graph indicate solar noon.

Ice cover is a significant factor in this location. Nares Strait is typically covered by sea ice for 11 months of the year (Jennings et al., 2011), limiting the access to Petermann Glacier. The ice is mobile from July to November and typically landfast from

December to June, when *ice arches*, curving structures connecting the landmasses on either side of the strait, form; these structures block the northern and southern entrances of Nares Strait (Münchow, 2016). During the period of this study, mobile ice restricted the ability to enter specific areas (Figure 9) and sometimes impacted the quality of acoustic data.

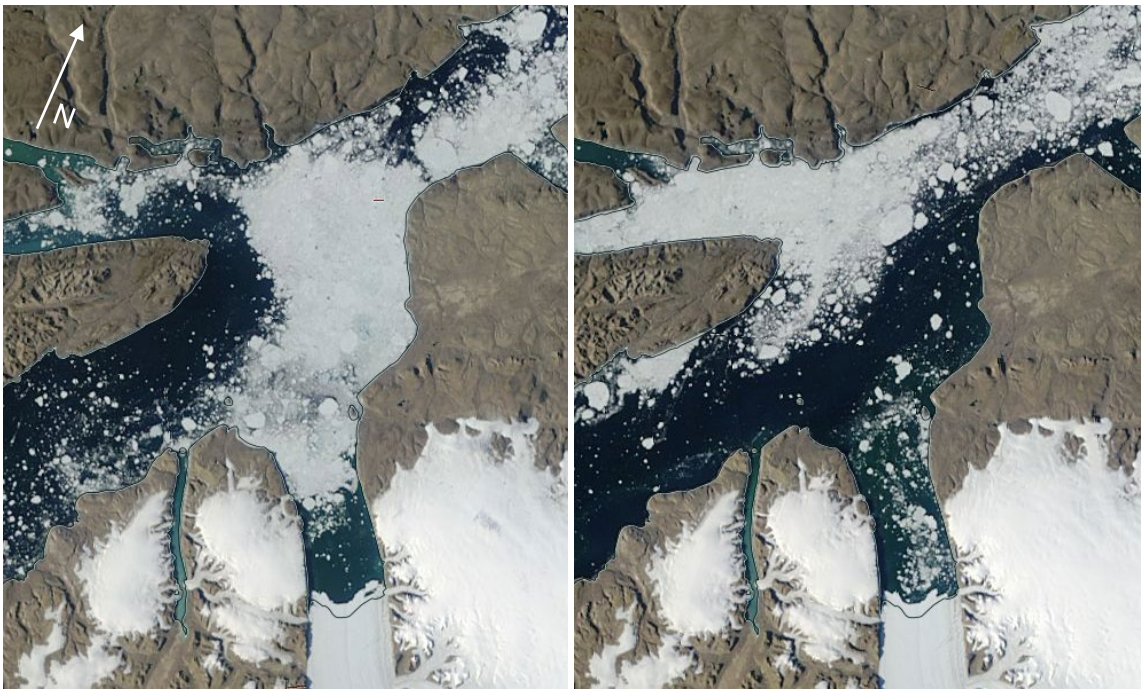

Figure 9: MODIS Terra Corrected Reflectance (True Color) images from August 2, 2015 (left) and August 11, 2015 (right) showing the variability of mobile ice in the study area. Images downloaded from NASA Worldview (https://worldview.earthdata.nasa.gov/). Note that the projection for these images is NSIDC Sea Ice Polar Stereographic (EPSG:3413); the white arrow indicates approximate north in both images.

2.2 Physical Setting

Petermann Fjord is a NNW-SSE oriented fjord filled laterally by the Petermann Glacier ice shelf to the SSE and opening to Hall Basin in the NNW (Figure 10, Figure 11). The fjord is ~ 40 km in length from the entrance to the ice shelf face and ~15 to ~23 km wide. Sedimentary rocks form steep walls above and below sea level on the eastern side of the fjord (Jakobsson et al., 2018; Figure 12). The western side of the fjord has

stepped walls, and wide terraced plateaus below sea level (Jakobsson et al., 2018; Figure 13). Seaward of the ice shelf terminus, two outlet glaciers draining an extension of the Greenland Ice Sheet are found on the eastern side of the fjord, and two outlet glaciers drain into the western side of the fjord (Jakobsson et al., 2018;Figure 11: Perspective view of Petermann Fjord, looking toward the fjord entrance to the northwest, and profile of the bathymetry across the deepest part of the fjord. Both the bathymetry and the profile are vertically exaggerated 2X. Figure 11 - Figure 13). The average depth in the fjord is 750 m; the western fjord terraces range from 300 m to 600 m depth and the maximum depth of 1158 m is found in the west-central fjord approximately 10 km seaward of the ice shelf face (Jakobsson et al., 2018; Figure 10).

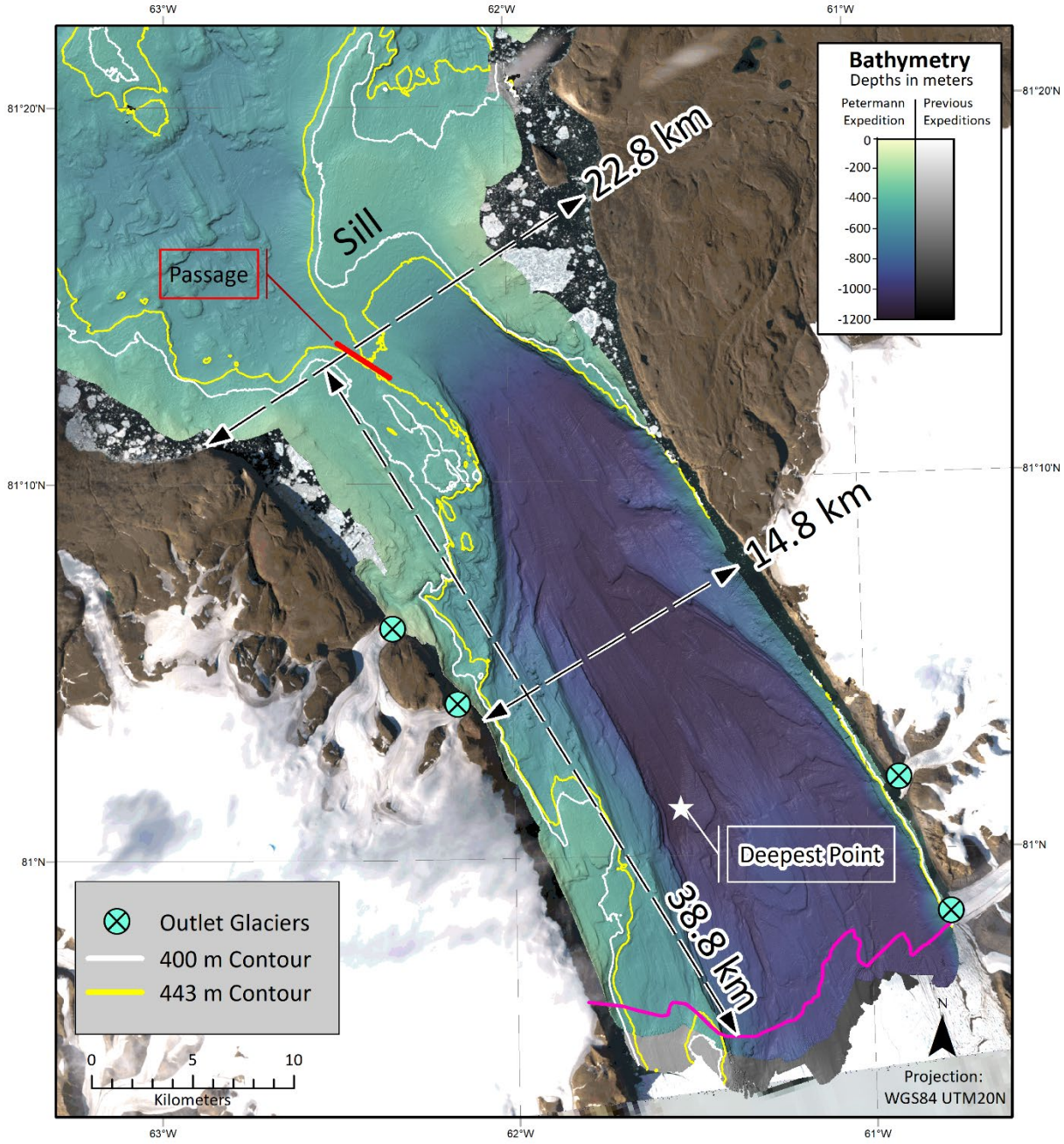

Figure 10: Petermann Fjord. Dashed lines with arrow end caps indicate where fjord dimension measurements were made. The bathymetric deep point is indicated by the white star. The magenta line is the August 2015 ice shelf margin. Imagery of the ice shelf does not continue to the magenta line because the imagery was masked based on the bathymetry, which extended beneath the ice shelf.

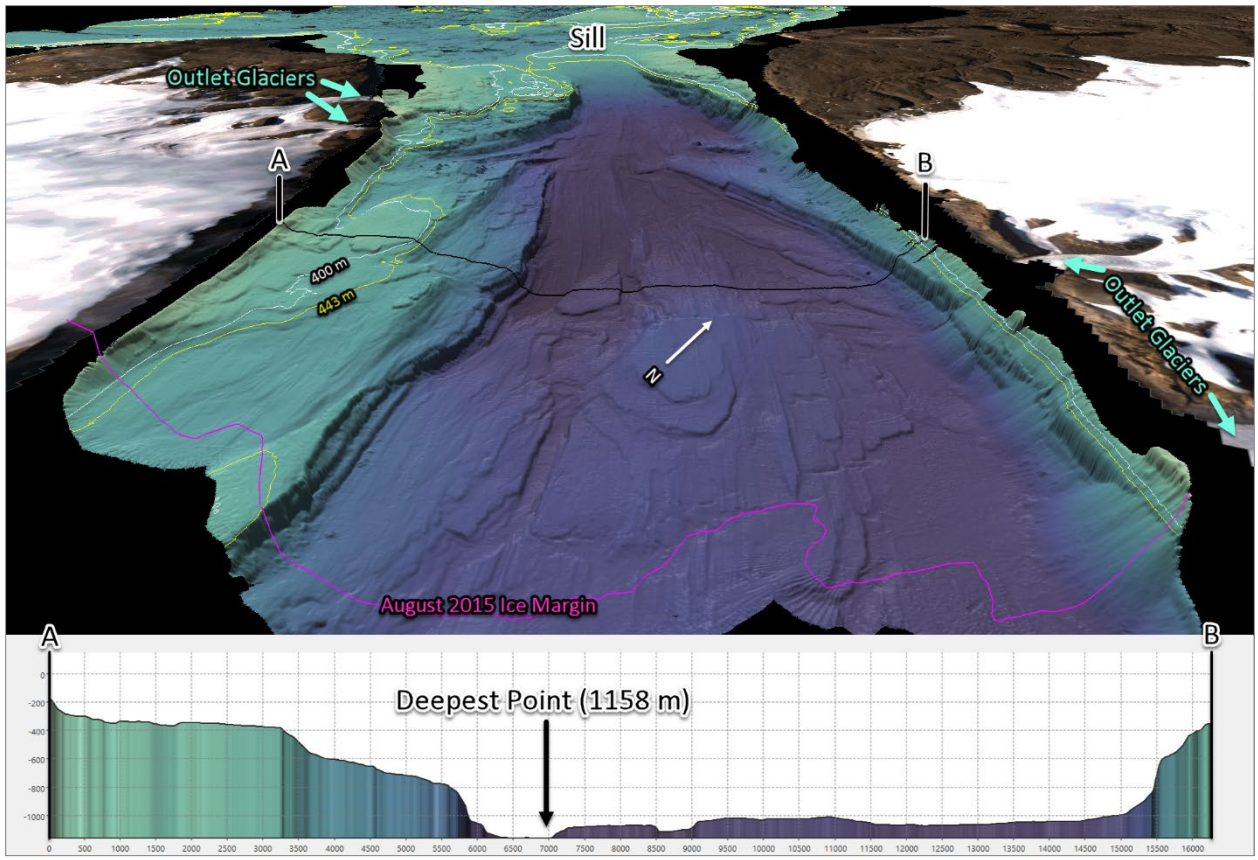

Figure 11: Perspective view of Petermann Fjord, looking toward the fjord entrance to the northwest, and profile of the bathymetry across the deepest part of the fjord. Both the bathymetry and the profile are vertically exaggerated 2X.

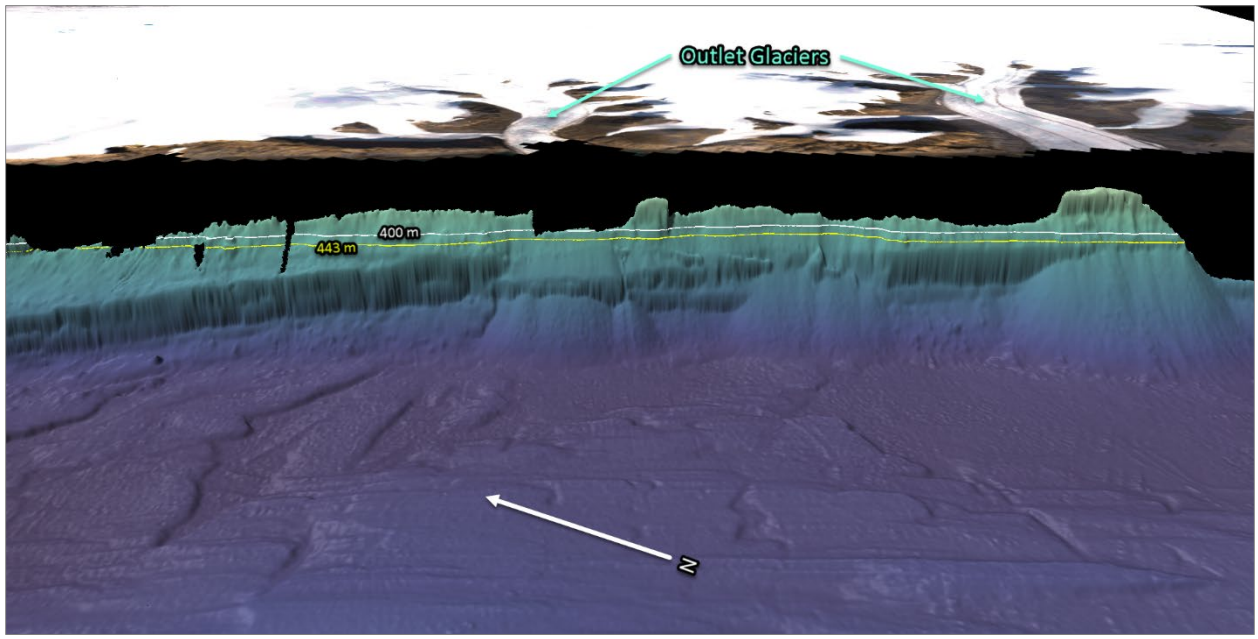

Figure 12: Perspective view of the steep eastern walls of the fjord, 2X vertical exaggeration. The bathymetric depths along the walls drop to ~1000 m in depth within 1500 m of the shoreline.

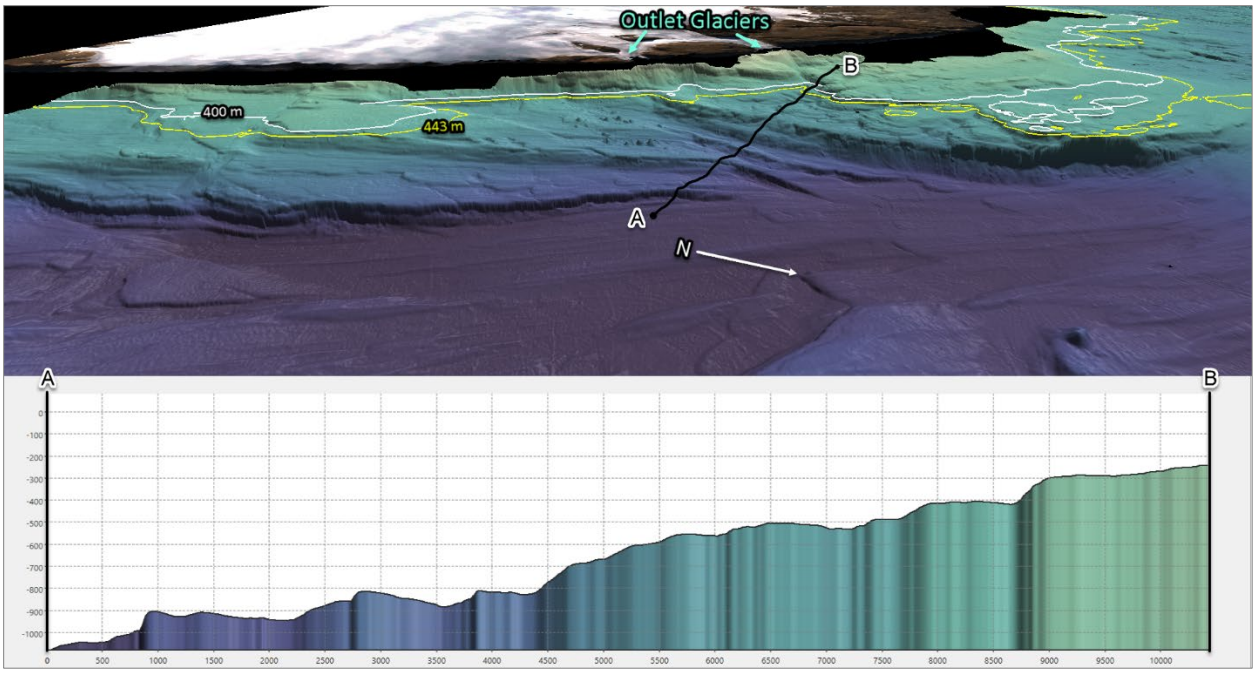

Figure 13: Perspective view and profile of the stepped walls and terraces on the western side of the fjord. Both the bathymetry and the profile are vertically exaggerated 2X.

Petermann Fjord is separated from Hall Basin by a *sill*, a shallow barrier between basins that may inhibit water movement (International Hydrographic Organization, 2019; Figure 10, Figure 11, Figure 14, Figure 15). The sill was formed as a Grounding Zone Wedge when the Petermann Glacier extended to the mouth of the fjord (Jakobsson et al., 2018). Most of the sill is shallower than 400 m, however there is a narrowing passage (< 200 m wide at its narrowest) down to 443 m depth (Jakobsson et al., 2018).

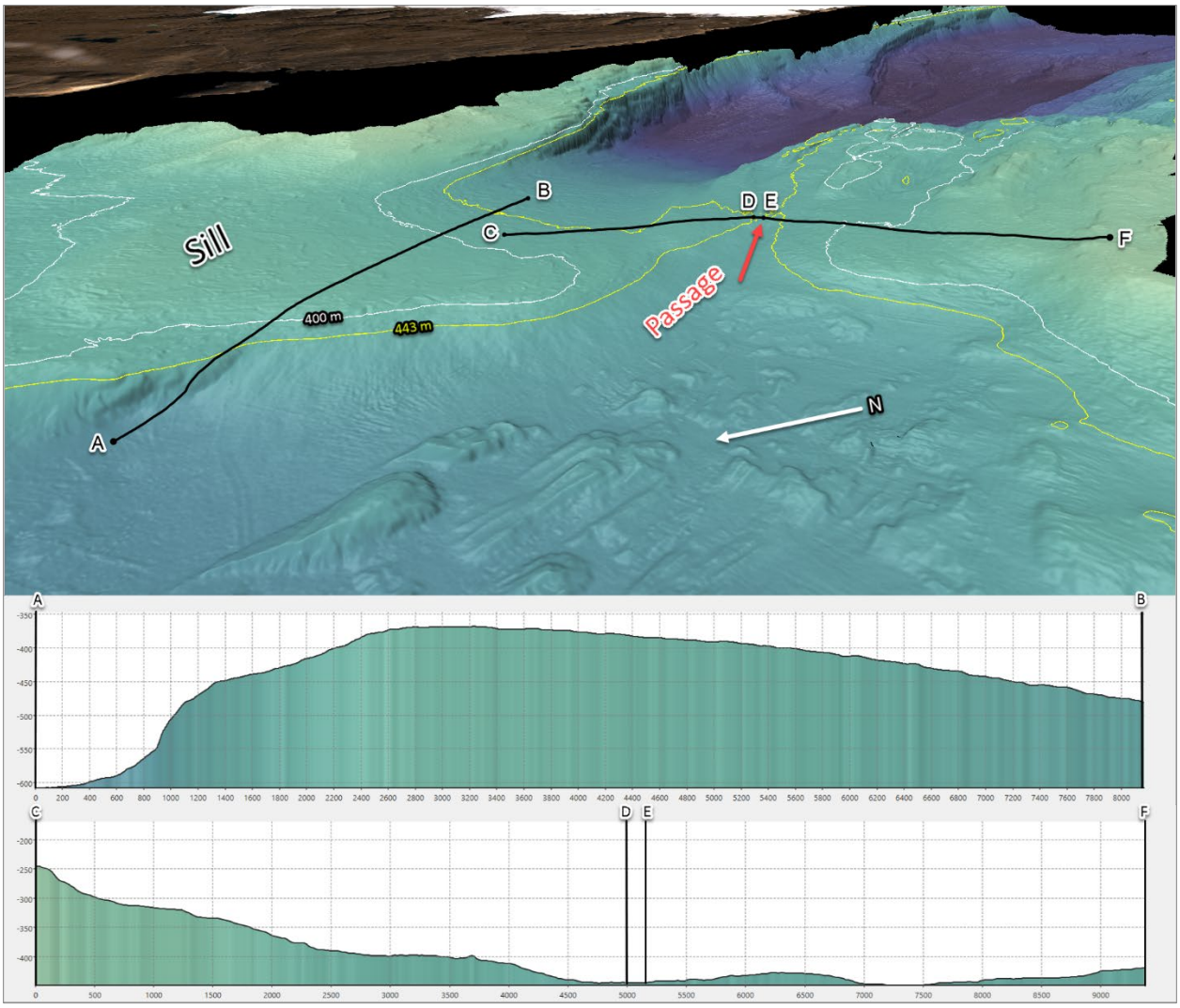

Figure 14: Perspective view and profiles of the sill and narrow deep passage to the fjord. Bathymetry is exaggerated 2X, profiles are exaggerated 5X. The gap between points D and E on the lower profile is ~150 m.

Hall Basin is designated by a widening of Nares Strait (Figure 15), approximately 71 km long and 51 km wide. The Robeson Channel section of Nares Strait is found to the north, and the Kennedy Channel section starts where Nares Strait continues to the south. The seafloor bathymetry is smooth and sediment covered in both channels (Figure 16, Figure 17), and rough and fractured between the two channels (Jakobsson et al., 2018; Figure 18). Bathymetric mapping in Hall Basin and Nares Strait during the Petermann Expedition was limited by operational priorities, shallow depths, and ice

cover (see Figure 7 and/or Figure 15, noting areas where bathymetry with pale yellow to blue colormap does not reach the shoreline visible in the underlying satellite image, and sections 3.1.1.2 through 3.1.1.5 for a description of mapping systems and methods). Prior mapping efforts by USCG *Healy* in 2003 (Rolling Deck to Repository (R2R), 2003) and CCGS *Amundsen* in 2013 (University of New Brunswick (UNB) Ocean Mapping Group, 2013) provides some coverage beyond the Petermann Expedition data, particularly near the mouth of Archer Fjord and Robeson Channel (see greyscale bathymetry in Figure 7 and Figure 15). The mean depth of the mapped areas of Hall Basin (including USCG *Healy* and CCGS *Amundsen* data) is 495 m. The max depth of 858 m is found in Nares Strait near the entrance to Archer Fjord (Figure 15). Several prominent *shoals*, localized areas of shallow bathymetric depth, are found at the tops of mounds in the rugged area of the basin. The shallowest mound borders Robeson Channels and reaches 193 m; this mound, which continues to the southwest as a linear ridge, marks the transition from rough to smooth topography that is an expression of an underlying transform fault (Tessensohn et al., 2006; Jakobsson et al., 2018). The bathymetry also decreases in depth along the eastern side of the basin and the eastern side of Kennedy Channel. Data collection stopped prior to the eastern edge of Hall Basin, but there is some indication that the bathymetry may continue as a shallow shelf moving toward the shore. A narrow section of mapping into Bessel Fjord (Figure 7, Figure 17) indicates that a shallow shelf exists along at least a portion of eastern Kennedy Channel.

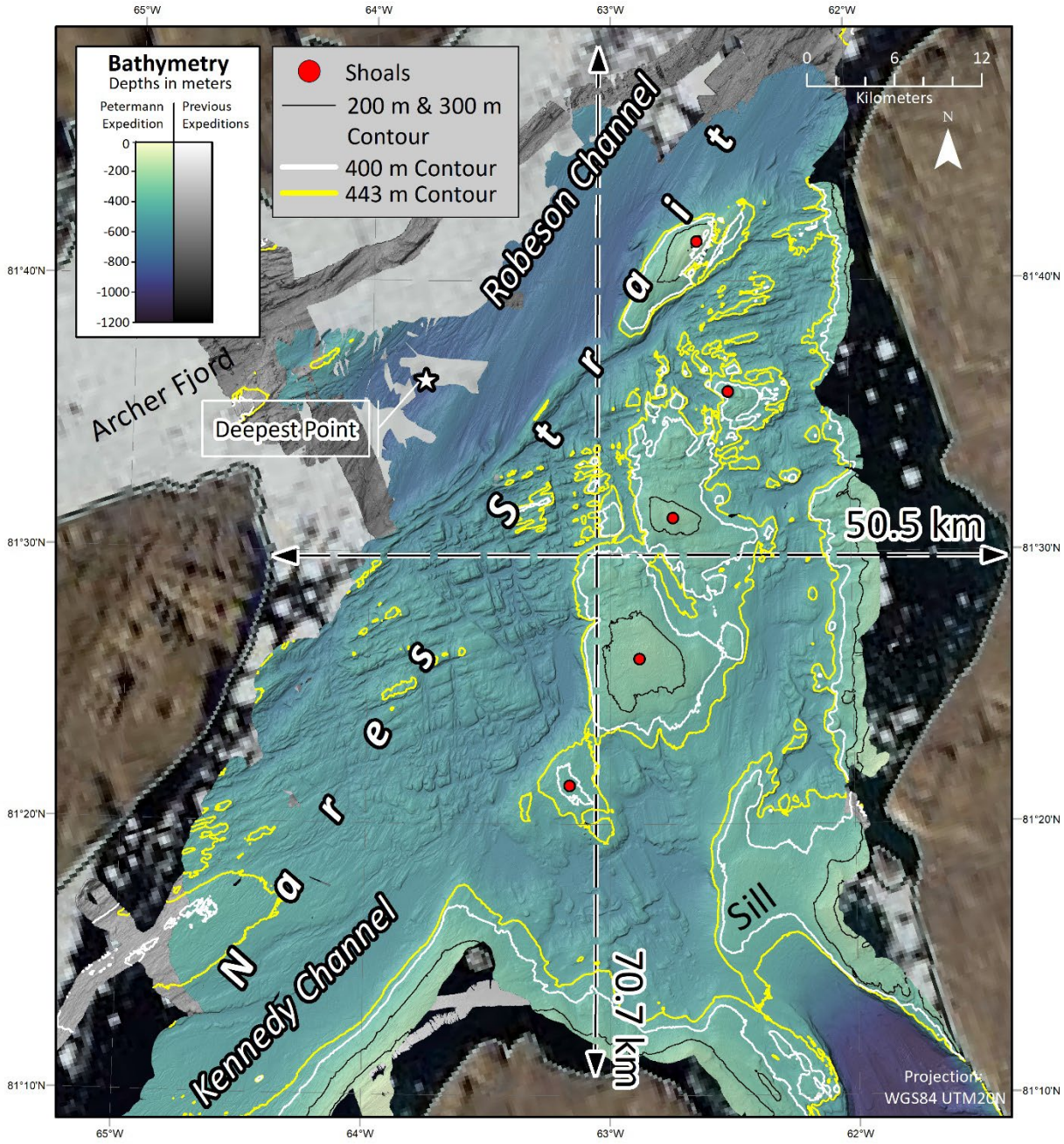

Figure 15: Hall Basin. Dashed lines with arrow end caps indicate where fjord dimension measurements were made. The red circles indicate prominent shoals (points of shallow bathymetric relief) in Hall Basin, which are marked with red arrows in Figure 16 and Figure 18.

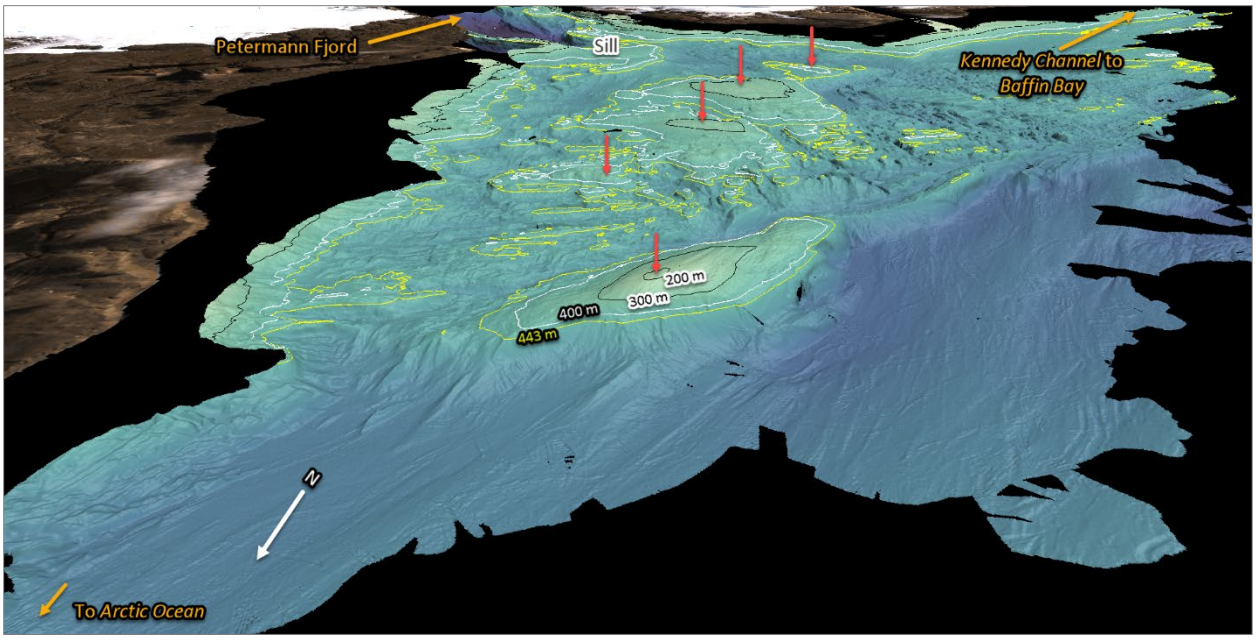

Figure 16: Perspective view of Hall Basin looking from Robeson Channel in the northeast (bottom left corner) toward Petermann Fjord (top center-left) and Kennedy Channel (top right). Red arrows indicate prominent shoals (points of shallow bathymetric relief) in Hall Basin. Bathymetry exaggerated 2X.

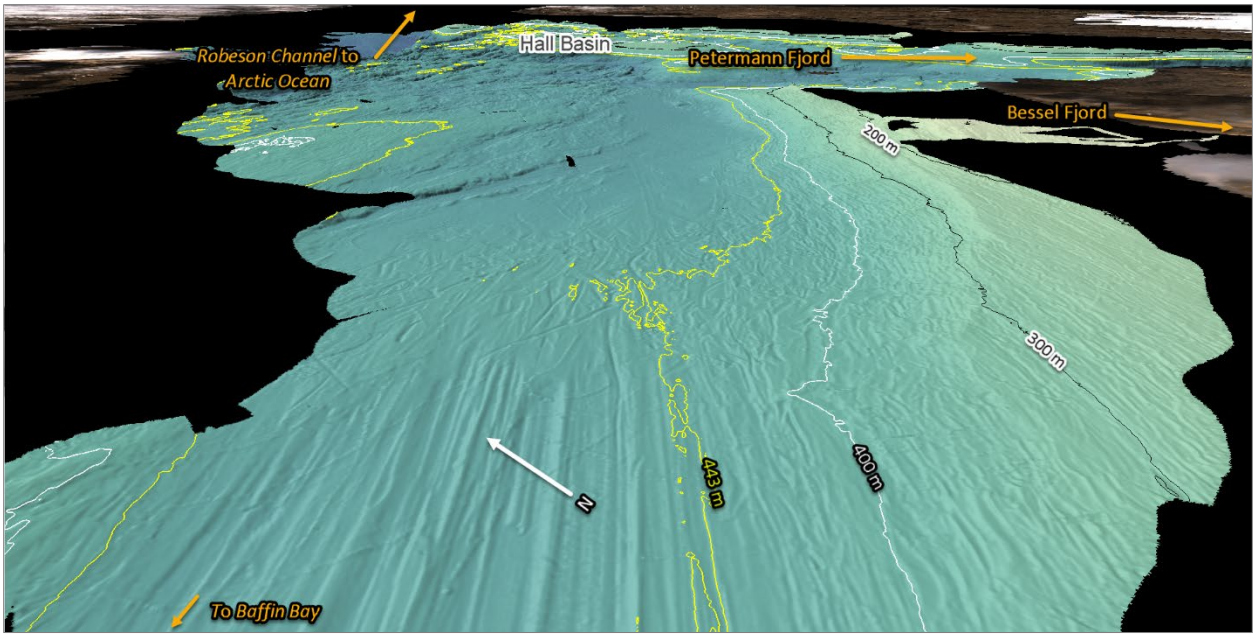

Figure 17: Perspective view of Kennedy Channel in the southwest (bottom of image) looking toward Hall Basin and Robeson Channel (top), and Petermann Fjord (right, top). Bathymetry exaggerated 2X.

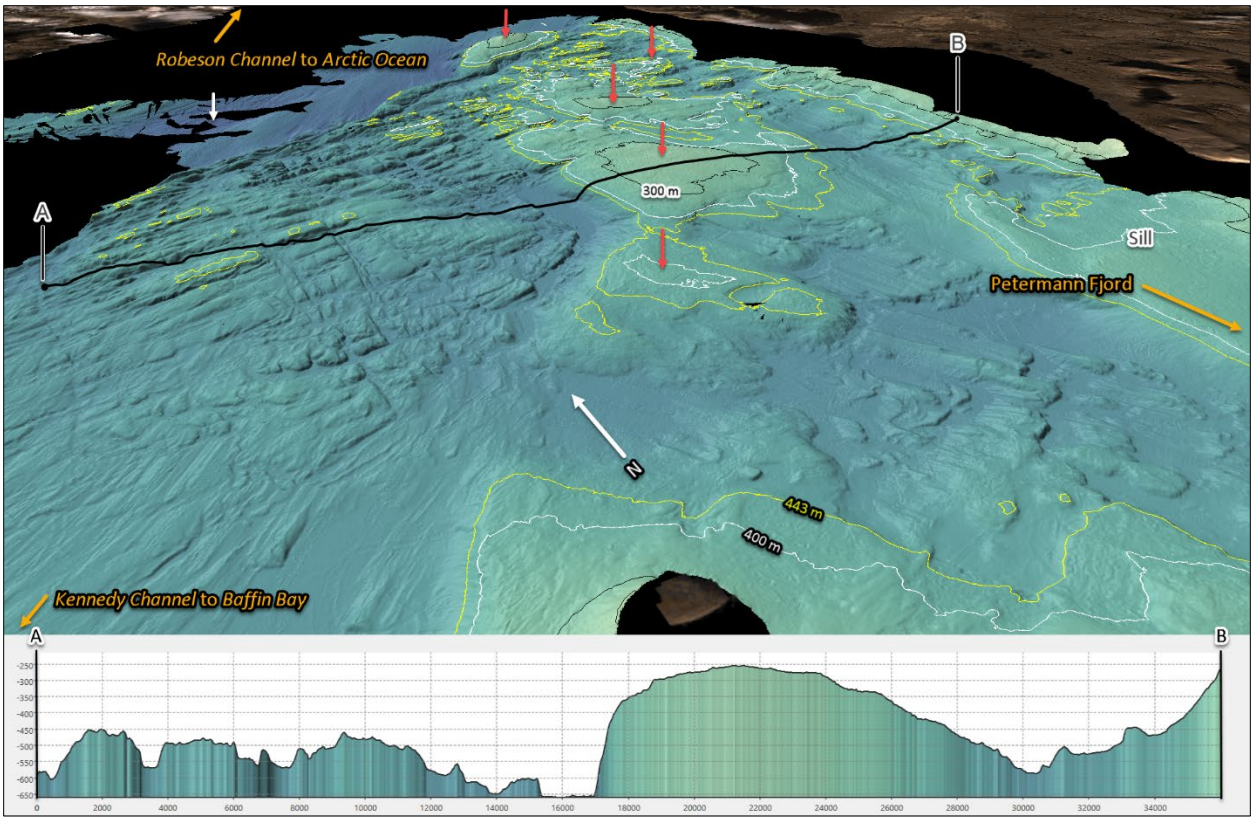

Figure 18: Perspective view of rough fractured bathymetry of Hall Basin. Red arrows indicate prominent shoals (points of shallow bathymetric relief) in Hall Basin. The white arrow indicates the deepest point that was mapped in Hall Basin/Nares Strait. Bathymetry exaggerated 2X, profile exaggerated 10X.

Petermann Glacier, the primary glacier feeding fresh water to Petermann Fjord, drains approximately 4% of the Greenland Ice Sheet (Rignot and Kanagaratnam, 2006; Hill et al., 2017, 2018; see Figure 19 for a map of the glacier extent). The glacier's floating ice shelf extends approximately 46 km from the grounding line (Figure 19). The glacier is approximately 600 m thick at the grounding line (Tinto et al., 2015) and is grounded somewhere between 400 and 600 m below sea level (Rignot and Steffen, 2008; Johnson et al., 2011; Straneo et al., 2012; Tinto et al., 2015; Münchow et al., 2016; Cai et al., 2017; Paden et al., 2019). The ice shelf has a mean thickness of ~300 m (Münchow et al., 2014; Washam et al., 2018) and is ~200 m thick at the terminus (Münchow et al., 2016).

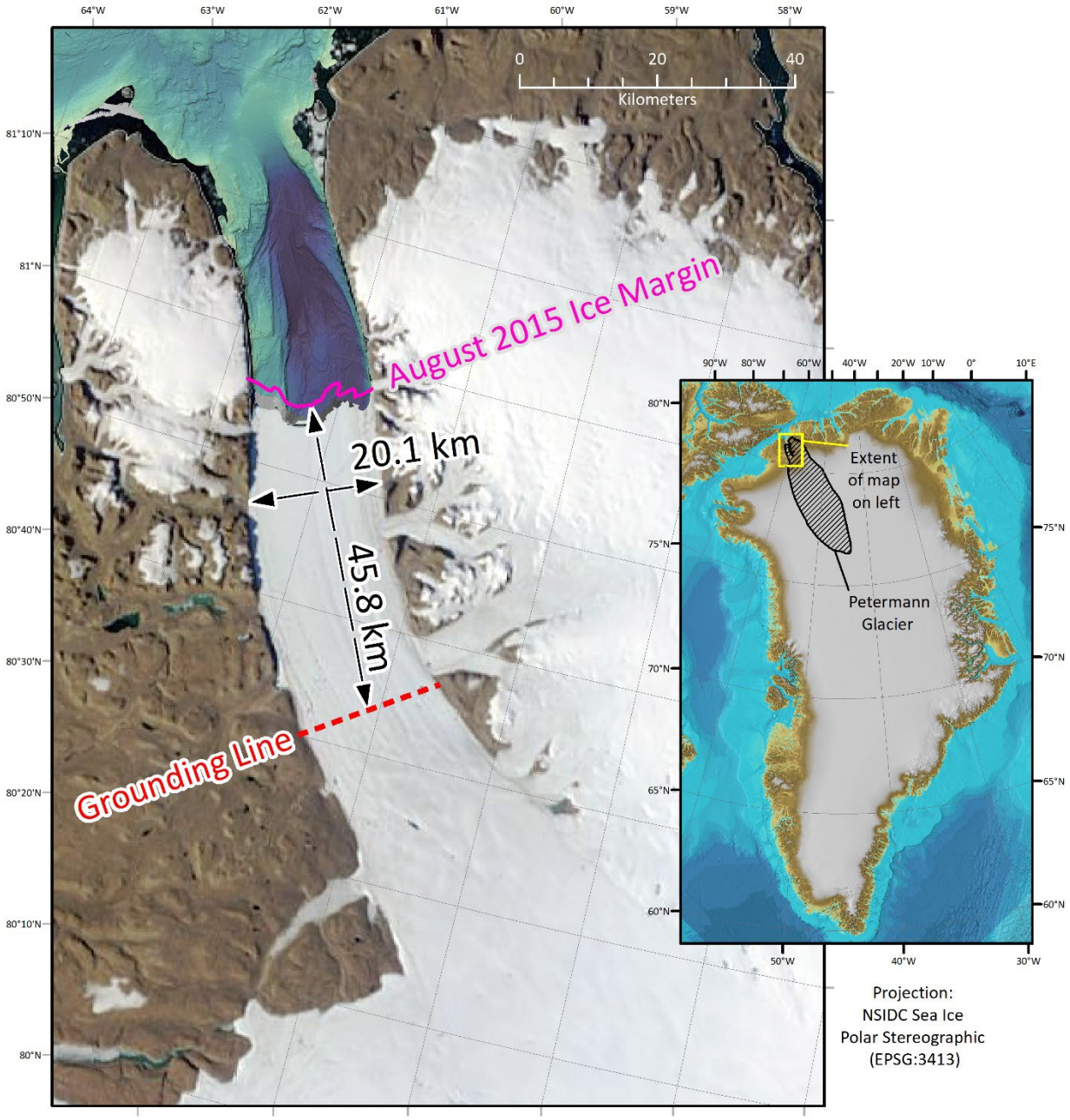

Figure 19: The Petermann Glacier floating ice shelf, left, and an overview map showing the extent of Petermann Glacier. The approximate position of the grounding line comes from Tinto et al., 2015. The extents of Petermann Glacier were taken from Hill et al., 2018. The location of the magenta line delineating the August 2015 ice margin differs from what appears to be the ice margin in the image because the image was masked based on the acquired bathymetry, which extended beneath the ice margin. Note that the projection for both maps is NSIDC Sea Ice Polar Stereographic North (EPSG: 3413) and that north should be inferred from direction of longitude meridians.

2.3 Regional Hydrography

The regional hydrography is influenced by the inflow of Winter Water and deeper Atlantic Water entering Nares Strait from the Lincoln Sea through Robeson Channel. Winter Water (also called Arctic Water or Polar Water in the literature, and more generically could be labeled Arctic Surface Water) is relatively fresh water made up of Pacific Water entering the Arctic via Barrow Strait that is seasonally influenced by runoff from major Siberian and North American rivers as well as ice melt (Aagaard et al., 1981; Jones et al., 2003; Münchow et al., 2007; Münchow, 2016; Johnson et al., 2011; Straneo et al., 2012; Straneo and Cenedese, 2015). The flow through Nares Strait is primarily southward, driven by winds and sea level drop from north to south along the strait (Sadler, 1976; Münchow et al., 2007; Münchow, 2016). Nares Strait functions as one of the export pathways for Winter Water into Baffin Bay and the North Atlantic (Aagaard and Carmack, 1989; Münchow et al., 2015; Shroyer et al., 2015; Münchow, 2016).

Atlantic Water enters the Arctic as relatively warm, relatively saline waters carried by the North Atlantic current via the Barents Sea or Fram Strait (Jones et al., 2003; Münchow et al., 2006; Straneo and Heimbach, 2013; Figure 20). It circles the Arctic Ocean counterclockwise, progressively moving deeper in the water column and losing some of its heat (Coachman and Barnes, 1963; Rudels et al., 1994; Jones et al., 1995; Polyakov et al., 2010; Talley et al., 2011), before arriving in the Lincoln Sea and entering Nares Strait at depth as a still relatively warm ($T > 0°$ C) and saline ($S > 34.6$)

water mass (Münchow et al., 2011; de Steur et al., 2013; Straneo and Heimbach, 2013; Münchow et al., 2014, 2016; Figure 21). Its passage into Nares Strait and further south is limited by the bathymetry, being partially restricted by a 290 m northern sill between the Lincoln Sea and Robeson Channel and completely blocked at the southern end of Kane Basin by another shallow sill at around 220 m depth (Jennings et al., 2011; Münchow et al., 2006, Münchow et al., 2011; Washam et al., 2018).

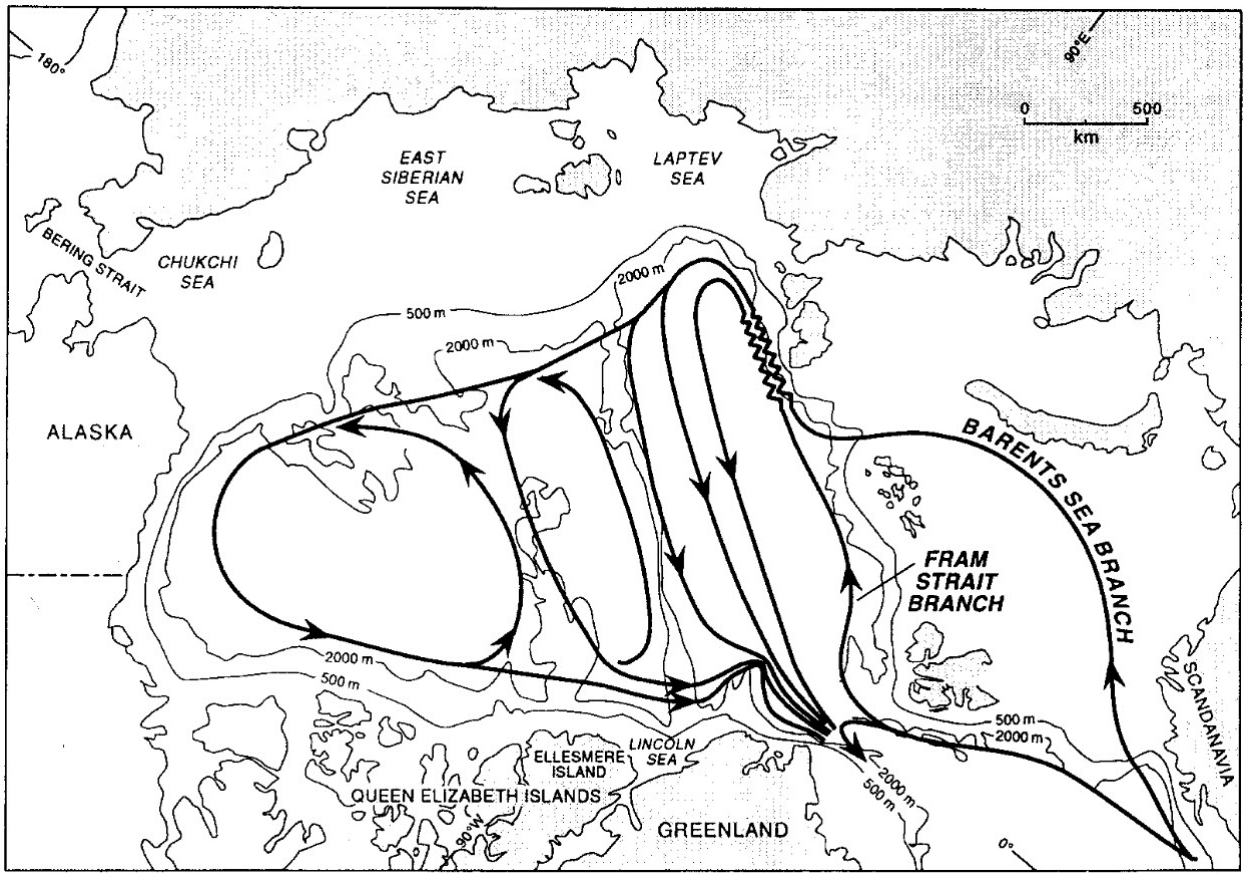

Figure 20: Diagram showing the inferred circulation in the Arctic Ocean of the Atlantic Layer and intermediate depth waters, between 200 and 1700 m (Rudels et al., 1994).

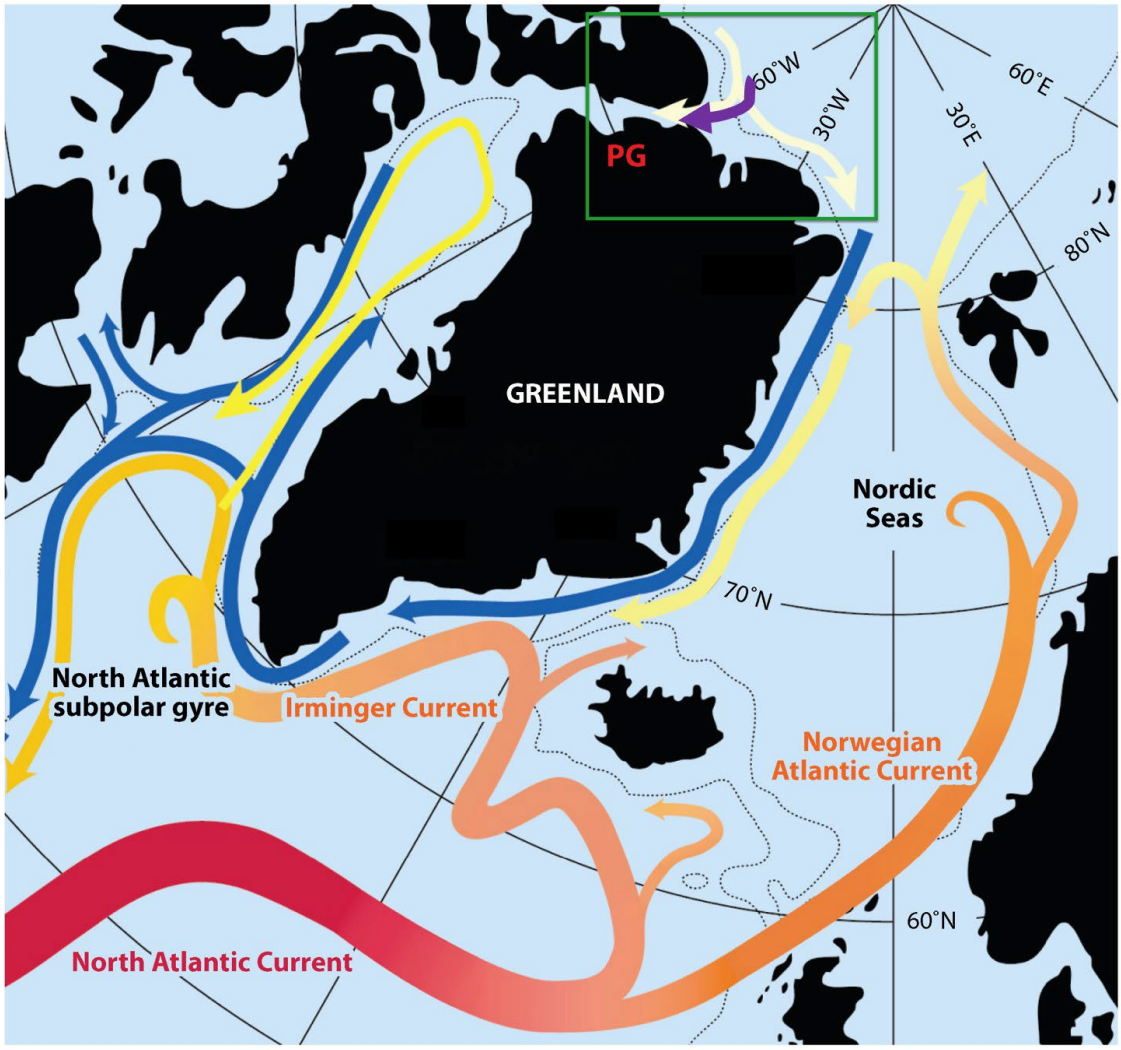

Figure 21: Large-scale ocean circulation around Greenland, with Atlantic Water pathways shown in red to pale yellow and Arctic-origin freshwater pathways shown in blue and purple (purple arrow added by this author). Note the incursion of Atlantic Water into Nares Strait after circling the Arctic, highlighted with a green box, and the label PG, showing the approximate location of Petermann Glacier. From Straneo and Cenedese, 2015, with green box added to emphasize the entrance to Nares Strait, purple arrow added to show pathway of freshwater from the Lincoln Sea into Nares Strait as described by Münchow, 2016 and others, and the locations of other glaciers removed.

After entering Nares Strait, Winter Water and Atlantic Water (collectively, the *Arctic outflow*) move through Hall Basin and into Petermann Fjord (Johnson et al., 2011; Straneo et al., 2012; Münchow et al., 2014). Flow is strongest along southwestern side of Nares Strait, along the coast of Ellesmere Island (Münchow et al., 2007; Heuzé et al., 2017). Water continues to the fjord entrance and into the southwestern side of the fjord mouth (Johnson et al., 2011; Heuzé et al., 2017). Here, the flow of the Atlantic Water is

partially restricted by the sill, however the warmer saltier water does enter the fjord below 150 m, renewing both deep and intermediate fjord waters (Johnson et al., 2011; Straneo et al., 2012; Heuzé et al., 2017). The warmer water moves through the fjord, flows under the base of the glacier on the southwestern side below 200 m (Heuzé et al., 2017) and interacts with the base of the glacier, causing enhanced basal melting, thinning, and calving (Straneo et al., 2012; Münchow et al., 2014). On the northeastern side of the fjord, at the glacial interface, basal meltwater-enriched water returns to the fjord between 100 and 280 m and flows outward, concentrated between 150 and 200 m, with a second outflow above 200 m on the southwest side of the terminus (Heuzé et al., 2017). This is supplemented by additional freshwater from subglacial discharge (also at depth) and surface runoff in summer (Washam et al., 2018). The meltwater leaves the fjord concentrated along the northeast side, entering Hall Basin and Nares Strait at depths between 75 and 250 m (Heuzé et al., 2017). The addition of freshwater to the seawater that exits the fjord creates a mass imbalance that must be compensated by deep inflow of the Atlantic Water at depth, similar to two-layer estuarine circulation (Farmer and Freeland, 1983; Washam et al., 2018). Once outside the fjord, most of the meltwater appears to follow the Greenland coast towards the Arctic, with high concentrations of meltwater found near that coast and to the middle of Hall Basin (Heuzé et al., 2017). Some of the meltwater exiting west of the sill may be recirculated into the fjord via a gyre detected in Hall Basin near the mouth of the fjord (Johnson et al., 2011; Heuzé et al., 2017). Figure 22 and Figure 23 summarize the hydrographic conditions in Petermann Fjord based on 2003, 2007 and 2009 data (Johnson et al., 2011) and 2015 Petermann Expedition data (Heuzé et al., 2017), respectively.

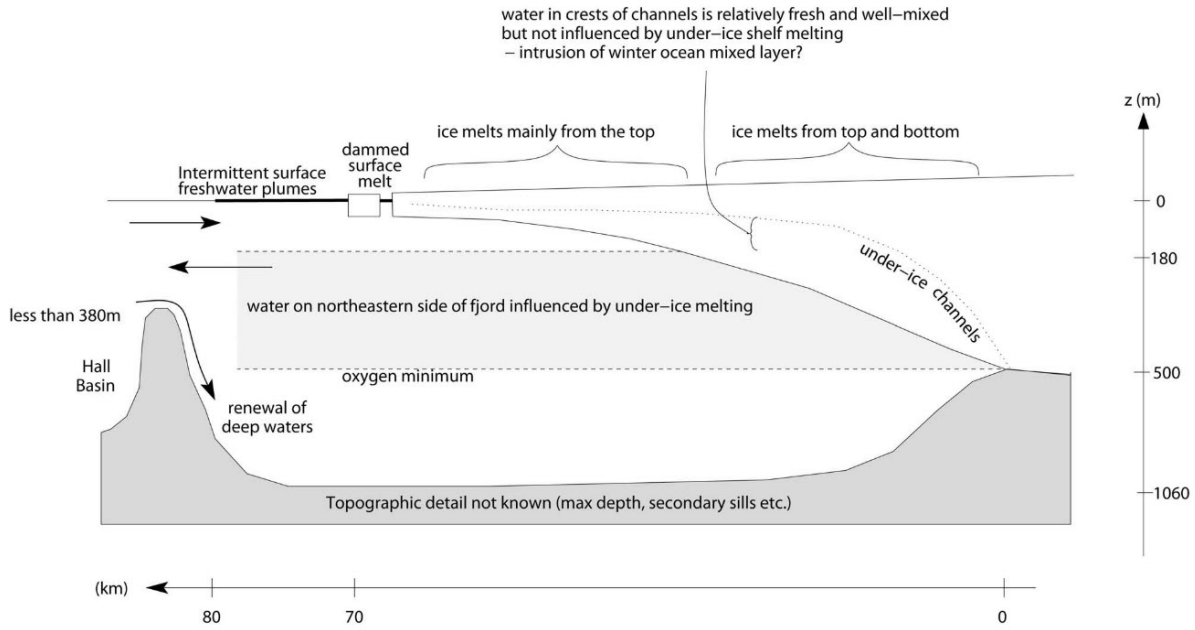

Figure 22: Schematic showing hydrographic conditions in Petermann Fjord, from Johnson et al. (2011).

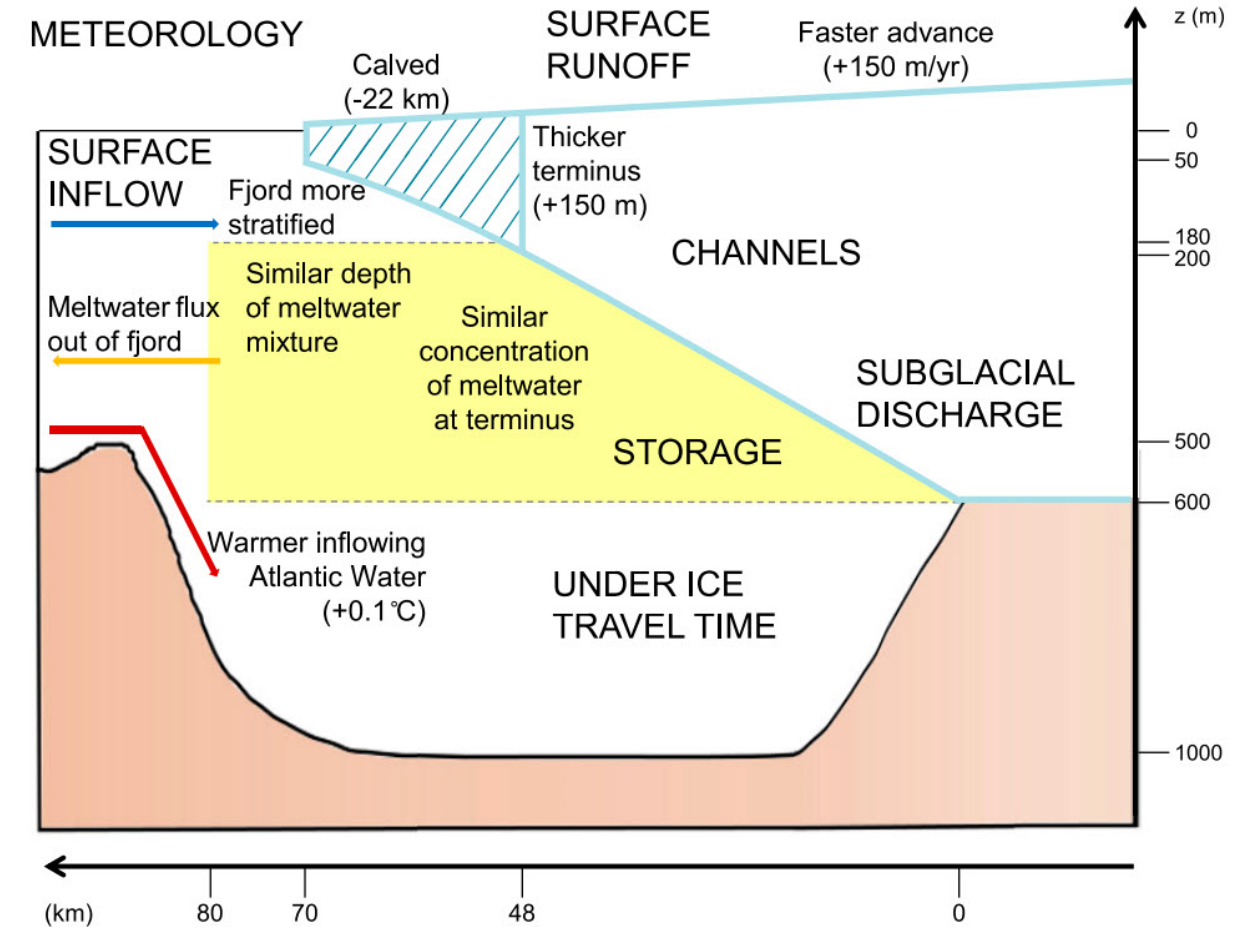

Figure 23: Schematic summarizing changes in Petermann Fjord since Johnson et al. (2011), from Heuzé et al. (2017). Captial letters indicate phenomena whose magnitude is unknown.

There are also four smaller outlet glaciers within the fjord that are seaward of the ice tongue (Figure 10). There has been no specific analysis of any contribution they might have to fjord hydrography, however our acoustic analysis implies that they can have a localized effect, adding nutrients or causing upwelling that attracts marine organisms to the location causing local increases in acoustic scattering (Figure 24).

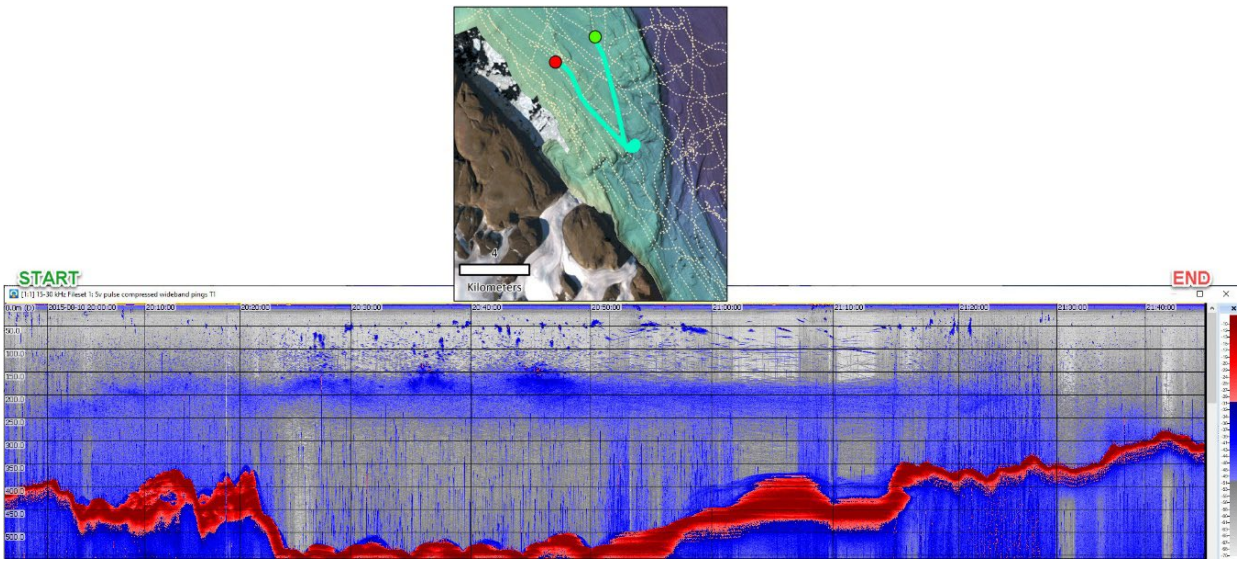

Figure 24: Example of enhanced biological scattering, possibly related to output from nearby outlet glaciers. The green and red dots on the map correspond to the start and end of the echogram, respectively.

2.4 Biological Community Inhabiting the Water Column

The fjords and bays at the margins of Arctic outlet glaciers physically aggregate plankton and the fish that prey on them, providing a concentrated foraging habitat for marine mammals (Lydersen et al., 2014; Laidre et al., 2018; Lomac-MacNair et al., 2018). Further, the fronts of tidewater glaciers found within some of those fjords and bays are considered foraging hotspots due to the effects of plumes of sub-glacial meltwater rising to the surface (Lydersen et al., 2014). Based on this, it could be expected that Hall Basin and Petermann Fjord would host many arctic species. Due to its remote nature and limited accessibility, however, few biological sampling studies have been conducted in Nares Strait, Hall Basin, or Petermann Fjord. During the Petermann 2015 Expedition, a dedicated marine mammal observer recorded 312 seals representing four species – bearded seal (*Erignathus barbatus*), hooded seal (*Crystophora cristata*), harp seal (*Pagophilus groenlandicicus*), and ringed seal (*Pusa hispida*) (Lomac-MacNair et al., 2018). The majority of the observed seals

(approximately 76%) were in the water (Lomac-MacNair et al., 2018), where they forage and feed in the upper water column and occasionally dive to depth. Bouchard et al. (2018) summarized ichthyoplankton and adult fish sampling from the CCGS *Amundsen* between 2005 and 2017, which included a sampling station and benthic trawl in Hall Basin (see Figure 25 for station location). Ichthyoplankton sampling yielded very low numbers of Gadidae (cod) larvae (Caroline Bouchard, personal communication, April 11, 2019); the trawl recovered Gadidae, Zoarcidae (eelpout), Liparidae (snailfish) and Cottidae (sculpin) (Bouchard et al., 2018). Unpublished zooplankton abundances collected on August 13, 2016, from the Hall Basin station were provided by the Fortier Lab at the University of Laval (Cyril Aubry, personal communication, April 18, 2019). A vertical tow with a 200 µ net starting at a depth of 451 m showed copepods to be dominant; of the 34 species identified, *Oithona similis*, *Microcalanus* sp., *Metridia longa*, *Oncaea notopus/parila*, and *Pseudocalanus* sp. were the most numerous. Of the 17 non-copepod species identified, appendicularians (*Fritillaria* sp., *Oikopleura* sp.), ostracods (*Boroecia maxima, Discoconchoecia elegans*), euphausiid nauplii and metanauplii, and chaetognaths (*Eukrohnia hamata*) were the most numerous. Polychaetes, cnidarians (*Melicertum octocostatum, Aglantha digitale, Lensia conoidae,* and unidentified sp.), echinoderm larvae, amphipods (*Themisto abyssorum*), and gastropods (*Limacina helicina*) were also present. Kalenitchenko et al. (2019) examined microbial eukaryotes, including phytoplankton, sampled in Nares Strait by the CCGS *Amundsen* during August 2014 (see Figure 25 for station location). They found high proportions of diatoms, as well as chlorophytes and haptophytes and heterotrophic flagellates such as choanoflagellates, Picozoa, and marine stramenopiles.

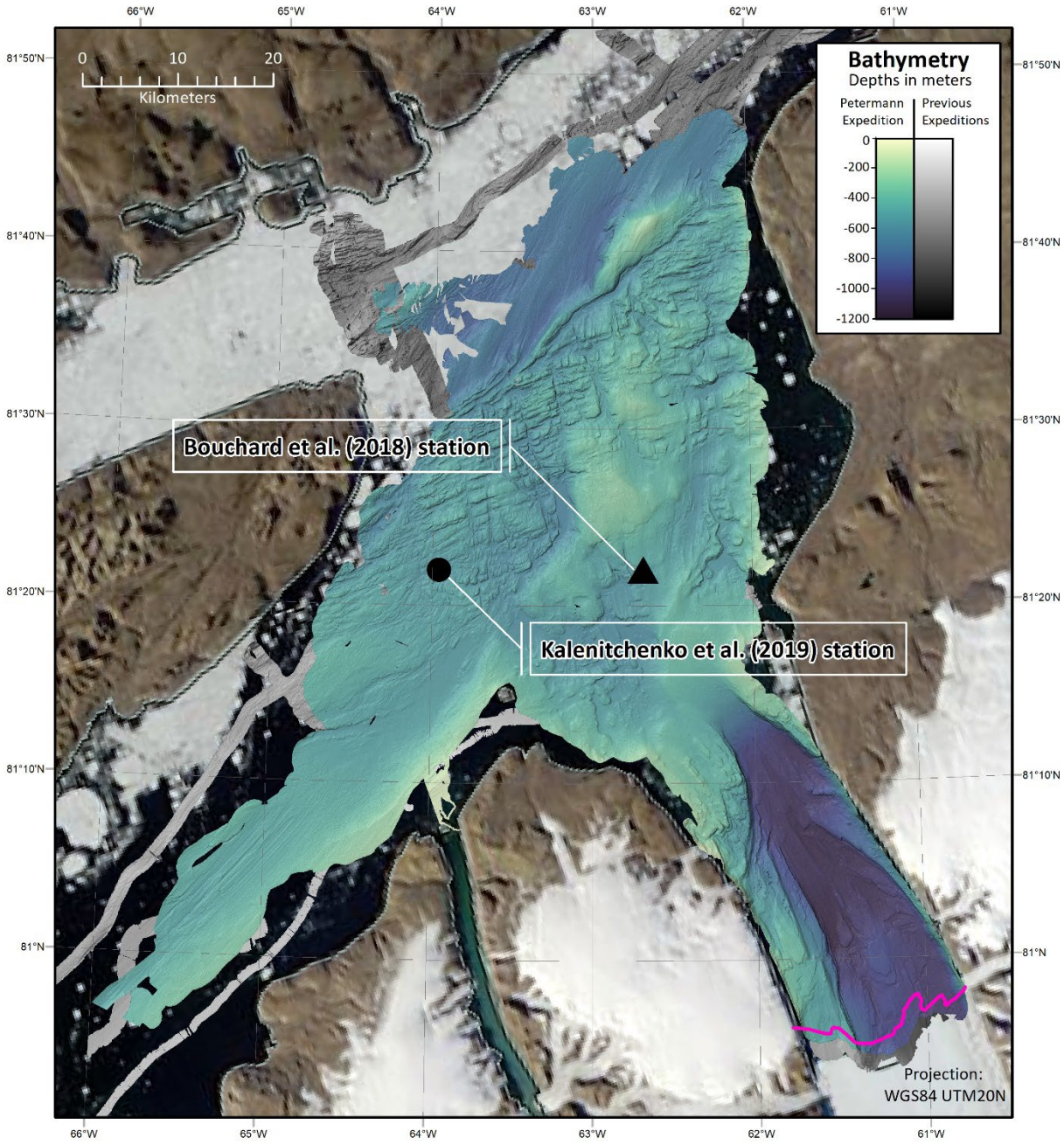

Figure 25: Locations of known biological samples (Bouchard et al., 2018; Kalenitchenko et al., 2019).

No other published reports of biological sampling in the study area could be found. One might expect some similarity to communities found in the Canadian Arctic Archipelago, Canadian and Eastern Arctic seas, and the fjords of Svalbard. These regions differ from Petermann, particularly in the water masses found there (which in

turn will affect the biological community present), but are better studied and are similar in that they are at high latitudes and influenced by the presence of Arctic water and Atlantic Water separated by a distinct halocline. In those regions, the base of the food web is dominated by algae – haptophytes, chyrsophytes (golden algae) and diatoms, present as ice algae and phytoplankton (Benoit et al., 2008; Falk-Petersen et al., 2008) – similar to what was found by Kalenitchenko et al. (2019) in Hall Basin. Copepods are the dominant zooplankton (Auel and Hagen, 2002; Benoit et al., 2008; Falk-Petersen et al., 2008; Kosobokova and Hirche, 2009; Kosobokova et al., 2011; Pomerleau et al., 2011; Berge et al., 2014; Lydersen et al., 2014). Other zooplankton include cnidarians, chaetognaths, amphipods, ctenophores, pteropods, decapods, appendicularians, and euphausiids (Welch et al., 1992; Auel and Hagen, 2002; Benoit et al., 2008; Falk-Petersen et al., 2008; Raskoff et al., 2010; Kosobokova et al., 2011; Berge et al., 2014; Lydersen et al., 2014; Knutsen et al., 2017). Polar cod (*Boreogadus saida*) have been found in high concentrations in the fjords and coastal seas of Spitsbergen (Falk-Petersen et al., 1986) and in Barrow Strait (Welch et al., 1993), and compromise 95% of the pelagic fish assemblage in the Canadian Arctic Seas (Benoit et al., 2008; Fortier et al., 2015; Geoffroy et al., 2016). Other fish include redfish, capelin, American plaice, sculpins, seasnails, eelblennies, and eelpouts (Falk-Petersen et al., 2008; Lydersen et al., 2014). Diving and pelagic seabirds include the fulmar, little auk, and black guillemot (Berge et al., 2014; Lydersen et al., 2014). In addition to seals, mammals living or spending time in the water column might include white whales, beluga whales, killer whales, narwhals, and polar bears (Welch et al., 1992; Lydersen et al., 2014).

CHAPTER 3 METHODS

3.1 Data Collection and Processing

3.1.1 Acoustic Data

3.1.1.1 Simrad EK80 split-beam echosounder

The water column acoustic data analyzed here were collected with a Simrad EK80 split-beam echosounder. The transducer was installed behind an ice window and aft of the ice knife on the bow of the IB *Oden* and operated for the entire 35 days of the voyage, for the purpose of acoustically mapping features in the water column. The system employed a wideband transceiver (WBT) and Simrad ES18-11 split-beam echosounder (SBES) transducer with a nominal frequency of 18 kHz and a nominal bandwidth of 15 to 30 kHz; testing and experience have found the system's actual useable bandwidth to be 16-26 kHz (Weidner et al, 2019). The system produces a linear frequency modulated (LFM) acoustic signal, with a -3dB beam width of 11° at 18 kHz, and a vertical range resolution of approximately 7.5 cm after pulse compression processing (Weidner et al., 2019). Data were monitored real-time by mapping watch standers using the Simrad EK80 software (version 1.8.0) and logged in the Simrad RAW format. Position and attitude information were collected using a Seapath Seatex 330 GNSS navigation and motion reference system; position was provided to the echosounder for real-time integration with the acoustic information. Pulse duration varied from 1.024 ms to 4.096 ms throughout the expedition, with the majority of data in the main study area collected with a pulse duration of 1.024 ms and transmission power

set to 2000W. Ping rate varied as the system was synced to the EM122 multibeam echosounder and SBP120 subbottom profiler.

3.1.1.2 Kongsberg EM122 multibeam echosounder

The hull-mounted Kongsberg EM122 multibeam echosounder (MBES) installed in IB *Oden* was also operated continuously over the entire 35 days of the voyage, for the primary purpose of seafloor mapping of submarine glacial landforms in order to reconstruct the glacial history of the area (Jakobsson et al., 2018). The system is 1°x1° and operates at 12 kHz, with the transmit array mounted along-ship in the ice knife forming the deepest part of *Oden's* hull and the receiver array mounted across-ship behind a titanium plate. Position and attitude information were collected using the Seapath Seatex 330 GNSS system and integrated with the acoustic information real-time. A Seatex MRU5 was used to log heave, pitch, roll and yaw. Sound speed profiles were generated from oceanographic information collected using a SeaBird 911+ CTD (see section 3.1.2.1) and supplemented with XBTs (eXpendable Bathy Thermographs) when necessary.

3.1.1.3 Kongsberg EM2040 multibeam echosounder

A Kongsberg EM2040 MBES is installed on a bow-mounted pole on the Research Vessel (RV) *Skidbladner*, a 6.4 m long survey launch that can be deployed from the IB *Oden*. The 1°x1° system operates in the frequency range of 200-400 kHz and can map to depths of approximately 500 m. The *Skidbladner* was deployed to map select shallow regions where the IB *Oden* could not operate. A Seatex MRU5+ was used to acquire motion, heading was acquired using two VS101 Hemisphere GPS

compasses, and main positioning acquired with a Hemisphere R320 GPS/GLONASS receiver. An Applied Microsystems Limited (AML) sound speed probe was mounted on the EM2040 transducer casing for continuous sound speed corrections related to beam forming, and a Valeport velocimeter was used for collecting sound speed profiles of the water column.

3.1.1.4 Acoustic survey design and execution

Over 4000 line km of EK80 and EM122 acoustic data were collected during the expedition (see Figure 7; the *Oden* track line is an indication of the acoustic data collected, as the echosounder was run continuously). The acoustic surveys were conducted in conjunction with many other ship-based experiments, including CTD casts and sediment coring. Mobile sea ice was also a factor (see Figure 9, and Figure 139 in Appendix B for images of changing ice conditions). This resulted in a very irregular ship track with many turns and sudden changes in speed and heading that are not ideal for seafloor mapping or water column surveying, but made the best use of the time available (see Figure 7 for the *Oden* ship track, and figures in Appendix A for examples of data quality issues due in part to ship operations). The three acoustic systems (SBES, MBES, and subbottom) were synchronized to reduce interference, however interference of the EM122 in the EK80 data was often a factor in the top 250 m of the water column (see Appendix A).

Approximately 131 line km of EM2040 data were collected by the RV *Skidbladner* during the expedition (Figure 26). The areas mapped by the *Skidbladner* were shallow regions of interest to the expedition team.

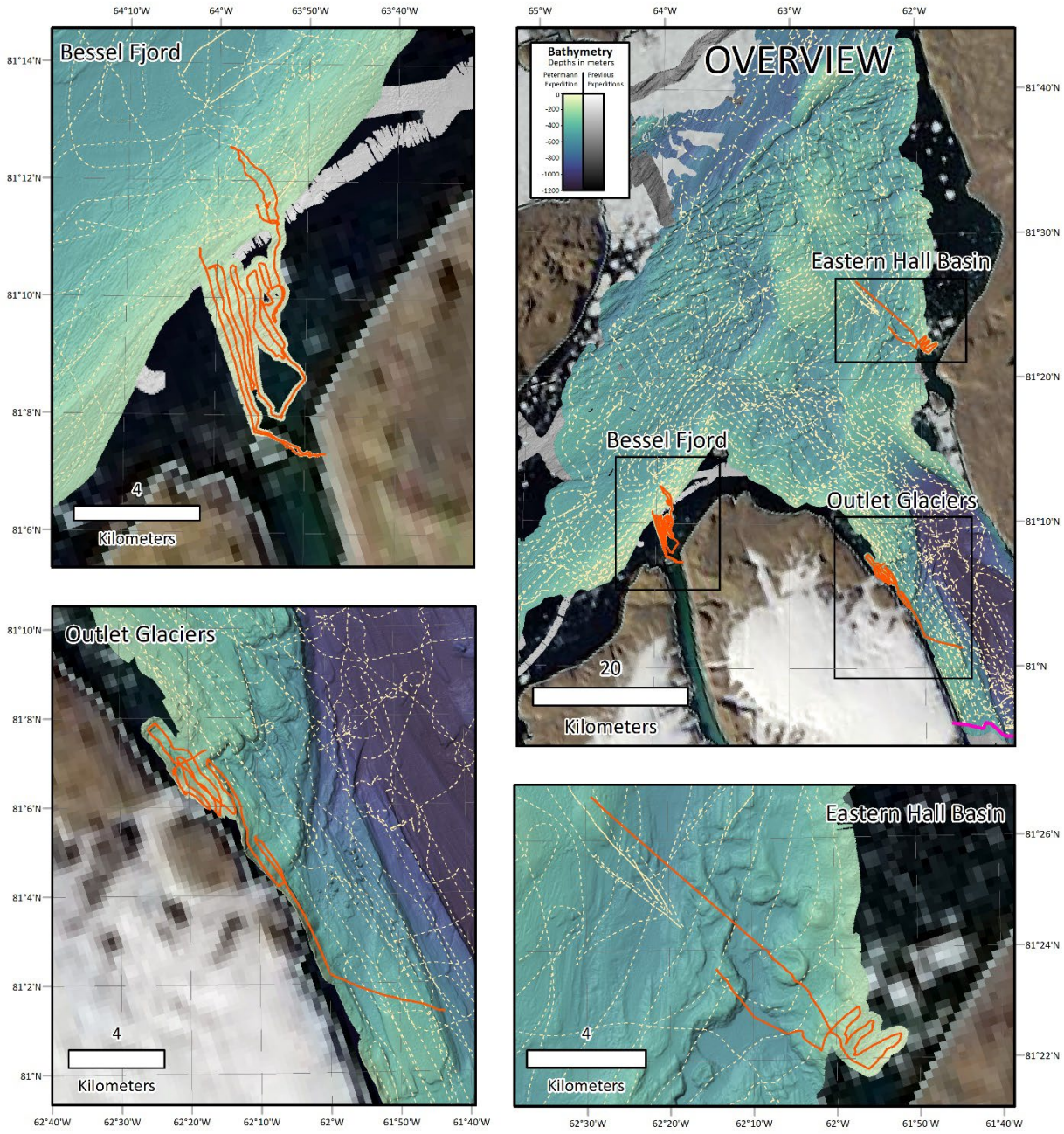

Figure 26: Areas mapped using the Kongsberg EM2040 MBES on the RV Skidbladner. Solid orange line is the RV Skidbladner track line, dotted cream-colored line is the IB Oden track line. Projection for all maps is WGS84 UTM 20N.

It is important to emphasize that the acoustic water column data was considered a “dataset of opportunity”, not specifically planned for in the expedition design and operations but collected nonetheless. Additionally, the EK80 18 kHz SBES installed specifically for water column mapping was selected based on availability (the CCOM

team had it available for use) and for its ability to detect bubbles, the primary goal of the water column mapping. This frequency of SBES (and single frequency acoustic surveys in general) is not, generally, the best approach for detecting and discriminating biology such as the scattering layer encountered on this expedition.

3.1.1.5 Echosounder Data Post-processing

The EK80 SBES data was processed using a combination of custom, open-source, and commercial software. The Simrad RAW files were converted to Generic Water Column (GWC) format using custom Python and navigation extraction routines compiled as plug-ins for QPS FMMidwater software version 7.6.1, 64-bit; these GWC files were specifically generated for use in the FMMidwater software. The custom Python and navigation extraction routines were written by Moe Doucet (formerly of QPS, Inc.) and Victoria Price-Doucet (formerly of CCOM) and can be made available through this author on request. Ranges from the transducer were calculated using a constant sound speed of 1500 m s^{-1} for all files. The Simrad RAW files were also reviewed in the Myriax Echoview software versions 8.0.95.32073 through 9.0.328.35283 and in the New Zealand National Institute of Water and Atmospheric Research's (NIWA) ESP3 software versions 1.0.1 through 1.8.1 (https://sourceforge.net/p/esp3/wiki/ESP3/). No pre-processing was required for these software tools, as both have direct support for the EK80 RAW format. Both programs calculated ranges from the transducer using a constant sound speed of 1500 m s^{-1} for the creation of echograms; we estimate that this could has caused the top of the layer to be misplaced in depth by up to 1.6 m for the shallowest layers and up to 26.8 m for the deepest layers (see Appendix A for more information). It should be noted that most

echograms shown in figures throughout this thesis are uncalibrated and show S_v values up to 7-9 dB higher than what was observed, due both to their uncalibrated nature as well as an incorrect default calibration gain value being applied in the EK80 software at the time of acquisition (see Appendix A, EK80 Data Calibration, for more information). The EK80 data was not corrected for pitch or roll; most values were less than 1.1° (see Appendix A) which would have little effect on the positioning of the horizontally extensive layers examined here. A depth offset of 8.2 m was added to points extracted from the EK80 data during later analysis (see section 3.2.1) to compensate for the transducer depth below water level; no other elevation changes (changes in draft, tide) were accounted for (see Appendix A for estimates of tide).

The EM122 and EM2040 MBES data were processed and integrated by Martin Jakobsson (Martin Jakobsson, personal communication, February 23, 2017) and provided as a 15 m resolution bathymetric grid (Figure 7 and all figures showing bathymetry unless otherwise noted). Prior to data analysis, the bathymetric surface was down-sampled from 15 m to 38 m using the 'RESAMPLER' application, 'BSPLINE' filter, in QPS FMCommand version 7.8.10 (Figure 27). This was done to compensate for the uncertainty of target positions in the EK80 data – the latitude and longitude assigned to targets by the processing software is that of the transducer position, however the targets detected can be anywhere within the 11° beam. The average scattering layer depth was 195 m, which corresponds to an approximate beam diameter of 38 m.

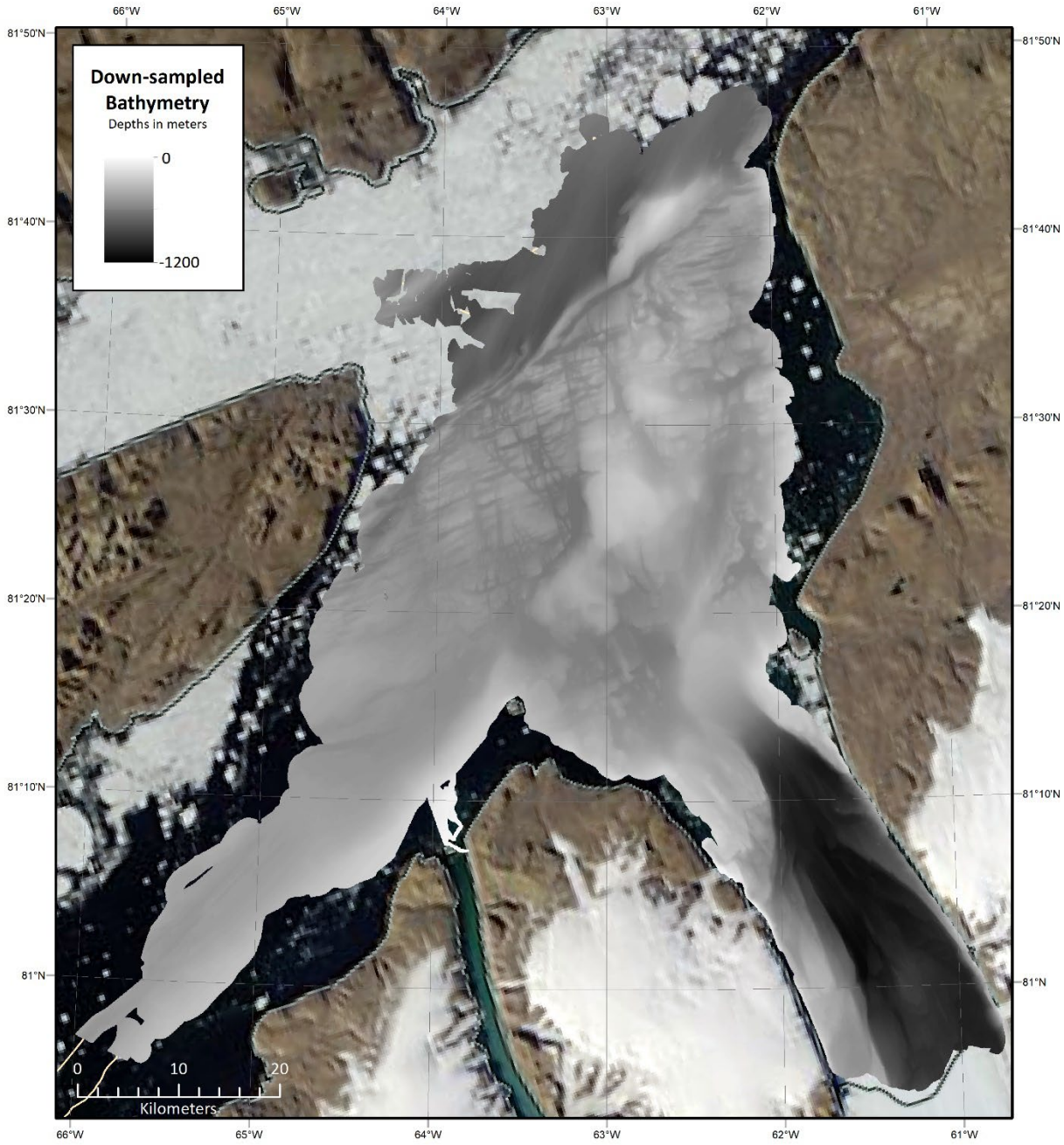

Figure 27: Down-sampled bathymetry used for analysis.

3.1.1.6 Echosounder Calibration

A standard sphere calibration was performed aboard the *Oden* just prior to returning to Thule Air Base on September 1, 2015, following the procedures of Foote et al. (1981). A 64 mm copper sphere was suspended under the *Oden* using monofilament

line and moved through the beam of the EK80. A calibration file was generated in ESP3 for the interrogation of targets in that software. See Appendix A for settings used to generate the ESP3 calibration file.

3.1.2 Environmental Variables

3.1.2.1 CTD Data

During the 2015 Petermann Expedition, a total of 46 ship-based CTD profiles of the water column (Figure 28) were collected in Petermann Fjord and Nares Strait using a Sea-Bird Electronics SBE 911+ integrated CTD and deck unit that sampled temperature, conductivity, pressure, and dissolved oxygen at 24 Hz. Profile 025 was omitted due to pump failures noted in the acquisition log, and another profile (001, the calibration cast), was omitted due to a large number of erroneous values. The remaining profiles were processed using SBEDataProcessing version 7.26.7. Raw HEX files were converted to CNV files using the instrument configuration file generated on the ship; primary conductivity, primary temperature, pressure, depth, raw oxygen, and pump status were extracted for downcasts only. It should be noted that the oxygen values prior to cast 26 were considered questionable by Heuzé et al. (2017) due to issues with the pump, which was replaced after cast 025 and prior to cast 026.

The casts were processed using the parameters suggested for the SBE 911+ in the Seasoft V2: SBE Data Processing Software Manual: a low pass filter was applied to the pressure data, the oxygen sensor values were aligned with the temperature and conductivity values, the files were corrected for thermal mass errors, automated loop editing was applied to remove values under a minimum velocity (when the sensor was

moving back upward), and a wild edit filter was applied to all variables to remove values with high standard deviations. Oxygen saturation in ml/l was derived using the internal SBE 43 calculations. Records where the pump was not functioning (pump status = 0) were manually deleted. The remaining records were smoothed using a 0.5 m vertical bin to create the final processed CNV files.

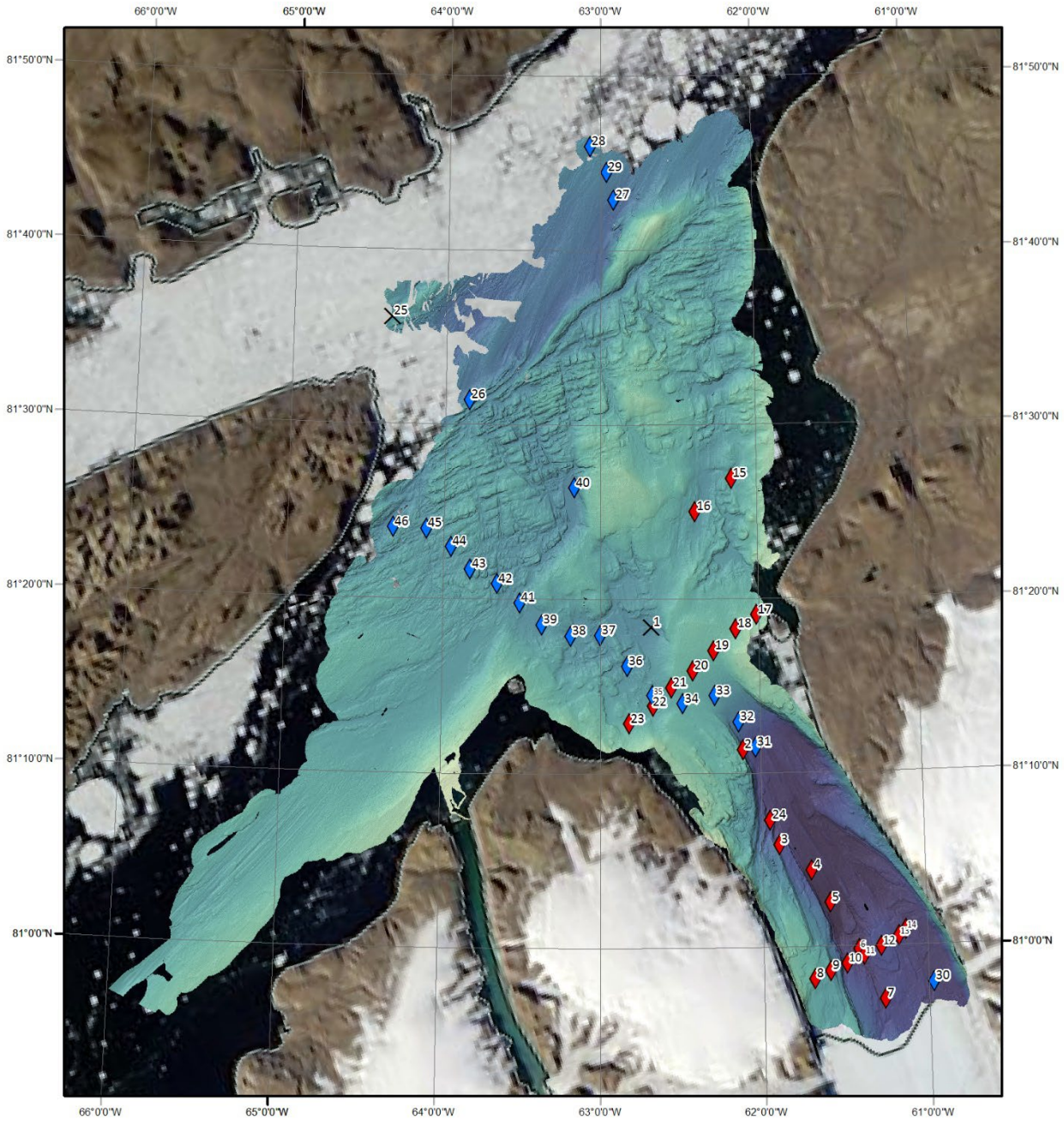

Figure 28: Location of CTD casts (also called 'CTD stations' in the text). A black X indicates a CTD cast that was not useable. Blue diamonds are CTD casts that included reliable oxygen measurements.

In-situ temperature and conductivity were converted to absolute temperature and absolute salinity using TEOS-10 equation of state as implemented in the Gibbs Seawater (GSW) Oceanographic Toolbox Version 3.06.10 for MATLAB (McDougall and

Barker, 2011). Absolute temperature, absolute salinity, and oxygen concentration were plotted relative to depth using MATLAB (Appendix D). Temperature-Salinity (T-S), Oxygen-Temperature (O-T) and Oxygen-Salinity (O-S) plots were generated using the GSW Oceanographic Toolbox in MATLAB (Appendix D).

3.1.2.2 Ship-based Radiation Data

Information about the ambient light levels was collected using a Biospherical Instruments QSR-2150 Photosynthetically Active Radiation (PAR) sensor and was used to provide relative values of light levels across the study area. This instrument was mounted on top of a shipping container located on the bridge roof (Figure 29). The QSR-2150 measures Quantum Scalar Irradiance over the PAR spectral region of 400 – 700 nm (Biospherical Instruments Inc., 2013). ASCII files were generated daily by the ship's technicians that included date, time, uncompensated PAR (in volts), supply voltage, and board temperature every five seconds. PAR values provided were not compensated for dark voltage or for shadows created by the ship itself (due to ship structures and equipment higher than the sensor). The last reported calibration for the instrument was August 5, 2010, lowering our confidence in the absolute values recorded by the instrument. For this reason, we present the data here as normalized PAR, scaled to a range of 0-1; based on the BSRN values in Alert (Figure 30), a reasonable range to associate with these scaled values is 1.5 – 220 W m^{-2}.

Figure 29: Location of the QSR-2150 on the ODEN. Image courtesy of Larry Mayer; sensor location provided by Axel Meiton.

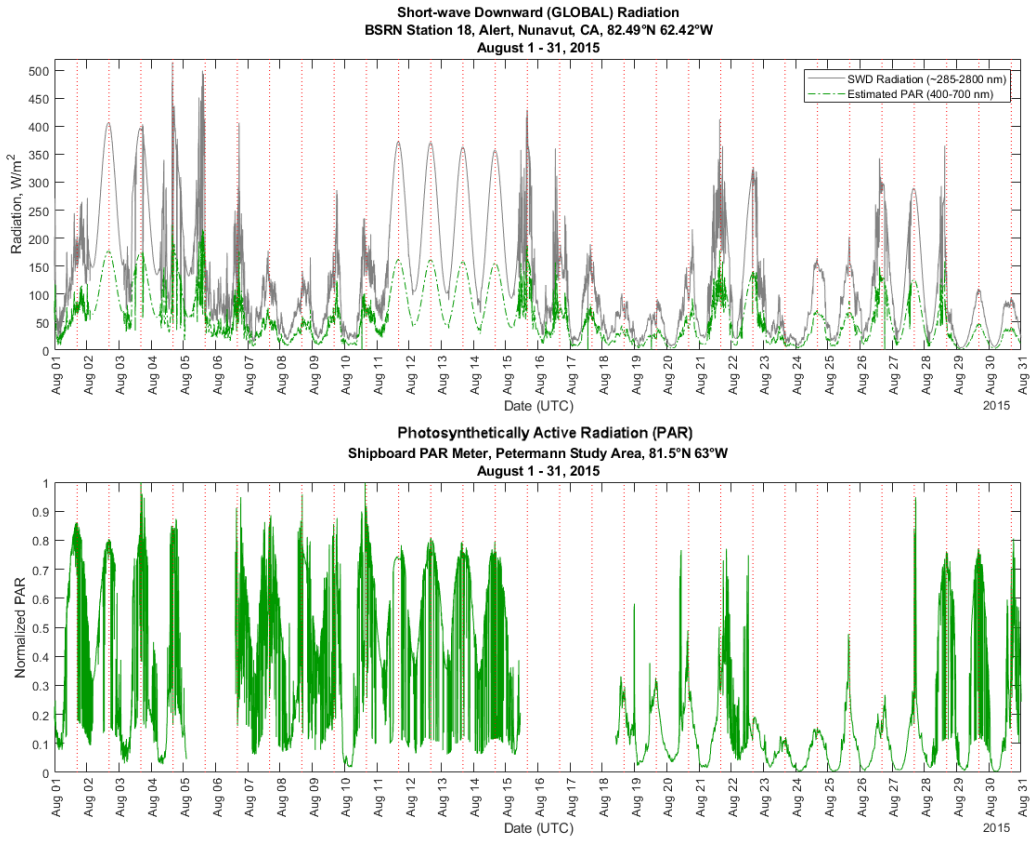

Figure 30: Top, BSRN data for Station #18, Alert Nunavut Canada; the location of the station is shown in Figure 6. The grey line shows the short-wave downward (SWD) radiation in watts m-2, the green line shows photosynthetically active radiation (PAR), estimated as 44% of SWD (Moon, 1940). Bottom, normalized PAR data as collected by the shipboard PAR sensor in the study location. Red vertical lines in each graph indicate solar noon. Note that this a repeat of Figure 8.

The insolation data was post-processed using MATLAB. Examination of the full timeseries revealed gaps in the data, lasting several hours to multiple days, which corresponded to empty or incomplete ASCII files (Figure 30). The full time series, therefore, had to be separated into sets that were continuous, and restricted by the dates the ship was in the main study area. This resulted in three separate insolation time series: Period 1, August 2 –August 5 (August 5 incomplete), Period 2, August 6 – August 15 (August 6 and August 15 incomplete), and Period 3, August 18 –August 28 (August 18 incomplete). The raw insolation time series was densely sampled (every five seconds) and had sharp spikes. The spikes may have been caused by changing cloud

conditions but could also have been influenced by the instrument being out of calibration, sometimes in shadow, or other installation or other unknown operational factors. In order to eliminate some of the spikes, new time series were created in MATLAB with the goal of capturing the overall diel pattern light signal. Data were grouped into hour bins, and the mean of each bin was calculated. The mean values per hour were smoothed using the 'SMOOTH' function and resampled to a sample per minute using the 'INTERP1' function (Figure 31 - Figure 33). Given the objective of simply trying to understand whether diel changes in light are related to changes in the depth of the scattering layer, this level of smoothing is a reasonable approach.

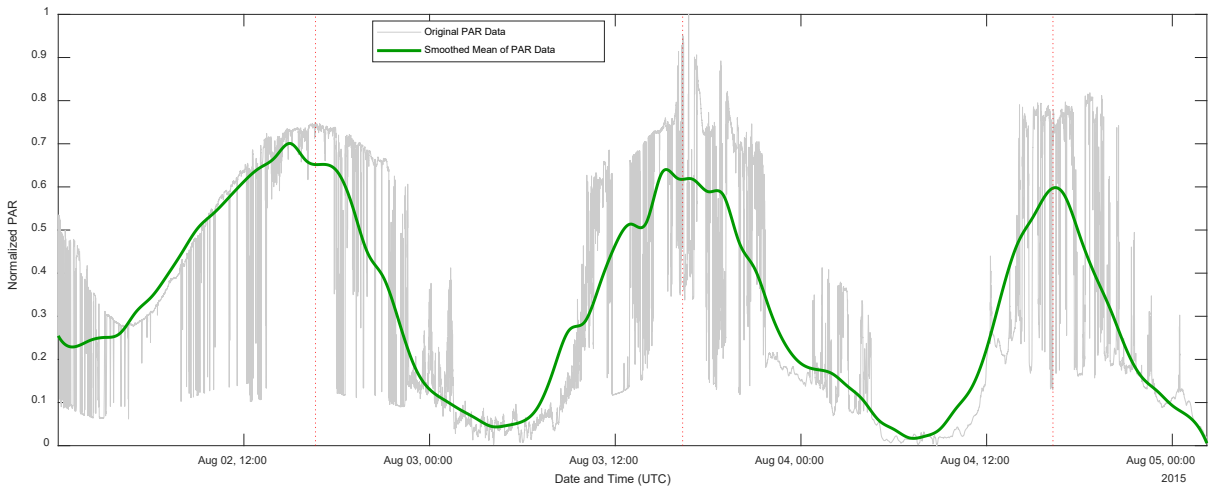

Figure 31: Original and smoothed mean PAR data for Period 1 (August 2 - August 5, 2015). Red dotted lines indicate solar noon.

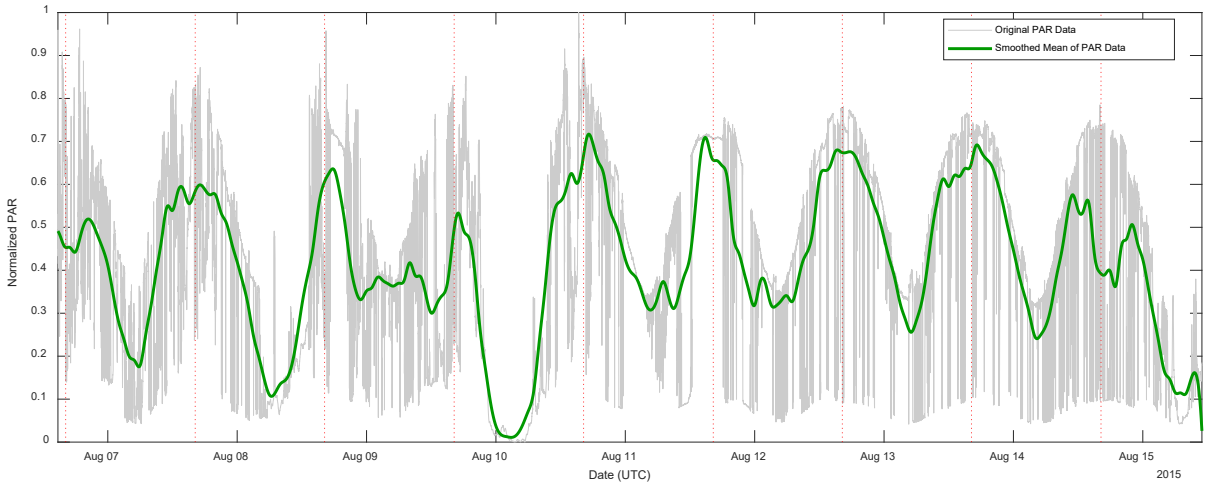

Figure 32: Original and smoothed mean PAR data for Period 2 (August 6 - August 15, 2015). Red dotted lines indicate solar noon.

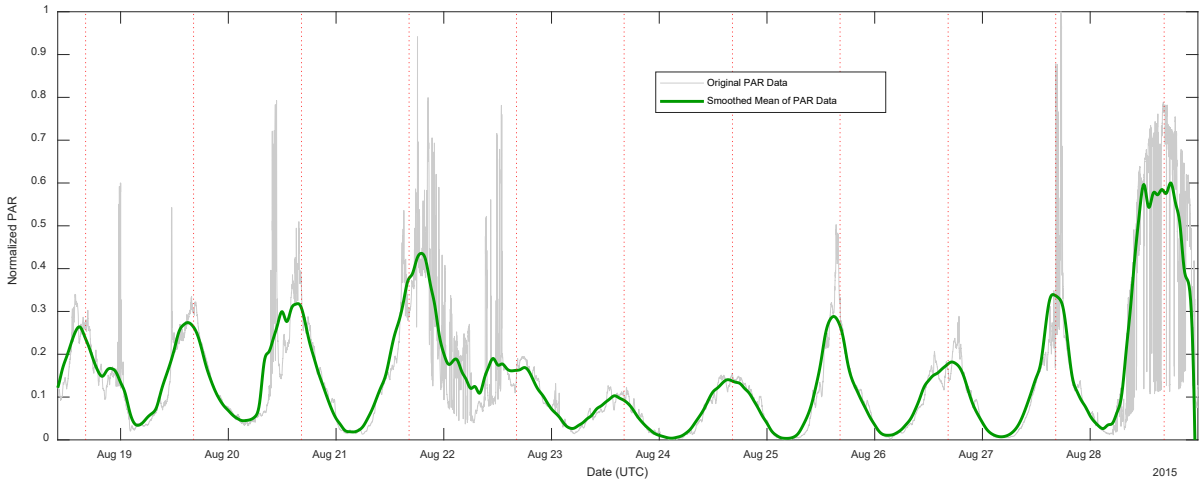

Figure 33: Original and smoothed mean PAR data for Period 3 (August 18 - August 28, 2015). Red dotted lines indicate solar noon.

During processing, it was noted that the PAR values for most of Period 3 were considerably lower than Periods 1 and 2. This appears to be related to increased cloud cover during that time period (see Figure 139 in Appendix B for satellite images taken during the study period).

3.1.3 K_d(490) Data

The diffuse attenuation coefficient for downwelling irradiance (K_d) is used to estimate light intensity at depth (Austin and Petzold, 1981; Simpson and Dickey, 1981; Lee et al., 2005). K_d is estimated from remotely sensed data by looking at the empirical relationships between K_d and the ratio of water-leaving radiance at two wavelengths as recorded by satellite-based ocean color sensors (Austin and Petzold, 1981; Mueller, 2000; Lee et al., 2005). K_d(490) looks specifically at light of wavelength 490 nm. For this project, we are using K_d(490) estimates derived from satellites bearing ocean color sensors as an indication of the relative turbidity in the water column and how it changes across the study area. Anecdotally, the water clarity in the fjord was less than that in Hall Basin and Nares Strait. This is in line with the increased glacial sediment load expected in Petermann Fjord and fjord outflow waters and appears to be corroborated by satellite imagery from the study period (Figure 34).

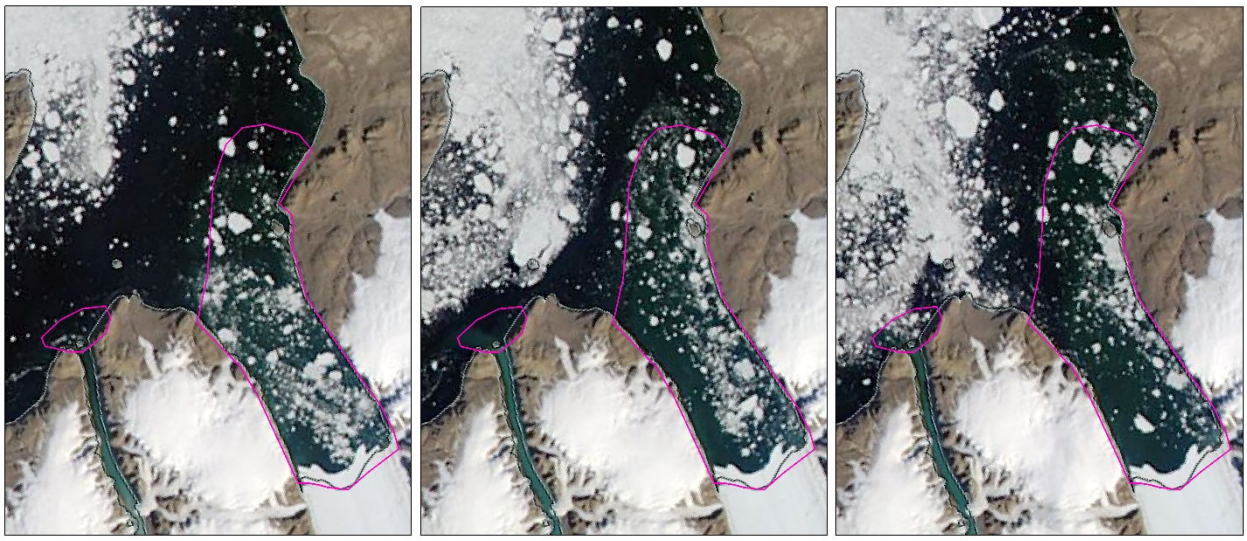

Figure 34: MODIS Aqua image from August 11, 12, and 13 2015, downloaded from NASA Worldview (https://worldview.earthdata.nasa.gov/). The pink line roughly outlines changes in water color between Petermann Fjord and a second smaller outlet fjord (Bessel Fjord) and Hall Basin, likely an indication of increased sediment load/turbidity and reduced water clarity that varies somewhat over time. Projection is WGS 84 UTM 20N.

The coverage provided by the K_d(490) products for this region during the study period was relatively sparse, due to the challenges of working in the Arctic – less satellite coverage compared to lower latitudes, mobile ice, extensive cloud cover, etc. (see Figure 139 in Appendix B and Figure 140 - Figure 145 in Appendix C for images of daily cloud cover and K_d(490) coverage). Two datasets were found to have the best coverage for this region. The European Space Agency (ESA) Ocean Colour – Climate Change Initiative (OC-CCI) dataset ("Ocean Colour Climate change Initiative dataset, Version 3.1") is a seamless integration of ocean color data from SeaWiFS, MERIS, MODIS Aqua, and VIIRS sensors at 4 km resolution (Grant et al., 2015). This dataset provided good overall month-binned coverage for August 2015. NASA's Ocean Biology Processing Group (OBPG) MODIS Terra dataset (NASA Goddard Space Flight Center, Ocean Ecology Laboratory) provides K_d(490) for that sensor at 4.6 km resolution and also had good month-binned coverage, including some additional coverage in

Petermann Fjord. Daily and binned monthly mean datasets were downloaded from their respective websites in NetCDF format. The NetCDF files were converted to ArcGIS GRID format and clipped to the study area extent for review in ArcMap.

3.2 Data Analysis

3.2.1 Determining Scattering Layer Presence and Depth

Water column backscatter timeseries files in generic water column (GWC) format for each EK80 line were loaded individually in FMMidwater for visualization and review (Figure 35). The Simrad RAW files were also reviewed in Echoview and, when necessary, ESP3. In Echoview, Mean Volume Backscattering Strength (S_v) pulse-compressed wideband echograms were generated for small contiguous groups of files (Figure 36); in ESP3, S_v echograms were generated. These echograms were used as a visual aid to selecting the scattering layer in FMMidwater; because multiple lines can be merged into one continuous echogram, they provided additional context that greatly aided scattering layer selection. GWC files and Echoview echogram images were generated for every file in the primary study area.

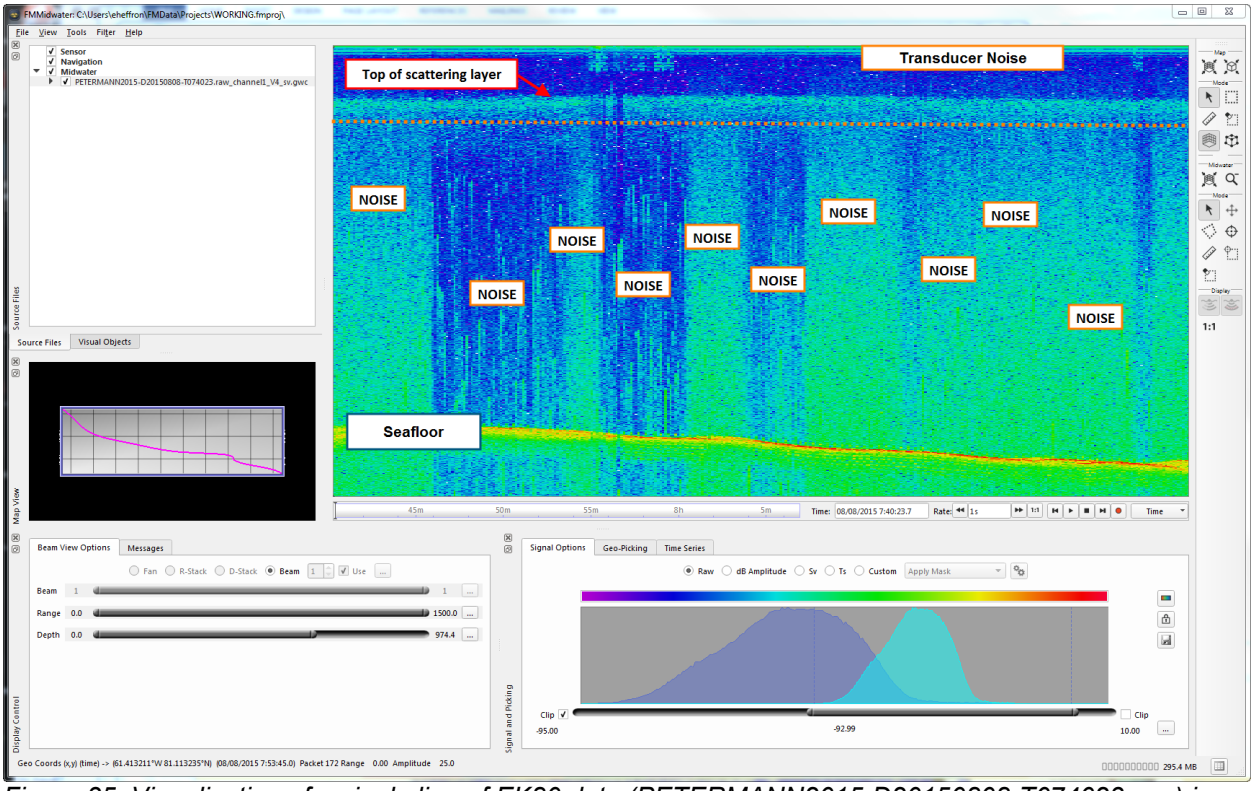

Figure 35: Visualization of a single line of EK80 data (PETERMANN2015-D20150808-T074023.raw) in FMMidwater. The scattering layer is visible in the top third of the image; it starts to dissipate under the dotted orange line. The seafloor is the strongest reflector and shows up as a yellow to red line in the echograms (labeled Seafloor). Unless the Oden was drifting, there was often quite a lot of noise in the water column (labeled NOISE). There is also a predictable band of noise in the top 20 m, known as the "transducer ringdown", labeled Transducer Noise. The data is colored by uncalibrated mean volume scattering (S_v); note that the signal option in the image says "Raw", but this was due to a software bug.

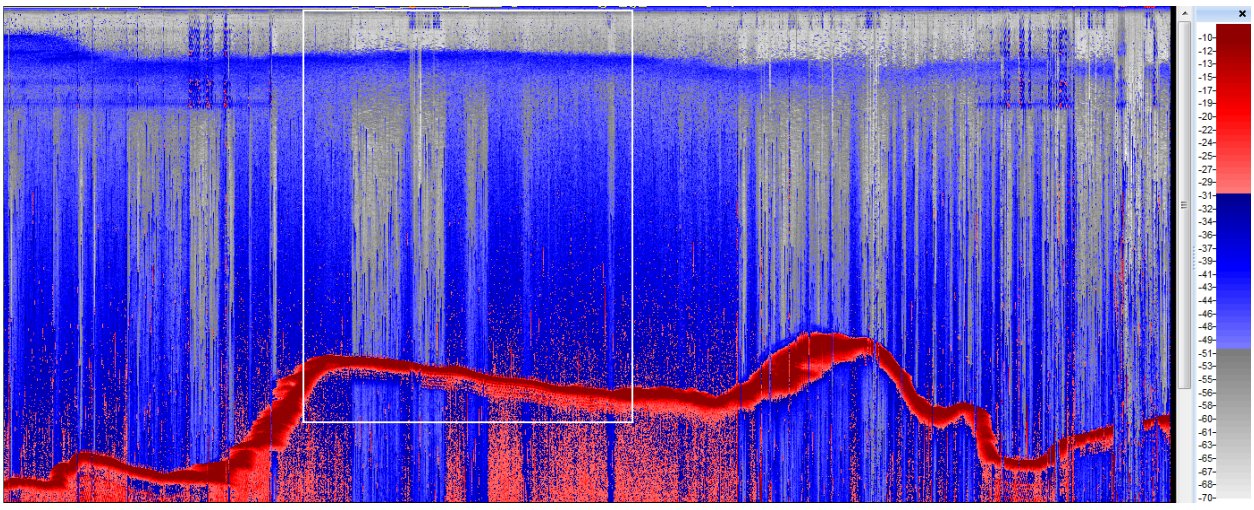

Figure 36: Visualization of five lines of EK80 data (PETERMANN2015-D20150808-T070926.raw through PETERMANN2015-D20150808-T082623.raw) in Echoview as an uncalibrated S_v pulse-compressed wideband echogram. Here, the seafloor shows up as a very strong red line. The white box indicates the line shown in Figure 35. The data is colored by uncalibrated S_v.

Each file was visually scrutinized using both FMMidwater and Echoview. When a scattering layer was detected, the FMMidwater Geo Pick tool was used to manually click along the top of the scattering layer (Figure 37), generating a table of latitude, longitude, range, amplitude (in S_v) and time for the selected points. The values in this table were exported in ASCII format for each line. Additionally, an ArcGIS feature dataset of the EK80 track lines was attributed as to scattering layer presence. EK80 lines with a visible scattering layer in any portion of the echogram were attributed as TRUE (scattering layer present).

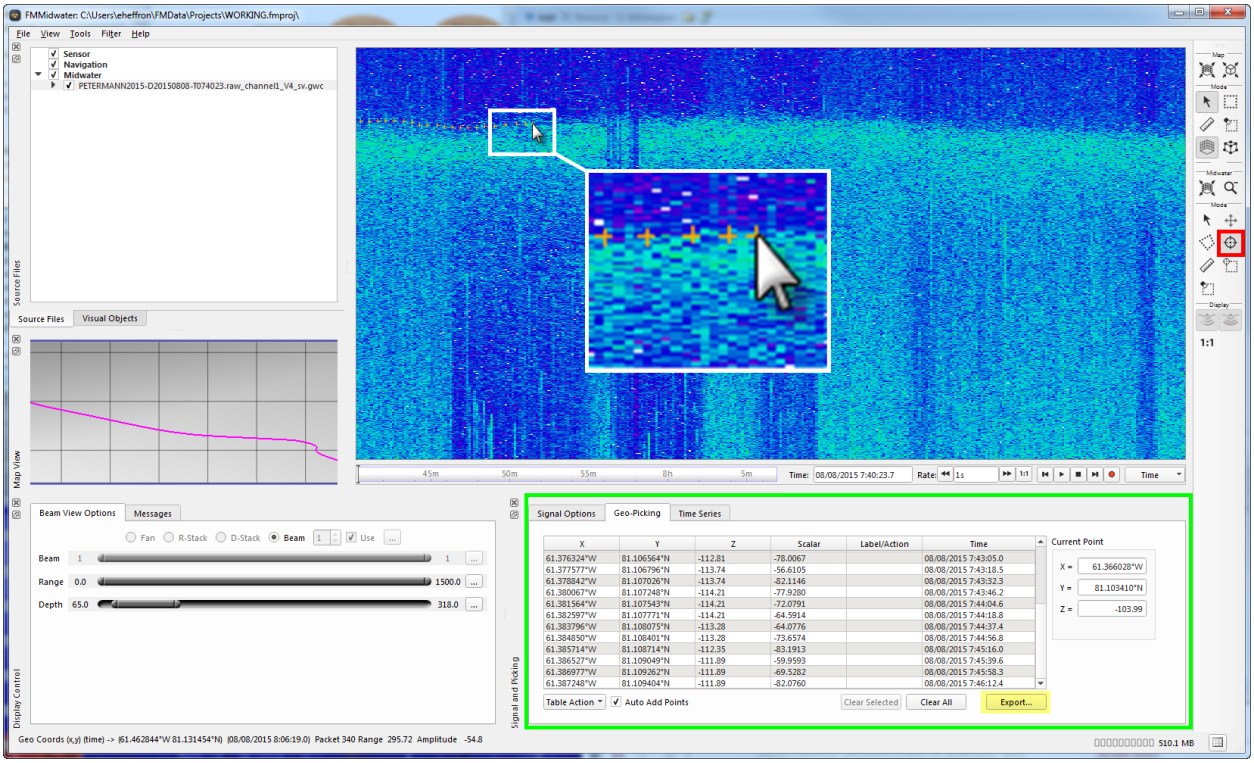

Figure 37: Picking the top of the scattering layer in FMMidwater. The Geo Pick tool (red box) was used to digitize the top of the layer, automatically populating a table with the latitude, longitude, and depth of the picks (green box) that was then exported to ASCII (highlighted in yellow).

Unequivocal identification and selection of the scattering layer was often hampered by data quality. In cases where no scattering layer was identified, it is possible that no coherent scattering layer was present or organisms were too diffuse,

but in some situations it could also be possible that a scattering layer was masked by noise. If there was no visible scattering layer and no indication of a scattering layer in previous or following echograms, these lines were attributed as FALSE (scattering layer not present). In some situations, an identifiable scattering layer in one line of EK80 data was seen to ‘disappear’ into noise for an extended period that included the following line. In these situations, the following EK80 line was attributed as UNKNOWN. Similarly, selecting the top of the scattering layer was often made more difficult by noise and interference; if there was some visible indication of a scattering layer but selecting it was too difficult, the layer was attributed as POSSIBLE (scattering layer possibly present). Images documenting these issues are provided in Appendix A.

There was also some question as to what level of scattering or grouping should constitute a “scattering layer”. Anytime it appeared that there was a mass of targets causing scattering, even if the target strength was quite low, the line was deemed to have a scattering layer. Example images showing the various levels of signal characterized as scattering layers are provided in Appendix A.

ASCII files were batch imported into ArcGIS. There, the Field Calculator tool was used to add an offset of -8.2 m to scattering layer points to compensate for transducer depth. The scattering layer points were binned at 10m intervals and colored by depth. The scattering layer points with applied transducer offset were also re-exported to ASCII files for other analysis documented below.

3.2.2 Bathymetry Analysis: Scattering Layer Depth vs. Bathymetric Depth and Slope

Correlation analysis was used to determine the linear dependence of the scattering layer depth on changes in bathymetry, specifically bathymetric depth and slope. The QPS Fledermaus version 7.8.10 ‘Calculate Slope’ tool, ‘Fitted Plane’ algorithm, was used to generate a grid of slope values for the 38 m bathymetric surface (Figure 38). The Esri ArcGIS Desktop version 10.7.1 ‘Extract Values to Points’ tool was then used to extract the slope and bathymetric grid values that corresponded to each scattering layer pick.

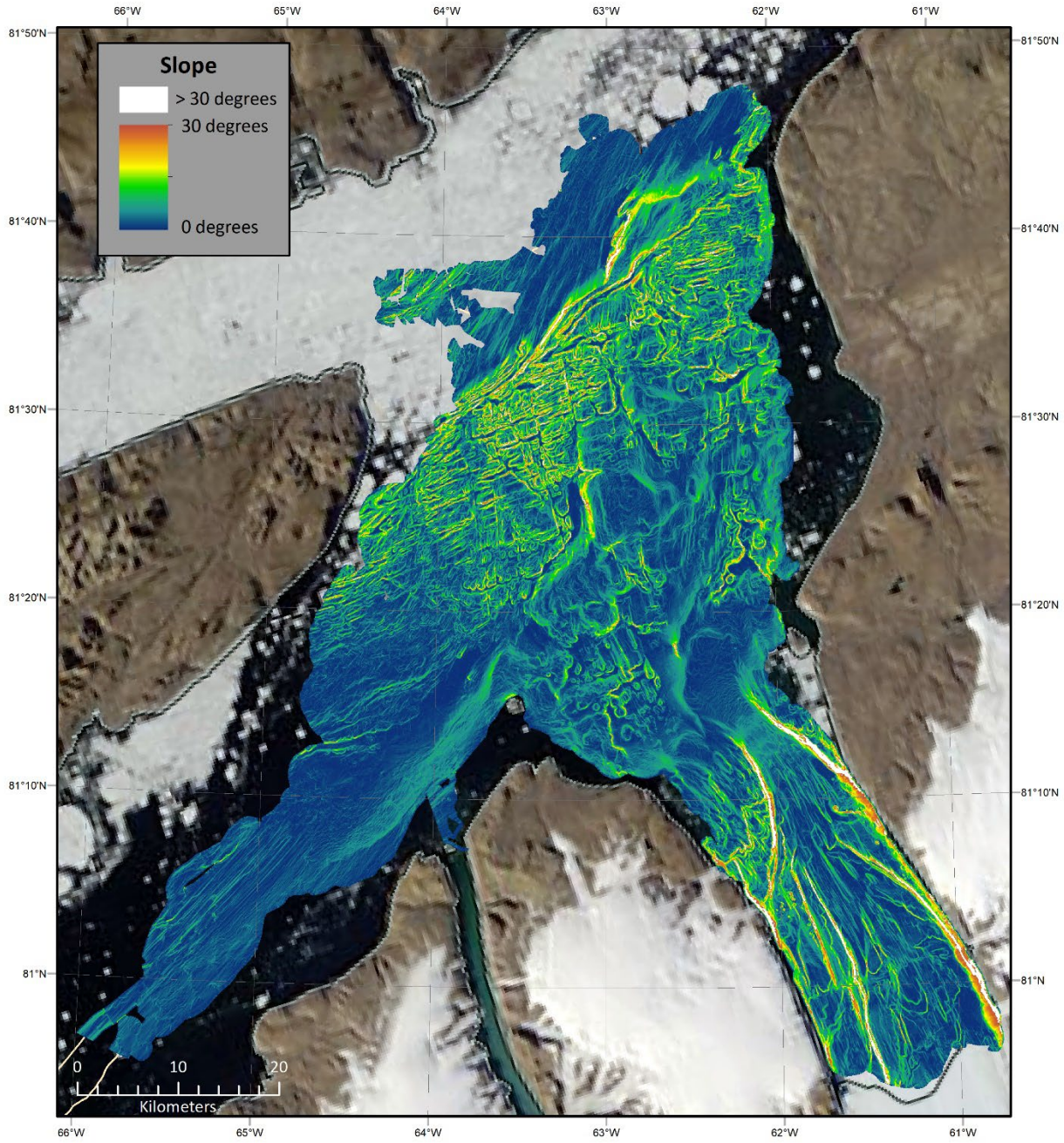

Figure 38: Bathymetric slope. Slope values ranged from 0 to 73 degrees. Mean slope for the study area was 5 degrees, and the majority of slope values were less than 30 degrees. Slopes greater than 30 degrees are shown in white. Projection is WGS 84 UTM 20N.

The MATLAB 'CORRCOEF' function was used to generate the Pearson's correlation coefficient (R) as well as the significance of the coefficient of correlation (P) for two variables per run: the scattering layer depth vs. the bathymetric depth, and the scattering layer vs. bathymetric slope. R is an indicator of how well the points in variable

x and variable y fit a straight line, with values of +/-1 indicating perfect correlation (x, y follows a straight line) and a value of 0 indicating no correlation (x, y have little or no tendency to lie on a straight line). P values less than 0.05 indicate that the correlation coefficient is significant and can be interpreted.

3.2.3 Statistical Analysis: Scattering Layer Depth vs. Ship-Based Radiation Data

Correlation analysis utilizing the MATLAB 'CORRCOEF' function was used to determine the linear dependence of the scattering layer depth on the ambient light levels measured with the shipboard PAR meter. For Period 1, only a single short section of data (< 62 minutes) was found to contain a scattering layer; this was too short to determine a diel pattern in the scattering layer depth, so no further processing was done for that time series. For the remaining two periods, the correlation was run twice. For the first run, all scattering layer points for that time period were used. For the second run, the scattering layer was divided into two regions – 'fjord influenced', and 'basin'. Polygons defining these regions were digitized using MODIS Aqua satellite images from August 11-13 where a change in water color was visible between the fjord and its primary outflow region, and the rest of the basin (Figure 39). The scattering layer points were extracted for each region based on these polygons.

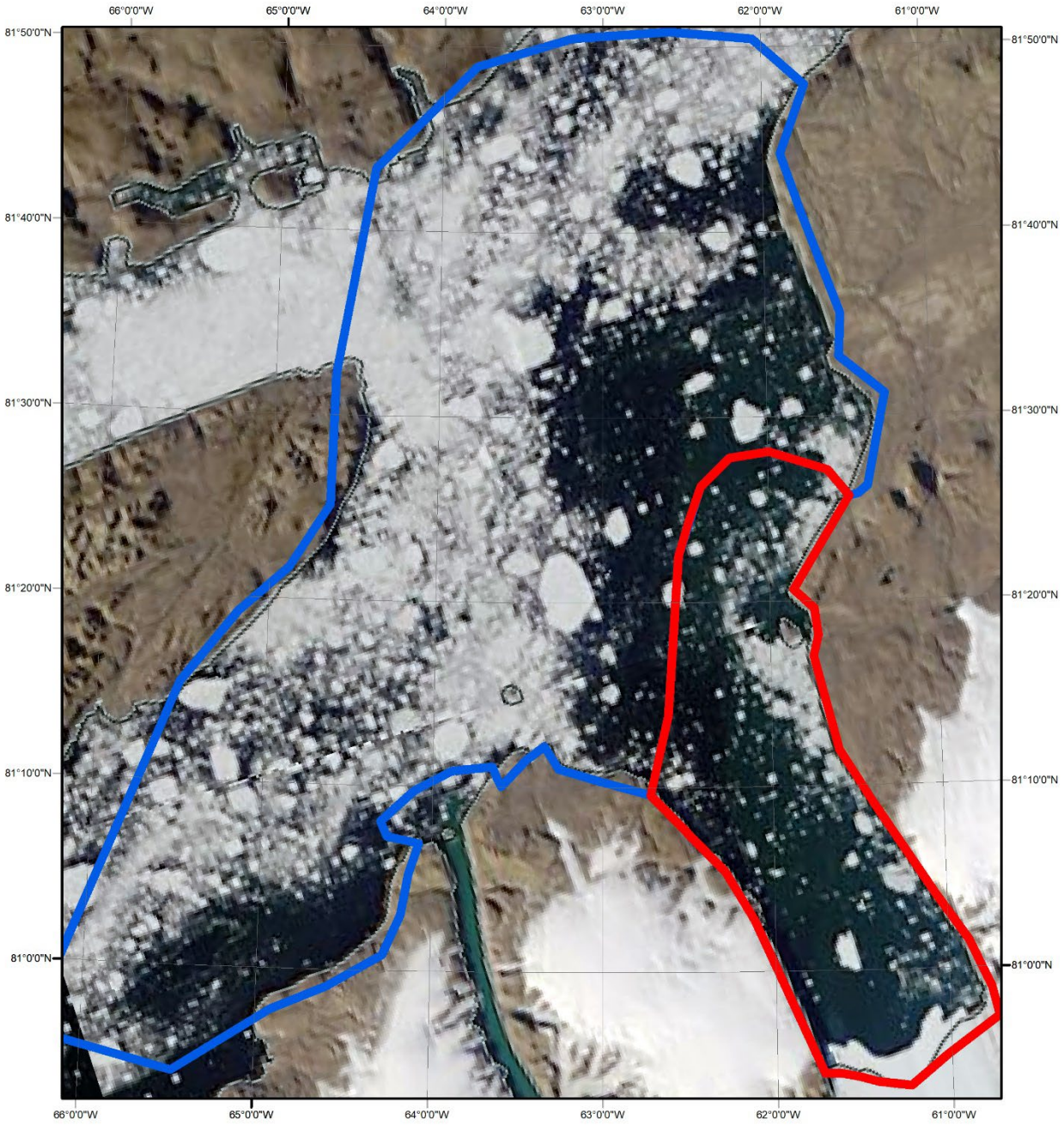

Figure 39: Polygons generated based on differences in water clarity. The red polygon indicates areas with green sediment-laden water, or 'fjord-influenced' locations. The blue area is typically clearer water, the 'basin'. Projection is WGS 84 UTM 20N.

3.2.4 Water Column Clarity Analysis: Scattering Layer Depth vs. Light Attenuation (K_d(490))

The OC-CCI dataset K_d(490) values ranged from 0.9 – 0.43 m^{-1} (Figure 40).

These values were used to clip the colormaps for both datasets in order to facilitate

visual comparison, though a few samples in the MODIS Terra dataset were outside of this range (see Appendix C); the results of this colormap clipping are presented in Figure 41. In addition to visual analysis, the MATLAB 'CORRCOEF' function was used to evaluate the linear correlation between $K_d(490)$ values in each dataset and scattering layer depth, across the entire study area. The ArcGIS 'Extract Values to Points' tool was used to find the $K_d(490)$ from each dataset that corresponded to the scattering layer pick position.

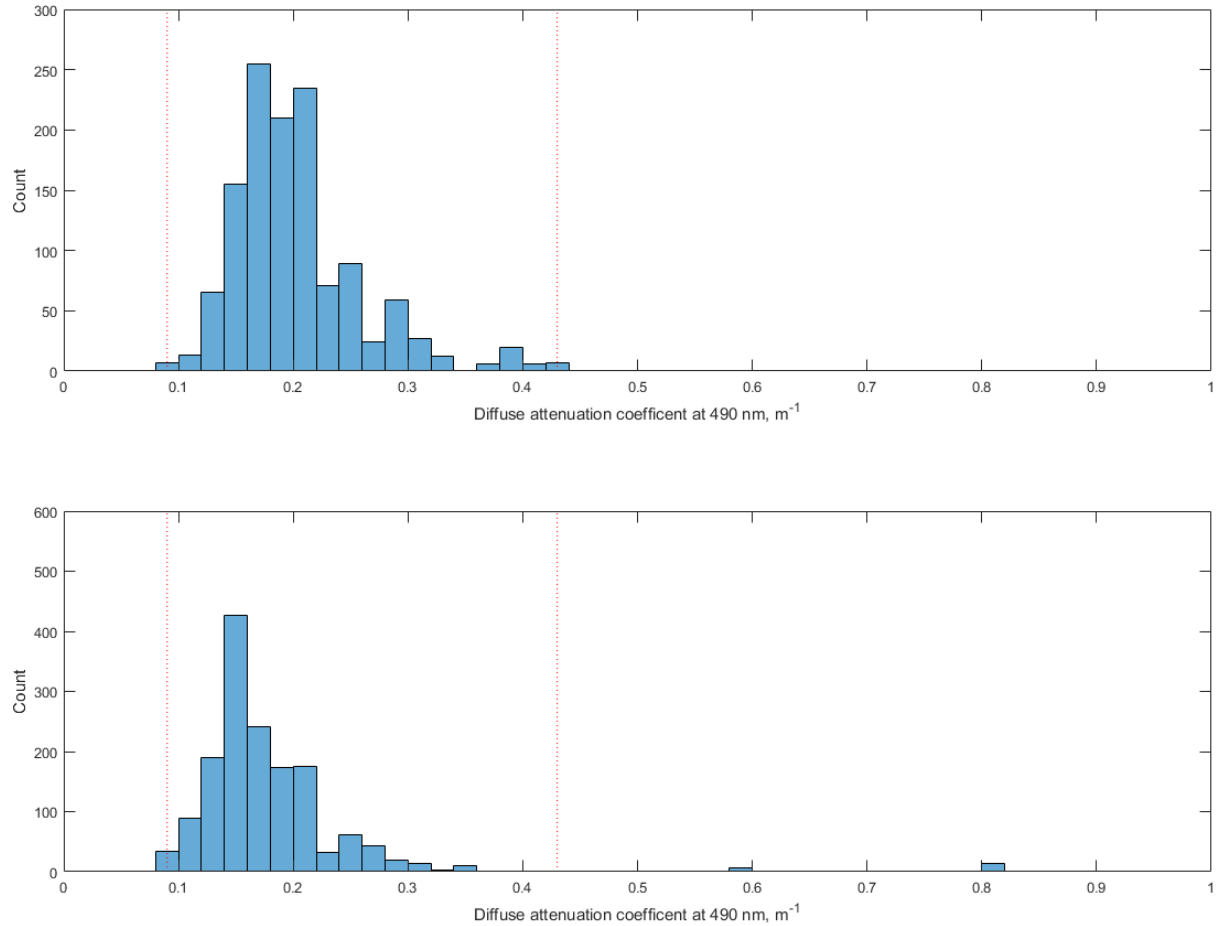

Figure 40: Distribution of monthly mean Kd(490) values, August 2015. Top, the OC-CCI dataset. Bottom, the MODIS Terra dataset. The red vertical lines indicate the minimum (0.9) and maximum (0.43) values used to clip the colormaps for Figure 41.

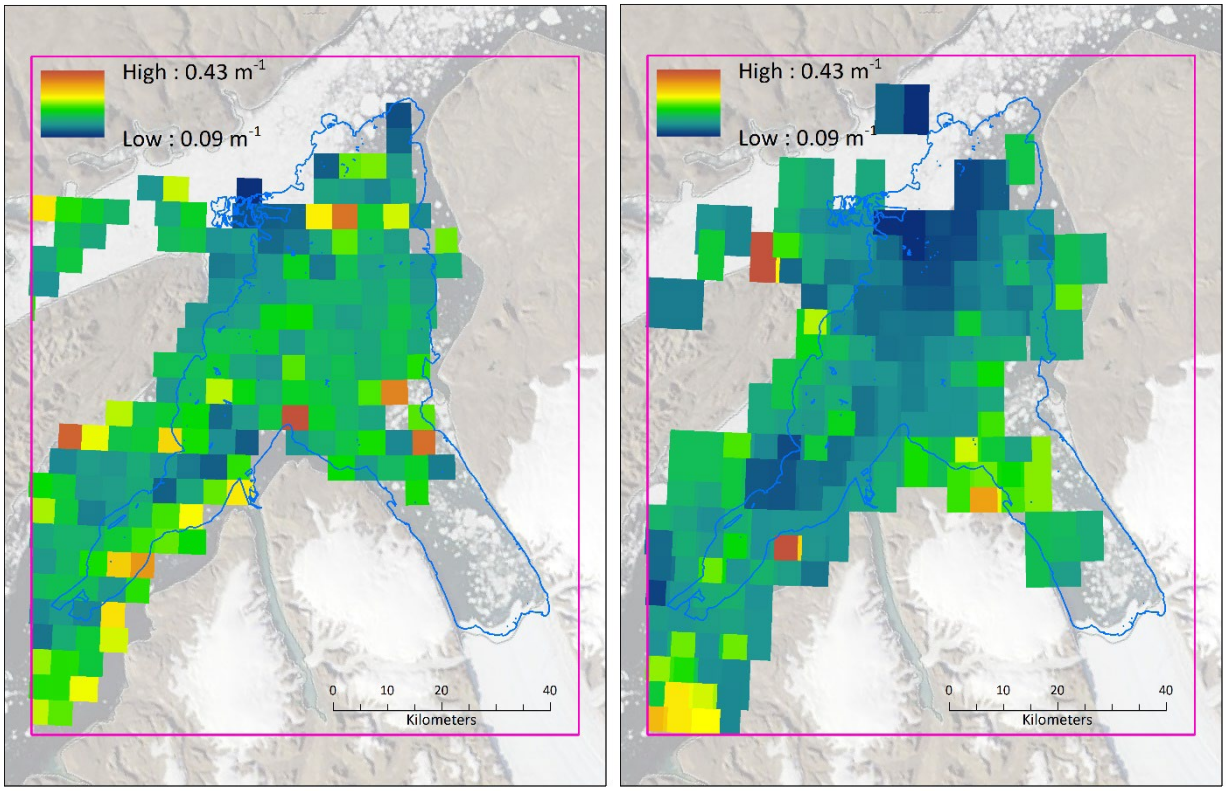

Figure 41: Left, OC-CCI $K_d(490)$ mean values for August 2015; each $K_d(490)$ pixel is 4 km x 4 km. Right, MODIS Terra $K_d(490)$ mean values for August 2015; each $K_d(490)$ pixel is 4.6 km x 4.6 km. The pink box was used to clip the grids to the same extent. The blue polygon shows the extent of the survey (where EK80 data was collected). Projection is WGS 84 UTM 20N.

3.2.5 Oceanography Analysis: Scattering Layer Depth vs. CTDs

The scattering layer extracted from the EK80 data during the time of CTD deployment was compared to the respective CTD for stations 003 – 024 and 030 - 044. For CTD 002, there was no scattering layer present during CTD deployment, however there was a scattering layer present in the EK80 data just prior, within 30 minutes and 220 m of CTD deployment; that scattering layer was used for analysis of station 002. For CTD station 026 – 029 and 045 – 046, no scattering layer was present at the time and location of deployment. The minimum, maximum, and average depth for the top of the scattering layer was overlaid on absolute temperature, absolute salinity, and oxygen

concentration relative to depth. Additionally, all scattering layer picks for each CTD station were overlaid on the corresponding T-S plots for the respective CTD station.

3.2.6 Examination of Scattering Layer Components

ESP3 (version 1.8.1) and Echoview (version 8.0.95.32073 through 9.0.328.35283) were used for more in-depth examination of the scattering layer components. As stated earlier, S_v pulse-compressed wideband echogram images were generated for small contiguous groups of files in Echoview. Echogram images were generated for all files in the primary study area and archived in a visual 'database', organized by day, where they could easily be reviewed and revisited (Figure 42).

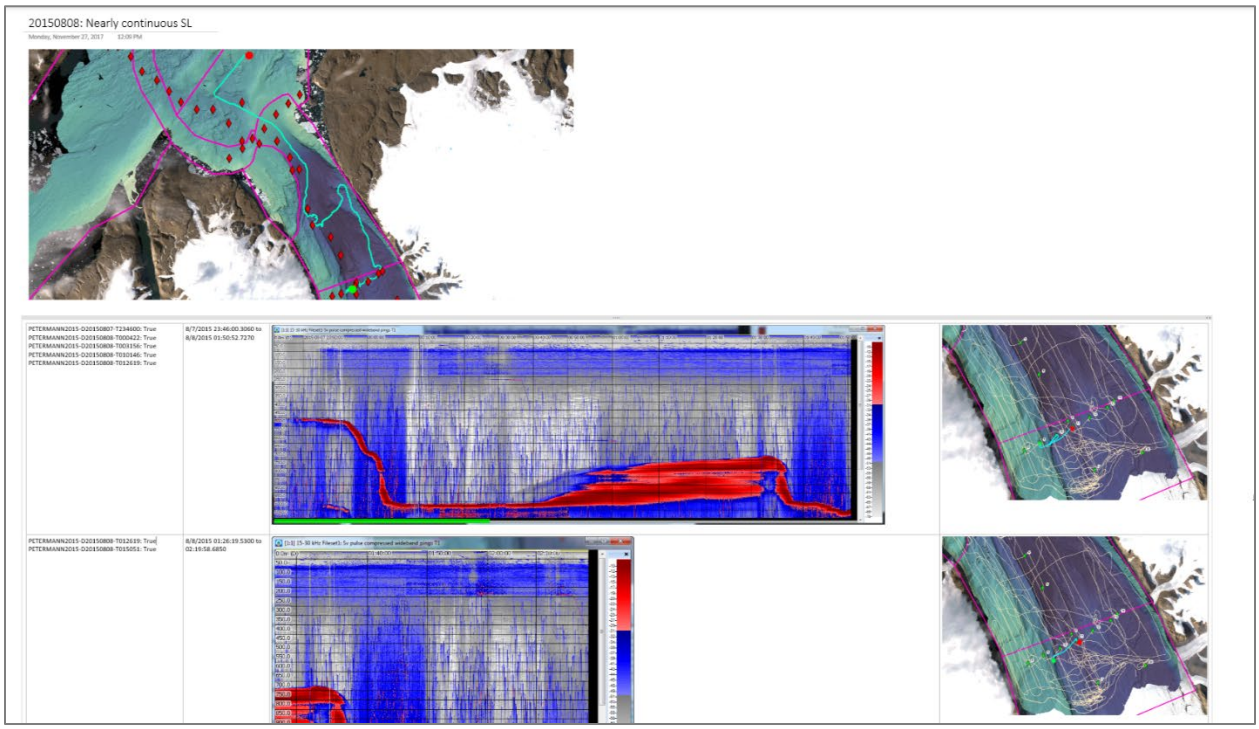

Figure 42: Screen capture of a portion of the echogram image "database" used for archive and review of echogram images. The screen capture shows the top of the database page for August 8, 2015, which includes the final line from August 7, 2015, and the first five lines of August 8. The map at the top is an overview of the trackline for the day, and maps on the right show the location of each echogram section. Echograms in image are not calibrated.

During analysis to determine scattering layer presence, it became evident that locations where the ship speed was quite low (< 1.5 knots) or where the ship was drifting were consistently easier to interpret, as increases in ship speed caused an increase in noise in the water column (see Figure 43 as well as Appendix A for additional examples). ESP3 was used to interrogate the ship speed and flag lines where speed was less than 1.0, 1.2, and 1.5 knots for the entire line, leaving 294 lines covering just less than 84 line km (Figure 44) and located mostly near CTD stations (Figure 45). The number of low-noise lines was further reduced to 174 lines covering just less than 57 line km once lines with no scattering layer were eliminated. The 174 lines subset was used exclusively during further examination of scattering layer components.

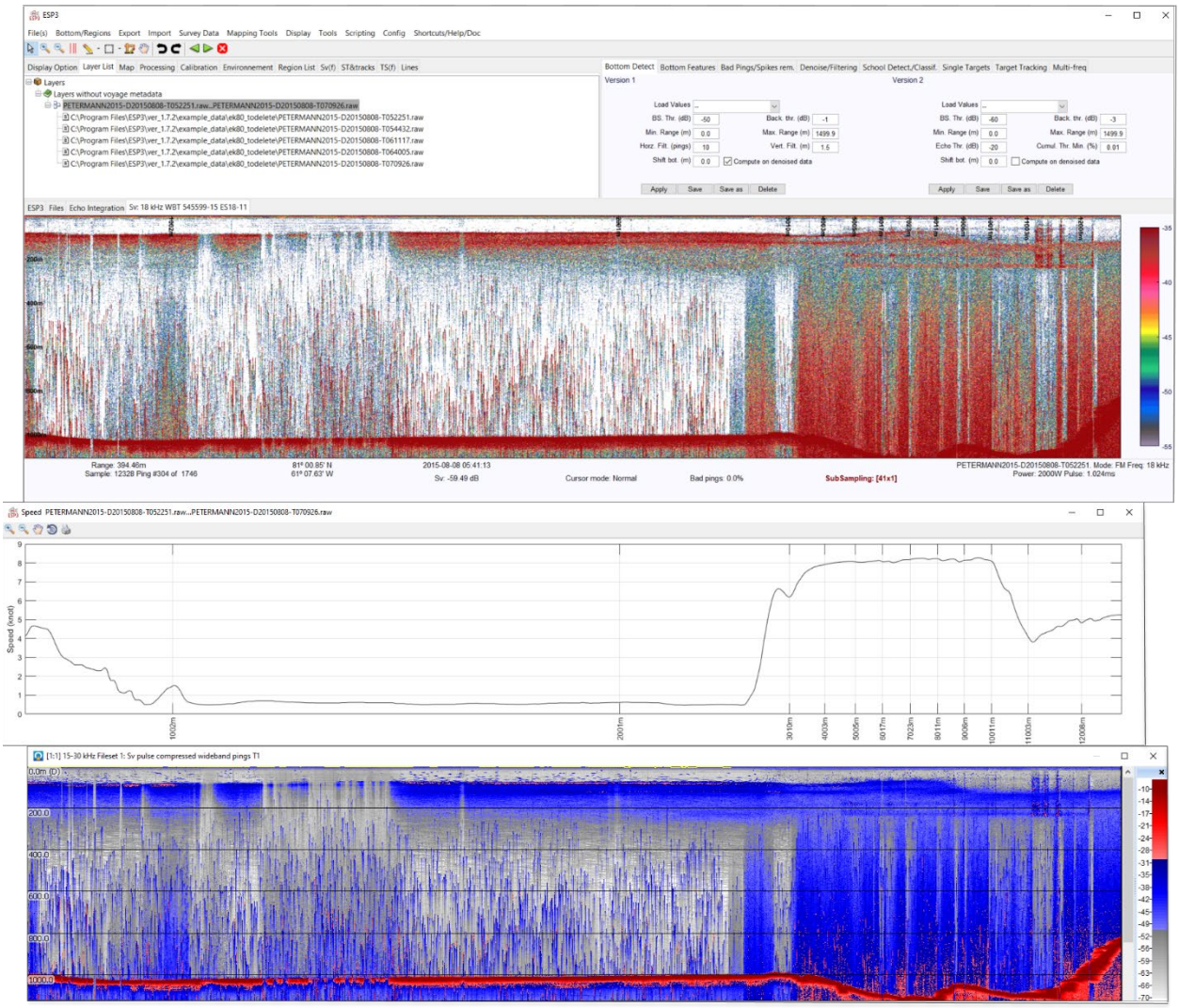

Figure 43: Using ESP3 to interrogate speed of ship during acquisition of EK80 data. The top image is an echogram in ESP3 for five lines. The middle image is the ship speed in knots for those five lines, calculated and plotted in ESP3. The bottom image is an echogram of the same five lines in Echoview. The images are offset on purpose in order to line up the start and end across the three images; note at the speed increases, the noise in the water column also increases. Note that in the top and bottom images, ESP3 and Echoview are set to use different color ramps and signal thresholds to improve visualization. Echograms in image are not calibrated.

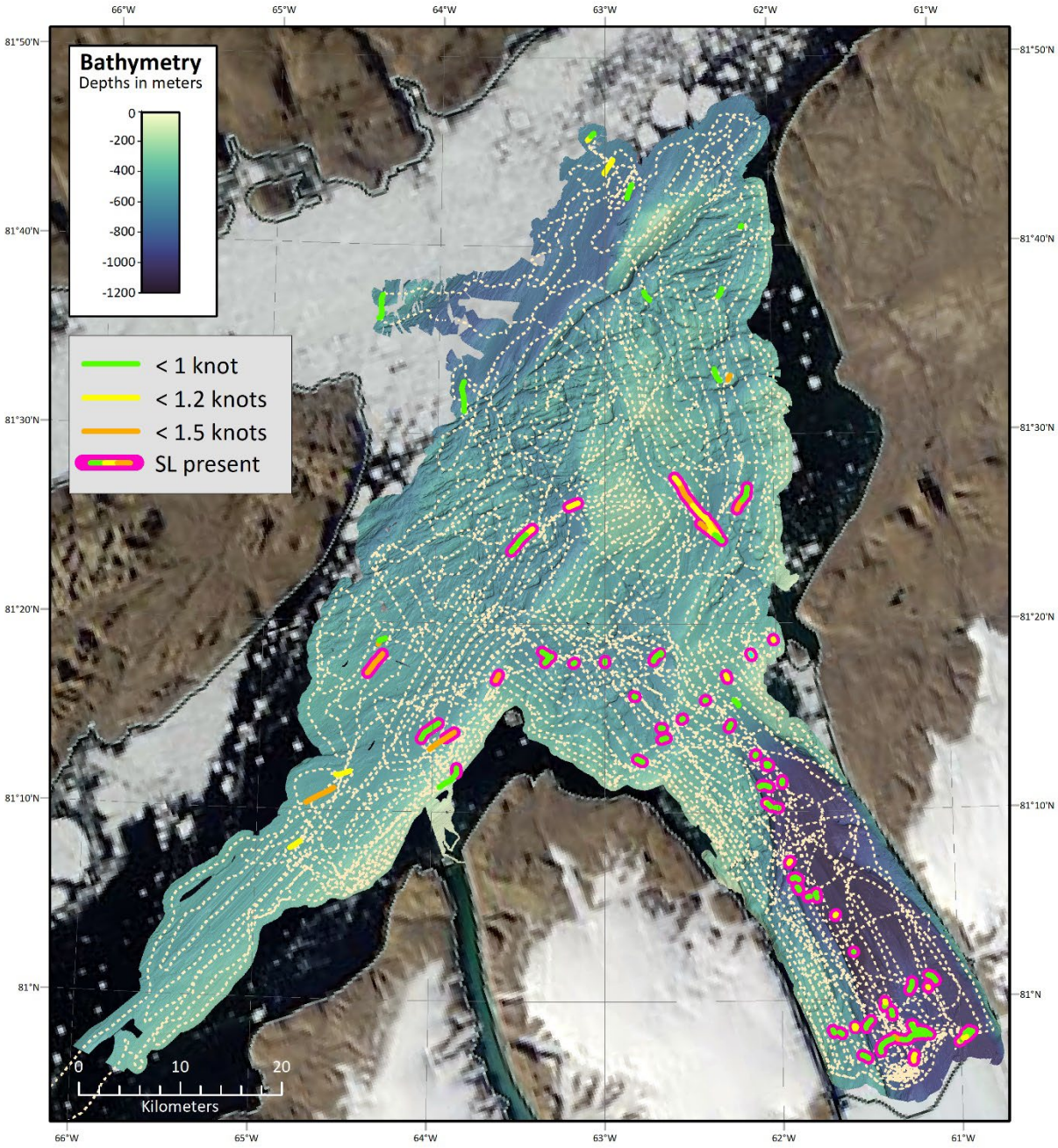

Figure 44: Tracklines where ship speed was less than 1.5 knots (green = less than 1 knot, yellow = less than 1.2 knots, orange = less than 1.5 knots) during data acquisition, with lines where a scattering layer was present highlighted in magenta. The dotted cream-colored line is the full ship trackline. Projection is WGS84 UTM 20N.

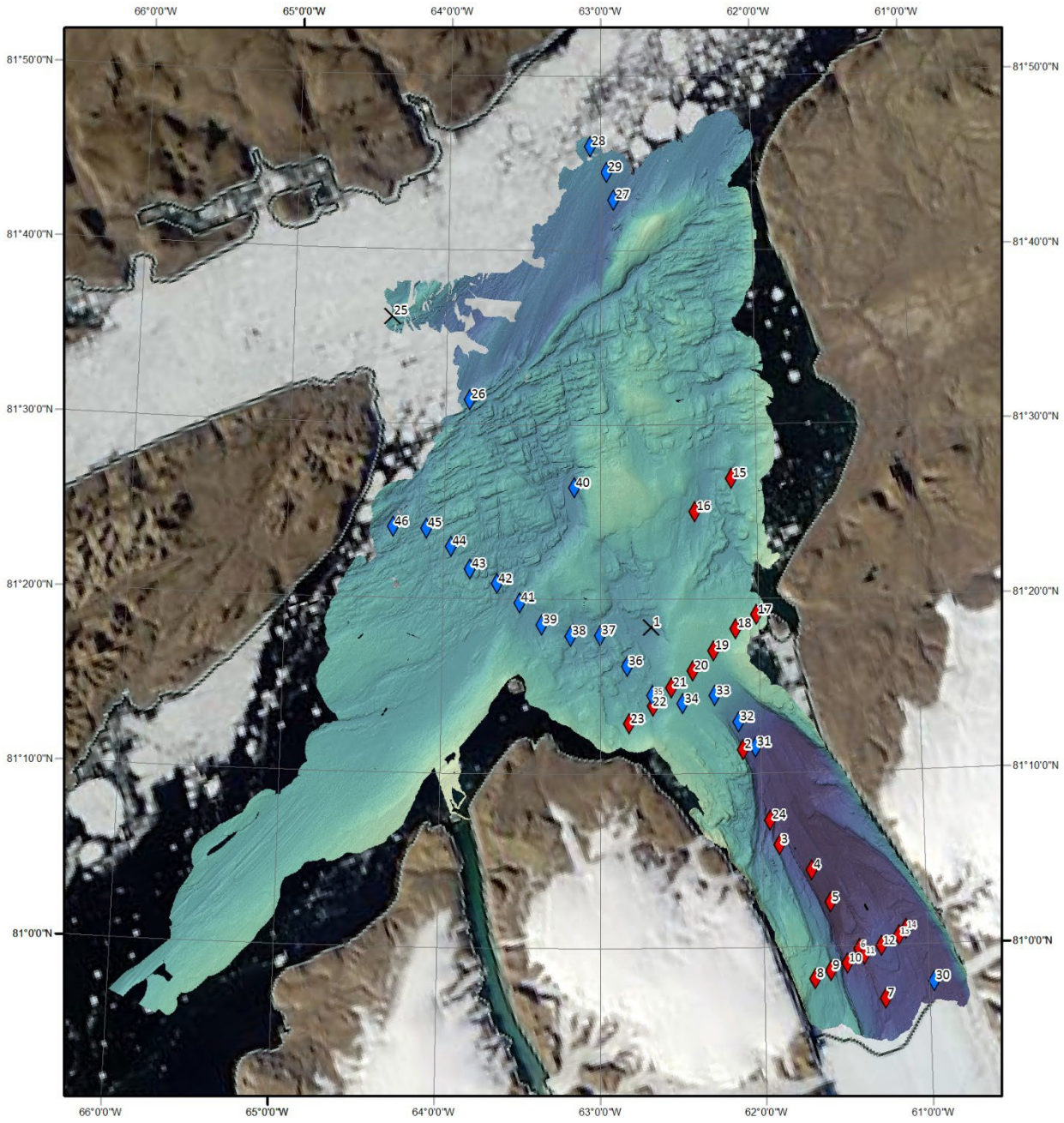

Figure 45: Location of CTD casts (also called 'CTD stations' in the text); note that is a repeat of Figure 28 included here for comparison to location of tracklines used for scattering layer component analysis, Figure 44. A black X indicates a CTD cast that was not useable. Blue diamonds are CTD casts that included reliable oxygen measurements.

ESP3 was then used to select individual targets and sections of the scattering layer from the reduced-speed lines for evaluation of the target strength (TS) and volume

scattering (S_v) across the sonar frequency range. Prior to running TS and S_v analysis, several pre-analysis processing steps were applied to the data (Figure 46). The ‘Bottom Detect Version 1’ default algorithm was applied, and the results reviewed and modified as needed in order to remove returns below the bottom from analysis. The ‘Spikes Removal’ algorithm was run on the file in an attempt to mitigate the contribution of sharp steam valve noise spikes to the signal (see Appendix A for further discussion of noise issues in the data). The water column from the seafloor to 10 m above and from the water surface to 30 m below was characterized as bad data in order to exclude it from analysis, due to high levels of noise associated with transducer ringing and seafloor reverberation. In some locations, the water column used for analysis was further restricted due to anomalously strong targets, high levels of noise, interference, or data gaps (see Appendix E for restrictions applied to each line).

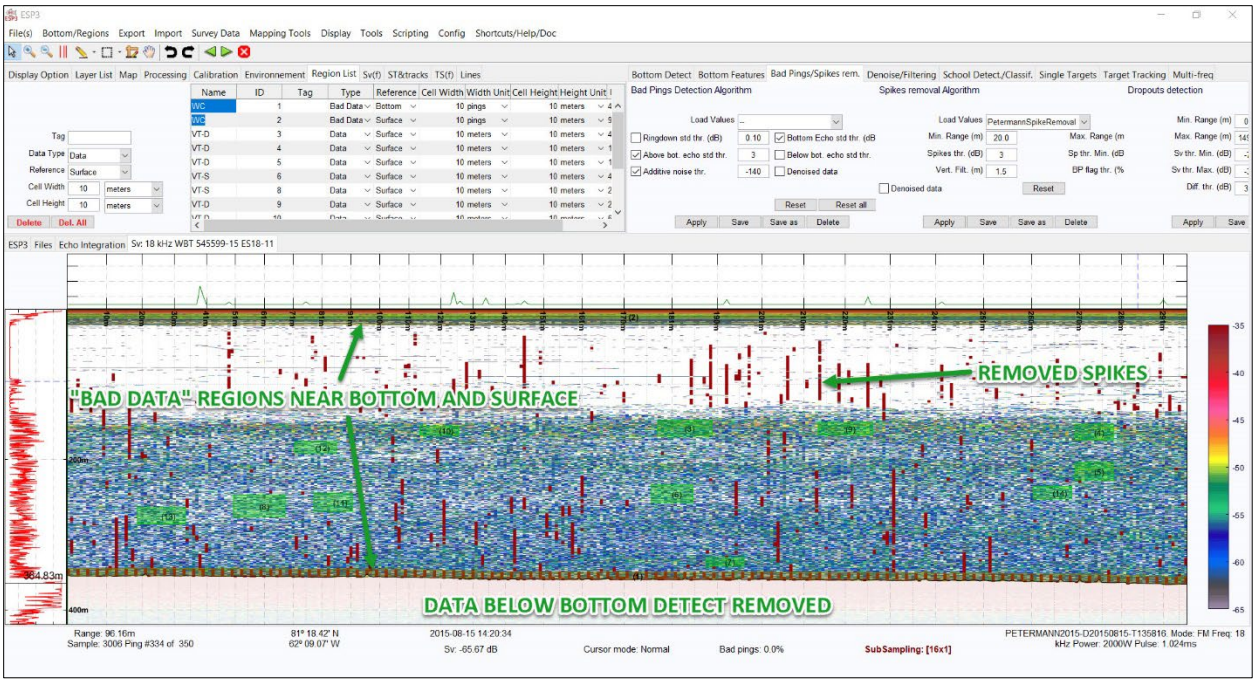

Figure 46: Echogram after pre-analysis processing. The dark red areas are spikes that have been removed. Green boxes are areas selected for analysis, as described in text following this figure. Note that the default gain has been adjusted in this figure as well as in the following two figures to bring reported signal levels closer to the calibrated signal level (see Appendix A for further discussion on the default gain and its impact on echogram images). Echogram is not calibrated.

For S_v analysis, selections were made in the densest part(s) (Figure 47) of the scattering layer as well as in areas within the layer where the density of scatterers appeared to be reduced (Figure 48). Once selections were made, the 'Display S_v Frequency Response' tool was used to interrogate the calibrated S_v values across the frequency range for the volume scatterers (Figure 49), and the results were exported to CSV files.

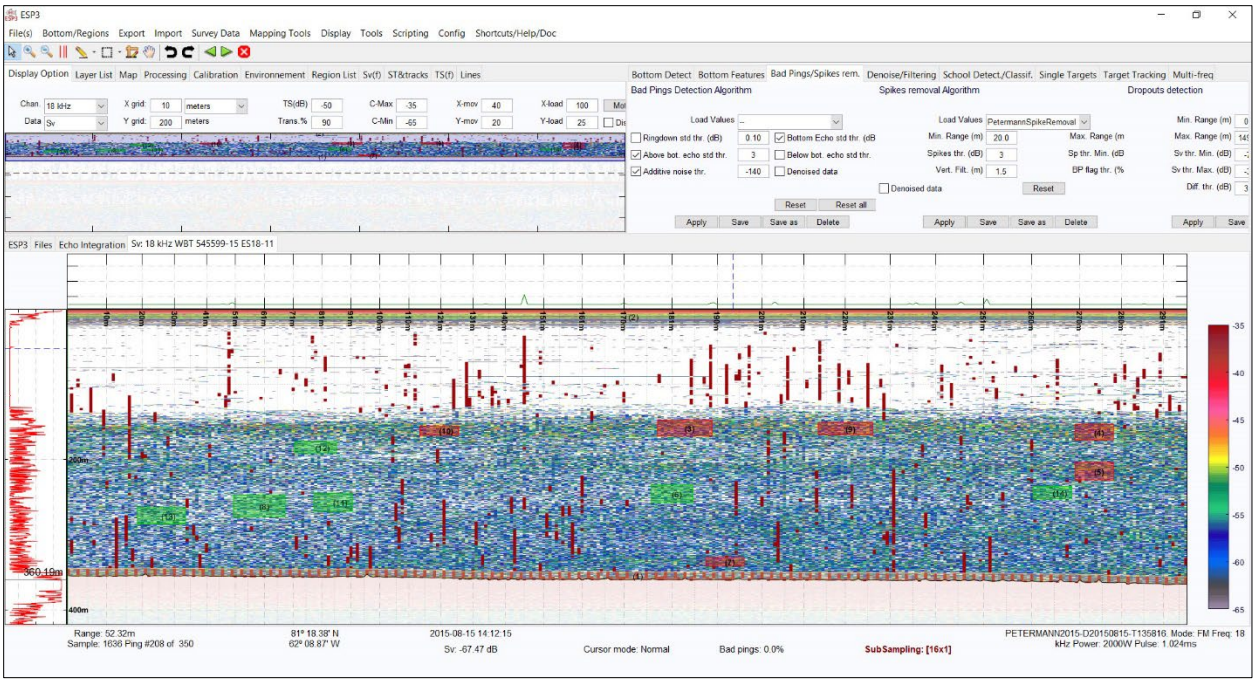

Figure 47: Higher density targets selected for S_v analysis, shown as filled red boxes; filled green boxes are lower density targets. Note that the default gain has been adjusted in this figure to bring reported signal levels closer to the calibrated signal level (see Appendix A for further discussion on the default gain and its impact on echogram images). Echogram is not calibrated.

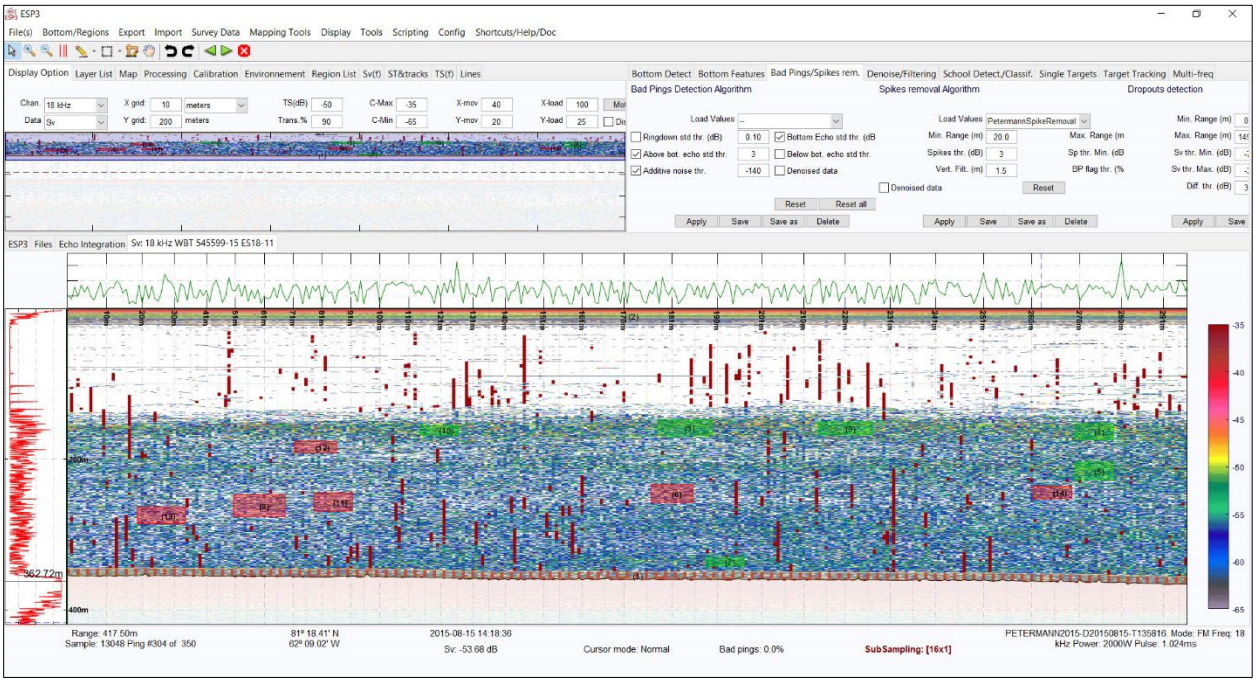

Figure 48: Lower density targets selected for S_v analysis, shown as filled red boxes; filled green boxes are higher density targets. Note that the default gain has been adjusted in this figure to bring reported signal levels closer to the calibrated signal level (see Appendix A for further discussion on the default gain and its impact on echogram images). Echogram is not calibrated.

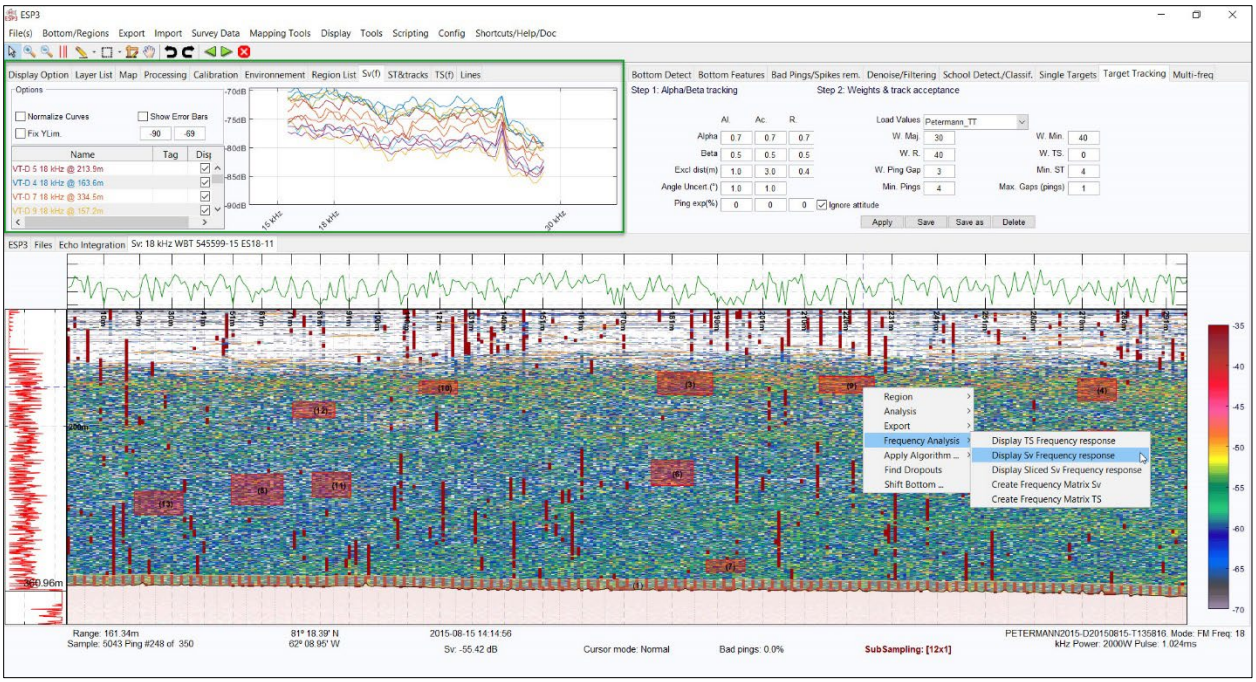

Figure 49: S_v Frequency response for volume targets. The resulting frequency response curves are shown on the upper left, highlighted by the green box. These curves were exported as CSV for each interrogated line. Echogram is not calibrated, but frequency response curves are.

Individual targets were selected from the unrestricted portion of the water column using the ‘Single Targets’ algorithm followed by the ‘Target Tracking’ algorithm, following processing procedures similar to those implemented by Geoffroy et al. (2016). First, the ‘Single Targets’ algorithm was implemented with parameters based on Geoffroy et al. (2016) and others (Parker-Stetter et al., 2009; Benoit et al., 2014) and adjusted slightly for this dataset (Table 1). An initial broad TS threshold was allowed (-100 to 0 dB) to provide an understanding of the range of individual target strengths for the region. This resulted in a Probability Density Function (PDF) with a bimodal distribution (Figure 50). Applying the ‘Target Tracking’ algorithm to these two distributions showed that most tracked targets from the lower TS distribution were concentrated in the water column above the primary scattering layer. In the example below, the lower TS targets were concentrated in the 30 – 160 m depth range (Figure

51), above the main scattering layer (Figure 52). The higher TS targets were also found above the scattering layer, but were more importantly the primary tracked targets within the depth range of the scattering layer (Figure 52). For this reason, the break between the distributions (Figure 50) was used for the minimum TS for the next step of the analysis. It should be noted that this TS value is uncalibrated, see Appendix E for more information on the use of uncalibrated TS as well as further discussion on and examples of why the higher TS distribution was selected.

Table 1: Parameters used for ESP3 Single Targets detection algorithm.

Parameters	**Values**
TS threshold, Maximum (uncalibrated dB)	-10
TS Threshold, Minimum (uncalibrated dB)	-55 to -42
PLDL (pulse length determination level, dB)	6
Minimum Normalized Pulse Length	0.7
Maximum Normalized Pulse Length	1.5
Maximum beam pattern correction (dB)	6
Across Angle Standard Deviation (degrees)	1.0
Along Angle Standard Deviation (degrees)	1.0

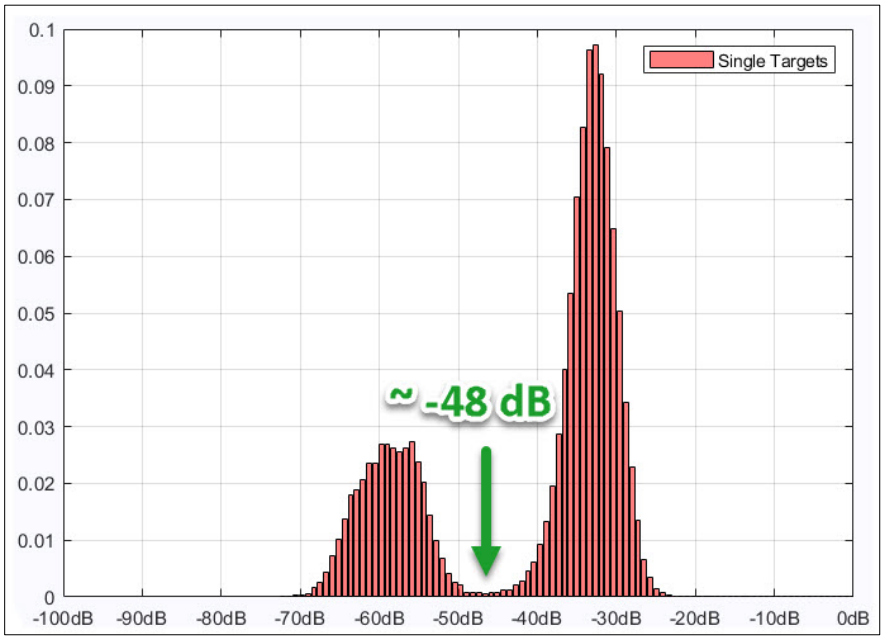

Figure 50: Probability density function for all single targets between 0 and -100 dB. In this example, the break between distributions occurs around -48 dB (uncalibrated).

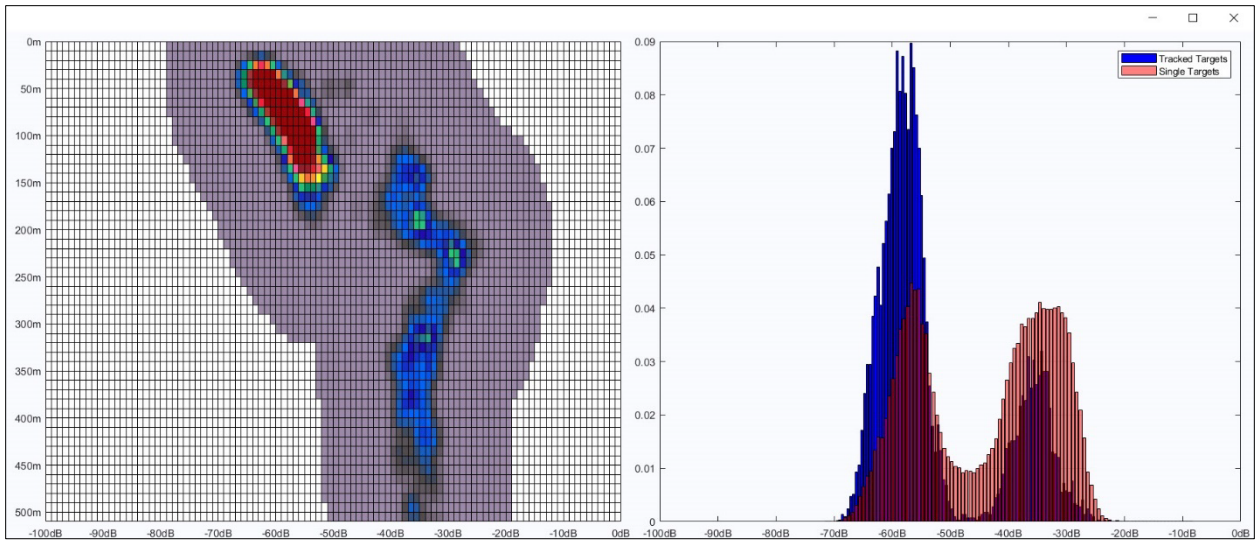

Figure 51: Distribution of tracked targets. The figure on the left shows the depth distribution for the tracked targets, colored by number of tracked targets. The figure at the right shows the results of the single target algorithm in red, and of those targets, those that meet the target tracking algorithm in blue.

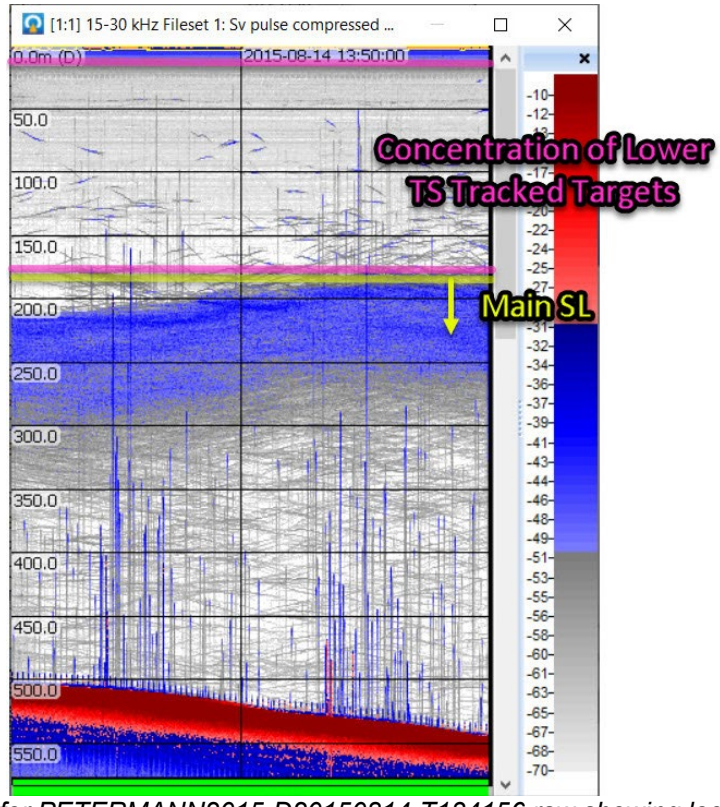

Figure 52: Echogram for PETERMANN2015-D20150814-T134156.raw showing location of main scattering layer compared to location of lower TS tracked targets.

Utilizing the minimum TS from the last step, a second run of the 'Single Targets' detection algorithm was performed (Figure 53). Next, the 'Target Tracking' algorithm

was applied, again using parameters utilized in earlier studies as a starting point (Benoit et al., 2014; Geoffroy et al., 2016) and adjusting them to improve the quality of retained targets (Figure 54; see Table 2 and Table 3 for parameters used). The 'Target Tracking' algorithm only retains single targets that can be tracked over several pings, minimizing the likelihood that single targets identified by the algorithm are from multiple closely-spaced targets (Simmonds and MacLennan, 2005; Geoffroy et al., 2016). The 'Produce TS(f) Curves from tracks' tool was used to produce *calibrated* TS curves of the retained tracks (Figure 55), which were then exported to CSV. It is important to note that it is only at this step that a calibration curve is applied to the data.

Table 2: Parameters for ESP3 Target Tracking algorithm, Weights and Track Acceptance.

Weights & Track Acceptance Parameter	**Values**
Weighting Major Axis	30
Weighting Minor Axis	40
Weighting Range	40
Weighting TS	0
Weighting Ping Gap	3
Minimum Single Targets (in a track)	4
Minimum Pings (in a track)	4
Maximum Gaps (between single targets, pings)	1

Table 3: Parameters for ESP3 Target Tracking algorithm, Alpha/Beta tracking.

Alpha/Beta Tracking Parameter	**Along**	**Across**	**Range**
Alpha (Gain sensitivity to unpredicted changes in position)	0.7	0.7	0.7
Beta (Gain sensitivity to unpredicted changes in velocity)	0.5	0.5	0.5
Exclusion distance (m)	1.0	3.0	0.4
Angle Uncertainty (degrees)	1.0	1.0	N/A
Ping expansion (%)	0	0	0

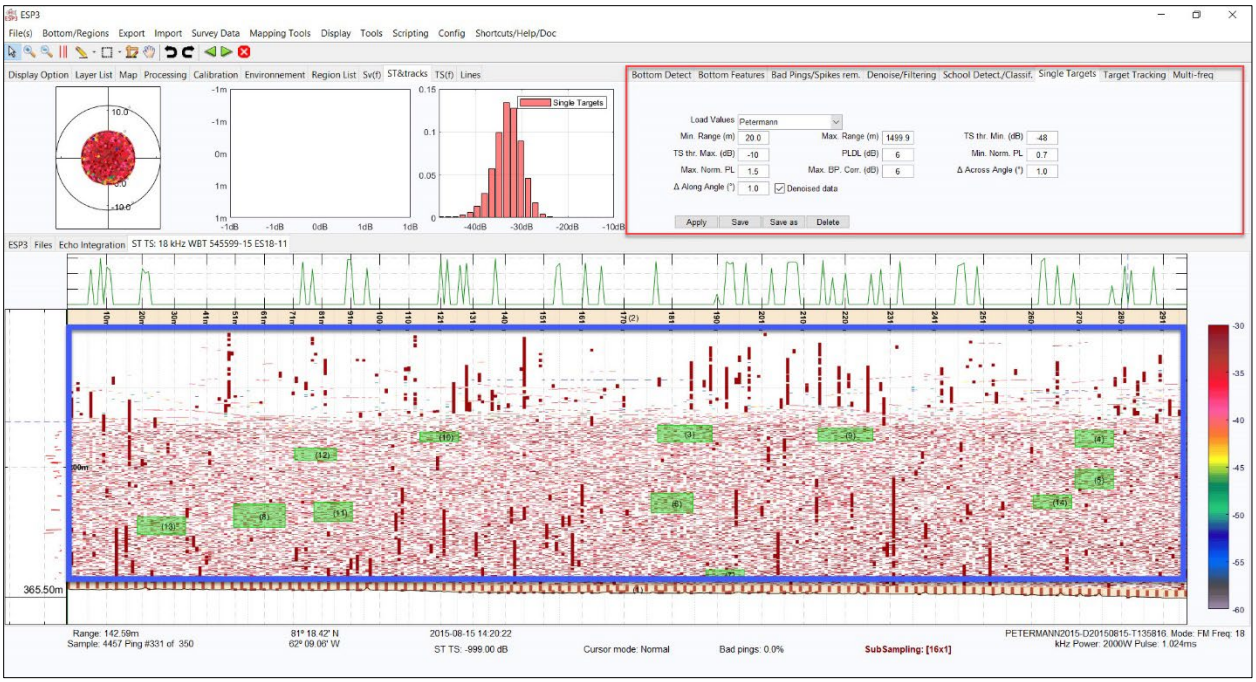

Figure 53: Results of single targets selection. The blue box is the water column region used for the analysis; it excludes the detections below the bottom detect as well as the "bad data" areas near the seafloor and surface. The red box, top right, highlights the parameters used for single target selection on this line, and the ST&tracks tab, top left, shows the dB distribution of single targets within the set threshold. Filled green boxes were areas selected for S_v analysis, described earlier. Echogram and PDF show uncalibrated values.

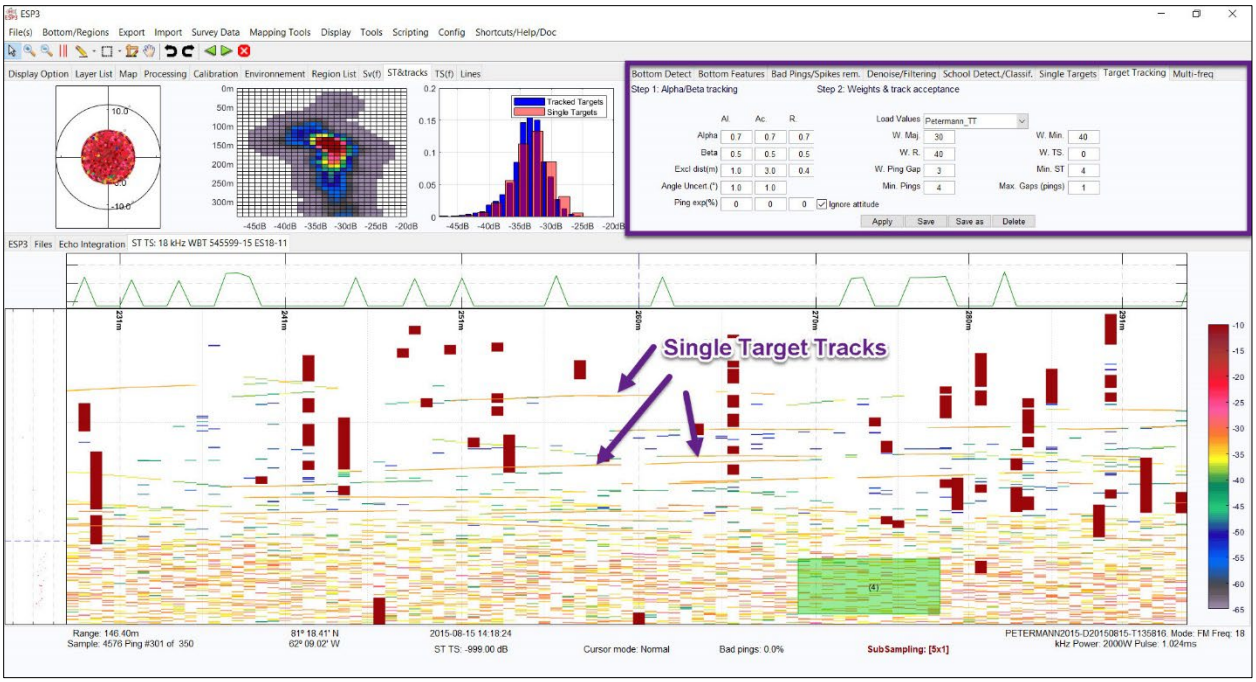

Figure 54: Results of Target Tracking, focusing on a small section of the echogram. The tracked targets are shown as yellow lines that are difficult to distinguish in the image. The purple box at the top right highlights the parameters used. Echogram and PDF display show uncalibrated values. The filled green box was an area selected for S_v analysis, described earlier.

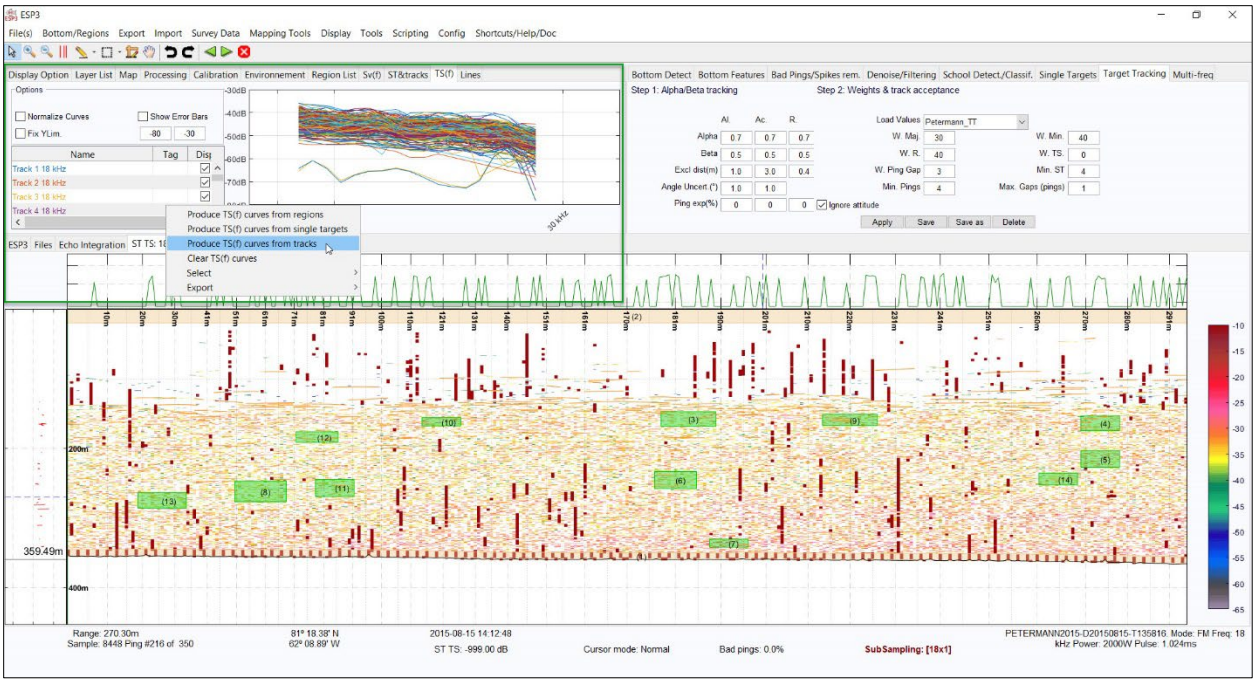

Figure 55: 'Produce TS(f) curves from tracks' tool and results. Echogram values are uncalibrated, frequency response curves are calibrated. Filled green boxes were areas selected for S_v analysis, described earlier.

The CSV files were evaluated and any records outside of the useable frequency range (16 – 26 kHz) as well as incomplete records (i.e., NaN values anywhere in the frequency response) were removed. This resulted in frequency response records for 16.11 – 25.63 kHz in TS (dB) for individual targets and 16.11 – 26 kHz in S_v (dB) for volume targets, as the sampling frequencies are automatically selected by the ESP3 software and differ for TS and S_v calculations. The results were taken into Microsoft Excel for conversion to σ_{bs},

$$\sigma_{bs} = 10^{\frac{TS_{dB}}{10}}$$

the backscattering cross-section, in m^2, and s_V,

$$s_V = 10^{\frac{S_{V_{dB}}}{10}}$$

the volume backscattering coefficient, in m^2 m^{-3}, translating values to the linear domain for calculation of averages (Simmonds and MacLennan, 2005; Parker-Stetter et al., 2009). All individual target TS values were used to calculate the average σ_{bs}; the average s_V was calculated for dense and sparse layers separately. The resulting average σ_{bs} and s_V near the nominal frequency of 18 kHz were, in turn, used to calculate the average density ($\hat{\rho}$) of targets in a layer, per m^3 (Parker-Stetter et al., 2009):

$$\hat{\rho} = \frac{\hat{s}_{V\ 18\ kHz}}{\hat{\sigma}_{bs\ 18\ kHz}}$$

The *acoustic sampling volume* (V), the volume of water column (m^3) ensonified by the beam and contributing to the returned signal at any instant (Simmonds and MacLennan, 2005; Parker-Stetter et al., 2009),

$$V = \psi\ R^2 * range\ resolution$$

was calculated, where ψ is the equivalent beam angle (0.02 steradians for this system) and R is the range (m), here the average depth of the portions of the scattering layer sampled for S_v. For a narrow band system, the *range resolution*, the difference in range between targets required for them to produce separate echoes, is calculated as $\frac{1}{2}c\tau$, where c is the sound speed (m s^{-1}) and τ is the pulse duration (Simmonds and MacLennan, 2005). For a broad band system such as the EK80 used here, the range resolution is estimated as the inverse of the bandwidth, ~ 7.5 cm for this system. Finally, the number of targets in the acoustic sampling volume was calculated by multiplying the average density ($\hat{\rho}$) by the acoustic sampling volume (V).

CHAPTER 4 RESULTS AND DISCUSSION

4.1 Distribution of the Scattering Layer

Figure 56 and Figure 57 summarize the presence/absence, geospatial distribution and depth distribution of the scattering layers during August 2015, based on manual selection in FMMidwater. The tops of the scattering layers ranged in depth from -45 m to -635 m (Figure 58), with a higher instance of scattering layers found in Petermann Fjord than in Hall Basin. The tops of the scattering layers in the 'fjord-influenced' area were found across the full depth range, but the highest numbers of picks were in the ranges of -80 to -90 m and -150 to -160 m (Figure 59). The tops of the scattering layers in the 'basin' area were found from -88 to -494 m, with the highest number of picks between -310 to -320 m (Figure 59). An absence of scattering layer presence was found along the western side of Nares Straight and in the center of Hall Basin. The distribution of scattering layer picks over time (Figure 60) indicates that scattering layers were found at all hours, with slightly fewer picks during the hours of lowest light levels.

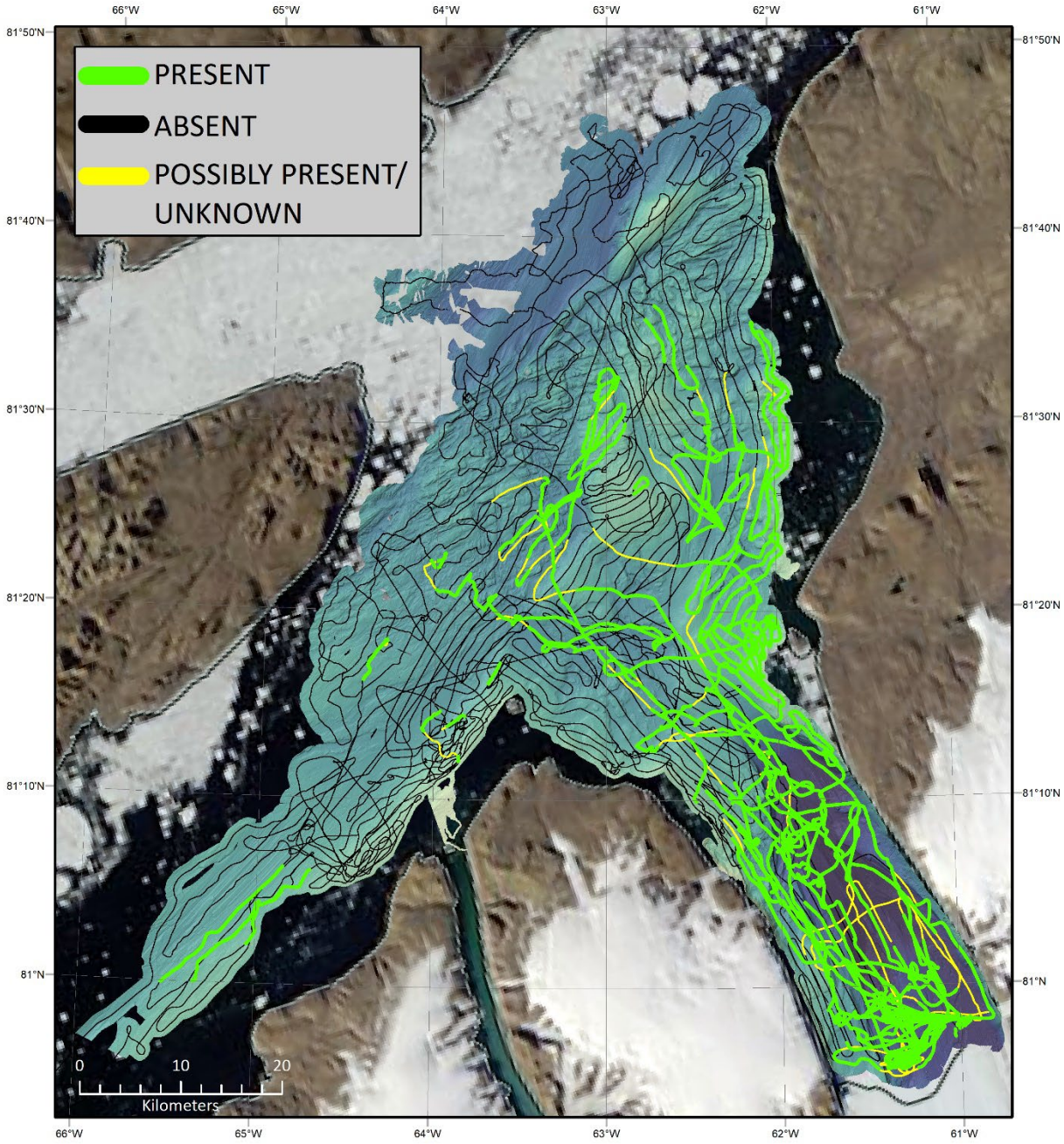

Figure 56: EK80 sonar track lines colored by scattering layer presence. Projection is WGS 84 UTM 20N.

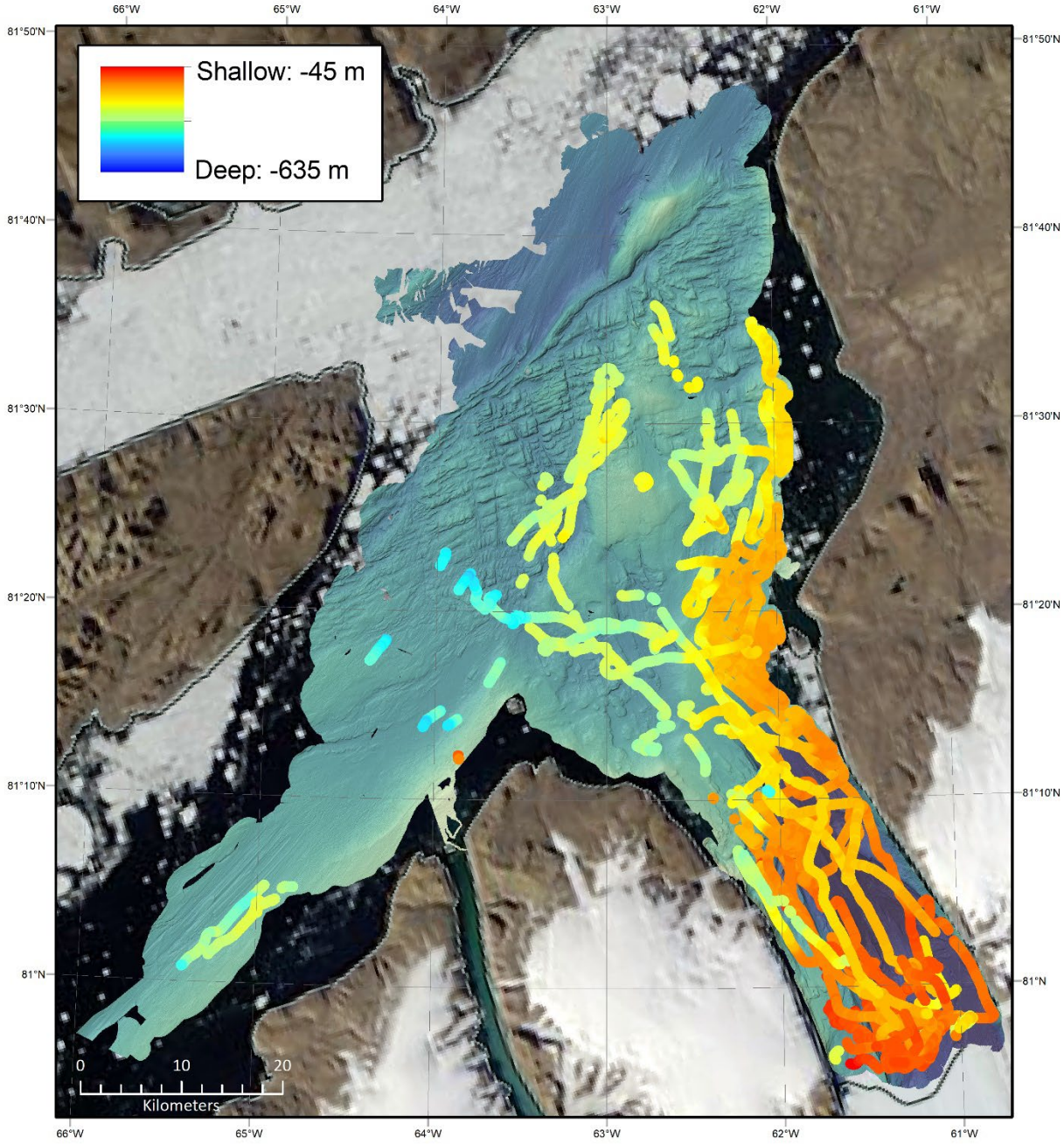

Figure 57: Map of scattering layer depth. Projection is WGS 84 UTM 20N.

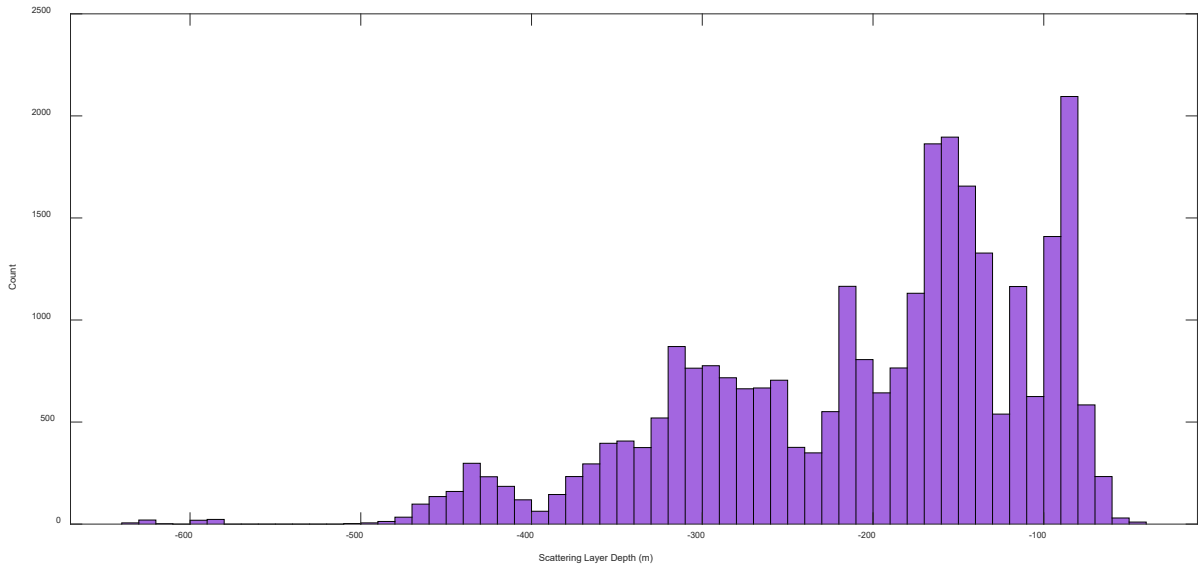

Figure 58: Distribution of scattering layer depths across the study area.

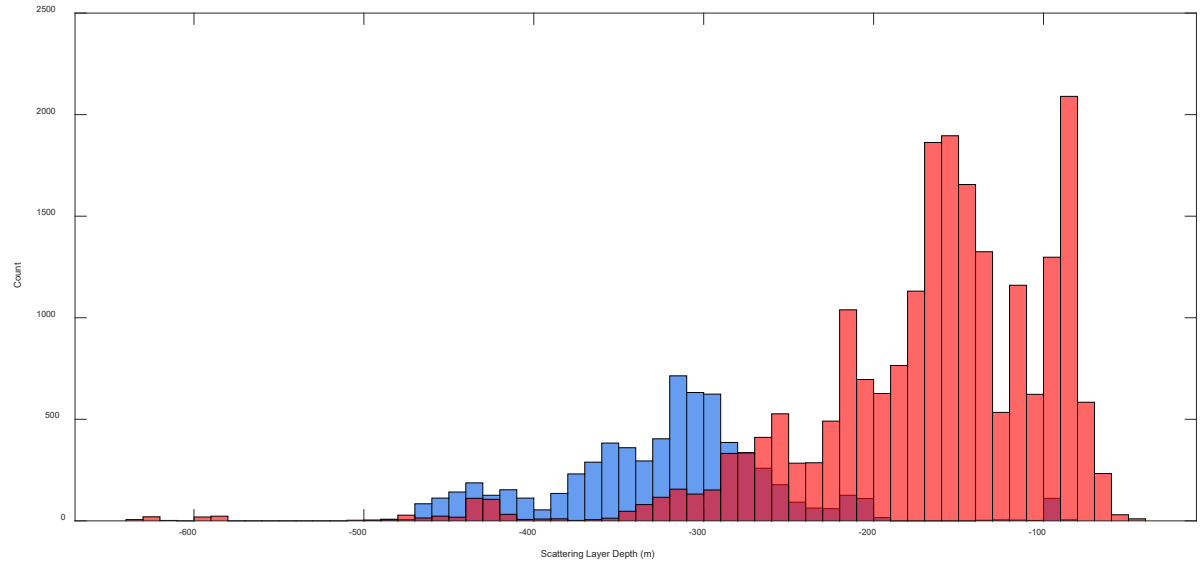

Figure 59: Distribution of scattering layer depth, 'fjord-influenced' shown in red, 'basin' shown in blue.

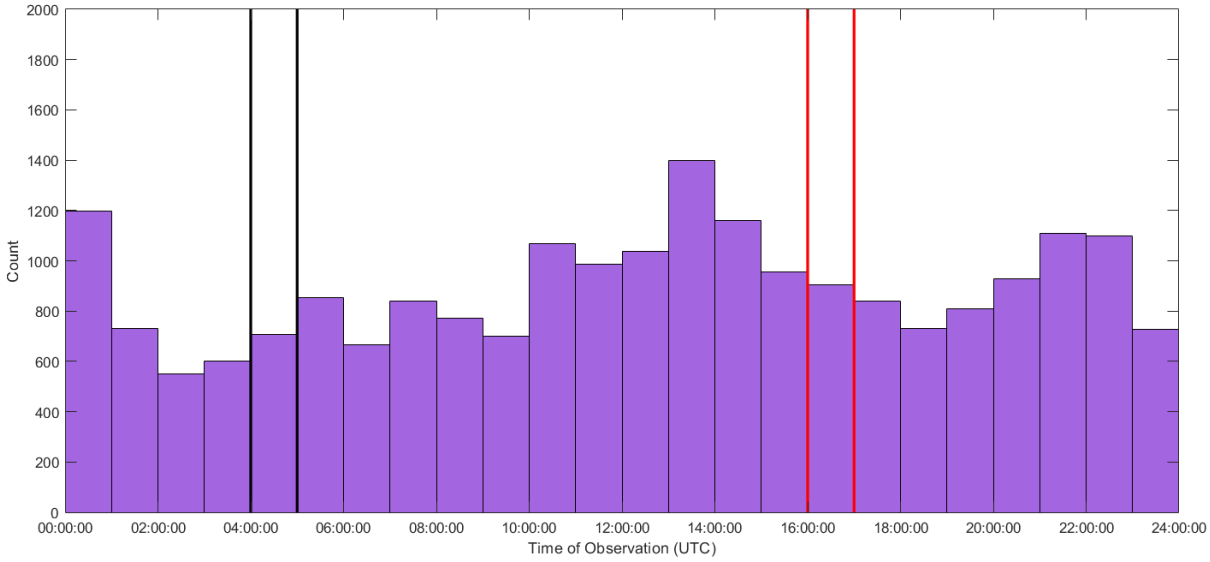

Figure 60: Distribution of scattering layer picks through time. The black lines indicate the time of lowest light levels, the red lines highest light levels (solar noon).

4.2 Relationship of Scattering Layer to Abiotic Factors

4.2.1 Correlation to bathymetry

The scatterplots of scattering layer depth vs. bathymetric depth and scattering layer depth vs. bathymetric slope do not indicate a linear relationship (Figure 61, Figure 62). The result of correlation test comparing scattering layer depth to bathymetric values was R = -0.38, P = 0, indicating no correlation (Figure 63). The result of the correlation test comparing scattering layer depth to bathymetric slope was R = 0.01, P = 3.141×10^{-70}, also indicating no correlation (Figure 64).

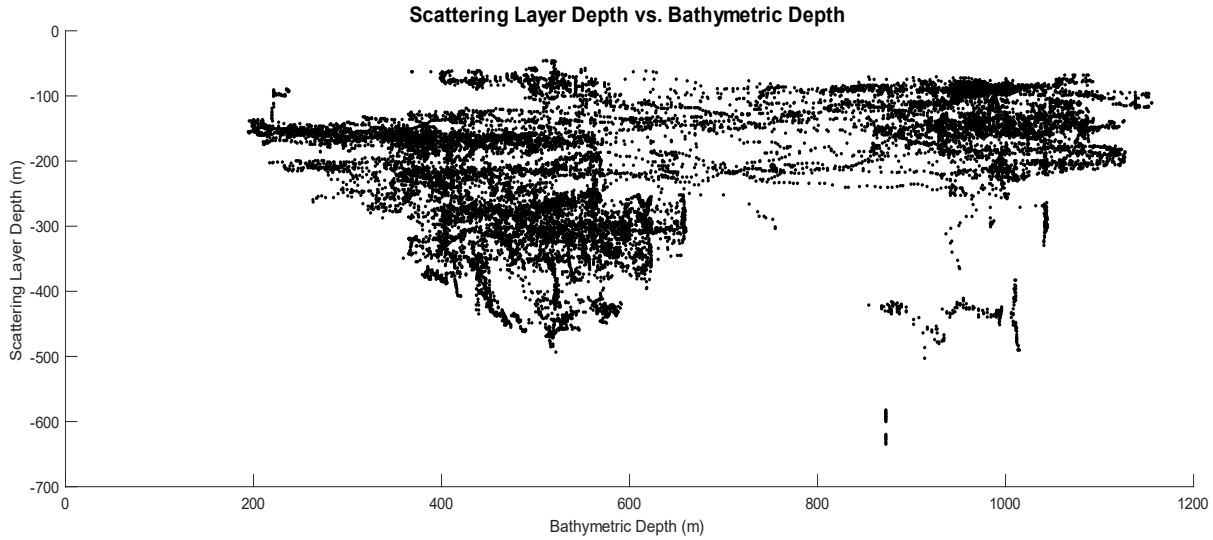

Figure 61: Scatterplot of scattering layer depth vs. bathymetric depths.

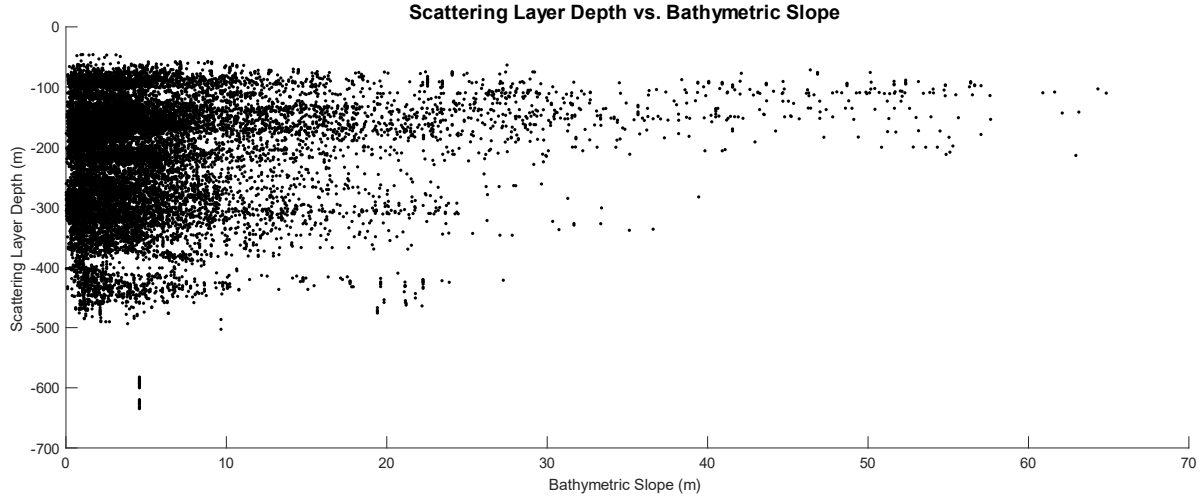

Figure 62: Scatterplot of scattering layer depth vs. bathymetric slope.

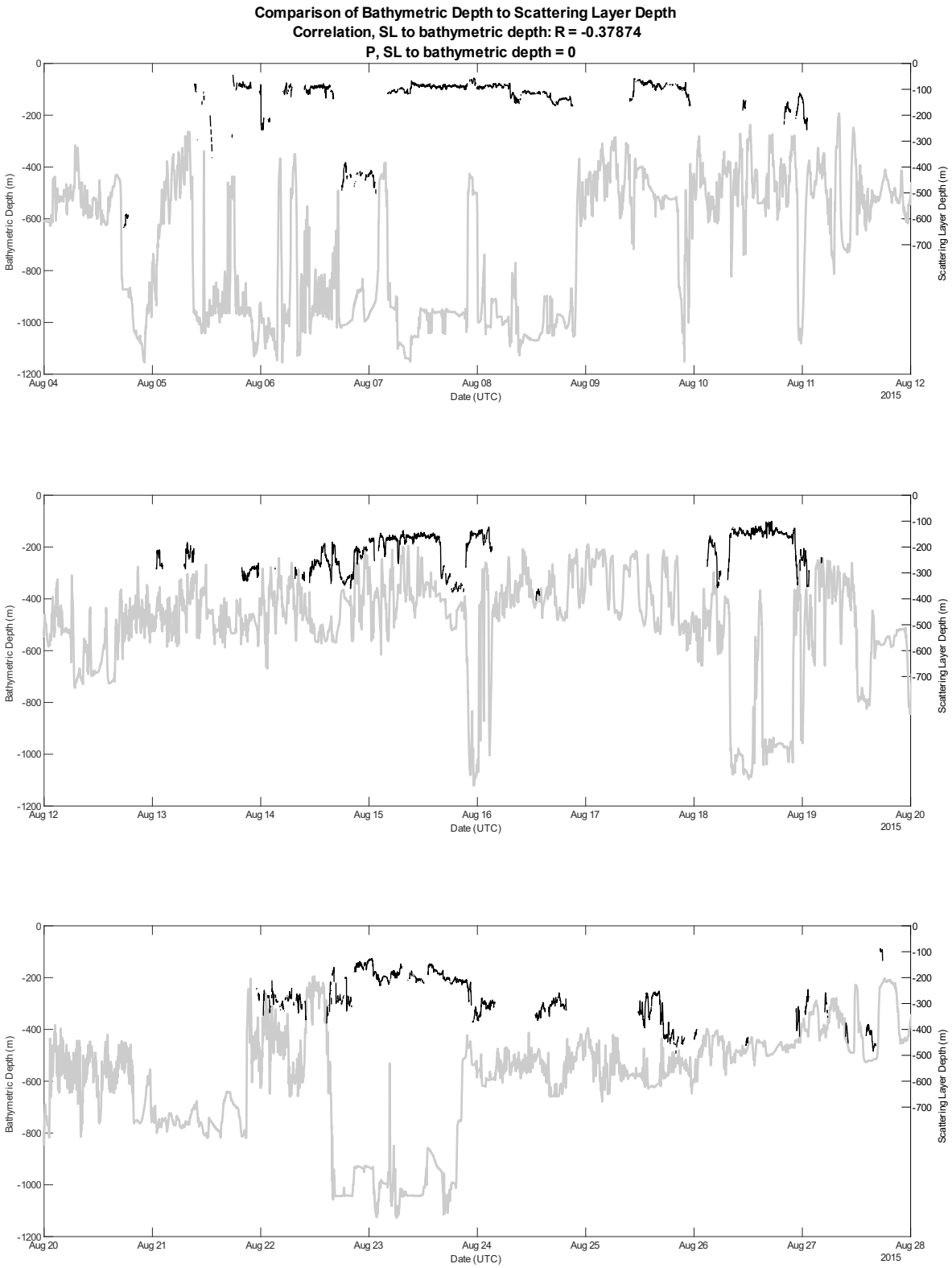

Figure 63: Comparison of scattering layer depth, shown as black lines, to bathymetric depth values, shown as a grey line, across the full study; graphs are broken in to overlapping nine-day periods for clarity. Note that the y-axis scales for the bathymetric depths (left) and scattering layer depths (right) are the same; the labels are a reflection of the actual data limits for each.

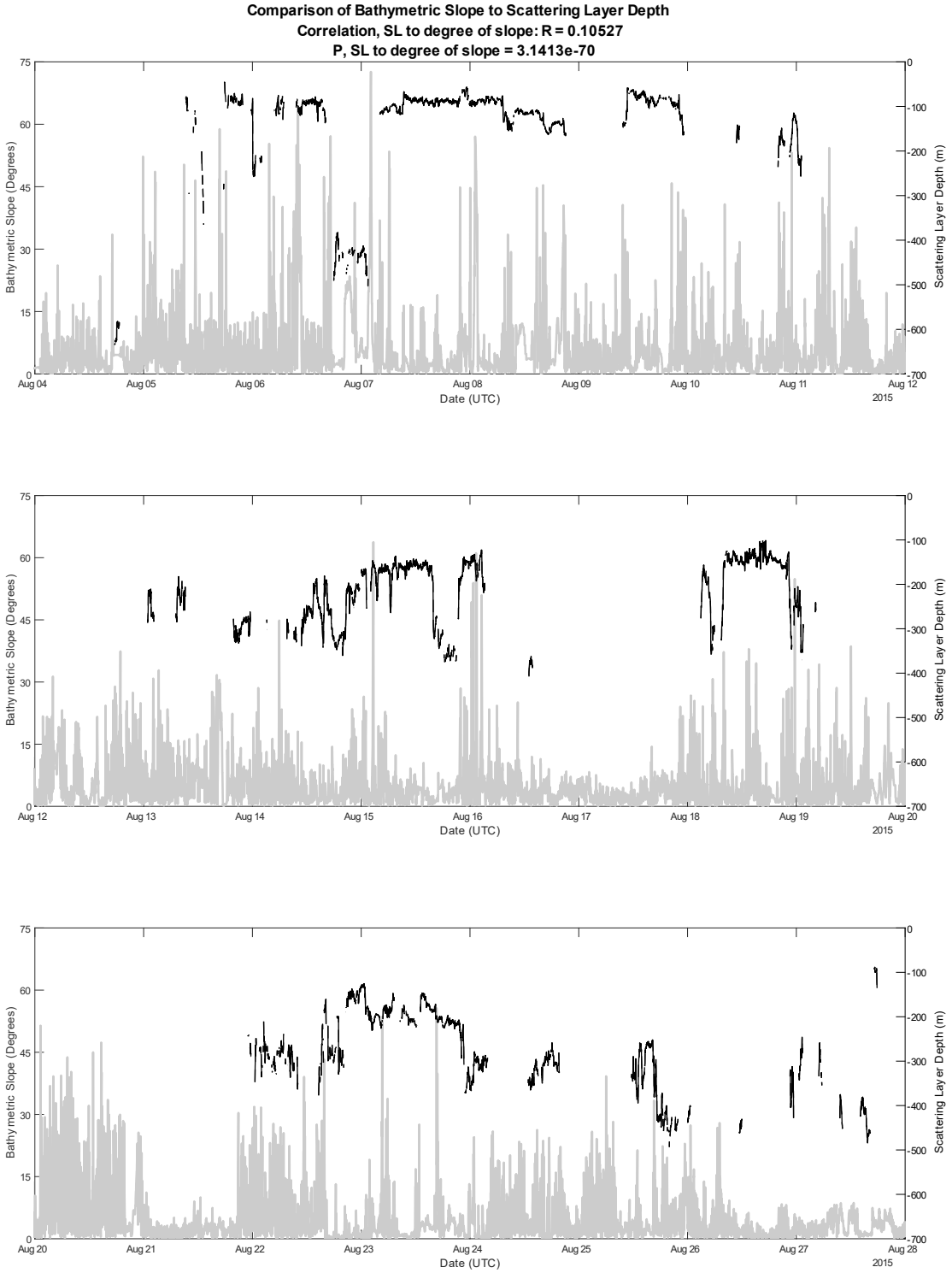

Figure 64: Comparison of scattering layer depth, shown as black lines, to bathymetric slope values, shown as a grey line, across the full study; graphs are broken in to overlapping nine-day periods for clarity. Note that the y-axis scales for the bathymetric slope (left) and scattering layer depths (right) are different.

4.2.2 Light as a factor in the scattering layer vertical distribution: Effects of light levels

The results of the first correlation test comparing all scattering layer picks for the time period to the PAR values for the same time period resulted in correlation coefficients of -0.146 and -0.053 and significance values of 6.199×10^{-27} and 0.00042 for Periods 2 and 3 respectively (Figure 65, Figure 66), indicating that results were significant and that there was no correlation. The results of the second correlation test, breaking the scattering layer into 'fjord-influenced' and 'basin' regions prior to running the correlation, resulted in correlation coefficients of -0.100 and 0.270 and significance values of 4.286×10^{-12} and 1.0239×10^{-42} for the 'fjord-influenced' region, Periods 2 and 3 respectively (Figure 67, Figure 68), indicating that the results were significant and that there was no correlation. For the 'basin-influenced' region, the results were 0.204 and 0.033 and significance values of 1.097×10^{-06} and 0.15212 (Figure 69, Figure 70), indicating the results for Period 2 were significant but did not indicate correlation while the results for Period 3 were not significant.

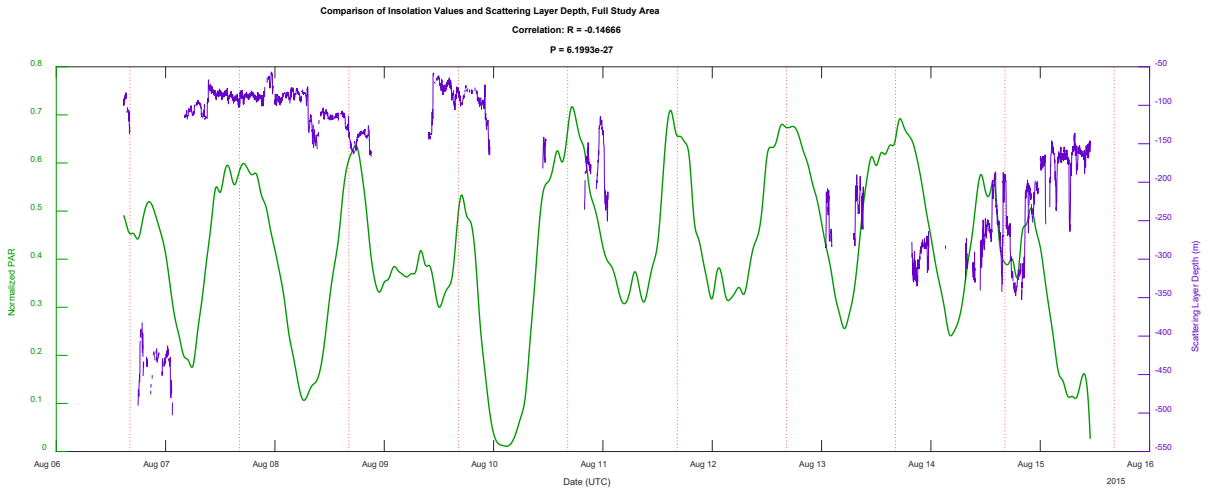

Figure 65: Comparison of scattering layer depth across the full study area to ship-based radiation values for Period 2 (August 6 – August 15, records for the 6th and 15th incomplete).

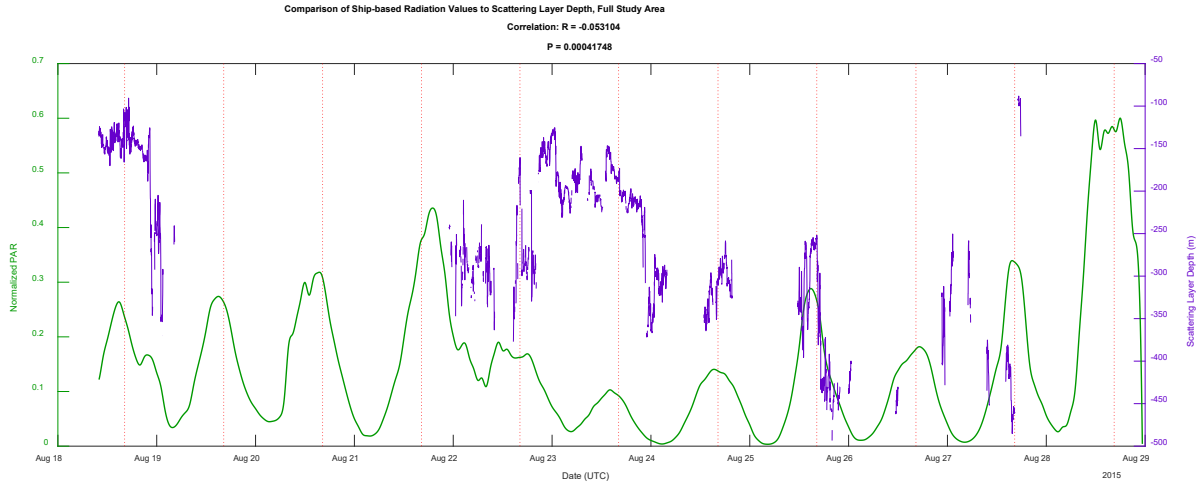

Figure 66: Comparison of scattering layer depth across the full study area to ship-based radiation values for Period 3 (August 18 - August 28, records for the 28th incomplete).

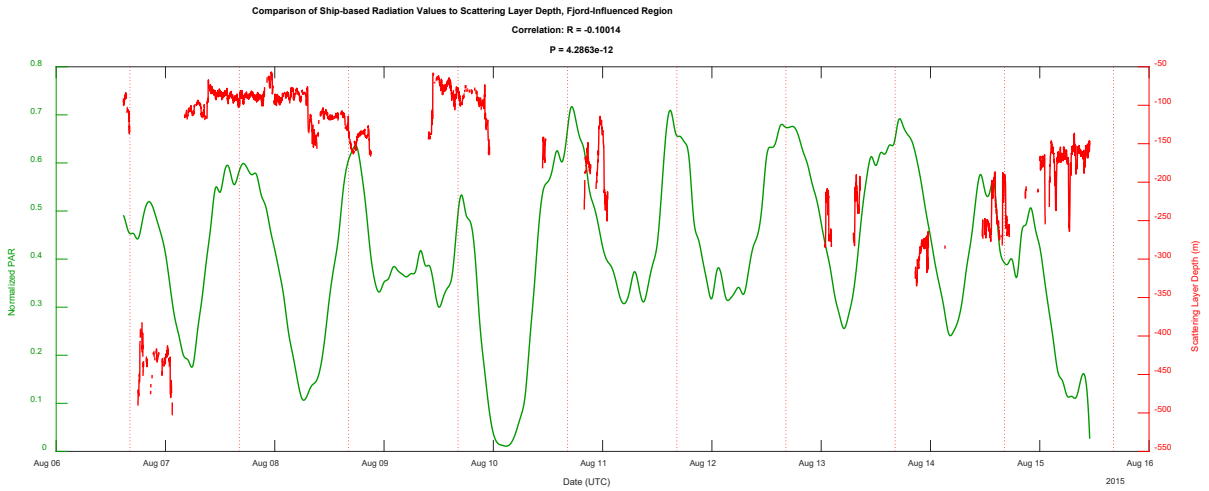

Figure 67: Comparison of scattering layer depth for the 'fjord-influenced' region to ship-based radiation values for Period 2 (August 6 – August 15, records for the 6th and 15th incomplete).

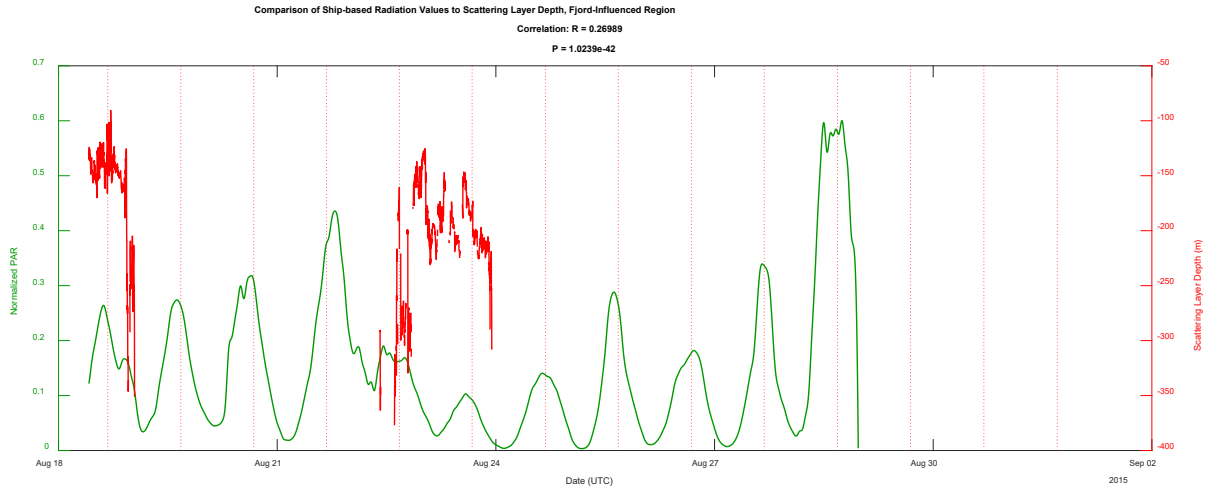

Figure 68: Comparison of scattering layer depth for the 'fjord-influenced' region to ship-based radiation values for Period 3 (August 18 - August 28, records for 28th incomplete).

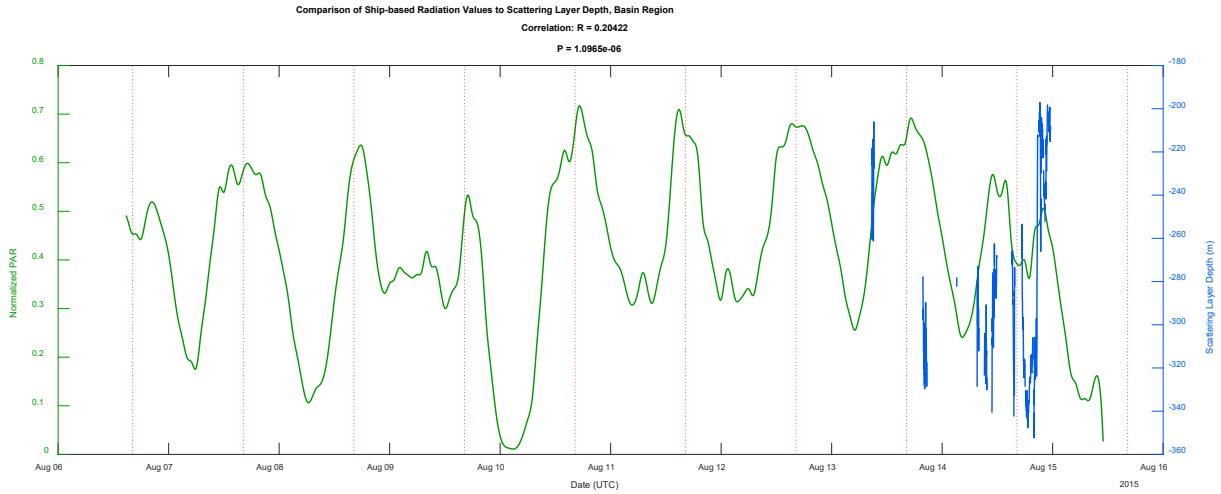

Figure 69: Comparison of scattering layer depth for the 'basin' region to ship-based radiation values for Period 2 (August 6 – August 15, records for the 6th and 15th incomplete).

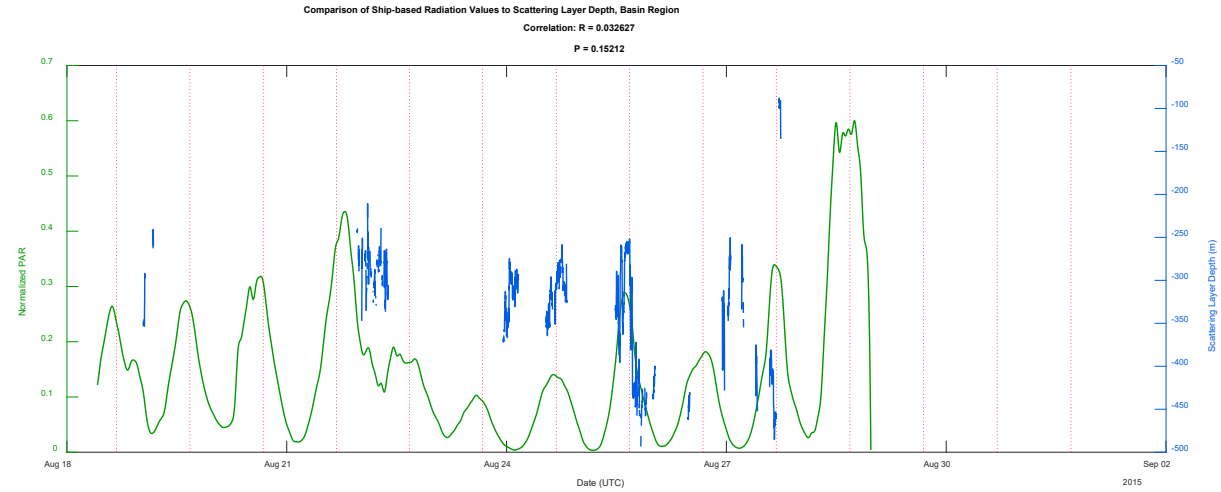

Figure 70: Comparison of scattering layer depth for the 'basin' region to ship-based radiation values for Period 3 (August 18 - August 28, records for 28th incomplete).

Scattering layers are often observed to migrate based on changes in light. If the scattering layer was following a nocturnal Diel Vertical Migration (DVM) pattern, with the layer increasing depth as light levels increased, we would expect to see an inverse correlation between scattering layer depth and light levels; if it was following a reverse DVM pattern, we would expect a positive correlation. The scattering layer in this study area was observed to change vertical position throughout the time series (as can be seen in the plots of scattering layer depth, Figure 65 - Figure 70), and light levels had a

discernable 24-hour cycle. Based on this analysis, however, the changes in vertical position do not appear to consistently correlate to the changes in light levels. The correlation coefficients resulting from the analysis comparing the scattering layer depth to ship-based radiation values were low (always less than +/- 0.3) and inconsistent, being sometimes positive and sometimes negative. While there does appear to an instance where the scattering layer appears to be reacting to changes in light (Figure 71), this appears to be the exception. The evidence implies that the change in light level over the 24-hour period was not enough to trigger migration and that the changing light level was not a significant factor in the position of the scattering layer in the study area over the course of the expedition. This is consistent with findings by other Arctic researchers who found DVM under midnight sun conditions to be absent or weak (Longhurst, 1976; Blachowiak-Samolyk et al., 2006; Cottier et al., 2006).

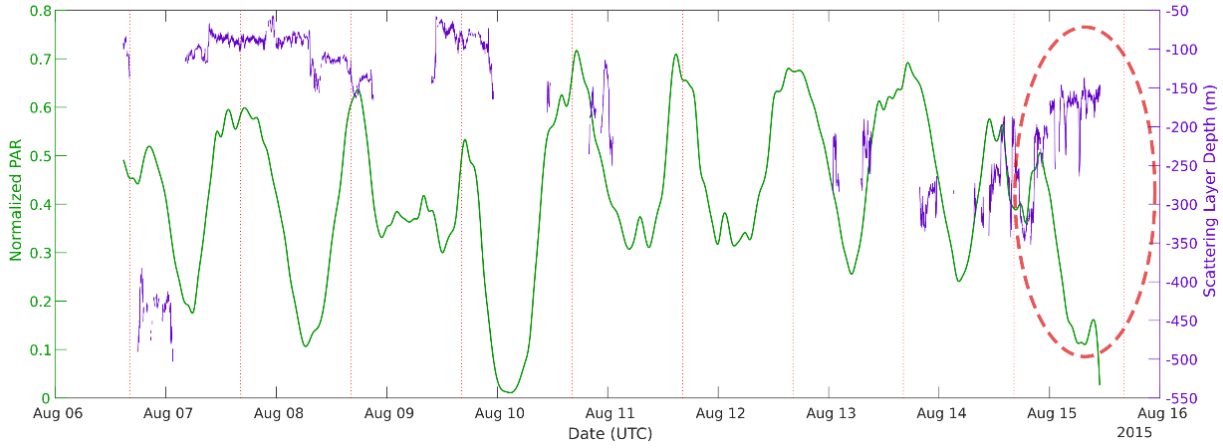

Figure 71: Example of scattering layer depth appearing to change depth in response to decreased light levels.

4.2.3 Light as a factor in the scattering layer vertical distribution: Effects of light attenuation

In the OC-CCI dataset, August 2015 $K_d(490)$ values appear to be similar throughout the study region, showing no consistent pattern of change in attenuation – though coverage in the fjord is limited (Figure 41). The MODIS Terra dataset has more complete coverage in the fjord and appears to show a slight increase in attenuation in the fjord, western Nares Strait, and east-central Hall Basin compared to the majority of Hall Basin. Open water basin values were around 0.11 – 0.15 m^{-1} (yellow circle, Figure 72) while fjord values were around 0.16 – 0.28 m^{-1} (solid red circle, Figure 72). The results of the linear correlation test were 0.165 and 0.228 with significance values of 2.266×10^{-85} and 4.049×10^{-193} for the OC-CCI and MODIS Terra datasets, respectively.

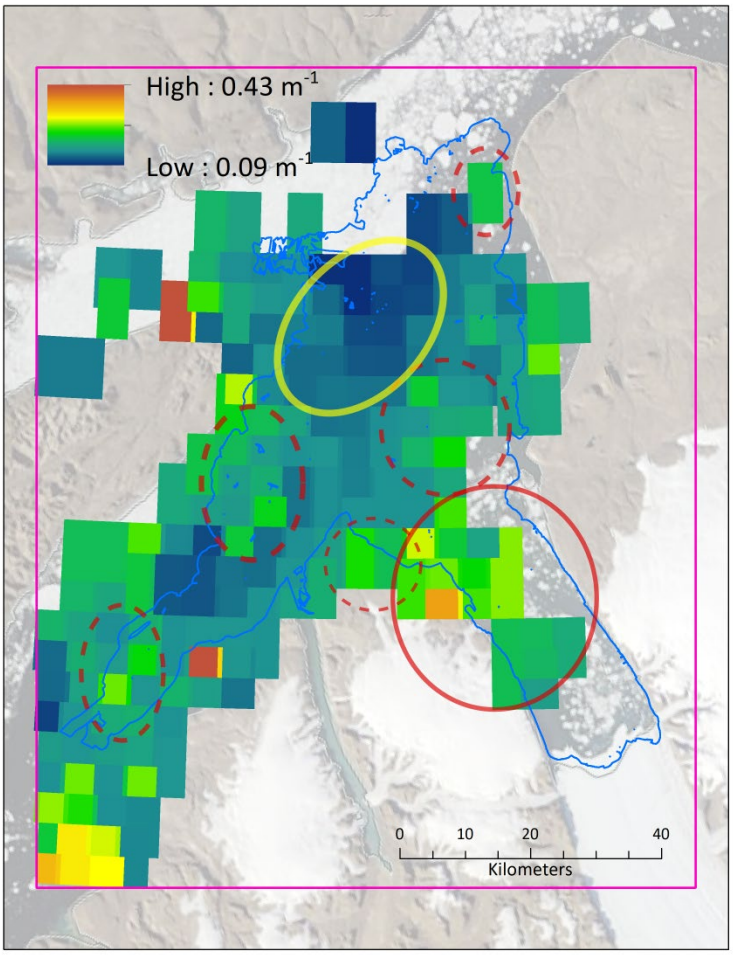

Figure 72: MODIS Terra K_d(490) mean values for August 2015. The solid red circle is the fjord area of higher attenuation mentioned in the text; dashed circles indicate other areas of higher attenuation. The yellow circle is an area of open water and lower attenuation. Projection is WGS 84 UTM 20N.

The MODIS Terra dataset showed higher average levels of light attenuation in the fjord than in most parts of Hall Basin for the month of August, and the scattering layer depth in the fjord does tend to be shallower, which seems to indicate that higher levels of attenuation may have some effect on the depth of water the organisms in the scattering layer choose to inhabit – though not consistently (Figure 73). The linear correlation between scattering layer depth and average K_d(490) was poor to weak, so it doesn't appear to be a strong driver of scattering layer depth. The water clarity does appear to fluctuate from day to day (see daily images, Appendix B) and the daily K_d(490) coverage is poor (Appendix C), so options for further investigation into water

clarity as the primary driver for scattering layer depth are limited (as least using these data sources), but the data available here implies that water clarity is not a strong driver of scattering layer depth.

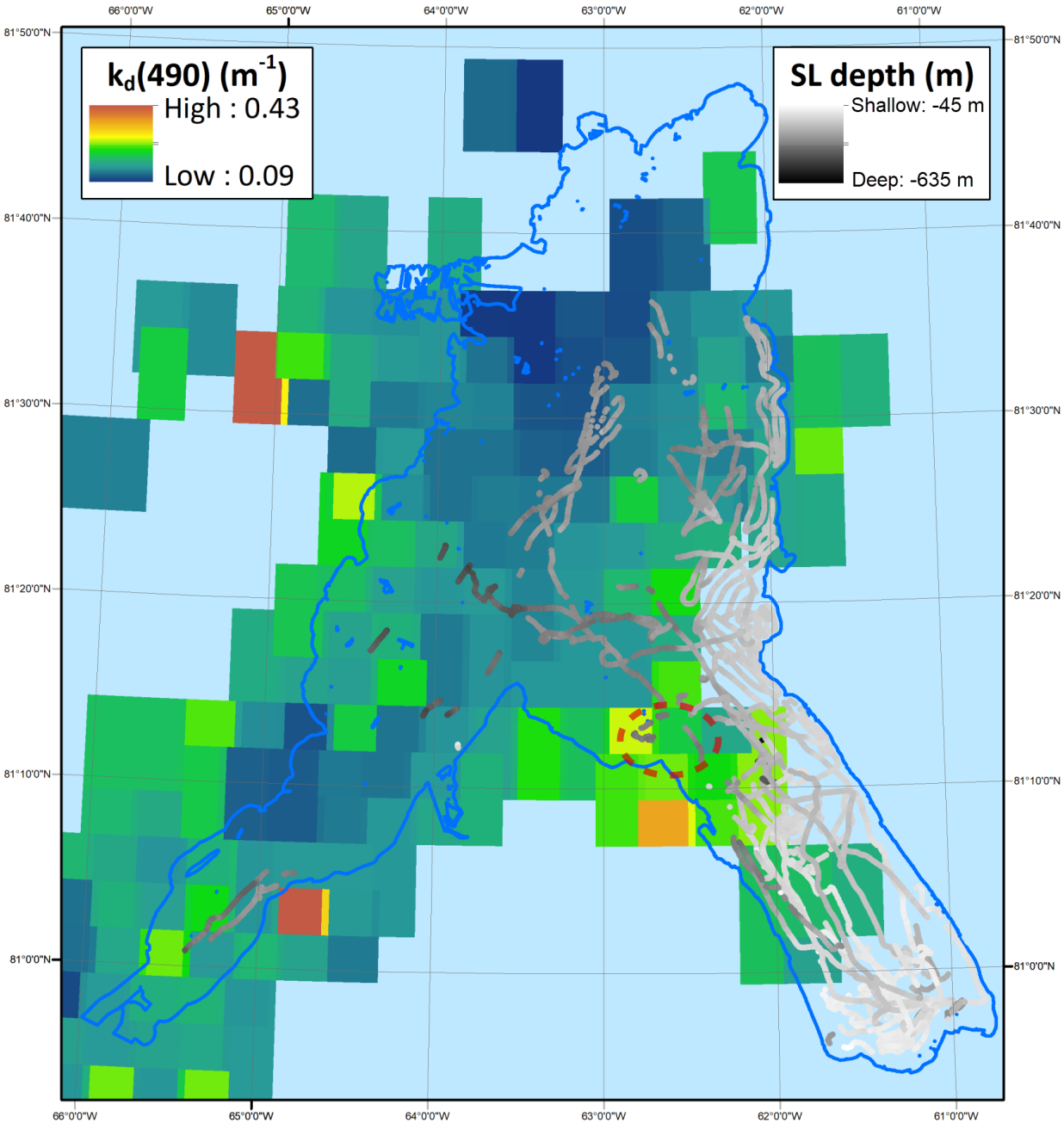

Figure 73: Scattering layer depth, here shown using a greyscale colormap, overlaid on MODIS Terra $K_d(490)$ data. The red circle highlights an area of high attenuation and a relatively deep scattering layer, which is inconsistent with the idea that shallower scattering layer depth is driven by higher attenuation. Projection is WGS 84 UTM 20N.

4.2.4 Water masses and circulation as factors in scattering layer distribution

When compared to water properties, the scattering layers identified during periods of CTD acquisition fell into two distinct groups and one transitional group. The first distinct group was associated with a deeper, more homogenous section of the water column, where temperature and salinity values were stabilizing and moving towards the higher temperature, higher salinity values associated with Atlantic Water ('homogeneous preference' scattering layers, Figure 74 - Figure 77). The Temperature-Salinity (T-S) diagrams (Figure 74, Figure 76, Figure 78, Figure 80, Figure 82) show the conservative temperature plotted against the absolute salinity for each CTD station. The picked points for the top of the scattering layer at that CTD are shown as open circles colored by depth, overlaid on the T-S line. A black 'x' shows the average depth for the top of the scattering layer. Overlain on each diagram are lines connecting the three water mass end members for the region, Winter Water (WW), Atlantic Water (AW), and Petermann Glacier Water (PGW), as defined by Heuzé et al. (2017; note that the WW and PGW end member values are not shown in the restricted T-S domain of the diagrams). Winter Water and Atlantic Water have been discussed previously (section 2.3). PGW is the theoretical end member associated with meltwater from the Petermann Glacier, representing the latent heat required to melt ice from Petermann Glacier with AW (Straneo et al., 2012; Heuzé et al., 2017). The water column in the region will have a mix of these three end members, distinguishable by their salinity and temperature characteristics measured during a CTD cast. T-S values closer to each end member are more like that end member, and T-S values that fall along the dotted lines between the

end members would theoretically be a mix of those two end members. In Figure 74, the scattering layer (highlighted with a yellow circle) is along the portion of the line after the transition, where the angle of the line has changed to be closer to a mix of AW and PGW. Further, the scattering layer is quite close to the AW end member. The T-S downplots (Figure 75, Figure 77, Figure 79, Figure 81, Figure 83) show similar information in a different way. Conservative temperature and absolute salinity are plotted against depth, with the depth range for all plots set to the maximum range observed across all CTD stations. In the top 150 m or so of the water column, temperature and salinity are changing quickly (the thermocline and halocline, labeled in Figure 75), leading to a more heterogenous water column. This top portion of the water column is where the WW is found. Below about 200 m the temperature and salinity start to steady, leading to a more homogeneous water column. This is where the AW is found. The PGW is found in the transition zone, between 100 and 280 m and concentrated between 150 and 200 m (Heuzé et al., 2017). The average depth of the top of the scattering layer in these plots is shown as a solid line, and the minimum and maximum depths of the top of the layer are shown as dashed lines. In Figure 75, the top of the scattering layer (highlighted in yellow) is at around 300 m, where the water column properties are more homogeneous. Figure 76 and Figure 77 show all CTDs in the homogenous preference group overlain on each other. In Figure 77, the position of the scattering layers shows that within the homogeneous preference group, there is still some association of the scattering layer with ongoing temperature change, but the salinity values are quite steady.

The second distinct group was associated with shallower portions of the water column where temperature and/or salinity were still changing considerably with depth (‘heterogenous preference’ scattering layers, Figure 78 - Figure 81), above 200 m, where Winter Water dominates (with possible influence of Petermann Glacier meltwater, depending on where you are in the region).

The transitional group was found at depths where water column properties were moving from colder, fresher, and more heterogeneous to warmer, saltier, and more homogeneous (Figure 82, Figure 83); this is the depth range where you would find the strongest concentrations of Petermann Glacier meltwater (again, depending on the region). In Figure 83, it can be seen that the salinity values are clearly moving to a more homogeneous state, however the temperature values are still changing with depth similar to the heterogenous profiles. T-S diagrams, T-S downplots, and oxygen plots for all CTD stations are provided in Appendix D.

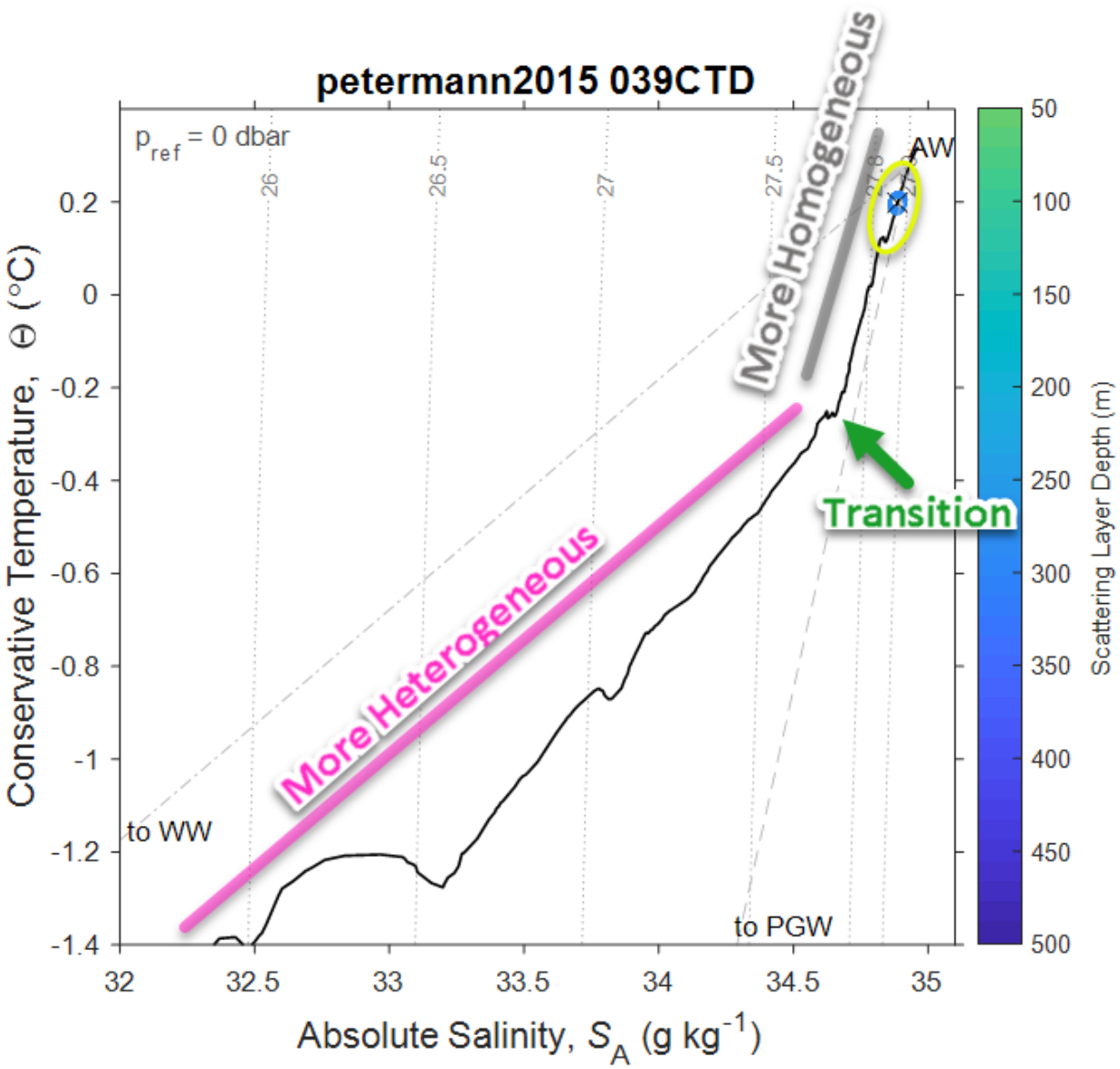

Figure 74: Temperature-Salinity (T-S) diagram for CTD 039, an example of a scattering layer associated with the more homogenous portion of the water column. The scattering layer picks corresponding to this CTD are highlighted with a yellow circle. They are plotted as open circles colored by depth; a black 'x' indicates the average depth for the top of the scattering layer in this location. Isobars are shown as labeled grey dotted lines.

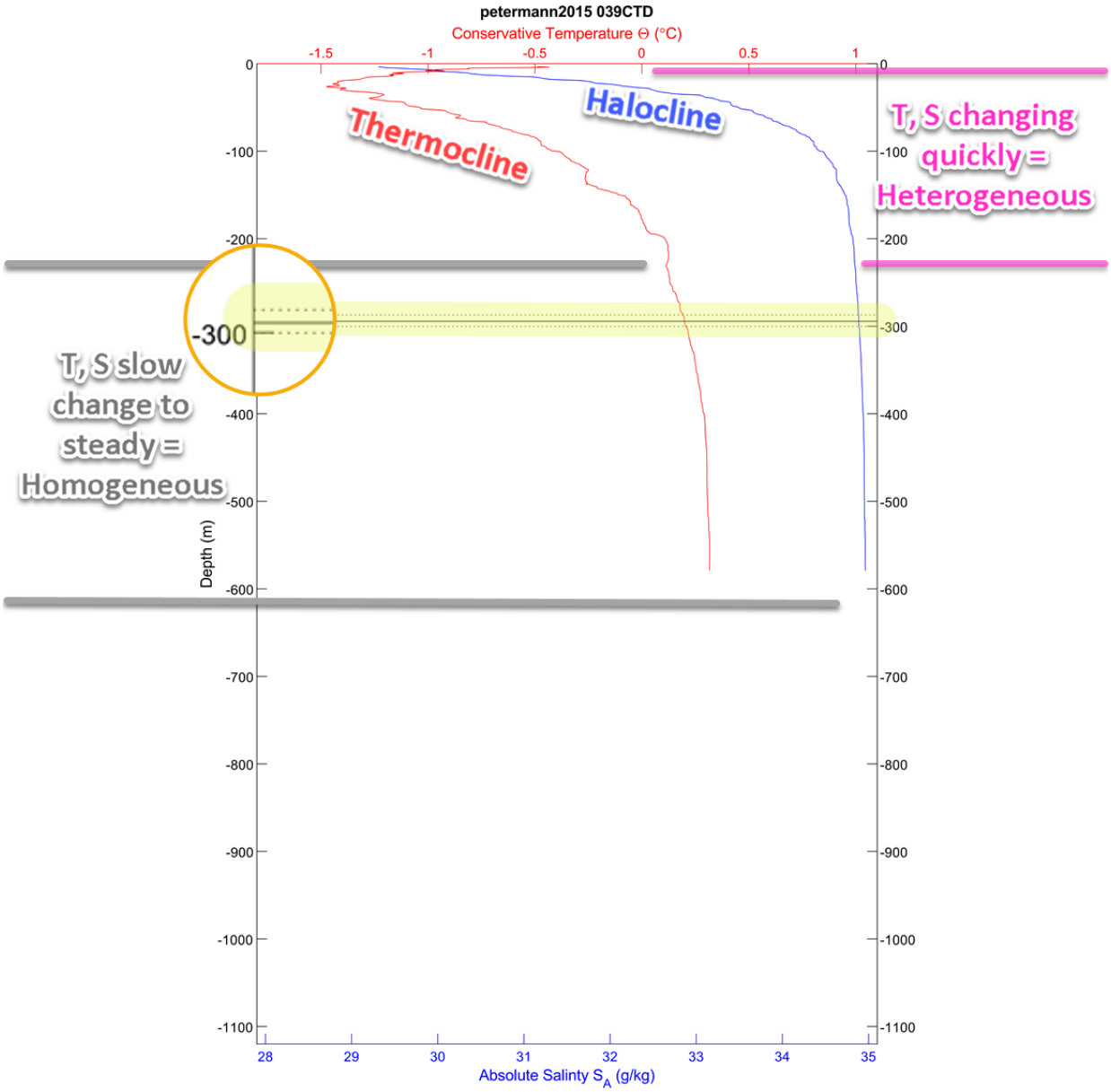

Figure 75: Temperature and salinity plotted by depth, CTD 039. The scattering layer depth, highlighted in yellow, is indicated by horizontal lines; the solid line is the average depth, the dotted lines are the shallowest and deepest depths, in all cases for the top of the scattering layer. The orange circle on the left shows a magnified version of the scattering layer depth lines.

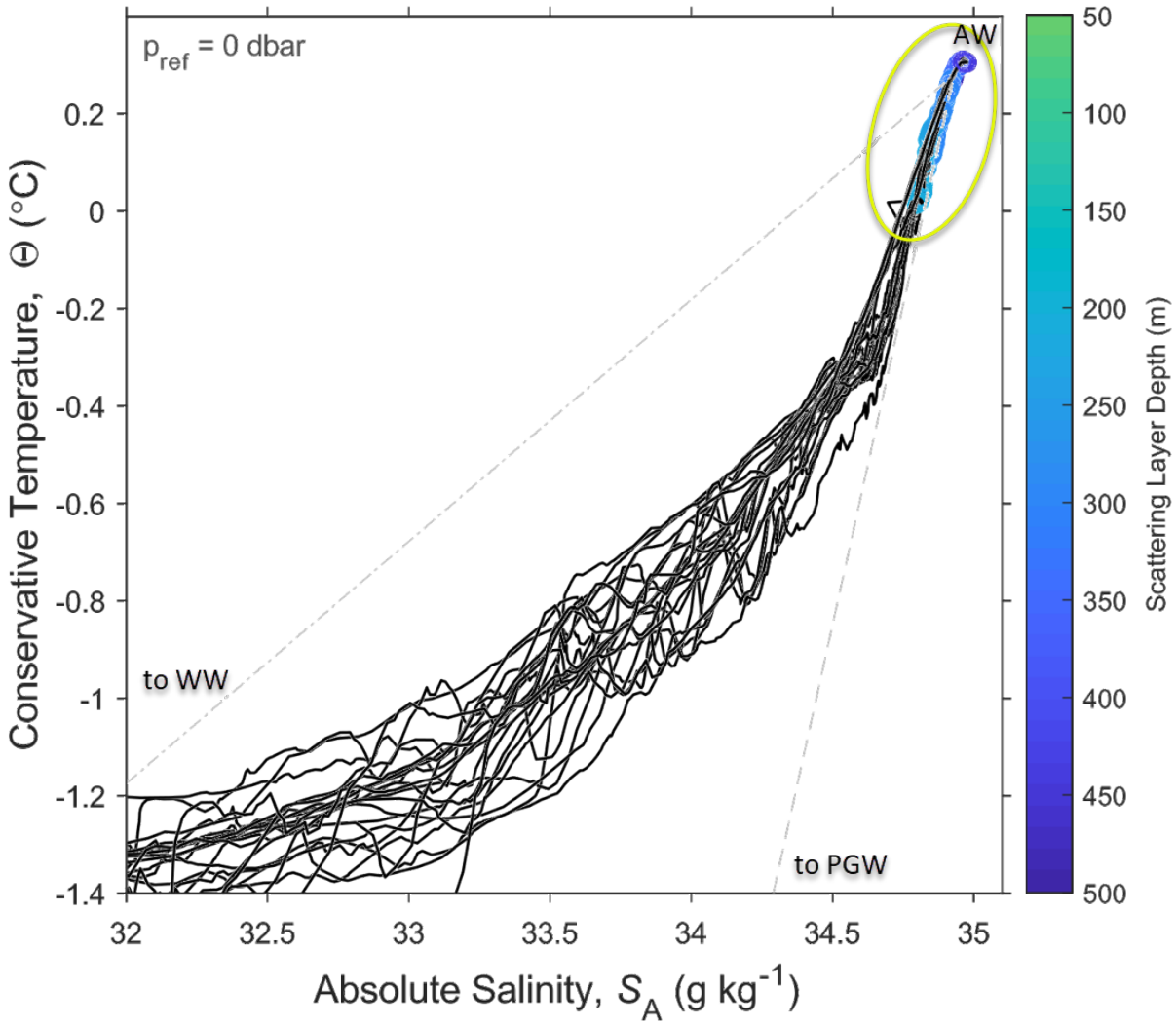

Figure 76: Overlaid T-S diagrams for CTDs associated with the 'homogeneous preference' scattering layers (CTDs 002, 015, 016, 020 – 023, 030 – 044). The scattering layer picks corresponding to each CTD, highlighted with a yellow circle, are plotted as open circles colored by depth.

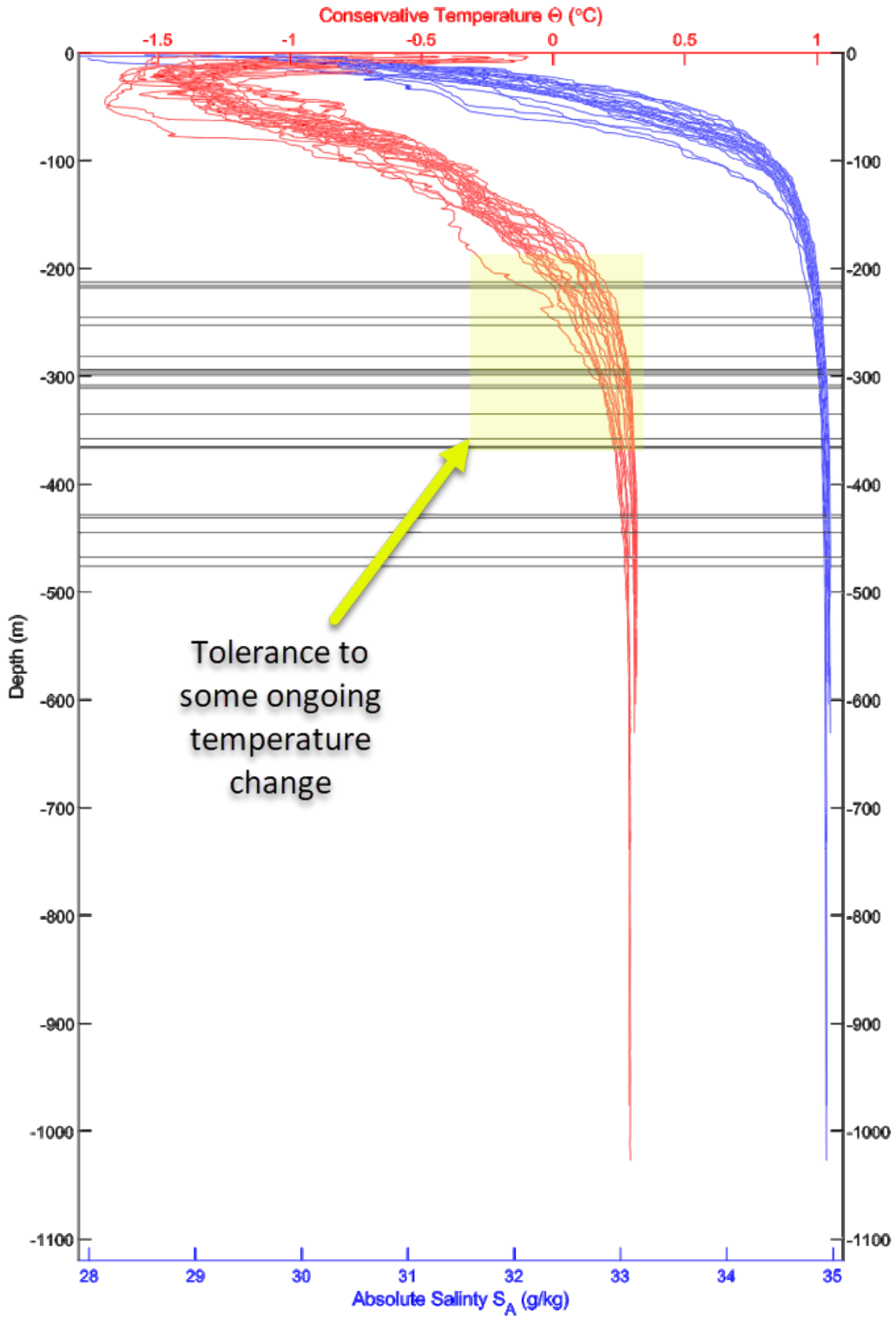

Figure 77: Overlaid temperature and salinity plots for CTDs associated with "homogeneous preference" scattering layers (CTDs 002, 015, 016, 020 – 023, 030 – 044). The average scattering layer depths are indicated by horizontal lines.

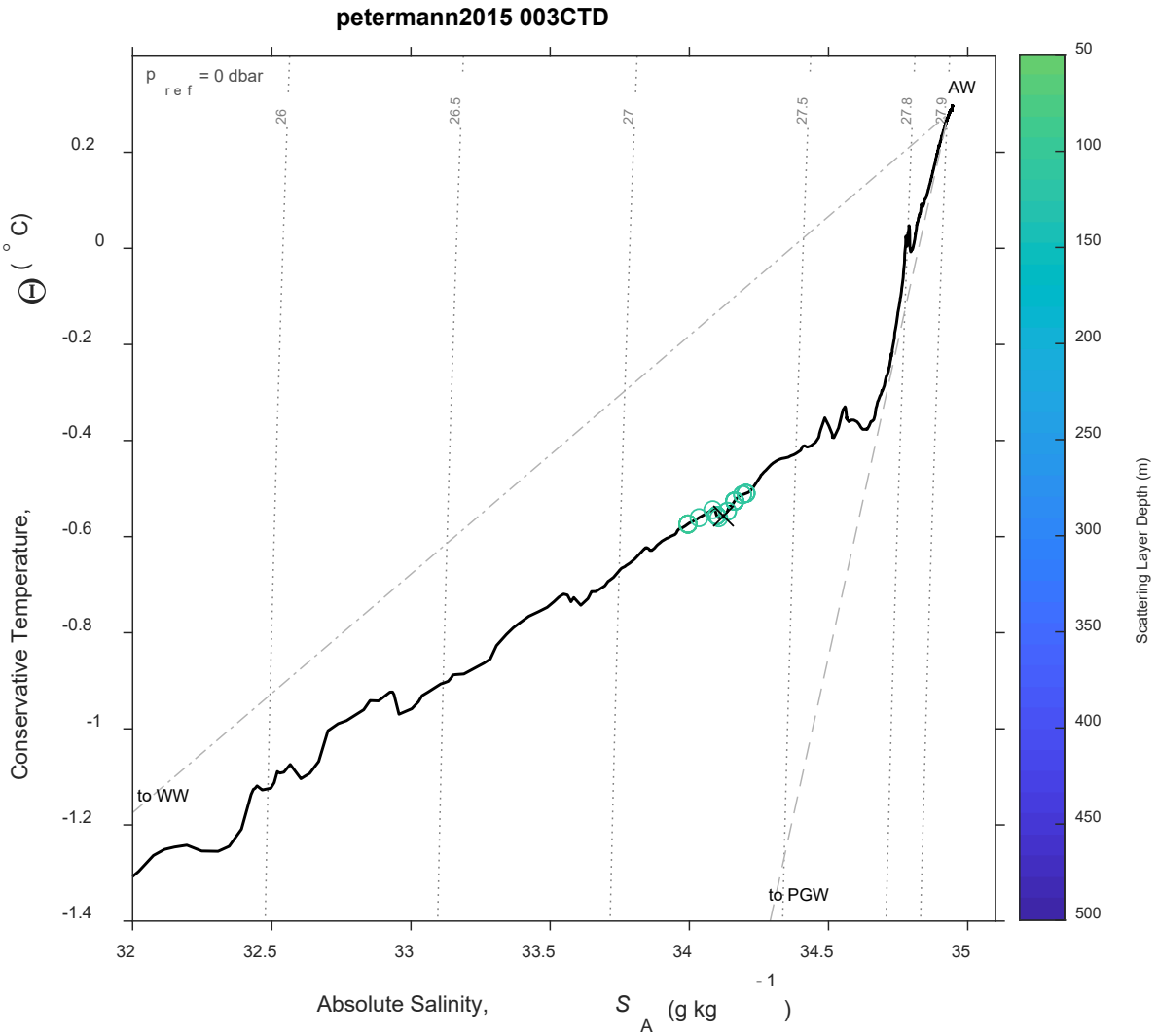

Figure 78: Temperature-Salinity (T-S) diagram for CTD 003, an example of a scattering layer associated with the more heterogenous portion of the water column. The scattering layer picks corresponding to this CTD are plotted as open circles colored by depth; a black 'x' indicates the average depth for the top of the scattering layer in this location. Isobars are shown as labeled grey dotted lines.

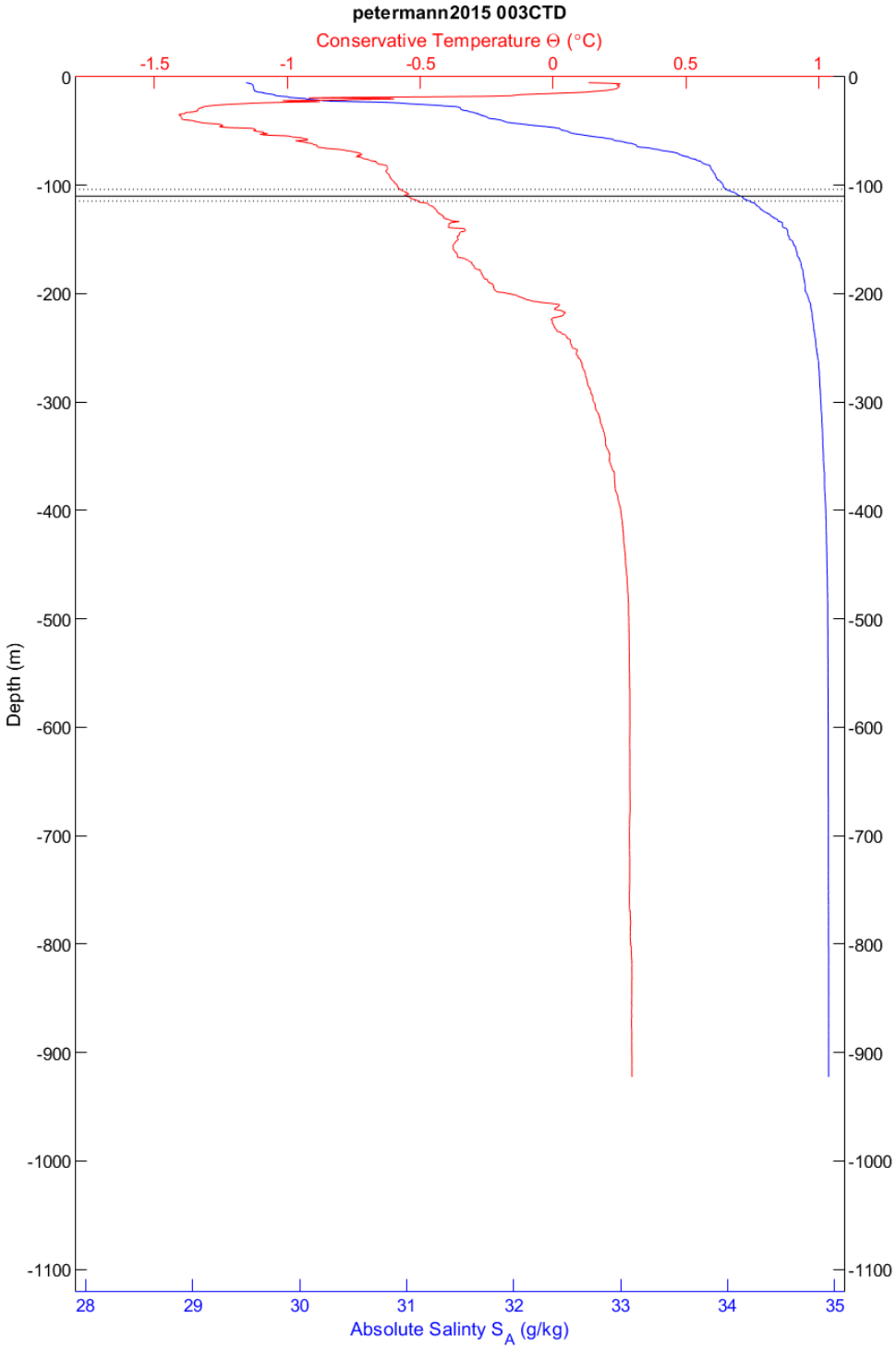

Figure 79: Temperature and salinity plotted by depth, CTD 003. The scattering layer depth is indicated by horizontal lines; the solid line is the average depth, the dotted lines are the shallowest and deepest depths, in all cases for the top of the scattering layer.

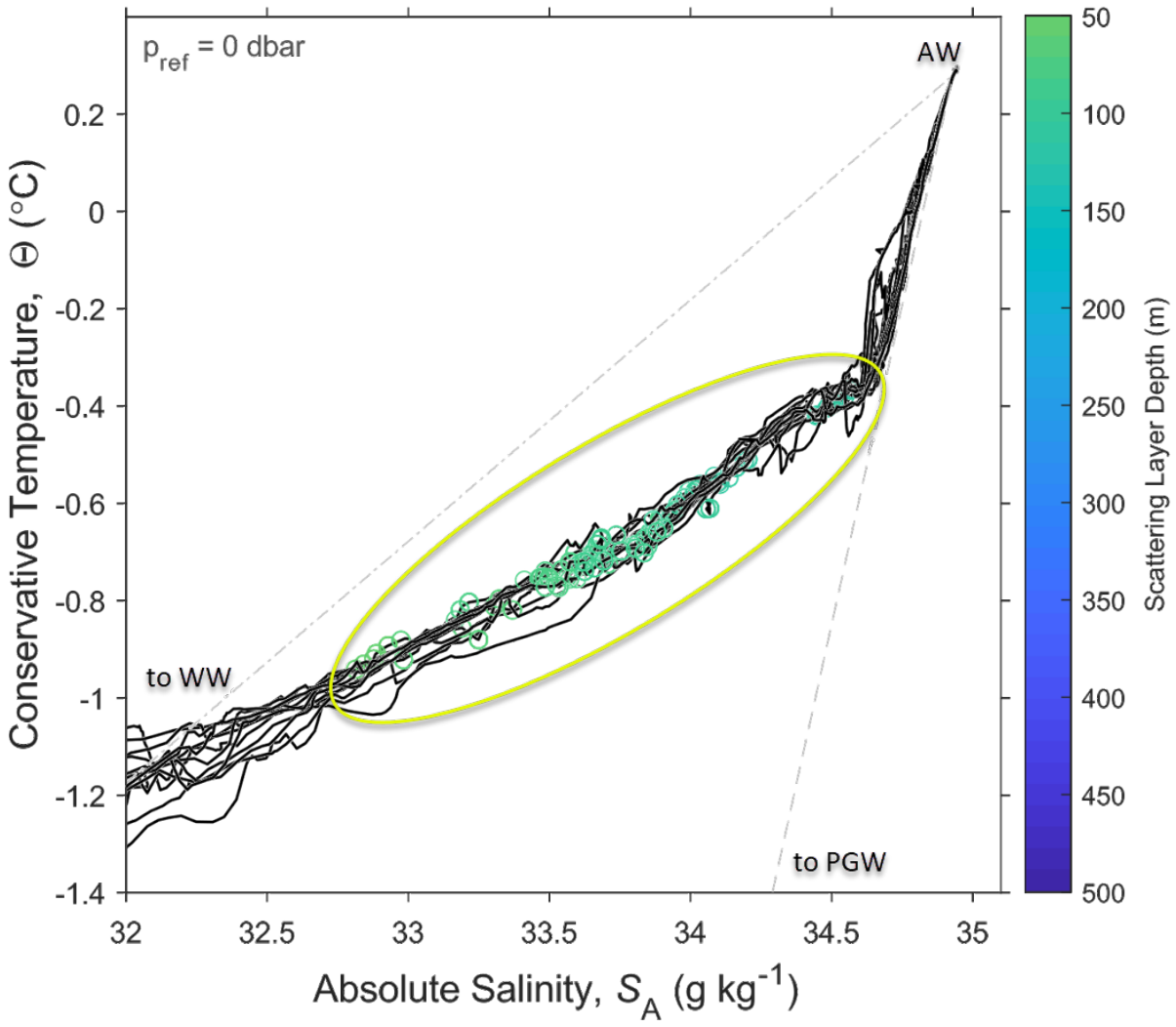

Figure 80: Overlaid T-S diagrams for CTDs associated with the 'heterogeneous preference' scattering layers (CTDs 003 – 014). The scattering layer picks corresponding to each CTD, highlighted with a yellow circle, are plotted as open circles colored by depth.

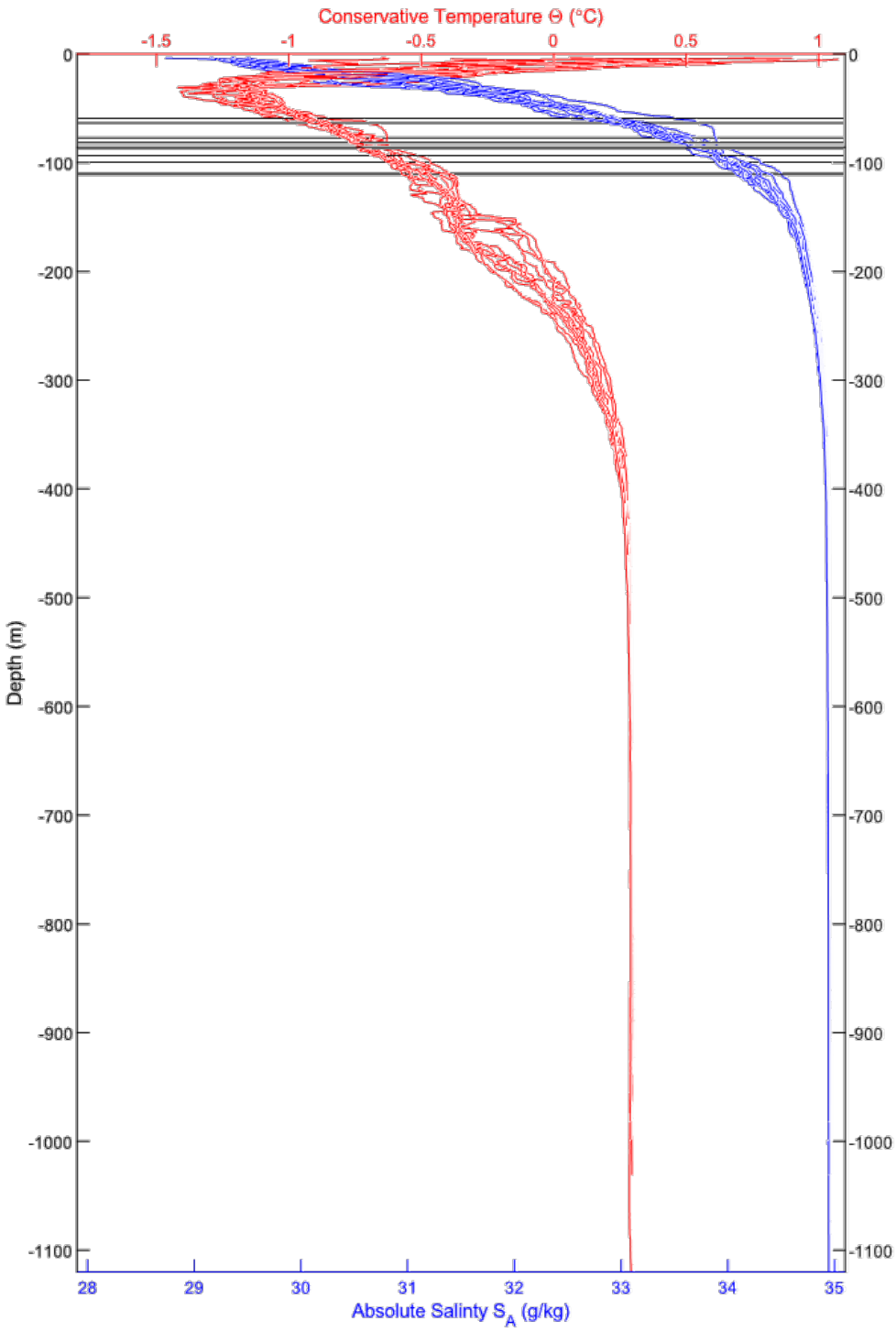

Figure 81: Overlaid temperature and salinity plots for CTDs associated with the "heterogenous preference" scattering layers (CTDs 003 – 014). The average scattering layer depths are indicated by horizontal lines.

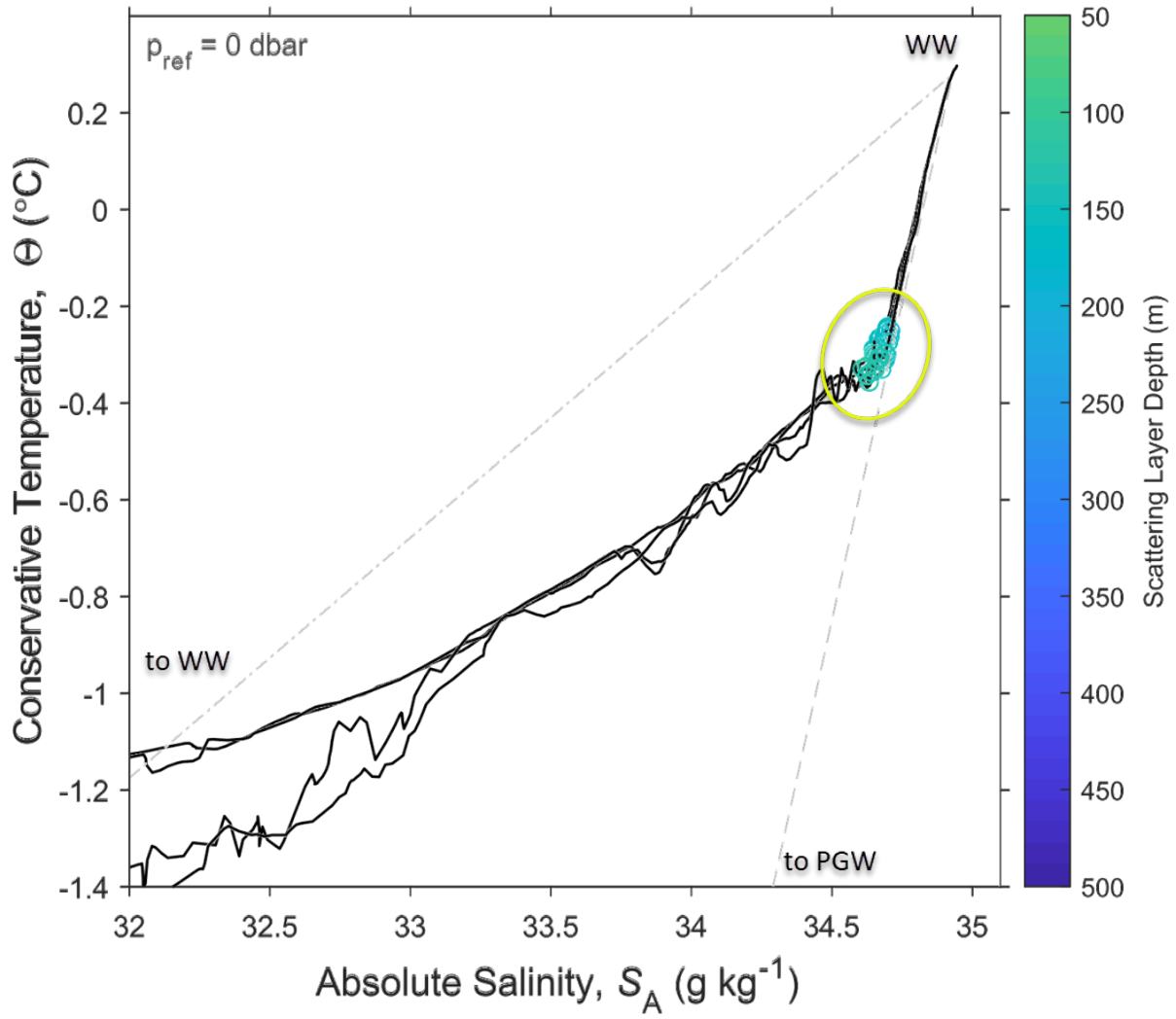

Figure 82: Overlaid T-S diagrams for CTDs associated with the 'transitional' scattering layers (CTDs 017 – 019, 024). The scattering layer picks corresponding to each CTD, highlighted with a yellow circle, are plotted as open circles colored by depth.

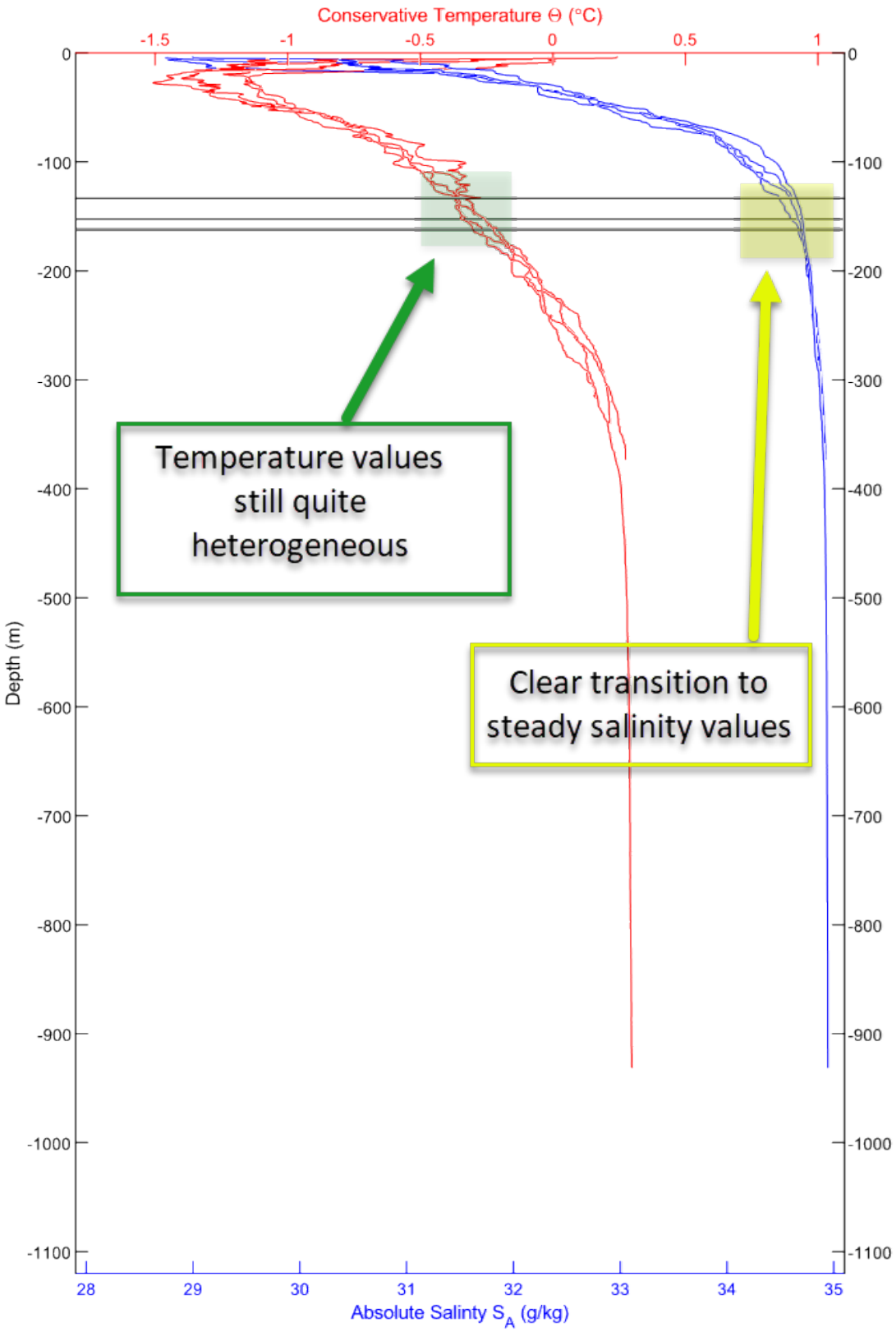

Figure 83: Overlaid temperature and salinity plots for CTDs associated with the "transitional" scattering layers (CTDs 017 – 019, 024). The average scattering layer depths are indicated by horizontal lines.

These CTD groups correspond with distinct locations in the study area. With a few exceptions, the deeper, warmer, saltier homogenous preference scattering layers are associated with Hall Basin and the western to central portion of the fjord entrance, the shallower, colder, fresher heterogenous preference scattering layers with the central fjord, and the transitional scattering layers with the far eastern side Hall Basin, just outside of the fjord entrance (Figure 84).

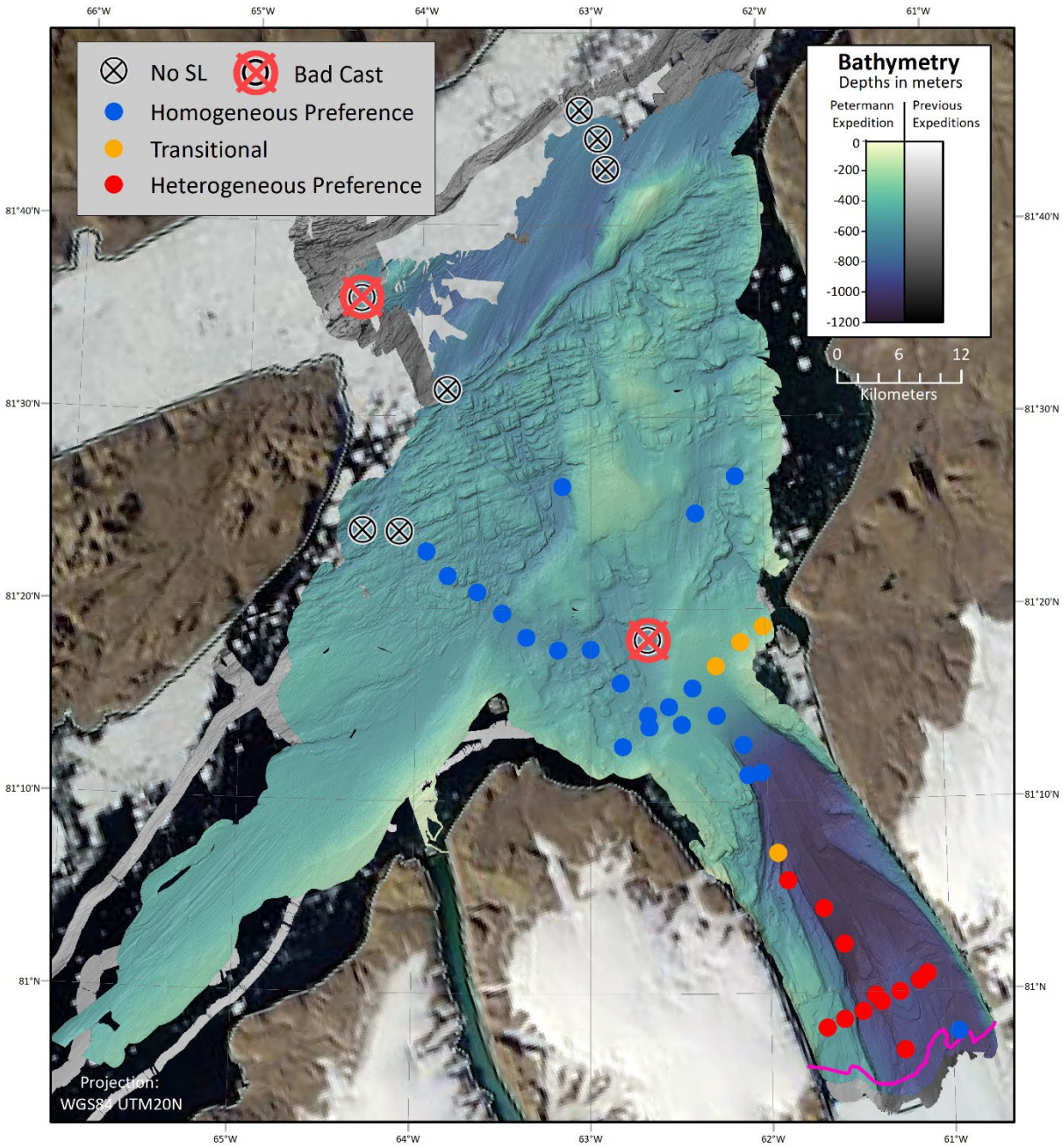

Figure 84: CTD locations colored by scattering layer group. Red circles indicate "heterogenous preference" layers, blue circles "homogenous preference" layers, and orange transitional layers. Black circles with "X" mark locations of CTDs with no associated scattering layers; when overlaid with a red circle and "X", it was considered a bad cast. Projection is WGS 84 UTM 20N.

There is a distinctive absence in scattering layer presence along the western edge of Hall Basin, towards Ellesmere Island (Figure 85). Heuzé et al. (2017) noted that the CTD casts in that area (026 – 029, 045, 046), which are directly in the Arctic outflow,

were the coldest and least oxygenated encountered during the expedition. It is possibly that the low oxygen levels she described are the reason for the lack of scattering layer at these CTD stations and in that area in general. It could also be related to the strength of the current here, as Münchow et al. (2007) noted that the strongest currents coming into Hall Basin from Kennedy Channel were within 10 km of the Ellesmere Island coast and extend to depths of over 300 m, with speeds in excess of 40 cm s^{-1}. Though some of this Arctic outflow sweeps towards Petermann Fjord to become fjord inflow (Johnson et al., 2011; Heuzé et al., 2017), it seems likely that a strong current continues to carry water along the Ellesmere Island coast down through Robeson Channel, creating an inhospitable environment for mobile organisms and effectively clearing out drifting components of the scattering layer (Figure 85). The portion of the Arctic outflow that turns in towards Hall Basin may transport some scatterers there where they concentrate as the currents reduce.

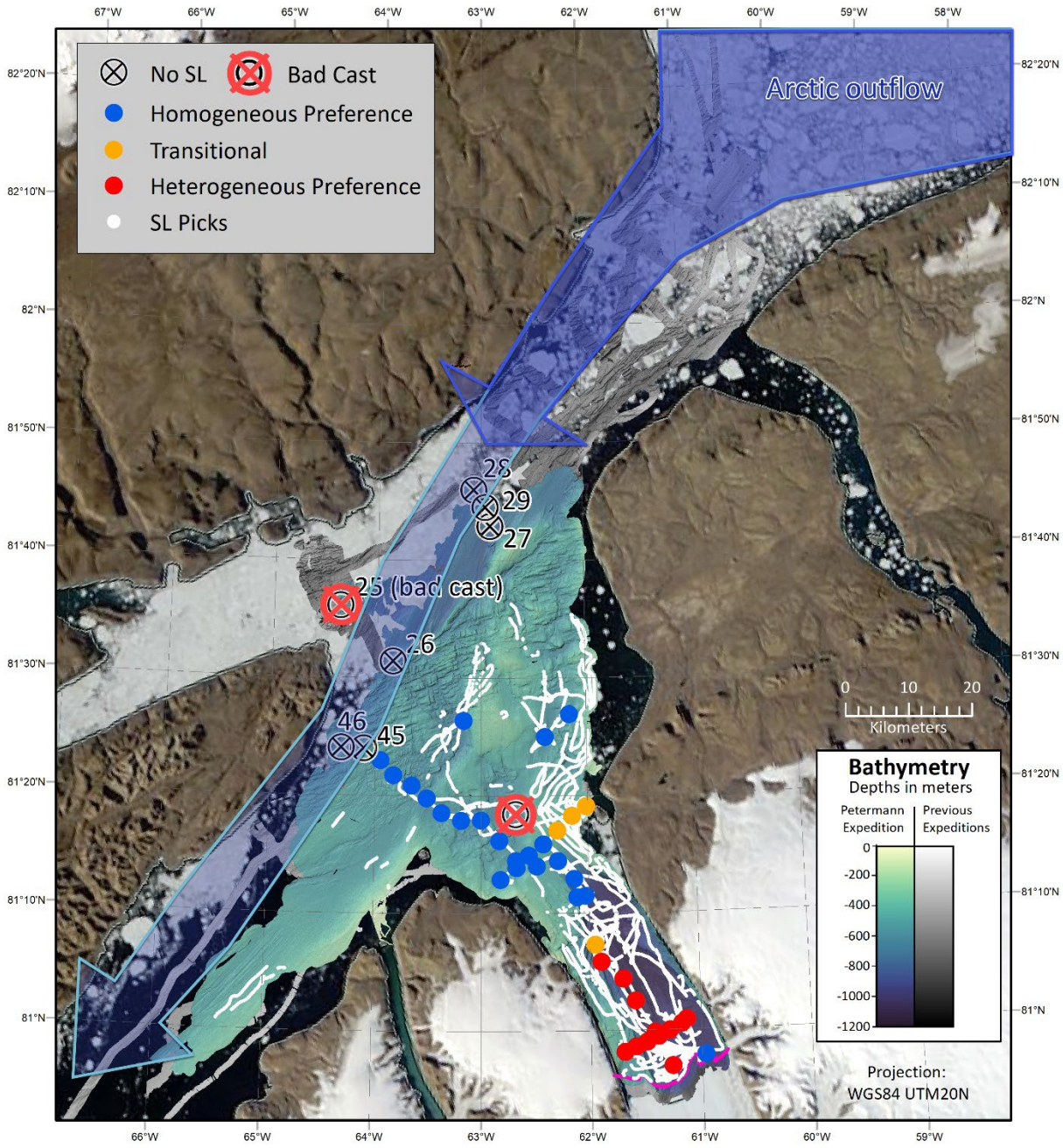

Figure 85: Relationship between lack of scattering layer and Arctic outflow. There is a distinctive gap in scattering layer presence along the western edge of the region. This may be related to low oxygen levels reported by Heuzé et al. (2017) that correspond to the casts with no scattering layer. It could also be related to the strength of the Arctic outflow in this area, as reported by Münchow et al. (2007). The darker blue arrow shows the strongest part of the outflow as reported in Münchow et al. (2007), within 10 km of the Ellesmere Island coast. The lighter blue arrow is the continuation of this outflow through Hall Basin (Münchow and Melling, 2008; Johnson et al., 2011; Heuzé et al., 2017), and possibly continuing into Robeson Channel.

A second distinctive absence of scattering layer appears near the center of Hall Basin (Figure 86). During preliminary analysis, we believed this gap might be due to the

gyre proposed by Johnson et al. (2011). Closer analysis showed the gyre detected by Johnson in 2011 to be further south (at least at that time), in a location not associated with a lack of scatterers in 2015 (Figure 87). It seems reasonable that there could be some migration in the location of the circulation gyre; the absence of scatterers could be related to what appears to be increased flow rates in that location, if surface currents were similar to what was observed by Johnson in 2011 (yellow circle on Johnson overlay, Figure 87). The absence of scatterers could also simply be related to the series of bathymetric highs in this region (Figure 88). The tops of the shoals and any changes in circulation they produce may impede on the preferred depth of the scattering layer (Figure 89).

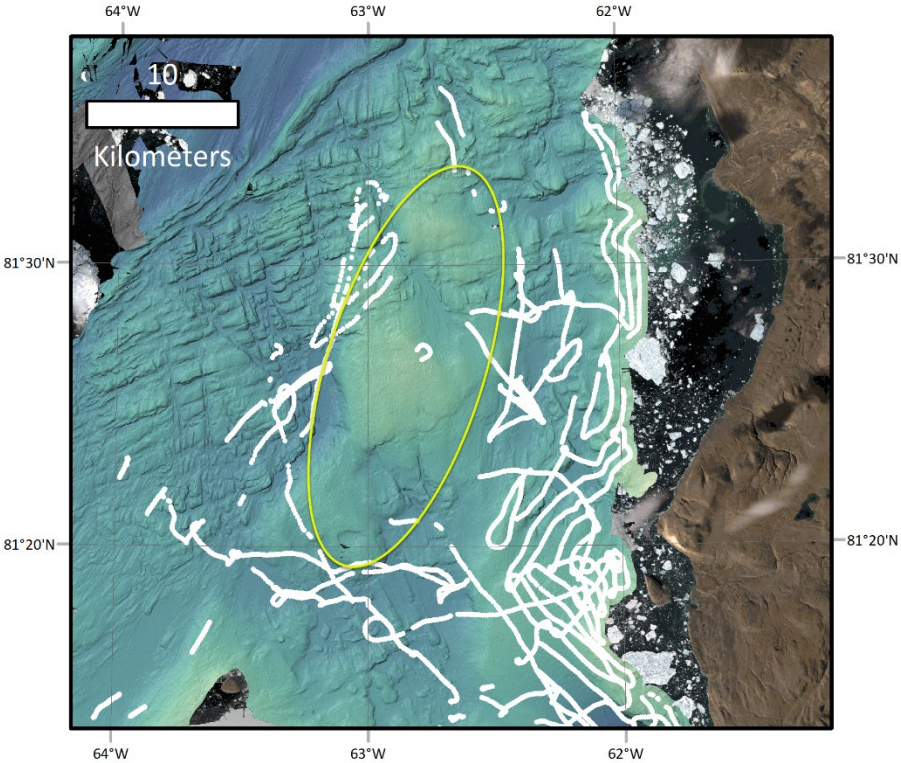

Figure 86: Distinctive absence in scatterers near the center of Hall Basin, highlighted by the yellow circle. Here, scattering layer picks are shown in white. Projection is WGS84 UTM 20N.

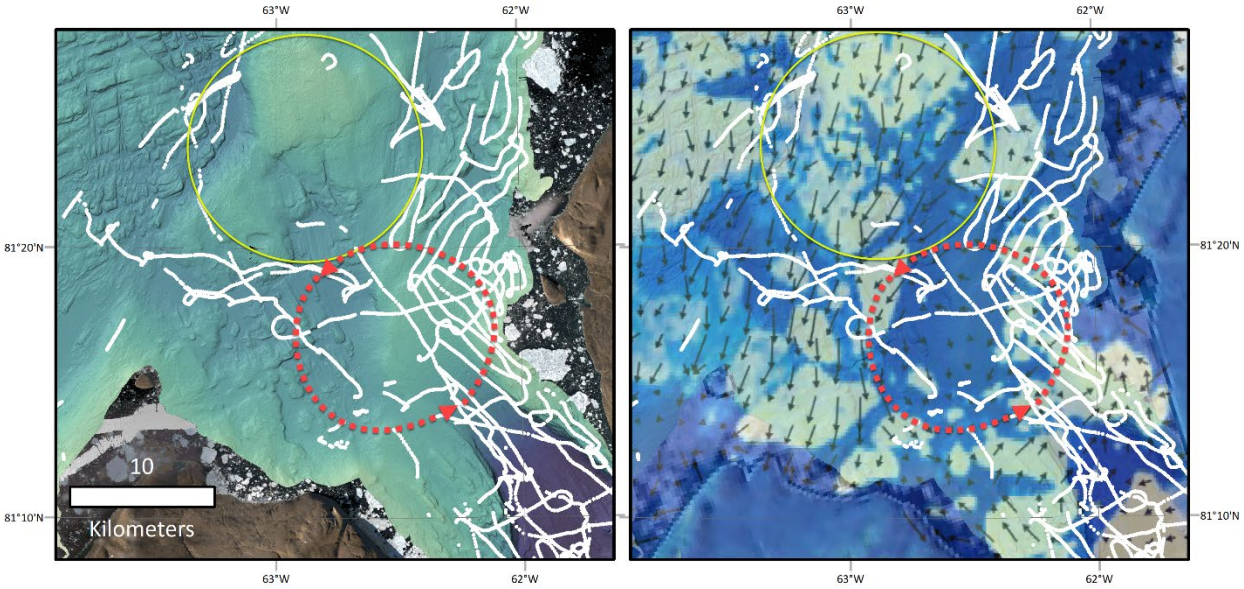

Figure 87: Comparison of location where scatterers are absent to Johnson et al. (2011) analysis of surface currents. The map on the left shows Petermann Expedition bathymetry with yellow-blue indicating shallow depths and dark purple deep, overlaid with scattering layer picks in white. The map on the right shows the same data overlaid with an analysis of surface currents from Johnson et al. (2011), with the arrows indicating current vectors and the length of the arrows indicative of relative strength. The area of absence, highlighted by the yellow circle, does not correspond to the gyre location (highlighted by the red circle), or at least to the location of the circulation gyre at the time of Johnson's analysis.

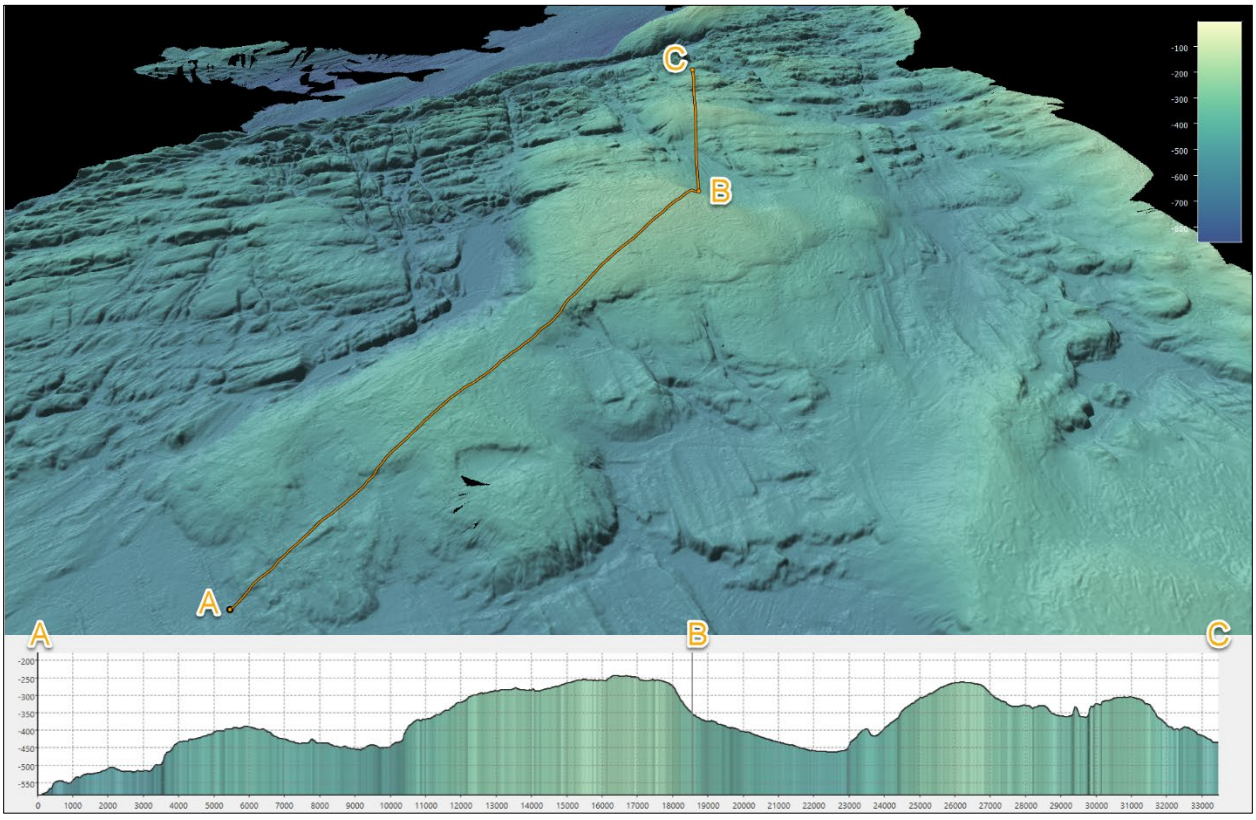

Figure 88: Perspective view and bathymetric profile along bathymetric highs in Hall Basin. The perspective view is facing north and is vertically exaggerated 3x. The profile is vertically exaggerated 10x.

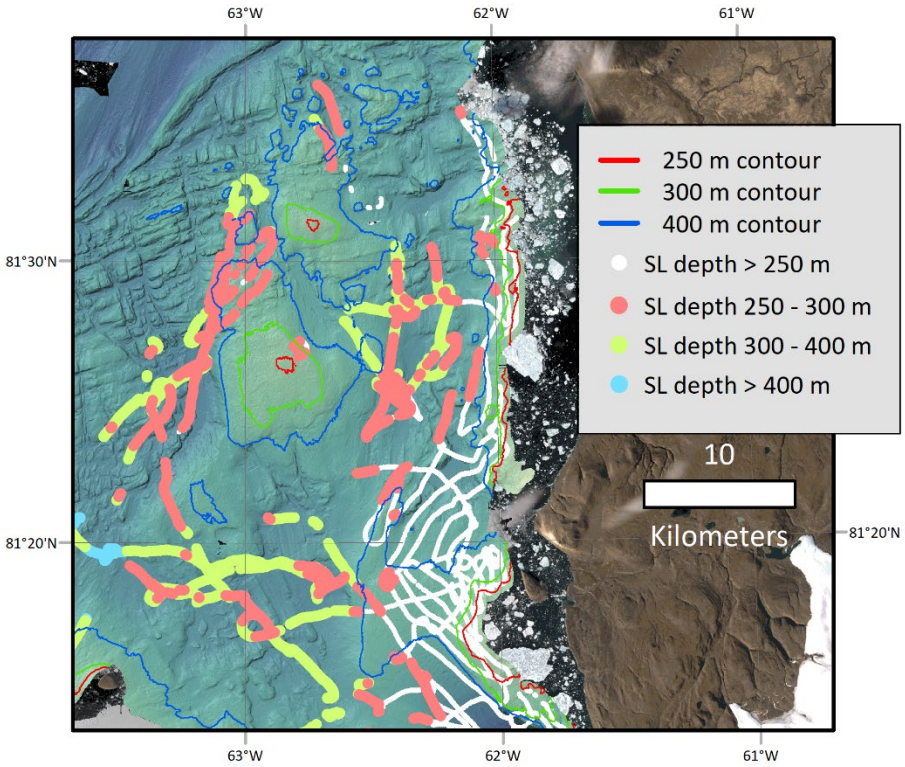

Figure 89: Scattering layer (SL) depth compared to bathymetric shoals in this region; the contours are in reference to the bathymetric depths.

The overall pattern of homogeneous preference, heterogenous preference, and transitional scattering layers observed at the CTD stations does appear to have relationship to the hydrography in the study area as described in 2.3 (Figure 90). The homogeneous preference scatterers, found in the deeper, warmer, saltier part of the water column, appear to be associated with areas where Arctic outflow has turned into Hall Basin and become the source for fjord inflow waters. The heterogeneous scatterers, found in the shallower, fresher, colder, parts of the water column, and transitional scatterers, where water column properties are transitioning from heterogeneous to homogeneous, appear to be associated with the meltwater-influenced fjord outflow. This apparent relationship could be interpreted to extend to the full scattering layer distribution (Figure 91).

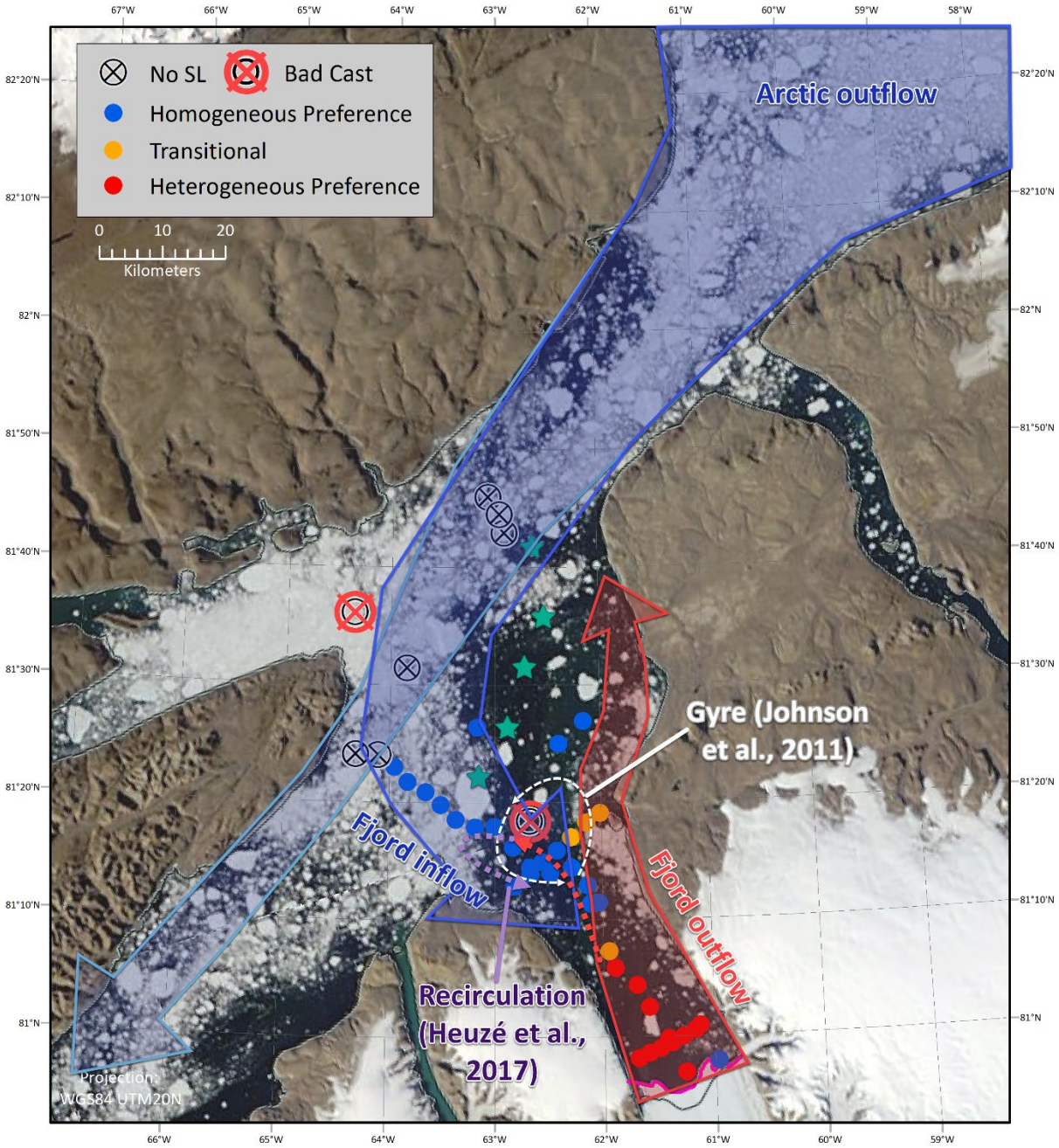

Figure 90: Arctic outflow, fjord inflow and meltwater influenced fjord outflow compared to scattering layer groups at CTD stations. Green stars show the location of bathymetric highs discussed above and in section 2.2. The dashed white arrow approximates the position of the gyre (Johnson et al., 2011), the dashed red to purple arrow the location of recirculation (Heuzé et al., 2017).

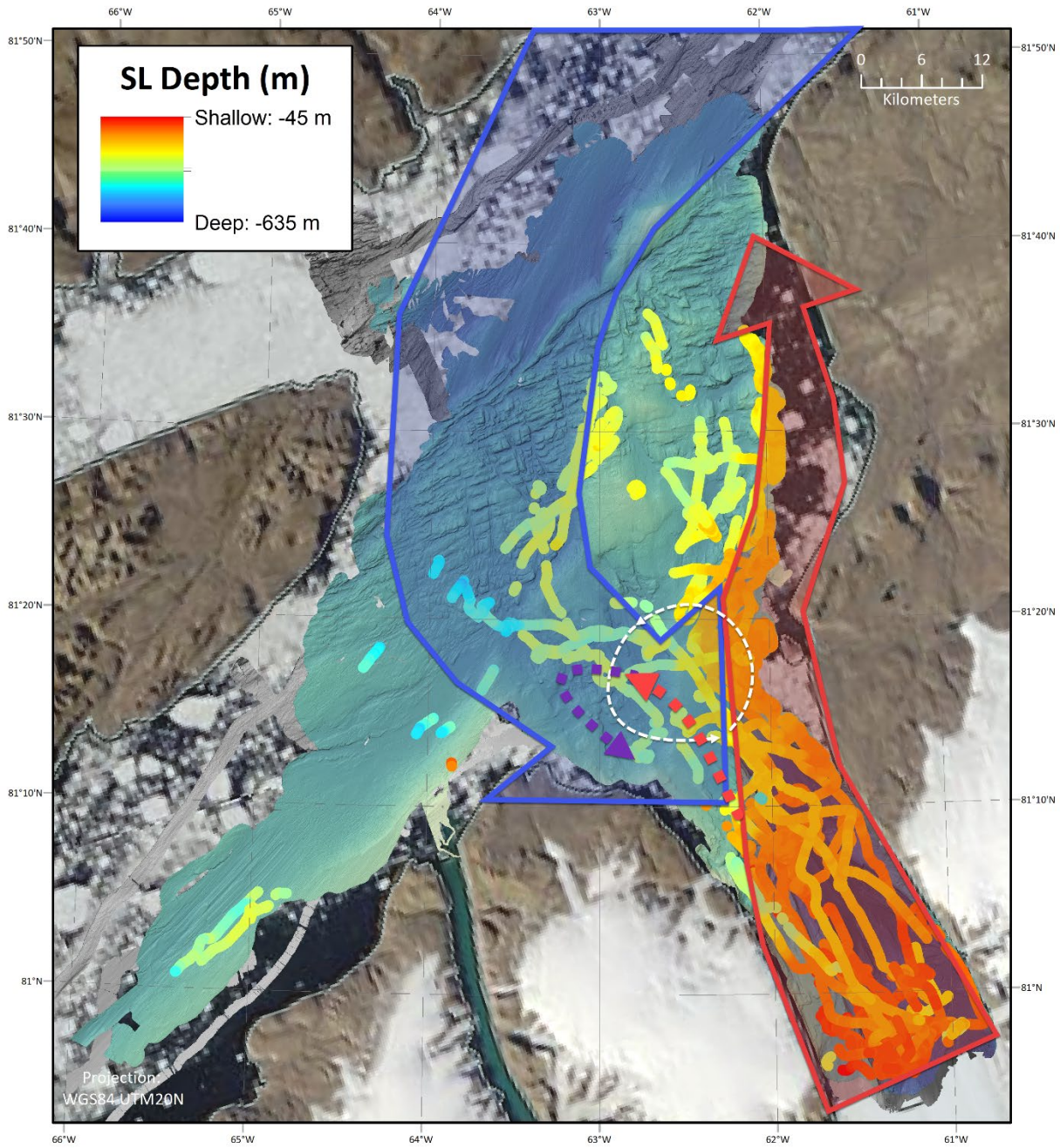

Figure 91: Arctic outflow, fjord inflow and meltwater influenced fjord outflow compared to the full scattering layer distribution. The dashed white arrow approximates the position of the gyre (Johnson et al., 2011), the dashed red to purple arrow the location of recirculation (Heuzé et al., 2017).

The transitional scattering layers are, for the most part, focused in one area. They are defined by their preference for the transitional portion of the water column, a sharp bend in the T-S diagram known as a “kink” or a “knickpoint”. Geospatially, three of the four stations occur where the fjord opens up into Hall Basin. There is a

concentration of scatterers in that region that are at the same general depth as those found at the CTD station (~ 140 – 170 m), and similar depth scattering layers continue up the coast (Figure 92). This water depth also has the strongest concentration of meltwater, broadly at 100 – 280 m with the highest concentration at 150 – 200 m (Heuzé et al., 2017). The scatterers may be attracted to this transitional area due to enhanced oxygen or nutrients provided by the meltwater, and the continuation along the coast may be tracking the coastal current inferred by Heuzé (2017).

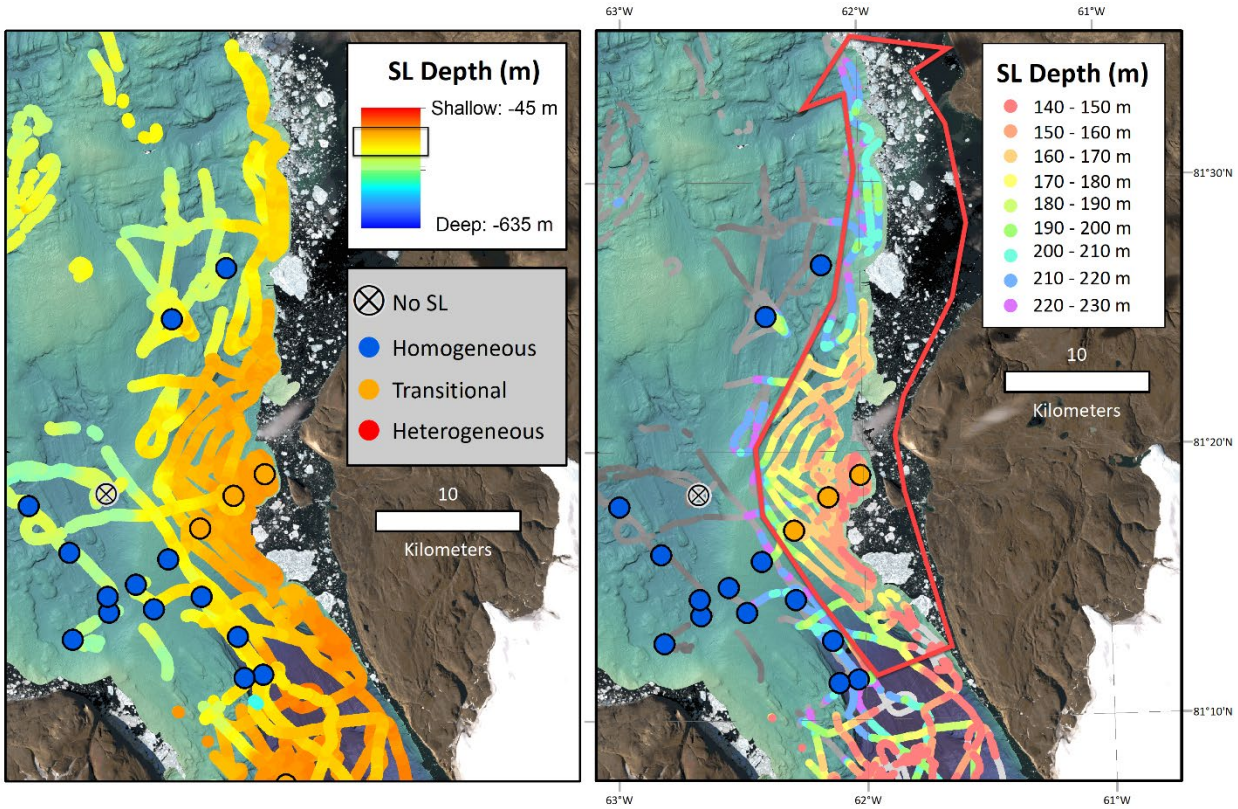

Figure 92: Scattering layers near the transitional CTDs 017 - 019. The map on the left shows all scattering layers colored by depth; the black box in the legend highlights the depth range of interest. The map on the right breaks apart that depth range; scatterers above and below the 140 – 230 m depth range are colored in greyscale with white being the shallowest and dark grey the deepest. The red arrow indicates the inferred path of outflow waters (Heuzé et al., 2017) after leaving the fjord.

Visual examination of echograms showed some additional interesting scattering layer behavior that could potentially be related to smaller scale hydrographic processes.

The first example, described in section 2.3, was an increase in scatterers that appeared to be related to outflow from a small outlet glacier (Figure 93). Another example was found near the face of the glacier. Many scattering layers here were patchy with variations in scattering strength (Figure 94). This could be a reflection of sub-glacial meltwater plumes rising to the surface, entraining and killing some plankton, causing stronger swimmers to migrate away from the plumes, all the while providing nutrients for phytoplankton blooms and creating a foraging hotspot, as proposed by Lydersen et al. (2014). The third example was found at the mouth of fjord, where the scattering layer was observed to suddenly drop in depth and weaken (Figure 95). This could be related to inflow/outflow water masses at the fjord mouth or could potentially be a reflection of the gyre described by Johnson et al. (2011). A final example was near the entrance to Bessel Fjord. At this location, an aggregation of scatterers appeared to be associated with some kind of release from seafloor, which the expedition team speculated to be gas or fresh water (Figure 96).

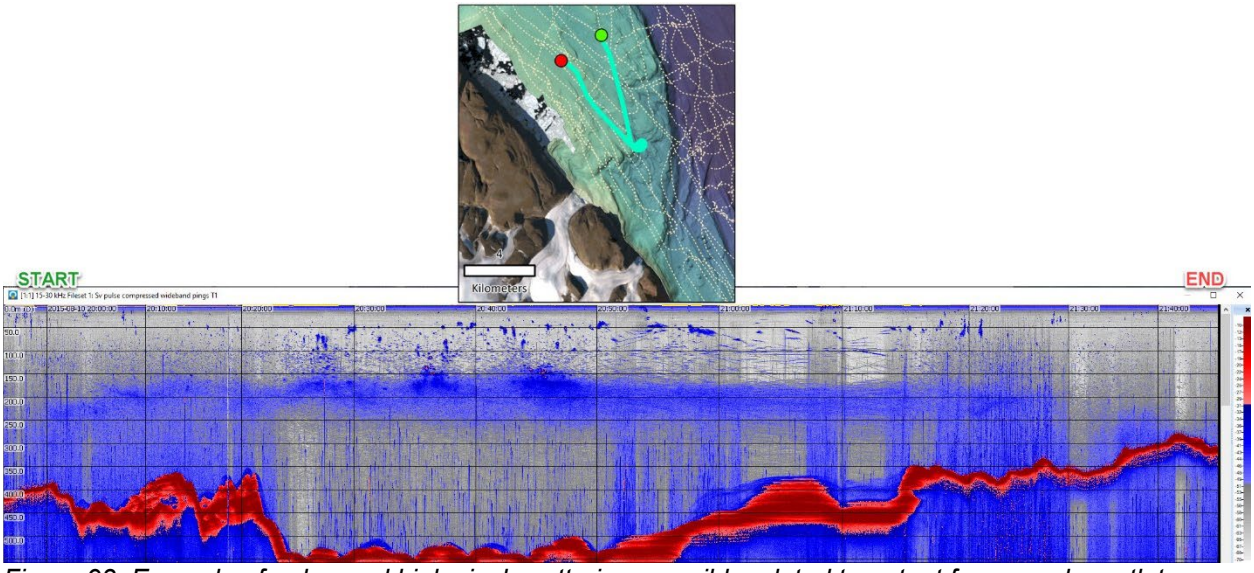

Figure 93: Example of enhanced biological scattering, possibly related to output from nearby outlet glaciers. The green and red dots on the map correspond to the start and end of the echogram, respectively. Note that this is a repeat of Figure 24.

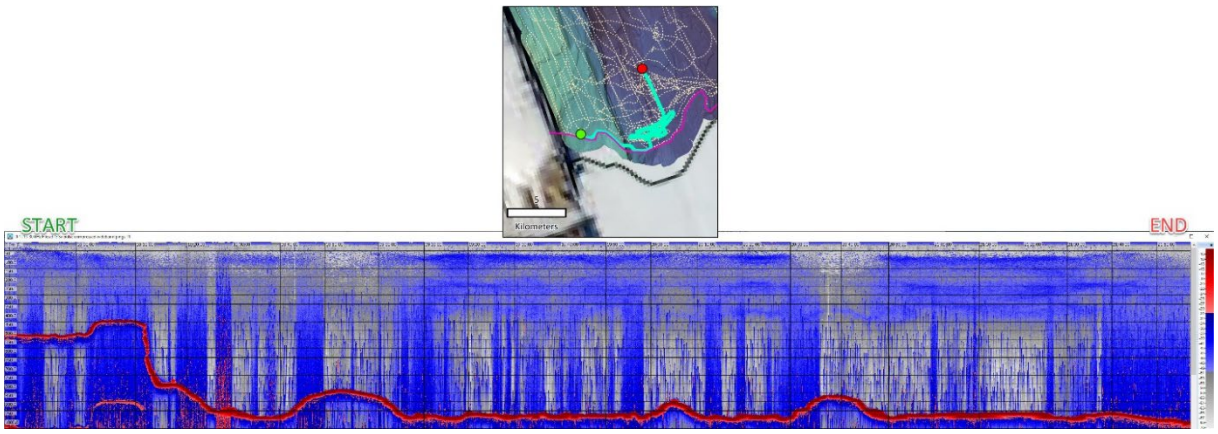

Figure 94: Patchy scattering layers associated with the glacier face. The start of the echogram aligns with the green dot on the map, the end with the red dot. Echogram is uncalibrated.

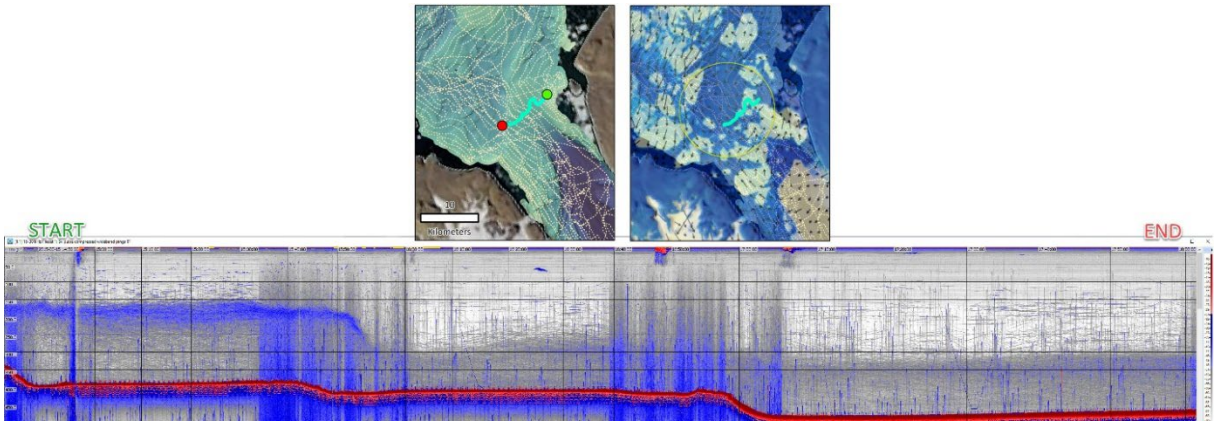

Figure 95: Depression and weakening of the scattering layer associated with the fjord entrance. This could potentially be related to the gyre described by Johnson et al. (2011), shown on map on top top right. Echogram is uncalibrated.

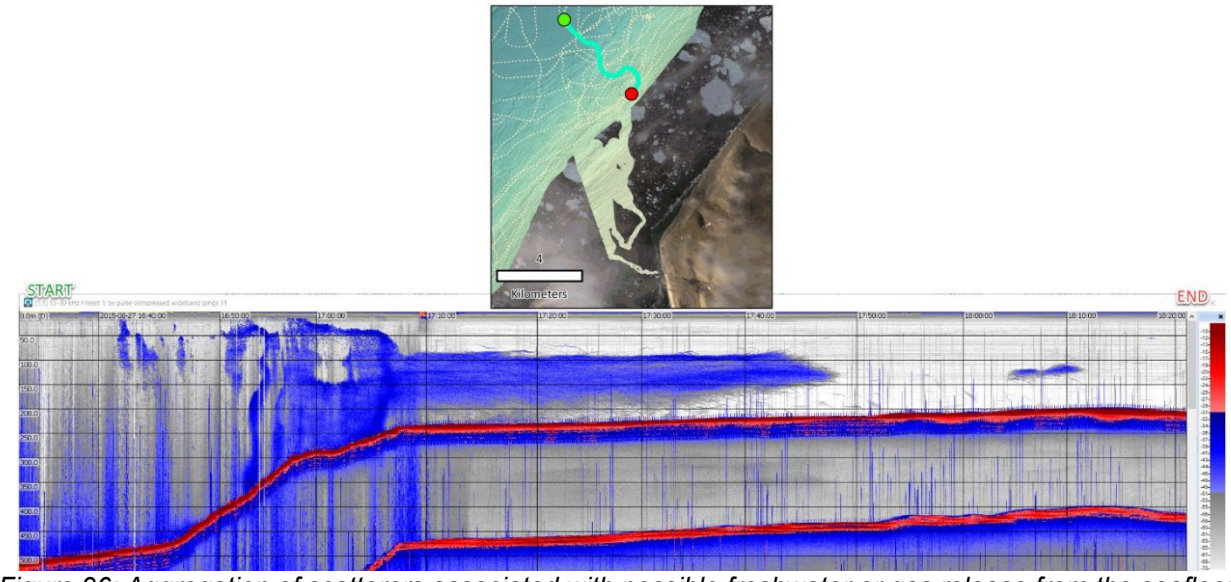

Figure 96: Aggregation of scatterers associated with possible freshwater or gas release from the seafloor. Echogram is uncalibrated.

4.3 What are the Scatterers?

Thus far, we have established a clear association between different scattering layer behavior and local water column properties, with the organisms in the scattering layers showing distinct preferences for deeper, warmer, saltier homogeneous portions of the water column, shallower, colder, fresher heterogeneous portions of the water column, or transitional water column environments where water column properties are moving from heterogeneous to homogeneous. We now explore the question of what the scattering layers consists of. Due to the lack of biological sampling, we are limited to information we can glean from the acoustics and our understanding of the regional setting and the organisms that inhabit it. As discussed in section 1.3.2, other researchers have been able to gain insight into the nature of scatters through analysis of S_v, TS and frequency response, including in Arctic environments (Geoffroy et al., 2011; Benoit et al., 2014; Geoffroy et al., 2016). We have attempted to do the same here, with an understanding of the limitations of this opportunistic data set – specifically, that it was not designed or optimized for bioacoustics analysis, and that no sampling occurred.

4.3.1 Visual indications

In many locations, individual targets could be visually recognized in the echograms. The individual targets were most discernable at slow speeds (Figure 97) above the scattering layer, however in many cases what at least appeared to be individual targets were visible within and below the scattering layer as well (Figure 98,

Figure 99). Individual tracks, indicating movement, are visible. There are also instances where targets have a hyperbolic echo shape often interpreted as individual fish on echograms (Figure 99). We believe that these individual targets are a component of the scattering layer.

Individual targets became less discernible with increased density, and perhaps also with depth. In Figure 99, individual targets are not resolvable below ~120 m; in this example density appears to be increasing as well, concentrating at 150 – 200 m. In Figure 100, individual targets are discernable above ~200 m, but are not discernable within the densest part of the scattering layer, between 200 – 375 m. This may be due to depth, weaker targets, or even a change in overall scattering layer composition. It was possible to find examples of visible individual targets at depths greater than 200 m, but the best examples were where targets were quite diffuse (Figure 101). Though we cannot be certain, we hypothesize that dense portions of the scattering layer are at least partially composed of the organisms we can discern as individual targets in other locations.

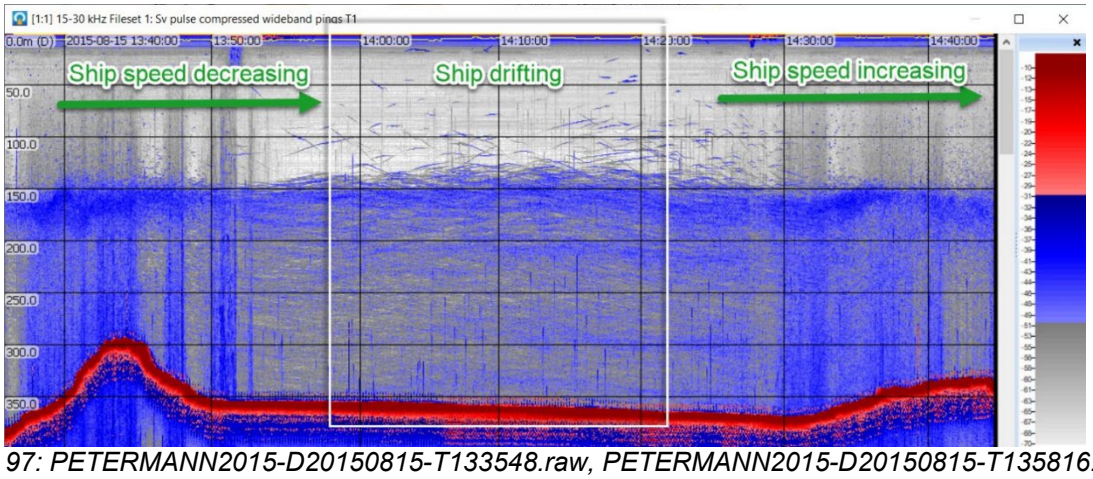

Figure 97: PETERMANN2015-D20150815-T133548.raw, PETERMANN2015-D20150815-T135816.raw, and PETERMANN2015-D20150815-T142141.raw shown in Echoview. Note how individual targets resolve as the ship slows and drifts (white box), and then lose resolution when the ship increases in speed again. Echogram is uncalibrated.

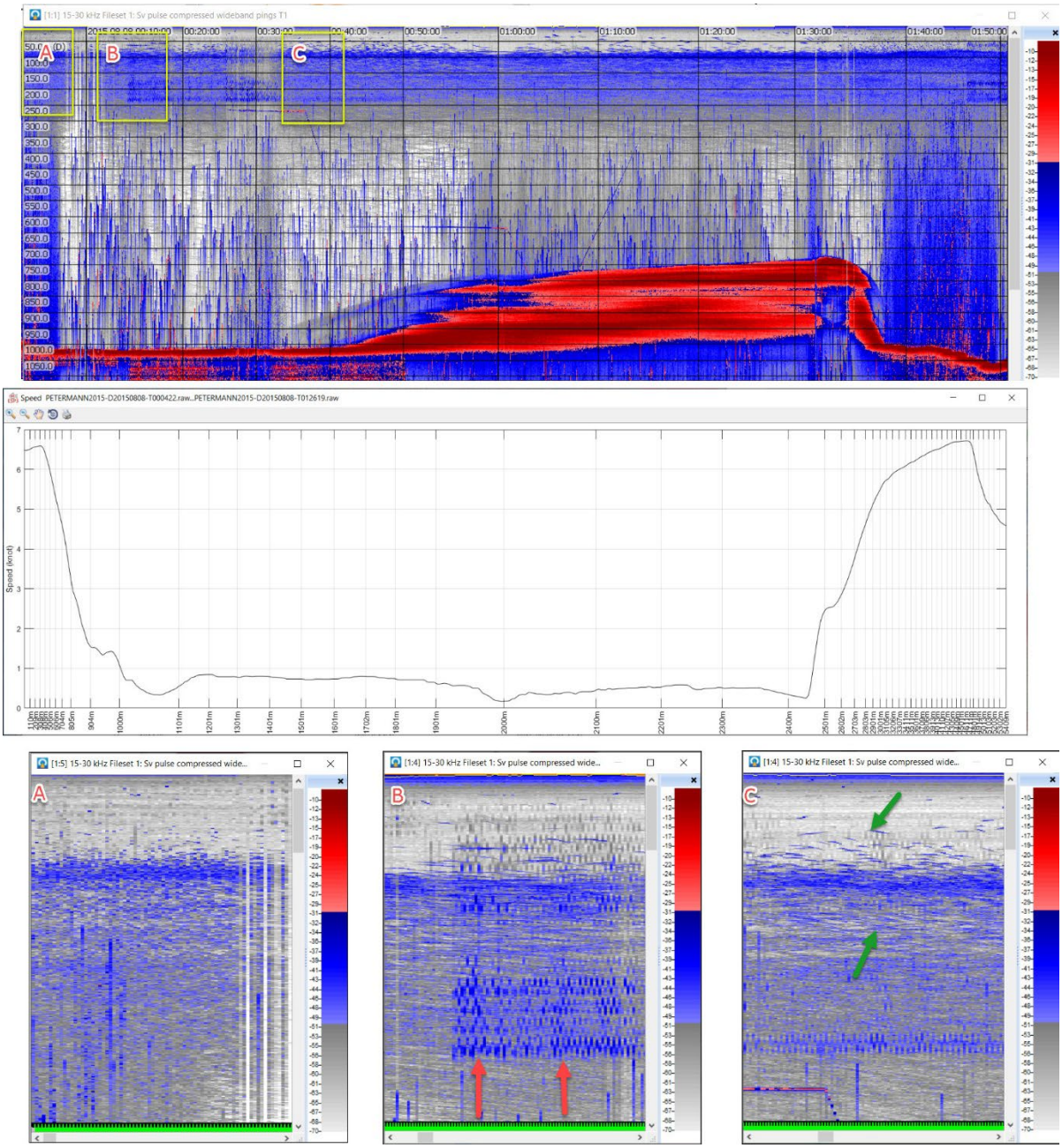

Figure 98: Top, combined echogram for lines PETERMANN2015-D20150808-T000422.raw through PETERMANN2015-D20150808-T012619.raw. Center, ship speed. Bottom, zoomed in portions of the echogram. At higher speeds, individuals are single pixels (A). As the ship slows, individual organism tracks are visible (B), though here they are partially overprinted by interference (red arrows). When the ship is drifting or moving at very slow speed (C), individual tracks are easily distinguished above the scattering layer and appear to be present within the scattering layer as well (green arrows). Also note the presence of an instrument (CTD) in the water column starting between B and C and also visible in the bottom left corner of C, as well as some continued interference in C. Echogram images are uncalibrated.

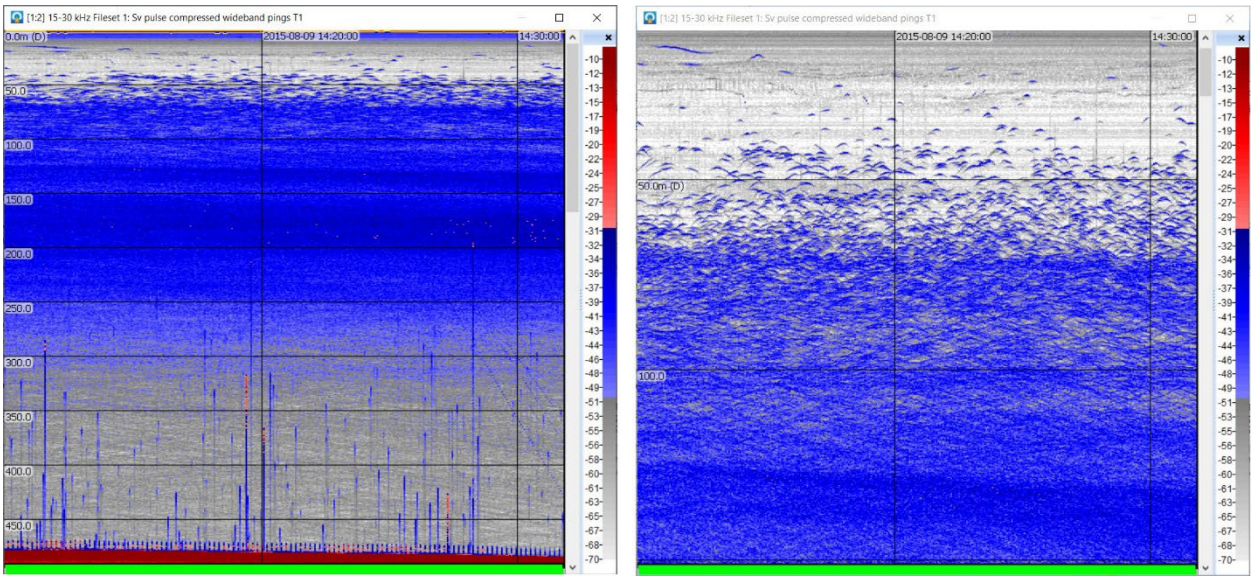

Figure 99: PETERMANN2015-D20150809-T141007.raw. The image on the left shows the full echogram above the seafloor, which covers approximately 170 m at a speed of 0.2 to 0.3 kn. The image on the right is a zoom on the top 150 m of the water column. Individual targets have a hyperbolic shape associated with individual targets and that is often interpreted as individual fish when environmental circumstances support that interpretation. The individual targets appear to be at least partially distinguishable down to at least 100 m. Between 100 and 150 m the scatter becomes very dense and strong and individual targets are no longer distinguishable. Echogram images are uncalibrated.

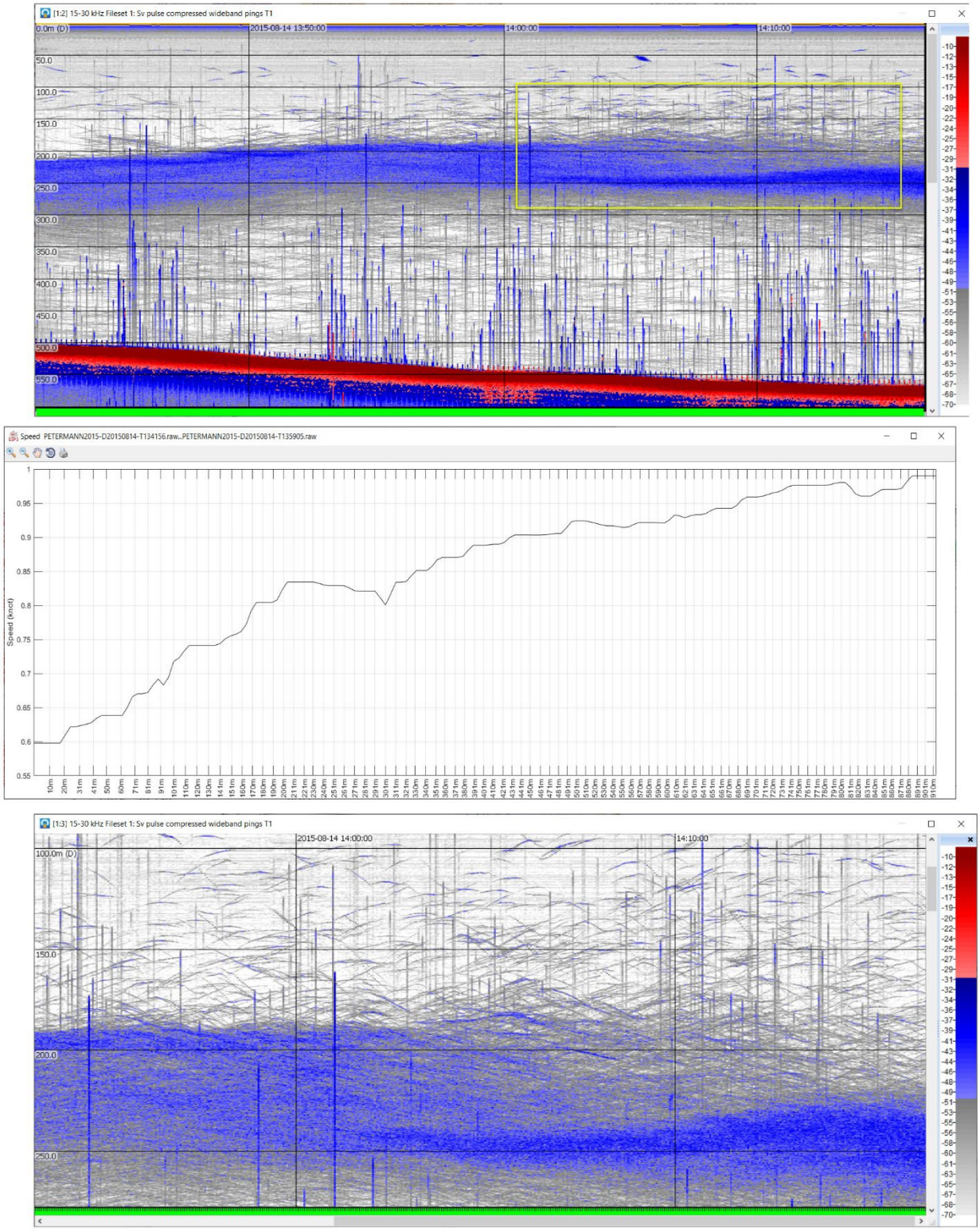

Figure 100: PETERMANN2015-D20150814-T134156.raw through PETERMANN2015-D20150814-T135905.raw. The top image shows the full echogram above the seafloor. The center image shows the speed during acquisition. The bottom image shows a zoom of a portion of the full echogram highlighted by the yellow box. Distance covered is approximately 910 m. Echogram images are uncalibrated.

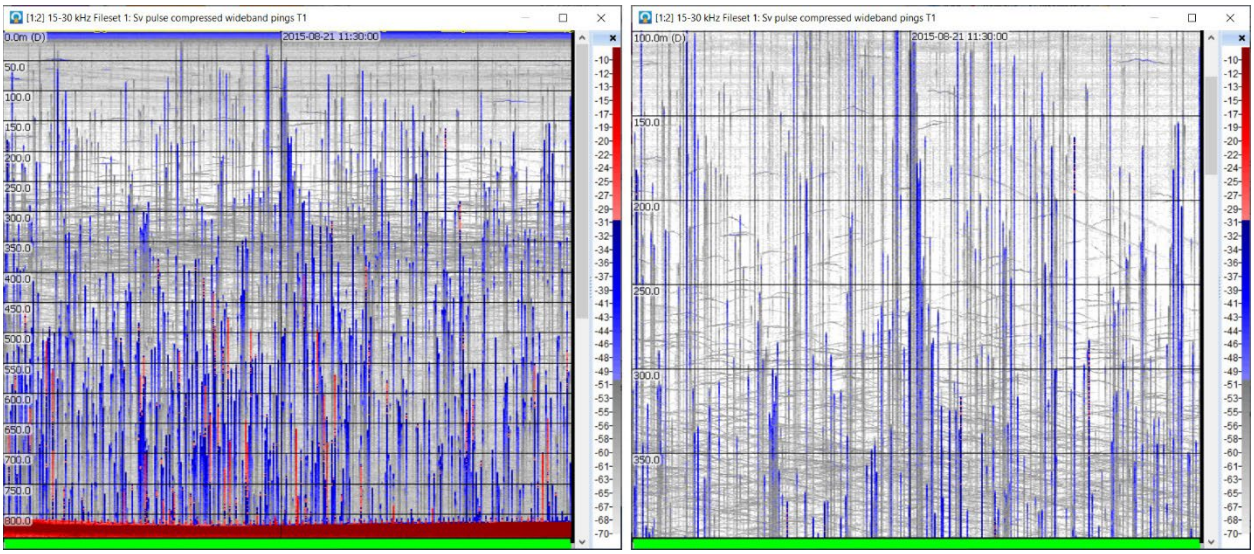

Figure 101: PETERMANN2015-D20150821-T112036.raw. The image on the left shows the full echogram above the seafloor. The image on the right is a zoom between 100 and 400 m. Individual targets are visible at depth, though targets strengths are very low and density is low. Distance covered is approximately 445 m at 0.6 – 0.9 kn. These scatterers were not classified as a scattering layer. Echogram images are uncalibrated.

4.3.2 Frequency Response, Target Strength, and Density Analysis

A total of 18 lines associated with 17 CTD stations were reviewed to determine target strength and frequency response of both individual targets and volume targets (Figure 102). Nine of the lines were associated with homogeneous preference scattering layers, six with the heterogeneous preference, and three with transitional. Two of the lines were associated with scattering layers that didn't fit the pattern matching inflow and outflow, found at CTDs 024 and 030 (locations highlighted with white circles, Figure 102). These two lines were not included in the group summaries found below. They are discussed separately in section 4.4. Details from the analysis of each line can be found in Appendix E.

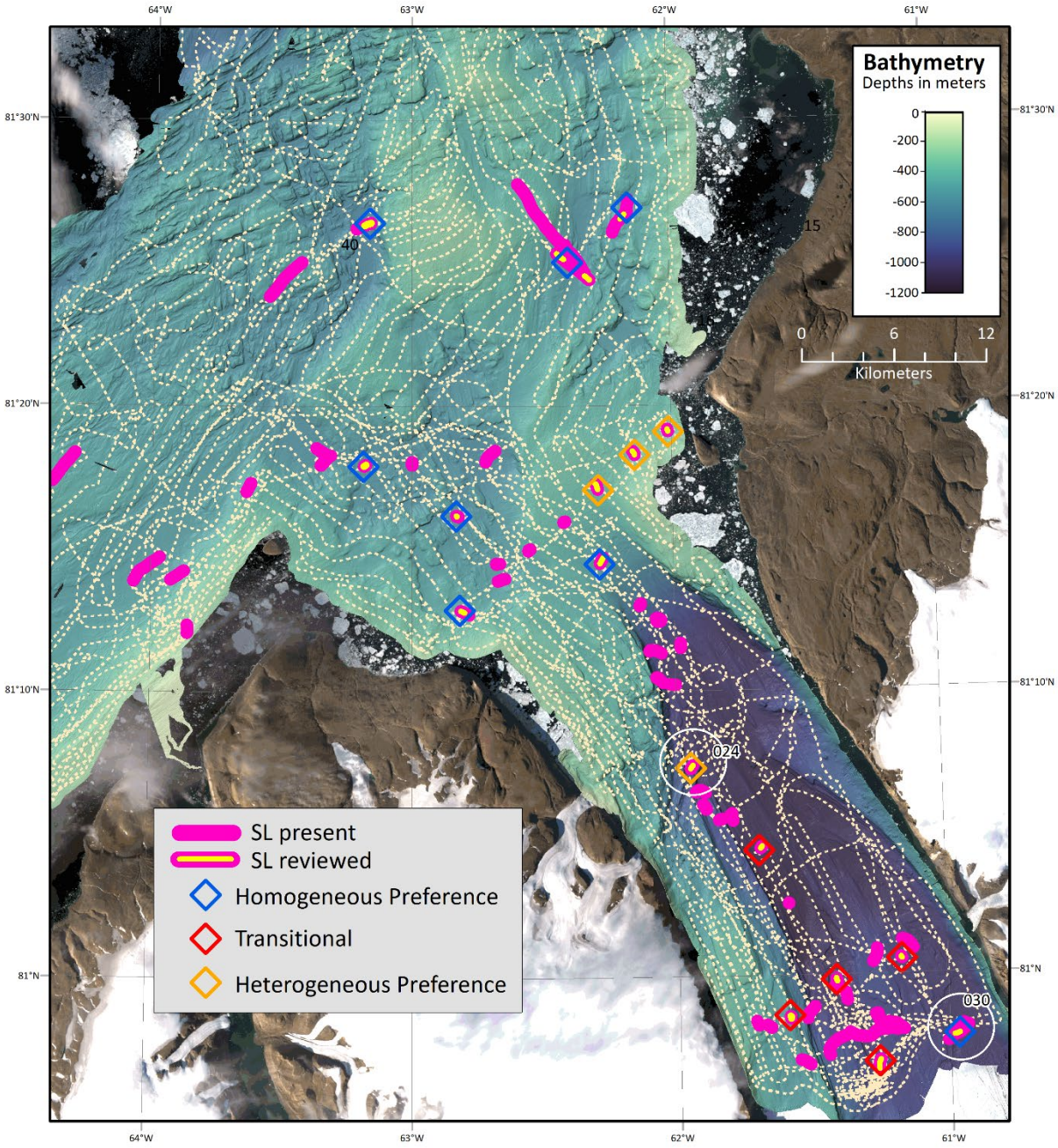

Figure 102: Lines evaluated for target strength and frequency response.

A total of 4960 individual targets were analyzed across the three groups. The frequency response curves were flat to slightly downward-sloping over this short frequency range (Figure 103 shows the average of all frequency responses per line; individual frequency response curves were also flat to slightly downward sloping and

can be found in Appendix E). In general, the shape of the frequency response over this short range provided little insight as to the nature of the targets; the slight downward trend suggests a resonance at frequencies lower than what was sampled, however the shape of the frequency response over this short range can't be said to provide any definitive insight into the nature of the targets.

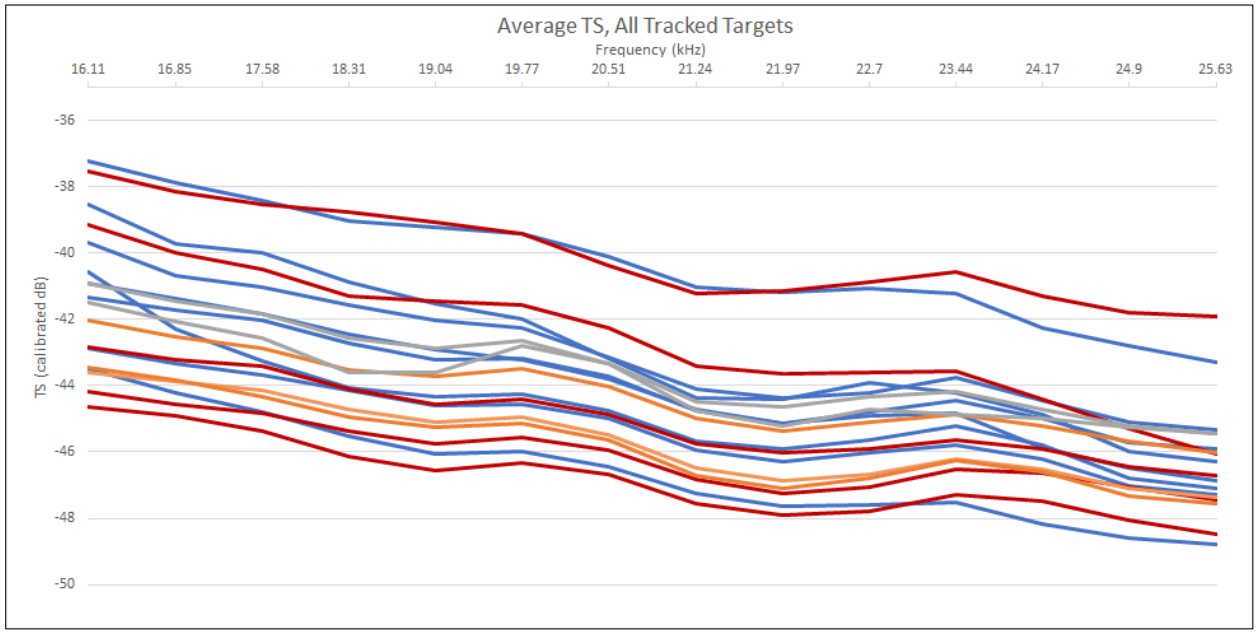

Figure 103: Average TS frequency response for tracked targets in each examined line. Blue indicates a homogeneous preference scattering layer, red a heterogeneous preference scattering layer, orange a transitional scattering layer, and grey an outlier.

A total of 1740 individual targets and 141 volume samples were analyzed for the eight lines associated with homogenous preference layers in the inflow region. Calibrated target strength of individual targets at ~18 kHz ranged from -65.25 to -26.76 dB, with an overall average of -42.04 dB; the largest number of samples were between -47 and -46 dB (Figure 104). Average calibrated S_v of volume samples at ~18 kHz ranged from -81.70 to -77.65 dB in less dense sections and -75.30 to -67.51 dB in higher density sections. Calculated average densities ranged from 0.00007 targets m^{-3} for less dense S_v samples to 0.003 targets m^{-3} for higher density S_v samples. At the

average depth of the homogenous layer samples (330 m), this would be the equivalent of 0.01 to 0.5 targets in an acoustic sampling volume of 163 m^3.

A total of 2172 individual targets and 77 volume samples were analyzed for the five lines associated with heterogeneous preference layers in the outflow region. Calibrated target strength of individual targets at ~18 kHz ranged from -75.88 to -27.77 dB, with an overall average of -43.05 dB; the largest number of samples were between -46 and -45 dB (Figure 104). Average calibrated S_v of volume samples at ~18 kHz ranged from -79.89 to -67.77 dB in less dense sections and -73.41 to -57.17 dB in higher density sections. Calculated average densities ranged from 0.0001 targets m^{-3} for less dense S_v samples to 0.02 targets m^{-3} for higher density S_v samples. At the average depth of the heterogenous layer samples (155 m), this would be the equivalent of 0.005 to 0.84 targets in an acoustic sampling volume of 36 m^3.

A total of 1048 individual targets and 43 volume samples were analyzed for the three lines associated with transitional layers. Calibrated target strength of individual targets at ~18 kHz ranged from -65.38 to -36.81 dB, with an overall average of -44.04 dB; the largest number of samples were between -45 and -44 dB (Figure 104). Average calibrated S_v of volume samples at ~18 kHz ranged from -76.92 to -75.42 dB in less dense sections and -71.57 to -70.34 dB in higher density sections. Calculated average densities ranged from 0.0006 targets m^{-3} for less dense S_v samples to 0.003 targets m^{-3} for higher density S_v samples. At the average depth of the transitional layer samples (210 m), this would be the equivalent of 0.04 to 0.2 targets in an acoustic sampling volume of 66 m^3.

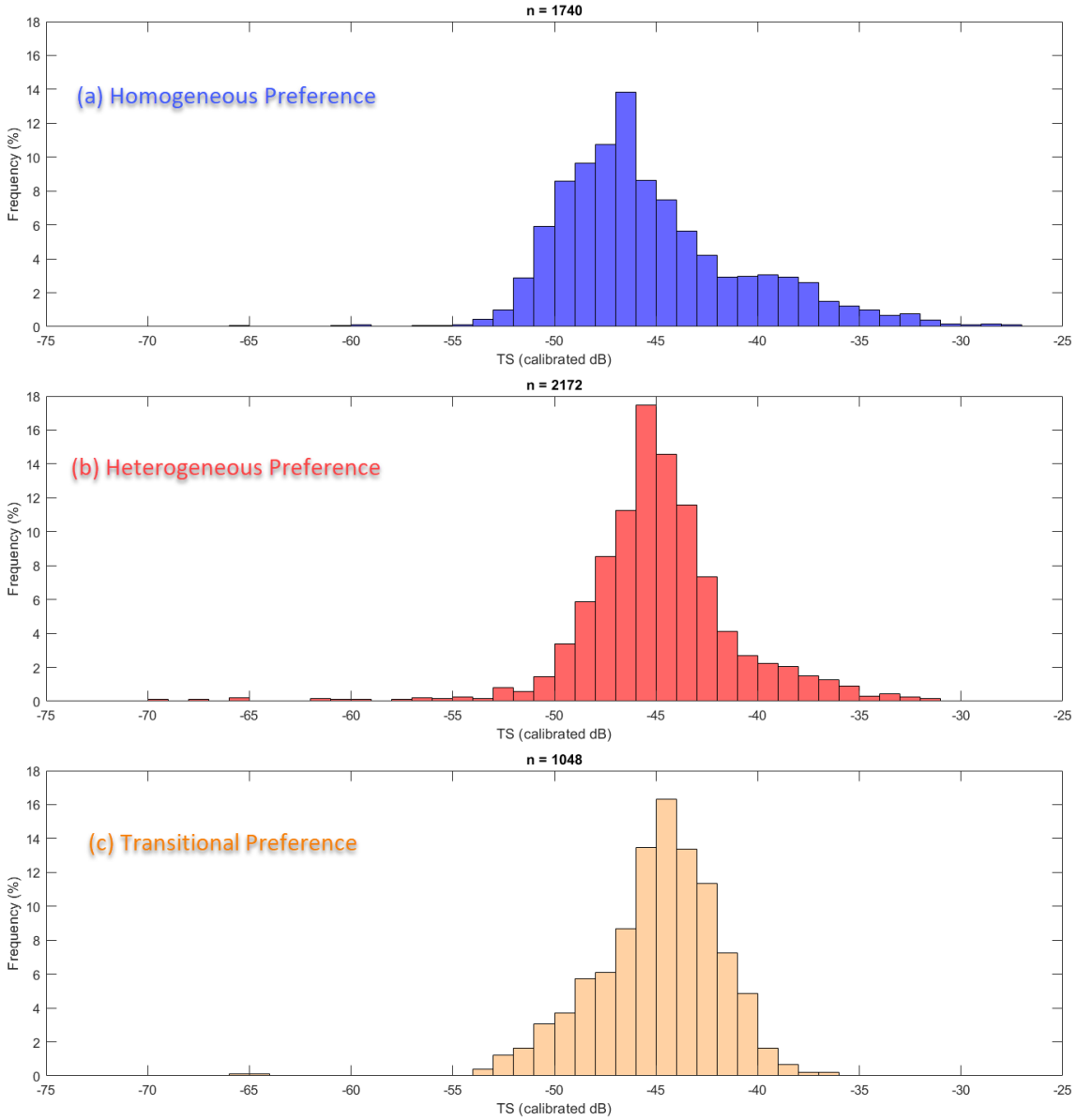

Figure 104: Frequency distribution for tracked single targets in (a) scattering layers with a homogeneous preference, (b) scattering layers with a heterogeneous preference, and (c) scattering layers with a transitional preference. The number of samples is listed above the corresponding distribution.

Average calibrated target strengths of -44.04 to -42.04 dB suggest relatively strong scatterers. If the target strengths can be attributed to fish, the potential species are relatively limited. Polar cod (*Boreogadus saida*) is a likely possibility, being the most widespread and abundant fish in the Arctic Ocean (Benoit et al., 2008, 2014; Geoffroy et al., 2011; Parker-Stetter et al., 2011). The overall target strength distributions are

within the ranges for polar cod observed by some researchers in late summer and early fall (Benoit et al., 2014; Geoffroy et al., 2016). The average target strength observed here, however, was quite a bit higher, -44.04 to -42.04 dB in this study compared to -55.3 to -48.23 dB (depending on depth, Geoffroy et al., 2016) and -49.28 dB (Benoit et al., 2014).

The calculated densities and number of targets per acoustic sampling volume seem very low when compared to the visual observations of relatively dense layers. Based on this, we believe the scattering layers are composed of a mix of large targets, possibly fish, and smaller weaker targets, such as smaller fish with swim bladders, fish without swim bladders, or zooplankton. The lower target strength distributions found during single target detections may be indicative of these smaller targets (see 3.2.6 and Appendix E). The frequency differencing methods typically used to separate fish and zooplankton populations (Benoit et al., 2014; Geoffroy et al., 2016) and the sampling to support that discrimination were not available to us, so confirmation and quantification of relative contributions isn't possible.

It is not clear what about the scatterer population is driving the vertical separation/preference for certain water mass characteristics. The similarities in target strength distributions for the majority of individual targets within the depth range of the scattering layers and limited diversity in the Arctic seems to preclude different species. Polar cod are known to segregate at different depths based on age, with age 1+ cod staying at depth and age-0 cod forming epipelagic layers before joining older fish at depth in late fall (Parker-Stetter et al., 2011; Benoit et al., 2014; Geoffroy et al., 2016). We did note a bimodal distribution in the preliminary stages of our analysis of scattering

layer components (Figure 105), noting that the individual tracked targets in the lower target strength distribution were more often found above (and near the top of) the primary scattering layer depth range (Figure 106); this was used as our justification for focusing on the higher target strength distribution in our analysis. It does seem that age segregation could be responsible for this initial bimodal distribution, and for the overlapping occurrence of both distributions in the 50 – 200 m epipelagic depth range, though it should also be noted that the estimated calibrated target strengths for the lower target strength distribution are quite low, around -65 to -90 dB, which may be quite low even for juvenile cod. There is some suggestion of this as well when looking at targets from both distributions plotted over depth; there is a visible increase in target strength with depth in the lower target strength distributions, and a less pronounced but still discernable increase in target strength with depth for the higher target strength distributions, to a depth of ~ 200 m (Figure 107). This pattern of an increase in target strength with depth is internal to each preference group, however, and does not explain the different vertical segregation specific to each group (heterogeneous generally shallower, transitional in the mid-depths, and homogeneous generally deeper).

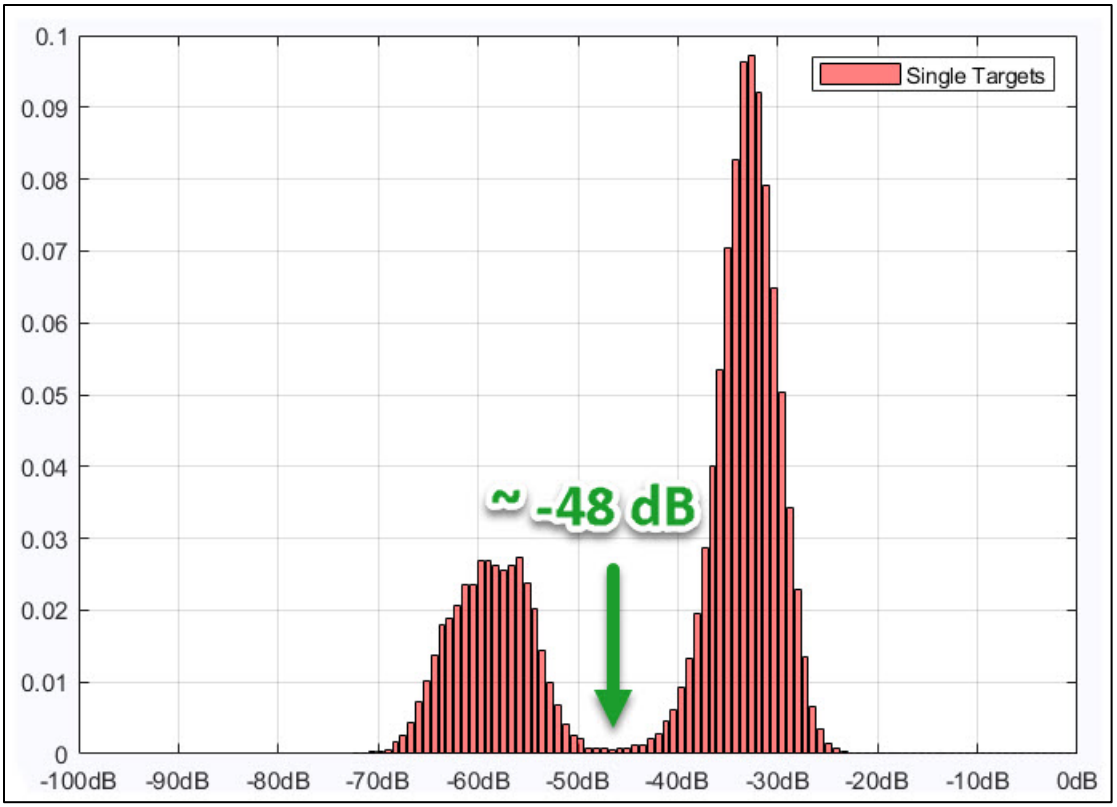

Figure 105: Probability density function for all single targets between 0 and -100 dB, showing a break between distributions around -48dB (uncalibrated). Figure repeated from section 3.2.6.

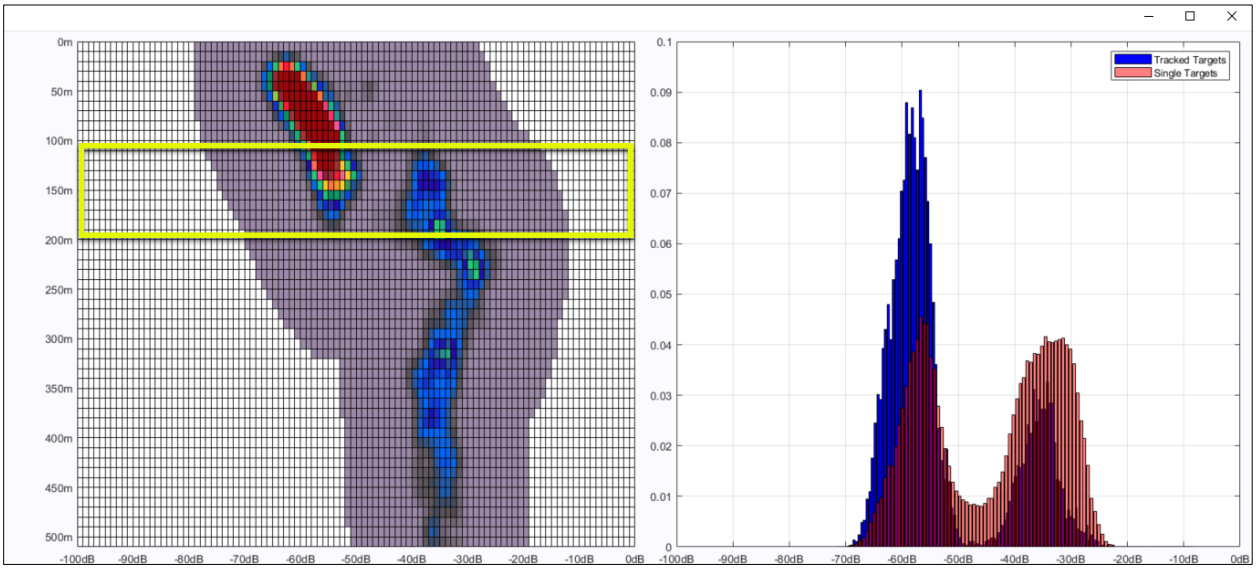

Figure 106: Distribution of tracked targets. The figure on the left shows the depth distribution for the tracked targets, colored by number of tracked targets. The figure at the right shows the results of the single target algorithm in red, and of those targets, those that meet the target tracking algorithm in blue. Figure repeated from section 3.2.6, with yellow box added to highlight area of depth overlap between target strength distributions.

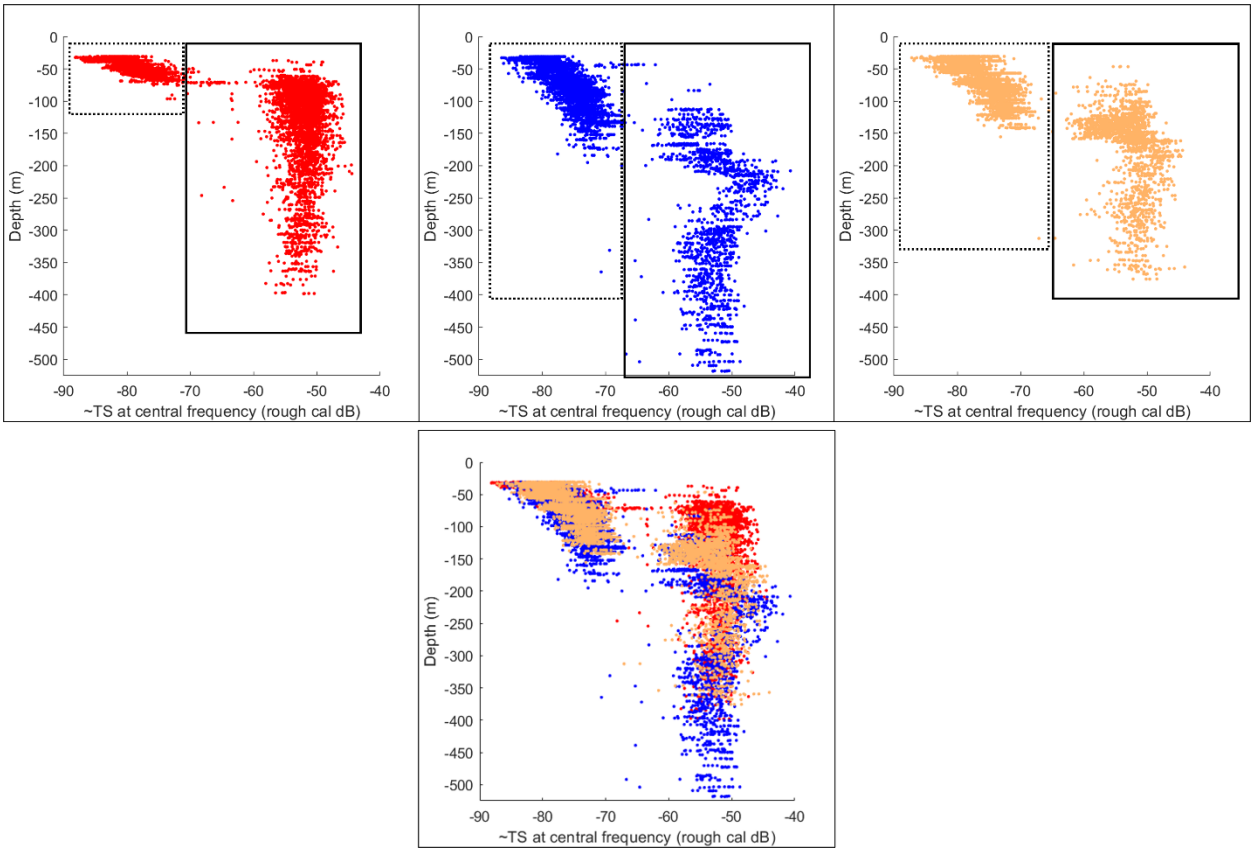

Figure 107: Target strength distribution over depth for both target strength distributions. Target strength values here are "roughly calibrated" (see Appendix A for a description of rough gain calibration in ESP3). Top row shows files individually; red dots are from a file with a heterogeneous preference layer (PETERMANN2015-D20150807-T093944), blue dots are from a file with a homogeneous preference layer (PETERMANN2015-D20150814-T134156), and orange dots are from a file with a transitional preference layer (PETERMANN2015-D20150815-T150617). Dashed boxes show the lower target strength distributions, solid boxes the higher target strength distributions (boxes are approximate). The bottom image shows the three files plotted together.

4.4 Analysis of Outliers

Two of the CTD stations, 024 and 030, did not fit the overall pattern of homogeneous preference layers being associated with inflow to the fjord and heterogeneous and transitional preference scattering layers being associated with outflow from the glacier and fjord (Figure 108). Station 030 fell into the homogeneous preference group, but is located very near to the ice shelf interface and the glacier outflow associated with heterogenous preference layers. Further examination of 030

showed that high levels of interference (caused by the multibeam sonar, see Appendix A for discussion of observed inference and causes) between 50 and 250 m prevented close examination of the top of the scattering layer, and perhaps biased the picks of the top of the layer to deeper depths (Figure 109). However, the depth of the scattering layer here, even accounting for masking by interference, is not within the depth range and temperature-salinity range of the surrounding heterogeneous preference layers. This station was one of the closest to ice interface, and thus the scattering layer position may be related to the dynamic processes at the ice front.

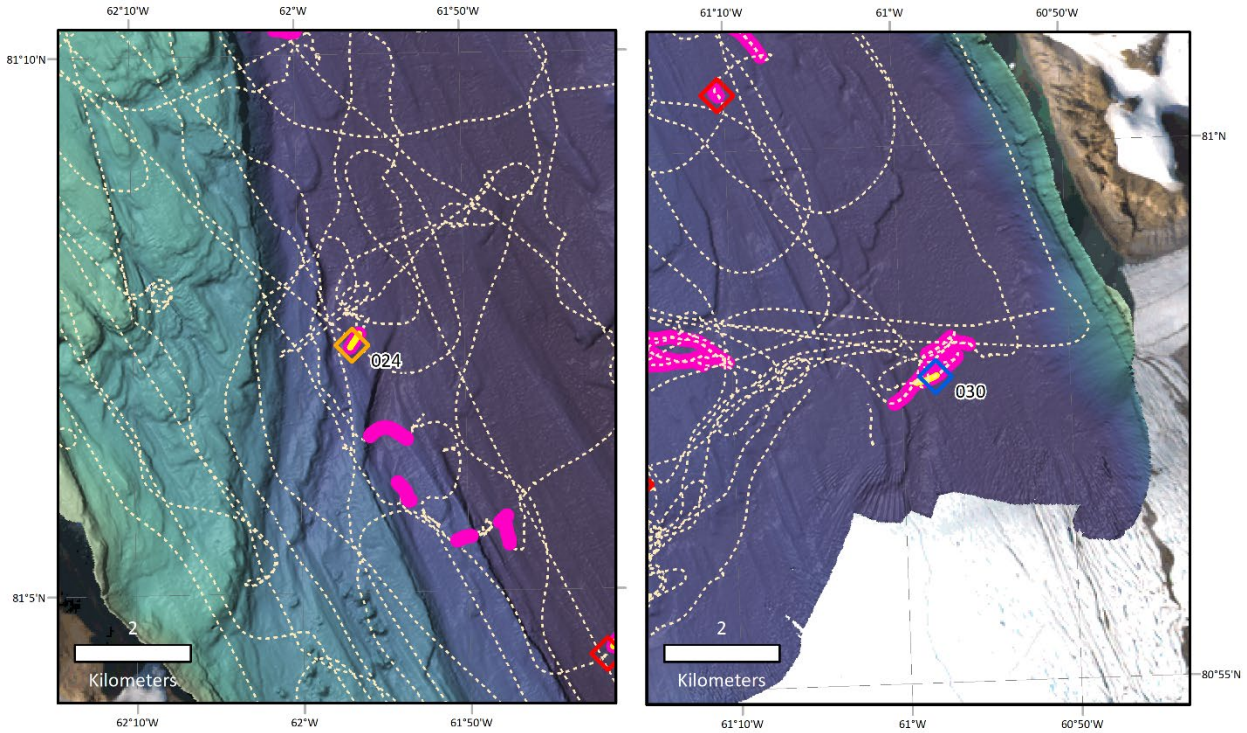

Figure 108: Location maps for the two "outlier" CTD stations, 024 and 030.

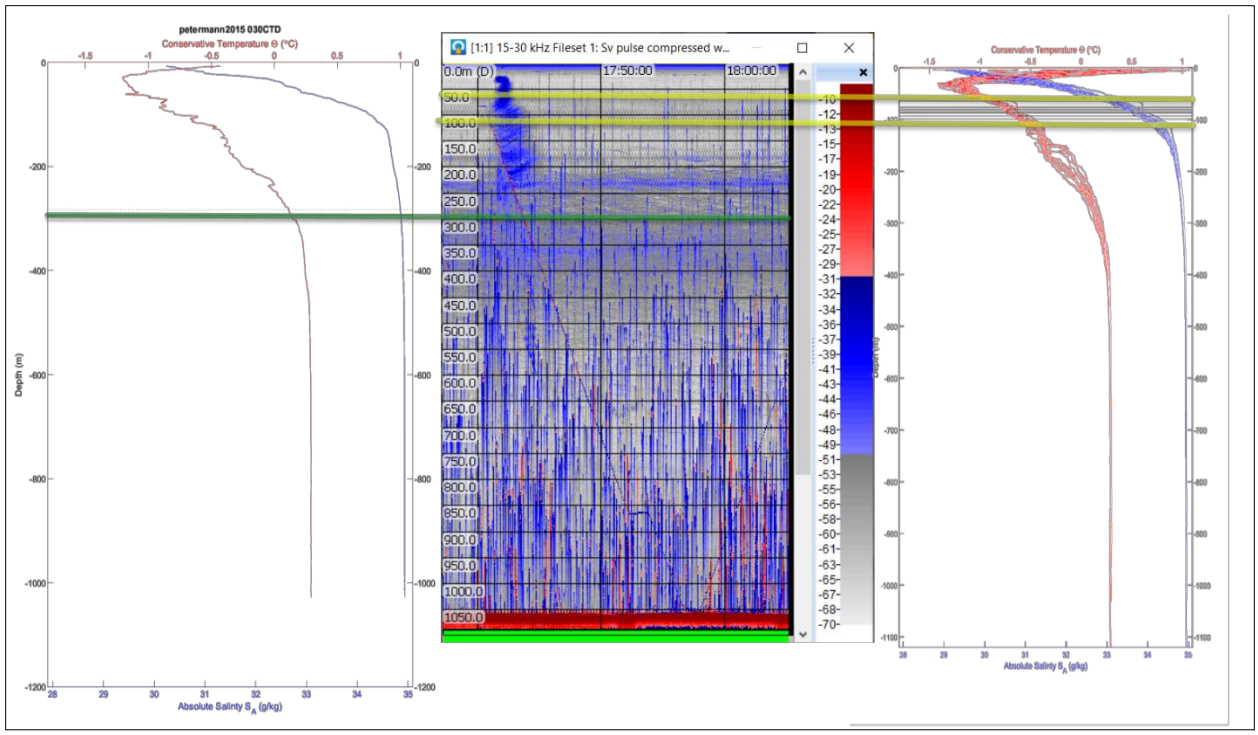

Figure 109: Comparison of PETERMANN2015-D20150822-T173712.raw (center) to the temperature and salinity downplot for station 030 (left) and to temperature and salinity downplots for all heterogeneous preference stations (right). The green line is the average depth of the scattering layer picks for this line. The yellow lines are the minimum and maximum average depths for scattering layer picks classified as heterogenous preference. Even accounting for masking by the interference, the scattering layer is well below the heterogenous portion of the water column.

The scattering layer at station 024 fell into the transitional preference group, and was the only station in the main part of the fjord to fall into that group. Comparison to the stacked temperature and salinity downplots for both the homogenous and heterogenous preference groups confirms that the layer falls right between the two (Figure 110). Possible explanations for the preference of the scattering layer here are that this station is the furthest “non-homogeneous” station from the glacier, so the scattering layer may have more in common with the transitional preference layers near the fjord entrance, possible influence from the outlet glaciers just to the west, and that the station lies near the west central portion of the fjord, where there is likely to be a transition zone between inflow and outflow (Figure 111).

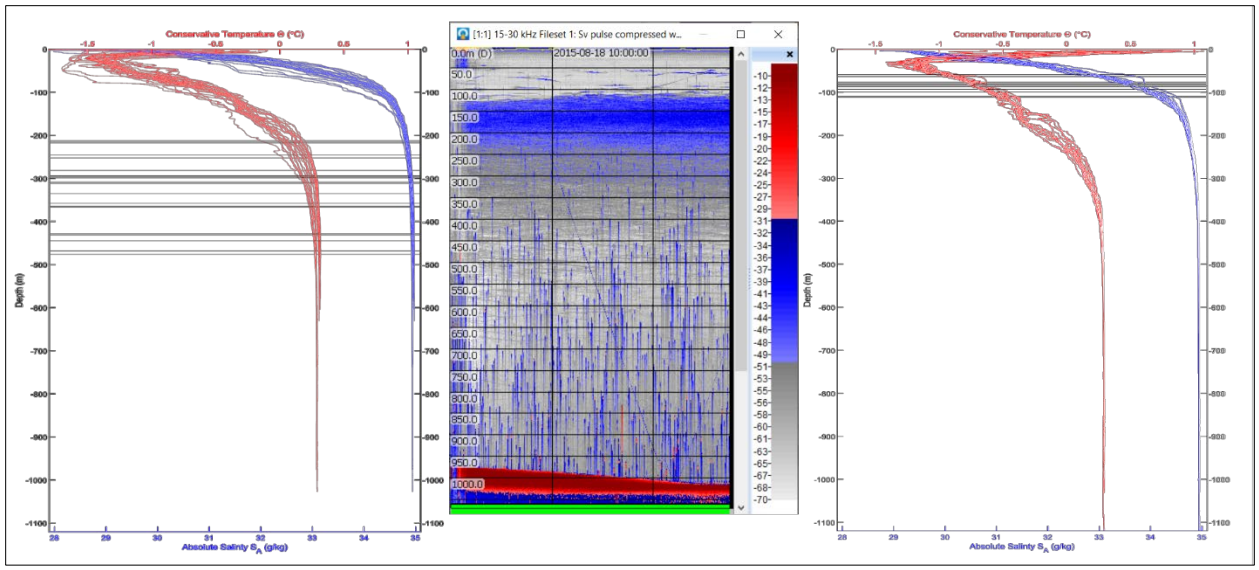

Figure 110: Comparison of PETERMANN2015-D20150818-T095013.raw (center) to the temperature and salinity downplots for all homogeneous preference stations (left) and all heterogenous preference stations (right).

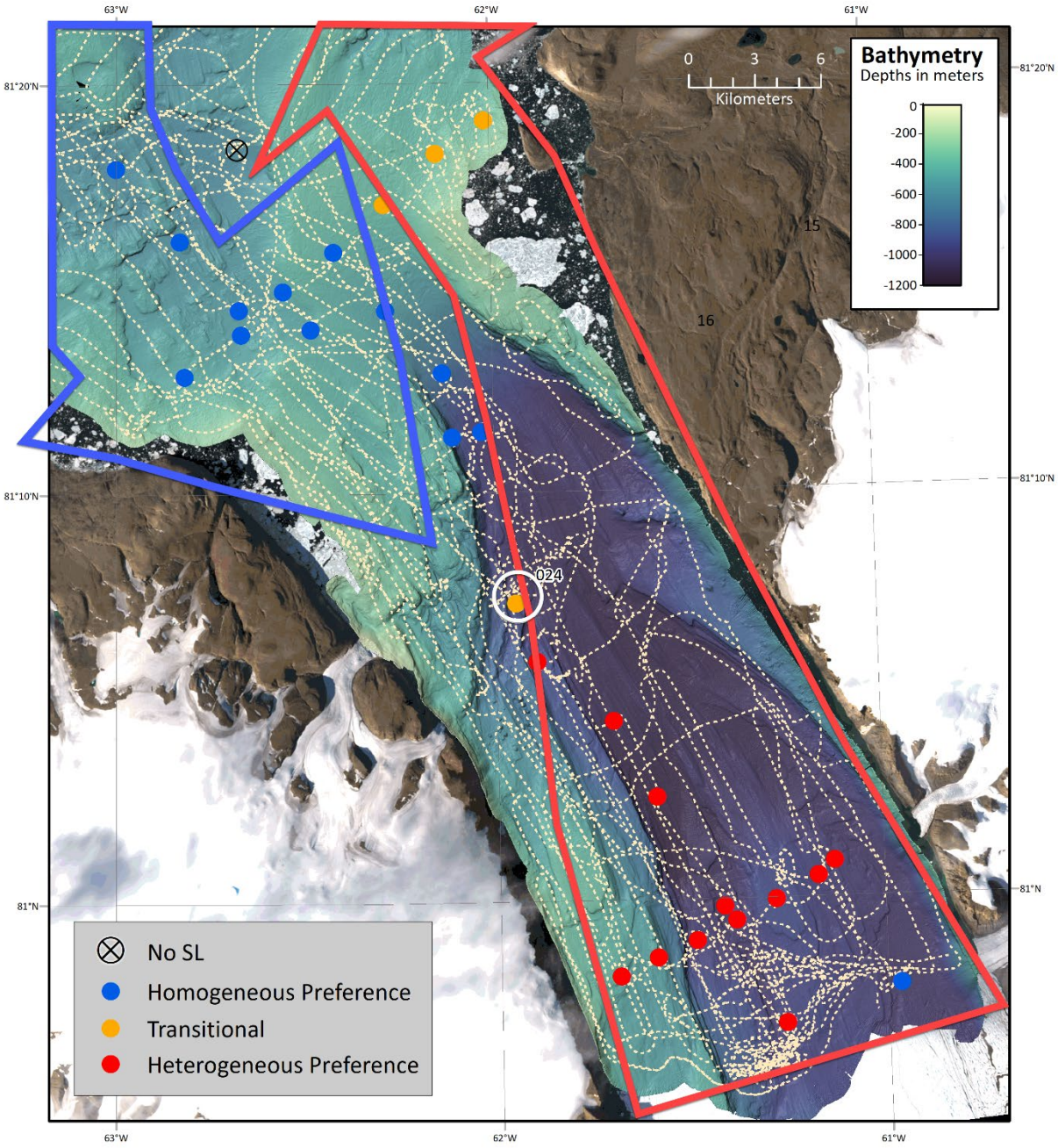

Figure 111: Location of station 024 in reference to other CTD stations and to generalized inflow/outflow.

4.5 Sources of Error

There are several potential sources of error in this study that should be mentioned, and if possible, addressed in the future. First, the echograms were not fully corrected for motion. Ship heave can cause a vertical displacement in observed

features, affecting out reported scattering layer depths. This can be addressed by applying a heave correction to the echograms. However, the magnitude of this error – a change in position of no more than 1-2 m vertically – would likely have very little effect on the scattering layer picks and results based on those picks. Second, the use of 1500 m s^{-1} for the generation of echograms could have caused the depth of the top of the scattering layer to be misplaced as much as 1.6 m for the shallowest layers and 26.8 m for the deepest layers. This potential depth misplacement is not large enough to push any of the layers into a different group (with regard to the homogeneous, heterogeneous and transitional groupings we applied); other parts of this analysis looked at relative depth compared to physical and environmental factors and would not be affected by these potential offsets. Third, the method for selecting the top of the scattering layer was subjective. Attempts were made to maintain some consistency, but the varying quality of the echograms made that nearly impossible. This can be addressed by using an automated approach to select layers based on objective criteria, though whether such an approach could be applied to these data is questionable, given the varying quality of the data. The subjective approach to picking the depth of the scattering layer also resulted in “jagged” layers with much apparent (small-scale) depth variability; some of this variability was likely real, but some of it was also an artifact of the picking process and echogram quality. A smoothing filter may help decrease this variability but, of course, would also remove real variability. Fourth, there may be better methods for compensating the light data. Shadows from the ship likely effected the signal; this could potentially be addressed by only using samples collected at certain ship headings, but is beyond the scope of this project.

Target strength calculations are often found to be biased in high-density conditions due to multiple scattering and shadowing (MacLennan, 1990; Parker-Stetter et al., 2009), and many of the single targets identified by the ESP3 ‘Single Targets’ algorithm were from areas of high concentration. The Sawada Index (Sawada et al., 1993) is one tool used for minimizing multiple target detections by identifying high-density cells and excluding them from Target Strength calculations. Geoffroy et al. (2016) found their methods combining single target detection followed by a fish tracking algorithm produced results similar to utilizing the Sawada Index. The methods used to identify single targets for Target Strength calculations here were similar to Geoffroy et al. (2016) and though some bias from multiple targets may still be present, it should be minimal.

CHAPTER 5 CONCLUSIONS

The scattering layers in Petermann Fjord and Hall Basin are found in distinct depth zones that differ consistently by location. Their depth distribution shows no correlation to changing light levels (over one month of the Arctic summer) demonstrating that at the time of observation, their depth distribution is not related to the time of day. Comparison of scattering layer depths to light attenuation in Hall Basin and Petermann Fjord show that there may be a weak relationship between scattering layer depths and the amount of light reaching depth in the water column, but based on the available data this relationship is not consistent and locally associated with areas of glacial runoff. There is, however, a strong and consistent relationship between the depth of the top of the scattering layer depths and water column properties, which separates the distribution of the scattering layer into three groups – a shallow 'heterogenous preference' group associated with relatively cold and lower salinity water, that is found in the top 200 m of the water column where fresh Polar Water is present and salinity and temperature are changing rapidly, a 'transitional' group in the 140 – 200 m region of the water column where temperature and salinity are starting to stabilize, and a 'homogeneous preference' group below 250 m where warm salty Atlantic water is present and temperature and salinity are relatively constant. The homogeneous group corresponds to the path of inflowing Atlantic water, while the transitional and heterogeneous groups correspond to the path of outflowing glacially-influenced waters. The influence of hydrographic processes on the scattering layer is further demonstrated locally where intense scattering layers near outlet glaciers and the patchy, multi-layer,

varied target strength scattering layers near the ice shelf interface hinted at intensified feeding areas and possible entrainment/die-off/foraging cycles described by Lydersen et al. (2014). Finally, the absence of scattering layers and sudden drops in the scattering layer depth in active areas such as the mouth of the fjord and along the western side of Hall Basin appear to be related to strong or recirculating flow clearing out drifting scatterers and creating an environment inhospitable to mobile organisms.

The results of this study show that in the remote area of the Arctic where logistics make it very difficult to make measurements, the depth distribution of the scattering layer can be used as an indication of water mass distribution and circulation patterns. This analysis expands the use of acoustic water column data and provides a more complete picture of regional hydrography that allows extrapolation beyond discrete CTD stations. Further, despite the lack of sampling and a restricted frequency band, we were able to discern some information regarding the composition of the scattering layers that seems to indicate potential fish aggregations, though definitive confirmation is not possible. Based on high individual target strengths but low volume scattering values and density calculations, we believe that the scattering layers are made up of fish interspersed with smaller fish and zooplankton. As the species observed in the high Arctic are limited, we believe the fish are likely polar cod (*Boreogadus saida*).

The conclusions described above have been drawn from what was, in essence, an opportunistic data set, not collected for the purposes of looking at the distribution or nature of the scattering layer. Further experiments, using optimized frequencies for bio-acoustic studies in conjunction with a carefully planned sampling program may provide

much more insight into the nature of the scattering layers in this environment and provide a deeper understanding of their association with water-mass properties.

LIST OF REFERENCES

Aagaard, K., and Carmack, E.C., 1989, The Role of Sea Ice and Other Fresh Water in the Arctic Circulation: Journal of Geophysical Research, v. 94, p. 14485–14498, doi:10.1029/JC094iC10p14485.

Aagaard, K., Coachman, L.K., and Carmack, E., 1981, On the halocline of the Arctic Ocean: Deep Sea Research Part A. Oceanographic Research Papers, v. 28A, p. 529–545, doi:10.1016/0198-0149(81)90115-1.

van Aken, H.M., Quadfasel, D., and Warpakowski, A., 1991, The Arctic Front in the Greenland Sea During February 1989: Hydrographic and Biological Observations: Journal of Geophysical Research, v. 96, p. 4739–4750, doi:10.1029/90JC02271.

Amundson, J.M., Fahnestock, M., Truffer, M., Brown, J., Lüthi, M.P., and Motyka, R.J., 2010, Ice mélange dynamics and implications for terminus stability, Jakobshavn Isbræ, Greenland: Journal of Geophysical Research, v. 115, p. 1–12, doi:10.1029/2009JF001405.

Auel, H., and Hagen, W., 2002, Mesozooplankton community structure, abundance and biomass in the central Arctic Ocean: Marine Biology, v. 140, p. 1013–1021, doi:10.1007/s00227-001-0775-4.

Austin, R.W., and Petzold, T.J., 1981, The Determination of the Diffuse Attenuation Coefficent of Sea Water Using the Coastal Zone Color Scanner, in Gower, J.F.R. ed., Oceanography from Space. Marine Science, vol 13, Boston, Springer, p. 239–256, doi:10.1007/978-1-4613-3315-9_29.

Bamber, J., van den Broeke, M., Ettema, J., Lenaerts, J., and Rignot, E., 2012, Recent large increases in freshwater fluxes from Greenland into the North Atlantic: Geophysical Research Letters, v. 39, p. 1–4, doi:10.1029/2012GL052552.

Benfield, M.C., Davis, C.S., Wiebe, P.H., Gallager, S.M., Lough, R.G., and Copley, N.J., 1996, Video Plankton Recorder estimates of copepod, pteropod and larvacean distributions from a stratified region of Georges Bank with comparative measurements from a MOCNESS sampler: Deep-Sea Research Part II: Topical Studies in Oceanography, v. 43, p. 1925–1945, doi:10.1016/S0967-0645(96)00044-6.

Benfield, M.C., Wiebe, P.H., Stanton, T.K., Davis, C.S., Gallager, S.M., and Greene, C.H., 1998, Estimating the spatial distribution of zooplankton biomass by combining Video Plankton Recorder and single-frequency acoustic data: Deep Sea Research Part II: Topical Studies in Oceanography, v. 45, p. 1175–1199, doi:10.1016/S0967-0645(98)00026-5.

Benn, D.I., and Evans, D.J.A., 2010, Glaciers and Glaciation: London, Hodder Education, 802 p.

Benoit, D., Simard, Y., and Fortier, L., 2008, Hydroacoustic detection of large winter aggregations of Arctic cod (Boreogadus saida) at depth in ice-covered Franklin Bay (Beaufort Sea): Journal of Geophysical Research, v. 113, p. 1–9, doi:10.1029/2007JC004276.

Benoit, D., Simard, Y., and Fortier, L., 2014, Pre-winter distribution and habitat characteristics of polar cod (Boreogadus saida) in southeastern Beaufort Sea: Polar Biology, v. 37, p. 149–

163, doi:10.1007/s00300-013-1419-0.

Benoit, D., Simard, Y., Gagné, J., Geoffroy, M., and Fortier, L., 2010, From polar night to midnight sun: Photoperiod, seal predation, and the diel vertical migrations of polar cod (Boreogadus saida) under landfast ice in the Arctic Ocean: Polar Biology, v. 33, p. 1505–1520, doi:10.1007/s00300-010-0840-x.

Benoit-Bird, K.J., and Au, W.W.L., 2003, Prey dynamics affect foraging by a pelagic predator (Stella longirostris) over a range of spatial and temporal scales: Behavioral Ecology and Sociobiology, v. 53, p. 364–373, doi:10.1007/s00265-003-0585-4.

Berge, J. et al., 2014, Arctic complexity: A case study on diel vertical migration of zooplankton: Journal of Plankton Research, v. 36, p. 1279–1297, doi:10.1093/plankt/fbu059.

Berge, J. et al., 2009, Diel vertical migration of Arctic zooplankton during the polar night: Biology Letters, v. 5, p. 69–72, doi:10.1098/rsbl.2008.0484.

Biospherical Instruments Inc., 2013, QSR-2150 Series with Digital Output: http://www.biospherical.com/images/pdf/qsr2150_2013.pdf (accessed May 2018).

Blachowiak-Samolyk, K., Kwasniewski, S., Richardson, K., Dmoch, K., Hansen, E., Hop, H., Falk-Petersen, S., and Mouritsen, L.T., 2006, Arctic zooplankton do not perform diel vertical migration (DVM) during periods of midnight sun: Marine Ecology Progress Series, v. 308, p. 101–116, doi:10.3354/meps308101.

Bouchard, C., Geoffroy, M., LeBlanc, M., and Fortier, L., 2018, Larval and adult fish assemblages along the Northwest Passage: the shallow Kitikmeot and the ice-covered Parry Channel as potential barriers to dispersal: Arctic Science, v. 4, p. 781–793, doi:10.1139/as-2018-0003.

Boyer, T.P. et al., 2019, World Ocean Database 2018 (A. V. Mishonov, Ed.): NOAA Atlas NESDIS 87, https://www.nodc.noaa.gov/OC5/WOD/pr_wod.html.

Brierley, A.S., 2014, Diel vertical migration: Current Biology, v. 24, p. R1074–R1076, doi:10.1016/j.cub.2014.08.054.

Cai, C., Rignot, E., Menemenlis, D., and Nakayama, Y., 2017, Observations and modeling of ocean-induced melt beneath Petermann Glacier Ice Shelf in northwestern Greenland: Geophysical Research Letters, v. 44, p. 8396–8403, doi:10.1002/2017GL073711.

Chu, D., Stanton, T.K., and Wiebe, P.H., 1992, Frequency dependence of sound backscattering from live individual zooplankton: ICES Journal of Marine Science, v. 49, p. 97–106, doi:10.1093/icesjms/49.1.97.

Church, J.A. et al., 2013, Sea Level Change, in Stocker, T.F., Qin, D., Plattner, G.K., Tignor, M., Allen, S.K., Boschung, J., Nauels, A., Xia, Y., Bex, V., and Midgley, P.M. eds., Climate Change 2013: The Physical Science Basis. Contribution of Working Group I to the Fifth Assessment Report of the Intergovernmental Panel on Climate Change, Cambridge, Cambridge University Press, p. 1137–1217.

Clay, C.S., and Horne, J.K., 1994, Acoustic models of fish: The Atlantic cod (Gadus morhua): The Journal of the Acoustical Society of America, v. 96, p. 1661–1668, doi:10.1121/1.410245.

Clay, C.S., and Medwin, H., 1977, Acoustical Oceanography: Principles and Applications: New York, Wiley, 544 p.

Coachman, L.K., and Barnes, C.A., 1963, The Movement of Atlantic Water in the Arctic Ocean: Arctic, v. 16, p. 9–16, doi:10.14430/arctic3517.

Cohen, J.H., and Forward Jr., R.B., 2005, Diel vertical migration of the marine copepod Calanopia americana. I. Twilight DVM and its relationship to the diel light cycle: Marine Biology, v. 147, p. 387–398, doi:10.1007/s00227-005-1569-x.

Cohen, J.H., and Forward Jr., R.B., 2019, Vertical Migration of Aquatic Animals, in Choe, J.C. ed., Encyclopedia of Animal Behavior (Second Edition), Academic Press, p. 546–552, doi:10.1016/B978-0-12-809633-8.01257-7.

Cohen, J.H., and Forward Jr., R.B., 2009, Zooplankton Diel Vertical Migration -- A Review of Proximate Control, in Gibson, R.N., Atkinson, R.J.A., and Gordon, J.D.M. eds., Oceanography and Marine Biology: An Annual Review, Taylor & Francis, v. 47, p. 77–110, doi:978-1420094213.

Colbo, K., Ross, T., Brown, C., and Weber, T., 2014, A review of oceanographic applications of water column data from multibeam echosounders: Estuarine, Coastal and Shelf Science, v. 145, p. 41–56, doi:10.1016/j.ecss.2014.04.002.

Cottier, F.R., Tarling, G.A., Wold, A., and Falk-Petersen, S., 2006, Unsynchronized and synchronized vertical migration of zooplankton in a high arctic fjord: Limnology and Oceanography, v. 51, p. 2586–2599, doi:10.4319/lo.2006.51.6.2586.

Cowen, R.K., Greer, A.T., Guigand, C.M., Hare, J.A., Richardson, D.E., and Walsh, H.J., 2013, Evaluation of the In Situ Ichthyoplankton Imaging System (ISIIS): Comparison with the traditional (bongo net) sampler: Fishery Bulletin, v. 111, p. 1–12, doi:10.7755/FB.111.1.1.

Cowen, R.K., and Guigand, C.M., 2008, In situ ichthyoplankton imaging system (ISIIS): system design and preliminary results: Limnology and Oceanography: Methods, v. 6, p. 126–132, doi:10.4319/lom.2008.6.126.

Daase, M., Falk-Petersen, S., Varpe, Ø., Darnis, G., Søreide, J.E., Wold, A., Leu, E., Berge, J., Philippe, B., and Fortier, L., 2013, Timing of reproductive events in the marine copepod Calanus glacialis: a pan-Arctic perspective: Canadian Journal of Fisheries and Aquatic Sciences, v. 70, p. 871–884, doi:10.1139/cjfas-2012-0401.

Darnis, G. et al., 2017, From polar night to midnight sun: Diel vertical migration, metabolism and biogeochemical role of zooplankton in a high Arctic fjord (Kongsfjorden, Svalbard): Limnology and Oceanography, v. 62, p. 1585–1605, doi:10.1002/lno.10519.

Driemel, A. et al., 2018, Baseline Surface Radiation Network (BSRN): structure and data description (1992–2017): Earth Systems Science Data, v. 10, p. 1491–1501, doi:10.5194/essd-10-1491-2018.

Dunstan, I.C., 1979, Underwater Sound Scattering by Marine Organisms. A Review: Australian Department of Defence Report MFL-R-756, p. 33, https://apps.dtic.mil/dtic/tr/fulltext/u2/a079954.pdf.

Engås, A., Skeide, R., and West, C.W., 1997, The ‘MultiSampler’: a system for remotely opening and closing multiple codends on a sampling trawl: Fisheries Research, v. 29, p. 295–298, doi:10.1016/S0165-7836(96)00545-0.

Falkner, K.K. et al., 2011, Context for the Recent Massive Petermann Glacier Calving Event: Eos, v. 92, p. 117–124, doi:10.1029/2011EO140001.

Falk-Petersen, S. et al., 2008, Vertical migration in high Arctic waters during autumn 2004: Deep-Sea Research Part II: Topical Studies in Oceanography, v. 55, p. 2275–2284, doi:10.1016/j.dsr2.2008.05.010.

Falk-Petersen, I., Frivoll, V., Guluksen, B., and Haug, T., 1986, Occurrence and size/age relations of polar cod, Boreogadus Saida (Lepechin), in Spitsbergen coastal waters: Sarsia, v. 71, p. 235–245, doi:10.1080/00364827.1986.10419693.

Farmer, D.M., and Freeland, H.J., 1983, The Physical Oceanography of Fjords: Progress in Oceanography, v. 12, p. 147–220, doi:10.1016/0079-6611(83)90004-6.

Fischer, J., and Visbeck, M., 1993, Seasonal variation of the daily zooplankton migration in the Greenland Sea: Deep-Sea Research I, v. 40, p. 1547–1557, doi:10.1016/0967-0637(93)90015-U.

Flagg, C.N., and Smith, S.L., 1989, On the use of the acoustic Doppler current profiler to measure zooplankton abundance: Deep Sea Research Part A. Oceanographic Research Papers, v. 36, p. 455–474, doi:10.1016/0198-0149(89)90047-2.

Foote, K.G., 1983, Linearity of fisheries acoustics, with addition theorems: Journal of the Acoustical Society of America, v. 73, p. 1932–1940, doi:10.1121/1.389583.

Foote, K.G., Knudsen, H.P., Vestnes, G., Brede, R., and Nielsen, R.L., 1981, Improved calibration of hydroacoustic equipment with copper spheres: International Council for the Exploration of the Sea, Fish Capture Committee, C.M. 1981/B:20, p. 1–18.

Foote, K.G., Knudsen, H.P., Vestnes, G., MacLennan, D.N., and Simmonds, E.J., 1987, Calibration of acoustic instruments for fish density estimation: a practical guide: ICES Cooperative Research Report, p. 1–63.

Fortier, L. et al., 2015, Arctic Change: Impacts on Marine Ecosystems and Contaminants., in Stern, G. and Gaden, A. eds., From Science to Policy in the Western and Central Canadian Arctic: An Integrated Regional Impact Study (IRIS) of Climate Change and Modernization, Quebec City, ArcticNet, p. 201–251, http://www.arcticnet.ulaval.ca/pdf/media/IRIS_FromScience_ArcticNet_lr.pdf (accessed October 2021).

Fortier, M., Fortier, L., Hattori, H., Saito, H., and Legendre, L., 2001, Visual predators and the diel vertical migration of copepods under Arctic sea ice during the midnight sun: Journal of Plankton Research, v. 23, p. 1263–1278, doi:10.1093/plankt/23.11.1263.

Forward Jr., R.B., 1988, Diel Vertical Migration: Zooplankton Photobiology and Behavior, in Barnes, M. ed., Oceanography and Marine Biology: An Annual Review, Volume 26, London, Aberdeen University Press, p. 361–393.

Geoffroy, M., Cottier, F.R., Berge, J., and Inall, M.E., 2017, AUV-based acoustic observations of the distribution and patchiness of pelagic scattering layers during midnight sun: ICES Journal of Marine Science, v. 74, p. 2342–2353, doi:10.1093/icesjms/fsw158.

Geoffroy, M., Majewski, A., LeBlanc, M., Gauthier, S., Walkusz, W., Reist, J.D., and Fortier, L., 2016, Vertical segregation of age-0 and age-1+ polar cod (Boreogadus saida) over the annual cycle in the Canadian Beaufort Sea: Polar Biology, v. 39, p. 1023–1037, doi:10.1007/s00300-015-1811-z.

Geoffroy, M., Robert, D., Darnis, G., and Fortier, L., 2011, The aggregation of polar cod (Boreogadus saida) in the deep Atlantic layer of ice-covered Amundsen Gulf (Beaufort

Sea) in winter: Polar Biology, v. 34, p. 1959–1971, doi:10.1007/s00300-011-1019-9.

Gjøsæter, H., Wiebe, P.H., Knutsen, T., and Ingvaldsen, R.B., 2017, Evidence of Diel Vertical Migration of Mesopelagic Sound-Scattering Organisms in the Arctic: Frontiers in Marine Science, v. 4, p. 1–14, doi:10.3389/fmars.2017.00332.

Grant, M. et al., 2015, Ocean Colour Climate Change Initiative (OC_CCI) – Phase Two: Product User Guide, p. 1–39, https://esa-oceancolour-cci.org/sites/esa-oceancolour-cci.org/alfresco.php?file=e9a4e5ab-39d4-4c8c-8065-ab705e32a182&name=OC-CCI-PUG-v2.0.3.pdf.

Greenlaw, C.F., 1979, Acoustical estimation of zooplankton populations: Limnology and Oceanography, v. 24, p. 226–242, doi:10.4319/lo.1979.24.2.0226.

Grenvald, J.C., Callesen, T.A., Daase, M., Hobbs, L., Darnis, G., Renaud, P.E., Cottier, F., Nielsen, T.G., and Berge, J., 2016, Plankton community composition and vertical migration during polar night in Kongsfjorden: Polar Biology, v. 39, p. 1879–1895, doi:10.1007/s00300-016-2015-x.

Harris, R.P., Wiebe, P.H., Lenz, J., Skjoldal, H.R., and Huntley, M. (Eds.), 2000, ICES Zooplankton Methodology Manual: Academic Press, 684 p., doi:10.1016/B978-012327645-2/50007-4.

Hays, G.C., 1995, Ontogenetic and seasonal variation in the diel migration of the copepods Metridia lucens and Metridia longa: Limnology and Oceanography, v. 40, p. 1461–1465, doi:10.4319/lo.1995.40.8.1461.

Hays, G.C., Warner, A.J., and Lefevre, D.L., 1996, Long-term changes in the diel vertical migration behaviour of zooplankton: Marine Ecology Progress Series, v. 141, p. 149–159, doi:10.3354/meps141149.

Hershey, J.B., and Backus, R.H., 1962, Sound Scattering by Marine Organisms, in Hill, M.N. ed., The Sea, Volume 1: Physical Oceanography, New York, Harvard University Press, p. 498–539.

Heuzé, C., Wåhlin, A., Johnson, H.L., and Münchow, A., 2017, Pathways of Meltwater Export from Petermann Glacier, Greenland: Journal of Physical Oceanography, v. 47, p. 405–418, doi:10.1175/JPO-D-16-0161.1.

Hill, E.A., Carr, J.R., and Stokes, C.R., 2017, A Review of Recent Changes in Major Marine-Terminating Outlet Glaciers in Northern Greenland: Frontiers in Earth Science, v. 4, p. 1–23, doi:10.3389/feart.2016.00111.

Hill, E.A., Gudmundsson, G.H., Carr, J.R., and Stokes, C.R., 2018, Velocity response of Petermann Glacier, northwest Greenland to past and future calving events: The Cryosphere, v. 12, p. 3907–3921, doi:10.5194/tc-12-3907-2018.

Hogg, A.E., Shepherd, A., Gourmelen, N., and Engdahl, M., 2016, Grounding line migration from 1992 to 2011 on Petermann Glacier, North-West Greenland: Journal of Glaciology, v. 62, p. 1104–1114, doi:10.1017/jog.2016.83.

Holliday, D. v., 1972, Resonance Structure in Echoes from Schooled Pelagic Fish: The Journal of the Acoustical Society of America, v. 51, p. 1322–1332, doi:10.1121/1.1912978.

Holliday, D. v., and Pieper, R.E., 1995, Bioacoustical oceanography at high frequencies: ICES Journal of Marine Science, v. 52, p. 279–296, doi:10.1016/1054-3139(95)80044-1.

Holliday, D. v., and Pieper, R.E., 1980, Volume scattering strengths and zooplankton distributions at acoustic frequencies between 0.5 and 3 MHz: The Journal of the Acoustical Society of America, v. 67, p. 135–146, doi:10.1121/1.384472.

Horne, J.K., 2000, Acoustic approaches to remote species identification: a review: Fisheries Oceanography, v. 9, p. 356–371, doi:10.1046/j.1365-2419.2000.00143.x.

Hunkins, K., 1965, The seasonal variation in the sound-scattering layer observed at Fletcher's Ice Island (T-3) with a 12-kc/s echo sounder: Deep-Sea Research and Oceanographic Abstracts, v. 12, p. 879–881, doi:10.1016/0011-7471(65)90810-7.

International Hydrographic Organization, 2019, Standardization of Undersea Feature Names: Guidelines, Proposal Form, Terminology, Edition 4.2.0: IHO Publication B-6, p. 43, https://iho.int/uploads/user/pubs/bathy/B-6_e4 2 0_2019_EF_clean_3Oct2019.pdf.

Jacobsen, H.P., and Norrbin, M.F., 2009, Fine-scale layer of hydromedusae is revealed by video plankton recorder (VPR) in a semi-enclosed bay in northern Norway: Marine Ecology Progress Series, v. 380, p. 129–135, doi:10.3354/meps07954.

Jakobsson, M. et al., 2020, Ryder Glacier in northwest Greenland is shielded from warm Atlantic water by a bathymetric sill: Communications Earth & Environment, v. 1, doi:10.1038/s43247-020-00043-0.

Jakobsson, M. et al., 2018, The Holocene retreat dynamics and stability of Petermann Glacier in northwest Greenland: Nature Communications, v. 9, doi:10.1038/s41467-018-04573-2.

Jennings, A.E., Sheldon, C.S., Cronin, T.M., Francus, P., Stoner, J., and Andrews, J., 2011, The Holocene History of Nares Strait: Oceanography, v. 24, p. 26–41, doi:10.5670/oceanog.2011.52.

Johnson, H.L., Münchow, A., Falkner, K.K., and Melling, H., 2011, Ocean circulation and properties in Petermann Fjord, Greenland: Journal of Geophysical Research: Oceans, v. 116, p. 1–18, doi:10.1029/2010JC006519.

Johnson, J. v., Prescott, P.R., and Hughes, T.J., 2004, Ice Dynamics Preceding Catastrophic Disintegration of the Floating Part of Jakobshavn Isbrae, Greenland: Journal of Glaciology, v. 50, p. 492–504, doi:10.3189/172756504781829729.

Jones, E.P., Rudels, B., and Anderson, L.G., 1995, Deep waters of the Arctic Ocean: origins and circulation: Deep-Sea Research Part I, v. 42, p. 737–760, doi:10.1016/0967-0637(95)00013-V.

Jones, E.P., Swift, J.H., Anderson, L.G., Lipizer, M., Civitarese, G., Falkner, K.K., Kattner, G., and McLaughlin, F., 2003, Tracing Pacific water in the North Atlantic Ocean: Journal of Geophysical Research, v. 108, doi:10.1029/2001JC001141.

Kalenitchenko, D., Joli, N., Potvin, M., Tremblay, J.-É., and Lovejoy, C., 2019, Biodiversity and species change in the Arctic Ocean: A view through the lens of Nares Strait: Frontiers in Marine Science, v. 6, p. 1–17, doi:10.3389/fmars.2019.00479.

Knutsen, T., Hosia, A., Falkenhaug, T., Skern-Mauritzen, R., Wiebe, P.H., Larsen, R.B., Aglen, A., and Berg, E., 2018, Coincident mass occurrence of gelatinous zooplankton in Northern Norway: Frontiers in Marine Science, v. 5, p. 5–8, doi:10.3389/fmars.2018.00158.

Knutsen, T., Wiebe, P.H., Gjøsæter, H., Ingvaldsen, R.B., and Lien, G., 2017, High Latitude Epipelagic and Mesopelagic Scattering Layers—A Reference for Future Arctic Ecosystem

Change: Frontiers in Marine Science, v. 4, p. 1–21, doi:10.3389/fmars.2017.00334.

Korneliussen, R.J. (Ed.), 2018, Acoustic target classification: ICES Cooperative Research Report No. 344, p. 104, http://doi.org/10.17895/ices.pub.4567.

Korneliussen, R.J., Heggelund, Y., Eliassen, I.K., Øye, O.K., Knutsen, T., and Dalen, J., 2009, Combining multibeam-sonar and multifrequency-echosounder data: Examples of the analysis and imaging of large euphausiid schools: ICES Journal of Marine Science, v. 66, p. 991–997, doi:10.1093/icesjms/fsp092.

Korneliussen, R.J., and Ona, E., 2002, An operational system for processing and visualizing multi-frequency acoustic data: ICES Journal of Marine Science, v. 59, p. 293–313, doi:10.1006/jmsc.2001.1168.

Kosobokova, K., and Hirche, H.J., 2009, Biomass of zooplankton in the eastern Arctic Ocean - A base line study: Progress in Oceanography, v. 82, p. 265–280, doi:10.1016/j.pocean.2009.07.006.

Kosobokova, K.N., Hopcroft, R.R., and Hirche, H.J., 2011, Patterns of zooplankton diversity through the depths of the Arctic's central basins: Marine Biodiversity, v. 41, p. 29–50, doi:10.1007/s12526-010-0057-9.

Kutschale, H., 1969, Arctic Hydroacoustics: Arctic, v. 22, p. 246–264, doi:10.14430/arctic3218.

La, H.S., Kang, M., Dahms, H.U., Ha, H.K., Yang, E.J., Lee, H., Kim, Y.N., Chung, K.H., and Kang, S.H., 2015, Characteristics of mesozooplankton sound-scattering layer in the Pacific Summer Water, Arctic Ocean: Deep-Sea Research Part II: Topical Studies in Oceanography, v. 120, p. 114–123, doi:10.1016/j.dsr2.2015.01.005.

Laidre, K.L., Northey, A.D., and Ugarte, F., 2018, Traditional Knowledge About Polar Bears (Ursus maritimus) in East Greenland: Changes in the Catch and Climate Over Two Decades: Frontiers in Marine Science, v. 5, p. 1–16, doi:10.3389/fmars.2018.00135.

Lavery, A.C., Chu, D., and Moum, J.N., 2009, Measurements of acoustic scattering from zooplankton and oceanic microstructure using a broadband echosounder: ICES Journal of Marine Science, v. 67, p. 379–394, doi:10.1093/icesjms/fsp242.

Lavery, A.C., Chu, D., and Moum, J.N., 2010, Observations of Broadband Acoustic Backscattering from Nonlinear Internal Waves: Assessing the Contribution from Microstructure: IEEE Journal of Oceanic Engineering, v. 35, p. 695–708, doi:10.1109/JOE.2010.2047814.

Lavery, A.C., Wiebe, P.H., Stanton, T.K., Lawson, G.L., Benfield, M.C., and Copley, N., 2007, Determining dominant scatterers of sound in mixed zooplankton populations: The Journal of the Acoustical Society of America, v. 122, p. 3304–3326, doi:10.1121/1.2793613.

Lee, Z.P., Du, K.P., and Arnone, R., 2005, A model for the diffuse attenuation coefficient of downwelling irradiance: Journal of Geophysical Research C: Oceans, v. 110, p. 1–10, doi:10.1029/2004JC002275.

Logerwell, E.A., and Wilson, C.D., 2004, Species discrimination of fish using frequency-dependent acoustic backscatter: ICES Journal of Marine Science, v. 61, p. 1004–1013, doi:10.1016/j.icesjms.2004.04.004.

Lomac-MacNair, K., Jakobsson, M., Mix, A., Freire, F., Hogan, K., Mayer, L., and Smultea, M.A., 2018, Seal Occurrence and Habitat Use during Summer in Petermann Fjord,

Northwestern Greenland: Arctic, v. 71, p. 334–348, doi:10.14430/arctic4735.

Longhurst, A.R., 1976, Vertical Migration, in Cushing, D.H. and Walsh, J.J. eds., The Ecology of the Seas, W.B. Saunders Company, p. 116–137.

Longhurst, A., Sameoto, D., and Herman, A., 1984, Vertical distribution of arctic zooplankton in summer: eastern Canadian archipelago: Journal of Plankton Research, v. 6, p. 137–168, doi:10.1093/plankt/6.1.137.

Ludvigsen, M., Berge, J., Geoffroy, M., Cohen, J.H., de La Torre, P.R., Nornes, S.M., Singh, H., Sørensen, A.J., Daase, M., and Johnsen, G., 2018, Use of an Autonomous Surface Vehicle reveals small-scale diel vertical migrations of zooplankton and susceptibility to light pollution under low solar irradiance: Science Advances, v. 4, p. eaap9887, doi:10.1126/sciadv.aap9887.

Lurton, X., 2010, An Introduction to Underwater Acoustics: Principles and Applications: Springer-Verlang Berlin Heidelberg, 680 p., doi:10.1007/978-3-642-13835-5.

Lydersen, C. et al., 2014, The importance of tidewater glaciers for marine mammals and seabirds in Svalbard, Norway: Journal of Marine Systems, v. 129, p. 452–471, doi:10.1016/j.jmarsys.2013.09.006.

MacLennan, D.N., 1990, Acoustical measurement of fish abundance: The Journal of the Acoustical Society of America, v. 87, p. 1–15, doi:10.1121/1.399285.

Madureira, L.S.P., Ward, P., and Atkinson, A., 1993, Differences in backscattering strength determined at 120 and 38 kHz for three species of Antarctic macroplankton: Marine Ecology Progress Series, v. 93, p. 17–24, doi:10.3354/meps093017.

Martin, L. v., Stanton, T.K., Wiebe, P.H., and Lynch, J.F., 1996, Acoustic classification of zooplankton: ICES Journal of Marine Science, v. 53, p. 217–224, doi:10.1121/1.413130.

McDougall, T.J., and Barker, P.M., 2011, Getting started with TEOS-10 and the Gibbs Seawater (GSW) Oceanographic Toolbox: SCOR/IAPSO WG127, 28 p., http://www.teos-10.org/pubs/gsw/pdf/Getting_Started.pdf.

McManus, M.A., Benoit-Bird, K.J., and Woodson, C.B., 2008, Behavior exceeds physical forcing in the diel horizontal migration of the midwater sound-scattering layer in Hawaiian waters: Marine Ecology Progress Series, v. 365, p. 91–101, doi:10.3354/meps07491.

Mix, A.C., Jakobsson, M., and Petermann 2015 Scientific party, 2022, Expedition report: Petermann 2015: Swedish Polar research Secretariat (manuscript in preparation).

Moon, P., 1940, Proposed standard solar-radiation curves for engineering use: Journal of the Franklin Institute, v. 230, p. 583–618, doi:10.1016/S0016-0032(40)90364-7.

Mueller, J.L., 2000, SeaWiFS Algorithm for the Diffuse Attenuation Coefficent, K (490), Using Water-Leaving Radiances at 490 and 555 nm, in Hooker, S.B. and Firestone, E.R. eds., SeaWiFS Postlaunch Calibration and Validation Analyses, Part 3, NASA Goddard Space Flight Center, v. 11, p. 49, https://oceancolor.gsfc.nasa.gov/SeaWiFS/TECH_REPORTS/PLVol11.pdf (accessed October 2021).

Münchow, A., 2016, Volume and Freshwater Flux Observations from Nares Strait to the West of Greenland at Daily Time Scales from 2003 to 2009: Journal of Physical Oceanography, v. 46, p. 141–157, doi:10.1175/JPO-D-15-0093.1.

Münchow, A., Falkner, K.K., and Melling, H., 2015, Baffin Island and West Greenland Current Systems in northern Baffin Bay: Progress in Oceanography, v. 132, p. 305–317, doi:10.1016/j.pocean.2014.04.001.

Münchow, A., Falkner, K.K., and Melling, H., 2007, Spatial continuity of measured seawater and tracer fluxes through Nares Strait, a dynamically wide channel bordering the Canadian Archipelago: Journal of Marine Research, v. 65, p. 759–788, doi:10.1357/002224007784219048.

Münchow, A., Falkner, K., Melling, H., Rabe, B., and Johnson, H., 2011, Ocean Warming of Nares Strait Bottom Waters off Northwest Greenland, 2003–2009: Oceanography, v. 24, p. 114–123, doi:10.5670/oceanog.2011.62.

Münchow, A., and Melling, H., 2008, Ocean current observations from Nares Strait to the west of Greenland: Interannual to tidal variability and forcing: Journal of Marine Research, v. 66, p. 801–833, doi:10.1357/002224008788064612.

Münchow, A., Melling, H., and Falkner, K.K., 2006, An Observational Estimate of Volume and Freshwater Flux Leaving the Arctic Ocean through Nares Strait: Journal of Physical Oceanography, v. 36, p. 2025–2041, doi:10.1175/JPO2962.1.

Münchow, A., Padman, L., and Fricker, H.A., 2014, Interannual changes of the floating ice shelf of Petermann Gletscher, North Greenland, from 2000 to 2012: Journal of Glaciology, v. 60, p. 489–499, doi:10.3189/2014JoG13J135.

Münchow, A., Padman, L., Washam, P., and Nicholls, K.W., 2016, The Ice Shelf of Petermann Gletscher, North Greenland, and its Connection to the Arctic and Atlantic Oceans: Oceanography, v. 29, p. 84–95, doi:10.5670/oceanog.2016.101.

Napp, J.M., Ortner, P.B., Pieper, R.E., and Holliday, D. v., 1993, Biovolume-size spectra of epipelagic zooplankton using a Multi-frequency Acoustic Profiling System (MAPS): Deep-Sea Research I, v. 40, p. 445–459, doi:10.1016/0967-0637(93)90141-O.

NASA Goddard Space Flight Center, Ocean Ecology Laboratory, O.B. processing G. Moderate-resolution Imaging Spectroradiometer (MODIS) Terra Downwelling Diffuse Attenuation Coefficient Data; 2018 Reprocessing: NASA OB.DAAC, doi:10.5067/TERRA/MODIS/L3B/KD/2018.

Ocean Colour Climate Change Initiative dataset, Version 3.1, www.esa-oceancolour-cci.org.

Ohman, M.D., 1990, The Demographic Benefits of Diel Vertical Migration by Zooplankton: Ecological Monographs, v. 60, p. 257–281, doi:10.2307/1943058.

Ohman, M.D., Frost, B.W., and Cohen, E.B., 1983, Reverse Diel Vertical Migration: An Escape from Invertebrate Predators: Science, v. 220, p. 1404–1407, doi:10.1126/science.220.4604.1404.

Ona, E., and Mitson, R.B., 1996, Acoustic sampling and signal processing near the seabed: the deadzone revisited: ICES Journal of Marine Science, v. 53, p. 677–690, doi:10.1006/jmsc.1996.0087.

Paden, J., Li, J., Leuschen, C., Rodriguez-Morales, F., and Hale, R., 2019, IceBridge MCoRDS L2 Ice Thickness, Version 1: doi:10.5067/GDQ0CUCVTE2Q.

Parker-Stetter, S.L., Horne, J.K., and Weingartner, T.J., 2011, Distribution of polar cod and age-0 fish in the U.S. Beaufort Sea: Polar Biology, v. 34, p. 1543–1557, doi:10.1007/s00300-

011-1014-1.

Parker-Stetter, S.L., Rudstam, L.G., Sullivan, P.J., and Warner, D.M., 2009, Standard operating procedures for fisheries acoustic surveys in the Great Lakes: Great Lakes Fish. Comm. Spec. Pub. 09-01, p. 180, http://www.glfc.org/pubs/SpecialPubs/Sp09_1.pdf.

Pedersen, G., and Korneliussen, R.J., 2009, The relative frequency response derived from individually separated targets of northeast Arctic cod (Gadus morhua), saithe (Pollachius virens,), and Norway pout (Trisopterus esmarkii): ICES Journal of Marine Science, v. 66, p. 1149–1154, doi:10.1093/icesjms/fsp070.

Pieper, R.E., Holliday, D. v., and Kleppel, G.S., 1990, Quantitative zooplankton distributions from multifrequency acoustics: Journal of Plankton Research, v. 12, p. 433–441, doi:10.1093/plankt/12.2.433.

Polyakov, I. v. et al., 2010, Arctic Ocean Warming Contributes to Reduced Polar Ice Cap: Journal of Physical Oceanography, v. 40, p. 2743–2756, doi:10.1175/2010JPO4339.1.

Pomerleau, C., Winkler, G., Sastri, A.R., Nelson, R.J., Vagle, S., Lesage, V., and Ferguson, S.H., 2011, Spatial patterns in zooplankton communities across the eastern Canadian sub-Arctic and Arctic waters: Insights from stable carbon (δ13C) and nitrogen (δ15N) isotope ratios: Journal of Plankton Research, v. 33, p. 1779–1792, doi:10.1093/plankt/fbr080.

Raskoff, K.A., Hopcroft, R.R., Kosobokova, K.N., Purcell, J.E., and Youngbluth, M., 2010, Jellies under ice: ROV observations from the Arctic 2005 hidden ocean expedition: Deep-Sea Research Part II: Topical Studies in Oceanography, v. 57, p. 111–126, doi:10.1016/j.dsr2.2009.08.010.

Rignot, E., and Kanagaratnam, P., 2006, Changes in the Velocity Structure of the Greenland Ice Sheet: Science, v. 311, p. 986–990, doi:10.1126/science.1121381.

Rignot, E., and Steffen, K., 2008, Channelized bottom melting and stability of floating ice shelves: Geophysical Research Letters, v. 35, p. 2–6, doi:10.1029/2007GL031765.

Rolling Deck to Repository (R2R), 2003, Multibeam collection for HLY0301: Multibeam data collected aboard Healy from 20-Jul-03 to 13-Aug-03, St. John's, Canada to Thule, Greenland: https://www.ngdc.noaa.gov/ships/healy/HLY0301_mb.html.

Rudels, B., Jones, E.P., Anderson, L.G., and Kattner, G., 1994, On the Intermediate Depth Waters of the Arctic Ocean, in Johannessen, O.M., Muench, R.D., and Overland, J.E. eds., The Polar Oceans and Their Role in Shaping the Global Environment, Geophysical Monograph Series, v. 85, p. 33–46, doi:10.1029/gm085p0033.

Sadler, H.E., 1976, Water, Heat, and Salt Transports through Nares Strait, Ellesmere Island: Journal of the Fisheries Research Board of Canada, v. 33, p. 2286–2295, doi:10.1139/f76-275.

Sawada, K., Furusawa, M., and Williamson, N.J., 1993, Conditions for the precise measurement of fish target strength in situ: Journal of the Marine Acoustic Society of Japan, v. 20, p. 73–79, doi:10.3135/jmasj.20.73.

Shepard, A. et al., 2012, A Reconciled Estimate of Ice Sheet Mass Balance: Science, v. 338, p. 1183–1189, doi:10.1126/science.1228102.

Shroyer, E.L., Samelson, R.M., Padman, L., and Münchow, A., 2015, Modeled ocean circulation in Nares Strait and its dependence on landfast-ice cover: Journal of Geophysical

Research: Oceans, v. 120, p. 7934–7959, doi:10.1002/2015JC011091.

Simmonds, J., and MacLennan, D., 2005, Fisheries Acoustics: Blackwell Science Ltd., 437 p.

Simmonds, E.J., Williamson, N.J., Gerlotto, F., and Aglen, A., 1992, Acoustic Survey Design and Analysis Procedure: A Comprehensive Review of Current Practice: ICES Cooperative Research Report No. 187, p. 127, https://www.ices.dk/sites/pub/Publication%20Reports/Cooperative%20Research%20Report%20(CRR)/CRR%20187.pdf (accessed October 2021).

Simpson, J.J., and Dickey, T.D., 1981, The Relationship between Downward Irradiance and Upper Ocean Structure: Journal of Physical Oceanography, v. 11, p. 309–323, doi:10.1175/1520-0485(1981)011<0309:trbdia>2.0.co;2.

Smith, S.L., and Schnack-Schiel, S.B., 1990, Polar Zooplankton, in Smith Jr., W.O. ed., Polar Oceanography, Part B: Chemistry, Biology, and Geology, San Diego, Academic Press, Inc., p. 527–598.

Søreide, J.E., Falk-Petersen, S., Hegseth, E.N., Hop, H., Carroll, M.L., Hobson, K.A., and Blachowiak-Samolyk, K., 2008, Seasonal feeding strategies of Calanus in the high-Arctic Svalbard region: Deep-Sea Research Part II: Topical Studies in Oceanography, v. 55, p. 2225–2244, doi:10.1016/j.dsr2.2008.05.024.

Stanton, T.K., Chu, D., Jech, J.M., and Irish, J.D., 2010, New broadband methods for resonance classification and high-resolution imagery of fish with swimbladders using a modified commercial broadband echosounder: ICES Journal of Marine Science, v. 67, p. 365–378, doi:10.1093/icesjms/fsp262.

Stanton, T.K., Chu, D., and Wiebe, P.H., 1996, Acoustic scattering characteristics of several zooplankton groups: ICES Journal of Marine Science, v. 53, p. 289–295, doi:10.1006/jmsc.1996.0037.

Stanton, T.K., Chu, D., and Wiebe, P.H., 1998a, Sound scattering by several zooplankton groups. II. Scattering models: The Journal of the Acoustical Society of America, v. 103, p. 236–253, doi:10.1121/1.421110.

Stanton, T.K., Chu, D., Wiebe, P.H., Martin, L. v., and Eastwood, R.L., 1998b, Sound scattering by several zooplankton groups. I. Experimental determination of dominant scattering mechanisms: The Journal of the Acoustical Society of America, v. 103, p. 225–235, doi:10.1121/1.421469.

Stanton, T.K., Wiebe, P.H., Chu, D., Benfield, M.C., Scanlon, L., Martin, L., and Eastwood, R.L., 1994, On acoustic estimates of zooplankton biomass: ICES Journal of Marine Science: Journal du Conseil, v. 51, p. 502–512, doi:10.1006/jmsc.1994.1051.

de Steur, L. et al., 2013, Hydrographic changes in the Lincoln Sea in the Arctic Ocean with focus on an upper ocean freshwater anomaly between 2007 and 2010: Journal of Geophysical Research: Oceans, v. 118, p. 4699–4715, doi:10.1002/jgrc.20341.

Straneo, F., and Cenedese, C., 2015, The Dynamics of Greenland's Glacial Fjords and Their Role in Climate: Annual Review of Marine Science, v. 7, p. 89–112, doi:10.1146/annurev-marine-010213-135133.

Straneo, F., and Heimbach, P., 2013, North Atlantic warming and the retreat of Greenland's outlet glaciers: Nature, v. 504, p. 36–43, doi:10.1038/nature12854.

Straneo, F., Sutherland, D.A., Holland, D., Gladish, C., Hamilton, G.S., Johnson, H.L., Rignot, E., Xu, Y., and Koppes, M., 2012, Characteristics of ocean waters reaching Greenland's glaciers: Annals of Glaciology, v. 53, p. 202–210, doi:10.3189/2012AoG60A059.

Stranne, C., Mayer, L., Jakobsson, M., Weidner, E., Jerram, K., Weber, T.C., Anderson, L.G., Nilsson, J., Björk, G., and Gårdfeldt, K., 2018, Acoustic mapping of mixed layer depth: Ocean Science, v. 14, p. 503–514, doi:10.5194/os-14-503-2018.

Stranne, C., Mayer, L., Weber, T.C., Ruddick, B.R., Jakobsson, M., Jerram, K., Weidner, E., Nilsson, J., and Gårdfeldt, K., 2017, Acoustic Mapping of Thermohaline Staircases in the Arctic Ocean: Scientific Reports, v. 7, p. 15192, doi:10.1038/s41598-017-15486-3.

SWERUS Scientific Party, 2016, SWERUS-C3 2014 Expedition Cruise Report - Leg 2 (of 2): https://bolin.su.se/data/swerus/reports/leg2/Cruise report SWERUS-C3 – Leg 2.pdf.

Talley, L.D., Pickard, G.L., Emery, W.J., and Swift, J.H., 2011, Descriptive physical oceanography: an introduction: Academic Press, 564 p.

Tessensohn, F., Jackson, R.H., and Reid, I.D., 2006, The Tectonic Evolution of Nares Strait: Implications of New Data: Polarforschung, v. 74, p. 191–198.

Tinto, K.J., Bell, R.E., Cochran, J.R., and Münchow, A., 2015, Bathymetry in Petermann fjord from Operation IceBridge aerogravity: Earth and Planetary Science Letters, v. 422, p. 58–66, doi:10.1016/j.epsl.2015.04.009.

University of New Brunswick (UNB) Ocean Mapping Group, 2013, Multibeam collection for 2013_Amundsen: Multibeam data collected aboard Amundsen from 26-Jul-13 to 05-Oct-13: https://www.ngdc.noaa.gov/ships/amundsen/2013_Amundsen_mb.html.

Urick, R.J., 1983, Principles of Underwater Sound: McGraw-Hill, 423 p.

Uye, S., Huang, C., and Onbé, T., 1990, Ontogenetic diel vertical migration of the planktonic copepod Calanus sinicus in the Inland Sea of Japan: Marine Biology, v. 104, p. 389–396, doi:10.1007/BF01314341.

van de Wal, R.S.W., Zhang, X., Mionobe, S., Jevrejeva, S., Riva, R.E.M., Little, C., Richter, K., and Palmer, M.D., 2019, Uncertainties in Long-Term Twenty-First Century Process-Based Coastal Sea-Level Projections: Surveys in Geophysics, v. 40, p. 1655–1671, doi:10.1007/s10712-019-09575-3.

Washam, P., Münchow, A., and Nicholls, K.W., 2018, A Decade of Ocean Changes Impacting the Ice Shelf of Petermann Gletscher, Greenland: Journal of Physical Oceanography, v. 48, p. 2477–2493, doi:10.1175/JPO-D-17-0181.1.

Watkins, J.L., and Brierley, A.S., 2002, Verification of the acoustic techniques used to identify Antarctic krill: ICES Journal of Marine Science, v. 59, p. 1326–1336, doi:10.1006/jmsc.2002.1309.

Webster, C.N., Varpe, Ø., Falk-Petersen, S., Berge, J., Stübner, E., and Brierley, A.S., 2013, Moonlit swimming: vertical distributions of macrozooplankton and nekton during the polar night: Polar Biology, v. 38, p. 75–85, doi:10.1007/s00300-013-1422-5.

Weidner, E., Weber, T.C., Mayer, L., Jakobsson, M., Chernykh, D., and Semiletov, I., 2019, A wideband acoustic method for direct assessment of bubble-mediated methane flux: Continental Shelf Research, v. 173, p. 104–115, doi:10.1016/j.csr.2018.12.005.

Welch, H.E., Bergmann, M.A., Siferd, T.D., Martin, K.A., Curtis, M.F., Crawford, R.E., Conover, R.J., and Hop, H., 1992, Energy Flow through the Marine Ecosystem of the Lancaster Sound Region, Arctic Canada: Arctic, v. 45, p. 343–357, doi:10.14430/arctic1413.

Welch, H.E., Crawford, R.E., and Hop, H., 1993, Occurrence of Arctic Cod (Boreogadus saida) and Their Vulnerability to Predation in the Canadian High Arctic: Arctic, v. 46, p. 331–339.

APPENDIX A EK80 DATA PROCESSING

A.1 Attitude and Elevation

EK80 data was acquired using the Simrad EK80 software (version 1.8.0). The software was set up to record ship position (latitude, longitude, and elevation) and attitude (roll, and pitch) as part of the RAW sonar files. Latitude and longitude were automatically integrated into the files (i.e., the data was georeferenced), however the elevation and attitude information was not. By not applying attitude data, we assume the sonar beam is always pointing directly down, ensonifying the water column immediately beneath the vessel. By not applying elevation information, we assume that the ship is transiting along a flat plane that maintains the same height. In reality, the pitch and roll change the ship and sonar beam orientation, causing a portion of the water column off the center track to be ensonified, and changes in elevation (heave and tides) introduce a change in the ship's height that will cause the ensonified targets to appear to move vertically. The result is that there is some offset between where the targets in the data are assumed to be, and where they actually are.

The attitude information for the period of August 1 – August 31 that was recorded (but not integrated) in the RAW files was interrogated to determine if it was necessary to apply pitch and roll to the RAW files. Roll during this period varied from 0° to -4.8/5.6° (Figure 112), with a mean value of -0.3°; 98.5% of the roll values fell between -1.1° and 0.5° (three standard deviations from the mean). The maximum offset these roll values would cause in the estimated target depth would be 0.48% of water depth, or 5.5 m at

the maximum survey depths of 1160 m. Pitch varied from 0° to -0.4°/1.6° (Figure 113), with a mean value of 0.3°; 99.9% of the pitch values fell between -0.3° and 1° (three standard deviations from the mean). The maximum offset these pitch values would cause in the estimated target depth would be 0.04 % of water depth, or 0.5 m at the maximum survey depths of 1160 m. These potential offsets, especially at the depths where the majority of our water column targets reside, were deemed small enough to justify not applying pitch and roll to the EK80 data.

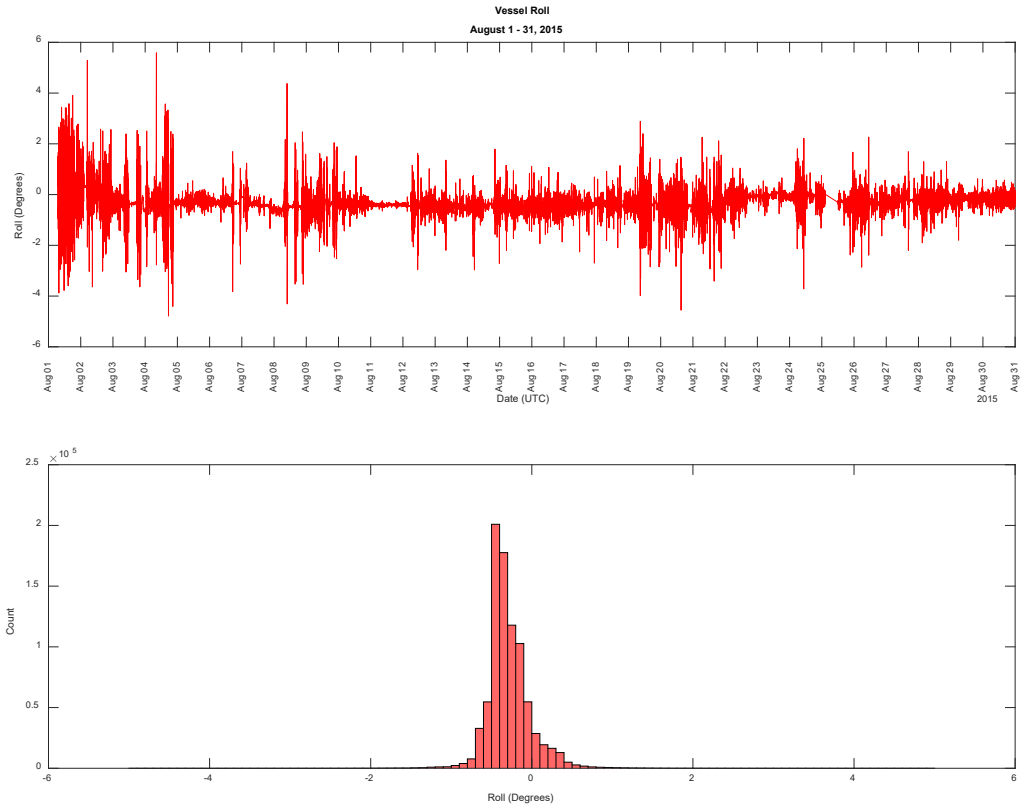

Figure 112: Roll values for the ODEN during the Petermann Expedition. Top, roll in degrees over the course of the expedition. Bottom, a histogram showing the frequency distribution of roll values for the expedition. Data is binned at 0.1 degrees.

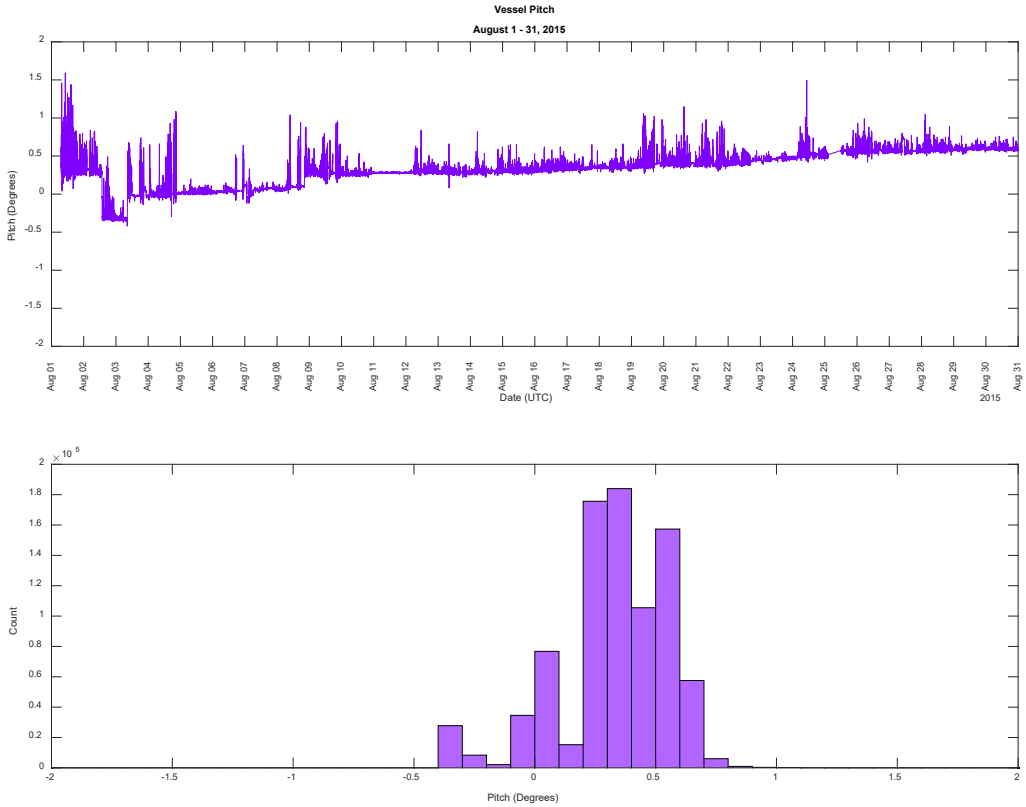

Figure 113: Pitch values for the ODEN during the Petermann Expedition. Top, pitch in degrees over the course of the expedition. Bottom, a histogram showing the frequency distribution of pitch values for the expedition. Data is binned at 0.1 degrees.

Elevation offsets during the survey included vessel heave and changing tides. Heave values varied from 0 m to -0.6 m/0.3 m (Figure 114); 98.1% of the heave values fell between -0.05 m and 0.05 m (three standard deviations from the mean). Elevation changes due to heave were therefore very low and were not applied to the data. Documented tide information for this location is poor. Geodetic GPS receivers deployed on the Petermann ice shelf for 13 days in August 2015 recorded vertical ice shelf displacements of up to +/- 1 m, dominated by the M_2 tide (Münchow et al., 2016). This can likely be taken as the maximum tidal elevation change, at least during the period of this study. Tidal offsets were not applied to the data.

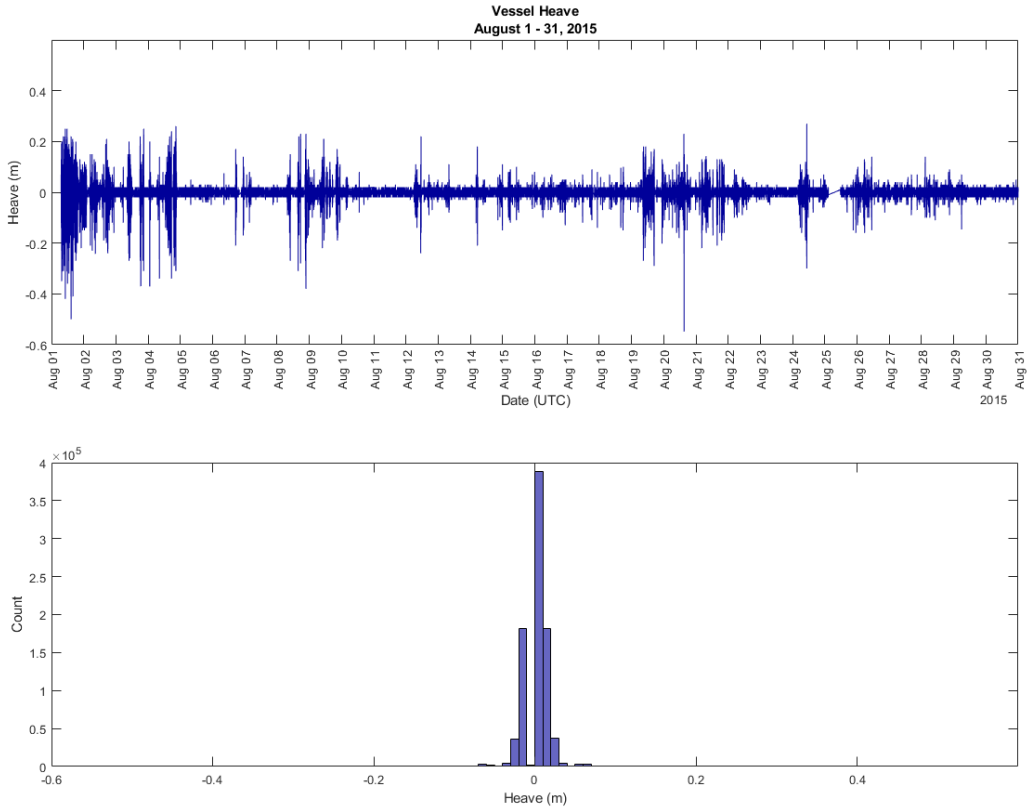

Figure 114: Heave values for the ODEN during the Petermann Expedition. Top, heave in meters over the course of the expedition. Bottom, a histogram showing the frequency distribution of heave values for the expedition. Data is binned at 0.01 meters.

Additionally, the ES18-11 transducer was mounted well below the sea surface waterline, and this transducer offset was not automatically applied to the EK80 RAW files. The depth of the transducer was estimated to be approximately 8.2 m below waterline, based on diagrams (Figure 115) and instrument offsets (Table 4) for the multibeam transducer (SWERUS Scientific Party, 2016). This offset was not applied to the raw data but was applied to the depth of the scattering layer selections during analysis.

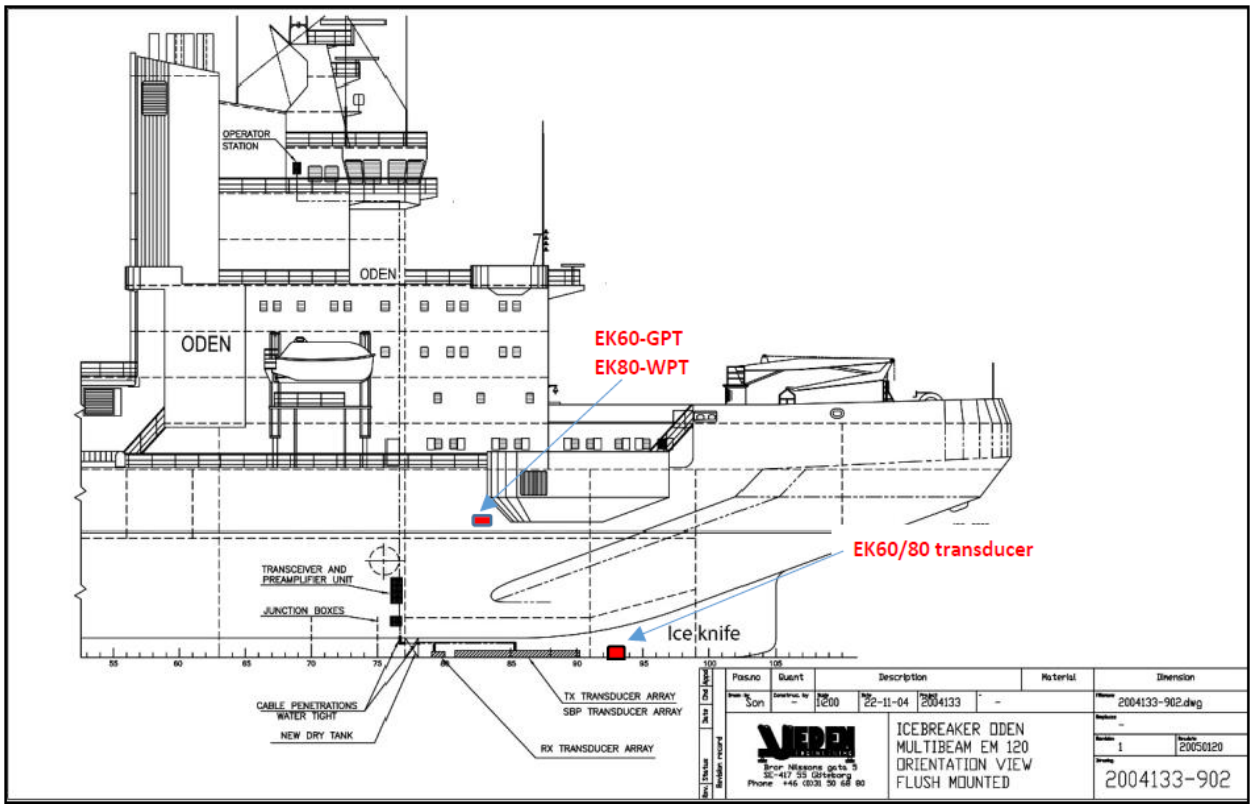

Figure 115: Location of the EK80 transducer on the ODEN (SWERUS Scientific Party, 2016).

Table 4: Offsets for the multibeam transducer on the ODEN, which were used to estimate the depth offset for the ES18-11 transducer. Adapted from SWERUS-C3 2-14 Expedition Cruise Report – Leg 2 (of 2) (2016).

	X	Y	Z
Reference point, MRU	0	0	0
EM120 TX Transducer	17.590	-2.374	9.459
Reference point to Waterline			1.3

A.2 Sound Speed

The various software programs used to process, visualize, and analyze the EK80 data – QPS FMMidwater software version 7.6.1 supplemented by custom Python and navigation extraction routines, Myriax Echoview software versions 8.0.95.32073 through 9.0.328.35283, and New Zealand National Institute of Water and Atmospheric Research's (NIWA) ESP3 software versions 1.0.1 through 1.8.1 – all utilized a single sound speed value of 1500 m s^{-1} for calculating ranges from the transducer and for the

generation of echograms. HydrOffice Sound Speed Manager v.2021.2.3 (https://www.hydroffice.org/soundspeed/main) was used to generate sound speed profiles for the regional, using the conductivity and temperature information in the processed CTD casts (see Section 3.1.2.1 and Appendix D for a description of CTD processing steps). Sound speed varied from lows of 1436 to 1441 m s^{-1} at 20 m depth to a steady 1467 m s^{-1} at 1000 m depth (Figure 116). The weighted harmonic mean (as calculated in Sound Speed Manager) ranged from 1450.4 to 1457.5 m s^{-1}. Using 1436 m s^{-1} as the slowest sound speed value for the water column in this region, the shallowest scattering layers (found at 45 m depth, 36.8 m from the transducer) could have been up to 1.6 m shallower than reported, and the deepest scattering layers (found at 635 m depth, 626.8 m from the transducer) could have been as much as 26.8 m shallower than reported. Using the slowest harmonic sound speed of 1450.4 m s^{-1}, the layers could have been 1.2 m and 20.7 m shallower than reported.

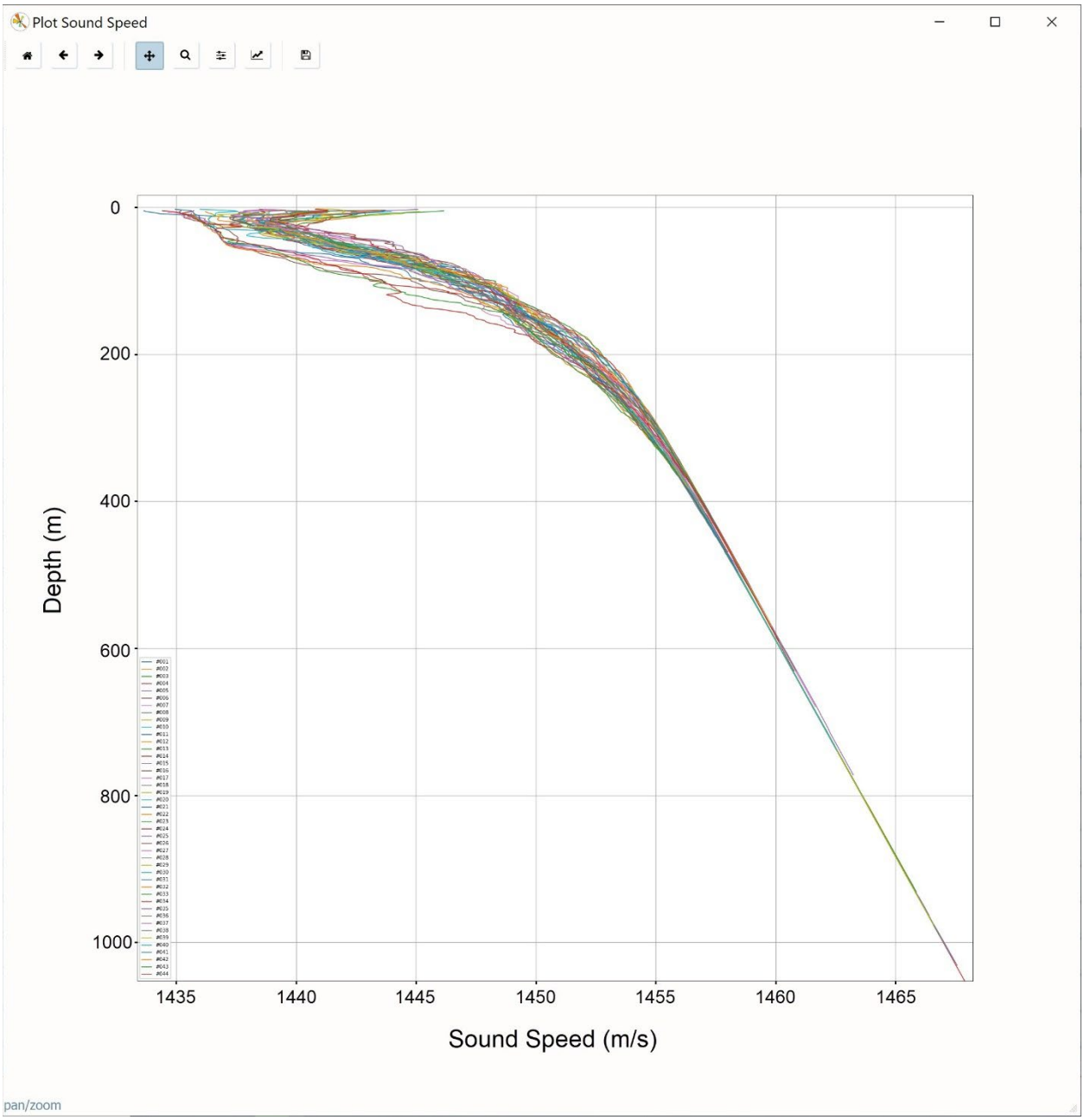

Figure 116: Sound speed profiles calculated from CTD casts.

A.3 EK80 Data Calibration

The ESP3 (version 1.8.1) 'Process TS Cal tool' was used to generate a calibration file for use in the ESP3 software, using data collected during deployment of the calibration sphere and utilizing a 1.024 ms pulse at 2000 W

(PETERMANN2015CALIB-D20150901-T214351.raw). The following values were used in the software's *Environment and Calibration* tabs prior to running the calibration:

Table 5: Values used for calibration processing in ESP3.

Sphere	64 mm copper
Depth *(of sphere)*	55 m
Temperature *(average, 8.4 – 54.6 m)*	1.12 ° C
Salinity *(average, 10 – 55 m)*	33.38 (unitless)

Temperature and salinity at the depth of the sphere are required as part of calibration, and are used to estimate sound speed, absorption, and attenuation. Notes from the expedition indicate that a CTD cast was taken near the calibration site, however this cast could not be located in the data archives. An XBT (serial number 334577) was taken approximately 120 km north of and 8 hours prior to arrival at the calibration site; an average of the temperatures recorded by that XBT between 8.4 m and 54.6 m was used. Salinity for the calibration site was estimated by averaging the World Ocean Database 2018 August and September 2015-2017 decadal objectively analyzed means between 10 and 55 m for the 0.25 degree node nearest the calibration site (Boyer et al., 2019).

Most of the calibration files collected were of low quality, in that the collected files were relatively short and the sphere was not moved thoroughly through the beam, understandable in that the files were collected in stormy conditions. During the calibration processing the ESP software provided a warning that targets within 0.3 degrees of the center of the beam were limited and that it had to extend the look radius to 1.6 degrees. Despite this, the software was able to generate a calibration file that could be used to calculate target strengths for individual targets and volumes (see Table 6 for calibration offset values and Figure 117 through Figure 120 for screen captures of

the calibration process and results). The dB offset was found to range from +1.00 dB to -18.91 dB across the frequency range, in that the observed sphere scattering strength was 1.00 dB lower to 18.91 dB higher than the theoretical values for the calibration sphere (Table 6). This was considerably higher than what is typically found during calibration. Upon further investigation, it was found that the default calibration gain value was set to 15.80 in the EK80 software during installation, whereas the appropriate default value for this transducer is closer to 22.9 dB. This setting was subsequently applied to all files during acquisition, causing the scattering level in all uncalibrated echograms to appear much stronger than it was. This does not affect the results of frequency response analysis, as the calculated calibration offset is applied during this type of analysis. It does, however, cause distortion in the real-time viewing of echograms and images made of those echograms, and in exports that don't utilize the calibration curve. As this discovery was made late in the analysis, the majority of echogram images have this issue and the scattering levels shown are artificially high. ESP3 allows for a generalized ("rough") real-time correction of echograms; Figure 121 provides an example of echograms with the default gain applied, and Figure 122 shows the same data with the gain adjusted to be closer to the standard value for this transducer and in line with the results of the calibration.

Table 6: Calibration offsets across the frequency range.

Frequency (kHz)	Sphere Theoretical TS (dB)	Observed TS (dB)	Difference (i.e., calibration offset, dB)
15.38	-36.64	-19.22	-17.42
16.11	-35.83	-16.92	-18.91
16.85	-35.35	-16.57	-18.78
17.58	-35.20	-16.93	-18.27
18.31	-35.36	-17.51	-17.85
19.04	-35.80	-18.70	-17.10
19.78	-36.46	-19.59	-16.87
20.51	-37.20	-20.09	-17.11
21.24	-37.77	-20.02	-17.75
21.97	-37.91	-20.06	-17.86
22.71	-37.55	-21.79	-15.76
23.44	-36.86	-22.94	-13.92
24.17	-36.11	-26.40	-9.72
24.90	-35.50	-30.07	-5.43
25.63	-35.12	-33.27	-1.86
26.37	-35.01	-35.18	0.18
27.10	-35.15	-36.10	0.95
27.83	-35.53	-36.53	1.00
28.56	-36.10	-36.21	0.12
29.30	-36.71	-37.54	0.83

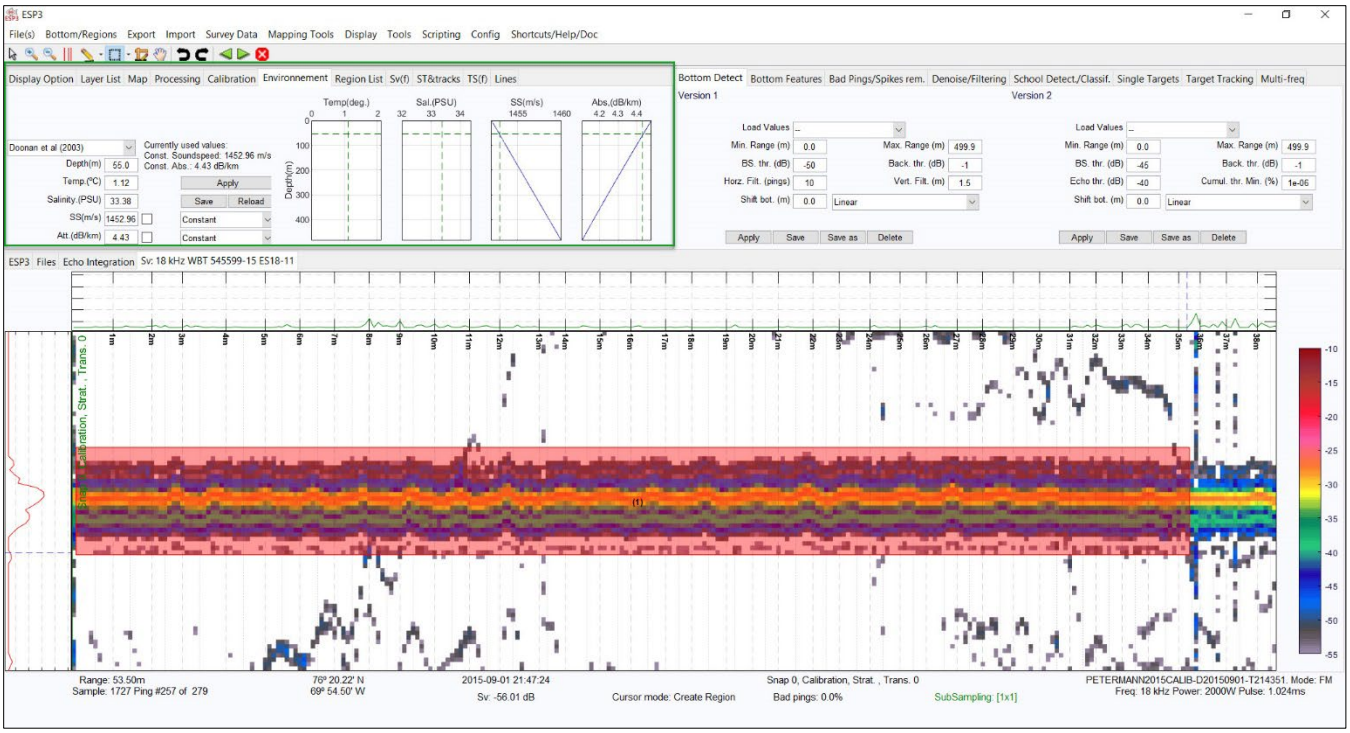

Figure 117: Selecting the sphere target for calibration in ESP3. A red region box is drawn around returns from the calibration sphere prior to running the data calibration. The environmental values used for the calibration are visible in the Environment tab, highlighted with a green box.

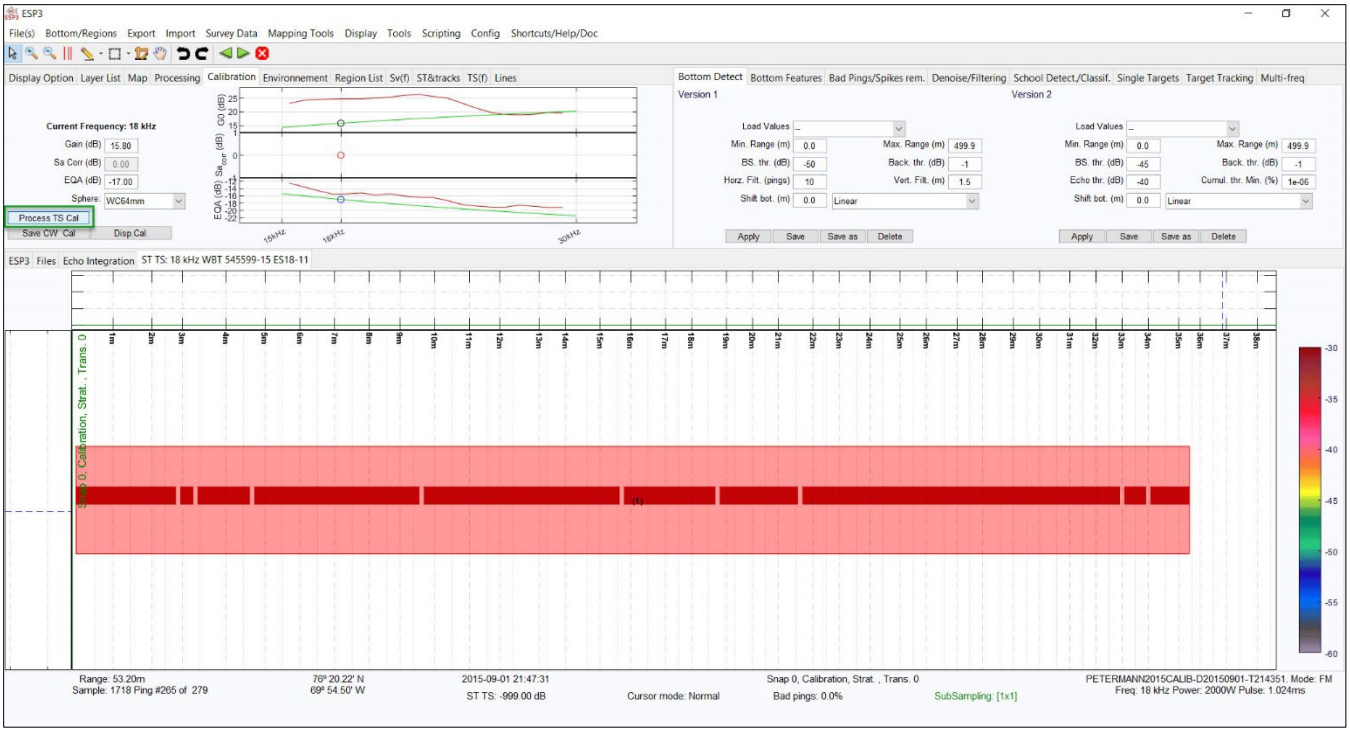

Figure 118: The calibration sphere is auto-extracted as a single target by the ESP software as the first step in the calibration processing. The green box is highlighting the Process TS Cal tool.

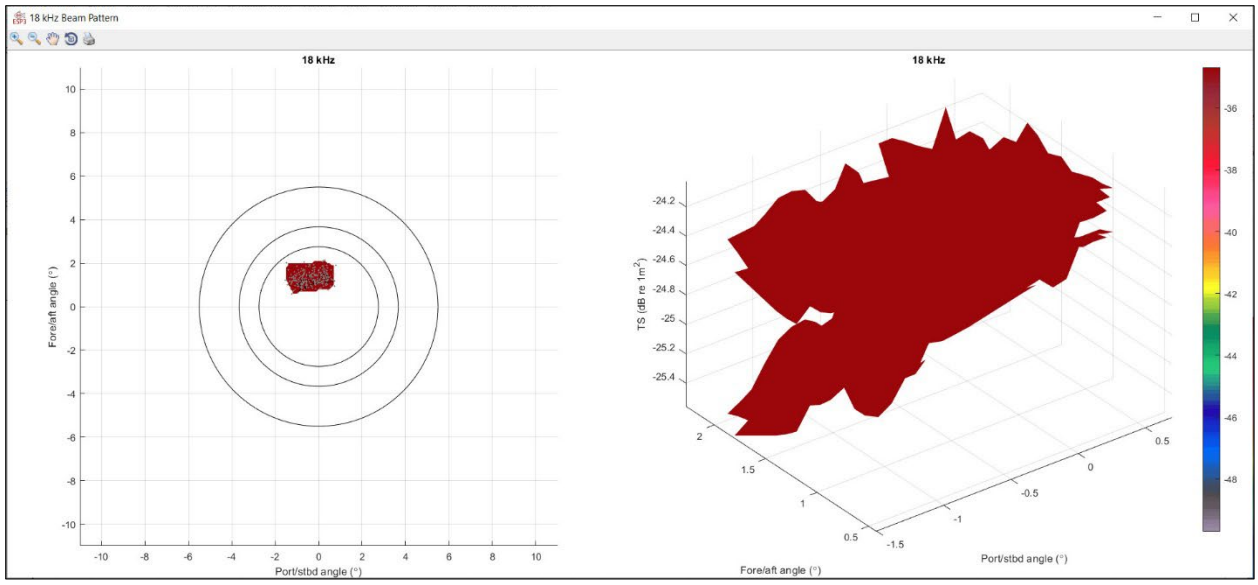

Figure 119: Coverage of the sphere within the beam (left) and beam pattern (right) extracted for the calibration sphere.

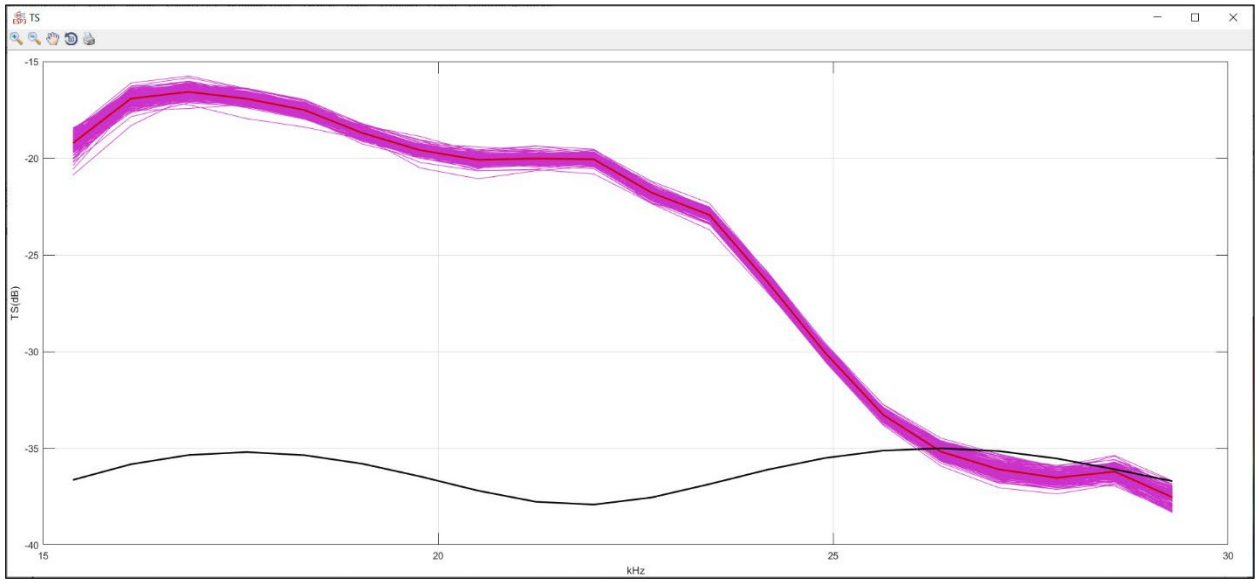

Figure 120: Target strength (TS) curve extracted from the EK80 data. The bottom black line is the theoretical TS for a 64 mm copper sphere. The magenta lines are the observed TS for the sphere, and the red line is the average of those observations.

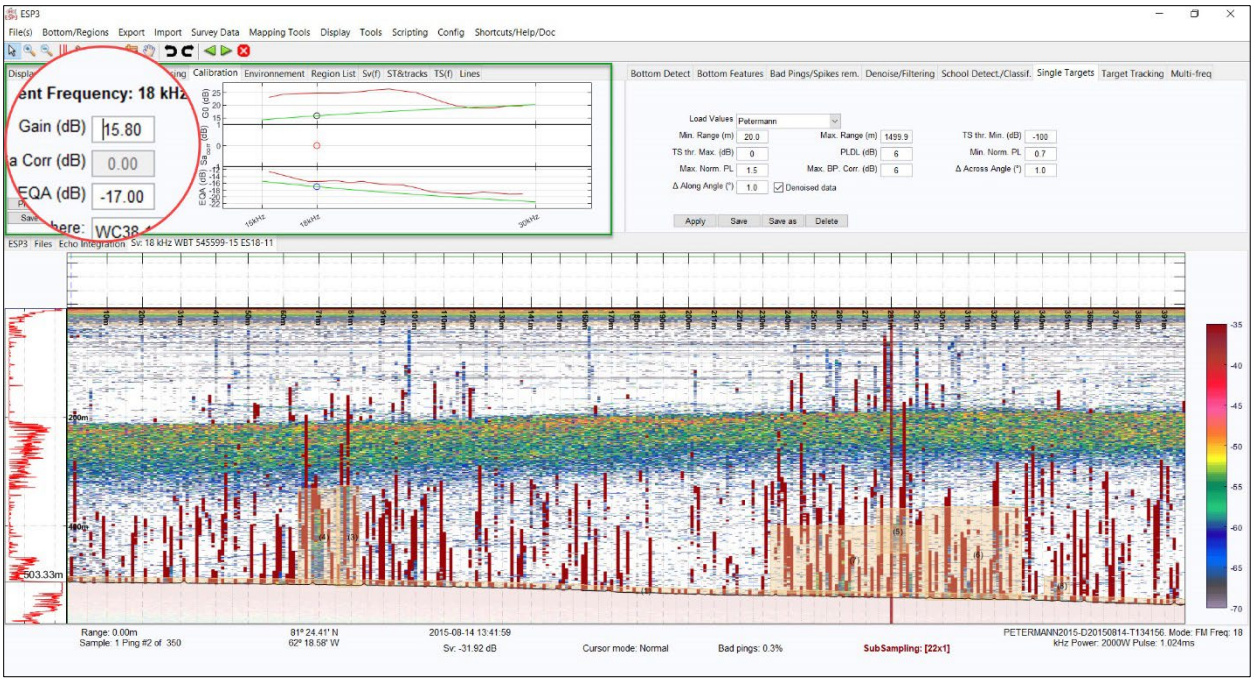

Figure 121: Example of echogram for EK80 file PETERMANN2015-D20150814-T134156 with the default gain value applied. The green box highlights the Calibration tab and the red circle highlights and magnifies the default gain value being applied; this is the gain being read directly from the EK80 file parameters.

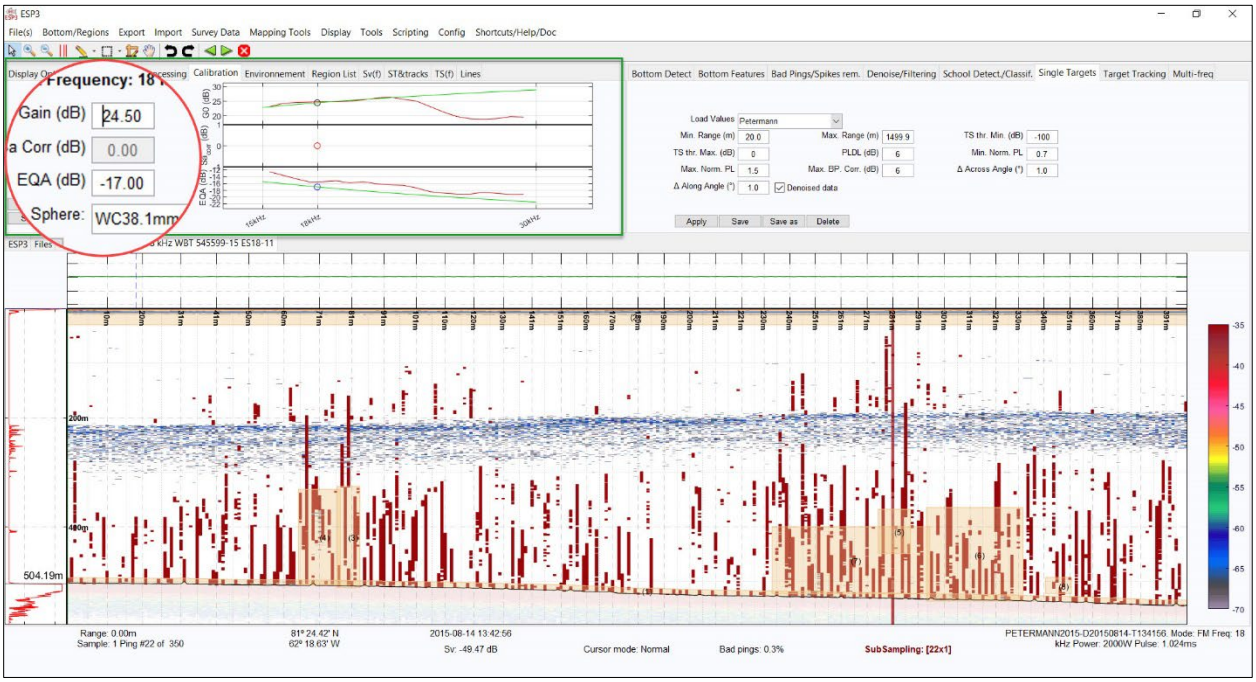

Figure 122: Example of echogram for the same file shown in Figure 121, with adjusted gain value applied. The green box highlights the Calibration tab and the red circle highlights and magnifies the new gain value being applied.

A.4 Data Issues

Processing of the EK80 files was hindered by the quality of data in many locations, as can be expected with data collected in the Arctic particularly when ice breaking is under way. Additionally, this was one of the first cruises utilizing the 18 kHz WBT and therefore there were occasional changes in setting such as pulse length and power while the mapping team attempted to find the best setting for the location and mapping priorities. Data quality was further compromised by persistent artifacts and interference from other systems. Quality also degraded considerably when the ship changed speed/direction, which happened almost continuously as the ship maneuvered around ice and moved on to stations; these quick changes generated a lot of noise in the water column. In some instances, the quality improved with continued steady speed.

A.4.1 Ship Noise

In nearly all of the EK80 data collected, there was an artifact in the water column that varied in severity but remained persistent even at very slow speeds (Figure 123). This is believed to be caused by the operation of the steam valves in the *Oden's* fuel and ballast water heating system (SWERUS Scientific Party, 2016). The artifact did not normally prevent the visual detection of features in the water column, but it did hamper attempts to do data filtering and automatic layer selection. This artifact could be partially removed prior to frequency response analysis using the ESP3 'Spikes removal' algorithm (Figure 124), however it can be assumed that some spikes remained and likely contributed to calculated values of S_v and TS during frequency response analysis.

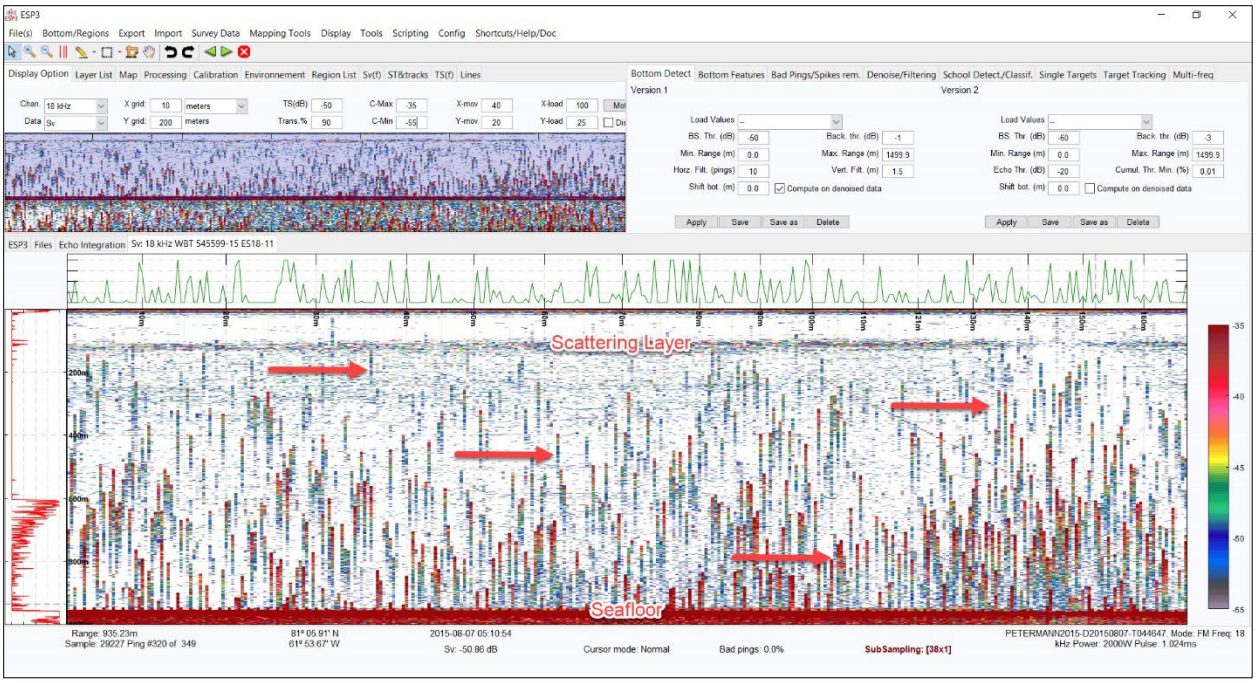

Figure 123: Steam valve noise showing up as sharp vertical spikes in scattering between the scattering layer and the seafloor when the ship is drifting (here, the speed is less than 0.3 knots). The red arrows point out a few examples, however the sharp spikes throughout the water column are all thought to be due to this noise source.

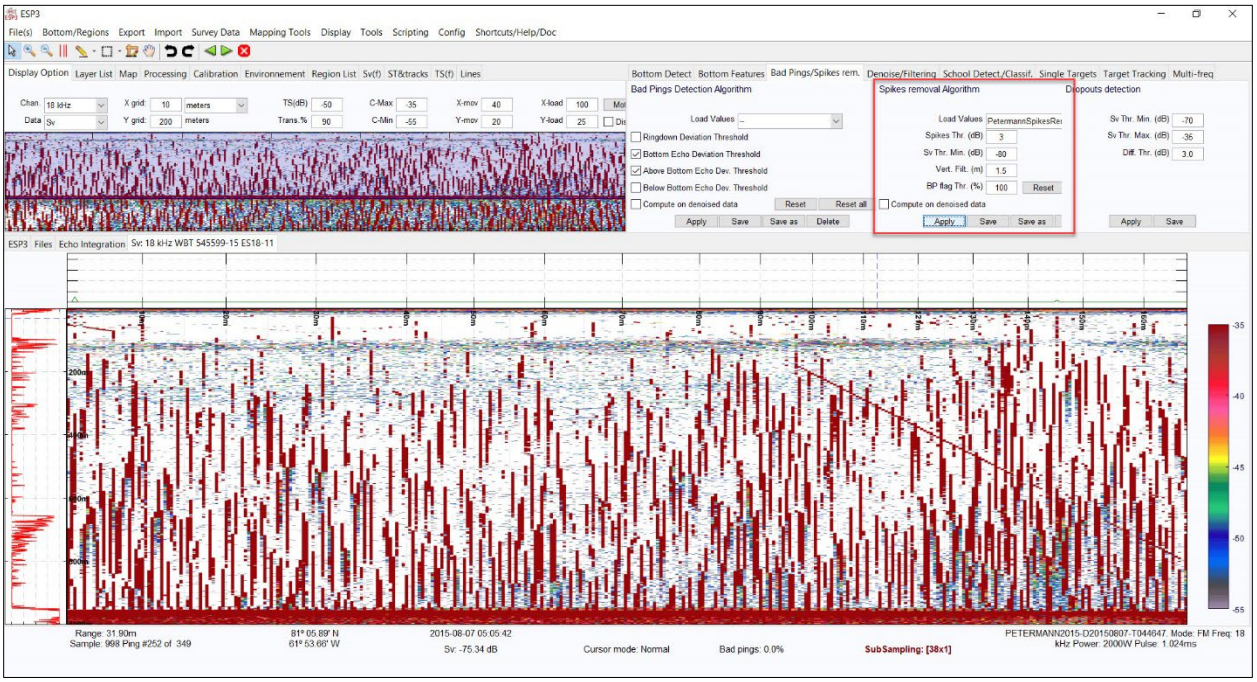

Figure 124: Data removed using the Spike removal Algorithm in ESP3. When the algorithm is applied, the areas covered by a dark red mask are removed from further signal analysis.

When the ship restarted its engine after being on station and increased its speed or transited at sustained high speeds (Figure 125), there was a drastic increase in noise in the water column. This noise masked the detection of targets at depth; in some instances, it made it impossible to determine if a scattering layer was present. The SWERUS Scientific Party (2016) also noted similar noise in the EK80 data in rough seas and at increased ship speeds which they attributed to bubbles sweeping past the transducer, also noting the noise tended to decrease dramatically on turns when bubbles were swept away from the transducer (SWERUS Scientific Party, 2016). Figure 126 shows an example of both where a sharp turn (and subsequent reduction in speed, though probably a secondary factor) greatly reduces noise in the water column, and where high levels of noise and an increase in the depth of the scattering layer ends up masking the presence of the scattering layer.

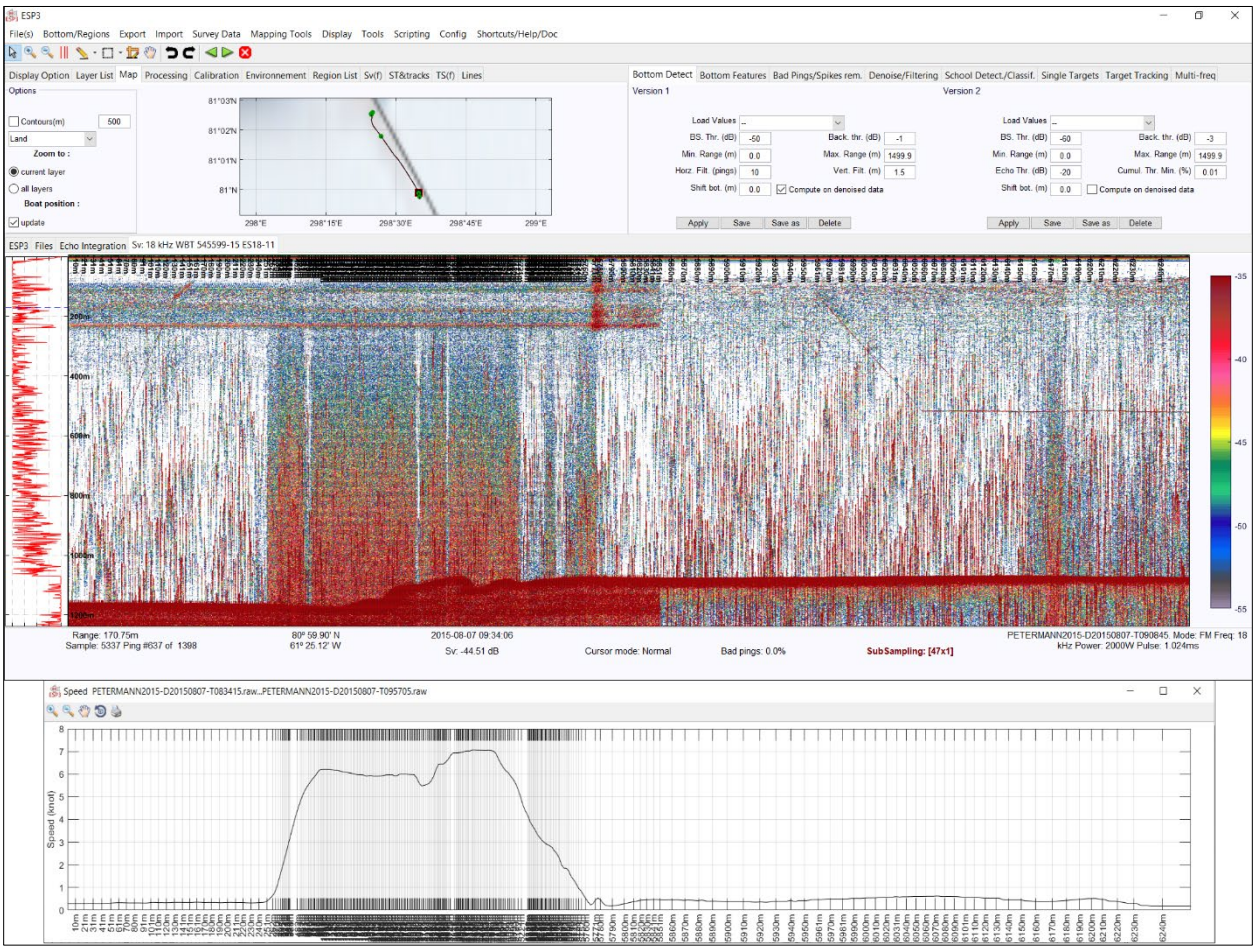

Figure 125: Increase in noise related to engines starting and increasing speed as the ship moved between stations.

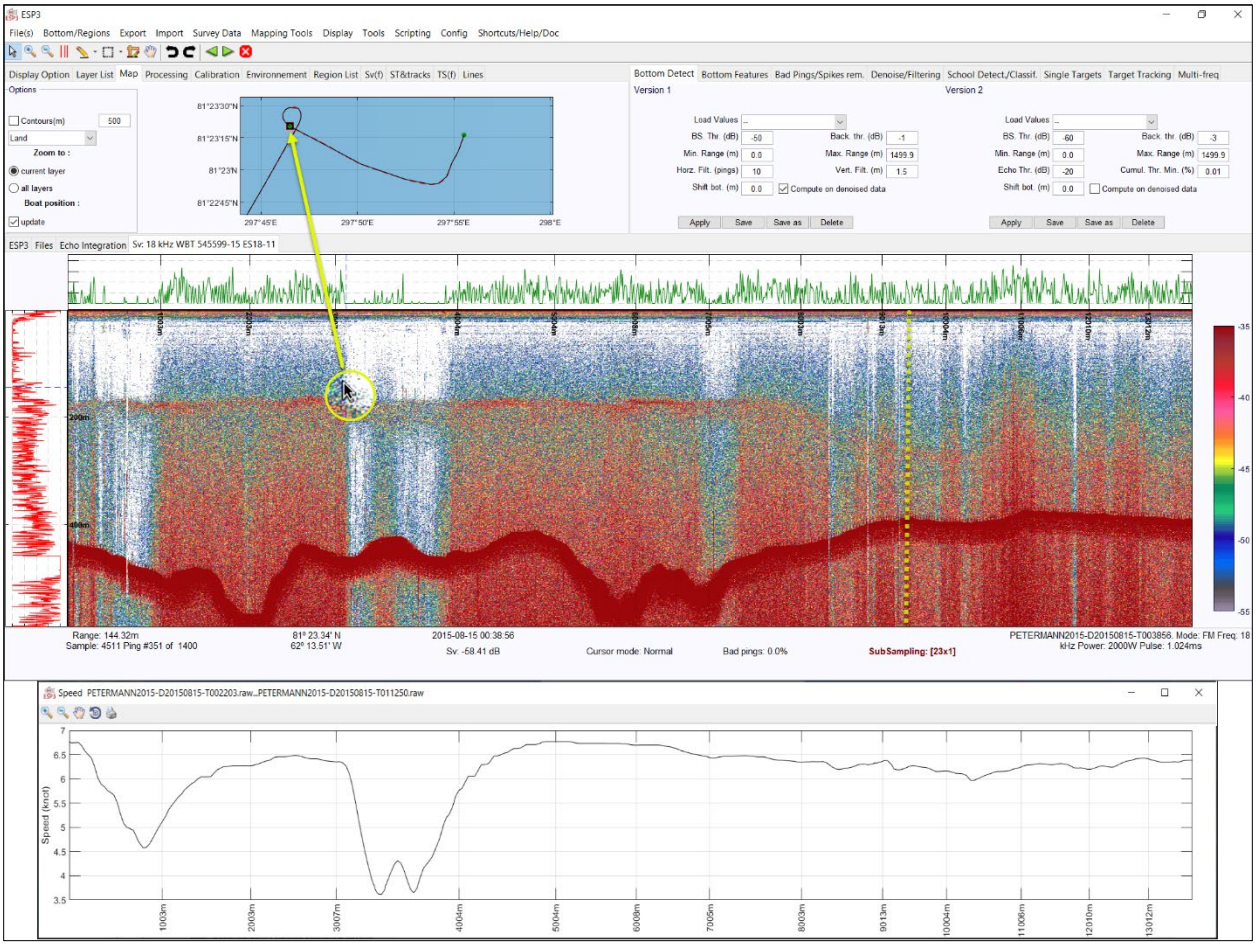

Figure 126: PETERMANN2015-D20150815-T002203 through PETERMANN2015-D20150815-T011250 in ESP3. The mouse position in the echogram corresponds to the start of a sharp turn visible in the Map tab. The dotted yellow line is the approximate location of a line change. The scattering layer is still visible in the line prior to the line change but becomes heavily masked with noise and possibly disappears after the line change.

A.4.2 EM122 Interference

In some locations, there was a persistent artifact in the upper water column, above 250 m, which manifested as straight lines with increased intensity every other ping (Figure 127); this interference was documented by watch standers as being related to periods when the EM122 was in Deep Mode (Kevin Jerram, personal communication, August 2017). In some instances, this interference was well above the scattering layer, but in other locations it overprinted the natural scattering (Figure 128), making manual

picking of the top of the layer difficult and automated picking of the top of the layer and schools nearly impossible.

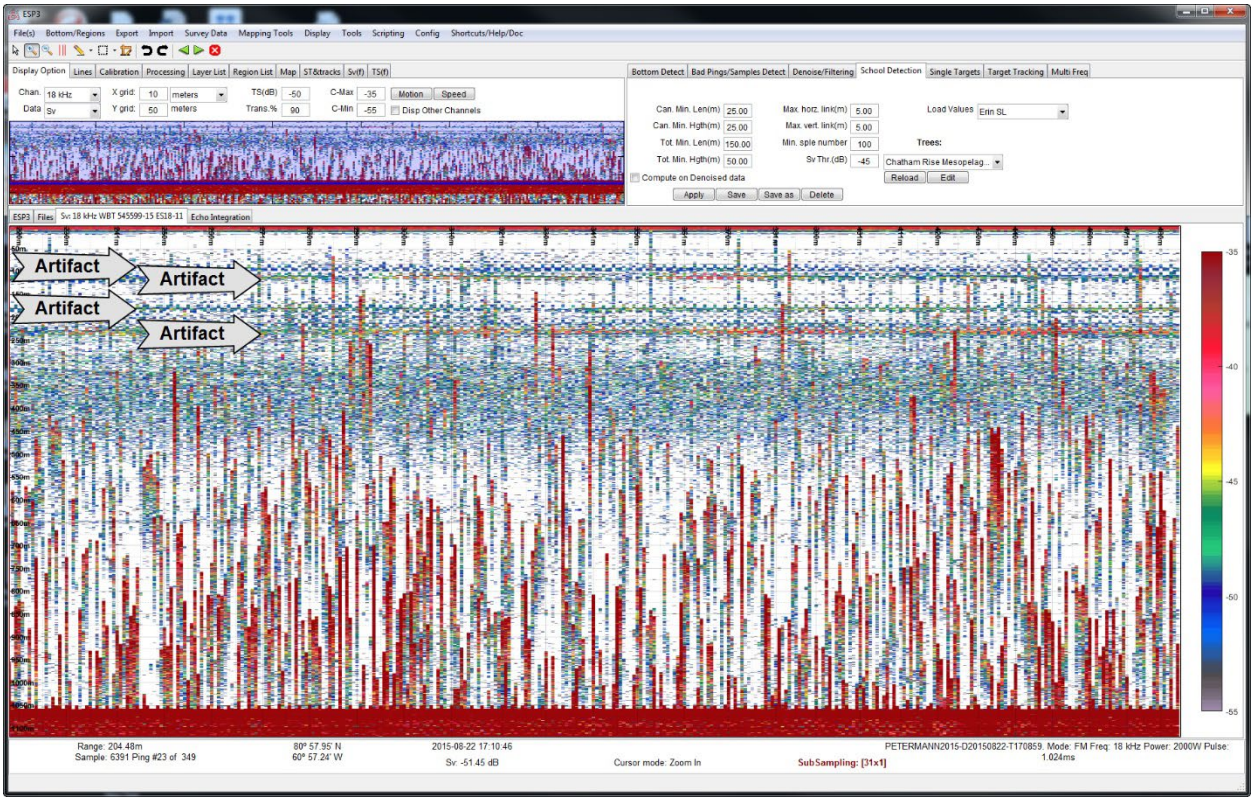

Figure 127: EM122 interference in the water column, shown in ESP3.

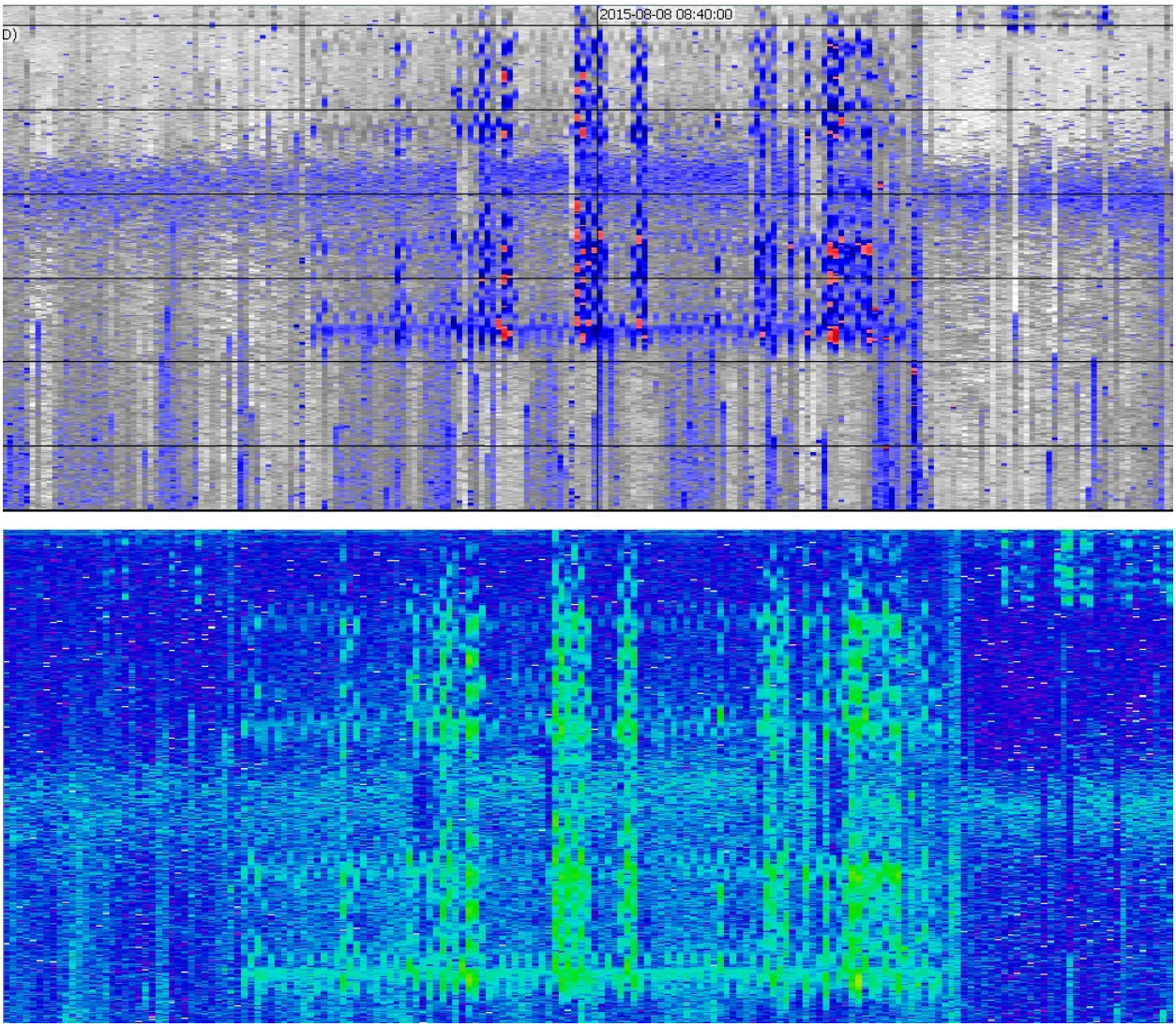

Figure 128: EM122 interference 'overprinted' on the scattering layer, as viewed in Echoview (top) and FMMidwater (bottom).

A.4.3 Other Instrumentation

The Peterman 2015 Expedition had several experiments under way. Other instruments entering the water would cause artifacts in the water column data, though this was typically easy to identify and did not greatly interfere with manual scattering layer selection. In the example below (Figure 129), the CTD can be seen entering the water.

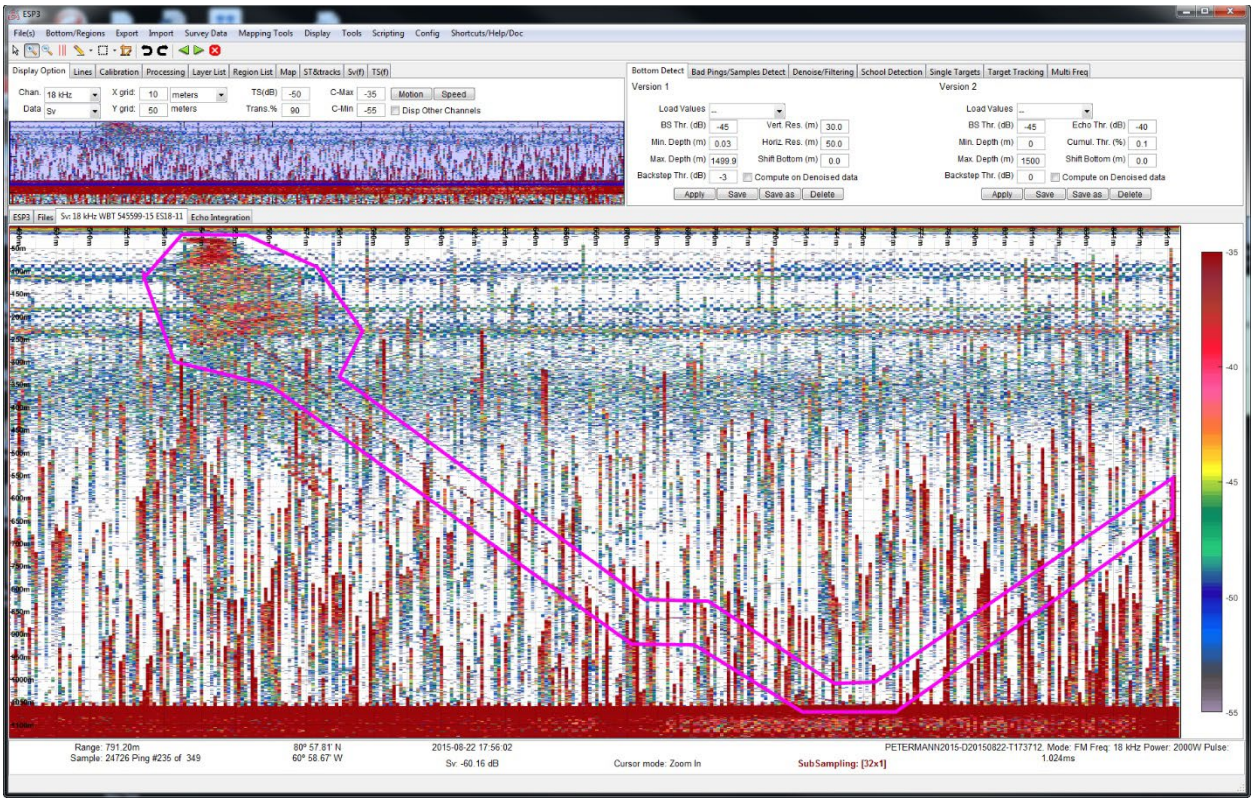

Figure 129: Noise in the water column caused by CTD deployment. Also note the EM122 interference in the top third of the water column.

A.5 Presence Classification

As noted in the main text, the decision as to whether or not a scattering layer was present was not always straight forward. Images are provided below to show various levels of scattering as well as examples of lines classified as “UNKNOWN” or “POSSIBLY”.

A.5.1 Scattering Layer Present (Classification: TRUE)

For a line to be classified as TRUE as to the presence of a scattering layer, there had to be the appearance that there was a coherent mass of targets scattering acoustic energy. Lines that only contained individual targets were not classified as TRUE. The

scattering layers varied in scattering intensity, possibly due to differences in density or composition (Figure 130 through Figure 132).

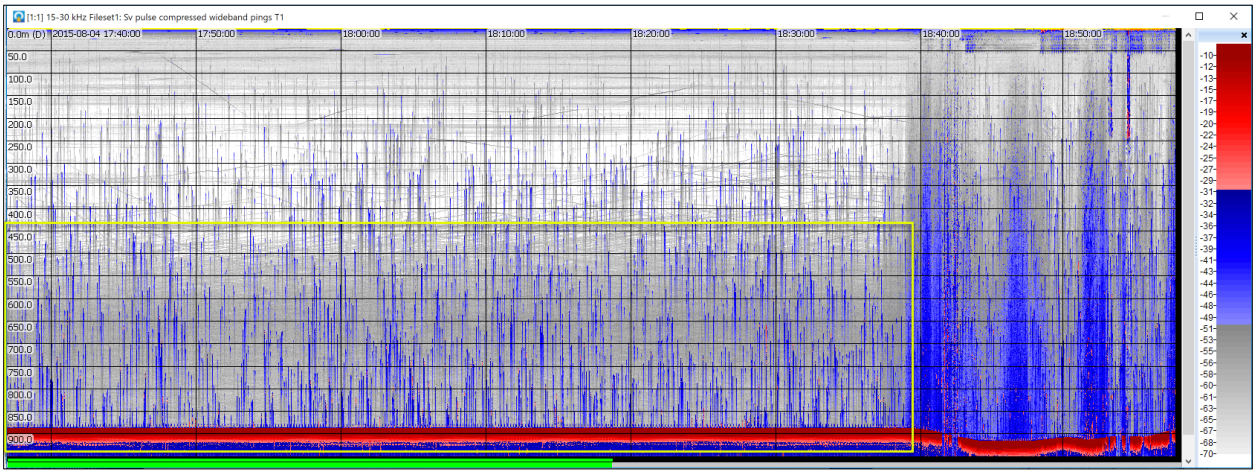

Figure 130: An example of a particularly weak but coherent area of scattering classified as a scattering layer. PETERMANN2015-D20150804-T173701 - PETERMANN2015-D20150804-T183045 shown in Echoview.

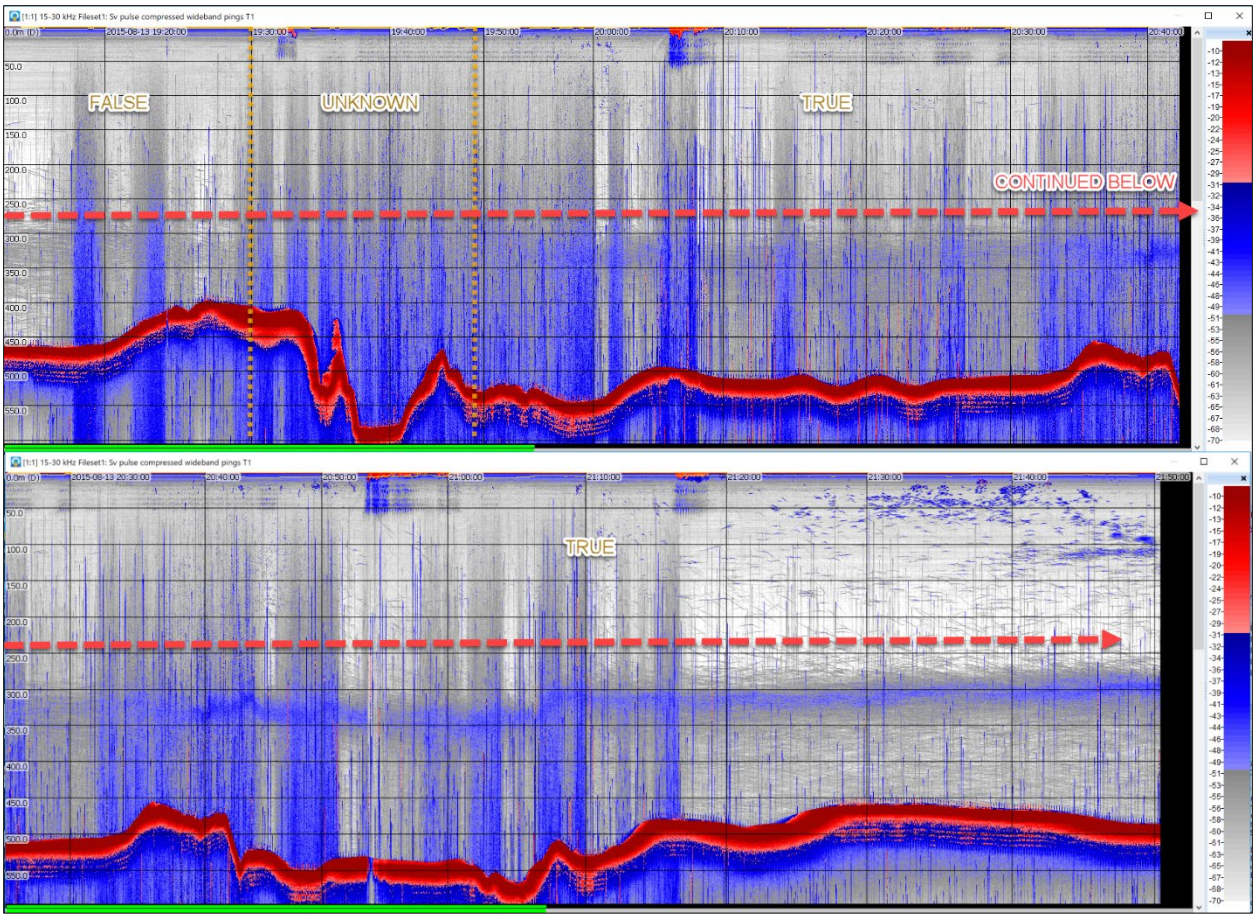

Figure 131: Example of individual scatterers (line classified as FALSE) concentrating into a coherent scattering layer. Lines PETERMANN2015-D20150813-T191317 - PETERMANN2015-D20150813-T202526, top, continuing to lines PETERMANN2015-D20150813-T202526 - PETERMANN2015-D20150813-T213419, bottom.

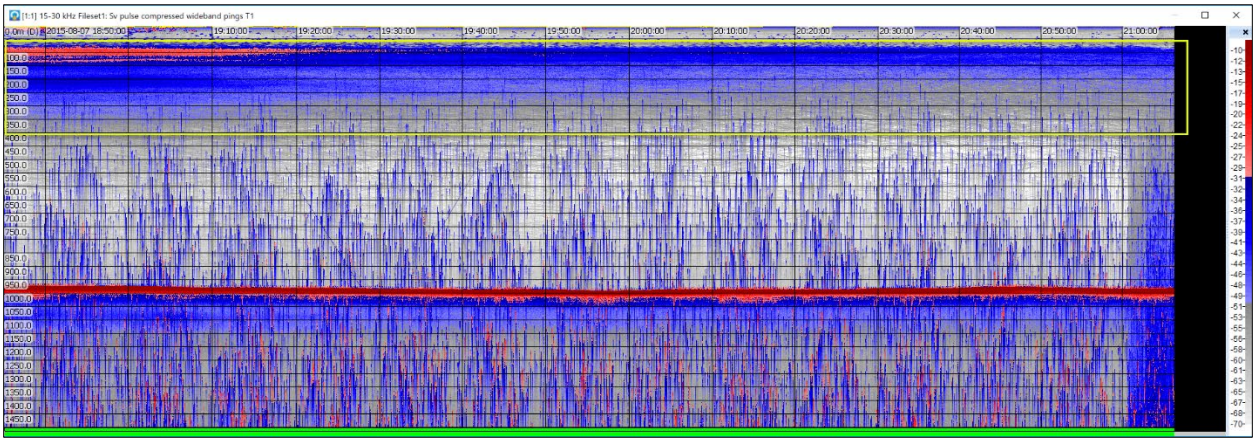

Figure 132: An example of a particularly strong scattering layer. PETERMANN2015-D20150807-T165156 - PETERMANN2015-D20150807-T184505 shown in Echoview.

A.5.2 Scattering Layer Not Present (Classification: FALSE)

If there was no coherent scattering visible, the line was classified as FALSE (Figure 133 - Figure 135). This may have been due to a lack of scattering layer or too low of a concentration of scatterers to reflect enough acoustic energy to appear as a coherent layer, but it could have also been due to persistent high levels of noise in the water column masking the existence of a layer.

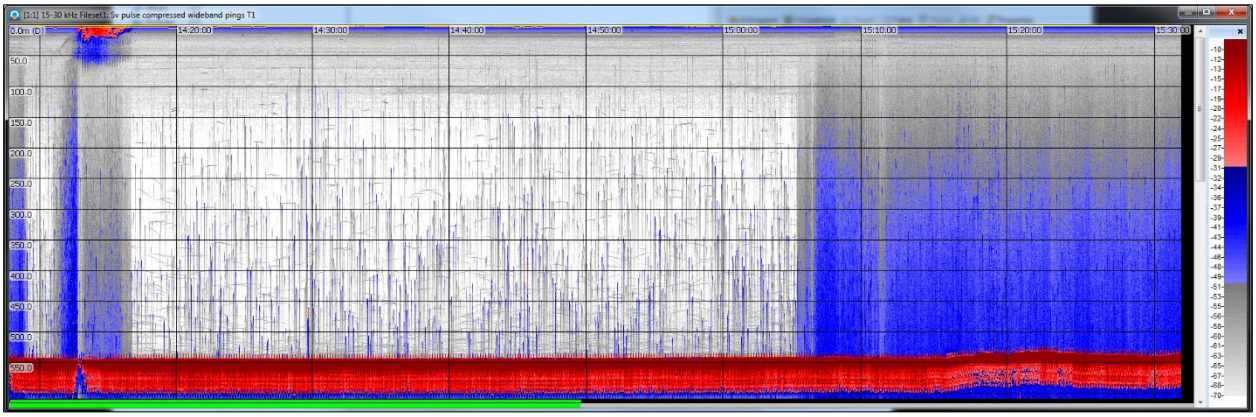

Figure 133: PETERMANN2015-D20150810-T140755 - PETERMANN2015-D20150810-T151554 shown in Echoview. These lines were classified as false; though there are many individual targets visible, there is no coherent scattering layer.

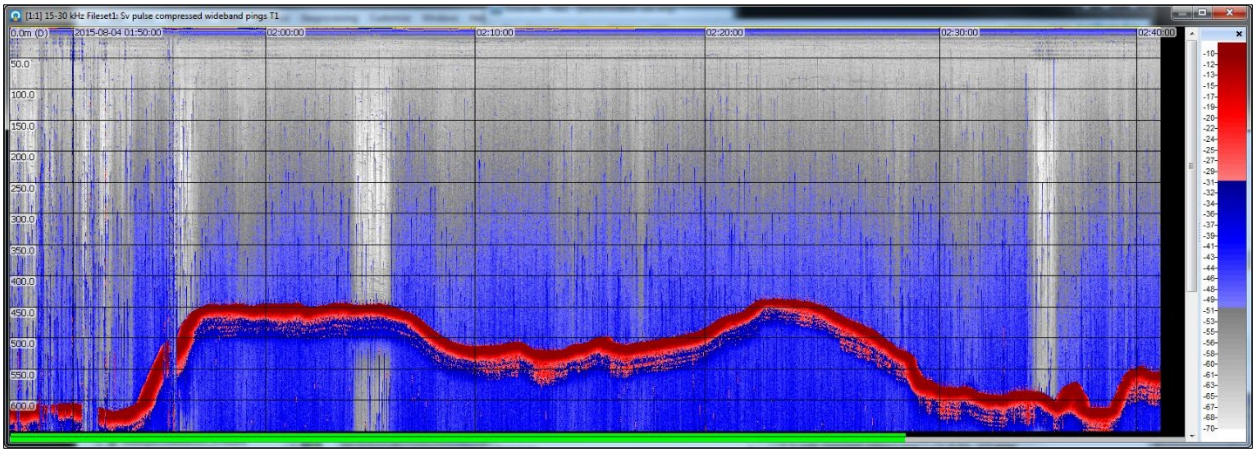

Figure 134: PETERMANN2015-D20150804-T01463 - PETERMANN2015-D20150804-T022256 shown in Echoview. These lines were classified as FALSE as there was no scattering layer present; though the files are noisy, the sections without noise seem to support the interpretation of no scattering layer.

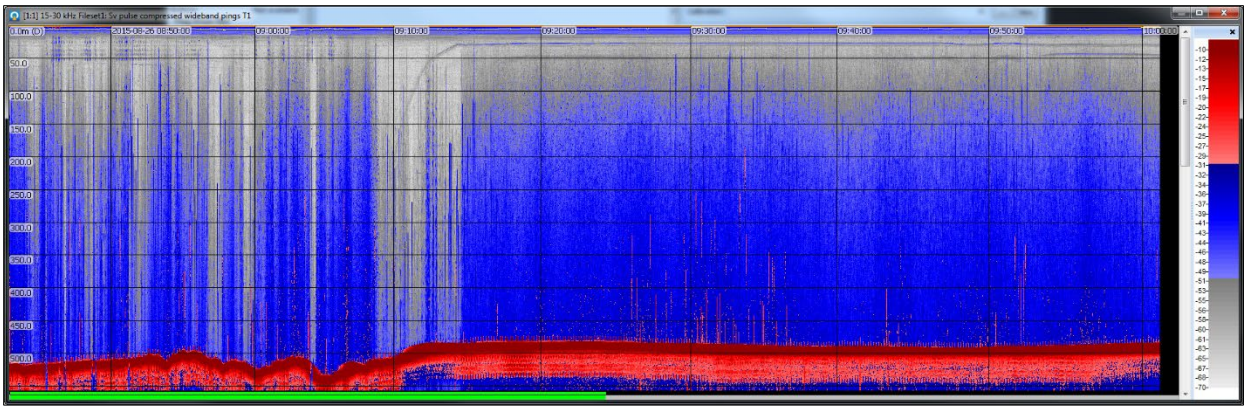

Figure 135: PETERMANN2015-D20150826-T084235- PETERMANN2015-D20150826-T094614 shown in Echoview. Extremely noisy files such as this could potentially mask scattering layers at depth.

A.5.3 Scattering Layer UNKNOWN or POSSIBLY present

In some instances, increases in noise masked scattering layers visible in previous or following lines. In these cases, masked lines with visible scattering layers just prior or following were classified as UNKNOWN (Figure 136). In regions where there appeared to be large concentrations of scatterers, but it was not possible to pick distinct layer, lines were classified as POSSIBLY (Figure 137). This was fairly common near the glacier ice face.

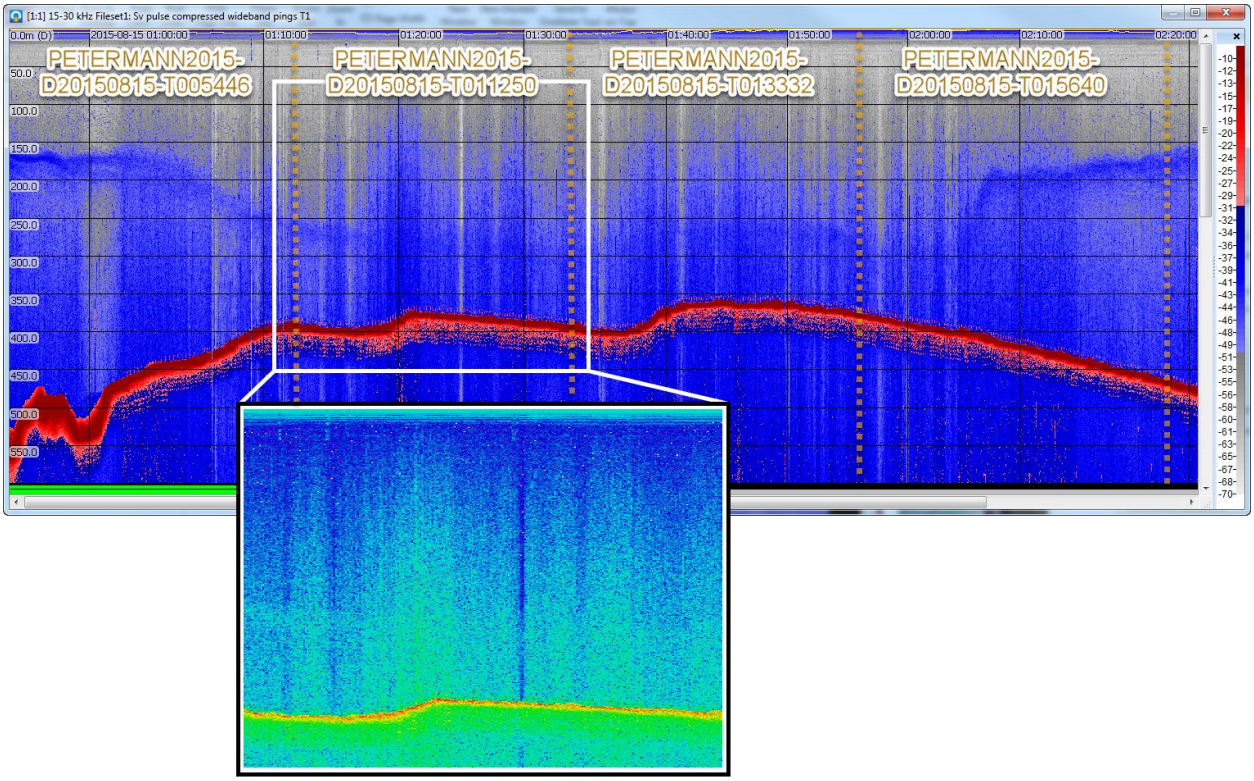

Figure 136: The top image shows lines PETERMANN2015-D20150815-T005446 through PETERMANN2015-D20150815-T021812 in Echoview; the inset shows part of that section, line PETERMANN2015-D20150815-T011250, in FMMidwater. The orange dotted lines show the approximate location of line changes, with the line names listed. Though there is some faint indication that the scattering layer visible at the start and end of the top images continues at depth, the overprint of noise makes it impossible to manually select the top of the layer. Lines PETERMANN2015-D20150815-T0005446 and PETERMANN2015-D20150815-T015640 were classified as TRUE, while PETERMANN2015-D20150815-T011250 and PETERMANN2015-D20150815-T013332 were classified as UNKNOWN.

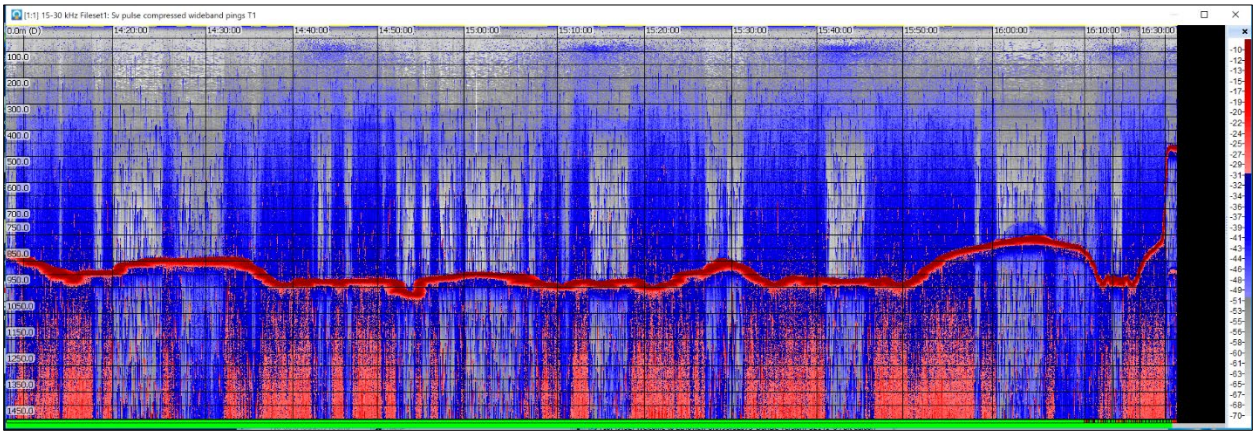

Figure 137: PETERMANN2015-D20150805-T14081 - PETERMANN2015-D20150805-T155440 in Echoview. This is an example of an area with large amounts of scatter where it was not possible to pick a line designating the top of a scattering layer.

APPENDIX B RADIATION DATA PROCESSING AND ANALYSIS

During the period 18 August to 25 August, there was a large overall reduction in the insolation values. There was also considerable spiking throughout the entire dataset. Comparisons to regional Baseline Surface Radiation Network (BSRN) data and review of the examples provided by the World Radiation Monitoring Center – Baseline Surface Radiation Network (WRMC-BSRN) seem to indicate that spikes and overall drops such as this are not unusual and correspond to mixed weather and cloudy days (Figure 138).

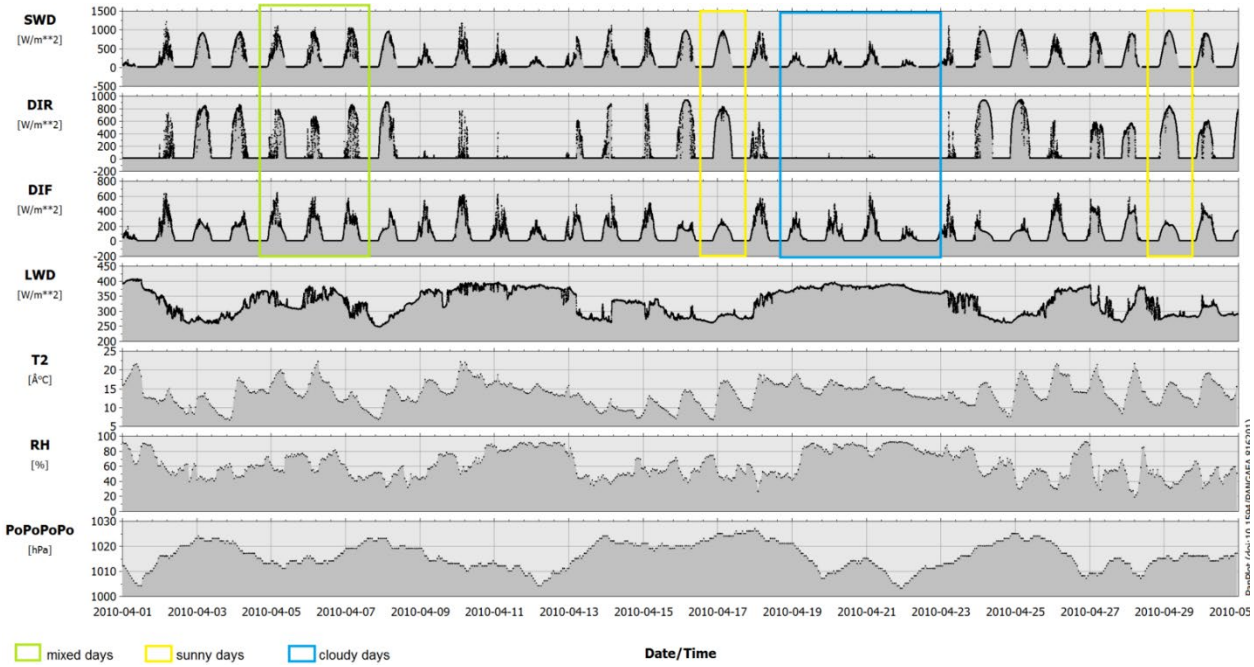

Figure 138: Data example from the WRMC-BSRN website showing changes in radiation levels on sunny, mixed, and cloudy days (https://bsrn.awi.de/data/data-example/).

Snapshots of TerraMODIS imagery were downloaded from NASA Worldview (https://worldview.earthdata.nasa.gov/) for the study area for each day of the expedition

(Figure 139). Evaluation of the images show an increase in cloud cover from August 18 – August 27 that may have been responsible for the observed decrease in measured Photosynthetically Active Radiation (PAR) values. This is further substantiated by the lack of diffuse attenuation coefficient data for the both the NASA OBPG TerraMODIS (NASA Goddard Space Flight Center, Ocean Ecology Laboratory) and ESA OC-CCI datasets ("Ocean Colour Climate change Initiative dataset, Version 3.1") (Appendix C, Figure 140 - Figure 145). The TerraMODIS $K_d(490)$ daily products (Figure 143 - Figure 145) are generated from the same satellite pass as the imagery, so a lack of data on days when the imagery shows increased cloud cover is not surprising. The ESA OC-CCI products (Figure 140 - Figure 142), however, are a composite from multiple satellites, indicating increased cloud cover during those satellite passes as well.

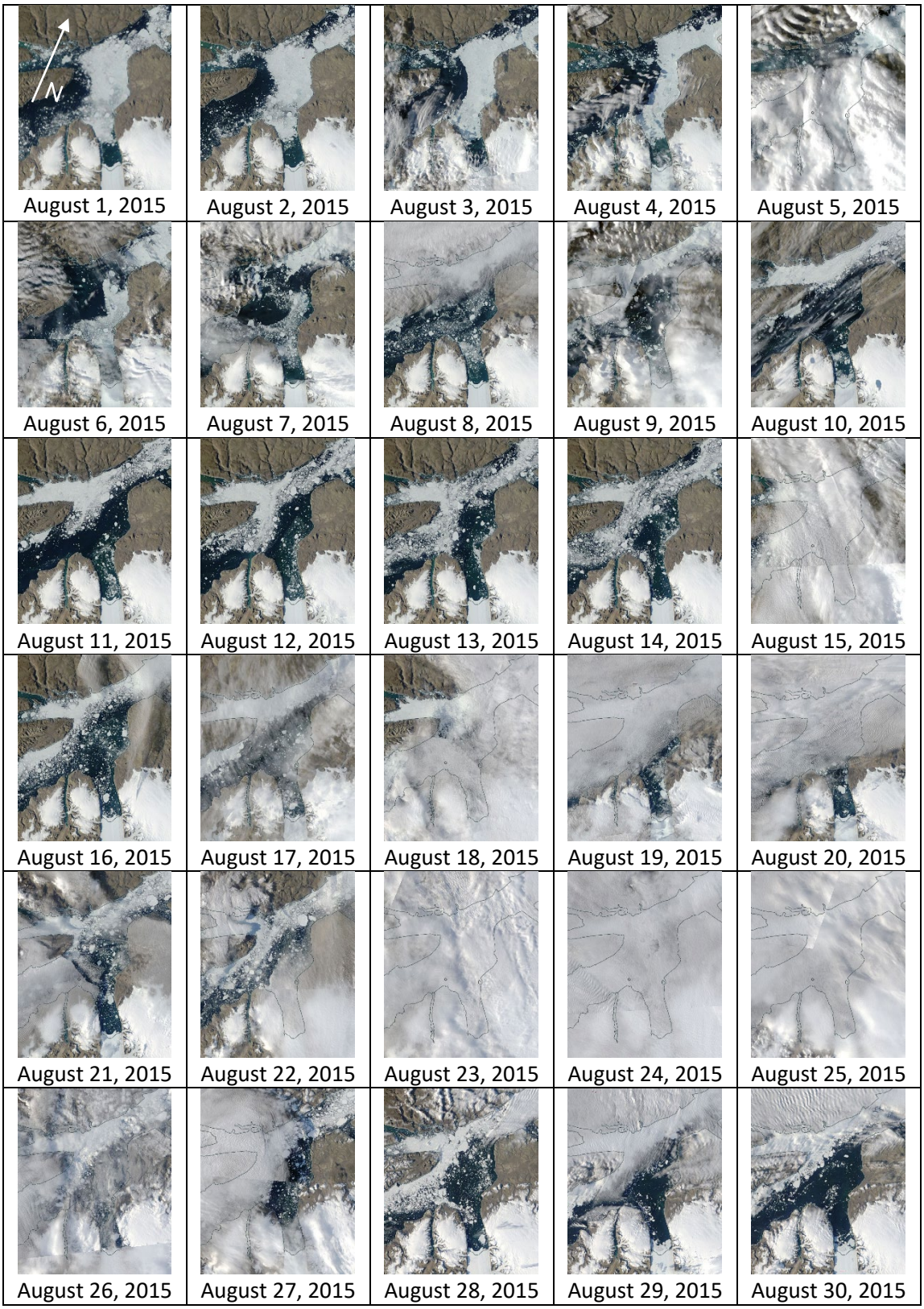

Figure 139: TerraMODIS images of the study site, August 1 - 30 2015. Images downloaded from NASA Worldview (https://worldview.earthdata.nasa.gov/).

APPENDIX C K_D(490) PROCESSING AND ANALYSIS

Diffuse attenuation coefficient at 490 nm (K_d(490)) from the ESA OC-CCI ("Ocean Colour Climate change Initiative dataset, Version 3.1") and MODIS Terra (NASA Goddard Space Flight Center, Ocean Ecology Laboratory) datasets were used to estimate turbidity in the water column across the study area. Daily and monthly mean values were downloaded. Daily values from August 2 - August 28, 2015, are presented here for reference (Figure 140 - Figure 147) but were not used for analysis due to the sporadic data. The colormaps were clipped to the range of data present in the OC-CCI datasets (0.09 – 0.56 m^{-1}, see Figure 146 for the full distributions of both datasets) to facilitate comparison, however four days of MODIS Terra data had a few pixels outside of that range (Figure 147).

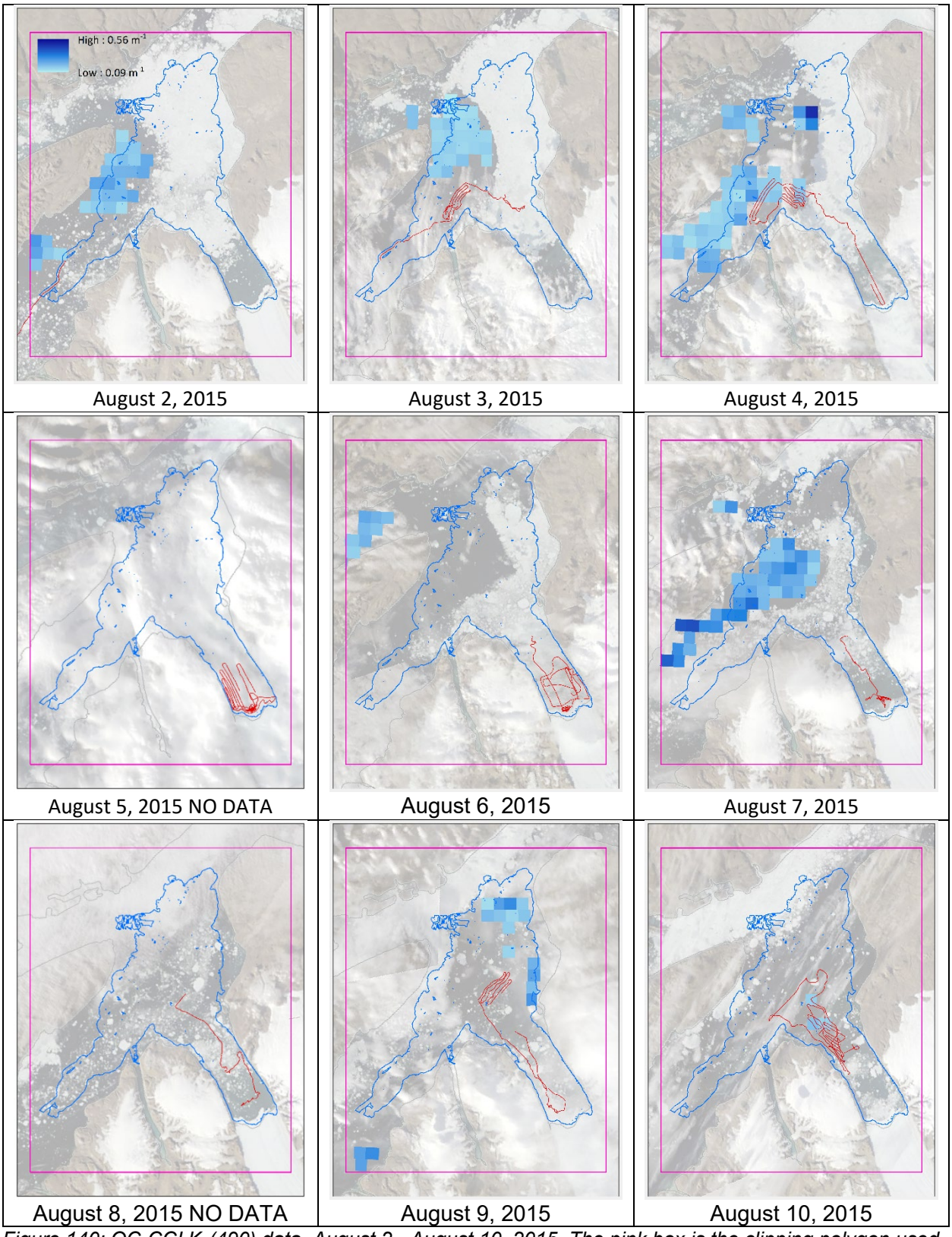

Figure 140: OC-CCI $K_d(490)$ data, August 2 - August 10, 2015. The pink box is the clipping polygon used to limit the dataset. The blue outline is the extent of the sonar data. The red line is the vessel track line for that day. The color bar in the top left image applies to all images. Projection is WGS84 UTM 20N.

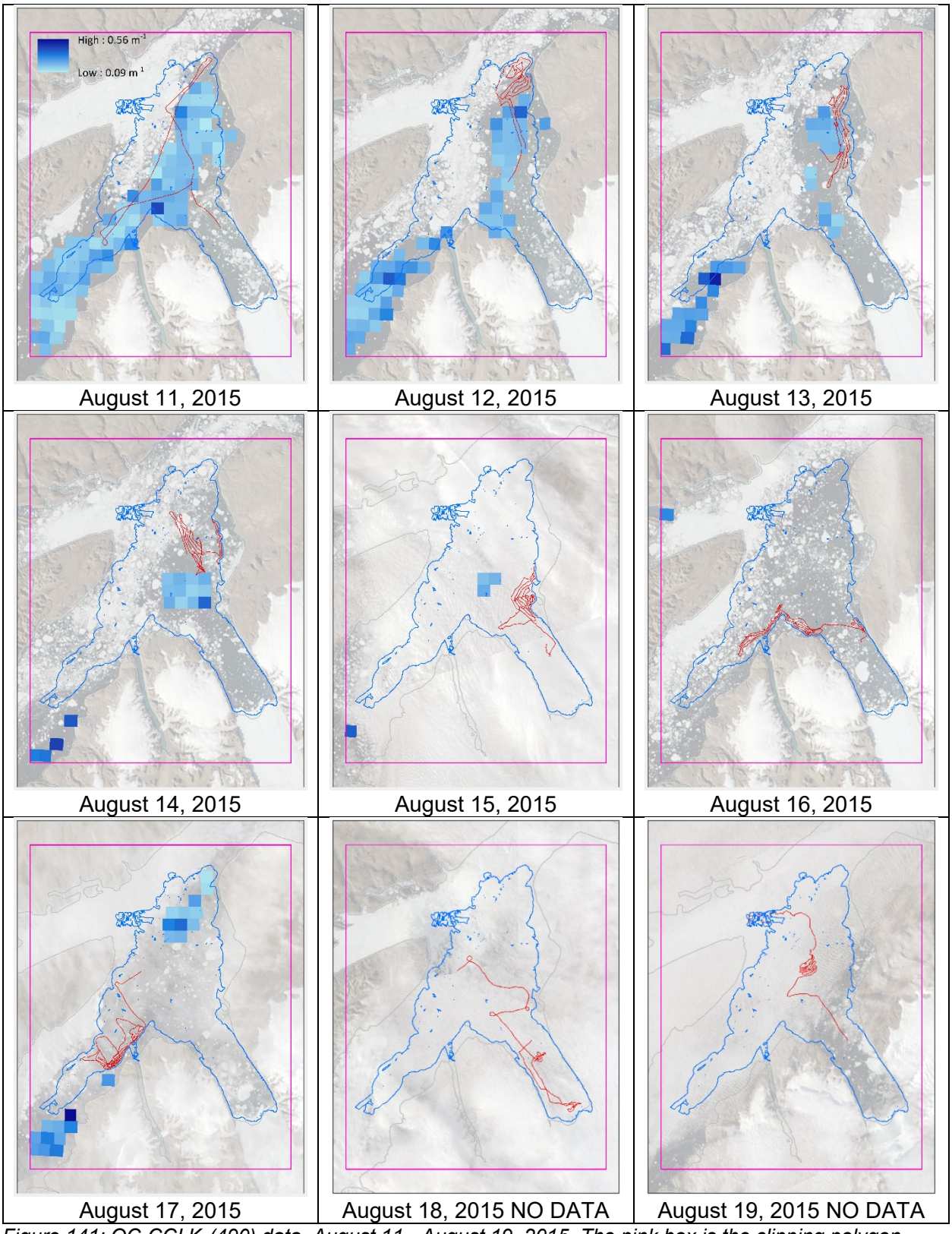

Figure 141: OC-CCI $K_d(490)$ data, August 11 - August 19, 2015. The pink box is the clipping polygon used to limit the dataset. The blue outline is the extent of the sonar data. The red line is the vessel track line for that day. The color bar in the top left image applies to all images. Projections is WGS84 UTM 20N.

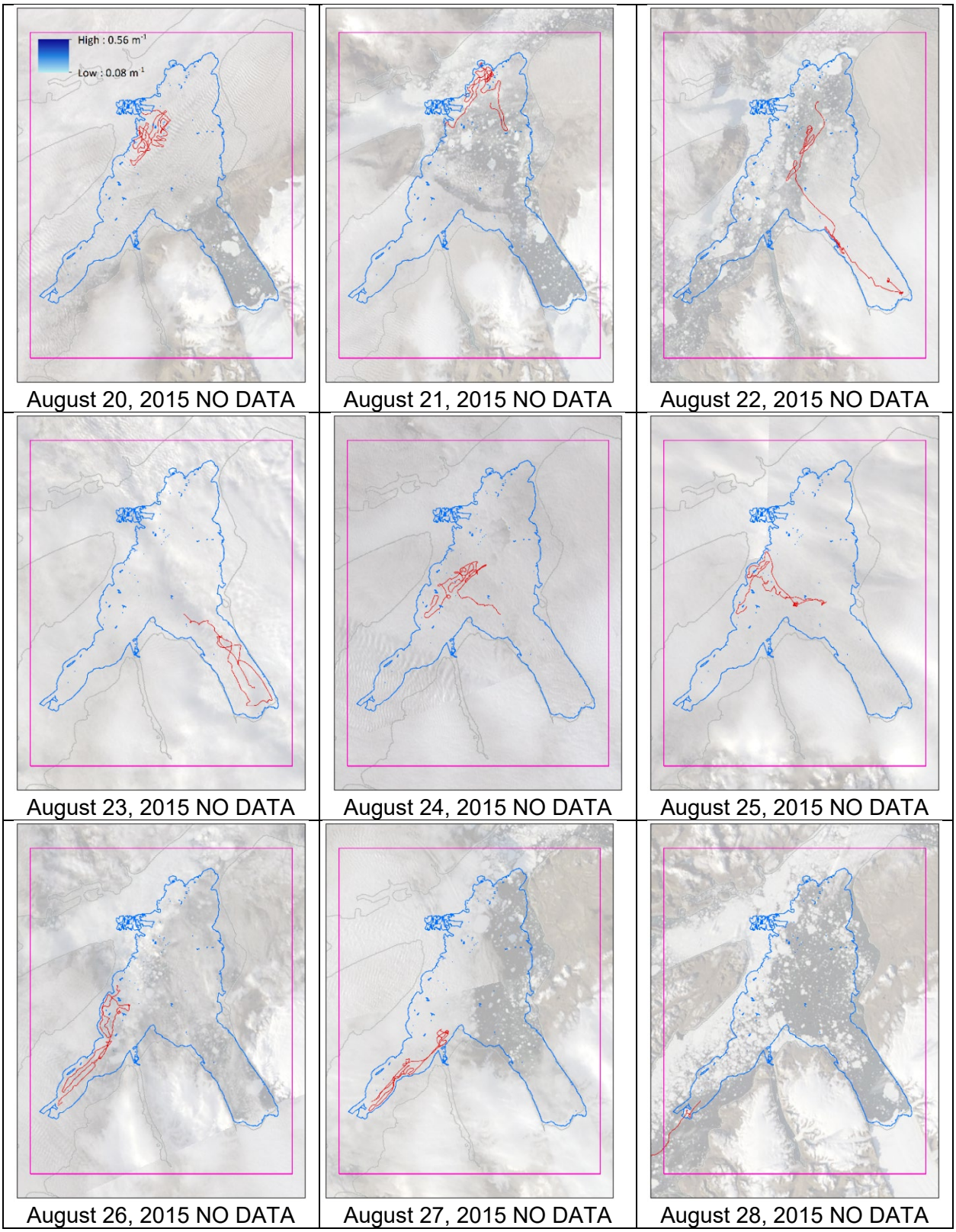

Figure 142: OC-CCI $K_d(490)$ data, August 20 - August 28, 2015. The pink box is the clipping polygon used to limit the dataset. The blue outline is the extent of the sonar data. The red line is the vessel track line for that day. The color bar in the top left image applies to all images. Projections is WGS84 UTM 20N.

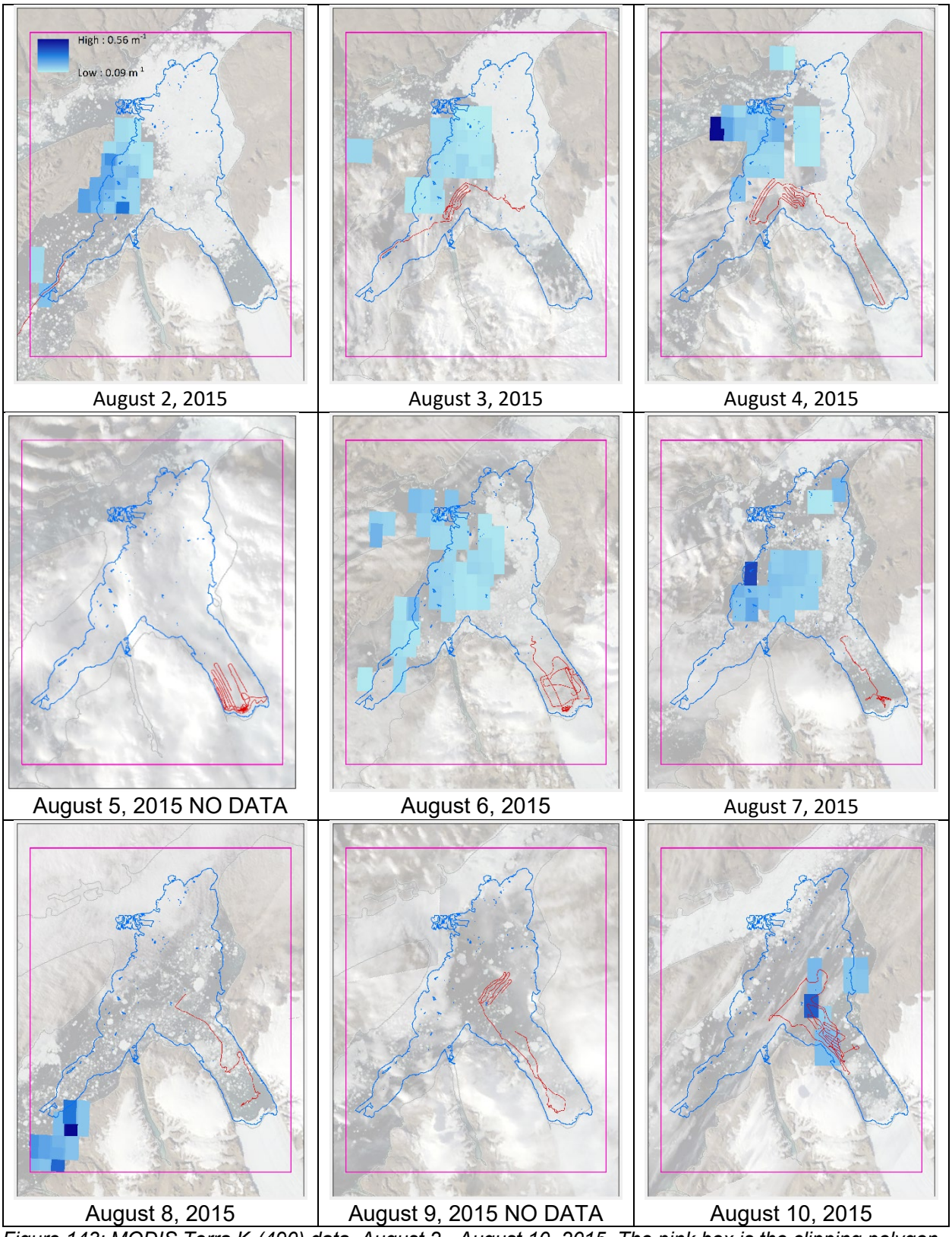

Figure 143: MODIS Terra $K_d(490)$ data, August 2 - August 10, 2015. The pink box is the clipping polygon used to limit the dataset. The blue outline is the extent of the sonar data. The red line is the vessel track line for that day. The color bar in the top left image applies to all images. Projection is WGS84 UTM 20N.

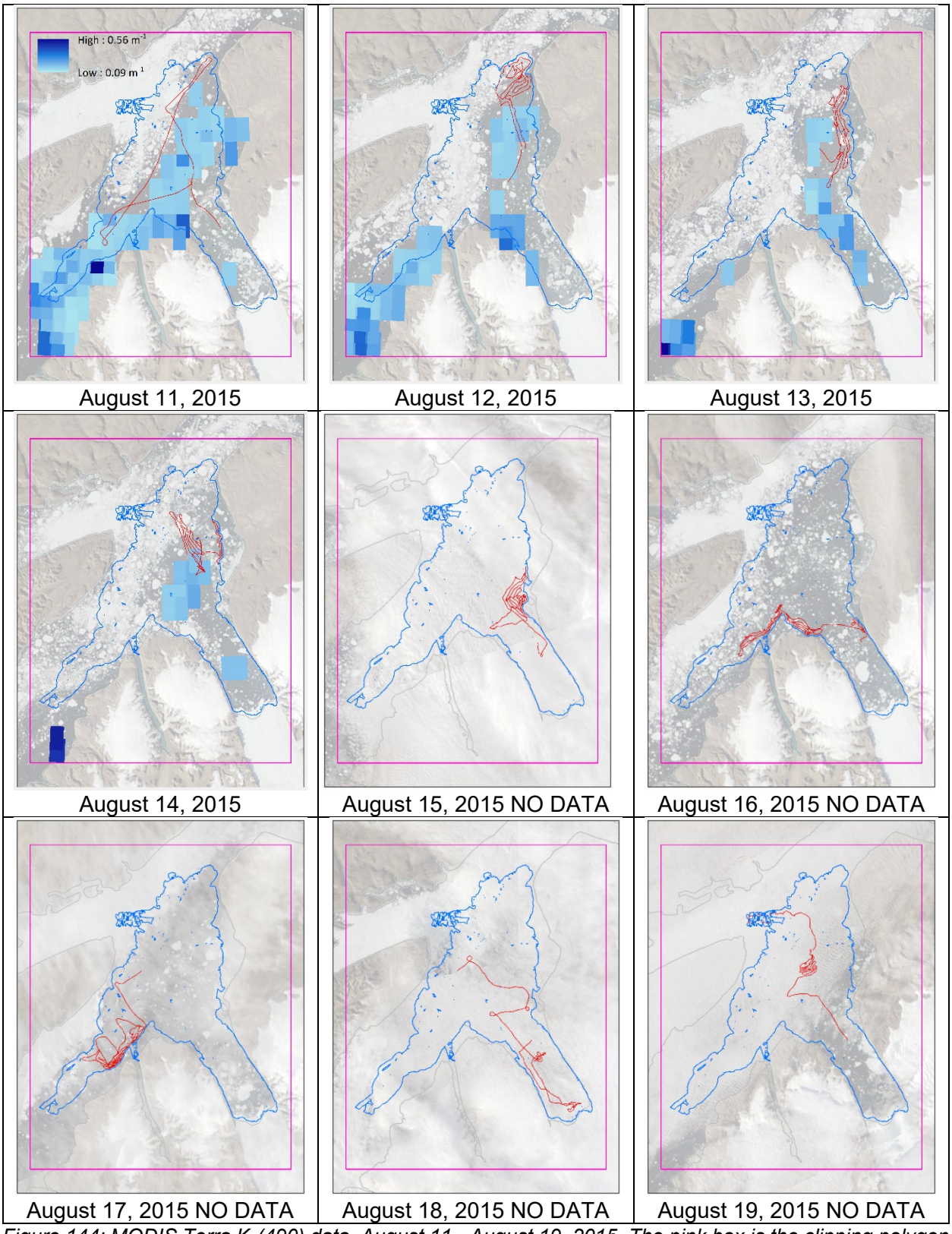

Figure 144: MODIS Terra $K_d(490)$ data, August 11 - August 19, 2015. The pink box is the clipping polygon used to limit the dataset. The blue outline is the extent of the sonar data. The red line is the vessel track line for that day. The color bar in the top left image applies to all images. Projection is WGS84 UTM 20N.

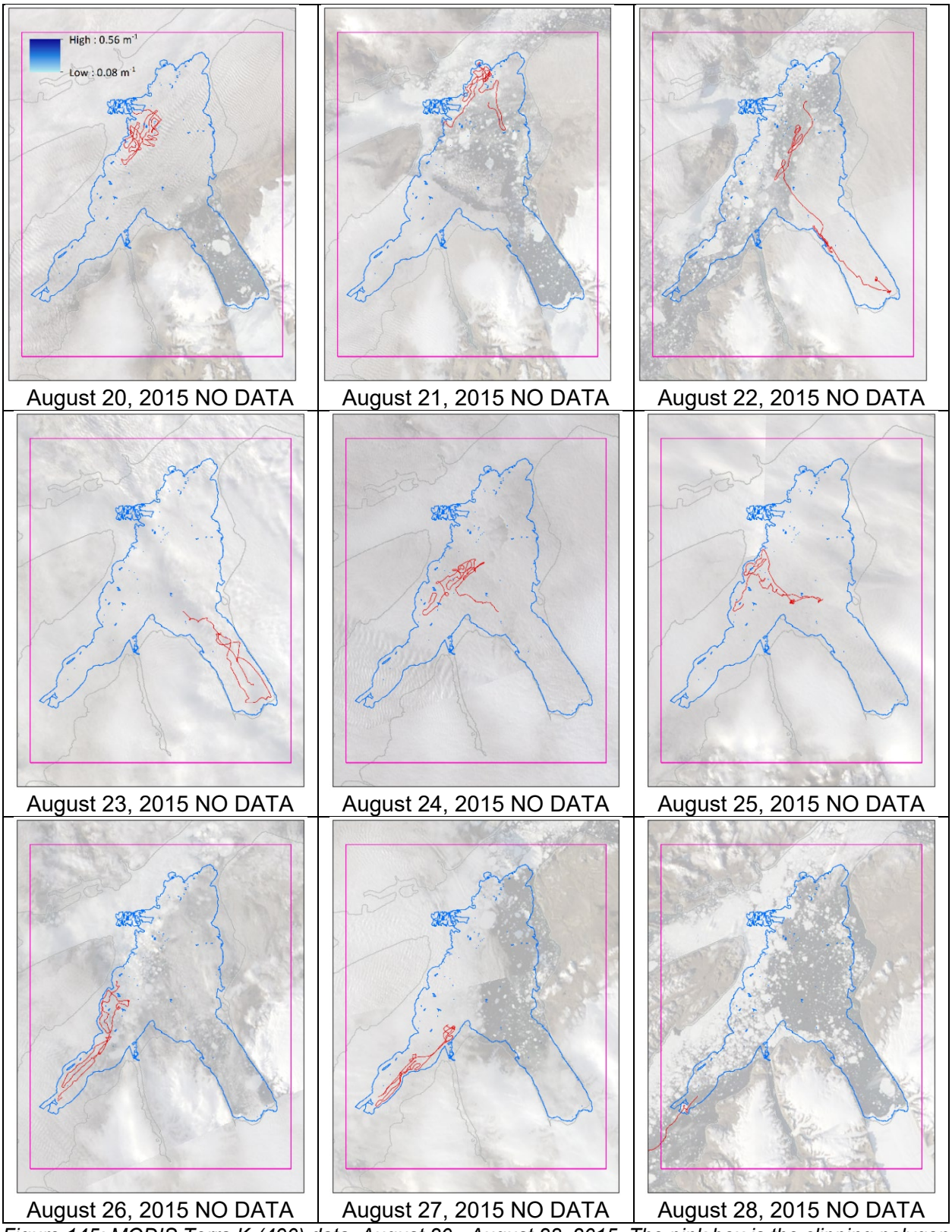

Figure 145: MODIS Terra $K_d(490)$ data, August 20 - August 28, 2015. The pink box is the clipping polygon used to limit the dataset. The blue outline is the extent of the sonar data. The red line is the vessel track line for that day. The color bar in the top left image applies to all images. Projection is WGS84 UTM 20N.

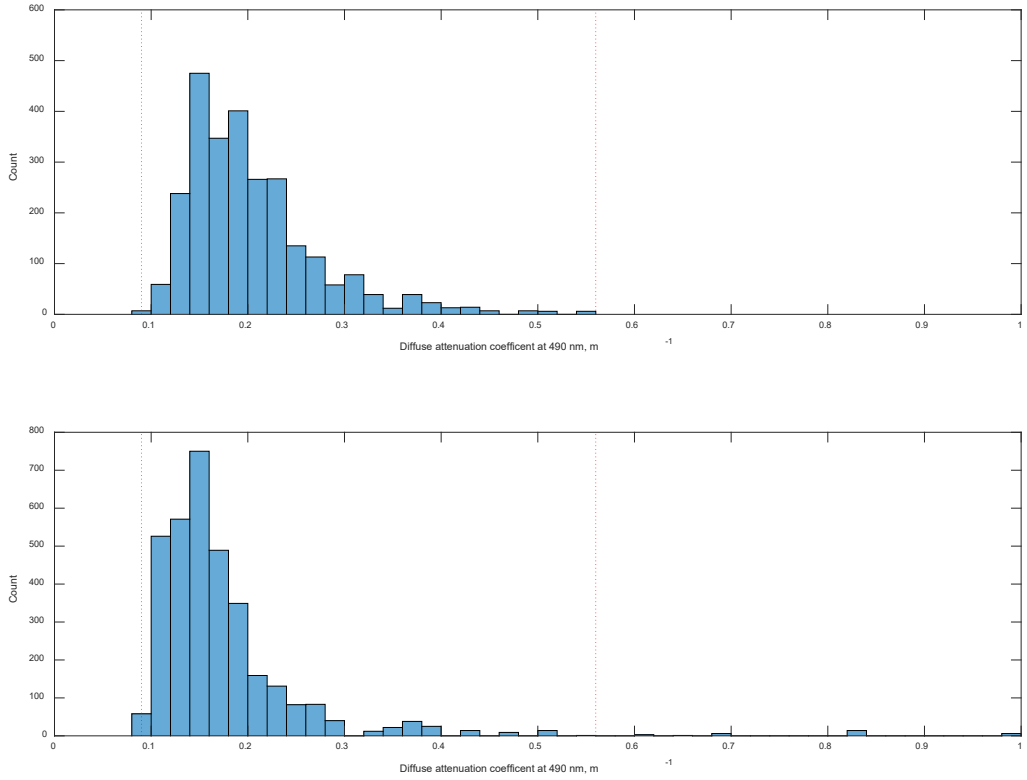

Figure 146: Distribution of daily $K_d(490)$ values, August 2-August 28, 2015. Top, the OC-CCI dataset. Bottom, the MODIS Terra dataset. The red vertical lines indicate the minimum (0.9) and maximum (0.56) values used to clip the colormaps for Figure 140 - Figure 145.

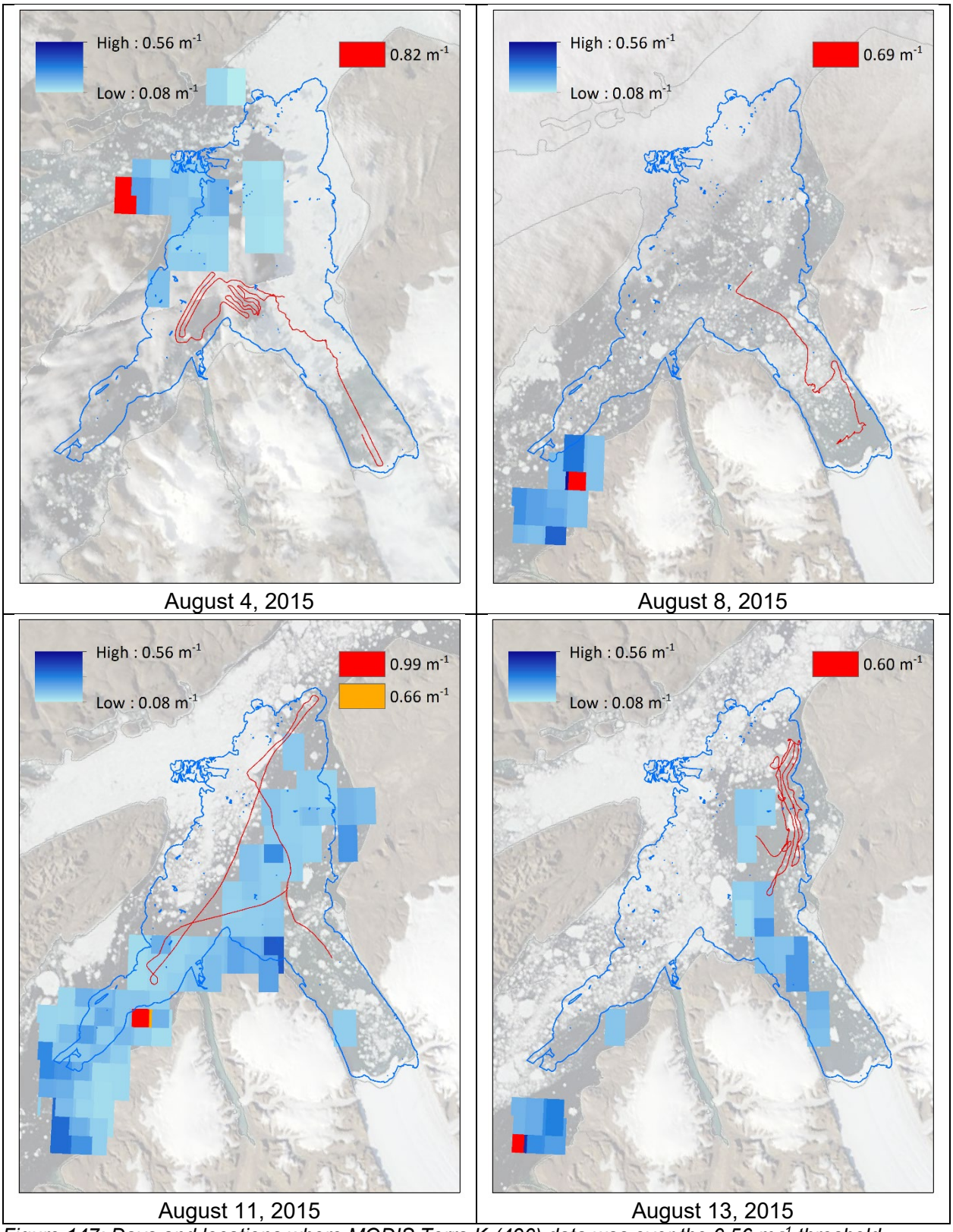

Figure 147: Days and locations where MODIS Terra $K_d(490)$ data was over the 0.56 m^{-1} threshold. Projection is WGS84 UTM 20N.

APPENDIX D CTD PROCESSING AND ANALYSIS

Temperature-Salinity (T-S) diagrams, Oxygen-Temperature (O-T) diagrams, and Oxygen- Salinity (O-S) diagrams as well as temperature vs. depth, salinity vs. depth, oxygen concentration vs. depth plots are provided here (Figure 148 - Figure 279) for each CTD station where reasonable data could be extracted; if a scattering layer was present, the location is included on the plots. Profile 001 and 025 were omitted due to erroneous values and pump failures. It should be noted that the oxygen values prior to cast 026, though presented here, were considered questionable by Heuzé et al. (2017) due to issues with the pump, which was replaced after cast 025 and prior to cast 026.

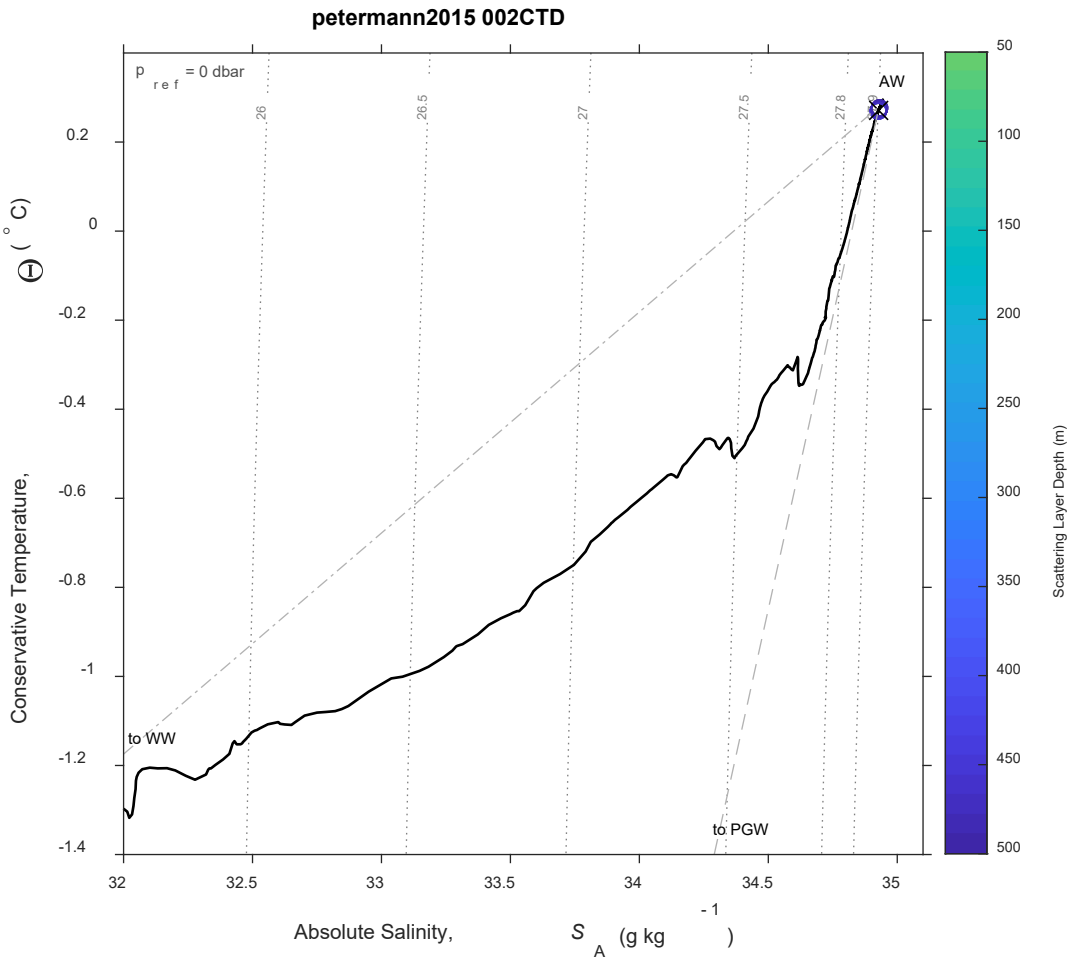

Figure 148: CTD 002, Temperature-Salinity (T-S) diagram. The scattering layer picks corresponding to this CTD are plotted as open circles colored by depth; a black 'X' indicates the average depth for the top of the scattering layer in this location. Note that this is the only location where the plotted scattering layers occurred prior to and 220 m distant from the CTD station. Isobars are shown as labeled grey dotted lines.

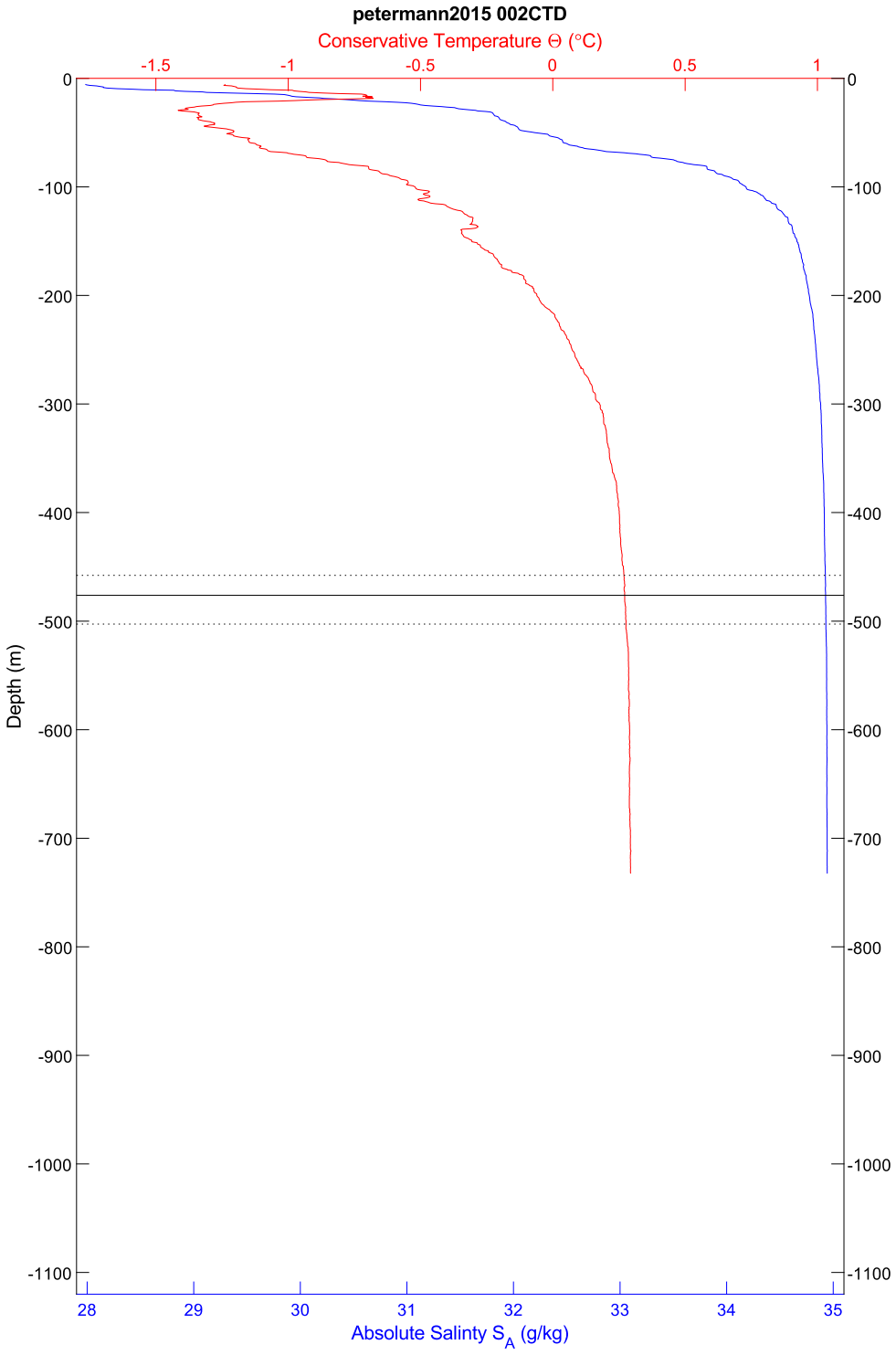

Figure 149: CTD 002, temperature and salinity plotted by depth. The scattering layer depth is indicated by horizontal lines; the solid line is the average depth, the dotted lines are the shallowest and deepest depths, in all cases for the top of the scattering layer.

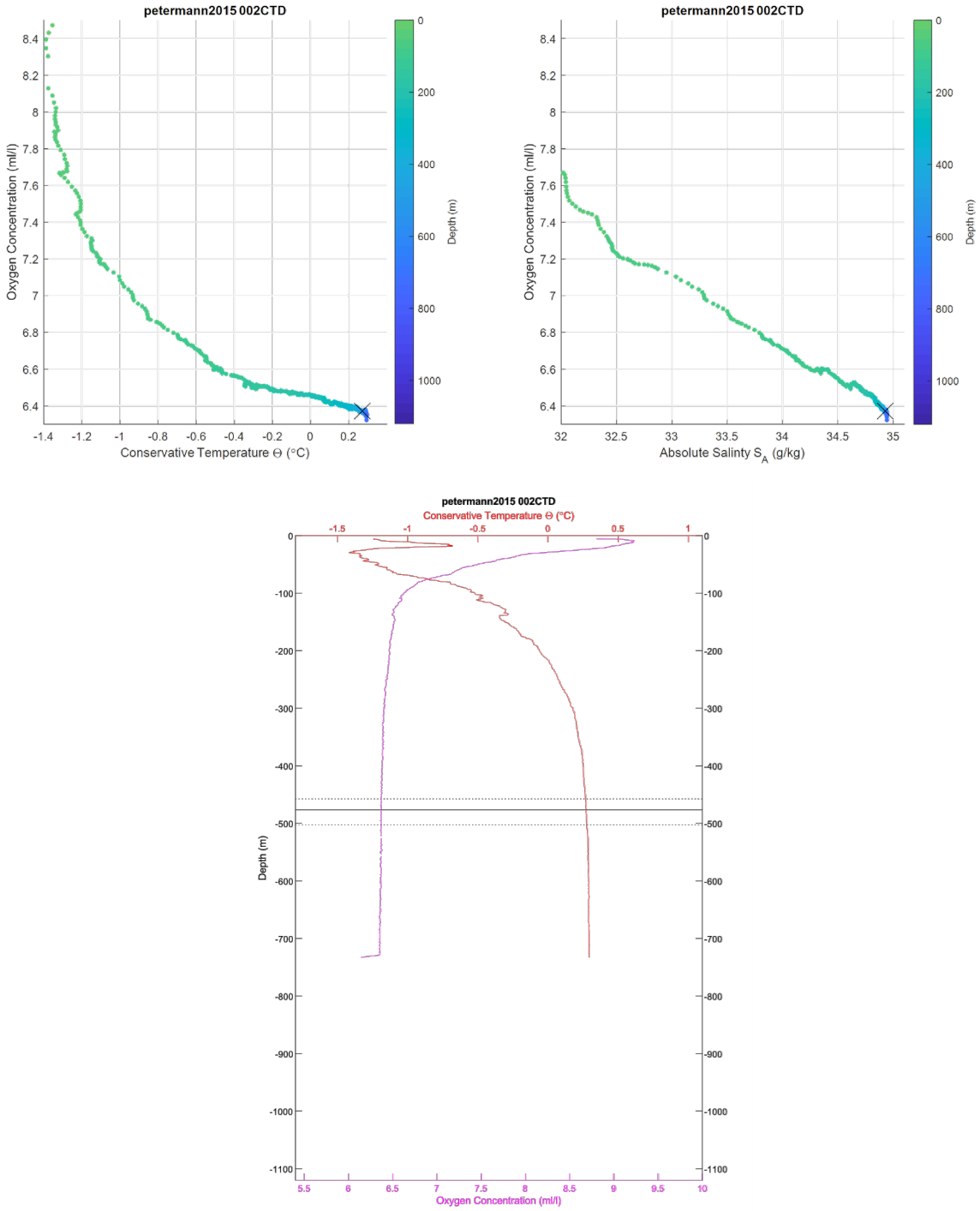

Figure 150: CTD 002. Top left, oxygen-temperature diagram, colored by depth. Top right, oxygen-salinity diagram, colored by depth. The black 'X' in the first two plots indicates the average depth for the top of the scattering layer in this location. Bottom center, temperature and oxygen plotted by depth. The scattering layer depth is indicated by horizontal lines; the solid line is the average depth, the dotted lines are the shallowest and deepest depths, in both cases for the top of the scattering layer. Note that oxygen values for this cast are considered questionable due to issues with the pump, which was replaced between cast 025 and 026.

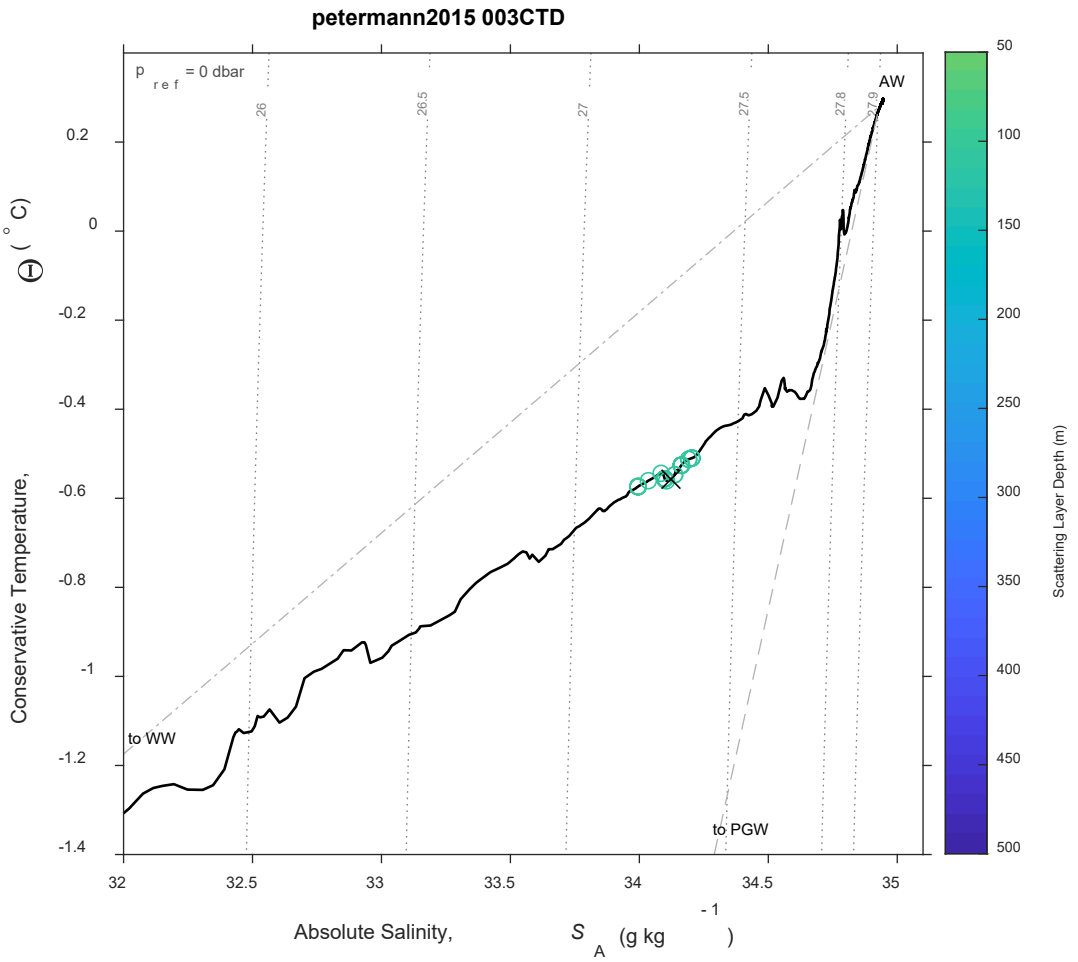

Figure 151: CTD 003, Temperature-Salinity (T-S) diagram. The scattering layer picks corresponding to this CTD are plotted as open circles colored by depth; a black 'X' indicates the average depth for the top of the scattering layer in this location. Isobars are shown as labeled grey dotted lines.

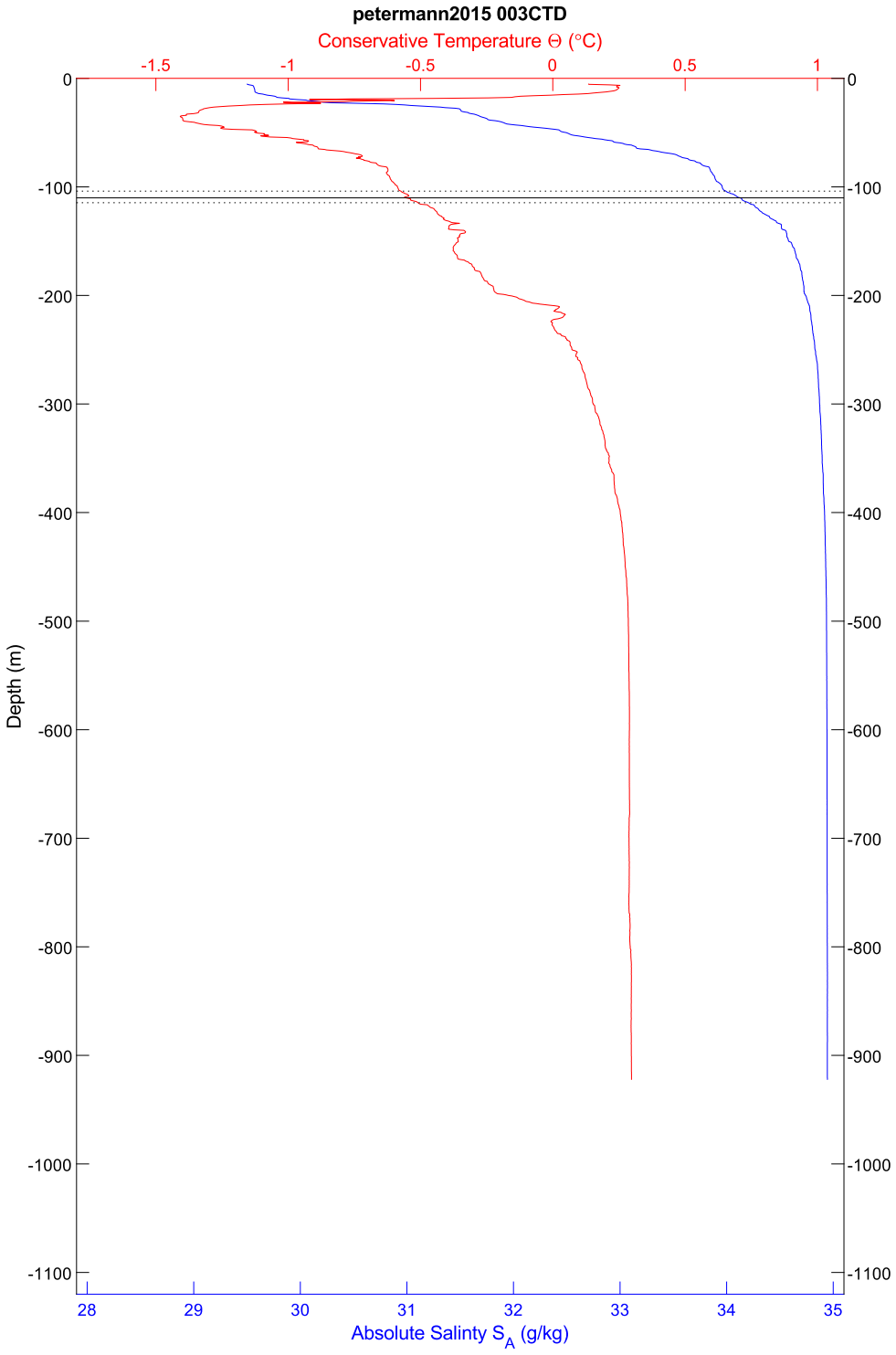

Figure 152: CTD 003, temperature and salinity plotted by depth. The scattering layer depth is indicated by horizontal lines; the solid line is the average depth, the dotted lines are the shallowest and deepest depths, in all cases for the top of the scattering layer.

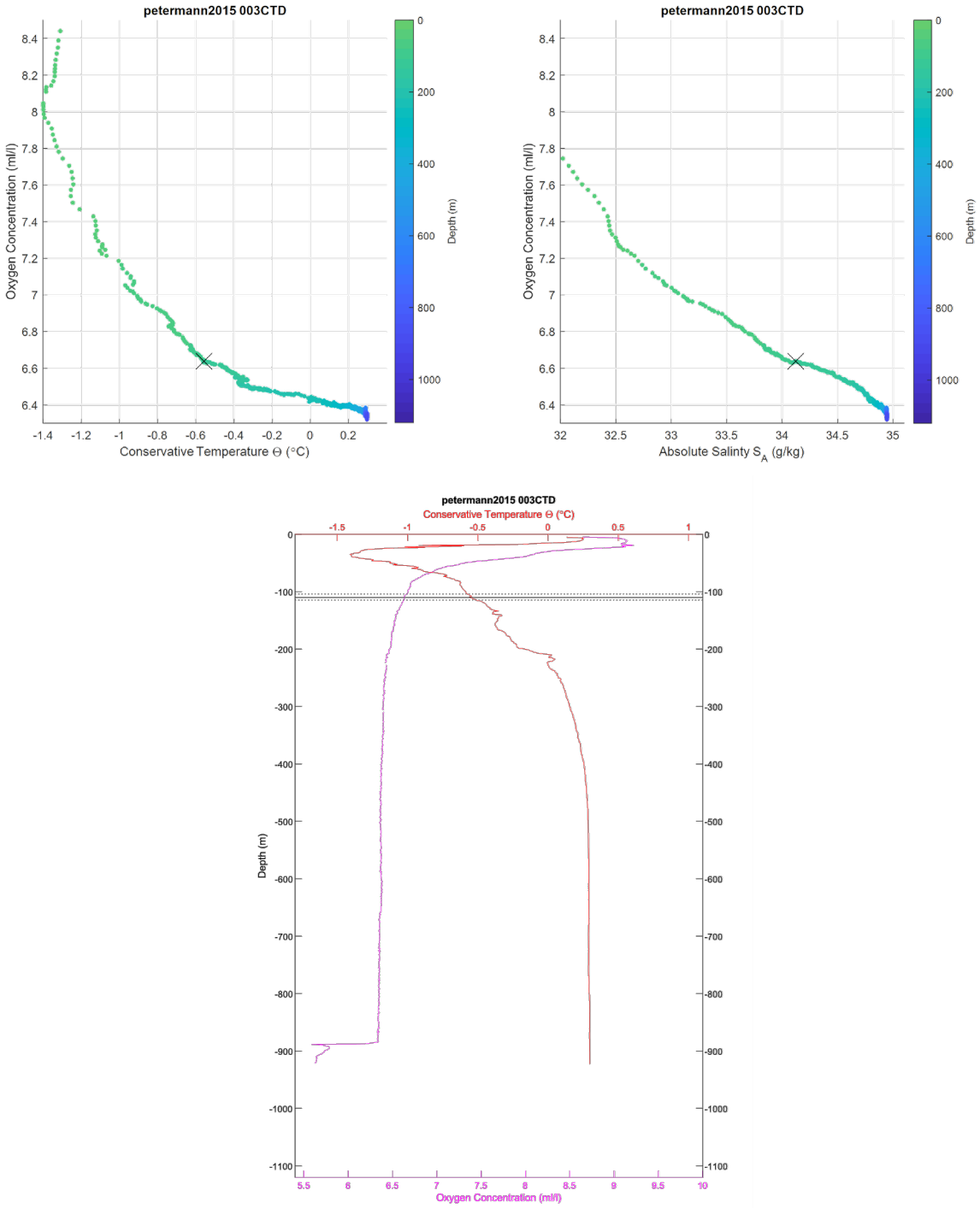

Figure 153: CTD 003. Top left, oxygen-temperature diagram, colored by depth. Top right, oxygen-salinity diagram, colored by depth. The black 'X' in the first two plots indicates the average depth for the top of the scattering layer in this location. Bottom center, temperature and oxygen plotted by depth. The scattering layer depth is indicated by horizontal lines; the solid line is the average depth, the dotted lines are the shallowest and deepest depths, in both cases for the top of the scattering layer. Note that oxygen values for this cast are considered questionable due to issues with the pump, which was replaced between cast 025 and 026.

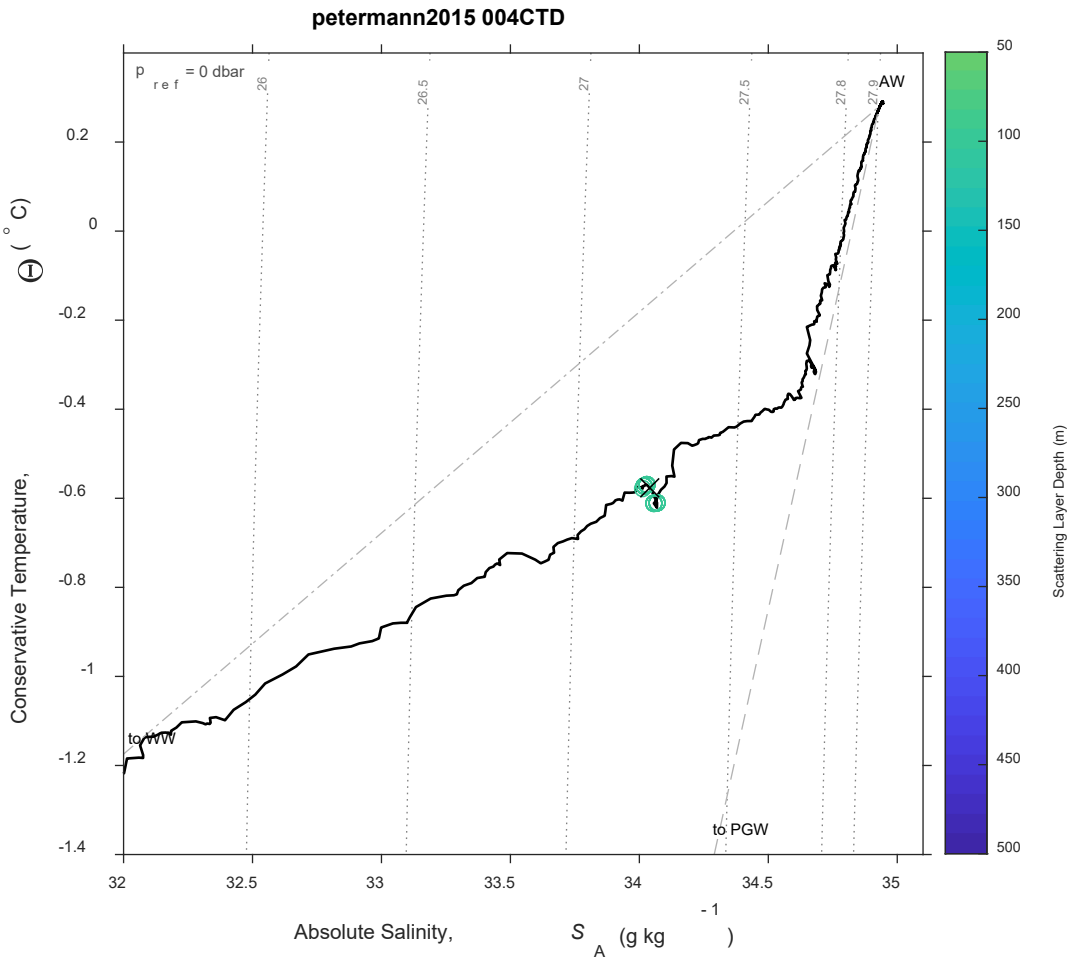

Figure 154: CTD 004, Temperature-Salinity (T-S) diagram. The scattering layer picks corresponding to this CTD are plotted as open circles colored by depth; a black 'X' indicates the average depth for the top of the scattering layer in this location. Isobars are shown as labeled grey dotted lines.

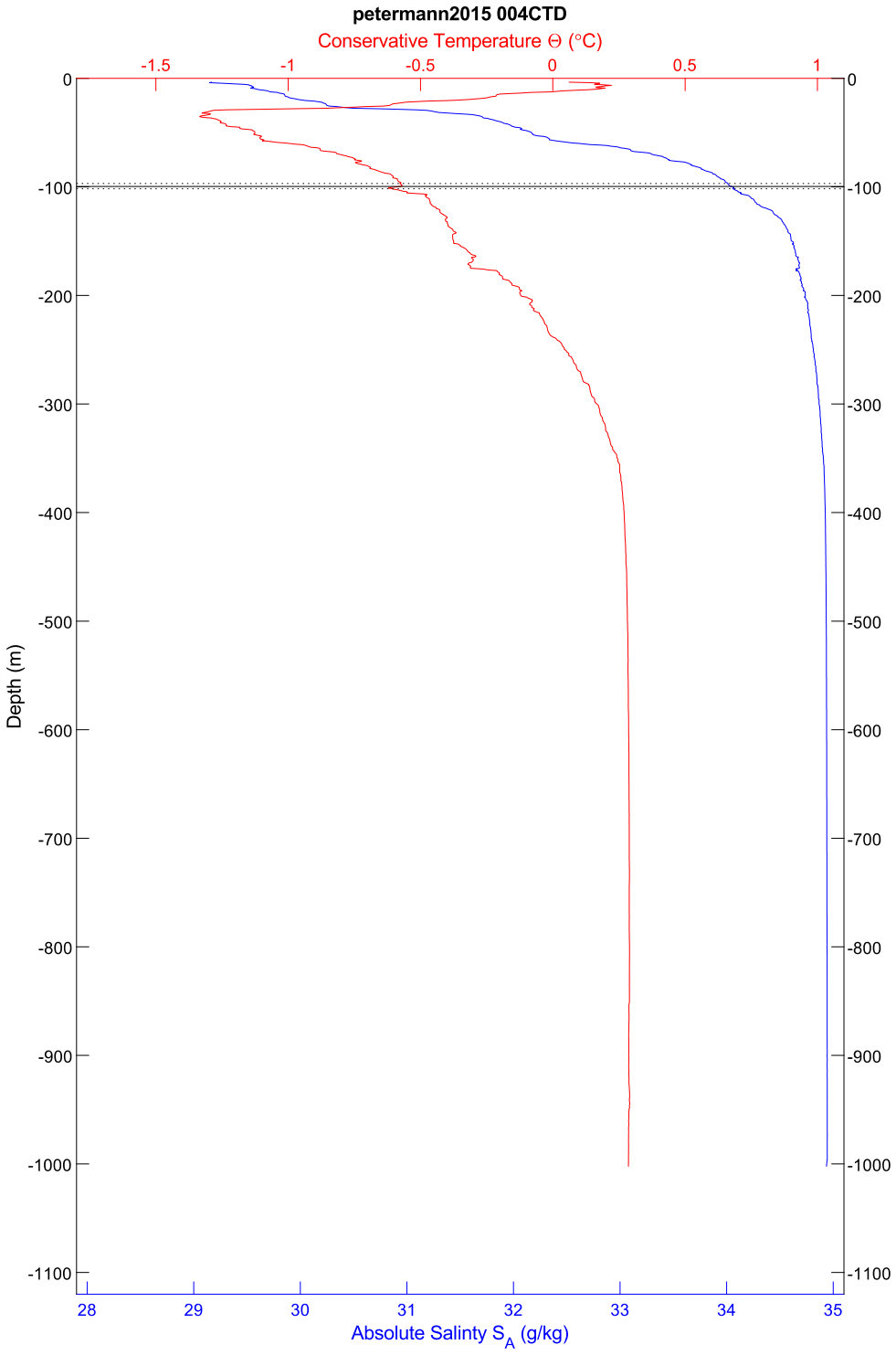

Figure 155: CTD 004, temperature and salinity plotted by depth. The scattering layer depth is indicated by horizontal lines; the solid line is the average depth, the dotted lines are the shallowest and deepest depths, in all cases for the top of the scattering layer.

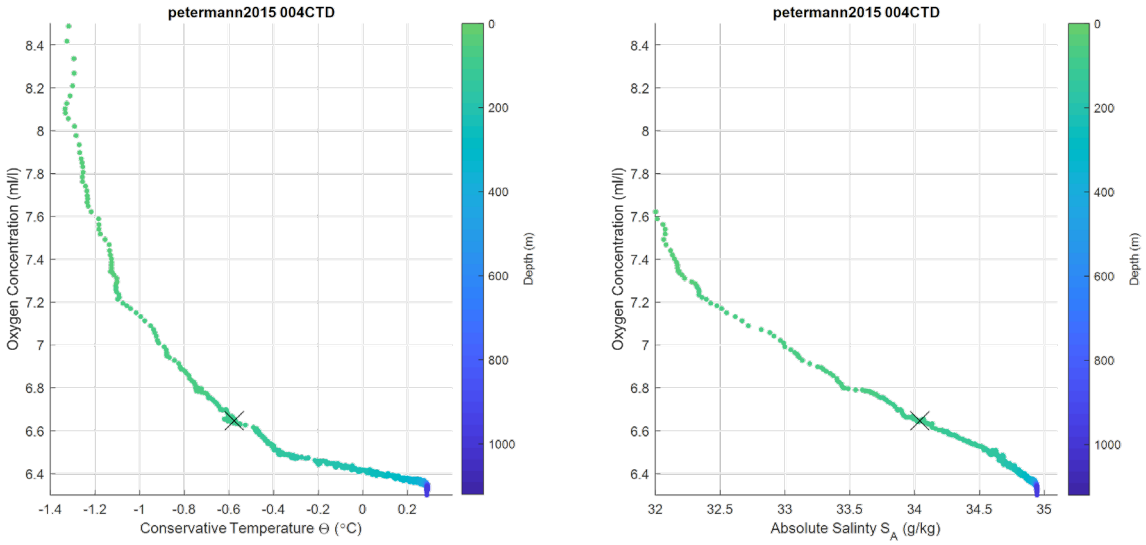

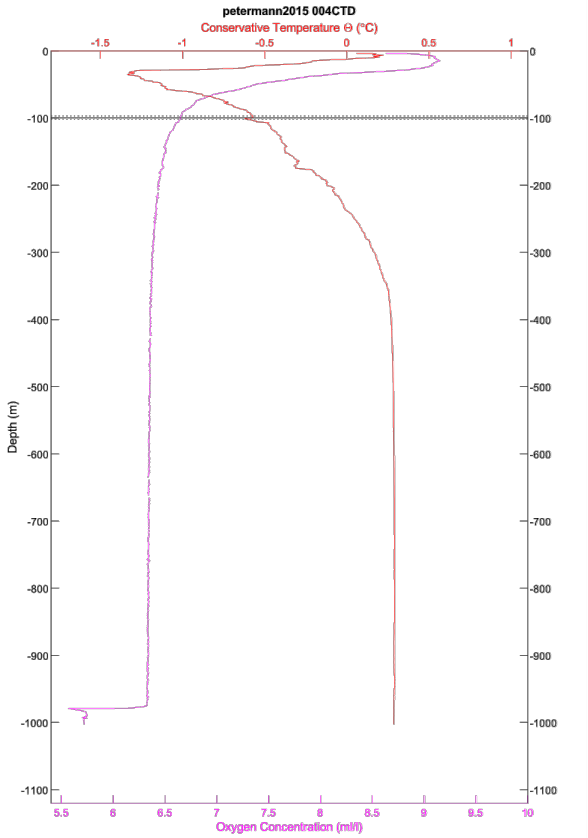

Figure 156: CTD 004. Top left, oxygen-temperature diagram, colored by depth. Top right, oxygen-salinity diagram, colored by depth. The black 'X' in the first two plots indicates the average depth for the top of the scattering layer in this location. Bottom center, temperature and oxygen plotted by depth. The scattering layer depth is indicated by horizontal lines; the solid line is the average depth, the dotted lines are the shallowest and deepest depths, in both cases for the top of the scattering layer. Note that oxygen values for this cast are considered questionable due to issues with the pump, which was replaced between cast 025 and 026.

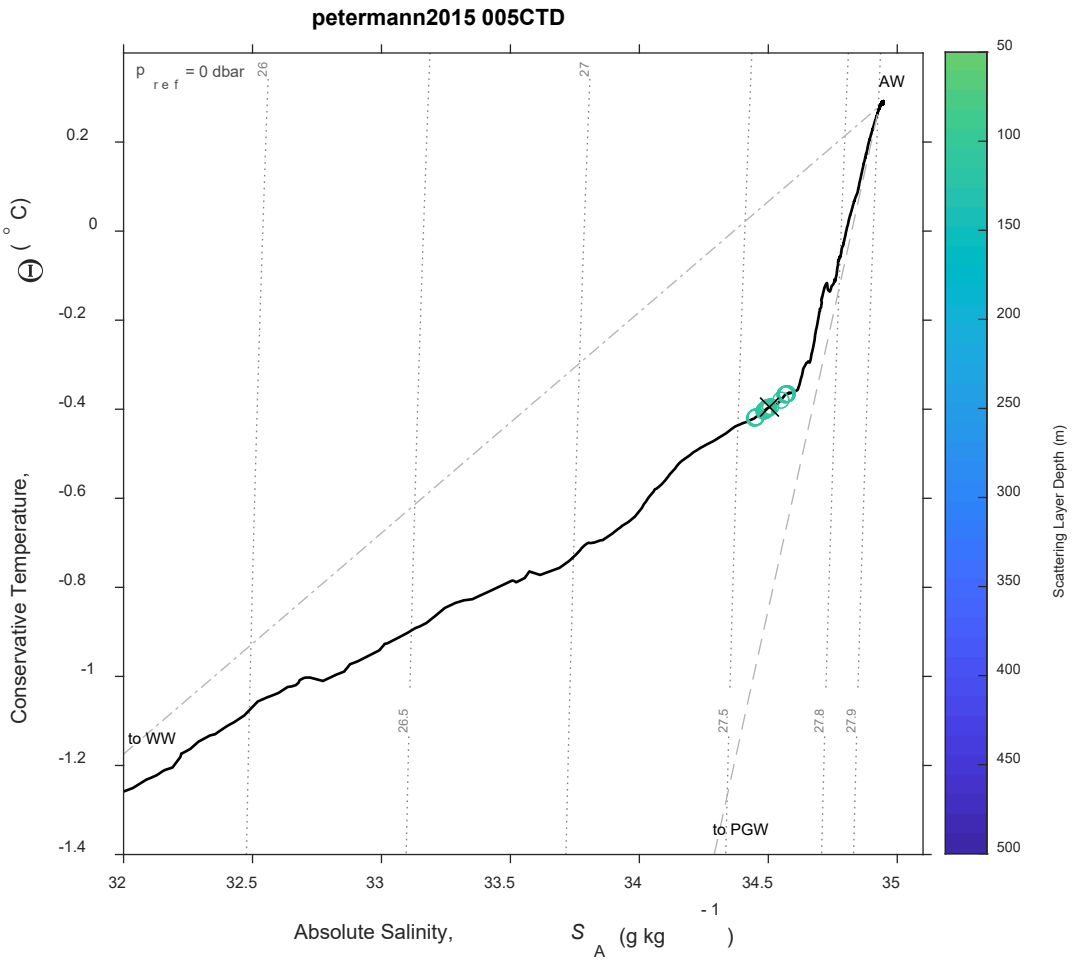

Figure 157: CTD 005, Temperature-Salinity (T-S) diagram. The scattering layer picks corresponding to this CTD are plotted as open circles colored by depth; a black 'X' indicates the average depth for the top of the scattering layer in this location. Isobars are shown as labeled grey dotted lines.

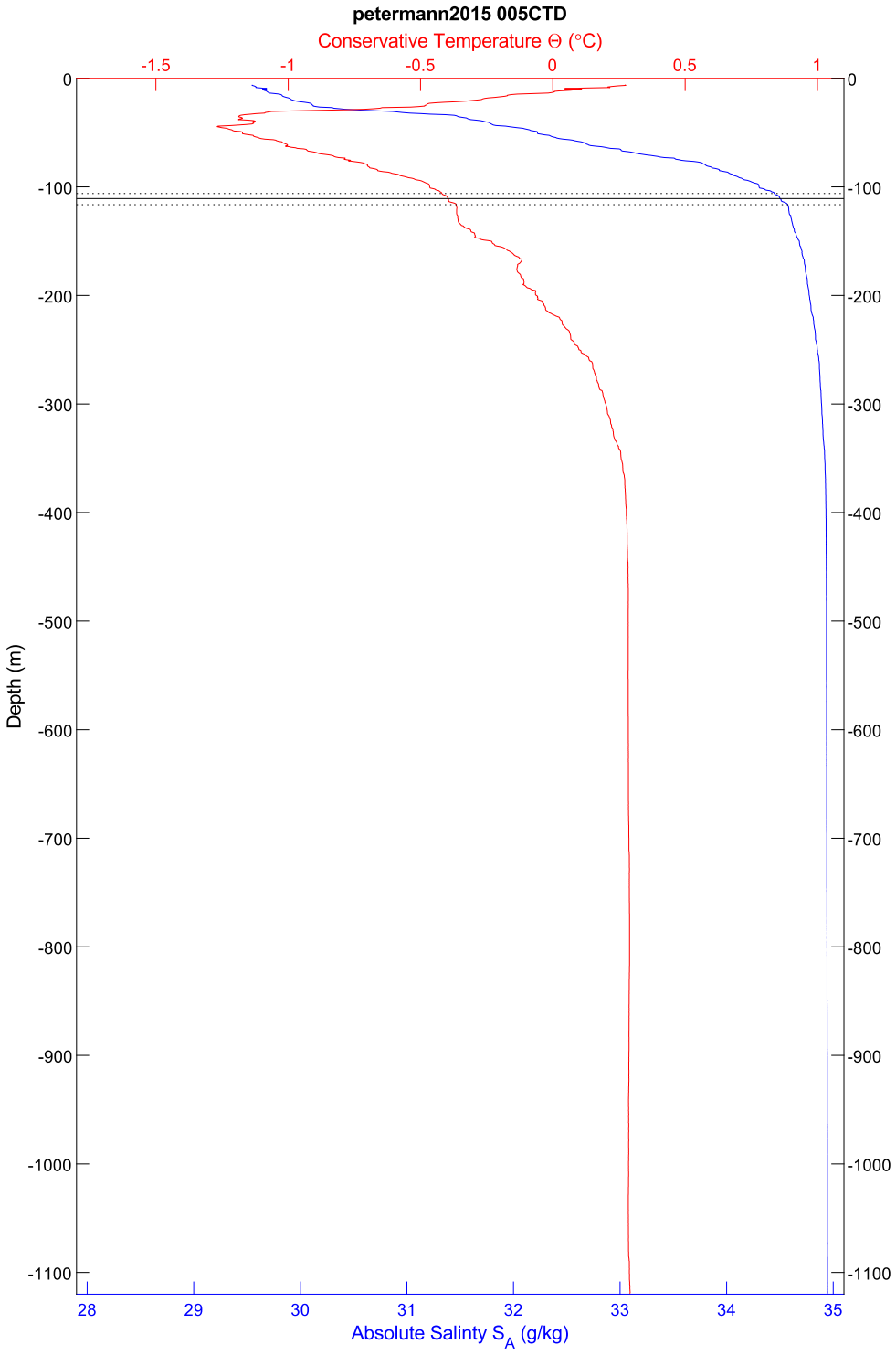

Figure 158: CTD 005, temperature and salinity plotted by depth. The scattering layer depth is indicated by horizontal lines; the solid line is the average depth, the dotted lines are the shallowest and deepest depths, in all cases for the top of the scattering layer.

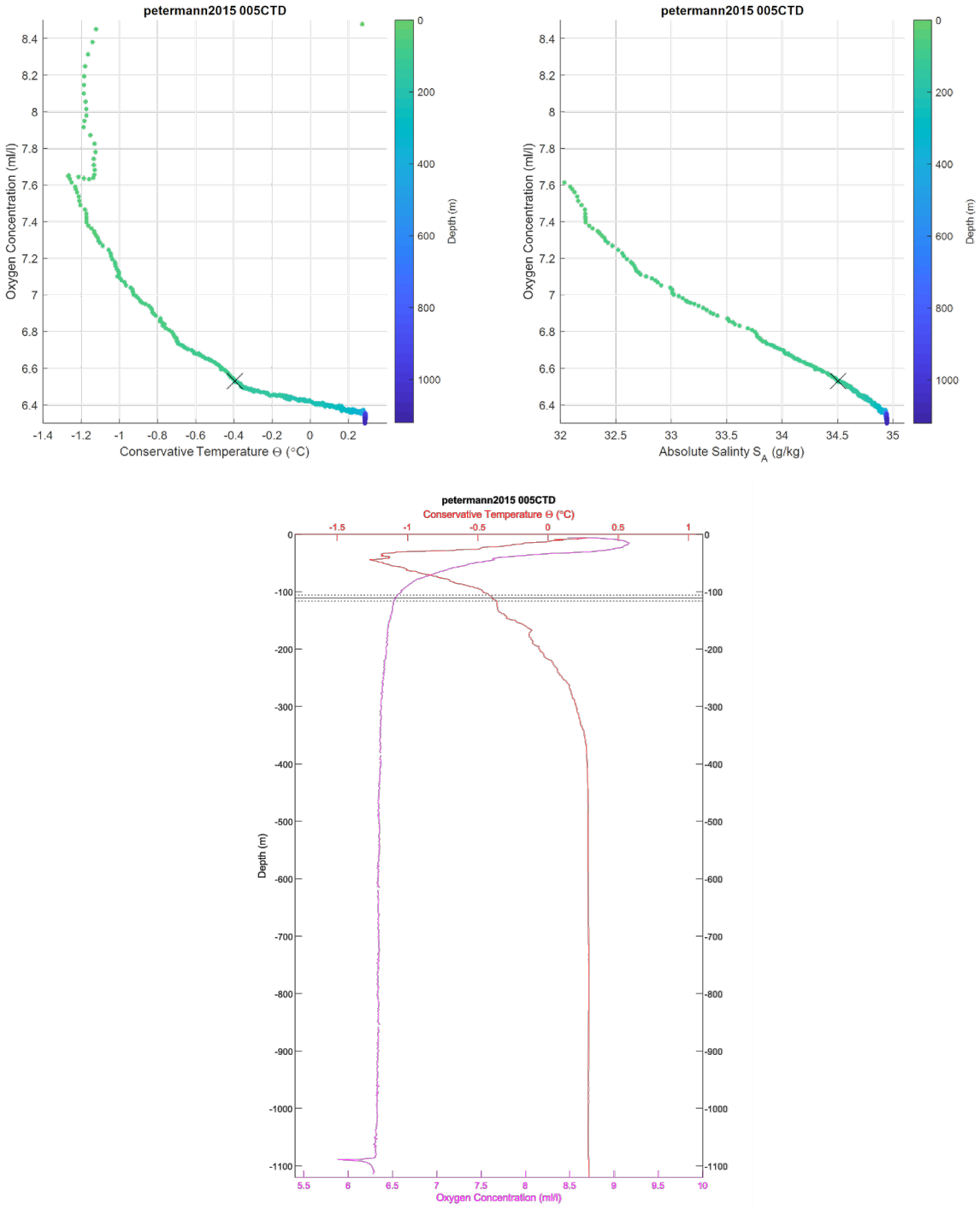

Figure 159: CTD 005. Top left, oxygen-temperature diagram, colored by depth. Top right, oxygen-salinity diagram, colored by depth. The black 'X' in the first two plots indicates the average depth for the top of the scattering layer in this location. Bottom center, temperature and oxygen plotted by depth. The scattering layer depth is indicated by horizontal lines; the solid line is the average depth, the dotted lines are the shallowest and deepest depths, in both cases for the top of the scattering layer. Note that oxygen values for this cast are considered questionable due to issues with the pump, which was replaced between cast 025 and 026.

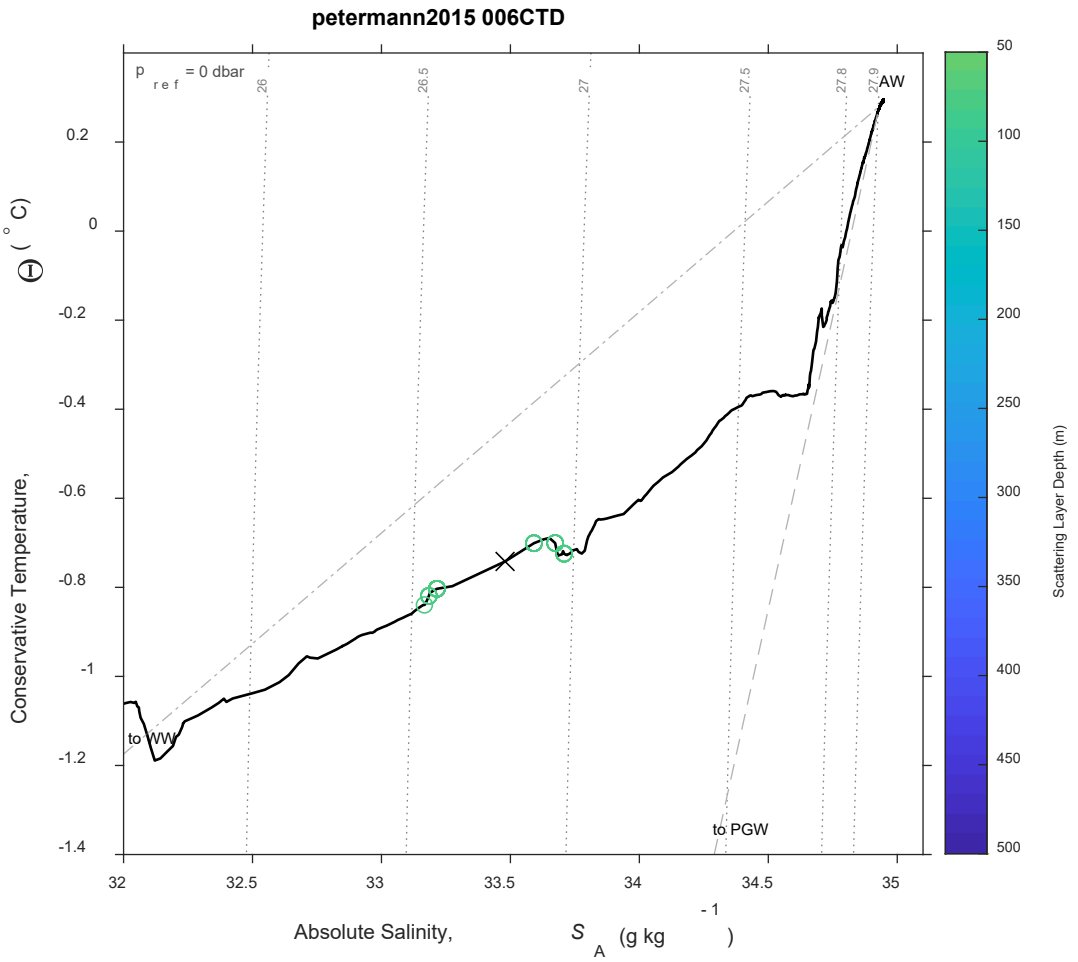

Figure 160: CTD 006, Temperature-Salinity (T-S) diagram. The scattering layer picks corresponding to this CTD are plotted as open circles colored by depth; a black 'X' indicates the average depth for the top of the scattering layer in this location. Isobars are shown as labeled grey dotted lines.

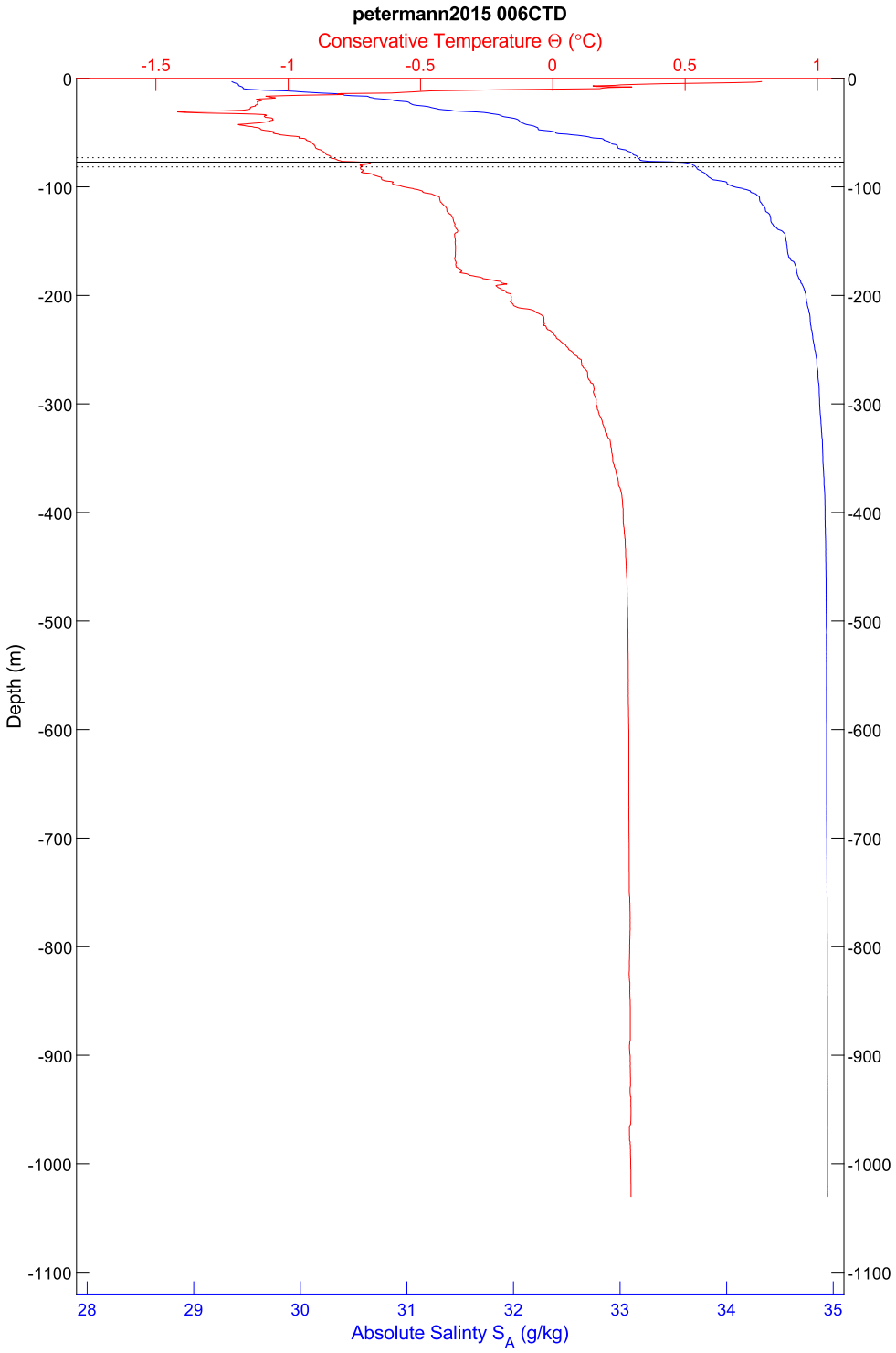

Figure 161: CTD 006, temperature and salinity plotted by depth. The scattering layer depth is indicated by horizontal lines; the solid line is the average depth, the dotted lines are the shallowest and deepest depths, in all cases for the top of the scattering layer.

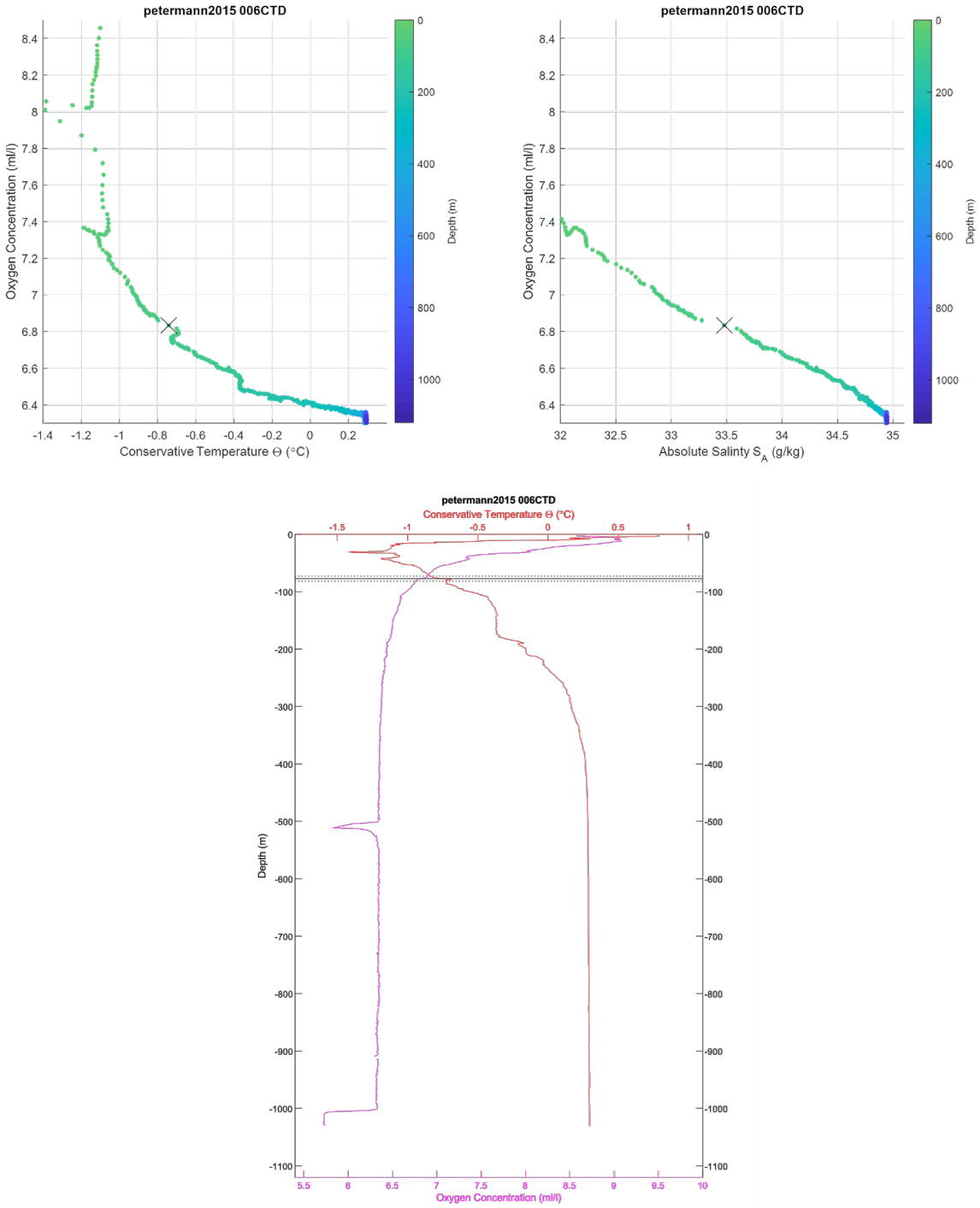

Figure 162: CTD 006. Top left, oxygen-temperature diagram, colored by depth. Top right, oxygen-salinity diagram, colored by depth. The black 'X' in the first two plots indicates the average depth for the top of the scattering layer in this location. Bottom center, temperature and oxygen plotted by depth. The scattering layer depth is indicated by horizontal lines; the solid line is the average depth, the dotted lines are the shallowest and deepest depths, in both cases for the top of the scattering layer. Note that oxygen values for this cast are considered questionable due to issues with the pump, which was replaced between cast 025 and 026.

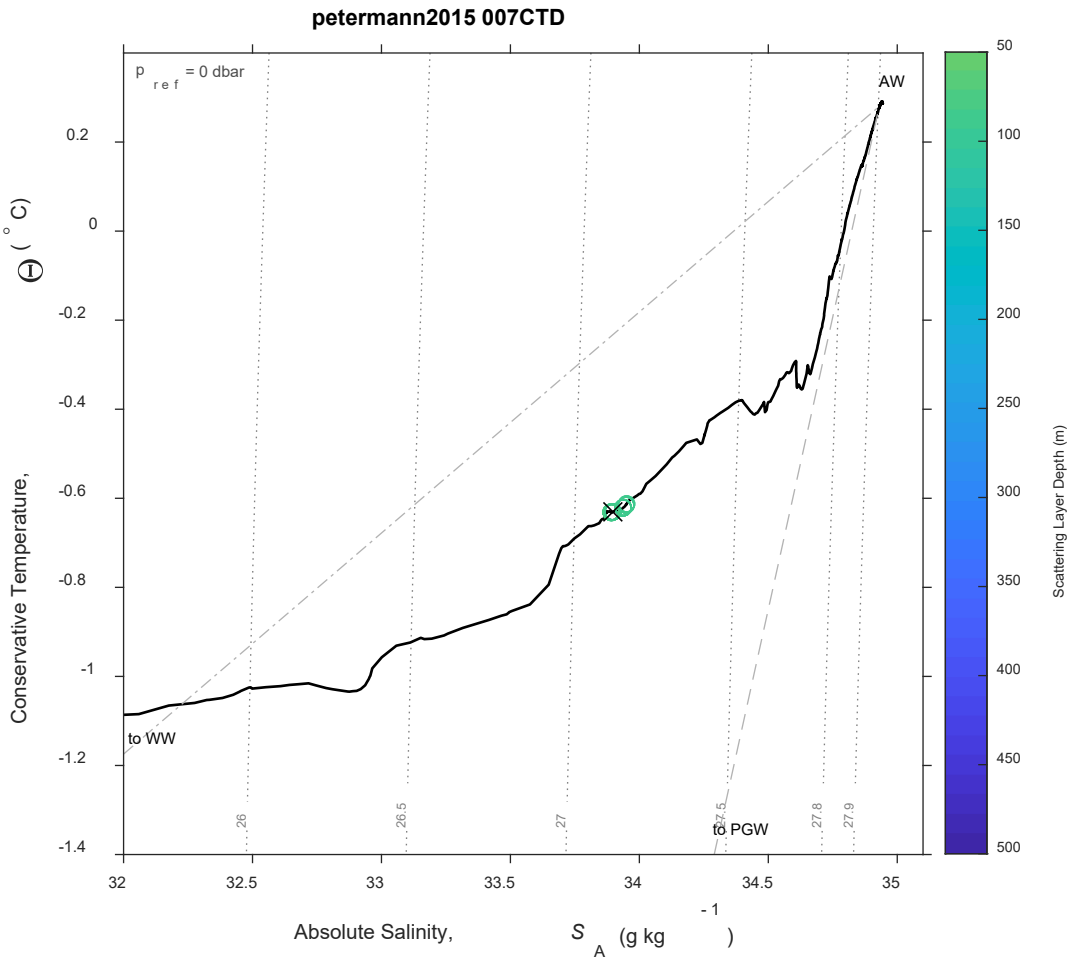

Figure 163: CTD 007, Temperature-Salinity (T-S) diagram. The scattering layer picks corresponding to this CTD are plotted as open circles colored by depth; a black 'X' indicates the average depth for the top of the scattering layer in this location. Isobars are shown as labeled grey dotted lines.

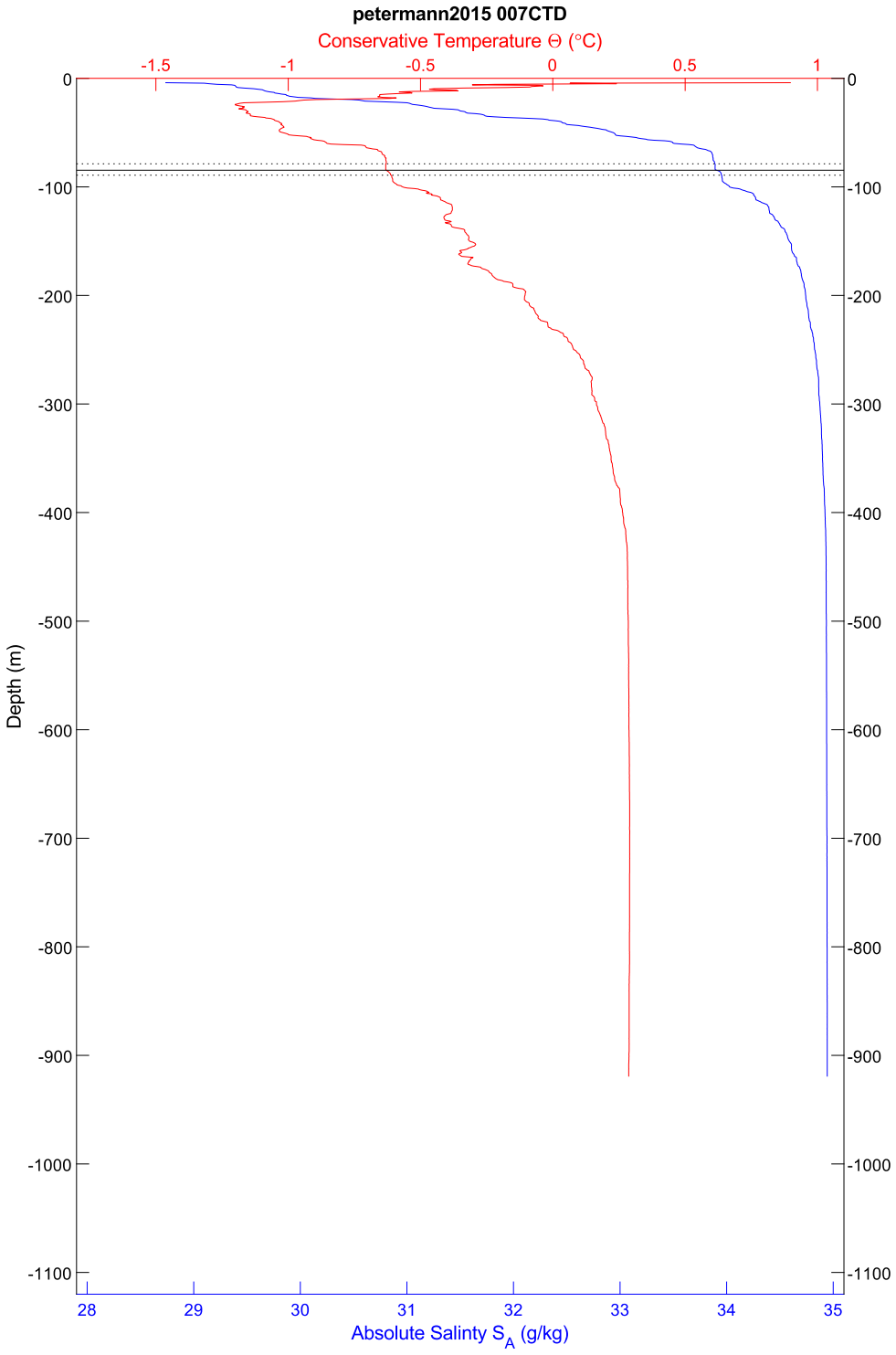

Figure 164: CTD 007, temperature and salinity plotted by depth. The scattering layer depth is indicated by horizontal lines; the solid line is the average depth, the dotted lines are the shallowest and deepest depths, in all cases for the top of the scattering layer.

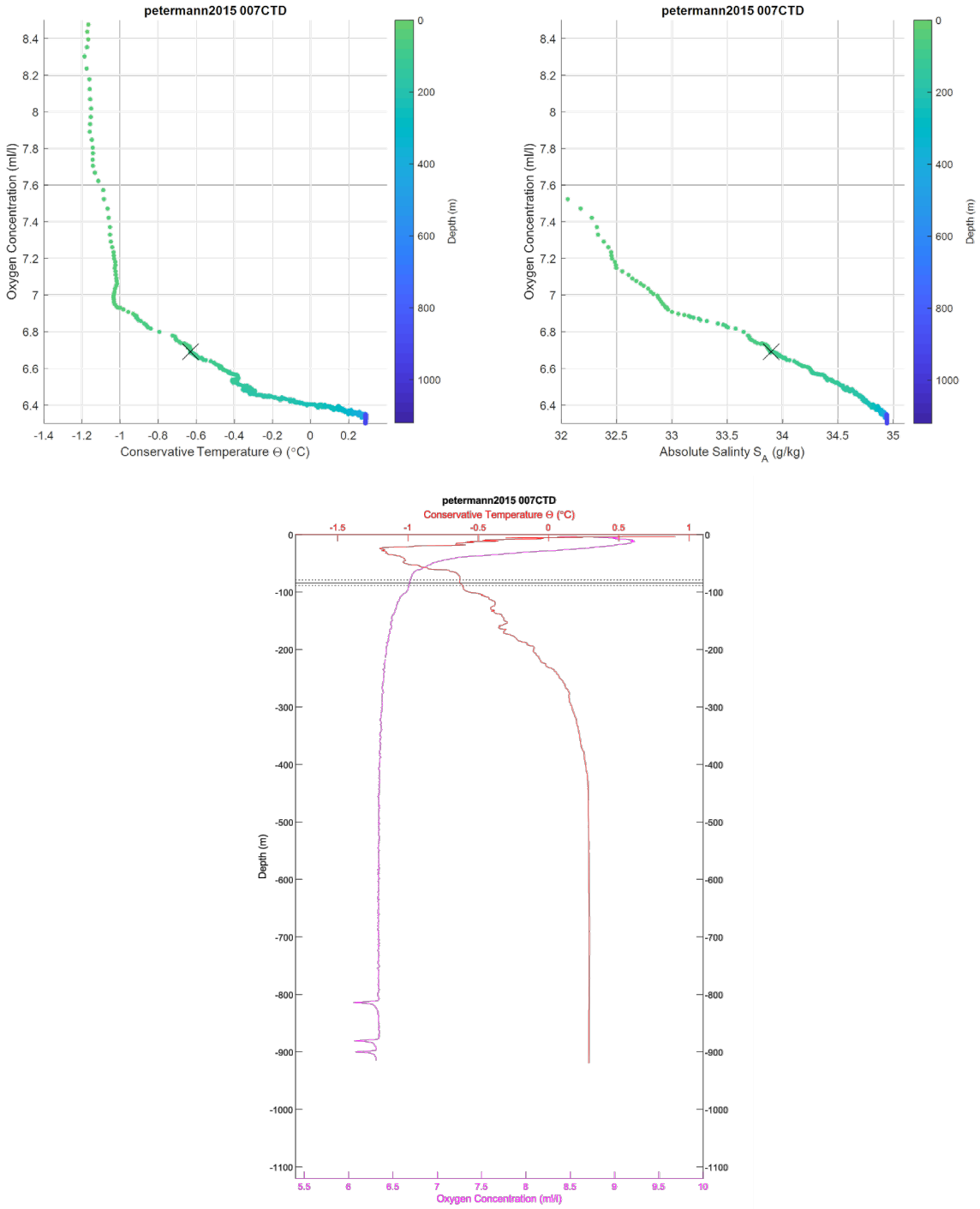

Figure 165: CTD 007. Top left, oxygen-temperature diagram, colored by depth. Top right, oxygen-salinity diagram, colored by depth. The black 'X' in the first two plots indicates the average depth for the top of the scattering layer in this location. Bottom center, temperature and oxygen plotted by depth. The scattering layer depth is indicated by horizontal lines; the solid line is the average depth, the dotted lines are the shallowest and deepest depths, in both cases for the top of the scattering layer. Note that oxygen values for this cast are considered questionable due to issues with the pump, which was replaced between cast 025 and 026.

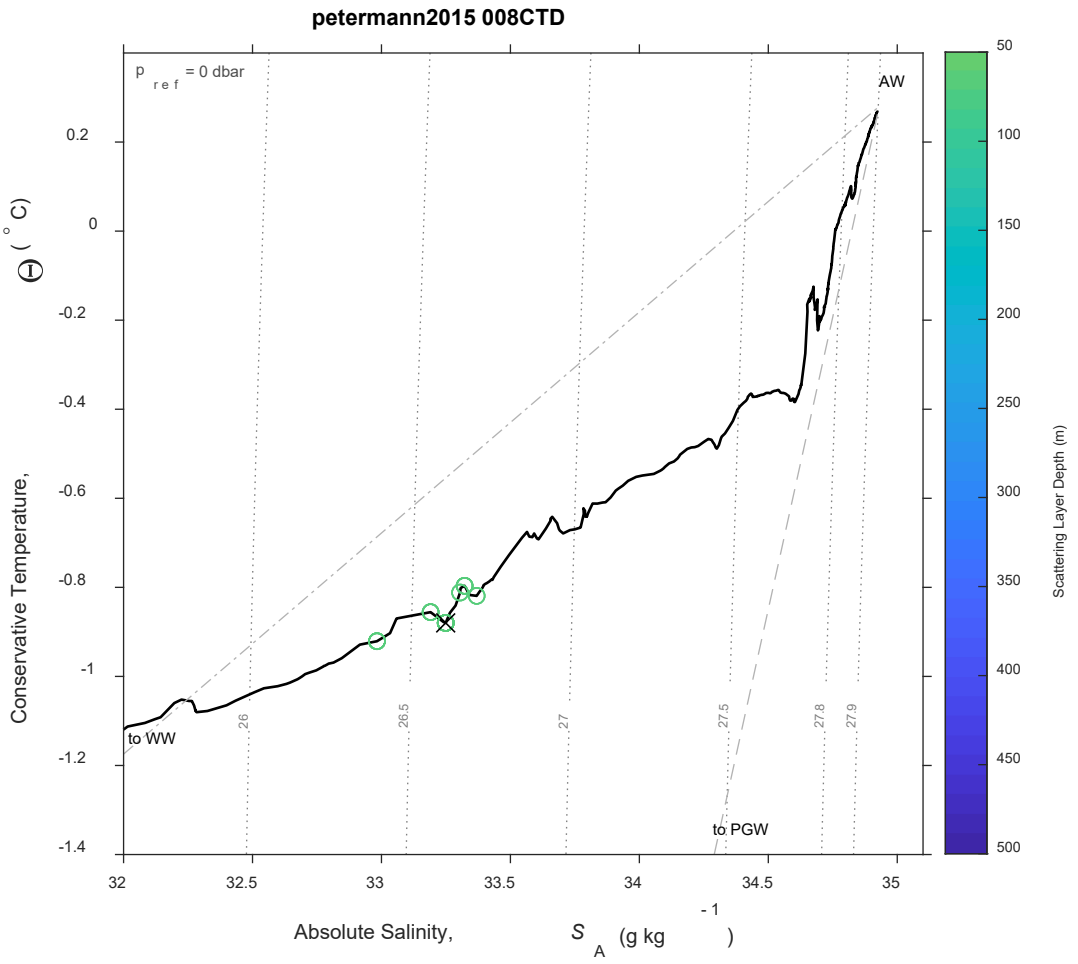

Figure 166: CTD 008, Temperature-Salinity (T-S) diagram. The scattering layer picks corresponding to this CTD are plotted as open circles colored by depth; a black 'X' indicates the average depth for the top of the scattering layer in this location. Isobars are shown as labeled grey dotted lines.

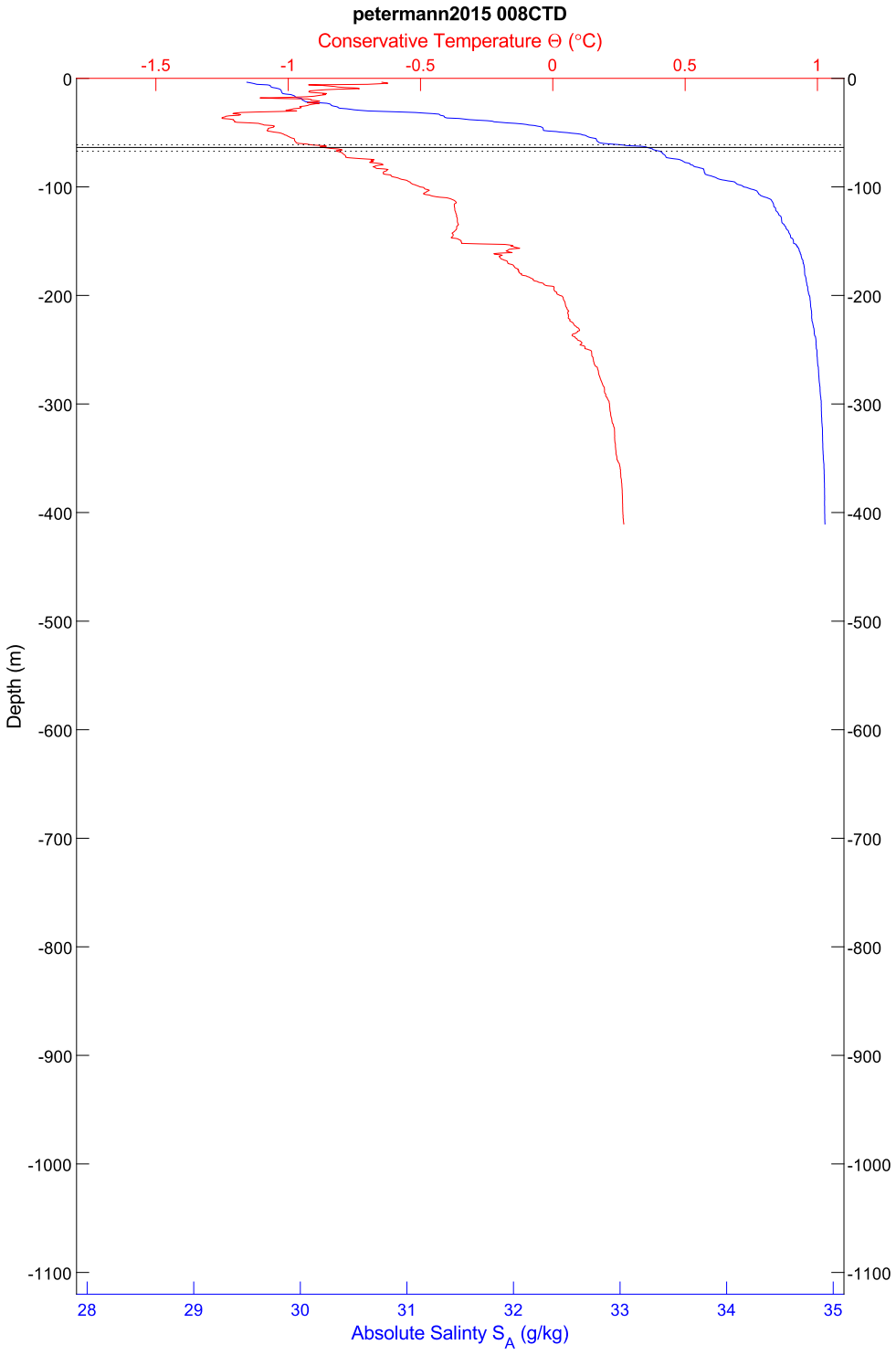

Figure 167: CTD 008, temperature and salinity plotted by depth. The scattering layer depth is indicated by horizontal lines; the solid line is the average depth, the dotted lines are the shallowest and deepest depths, in all cases for the top of the scattering layer.

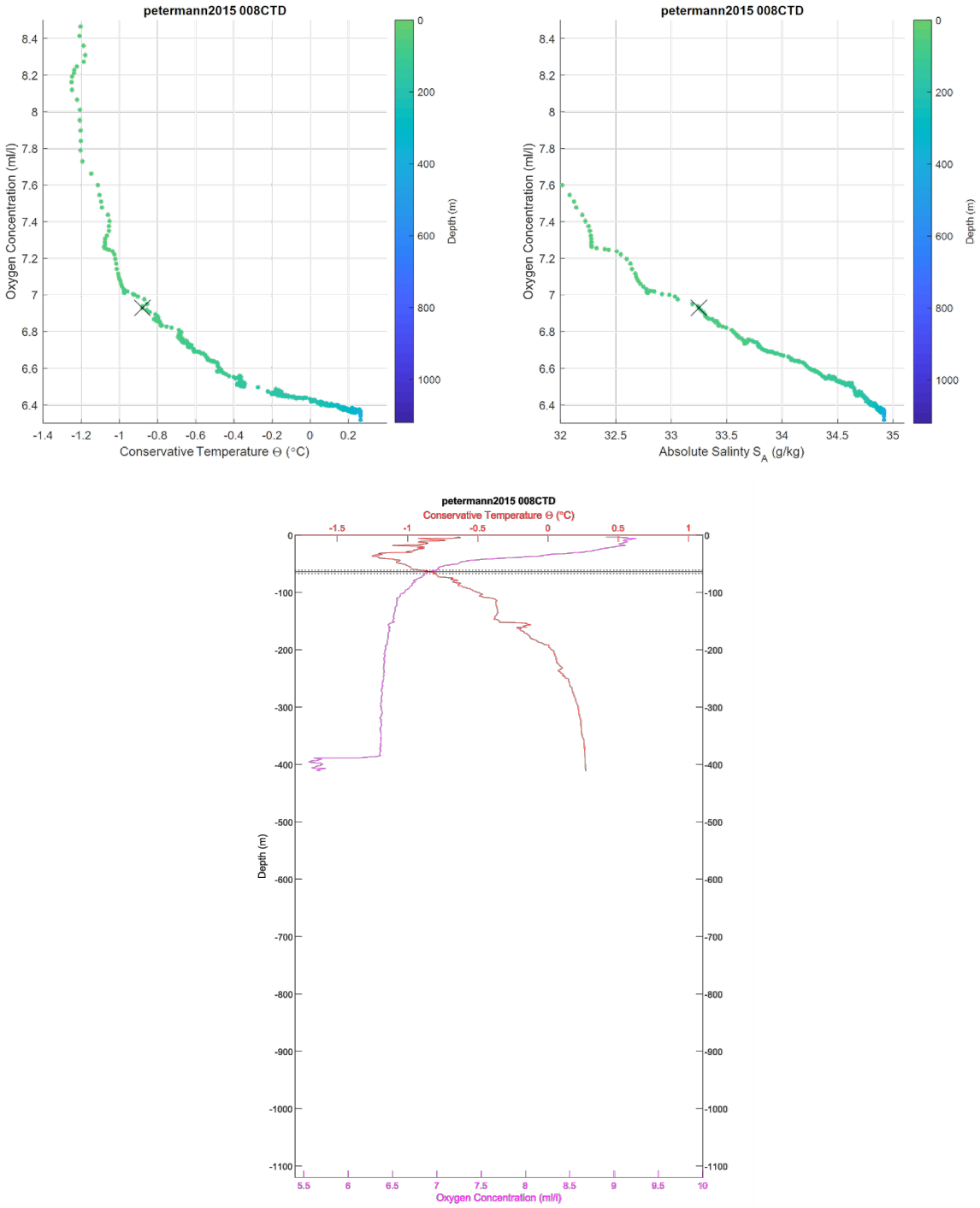

Figure 168: CTD 008. Top left, oxygen-temperature diagram, colored by depth. Top right, oxygen-salinity diagram, colored by depth. The black 'X' in the first two plots indicates the average depth for the top of the scattering layer in this location. Bottom center, temperature and oxygen plotted by depth. The scattering layer depth is indicated by horizontal lines; the solid line is the average depth, the dotted lines are the shallowest and deepest depths, in both cases for the top of the scattering layer. Note that oxygen values for this cast are considered questionable due to issues with the pump, which was replaced between cast 025 and 026.

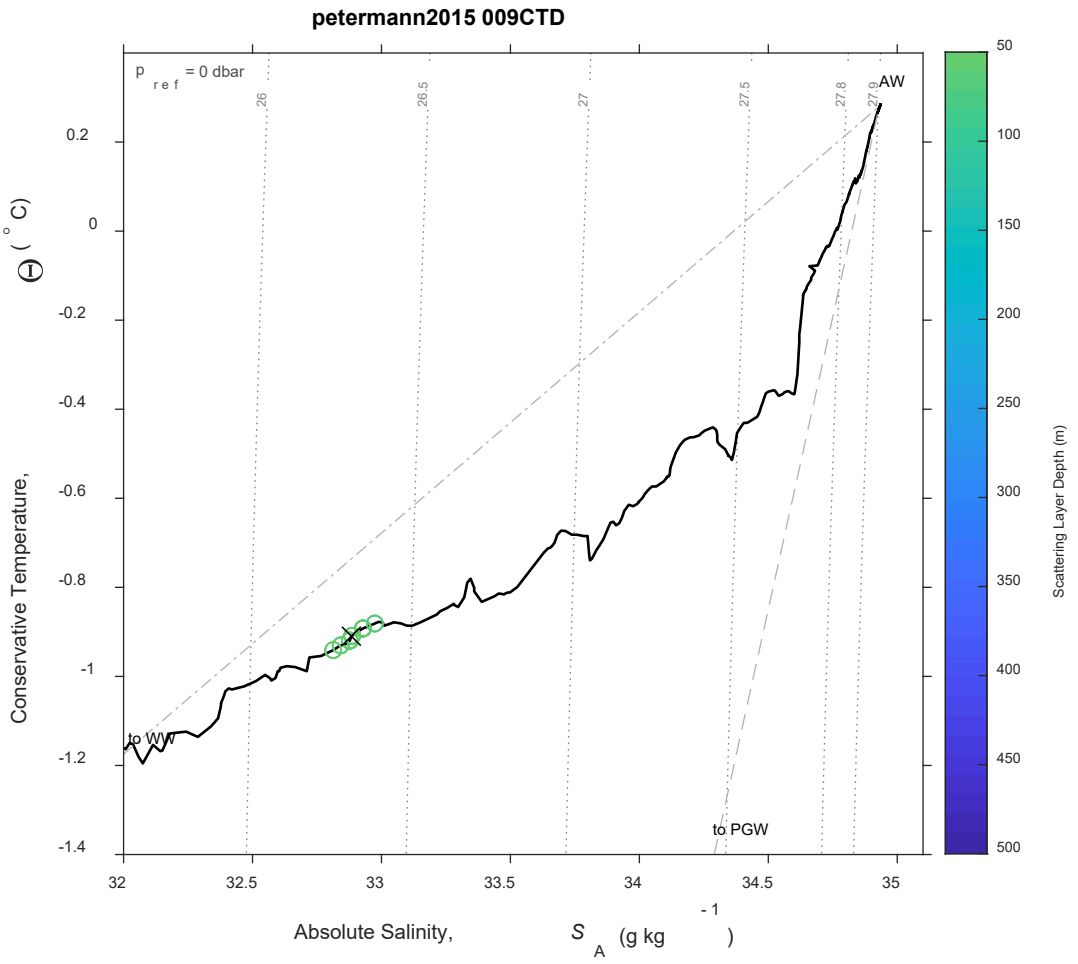

Figure 169: CTD 009, Temperature-Salinity (T-S) diagram. The scattering layer picks corresponding to this CTD are plotted as open circles colored by depth; a black 'X' indicates the average depth for the top of the scattering layer in this location. Isobars are shown as labeled grey dotted lines.

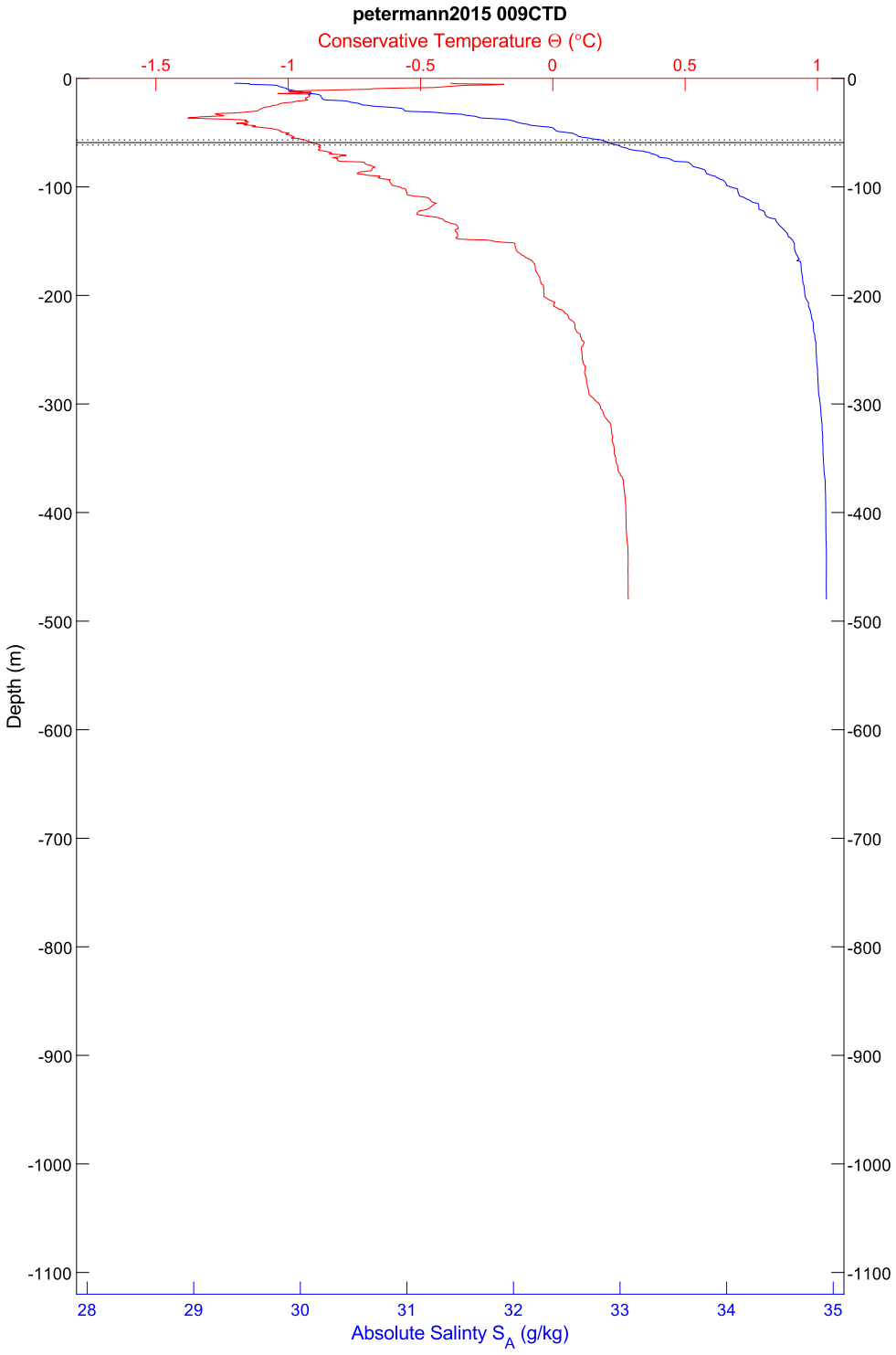

Figure 170: CTD 009, temperature and salinity plotted by depth. The scattering layer depth is indicated by horizontal lines; the solid line is the average depth, the dotted lines are the shallowest and deepest depths, in all cases for the top of the scattering layer.

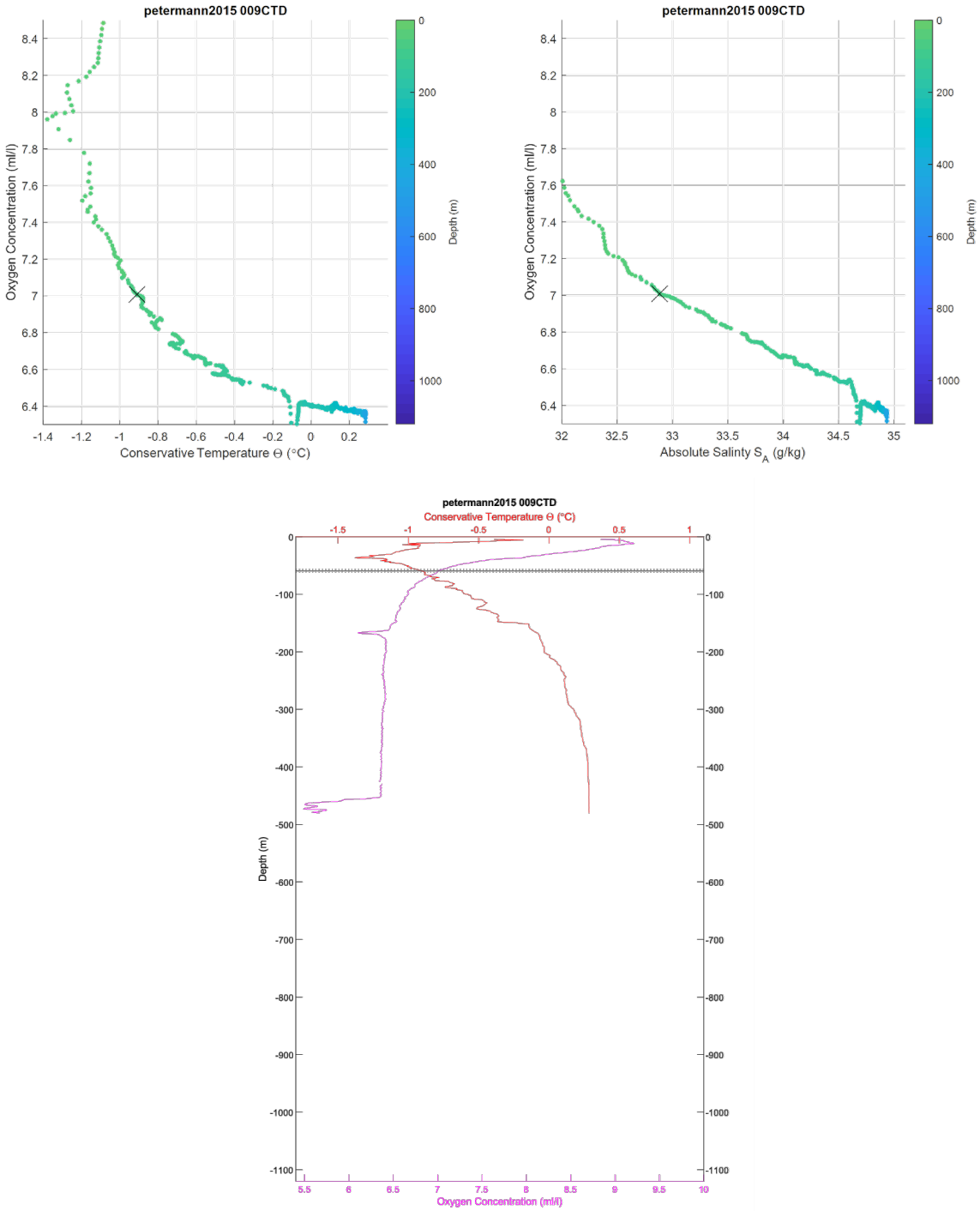

Figure 171: CTD 009. Top left, oxygen-temperature diagram, colored by depth. Top right, oxygen-salinity diagram, colored by depth. The black 'X' in the first two plots indicates the average depth for the top of the scattering layer in this location. Bottom center, temperature and oxygen plotted by depth. The scattering layer depth is indicated by horizontal lines; the solid line is the average depth, the dotted lines are the shallowest and deepest depths, in both cases for the top of the scattering layer. Note that oxygen values for this cast are considered questionable due to issues with the pump, which was replaced between cast 025 and 026.

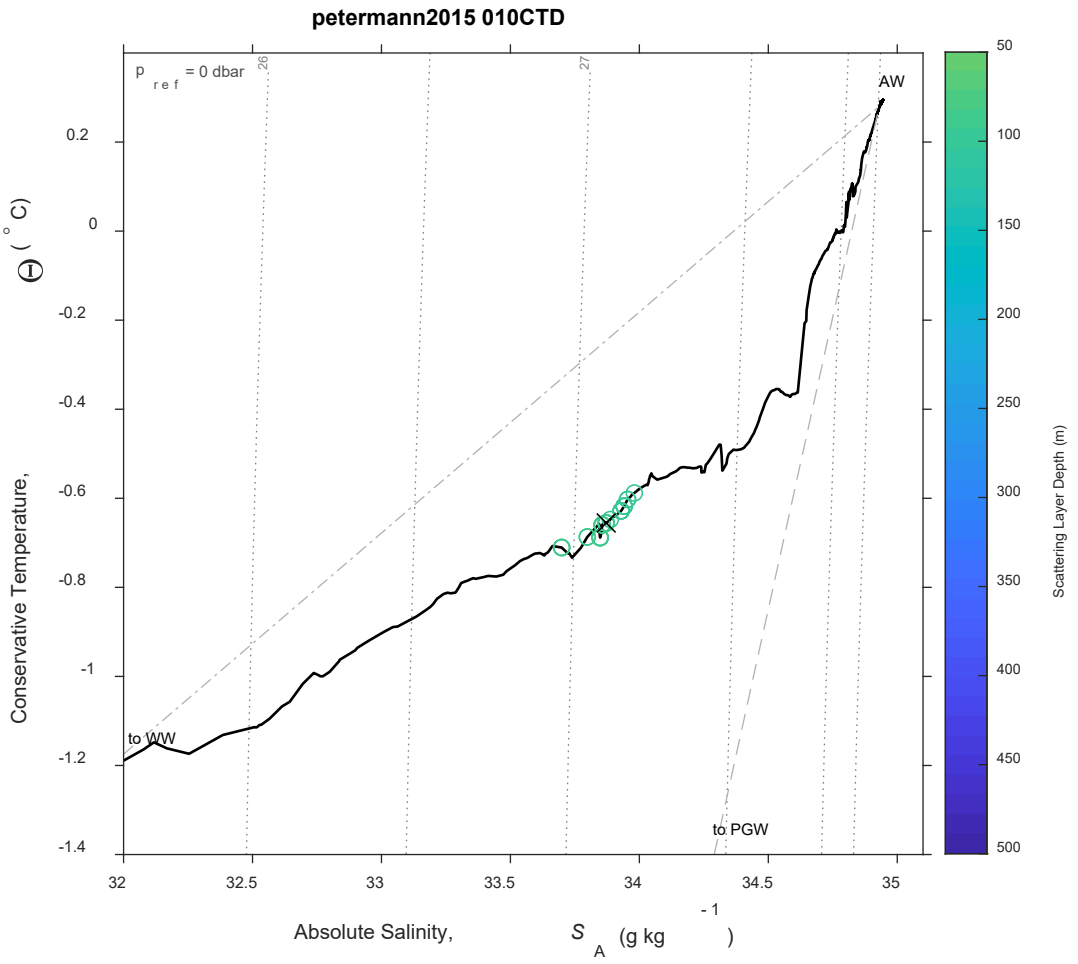

Figure 172: CTD 010, Temperature-Salinity (T-S) diagram. The scattering layer picks corresponding to this CTD are plotted as open circles colored by depth; a black 'X' indicates the average depth for the top of the scattering layer in this location. Isobars are shown as labeled grey dotted lines.

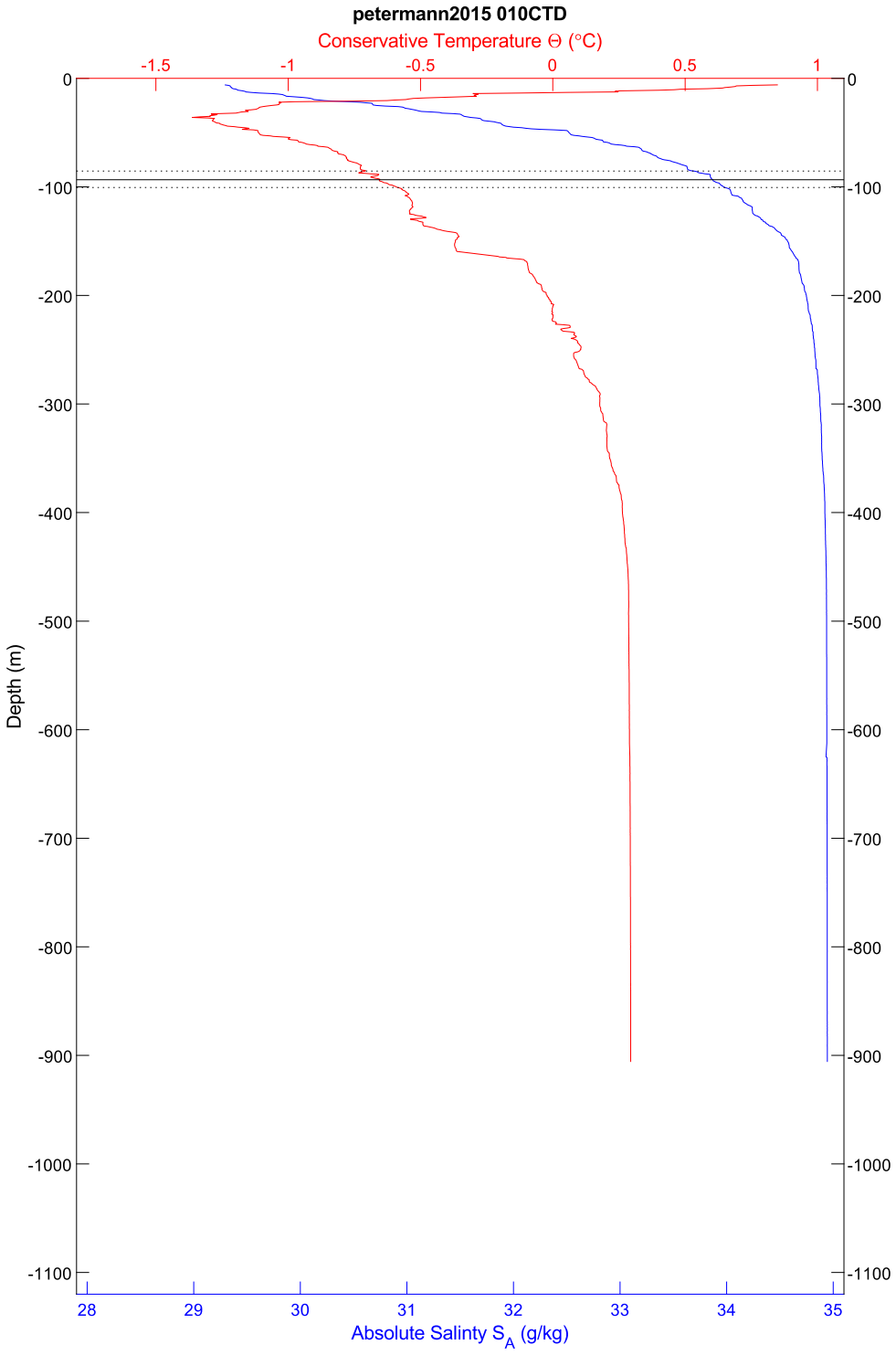

Figure 173: CTD 010, temperature and salinity plotted by depth. The scattering layer depth is indicated by horizontal lines; the solid line is the average depth, the dotted lines are the shallowest and deepest depths, in all cases for the top of the scattering layer.

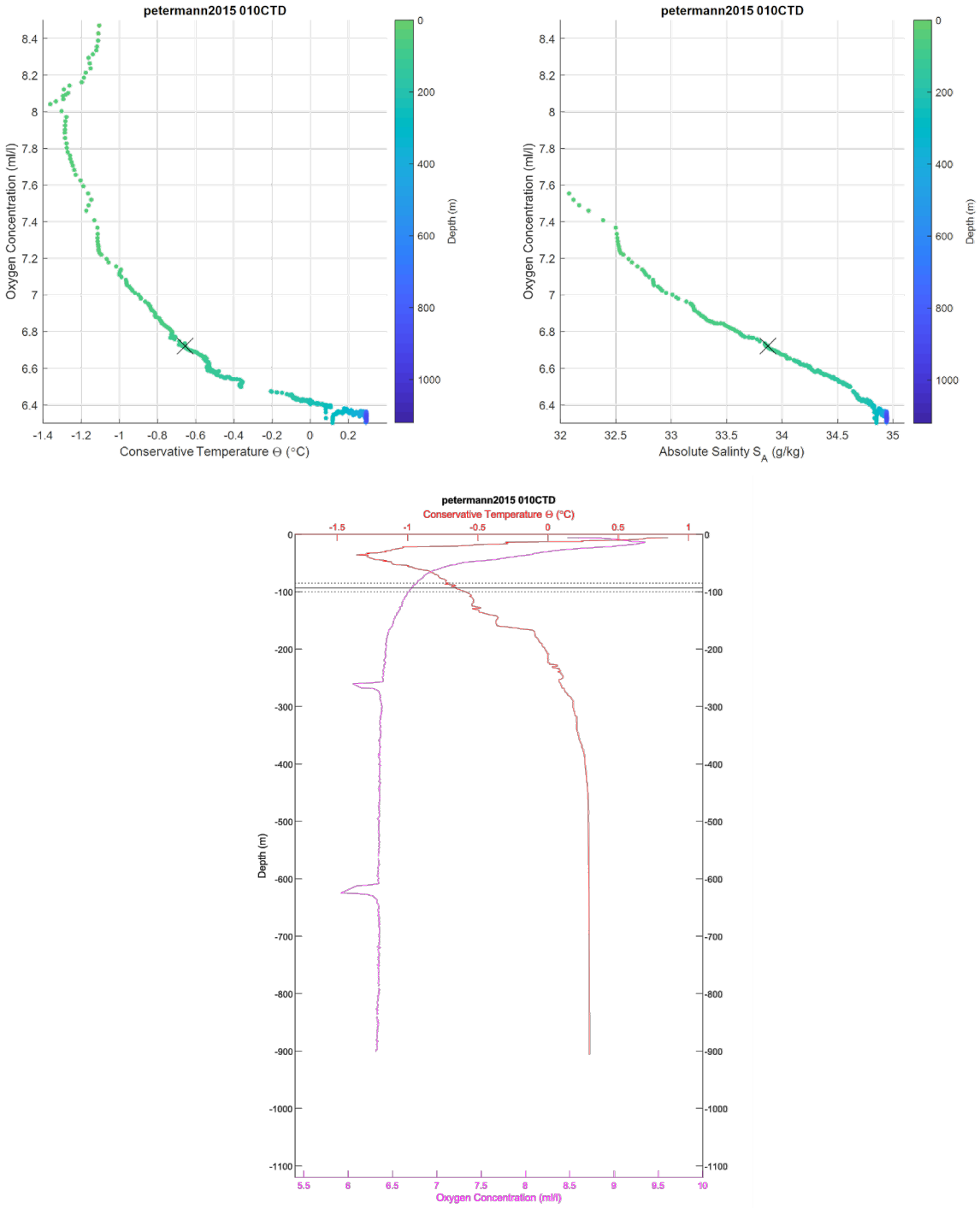

Figure 174: CTD 010. Top left, oxygen-temperature diagram, colored by depth. Top right, oxygen-salinity diagram, colored by depth. The black 'X' in the first two plots indicates the average depth for the top of the scattering layer in this location. Bottom center, temperature and oxygen plotted by depth. The scattering layer depth is indicated by horizontal lines; the solid line is the average depth, the dotted lines are the shallowest and deepest depths, in both cases for the top of the scattering layer. Note that oxygen values for this cast are considered questionable due to issues with the pump, which was replaced between cast 025 and 026.

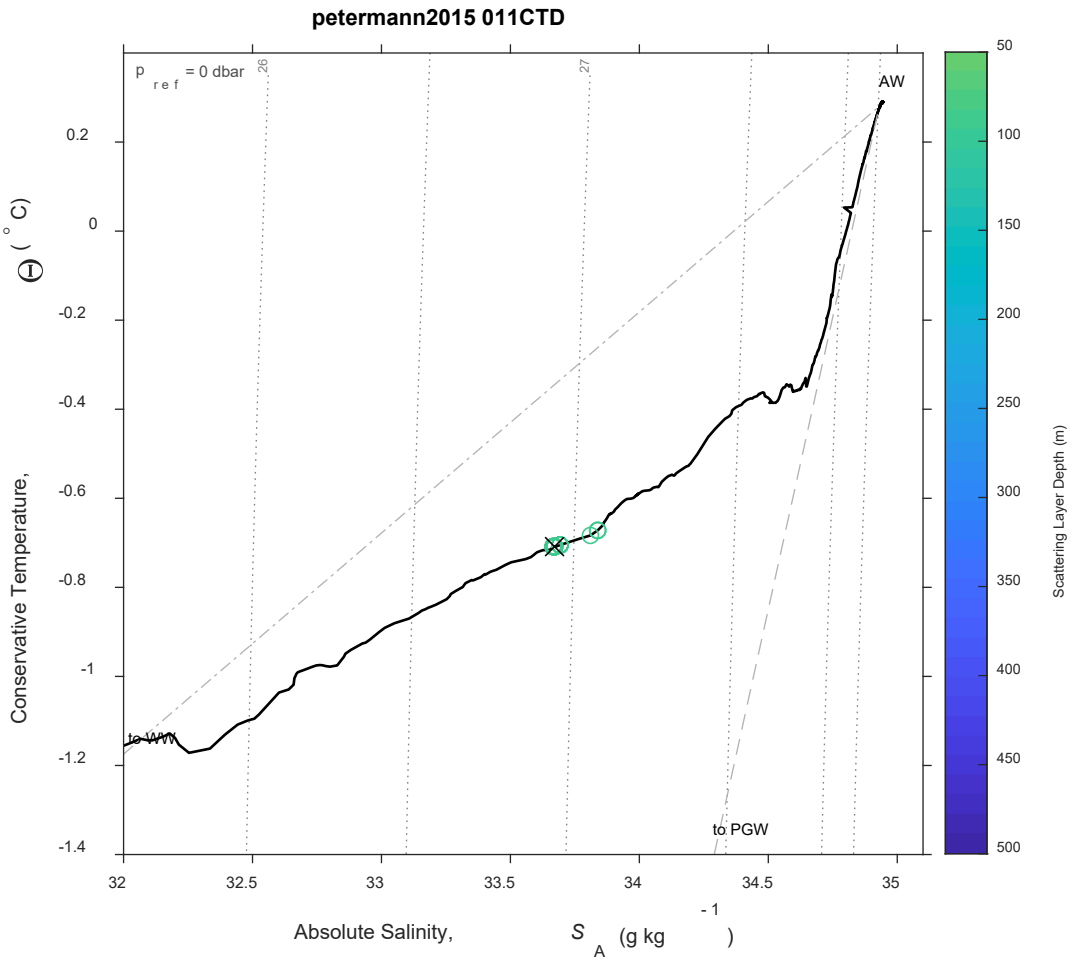

Figure 175: CTD 011, Temperature-Salinity (T-S) diagram. The scattering layer picks corresponding to this CTD are plotted as open circles colored by depth; a black 'X' indicates the average depth for the top of the scattering layer in this location. Isobars are shown as labeled grey dotted lines.

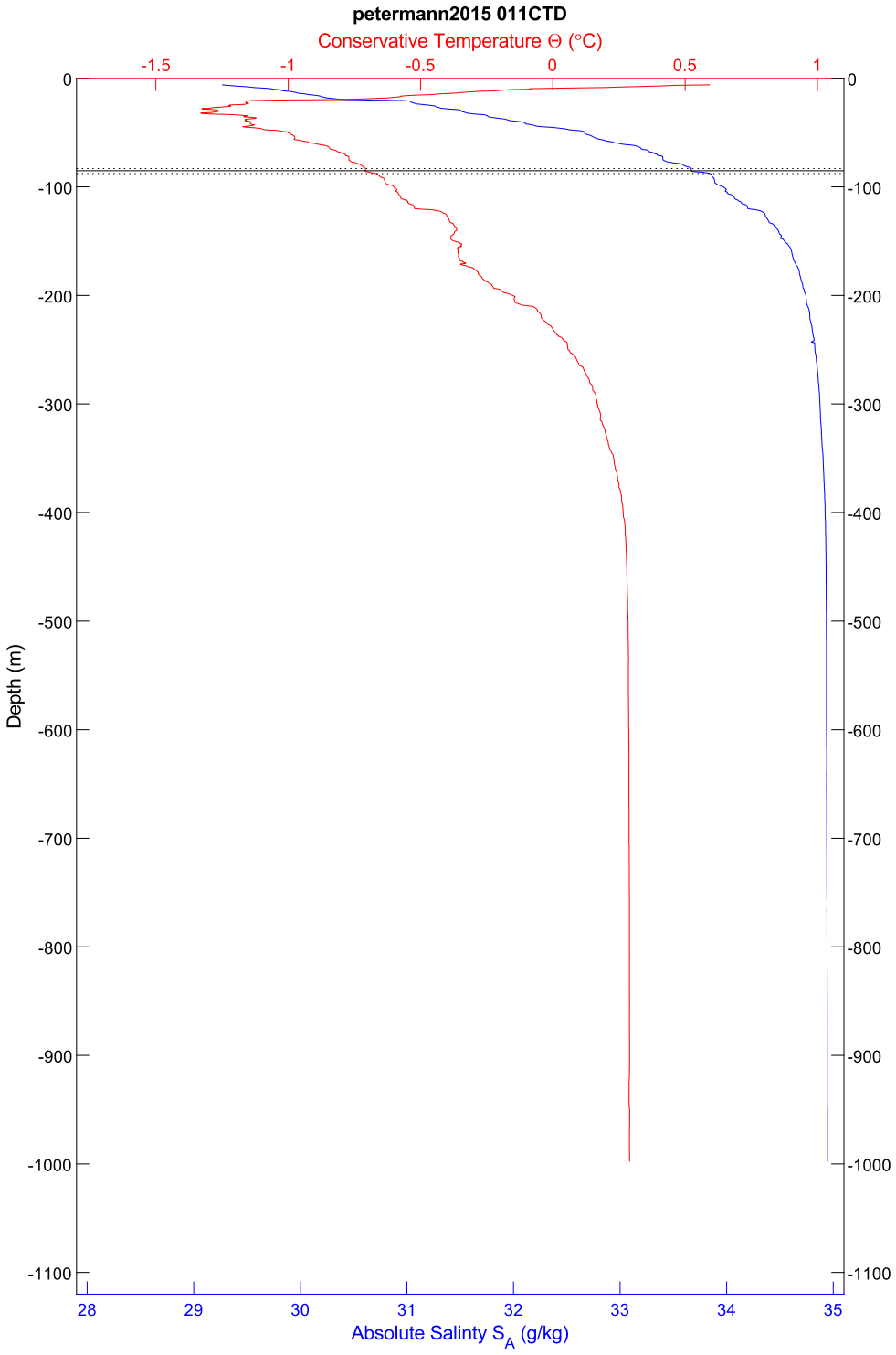

Figure 176: CTD 011, temperature and salinity plotted by depth. The scattering layer depth is indicated by horizontal lines; the solid line is the average depth, the dotted lines are the shallowest and deepest depths, in all cases for the top of the scattering layer.

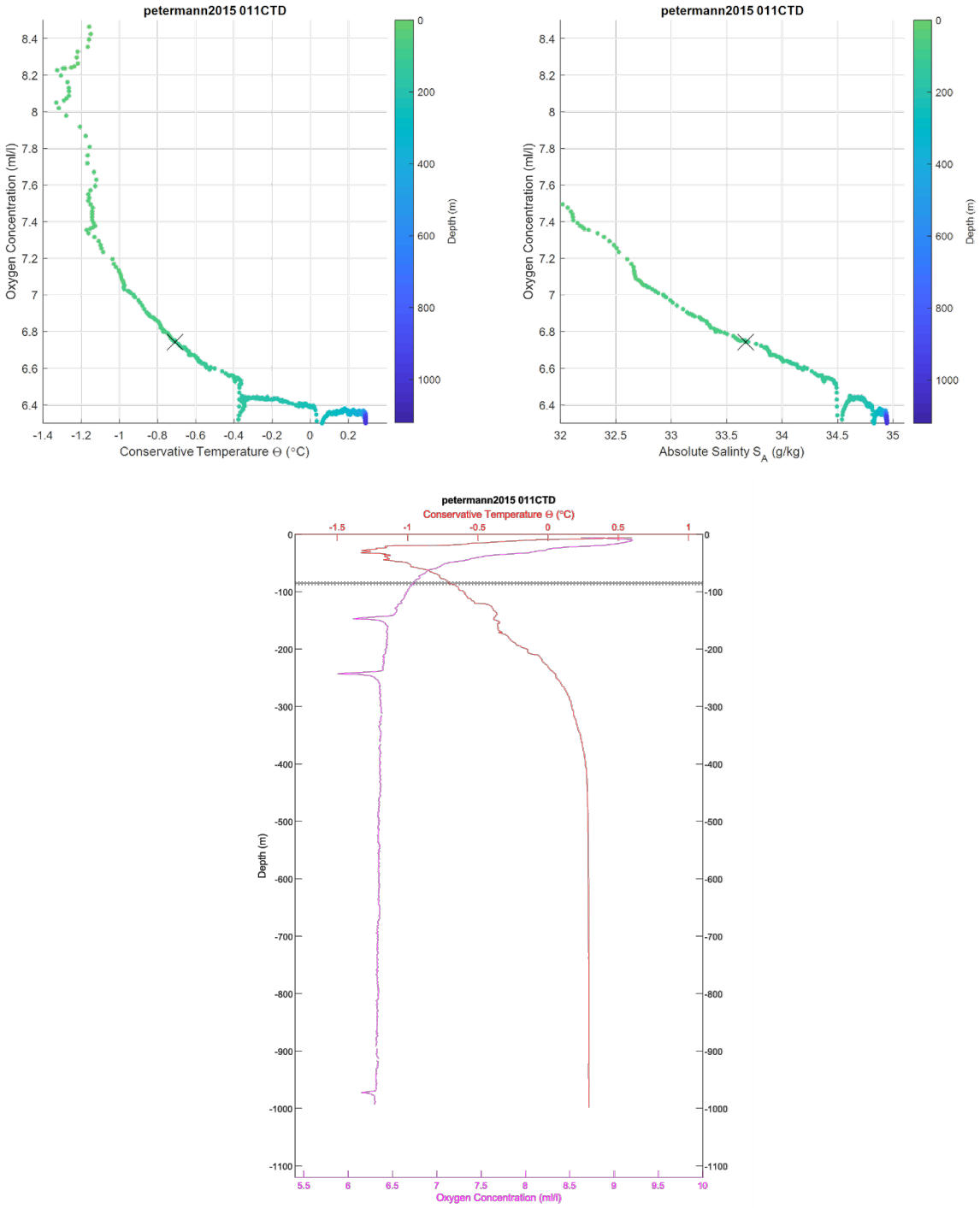

Figure 177: CTD 011. Top left, oxygen-temperature diagram, colored by depth. Top right, oxygen-salinity diagram, colored by depth. The black 'X' in the first two plots indicates the average depth for the top of the scattering layer in this location. Bottom center, temperature and oxygen plotted by depth. The scattering layer depth is indicated by horizontal lines; the solid line is the average depth, the dotted lines are the shallowest and deepest depths, in both cases for the top of the scattering layer. Note that oxygen values for this cast are considered questionable due to issues with the pump, which was replaced between cast 025 and 026.

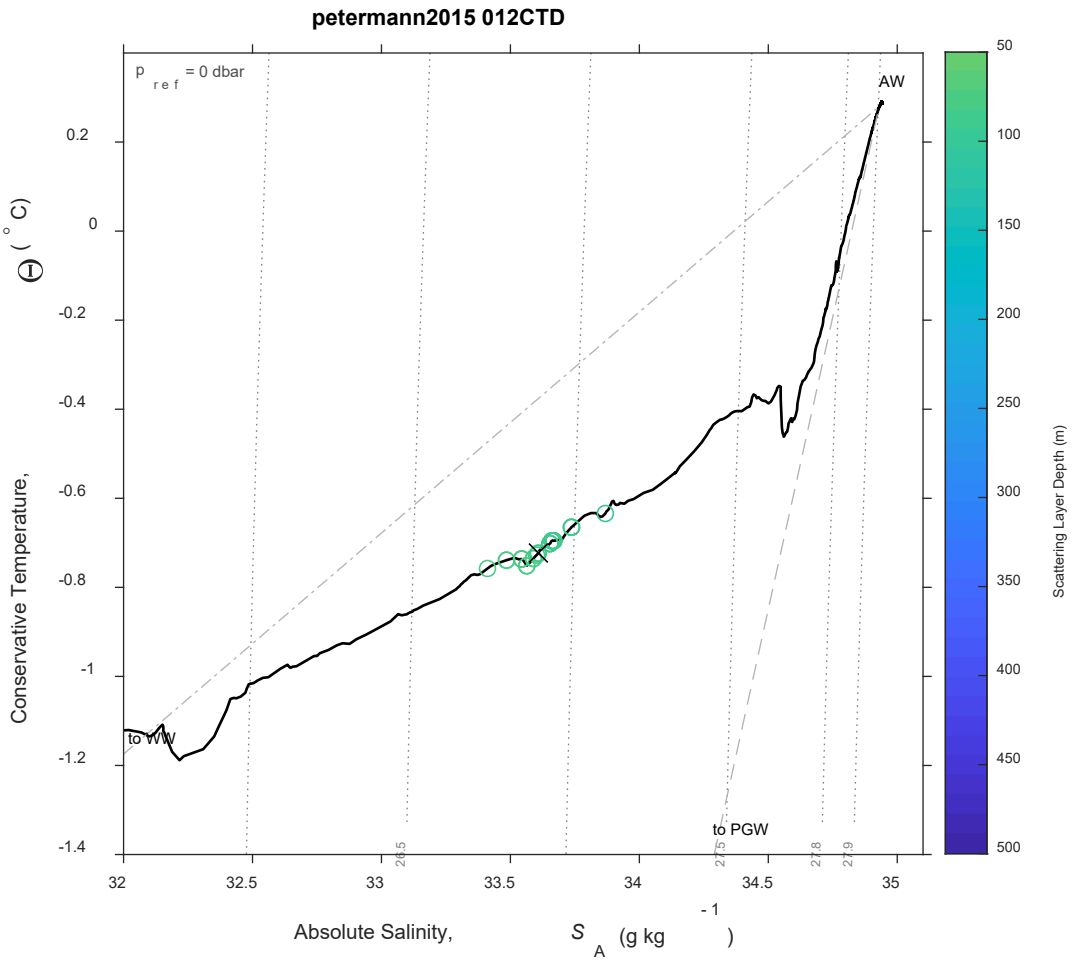

Figure 178: CTD 012, Temperature-Salinity (T-S) diagram. The scattering layer picks corresponding to this CTD are plotted as open circles colored by depth; a black 'X' indicates the average depth for the top of the scattering layer in this location. Isobars are shown as labeled grey dotted lines.

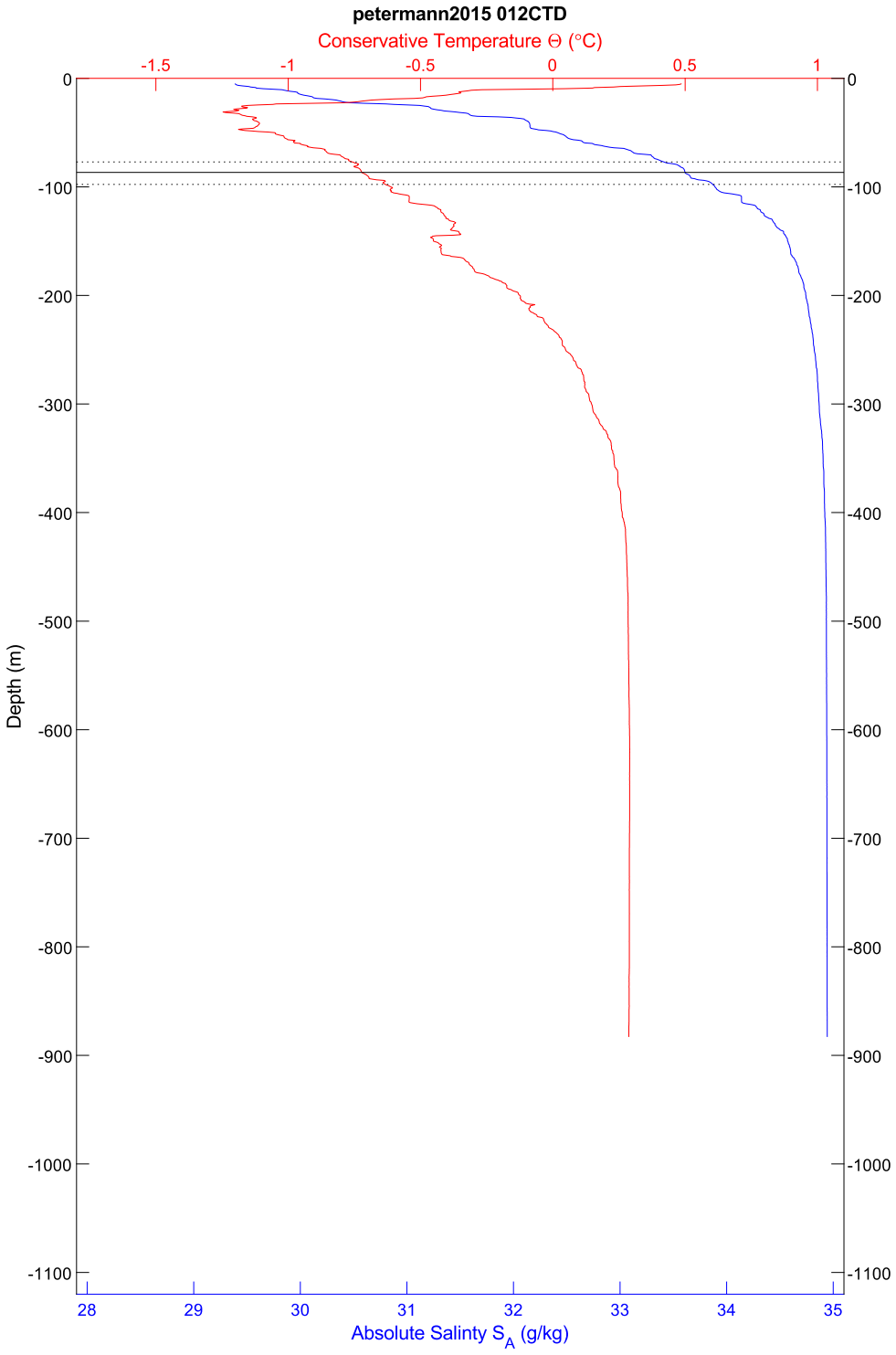

Figure 179: CTD 012, temperature and salinity plotted by depth. The scattering layer depth is indicated by horizontal lines; the solid line is the average depth, the dotted lines are the shallowest and deepest depths, in all cases for the top of the scattering layer.

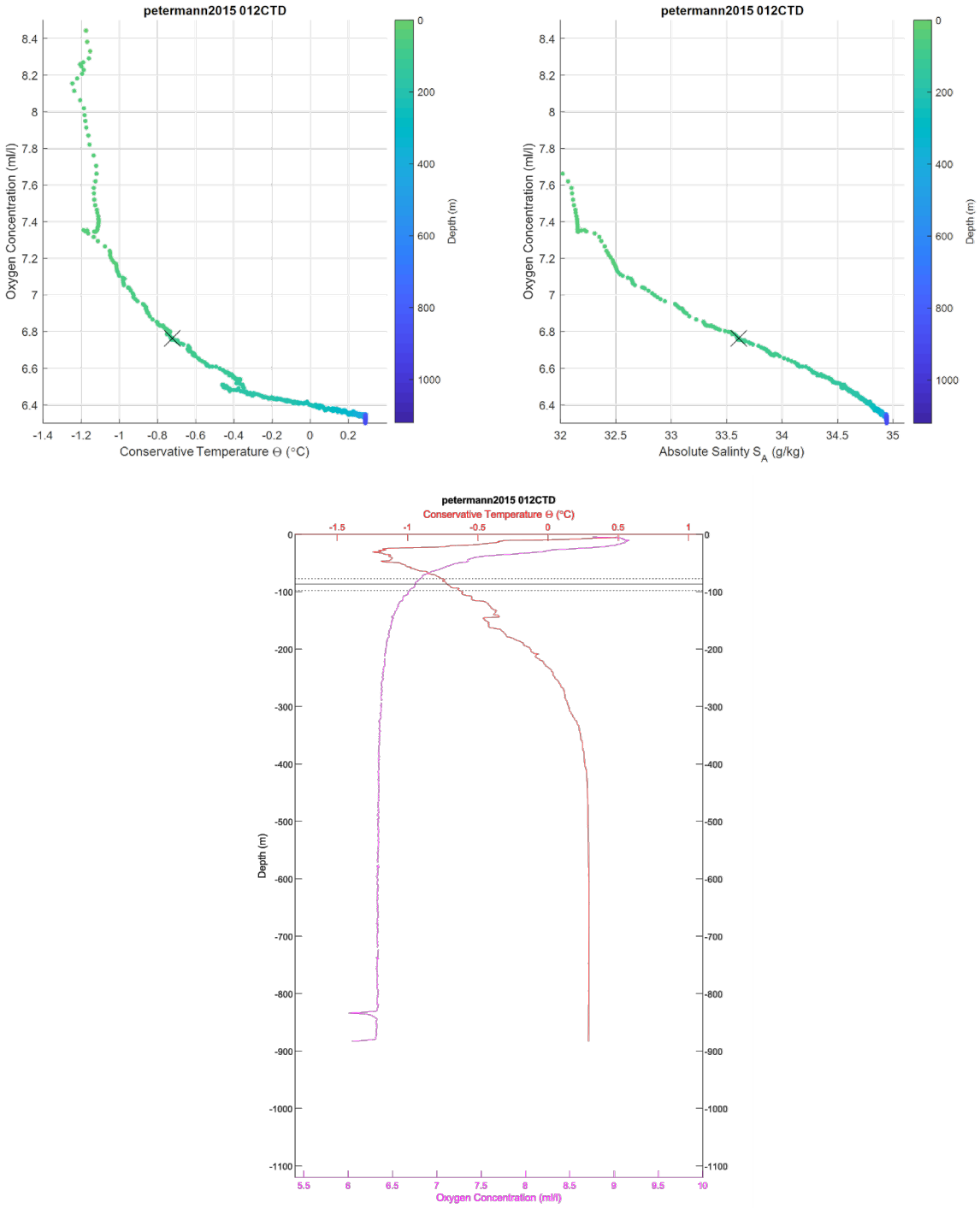

Figure 180: CTD 012. Top left, oxygen-temperature diagram, colored by depth. Top right, oxygen-salinity diagram, colored by depth. The black 'X' in the first two plots indicates the average depth for the top of the scattering layer in this location. Bottom center, temperature and oxygen plotted by depth. The scattering layer depth is indicated by horizontal lines; the solid line is the average depth, the dotted lines are the shallowest and deepest depths, in both cases for the top of the scattering layer. Note that oxygen values for this cast are considered questionable due to issues with the pump, which was replaced between cast 025 and 026.

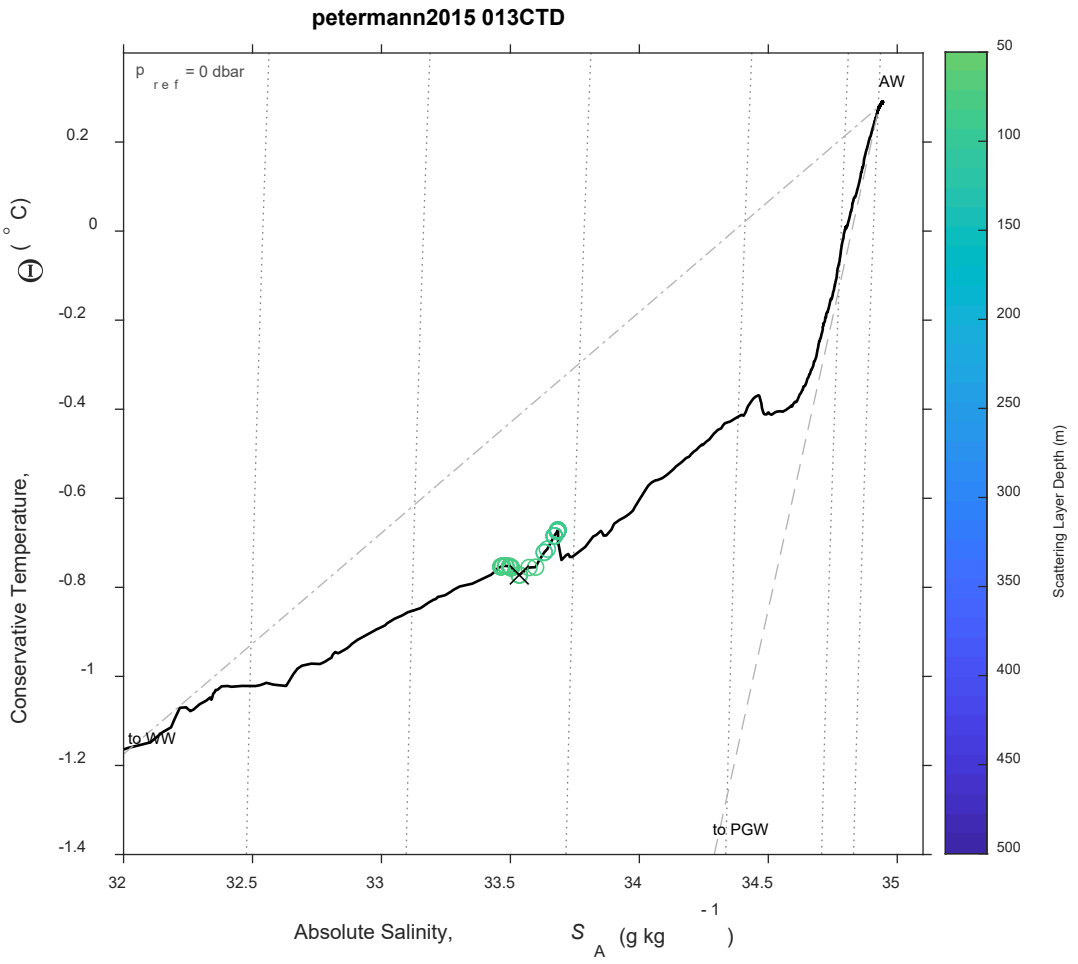

Figure 181: CTD 013, Temperature-Salinity (T-S) diagram. The scattering layer picks corresponding to this CTD are plotted as open circles colored by depth; a black 'X' indicates the average depth for the top of the scattering layer in this location. Isobars are shown as labeled grey dotted lines.

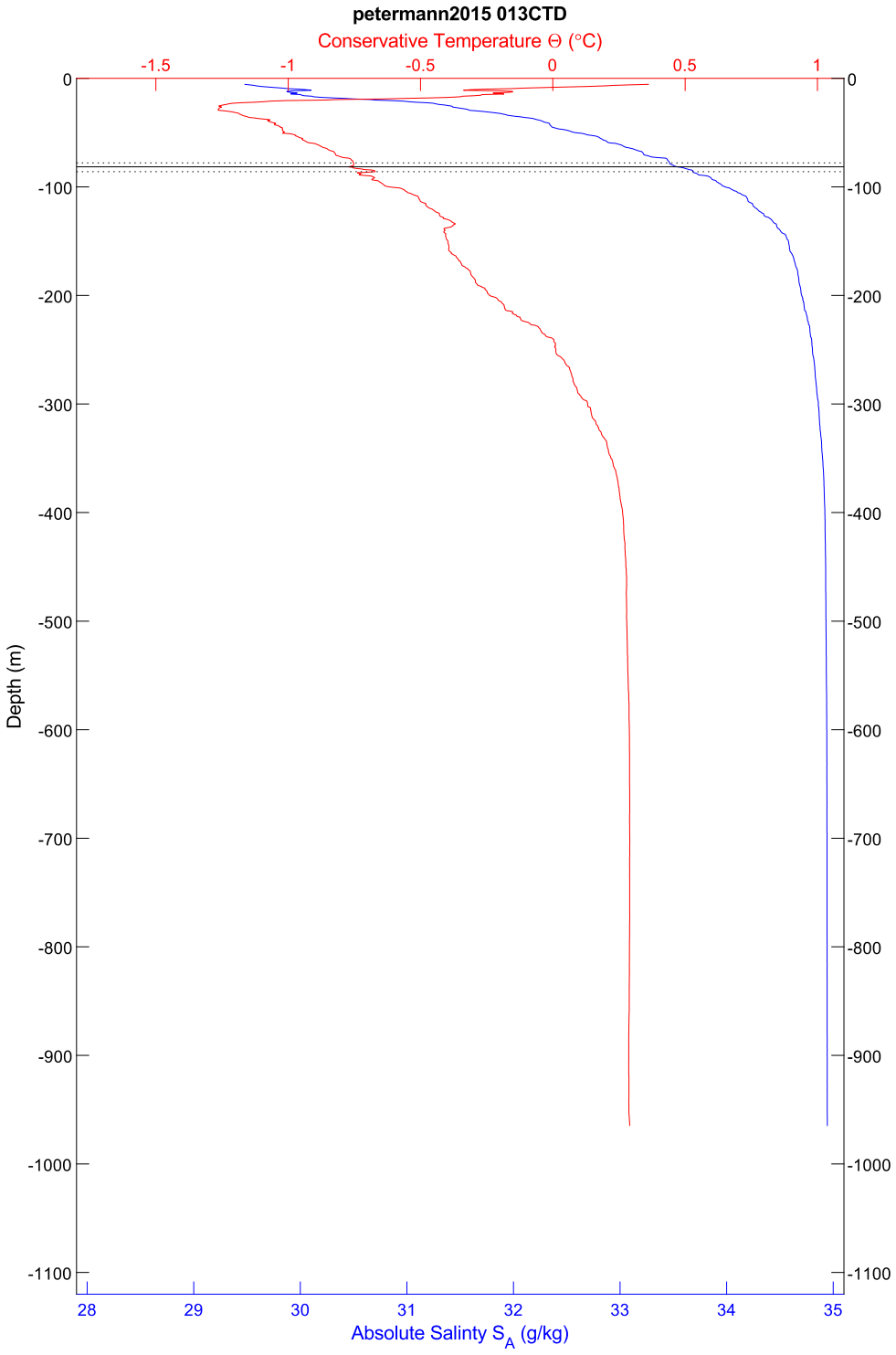

Figure 182: CTD 013, temperature and salinity plotted by depth. The scattering layer depth is indicated by horizontal lines; the solid line is the average depth, the dotted lines are the shallowest and deepest depths, in all cases for the top of the scattering layer.

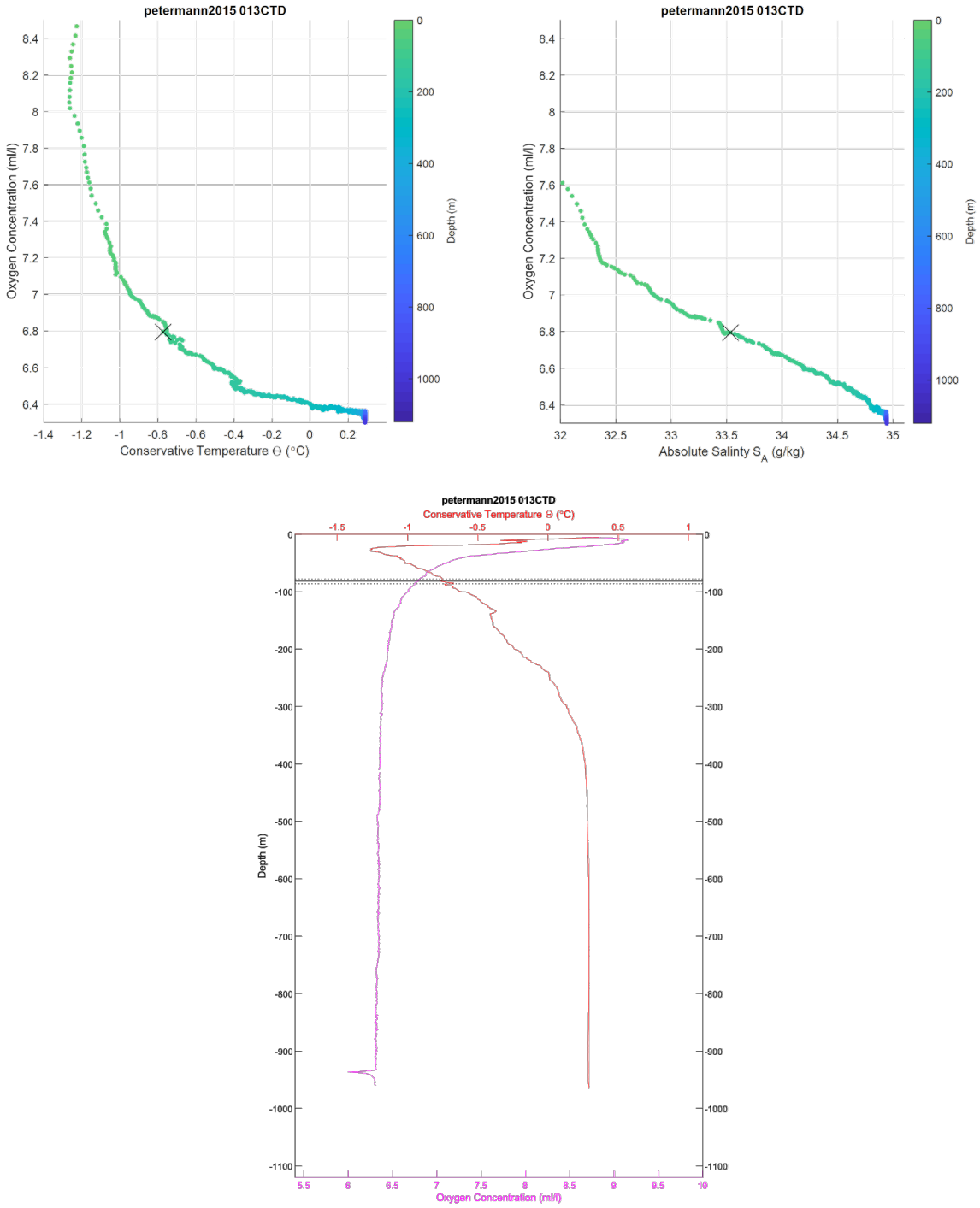

Figure 183: CTD 013. Top left, oxygen-temperature diagram, colored by depth. Top right, oxygen-salinity diagram, colored by depth. The black 'X' in the first two plots indicates the average depth for the top of the scattering layer in this location. Bottom center, temperature and oxygen plotted by depth. The scattering layer depth is indicated by horizontal lines; the solid line is the average depth, the dotted lines are the shallowest and deepest depths, in both cases for the top of the scattering layer. Note that oxygen values for this cast are considered questionable due to issues with the pump, which was replaced between cast 025 and 026.

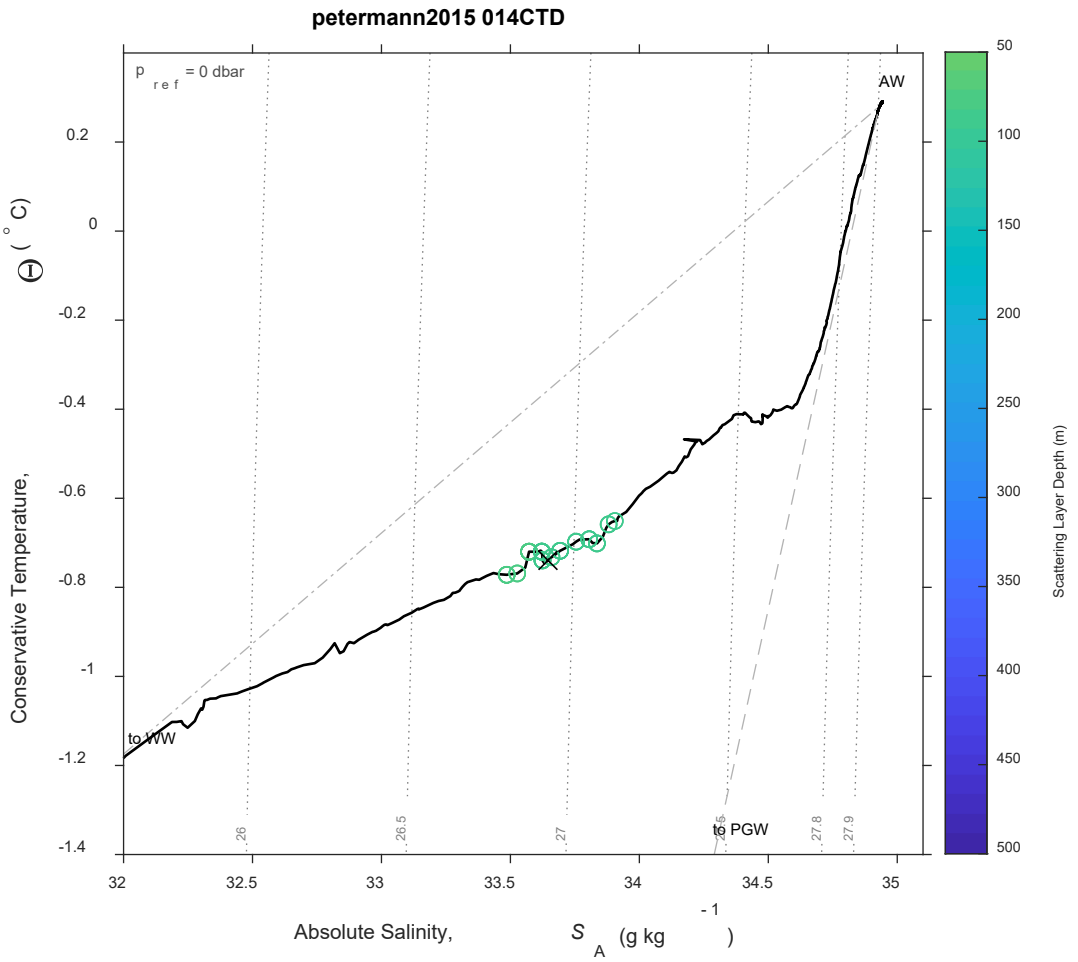

Figure 184: CTD 014, Temperature-Salinity (T-S) diagram. The scattering layer picks corresponding to this CTD are plotted as open circles colored by depth; a black 'X' indicates the average depth for the top of the scattering layer in this location. Isobars are shown as labeled grey dotted lines.

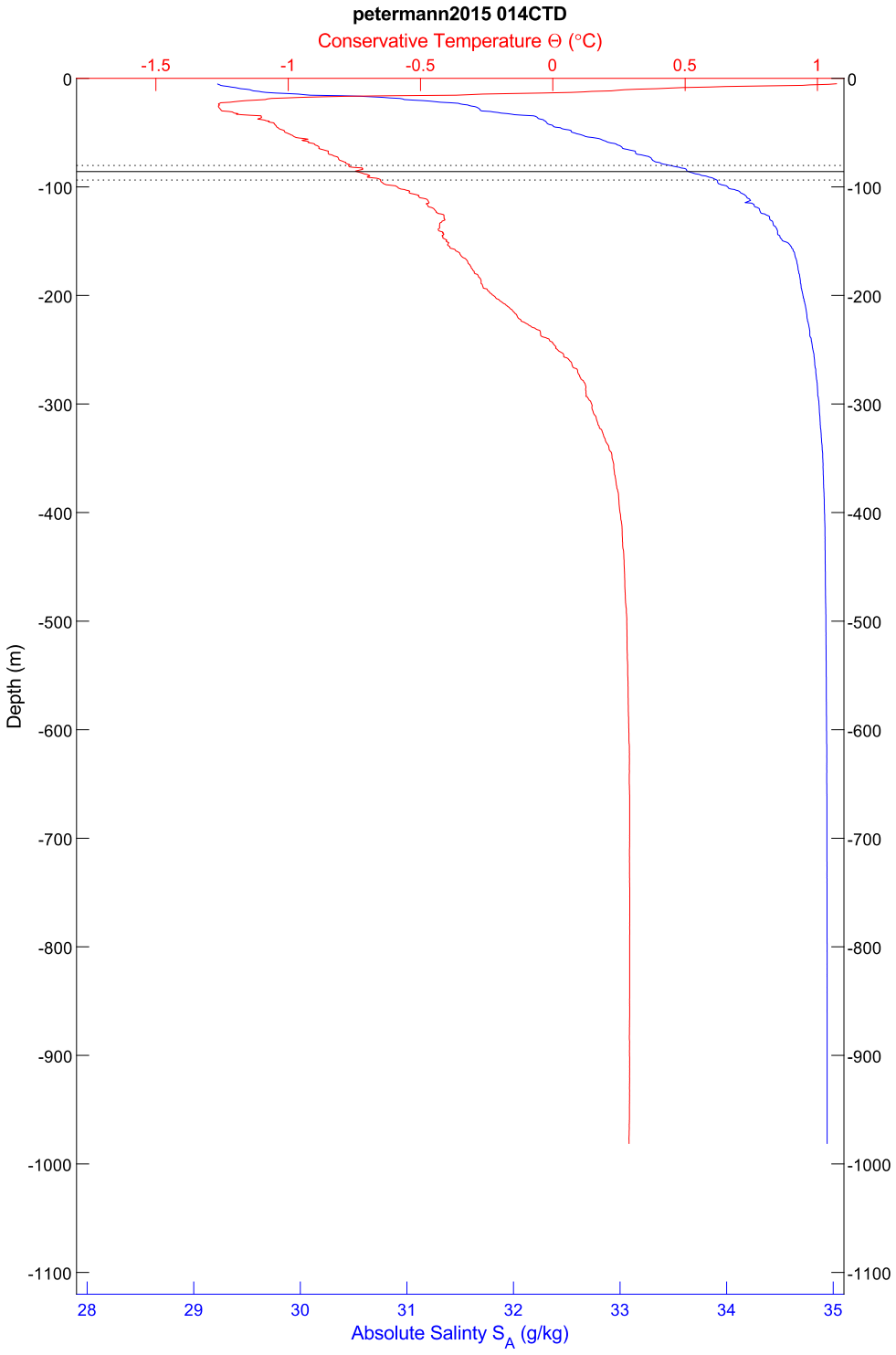

Figure 185: CTD 014, temperature and salinity plotted by depth. The scattering layer depth is indicated by horizontal lines; the solid line is the average depth, the dotted lines are the shallowest and deepest depths, in all cases for the top of the scattering layer.

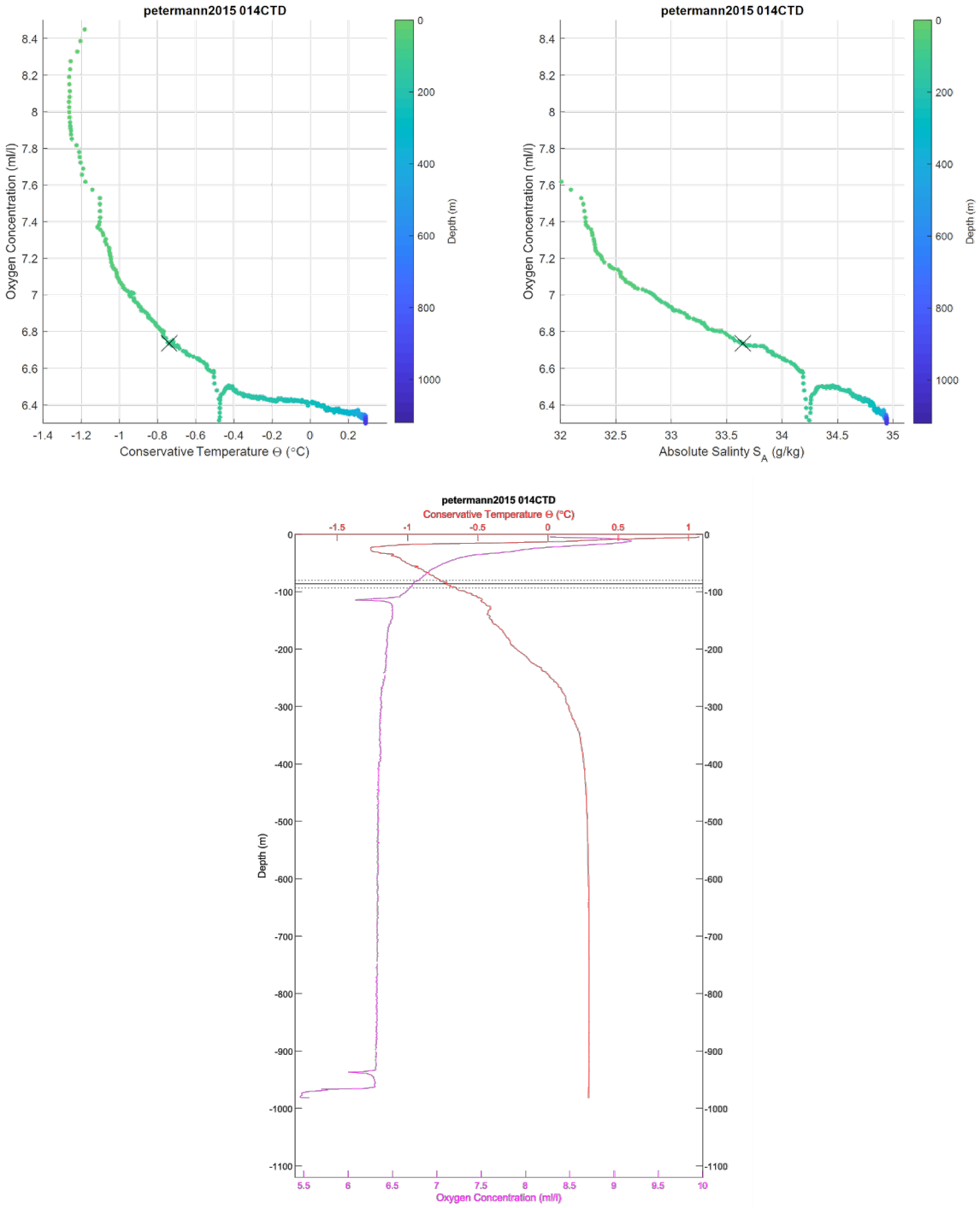

Figure 186: CTD 014. Top left, oxygen-temperature diagram, colored by depth. Top right, oxygen-salinity diagram, colored by depth. The black 'X' in the first two plots indicates the average depth for the top of the scattering layer in this location. Bottom center, temperature and oxygen plotted by depth. The scattering layer depth is indicated by horizontal lines; the solid line is the average depth, the dotted lines are the shallowest and deepest depths, in both cases for the top of the scattering layer. Note that oxygen values for this cast are considered questionable due to issues with the pump, which was replaced between cast 025 and 026.

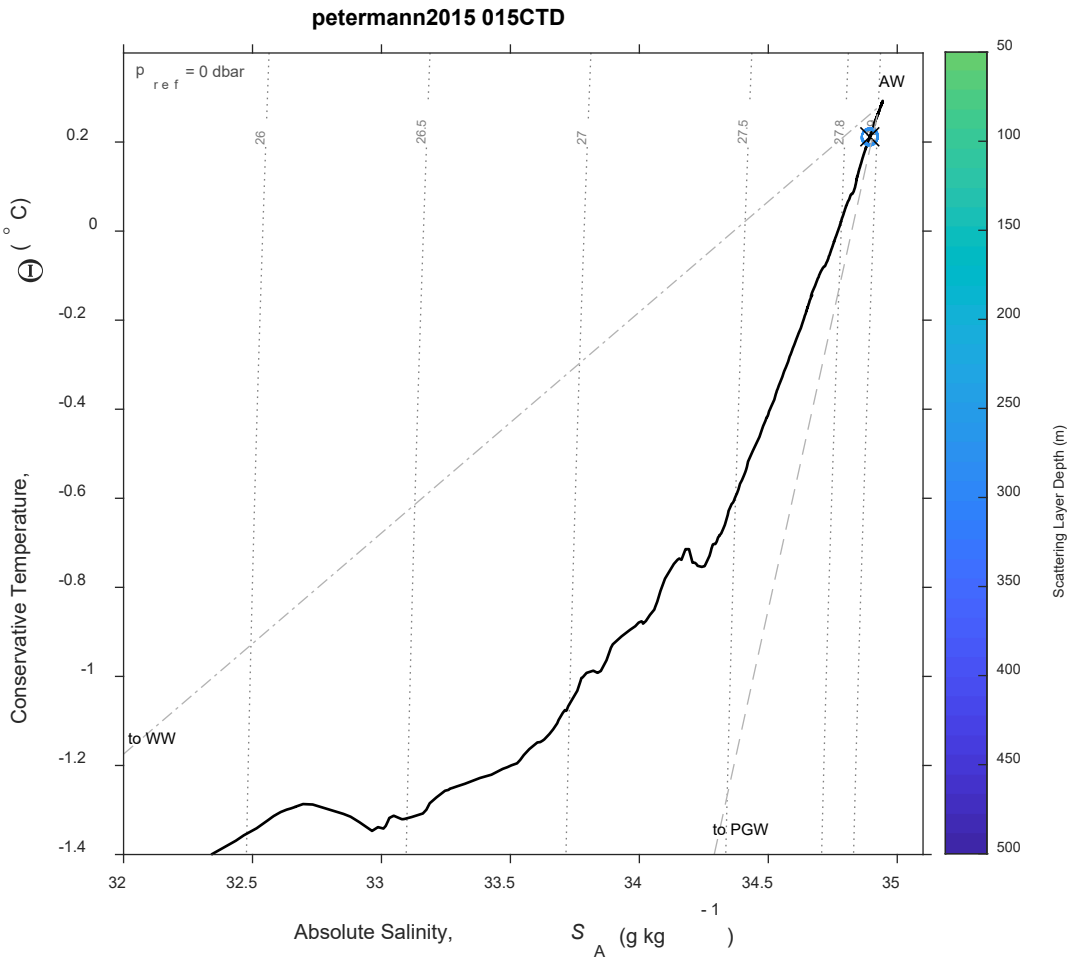

Figure 187: CTD 015, Temperature-Salinity (T-S) diagram. The scattering layer picks corresponding to this CTD are plotted as open circles colored by depth; a black 'X' indicates the average depth for the top of the scattering layer in this location. Isobars are shown as labeled grey dotted lines.

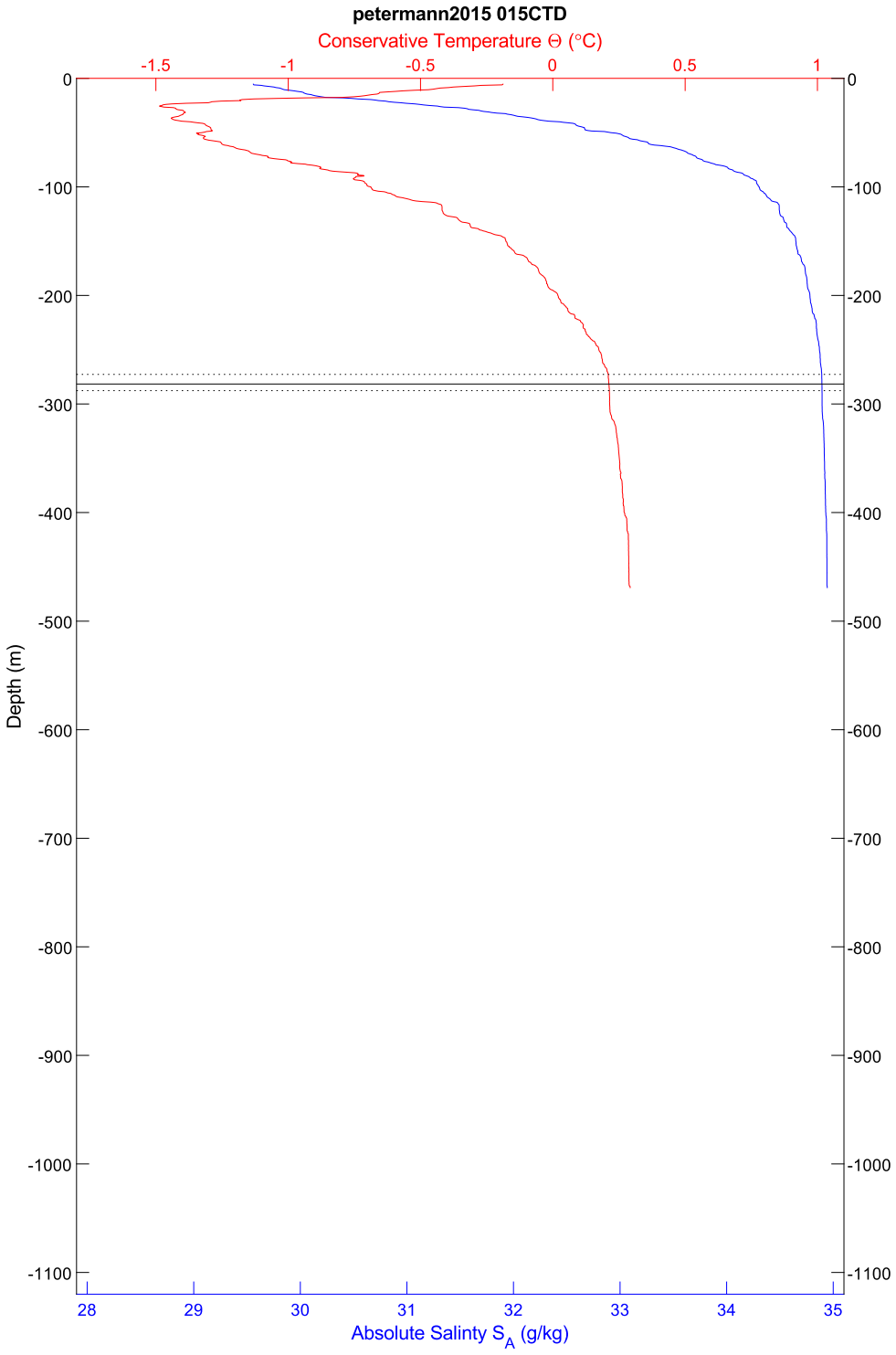

Figure 188: CTD 015, temperature and salinity plotted by depth. The scattering layer depth is indicated by horizontal lines; the solid line is the average depth, the dotted lines are the shallowest and deepest depths, in all cases for the top of the scattering layer.

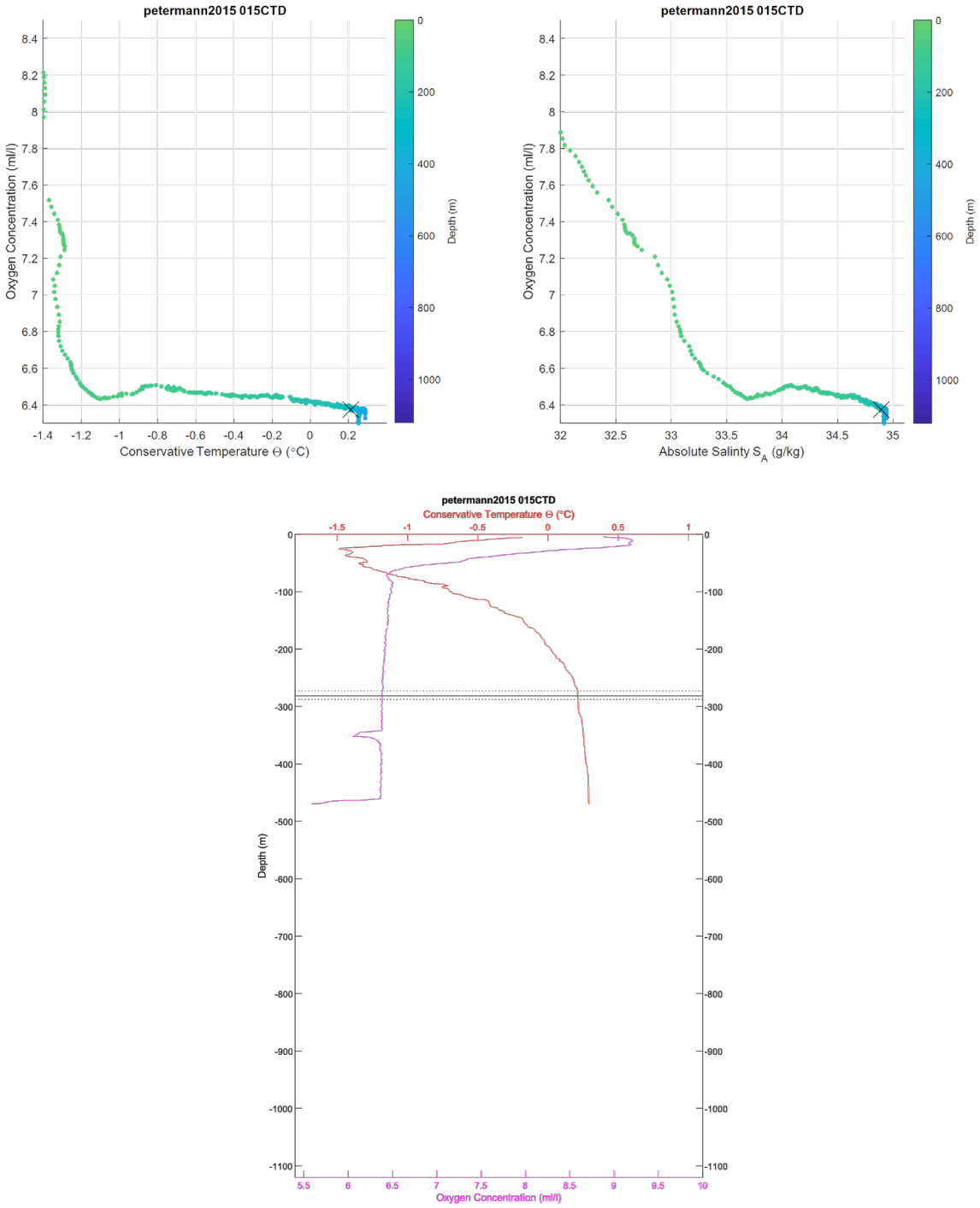

Figure 189: CTD 015. Top left, oxygen-temperature diagram, colored by depth. Top right, oxygen-salinity diagram, colored by depth. The black 'X' in the first two plots indicates the average depth for the top of the scattering layer in this location. Bottom center, temperature and oxygen plotted by depth. The scattering layer depth is indicated by horizontal lines; the solid line is the average depth, the dotted lines are the shallowest and deepest depths, in both cases for the top of the scattering layer. Note that oxygen values for this cast are considered questionable due to issues with the pump, which was replaced between cast 025 and 026

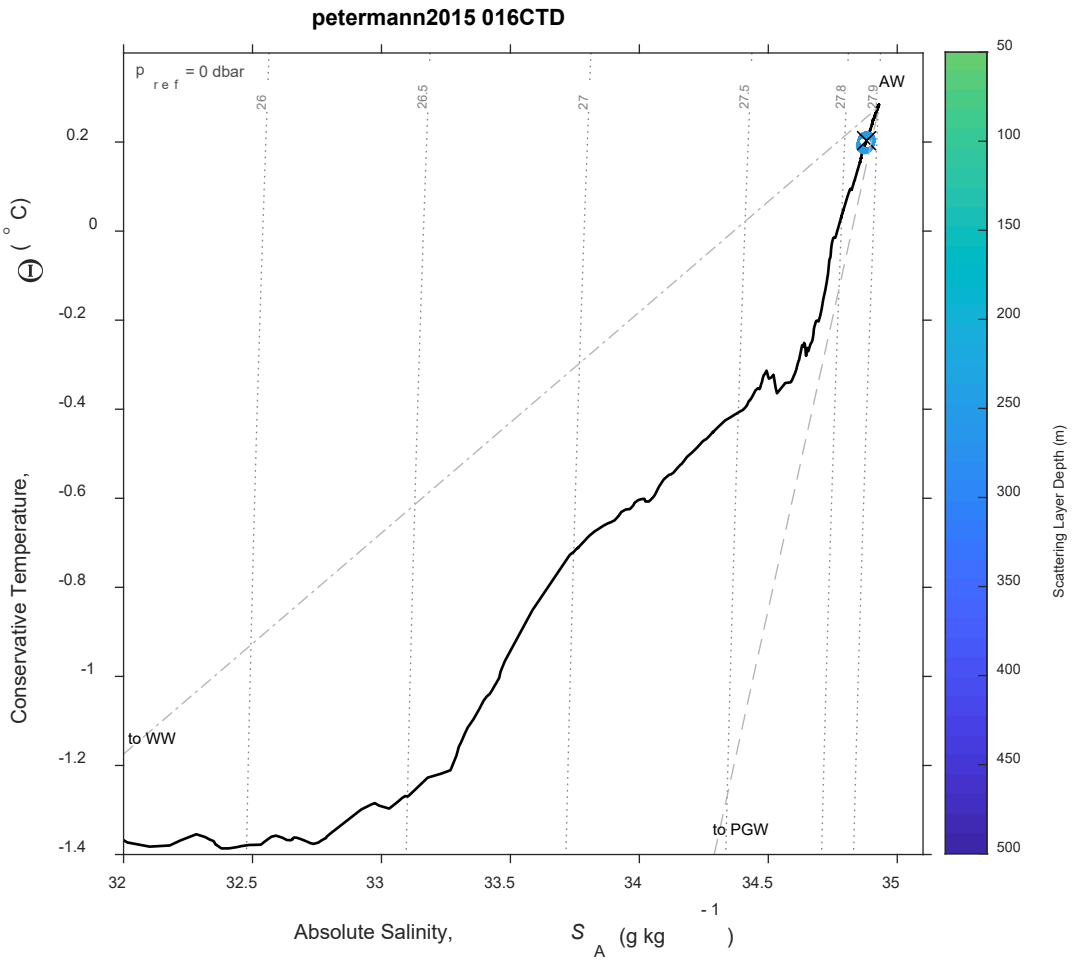

Figure 190: CTD 016, Temperature-Salinity (T-S) diagram. The scattering layer picks corresponding to this CTD are plotted as open circles colored by depth; a black 'X' indicates the average depth for the top of the scattering layer in this location. Isobars are shown as labeled grey dotted lines.

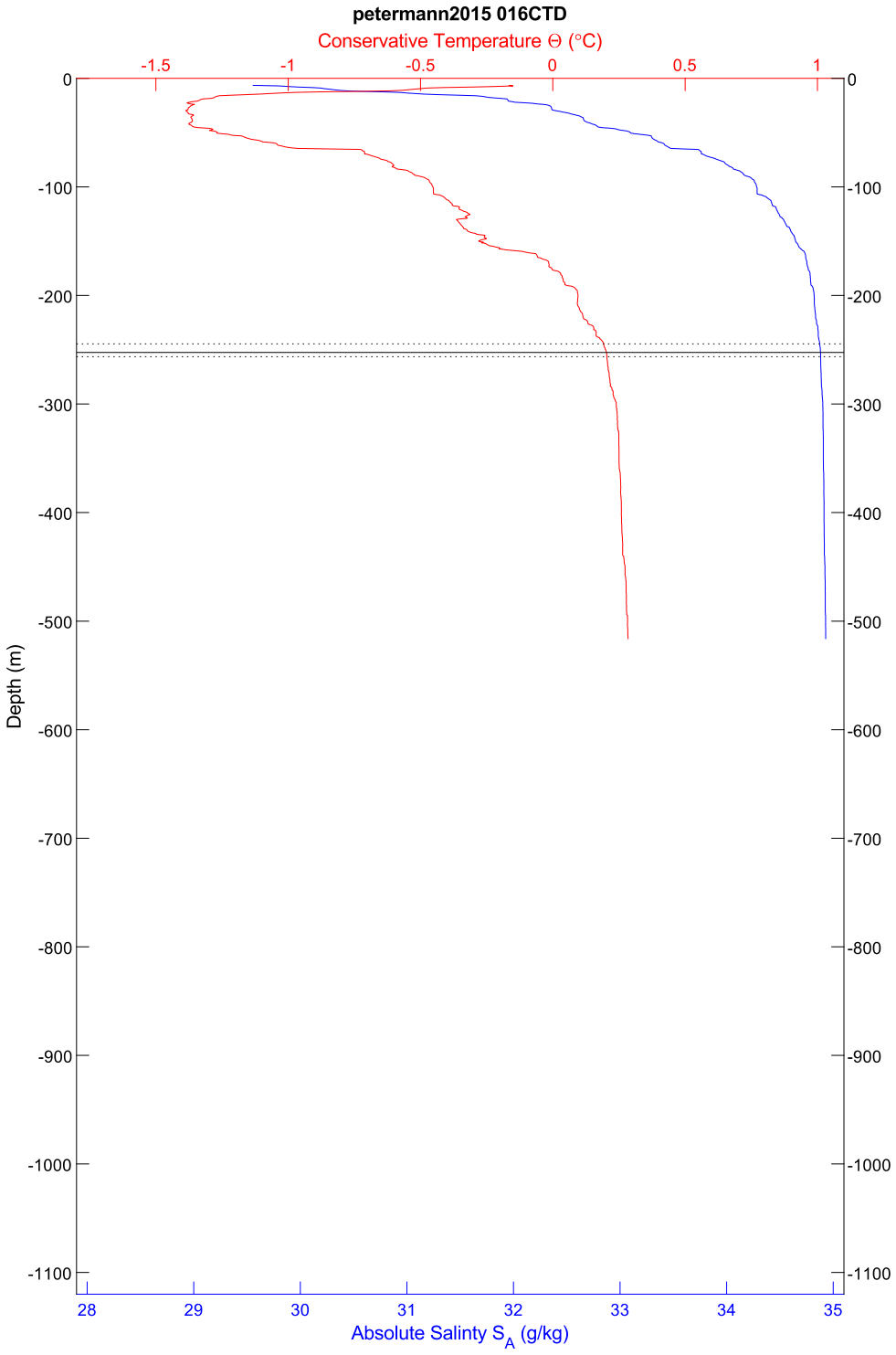

Figure 191: CTD 016, temperature and salinity plotted by depth. The scattering layer depth is indicated by horizontal lines; the solid line is the average depth, the dotted lines are the shallowest and deepest depths, in all cases for the top of the scattering layer.

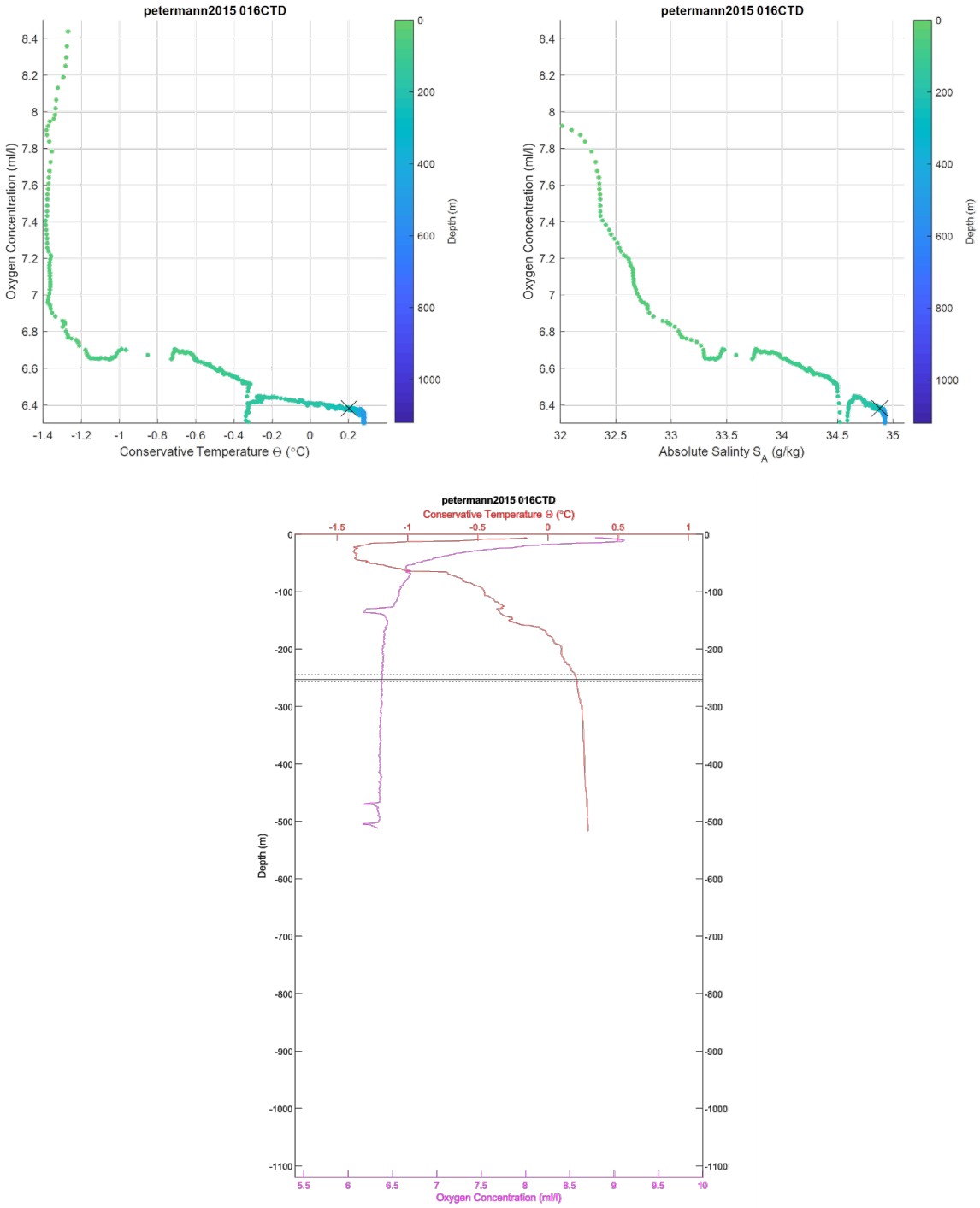

Figure 192: CTD 016. Top left, oxygen-temperature diagram, colored by depth. Top right, oxygen-salinity diagram, colored by depth. The black 'X' in the first two plots indicates the average depth for the top of the scattering layer in this location. Bottom center, temperature and oxygen plotted by depth. The scattering layer depth is indicated by horizontal lines; the solid line is the average depth, the dotted lines are the shallowest and deepest depths, in both cases for the top of the scattering layer. Note that oxygen values for this cast are considered questionable due to issues with the pump, which was replaced between cast 025 and 026.

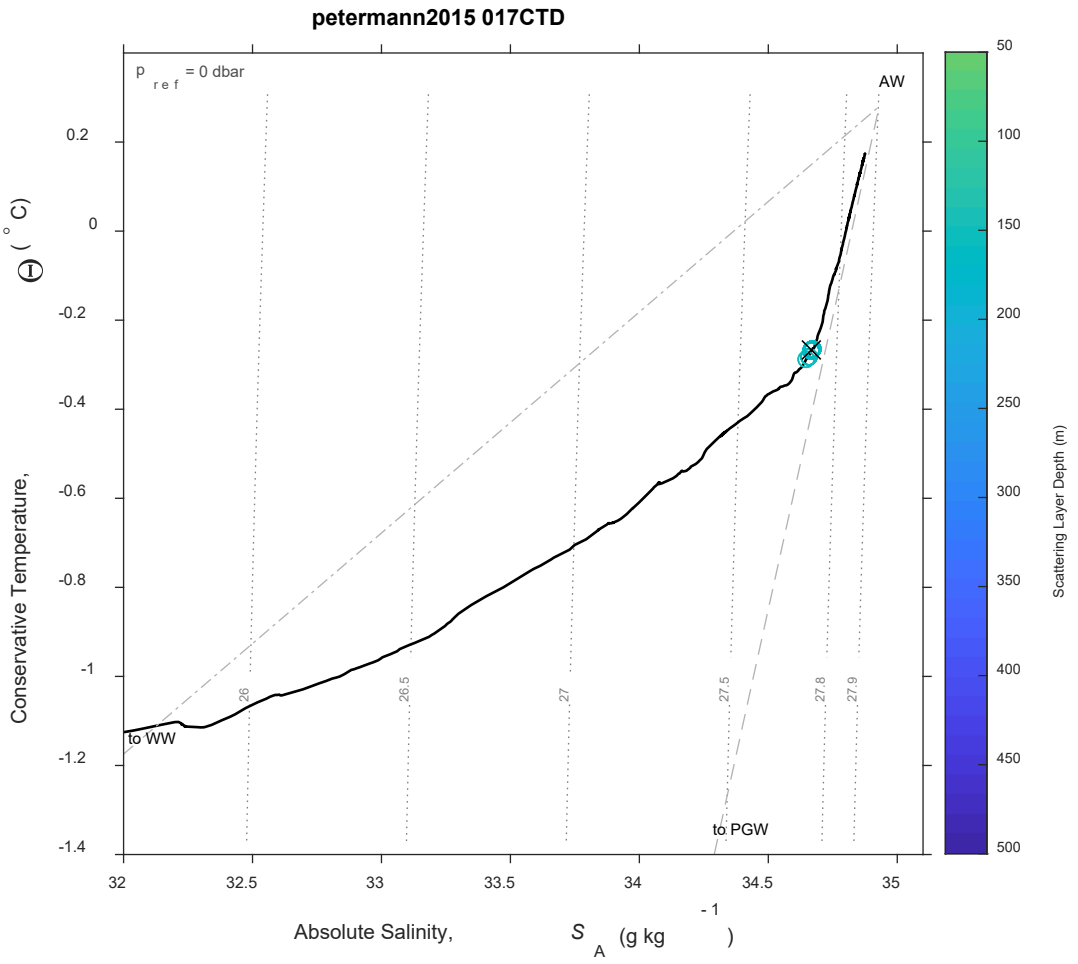

Figure 193: CTD 017, Temperature-Salinity (T-S) diagram. The scattering layer picks corresponding to this CTD are plotted as open circles colored by depth; a black 'X' indicates the average depth for the top of the scattering layer in this location. Isobars are shown as labeled grey dotted lines.

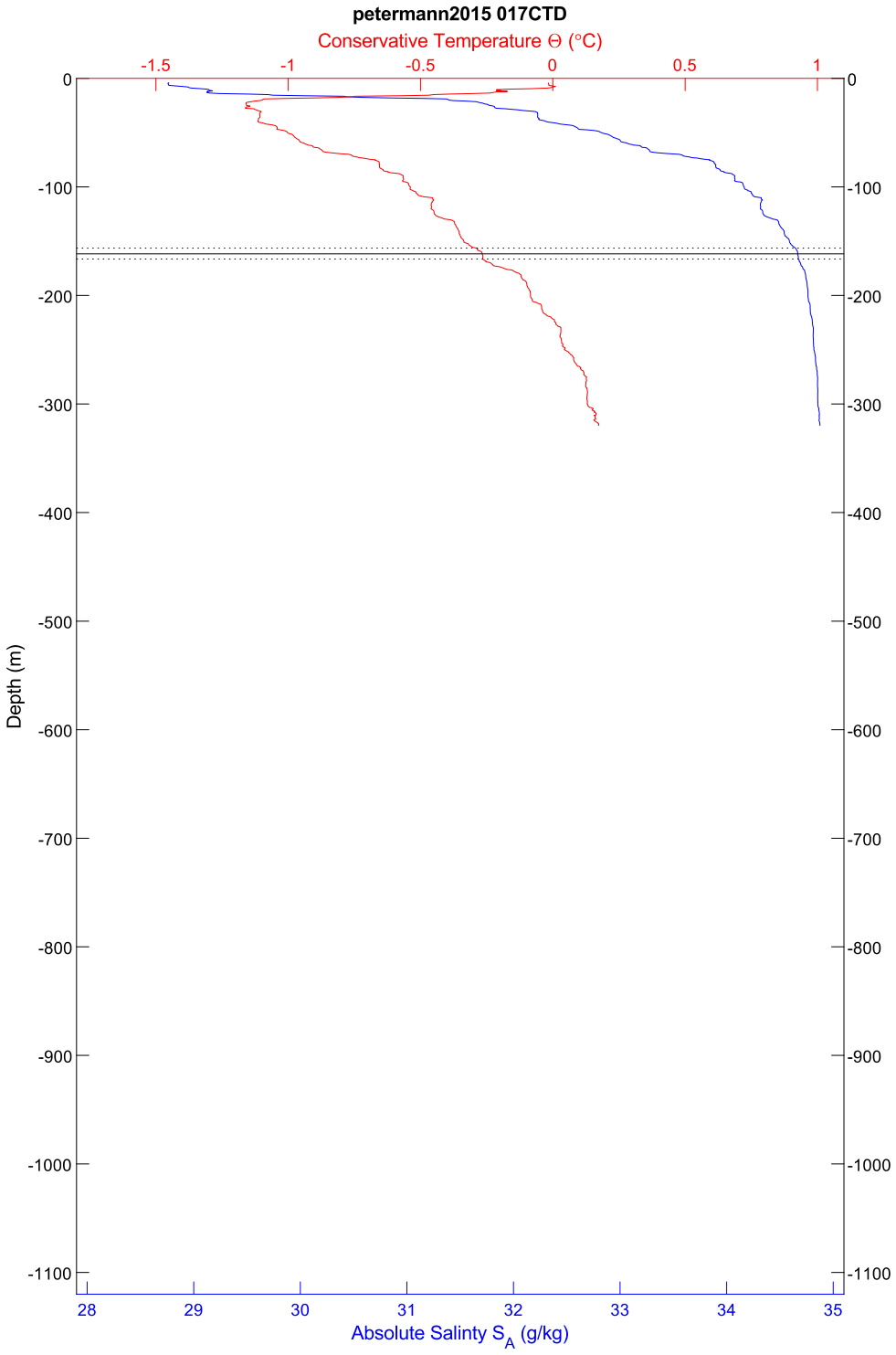

Figure 194: CTD 017, temperature and salinity plotted by depth. The scattering layer depth is indicated by horizontal lines; the solid line is the average depth, the dotted lines are the shallowest and deepest depths, in all cases for the top of the scattering layer.

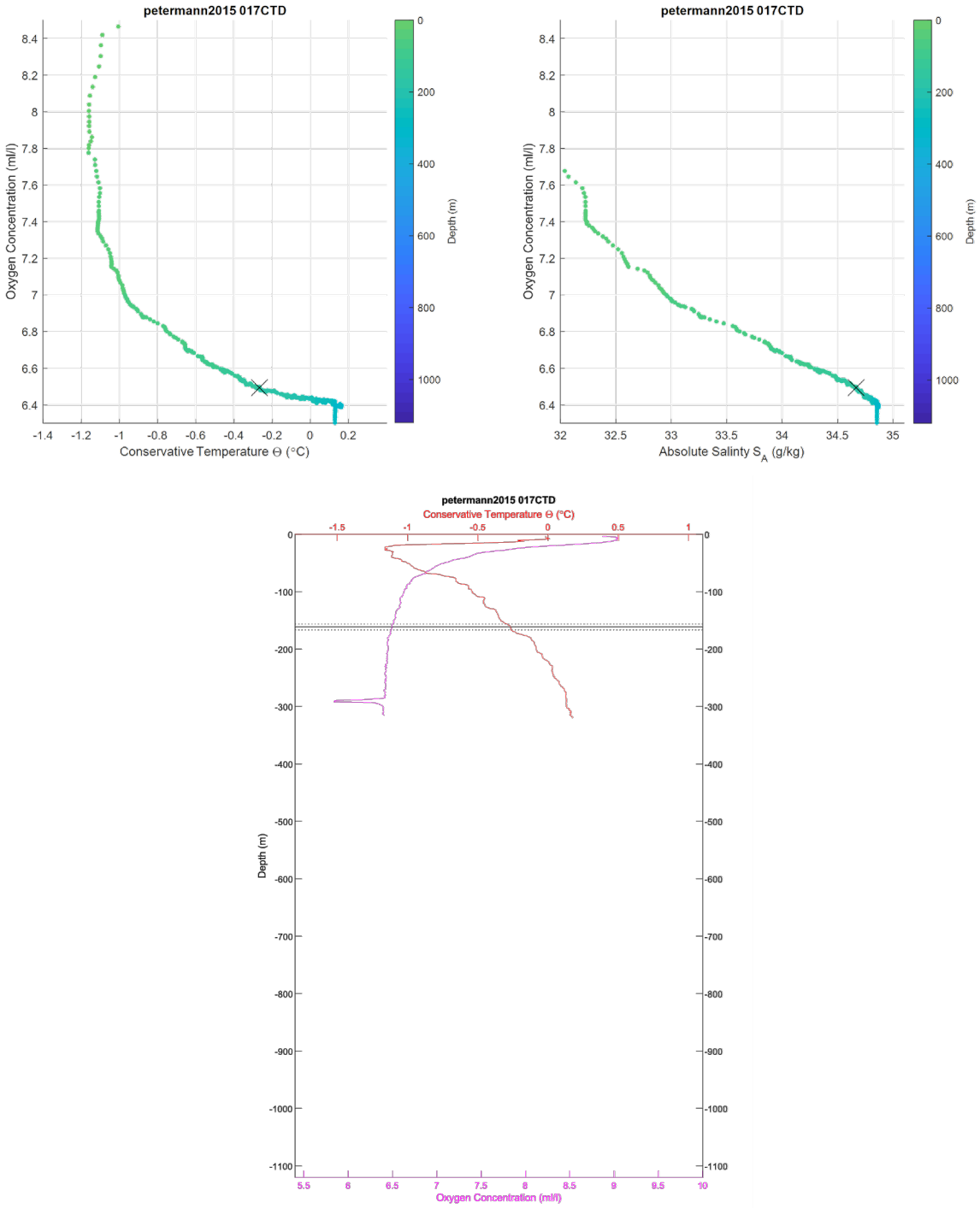

Figure 195: CTD 017. Top left, oxygen-temperature diagram, colored by depth. Top right, oxygen-salinity diagram, colored by depth. The black 'X' in the first two plots indicates the average depth for the top of the scattering layer in this location. Bottom center, temperature and oxygen plotted by depth. The scattering layer depth is indicated by horizontal lines; the solid line is the average depth, the dotted lines are the shallowest and deepest depths, in both cases for the top of the scattering layer. Note that oxygen values for this cast are considered questionable due to issues with the pump, which was replaced between cast 025 and 026.

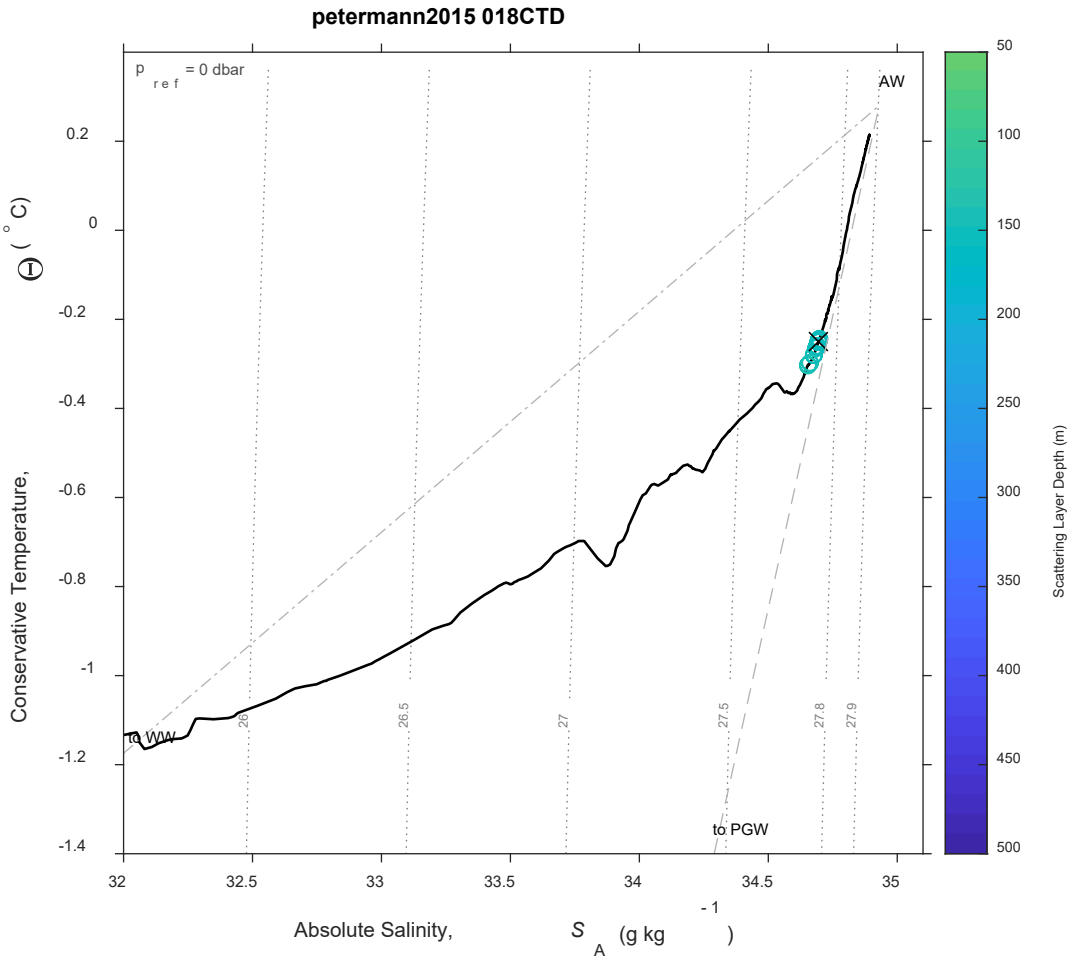

Figure 196: CTD 018, Temperature-Salinity (T-S) diagram. The scattering layer picks corresponding to this CTD are plotted as open circles colored by depth; a black 'X' indicates the average depth for the top of the scattering layer in this location. Isobars are shown as labeled grey dotted lines.

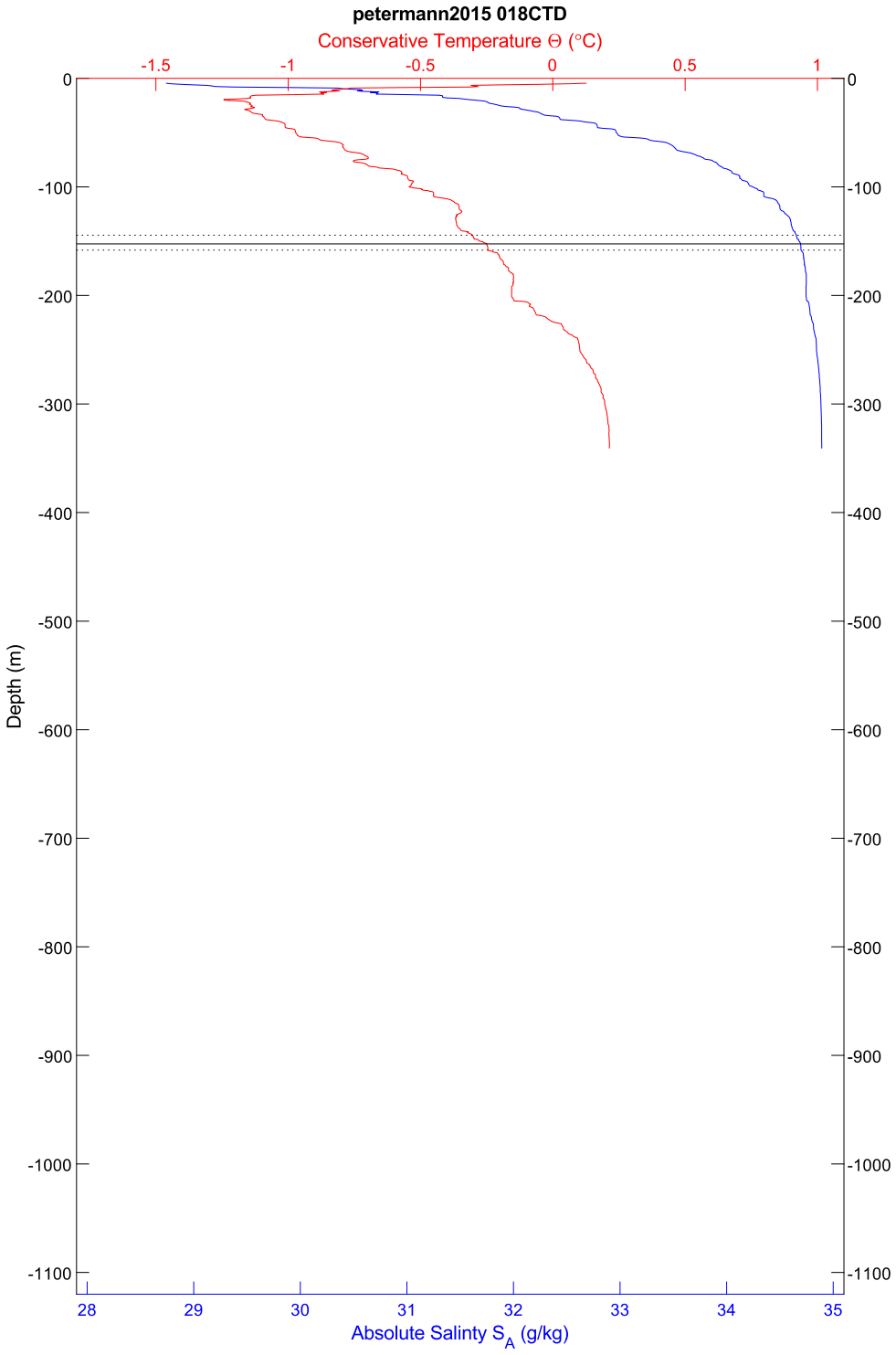

Figure 197: CTD 018, temperature and salinity plotted by depth. The scattering layer depth is indicated by horizontal lines; the solid line is the average depth, the dotted lines are the shallowest and deepest depths, in all cases for the top of the scattering layer.

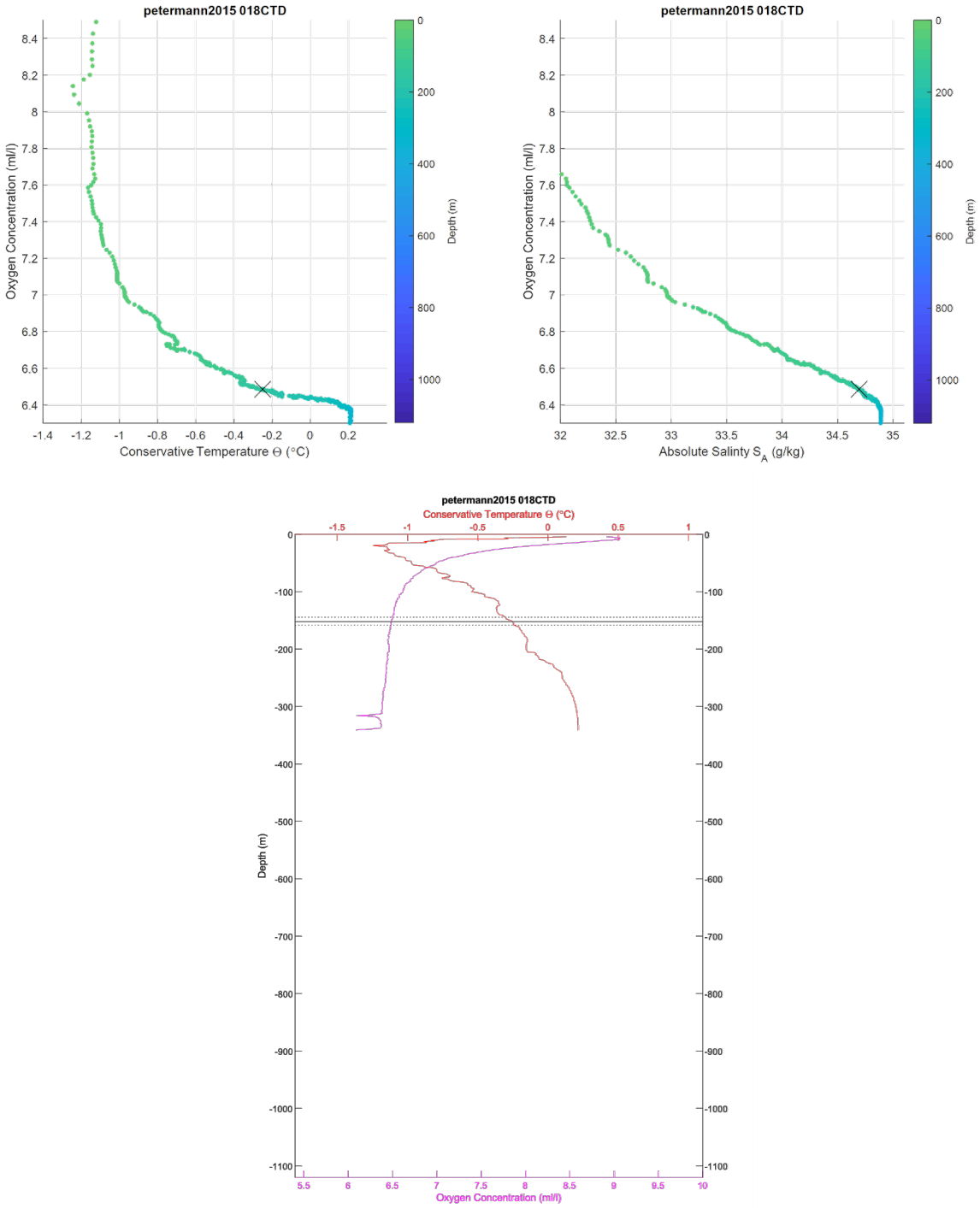

Figure 198: CTD 018. Top left, oxygen-temperature diagram, colored by depth. Top right, oxygen-salinity diagram, colored by depth. The black 'X' in the first two plots indicates the average depth for the top of the scattering layer in this location. Bottom center, temperature and oxygen plotted by depth. The scattering layer depth is indicated by horizontal lines; the solid line is the average depth, the dotted lines are the shallowest and deepest depths, in both cases for the top of the scattering layer. Note that oxygen values for this cast are considered questionable due to issues with the pump, which was replaced between cast 025 and 026.

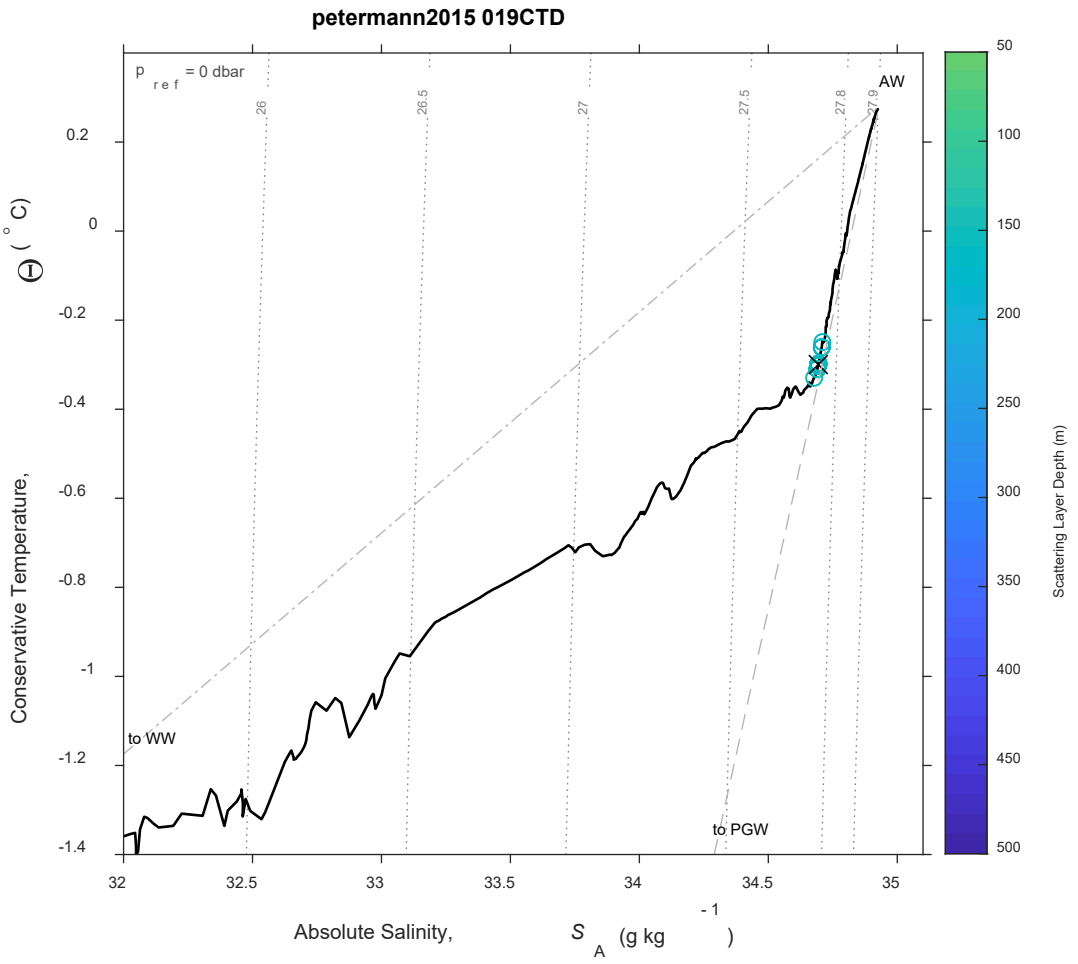

Figure 199: CTD 019, Temperature-Salinity (T-S) diagram. The scattering layer picks corresponding to this CTD are plotted as open circles colored by depth; a black 'X' indicates the average depth for the top of the scattering layer in this location. Isobars are shown as labeled grey dotted lines.

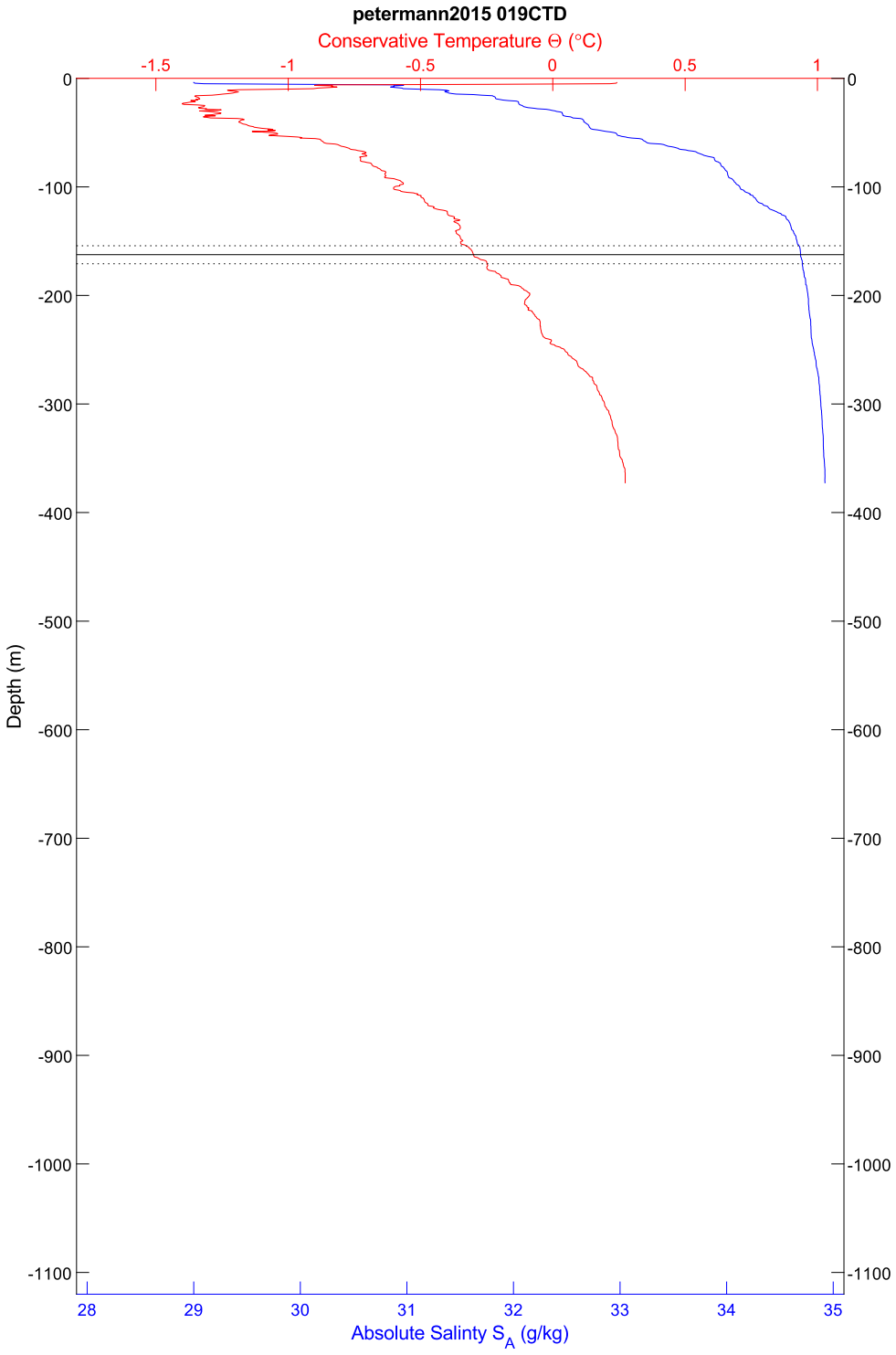

Figure 200: CTD 019, temperature and salinity plotted by depth. The scattering layer depth is indicated by horizontal lines; the solid line is the average depth, the dotted lines are the shallowest and deepest depths, in all cases for the top of the scattering layer.

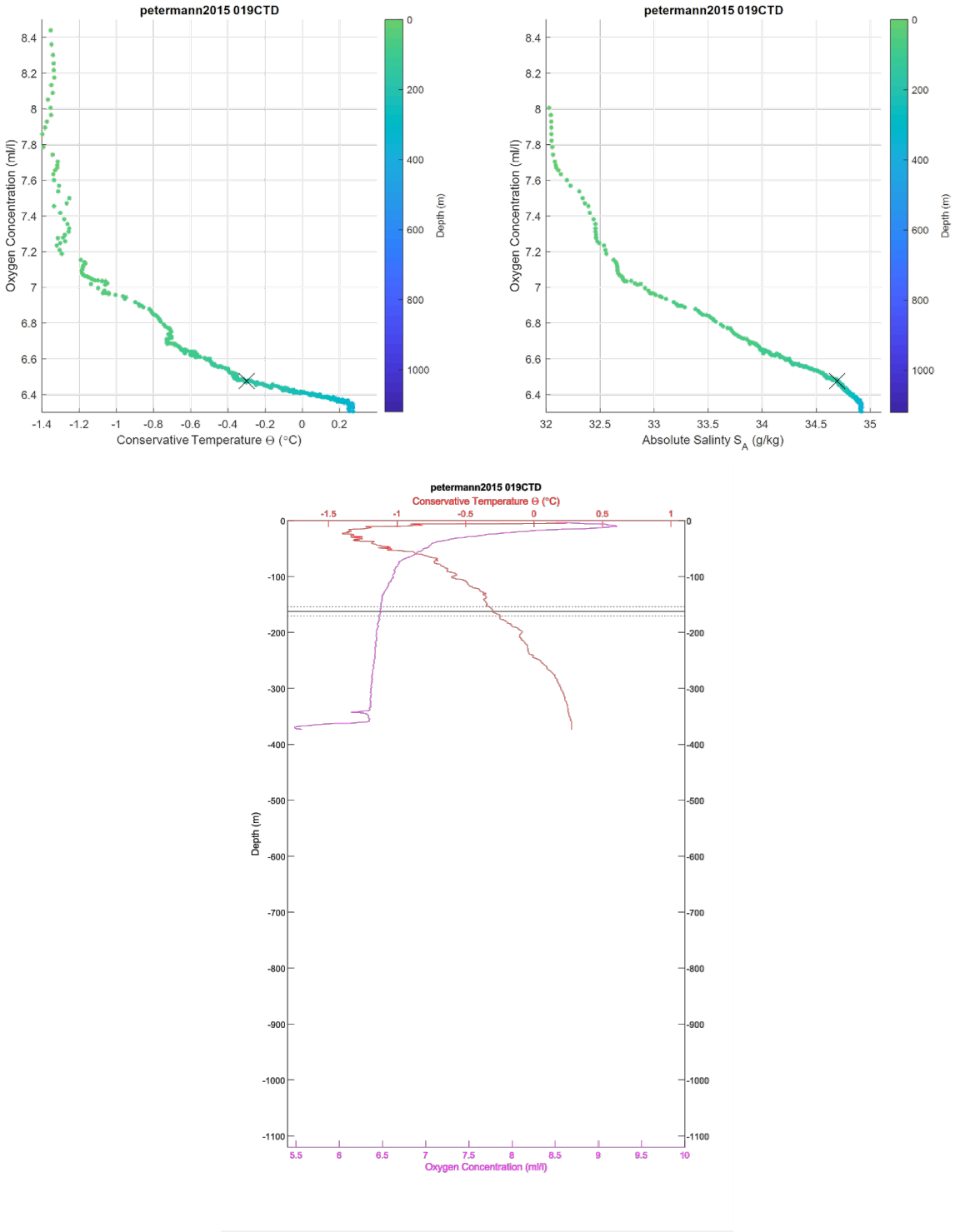

Figure 201: CTD 019. Top left, oxygen-temperature diagram, colored by depth. Top right, oxygen-salinity diagram, colored by depth. The black 'X' in the first two plots indicates the average depth for the top of the scattering layer in this location. Bottom center, temperature and oxygen plotted by depth. The scattering layer depth is indicated by horizontal lines; the solid line is the average depth, the dotted lines are the shallowest and deepest depths, in both cases for the top of the scattering layer. Note that oxygen values for this cast are considered questionable due to issues with the pump, which was replaced between cast 025 and 026.

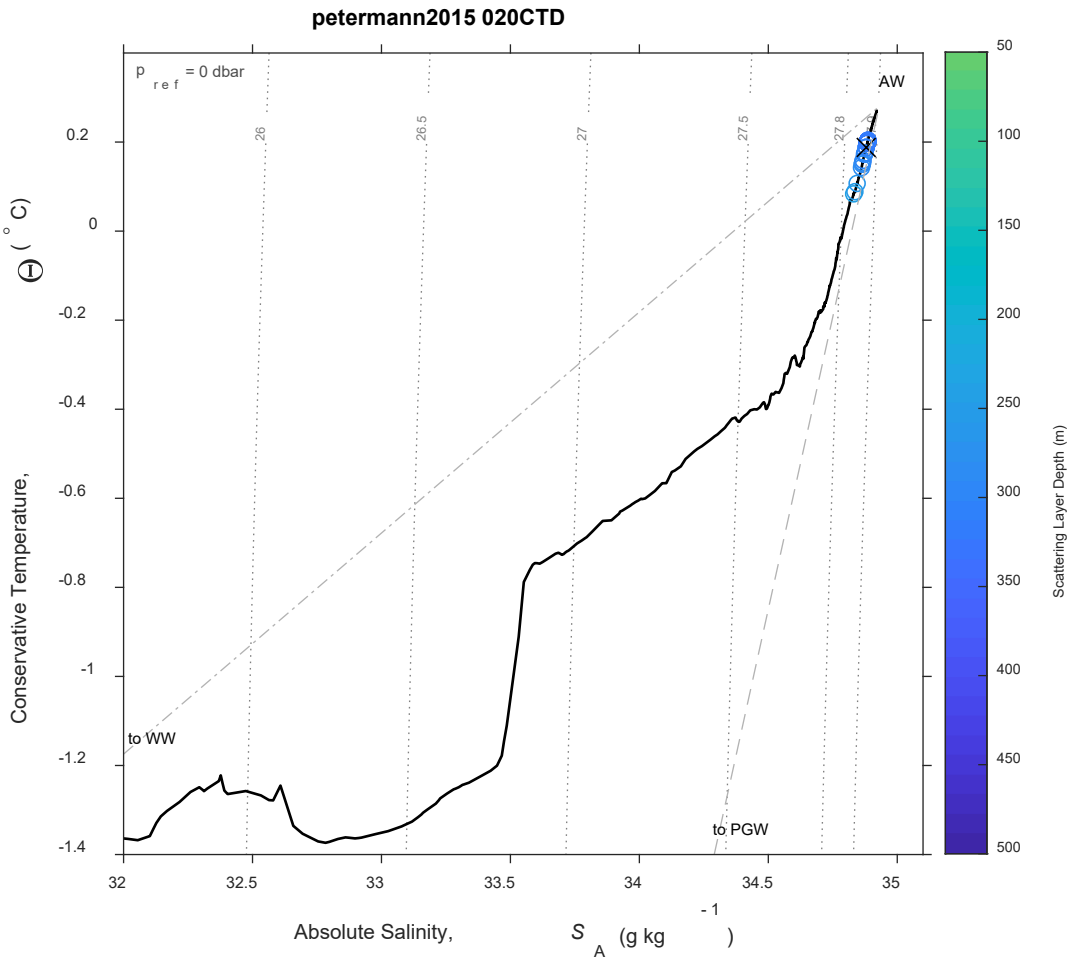

Figure 202: CTD 020, Temperature-Salinity (T-S) diagram. The scattering layer picks corresponding to this CTD are plotted as open circles colored by depth; a black 'X' indicates the average depth for the top of the scattering layer in this location. Isobars are shown as labeled grey dotted lines.

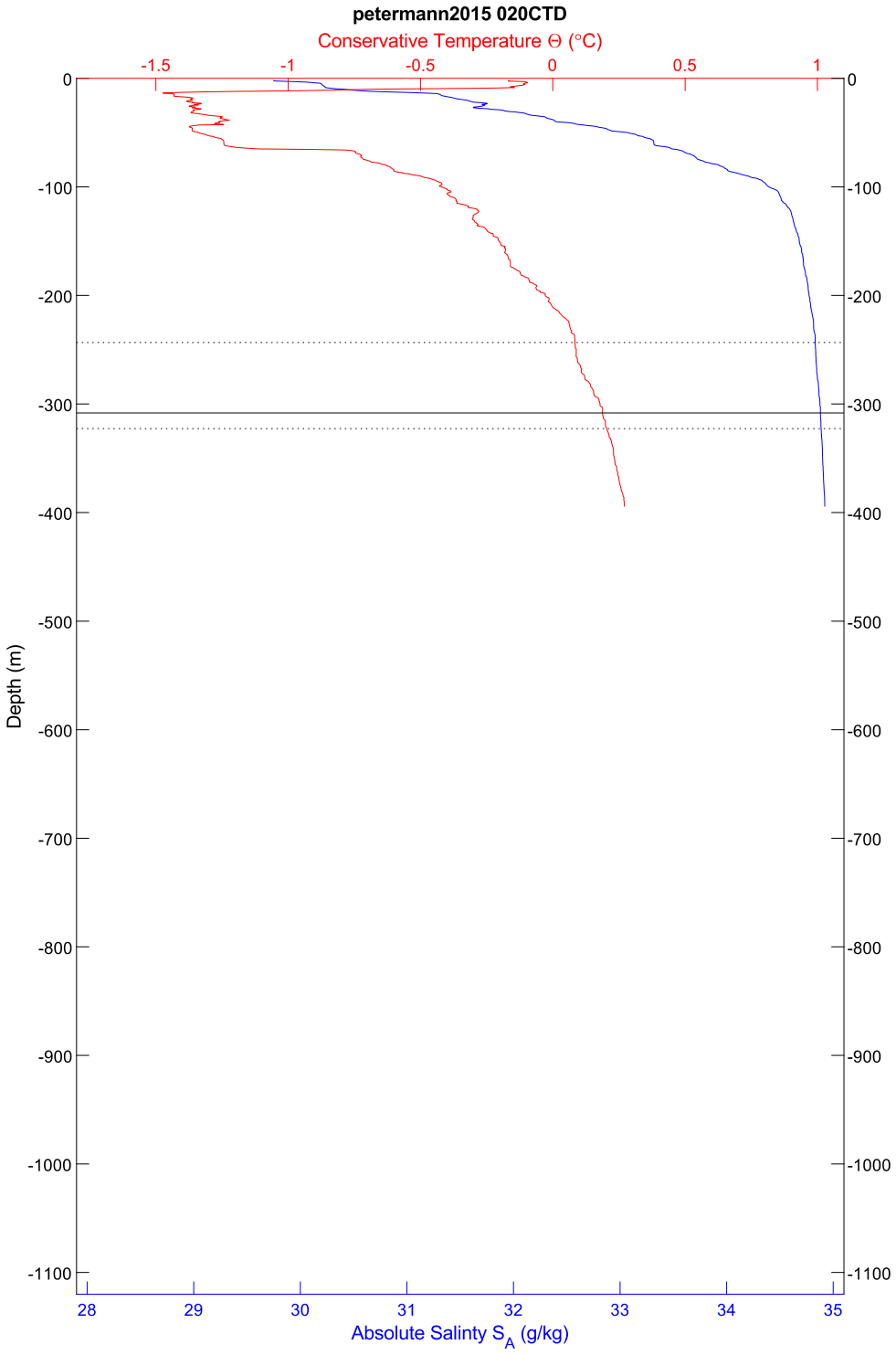

Figure 203: CTD020, temperature and salinity plotted by depth. The scattering layer depth is indicated by horizontal lines; the solid line is the average depth, the dotted lines are the shallowest and deepest depths, in all cases for the top of the scattering layer.

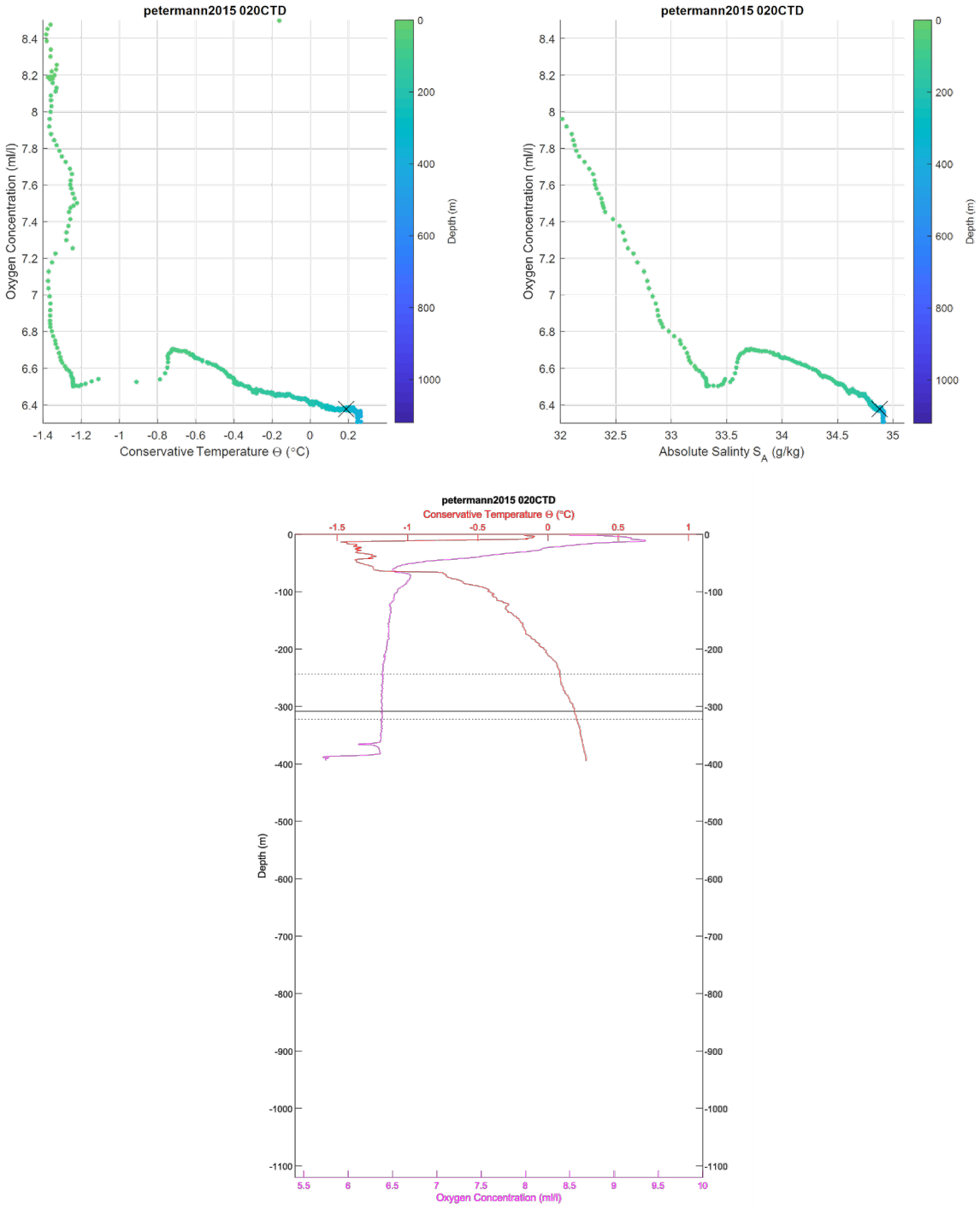

Figure 204: CTD 020. Top left, oxygen-temperature diagram, colored by depth. Top right, oxygen-salinity diagram, colored by depth. The black 'X' in the first two plots indicates the average depth for the top of the scattering layer in this location. Bottom center, temperature and oxygen plotted by depth. The scattering layer depth is indicated by horizontal lines; the solid line is the average depth, the dotted lines are the shallowest and deepest depths, in both cases for the top of the scattering layer. Note that oxygen values for this cast are considered questionable due to issues with the pump, which was replaced between cast 025 and 026.

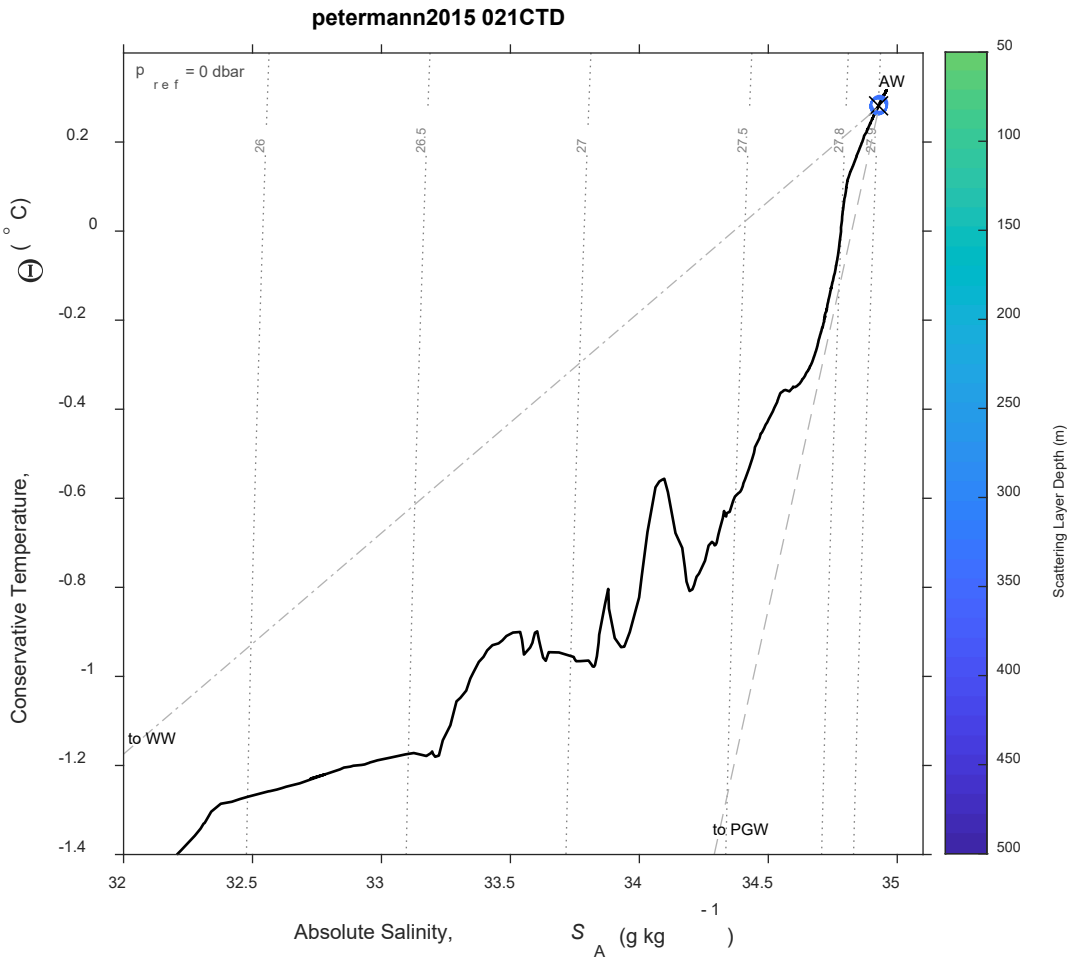

Figure 205: CTD 021, Temperature-Salinity (T-S) diagram. The scattering layer picks corresponding to this CTD are plotted as open circles colored by depth; a black 'X' indicates the average depth for the top of the scattering layer in this location. Isobars are shown as labeled grey dotted lines.

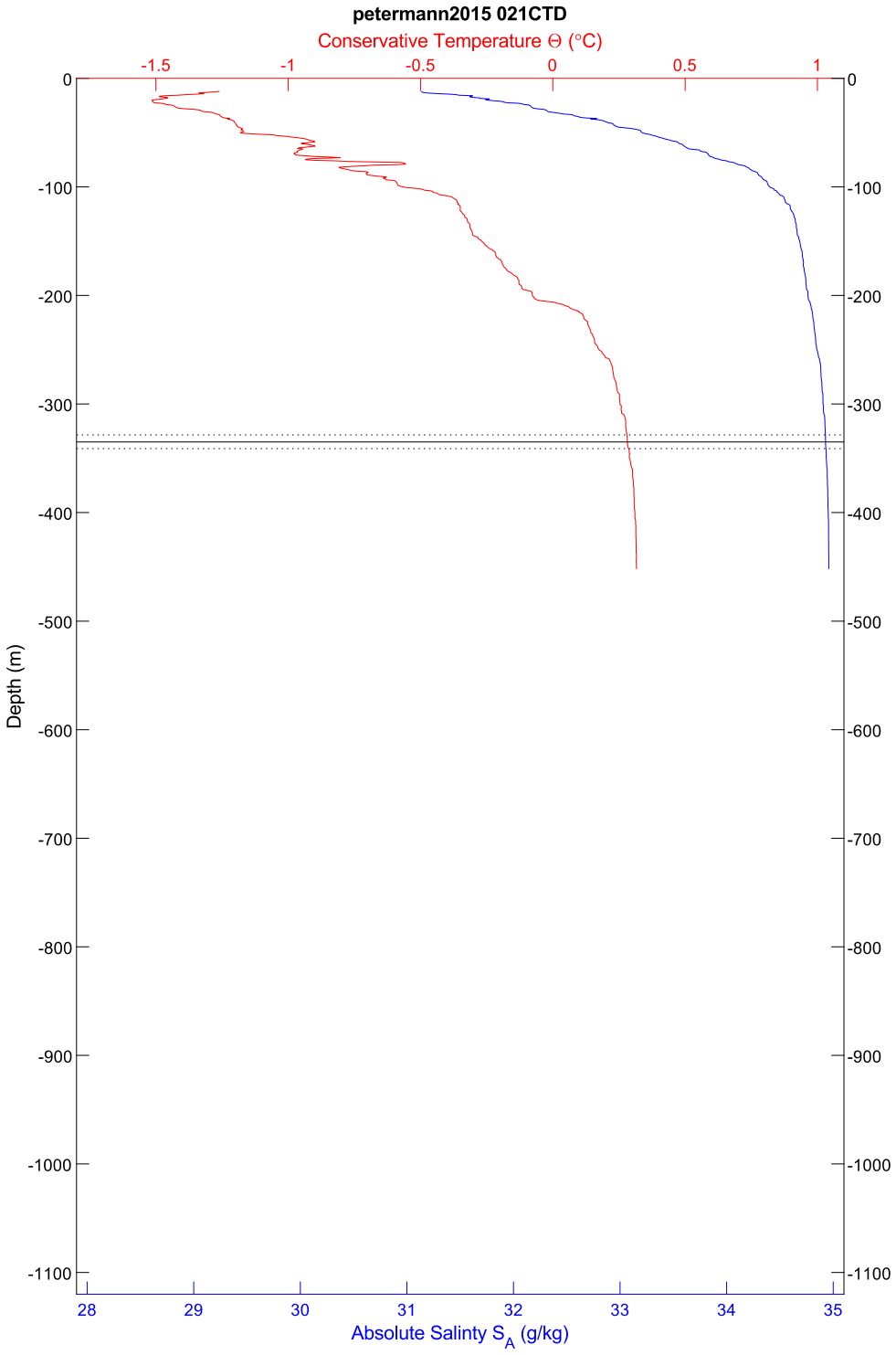

Figure 206: CTD 021, temperature and salinity plotted by depth. The scattering layer depth is indicated by horizontal lines; the solid line is the average depth, the dotted lines are the shallowest and deepest depths, in all cases for the top of the scattering layer.

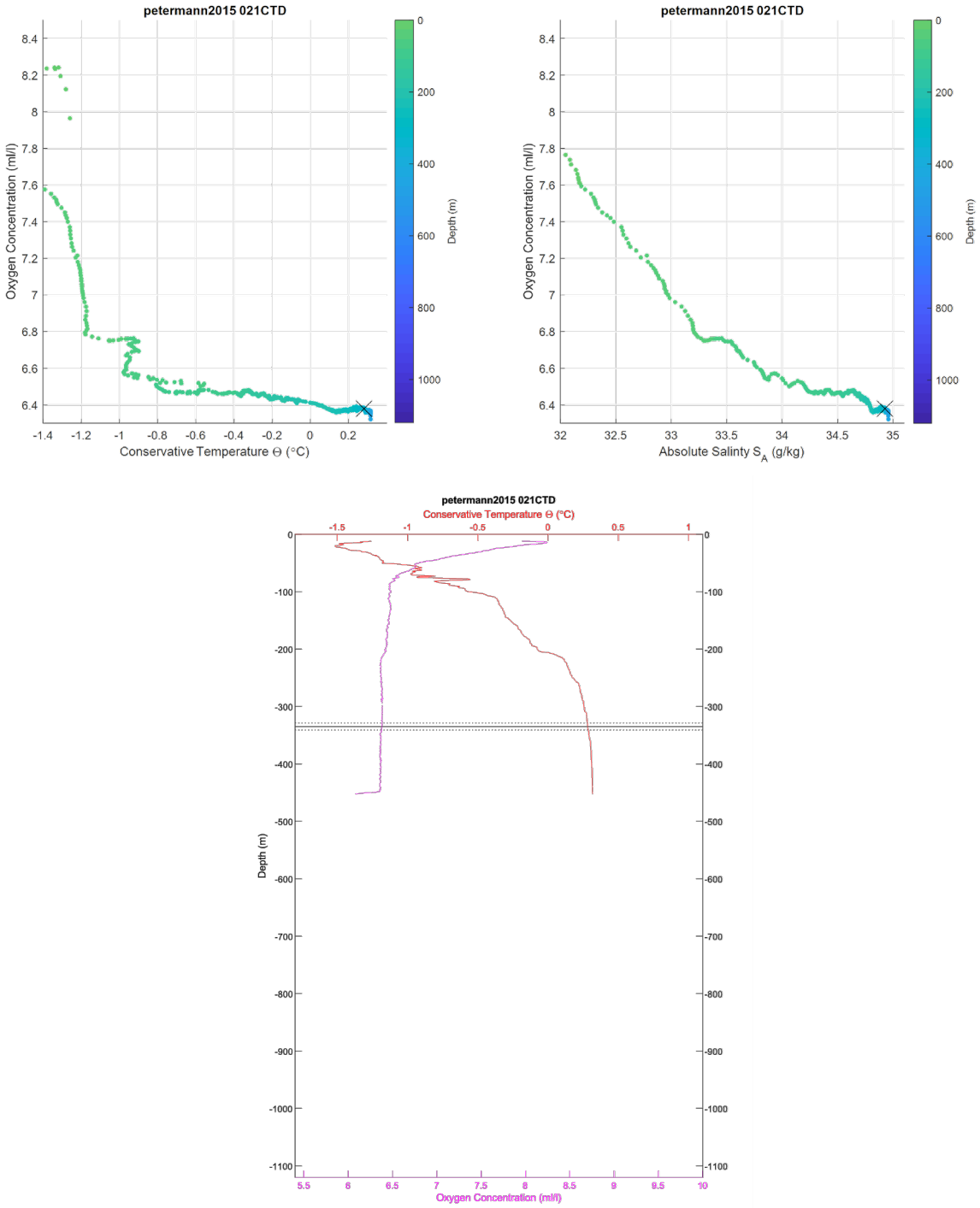

Figure 207: CTD 021. Top left, oxygen-temperature diagram, colored by depth. Top right, oxygen-salinity diagram, colored by depth. The black 'X' in the first two plots indicates the average depth for the top of the scattering layer in this location. Bottom center, temperature and oxygen plotted by depth. The scattering layer depth is indicated by horizontal lines; the solid line is the average depth, the dotted lines are the shallowest and deepest depths, in both cases for the top of the scattering layer. Note that oxygen values for this cast are considered questionable due to issues with the pump, which was replaced between cast 025 and 026.

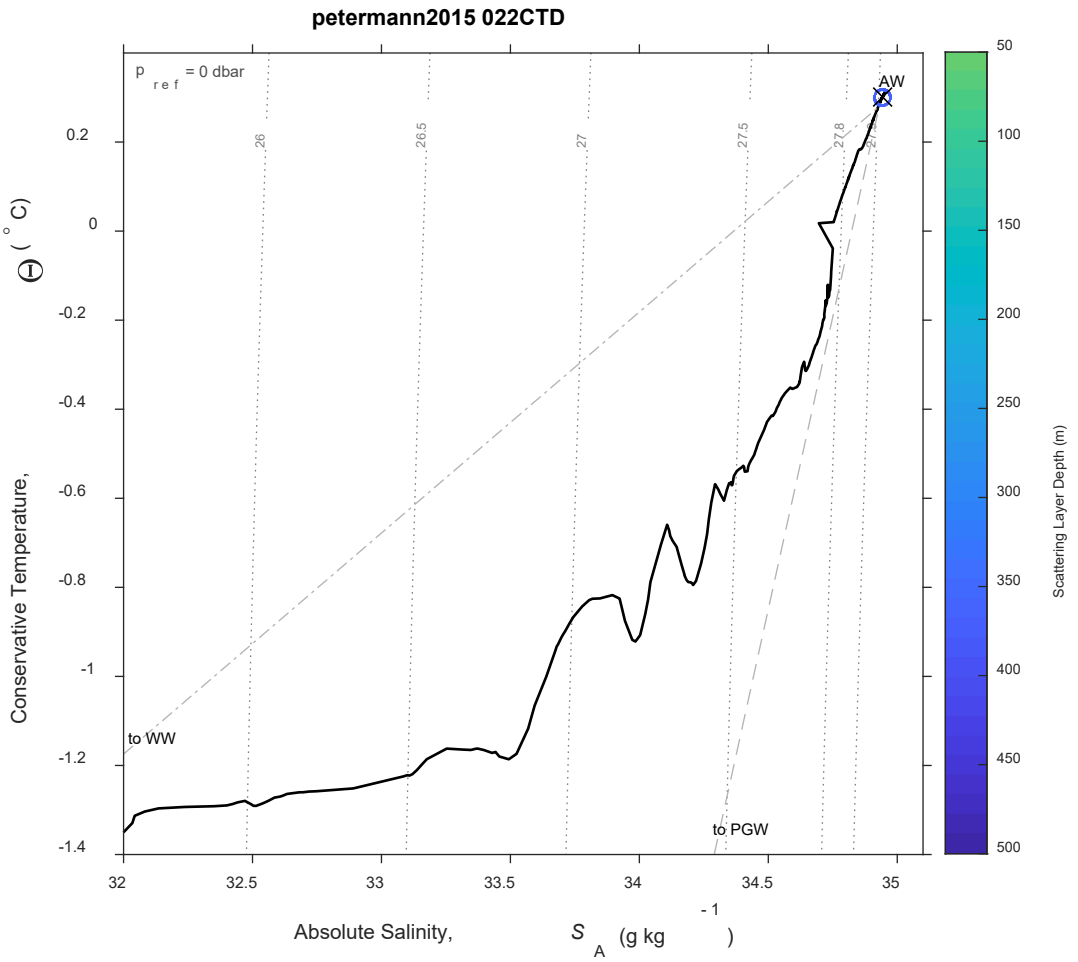

Figure 208: CTD 022, Temperature-Salinity (T-S) diagram. The scattering layer picks corresponding to this CTD are plotted as open circles colored by depth; a black 'X' indicates the average depth for the top of the scattering layer in this location. Isobars are shown as labeled grey dotted lines.

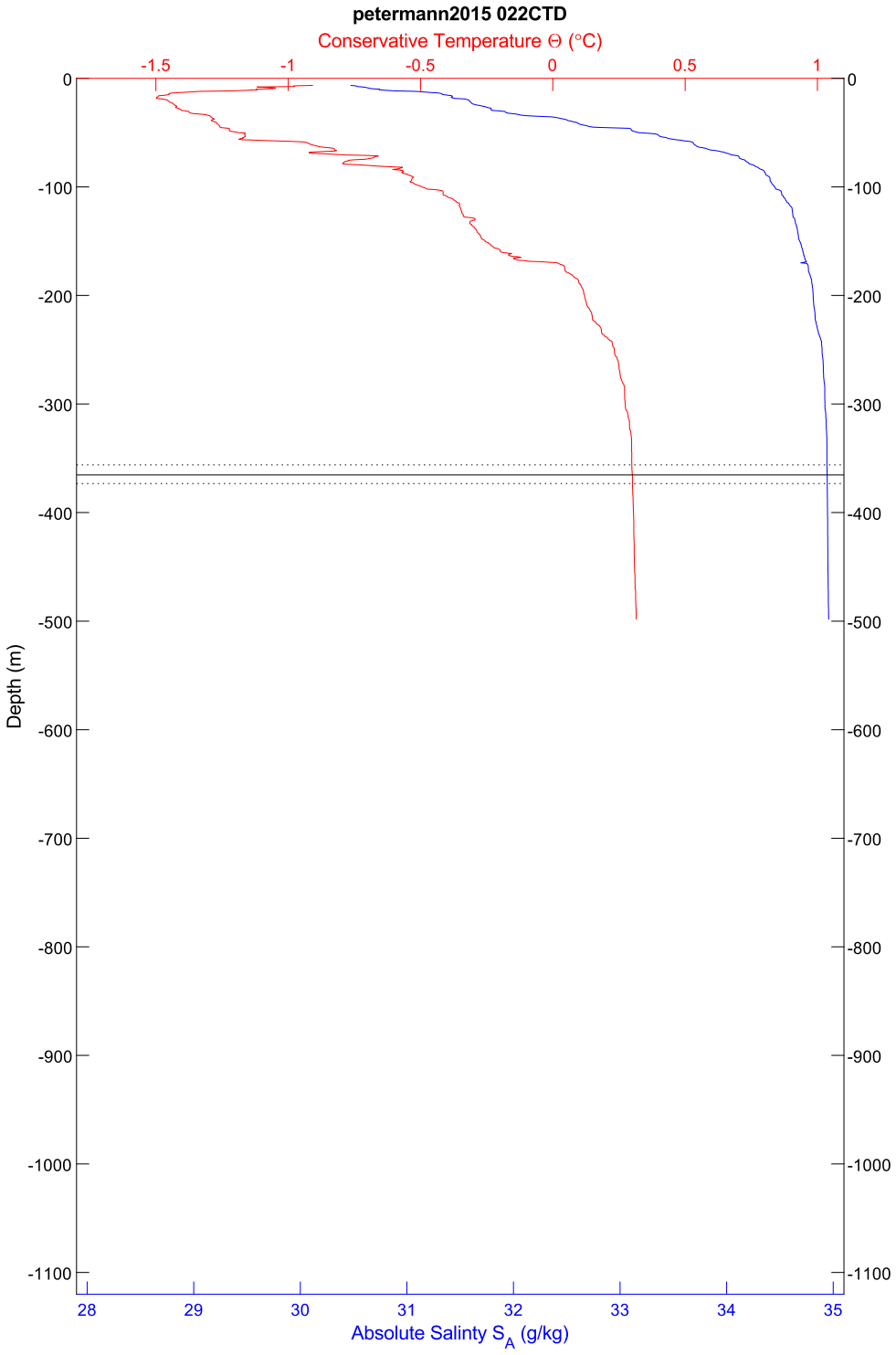

Figure 209: CTD 022, temperature and salinity plotted by depth. The scattering layer depth is indicated by horizontal lines; the solid line is the average depth, the dotted lines are the shallowest and deepest depths, in all cases for the top of the scattering layer.

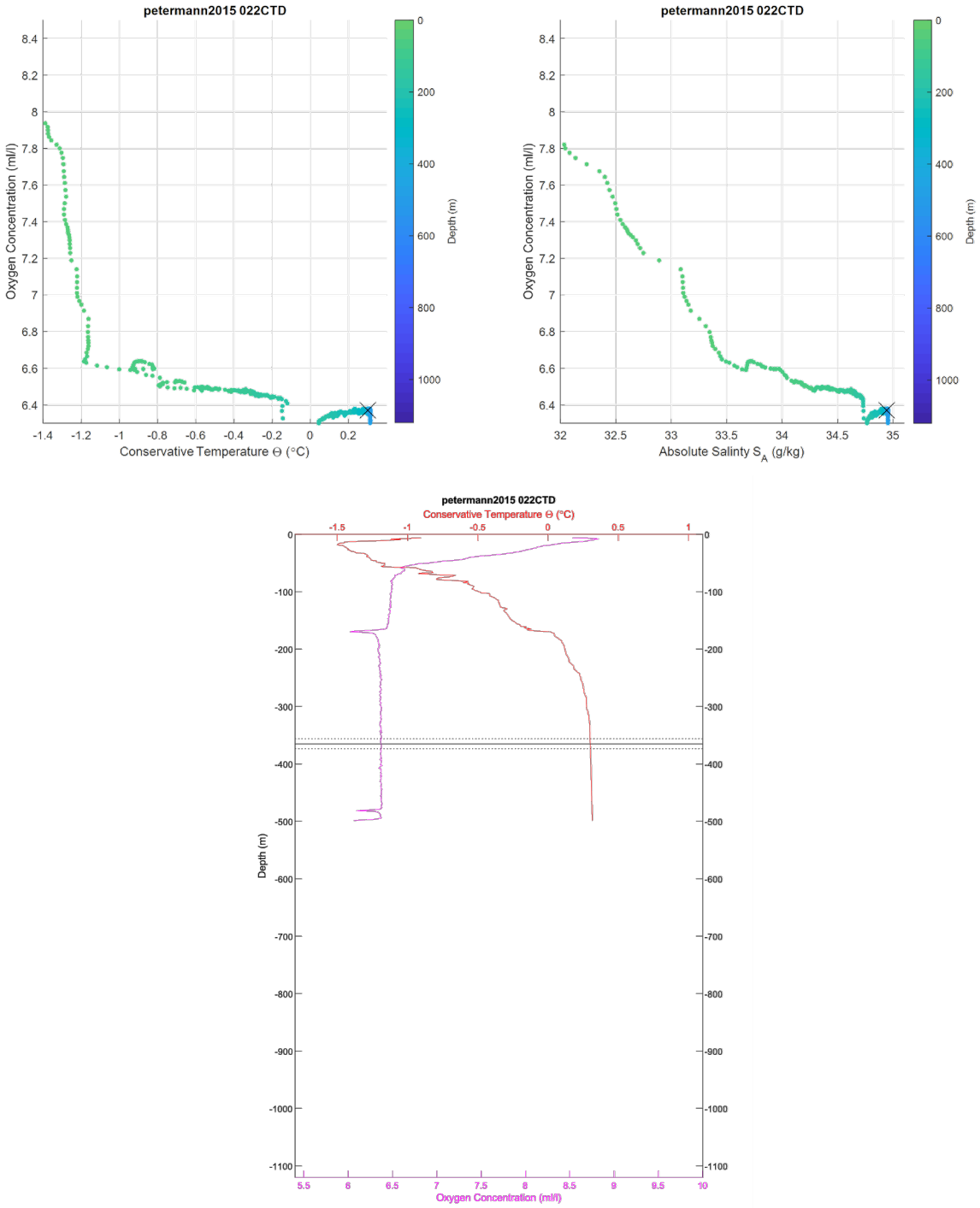

Figure 210: CTD 022. Top left, oxygen-temperature diagram, colored by depth. Top right, oxygen-salinity diagram, colored by depth. The black 'X' in the first two plots indicates the average depth for the top of the scattering layer in this location. Bottom center, temperature and oxygen plotted by depth. The scattering layer depth is indicated by horizontal lines; the solid line is the average depth, the dotted lines are the shallowest and deepest depths, in both cases for the top of the scattering layer. Note that oxygen values for this cast are considered questionable due to issues with the pump, which was replaced between cast 025 and 026.

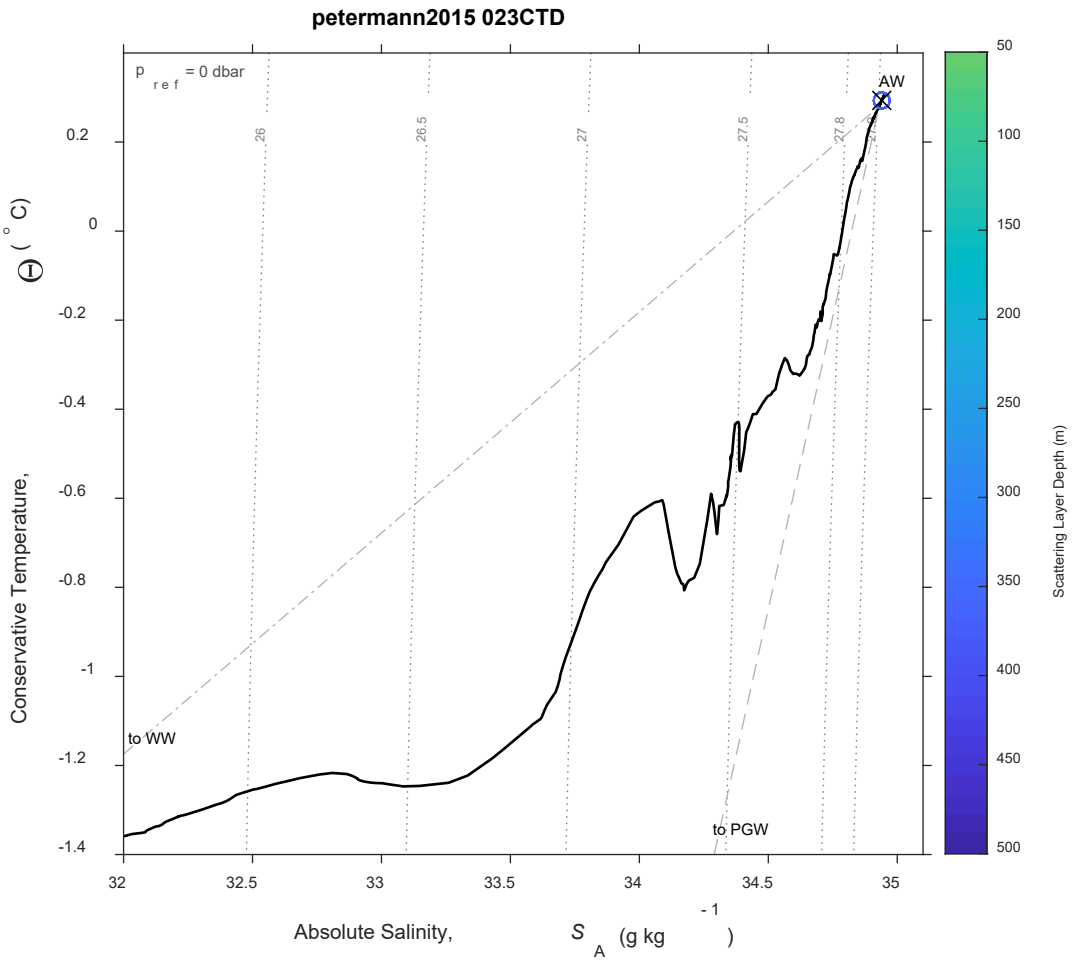

Figure 211: CTD 023, Temperature-Salinity (T-S) diagram. The scattering layer picks corresponding to this CTD are plotted as open circles colored by depth; a black 'X' indicates the average depth for the top of the scattering layer in this location. Isobars are shown as labeled grey dotted lines.

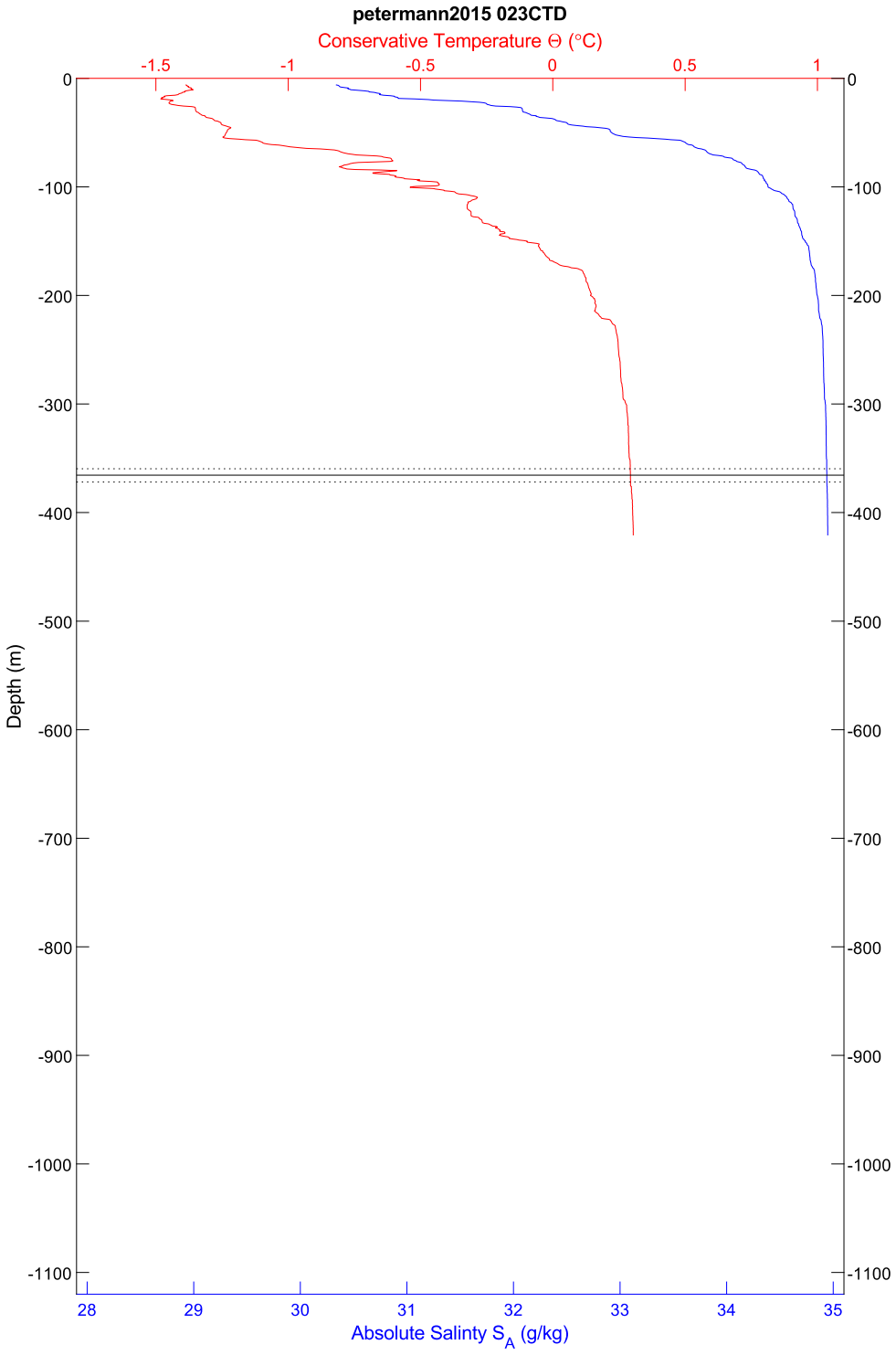

Figure 212: CTD 023, temperature and salinity plotted by depth. The scattering layer depth is indicated by horizontal lines; the solid line is the average depth, the dotted lines are the shallowest and deepest depths, in all cases for the top of the scattering layer.

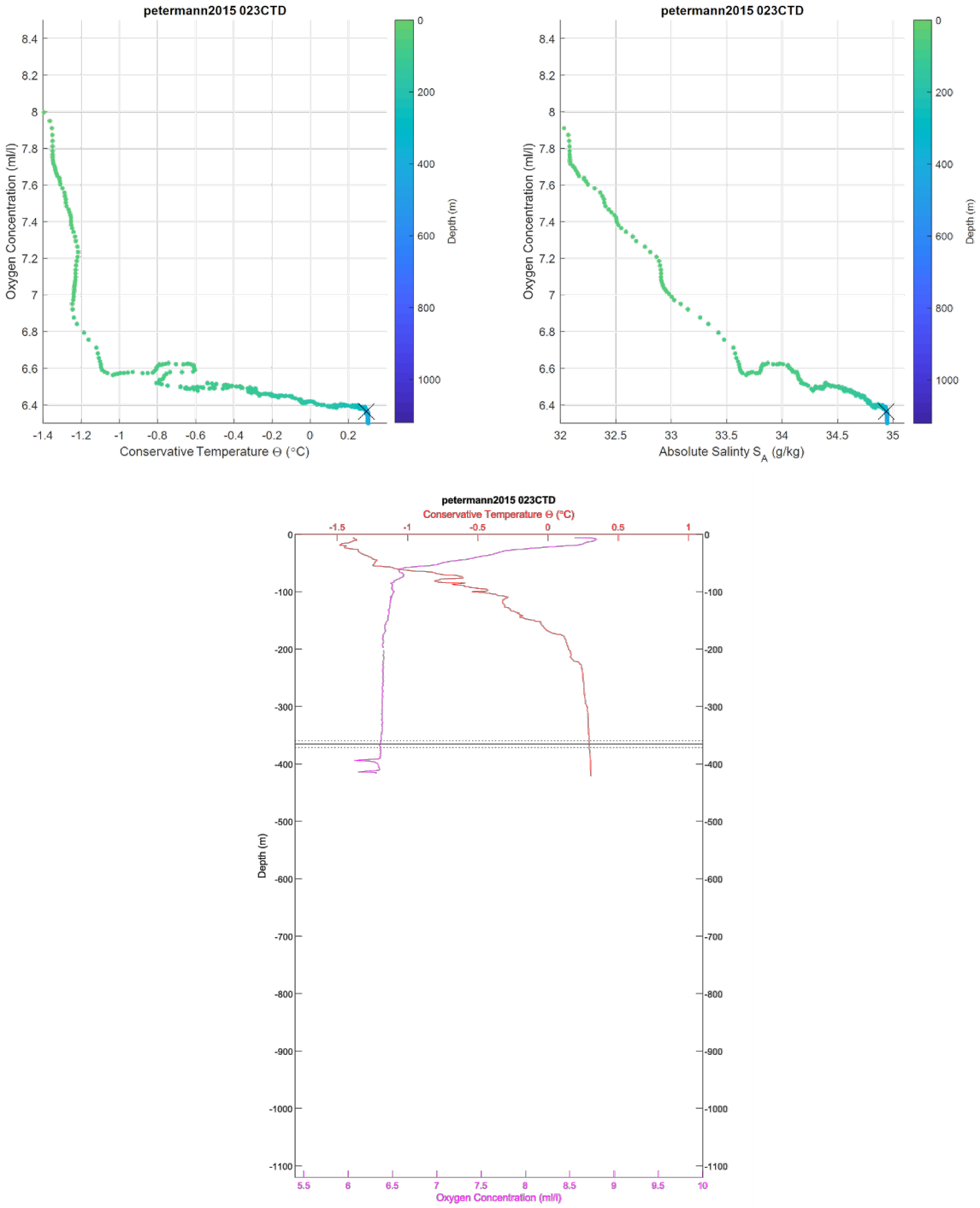

Figure 213: CTD 023. Top left, oxygen-temperature diagram, colored by depth. Top right, oxygen-salinity diagram, colored by depth. The black 'X' in the first two plots indicates the average depth for the top of the scattering layer in this location. Bottom center, temperature and oxygen plotted by depth. The scattering layer depth is indicated by horizontal lines; the solid line is the average depth, the dotted lines are the shallowest and deepest depths, in both cases for the top of the scattering layer. Note that oxygen values for this cast are considered questionable due to issues with the pump, which was replaced between cast 025 and 026.

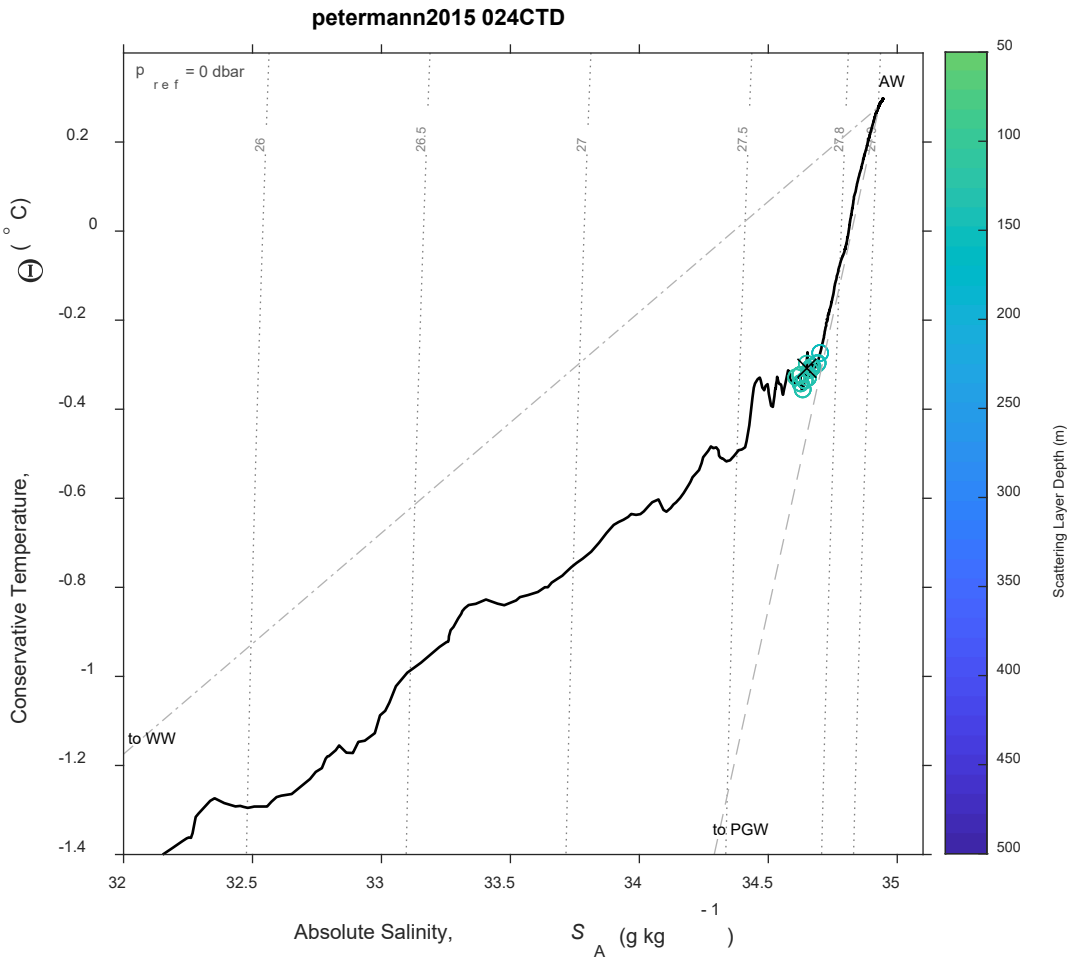

Figure 214: CTD 024, Temperature-Salinity (T-S) diagram. The scattering layer picks corresponding to this CTD are plotted as open circles colored by depth; a black 'X' indicates the average depth for the top of the scattering layer in this location. Isobars are shown as labeled grey dotted lines.

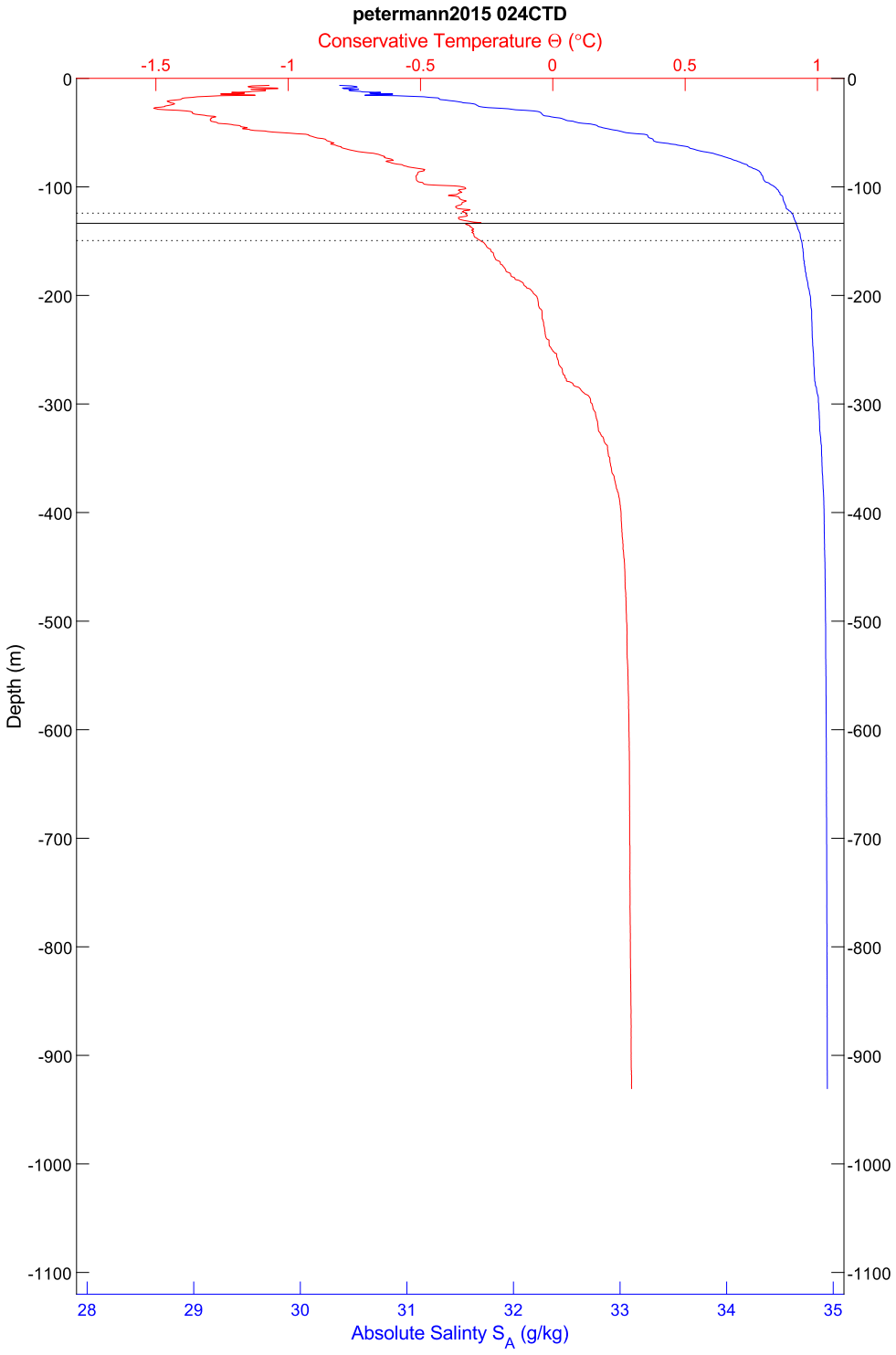

Figure 215: CTD 024, temperature and salinity plotted by depth. The scattering layer depth is indicated by horizontal lines; the solid line is the average depth, the dotted lines are the shallowest and deepest depths, in all cases for the top of the scattering layer.

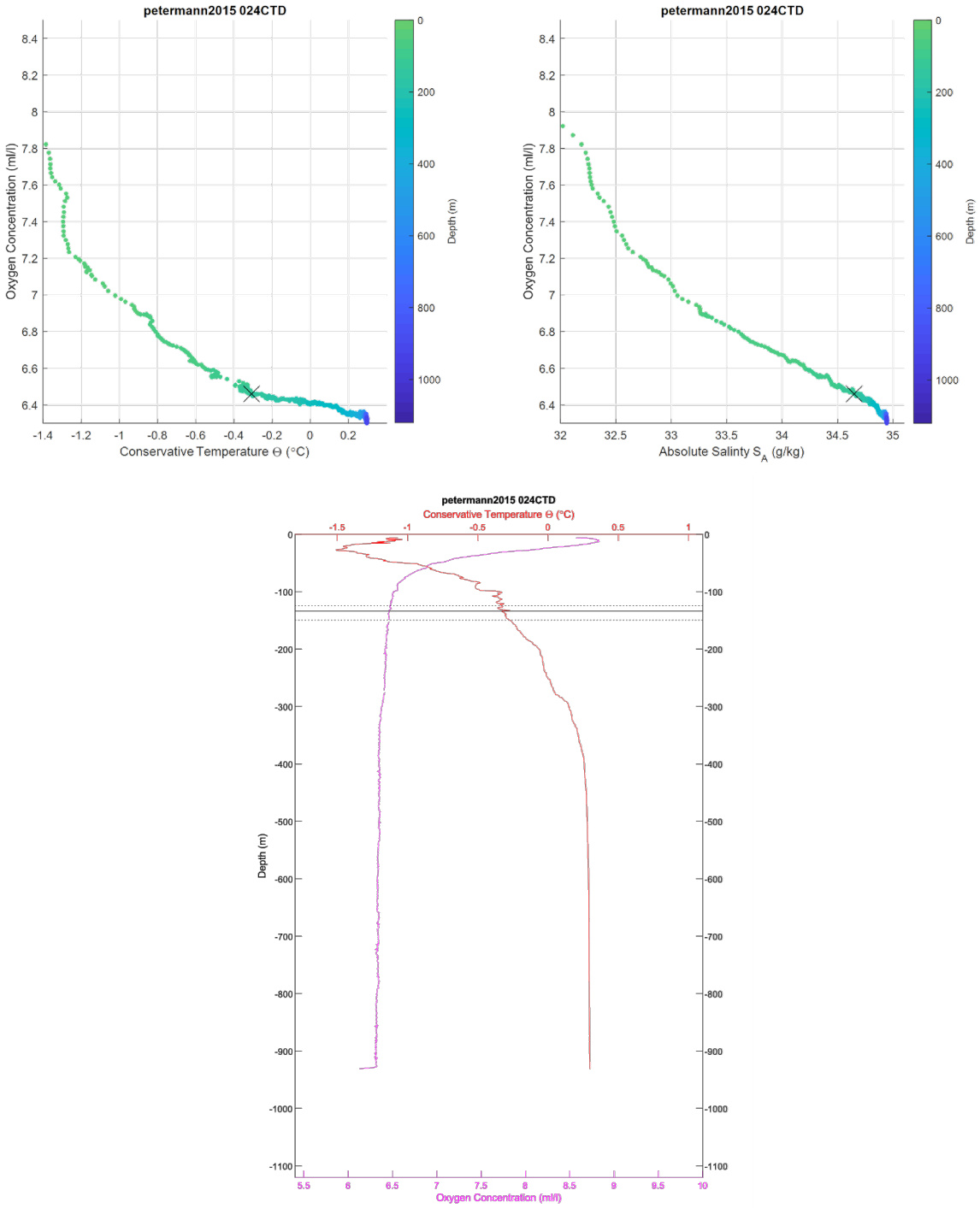

Figure 216: CTD 024. Top left, oxygen-temperature diagram, colored by depth. Top right, oxygen-salinity diagram, colored by depth. The black 'X' in the first two plots indicates the average depth for the top of the scattering layer in this location. Bottom center, temperature and oxygen plotted by depth. The scattering layer depth is indicated by horizontal lines; the solid line is the average depth, the dotted lines are the shallowest and deepest depths, in both cases for the top of the scattering layer. Note that oxygen values for this cast are considered questionable due to issues with the pump, which was replaced between cast 025 and 026.

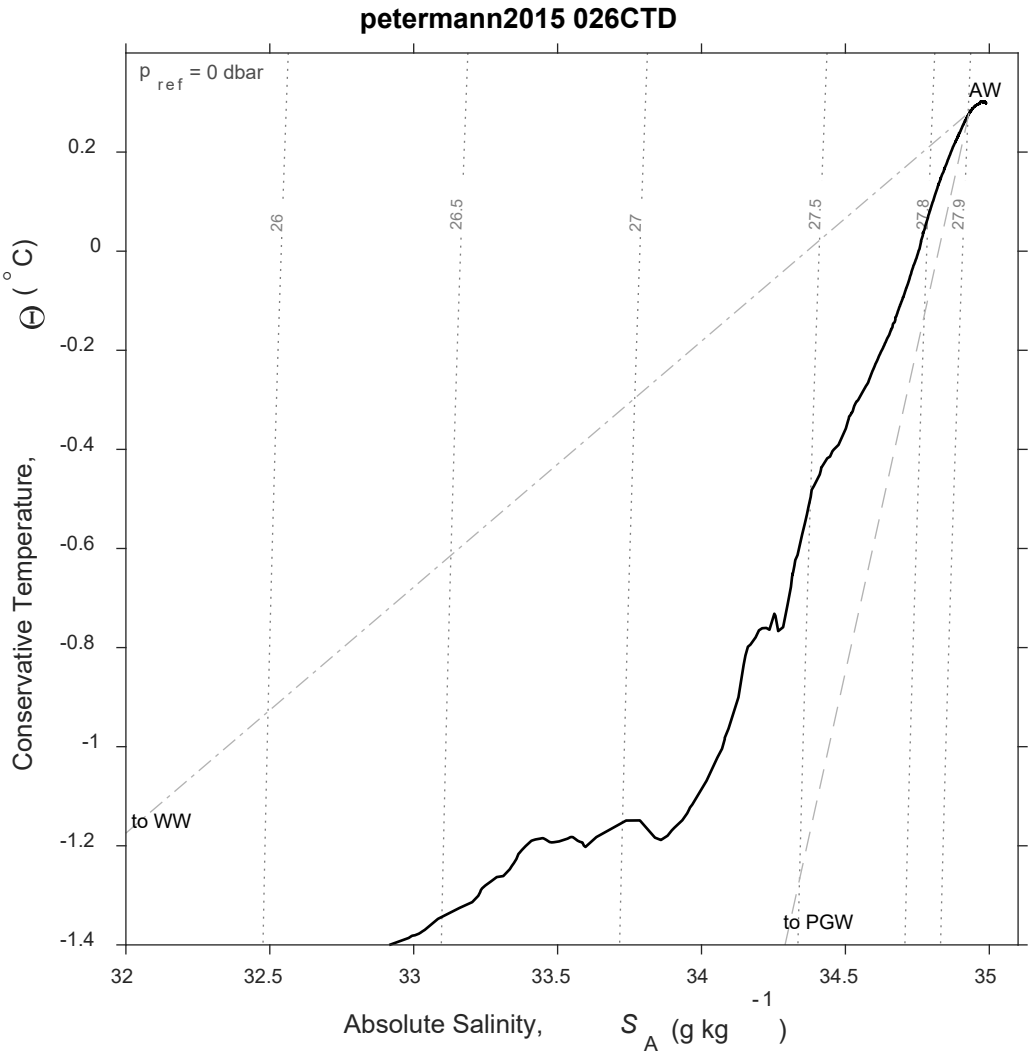

Figure 217: CTD 026, Temperature-Salinity (T-S) diagram. Isobars are shown as labeled grey dotted lines. There was no scattering layer associated with this CTD station.

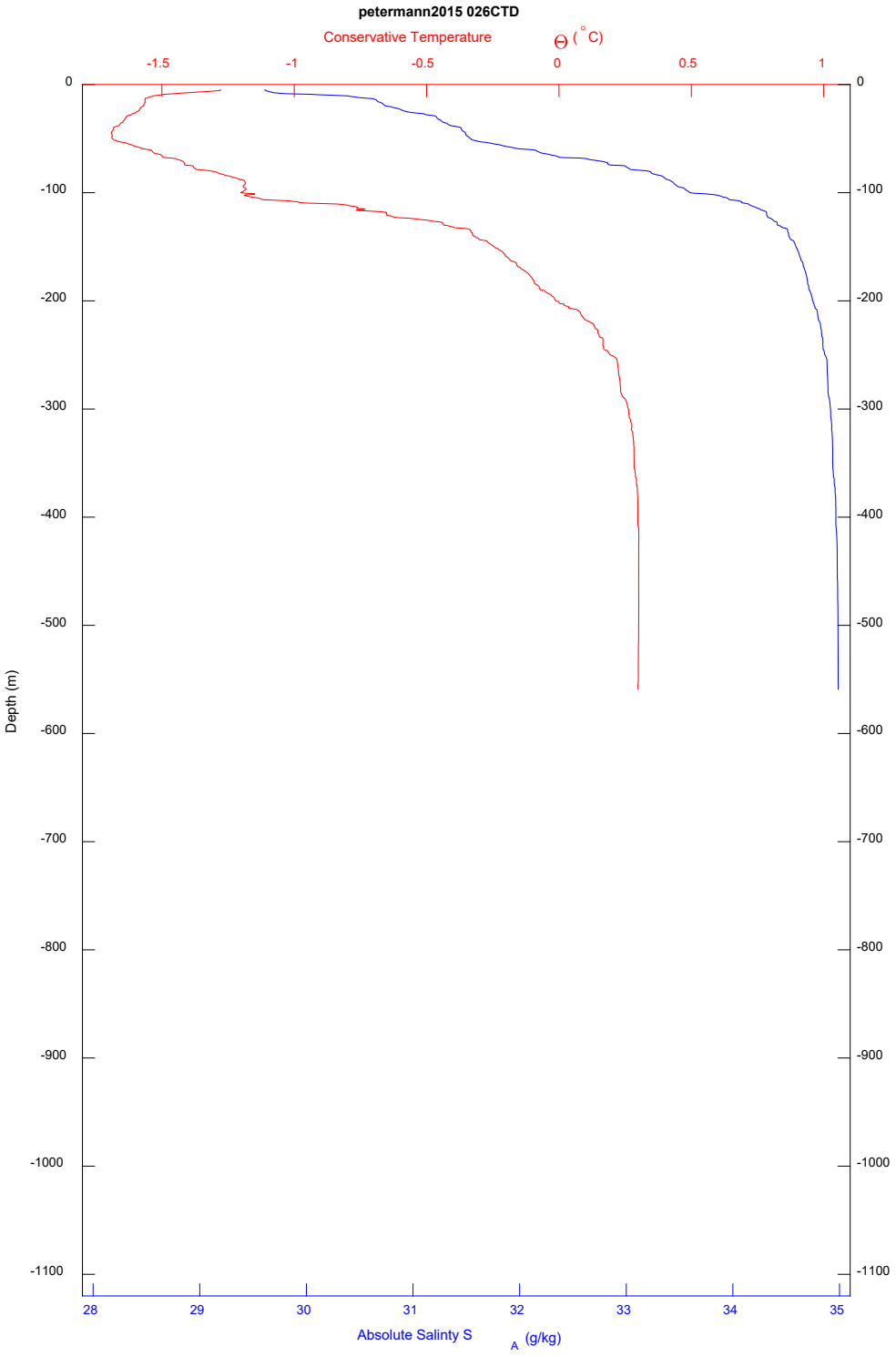

Figure 218: CTD 026, temperature and salinity plotted by depth. There was no scattering layer associated with this CTD station.

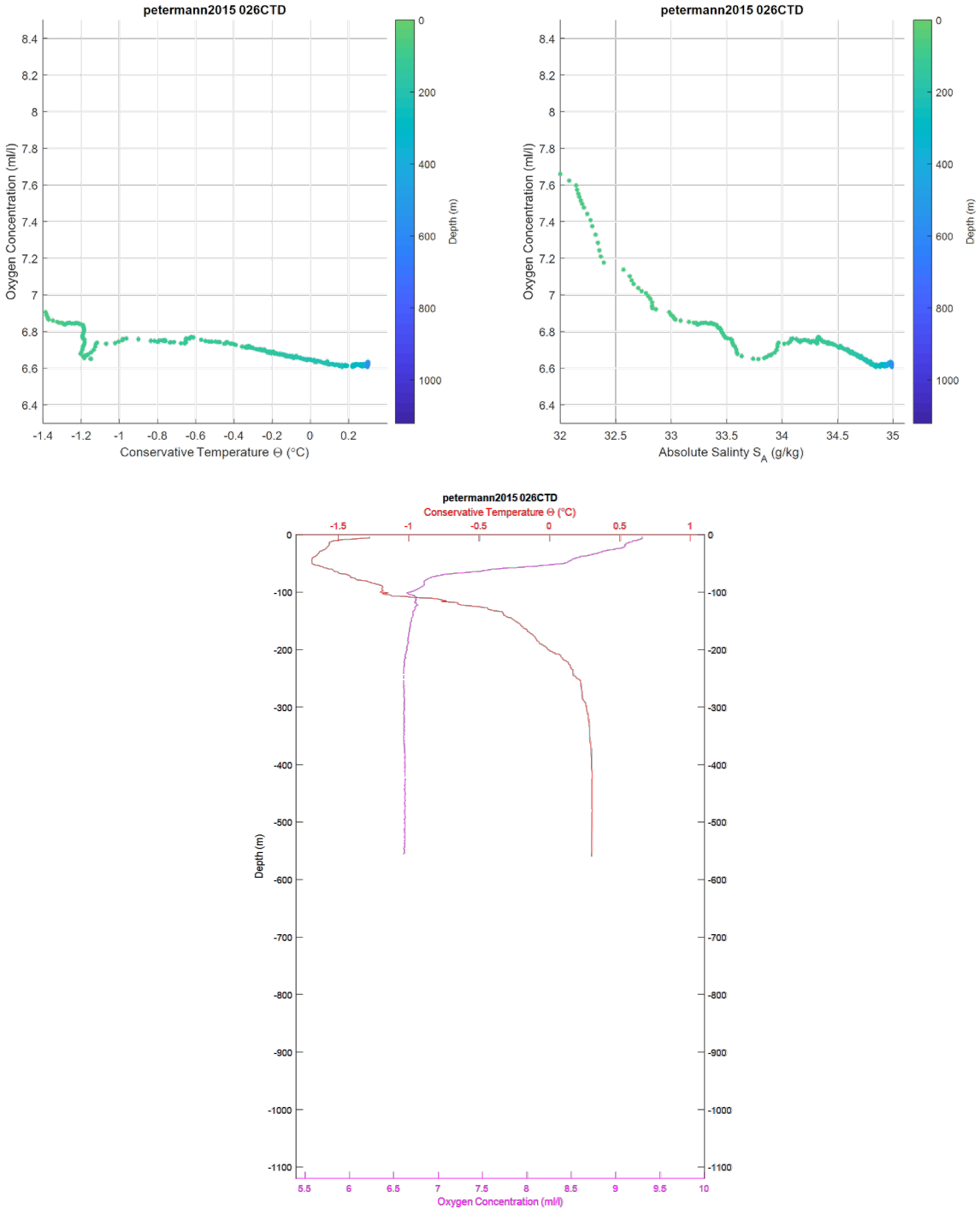

Figure 219: CTD 026. Top left, oxygen-temperature diagram, colored by depth. Top right, oxygen-salinity diagram, colored by depth. Bottom center, temperature and oxygen plotted by depth. There was no scattering layer associated with this CTD station.

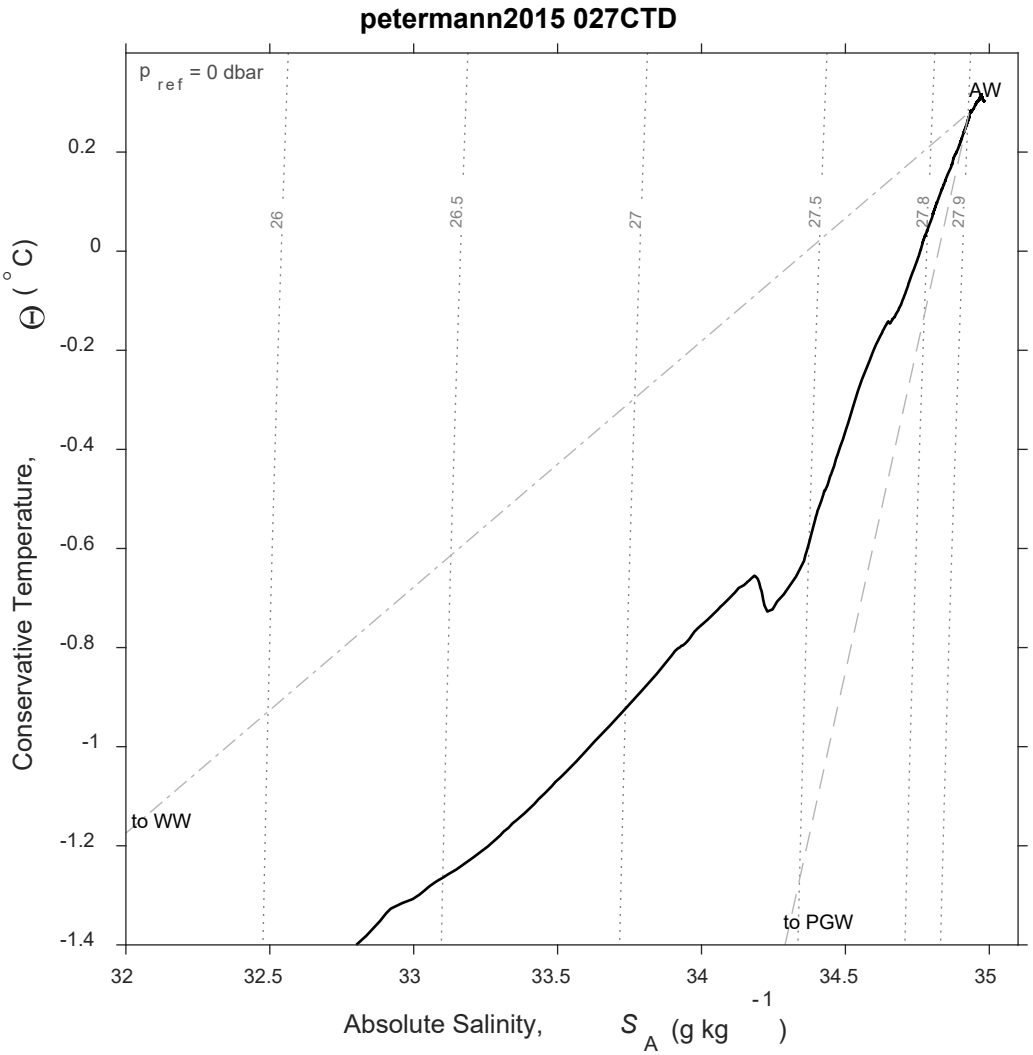

Figure 220: CTD 027, Temperature-Salinity (T-S) diagram. Isobars are shown as labeled grey dotted lines. There was no scattering layer associated with this CTD station.

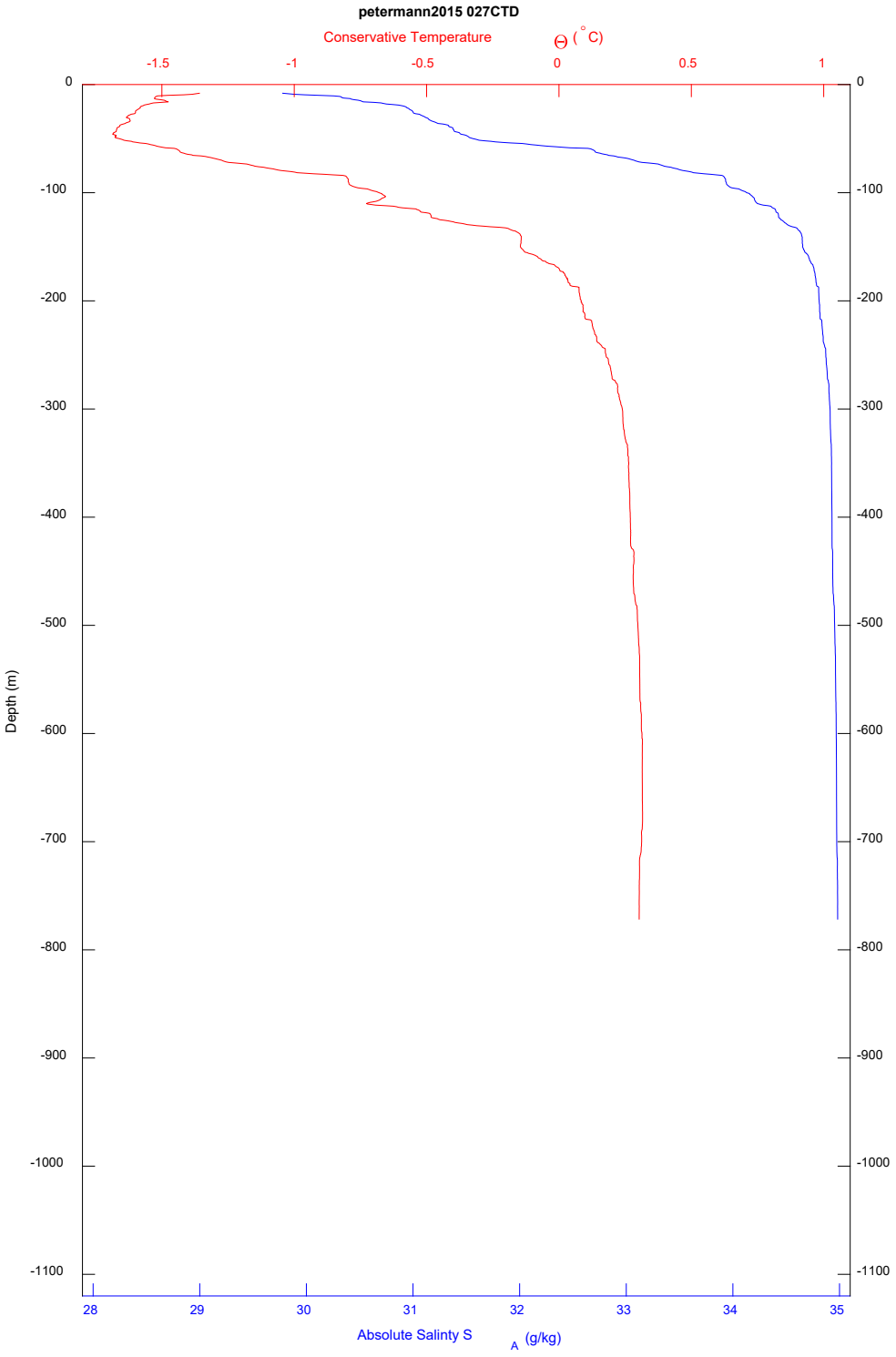

Figure 221: CTD 027, temperature and salinity plotted by depth. There was no scattering layer associated with this CTD station.

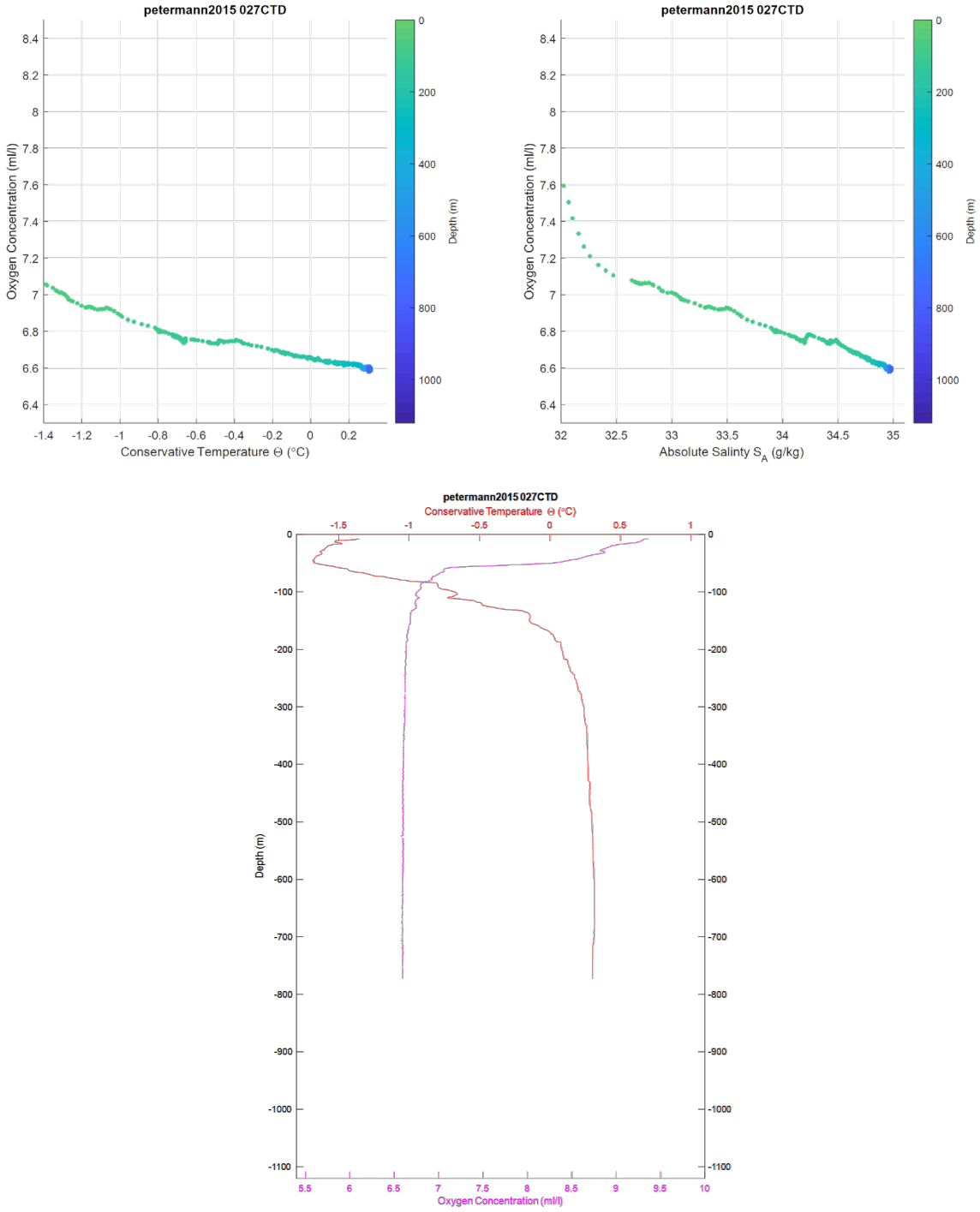

Figure 222: CTD 027. Top left, oxygen-temperature diagram, colored by depth. Top right, oxygen-salinity diagram, colored by depth. Bottom center, temperature and oxygen plotted by depth. There was no scattering layer associated with this CTD station.

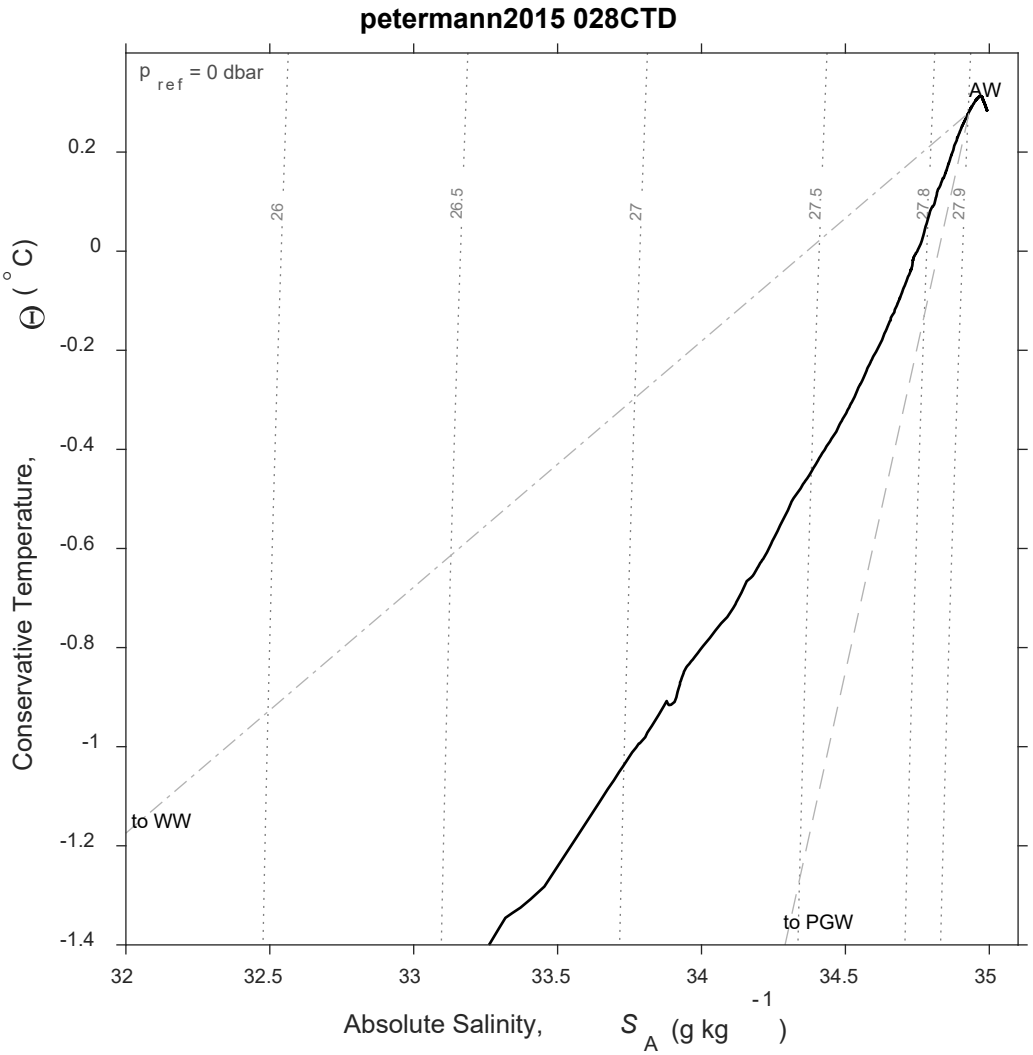

Figure 223: CTD 028, Temperature-Salinity (T-S) diagram. Isobars are shown as labeled grey dotted lines. There was no scattering layer associated with this CTD station.

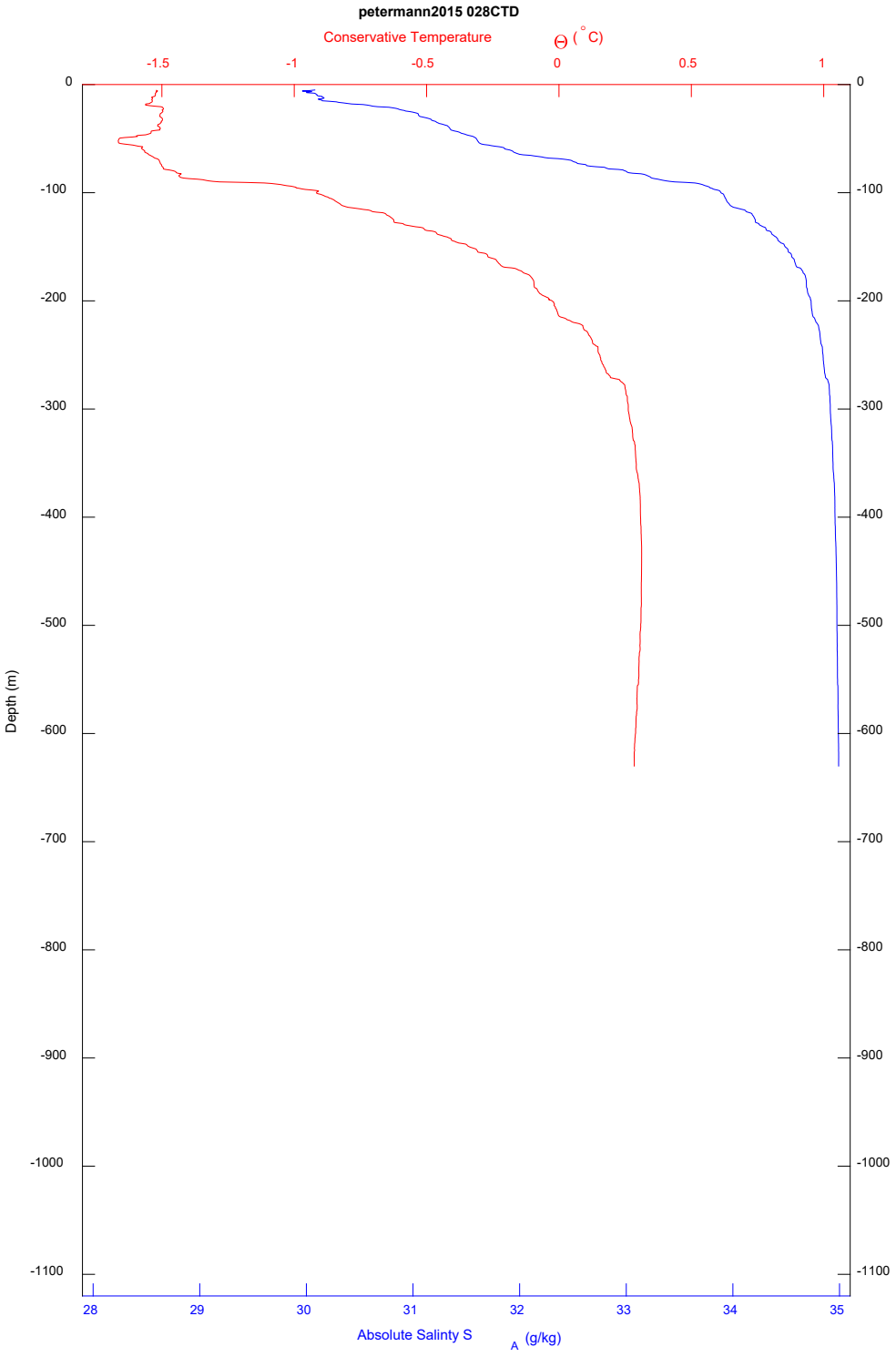

Figure 224: CTD 028, temperature and salinity plotted by depth. There was no scattering layer associated with this CTD station.

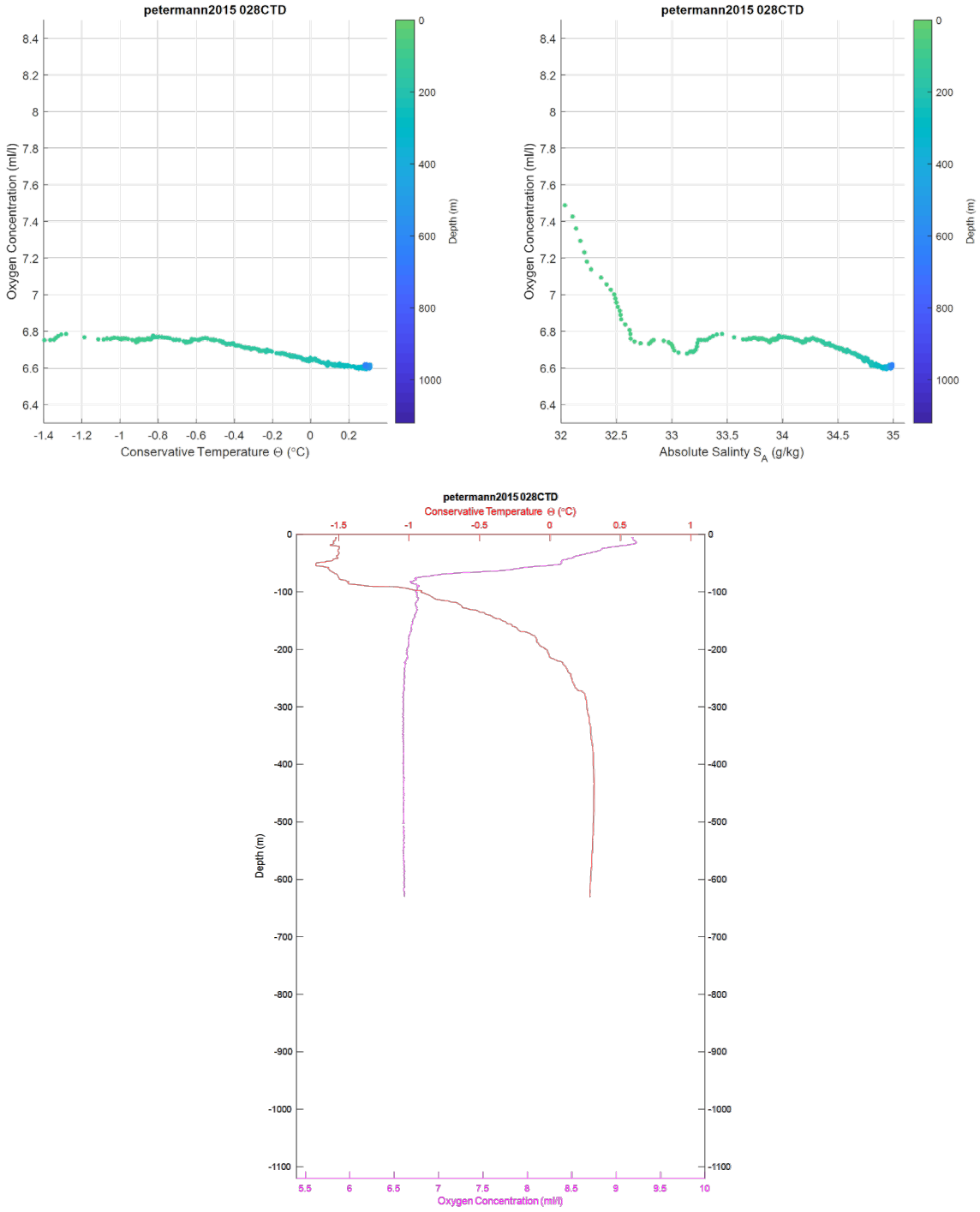

Figure 225: CTD 028. Top left, oxygen-temperature diagram, colored by depth. Top right, oxygen-salinity diagram, colored by depth. Bottom center, temperature and oxygen plotted by depth. There was no scattering layer associated with this CTD station.

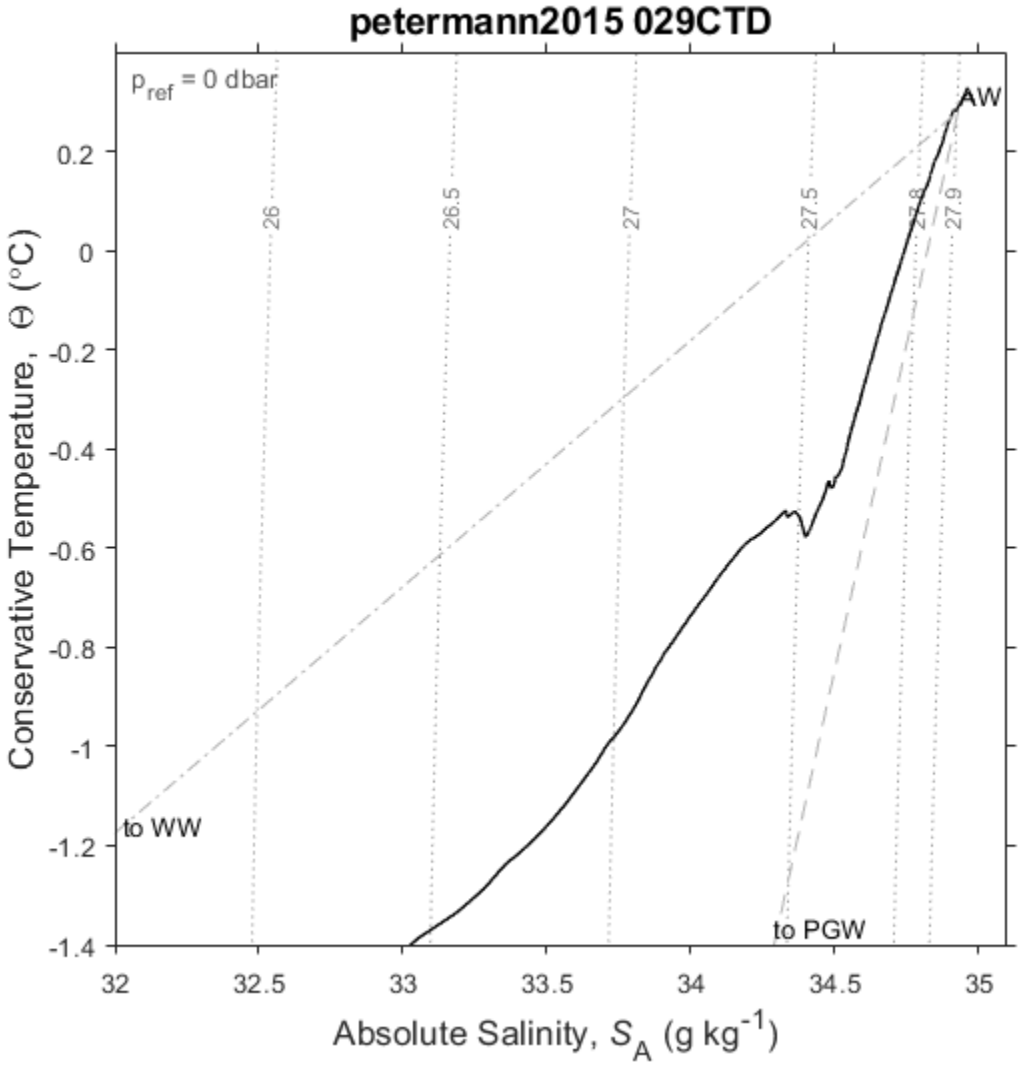

Figure 226: CTD 029, Temperature-Salinity (T-S) diagram. Isobars are shown as labeled grey dotted lines. There was no scattering layer associated with this CTD station.

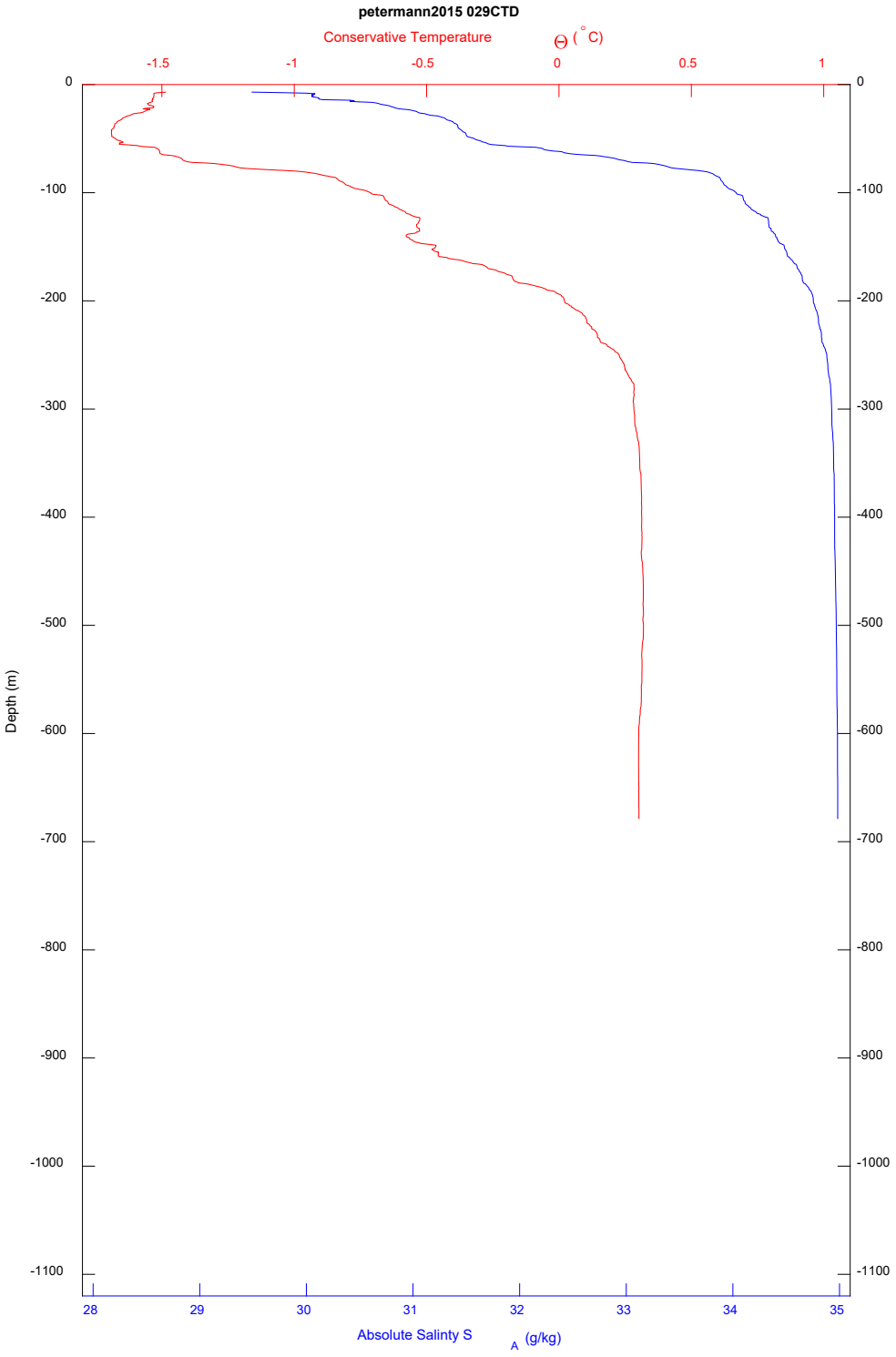

Figure 227: CTD 029, temperature and salinity plotted by depth. There was no scattering layer associated with this CTD station

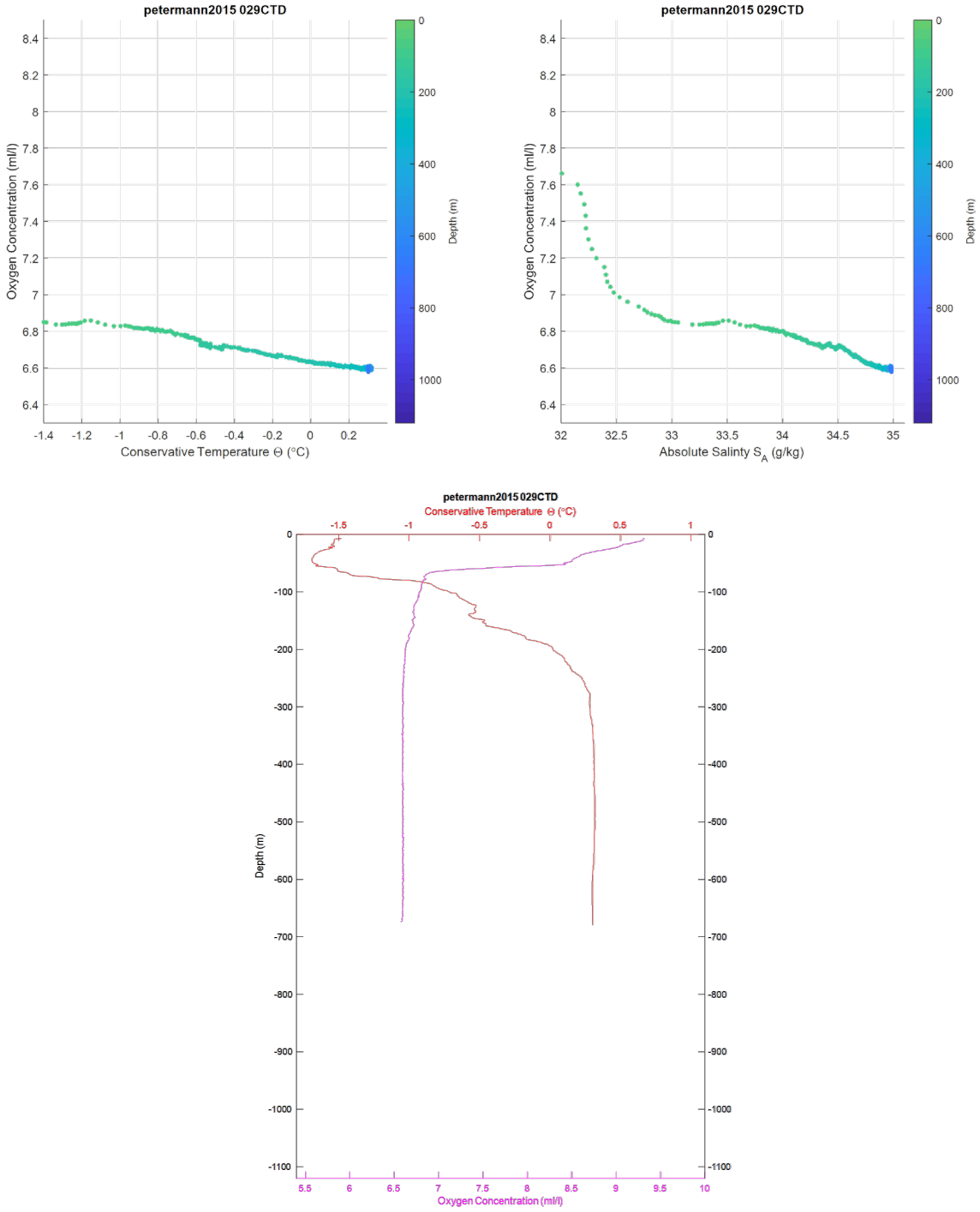

Figure 228: CTD 029. Top left, oxygen-temperature diagram, colored by depth. Top right, oxygen-salinity diagram, colored by depth. Bottom center, temperature and oxygen plotted by depth. There was no scattering layer associated with this CTD station.

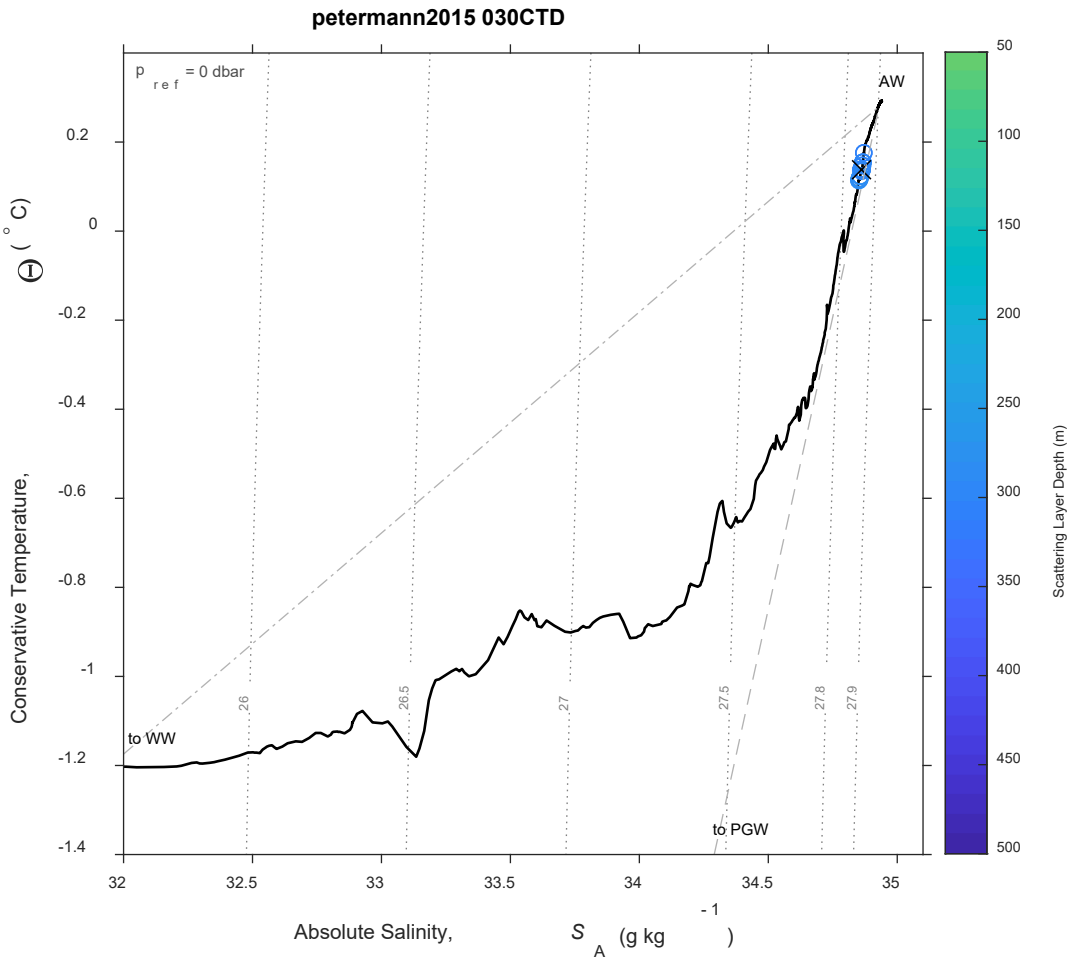

Figure 229: CTD 030, Temperature-Salinity (T-S) diagram. The scattering layer picks corresponding to this CTD are plotted as open circles colored by depth; a black 'X' indicates the average depth for the top of the scattering layer in this location. Isobars are shown as labeled grey dotted lines.

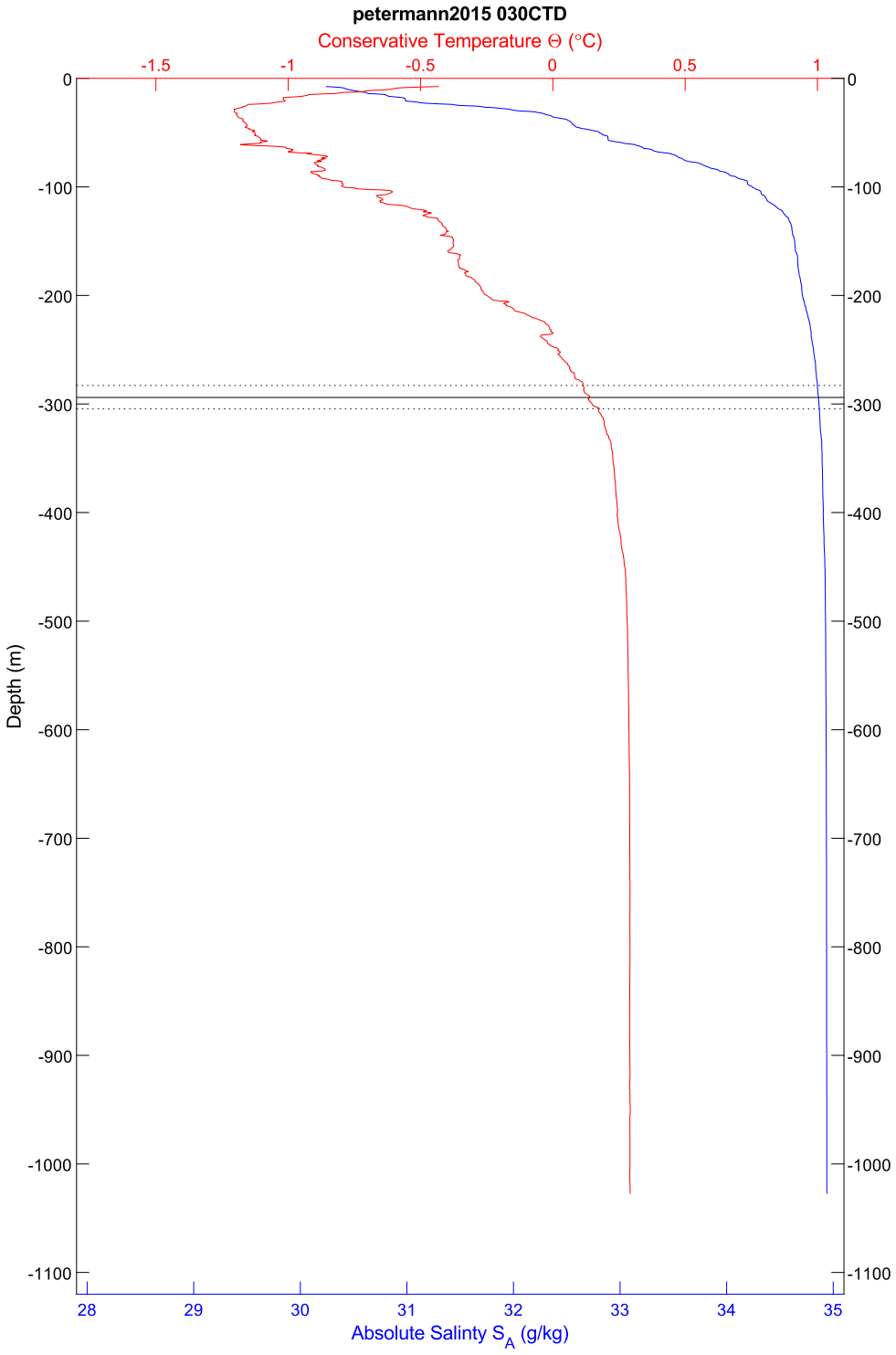

Figure 230: CTD 030, temperature and salinity plotted by depth. The scattering layer depth is indicated by horizontal lines; the solid line is the average depth, the dotted lines are the shallowest and deepest depths, in all cases for the top of the scattering layer.

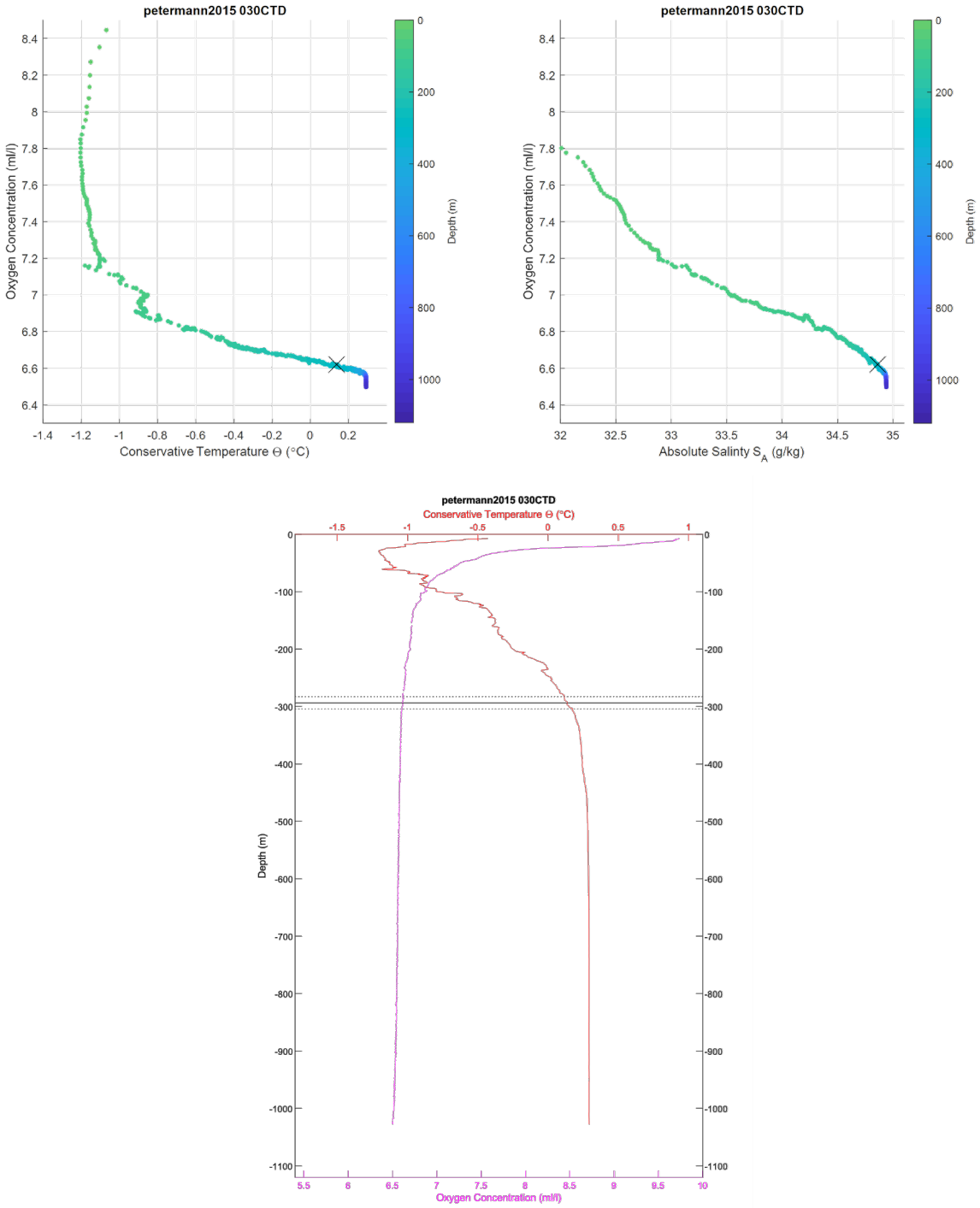

Figure 231: CTD 030. Top left, oxygen-temperature diagram, colored by depth. Top right, oxygen-salinity diagram, colored by depth. The black 'X' in the first two plots indicates the average depth for the top of the scattering layer in this location. Bottom center, temperature and oxygen plotted by depth. The scattering layer depth is indicated by horizontal lines; the solid line is the average depth, the dotted lines are the shallowest and deepest depths, in both cases for the top of the scattering layer.

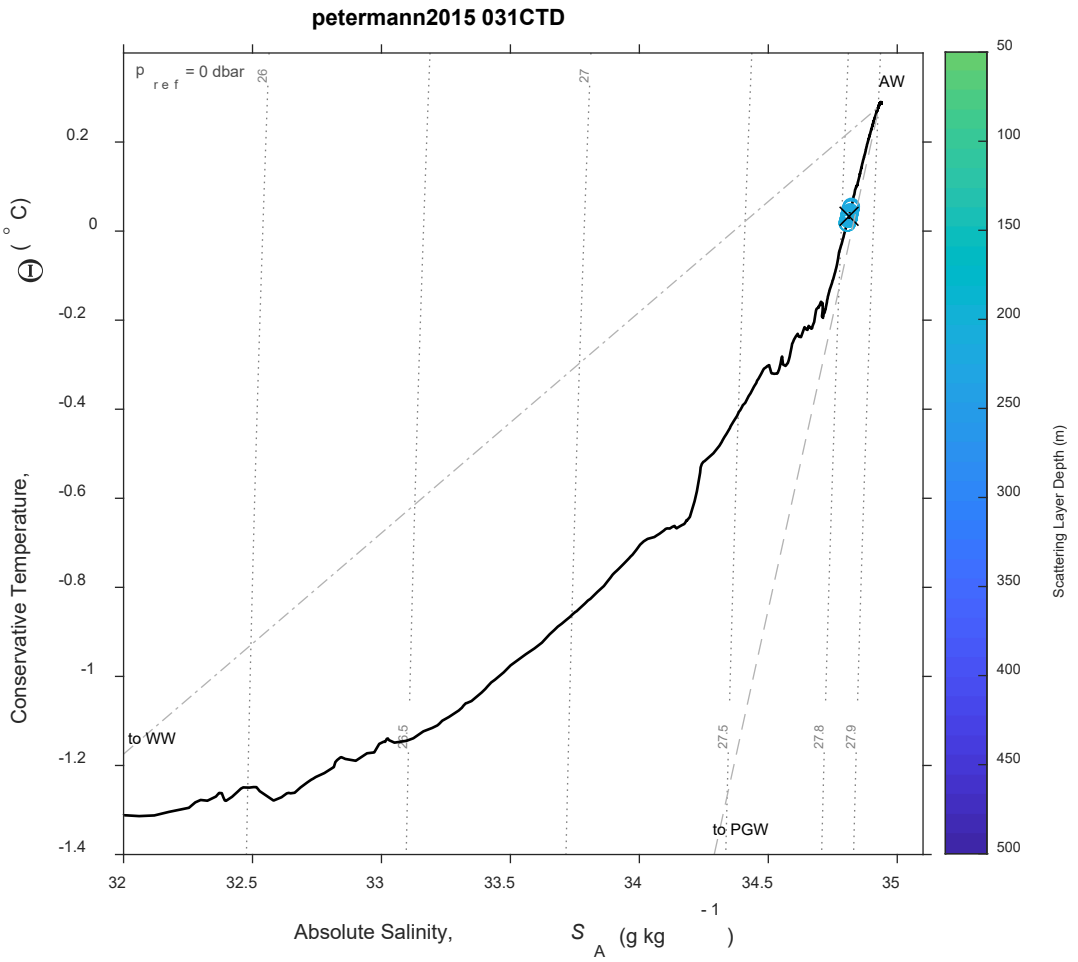

Figure 232: CTD 031, Temperature-Salinity (T-S) diagram. The scattering layer picks corresponding to this CTD are plotted as open circles colored by depth; a black 'X' indicates the average depth for the top of the scattering layer in this location. Isobars are shown as labeled grey dotted lines.

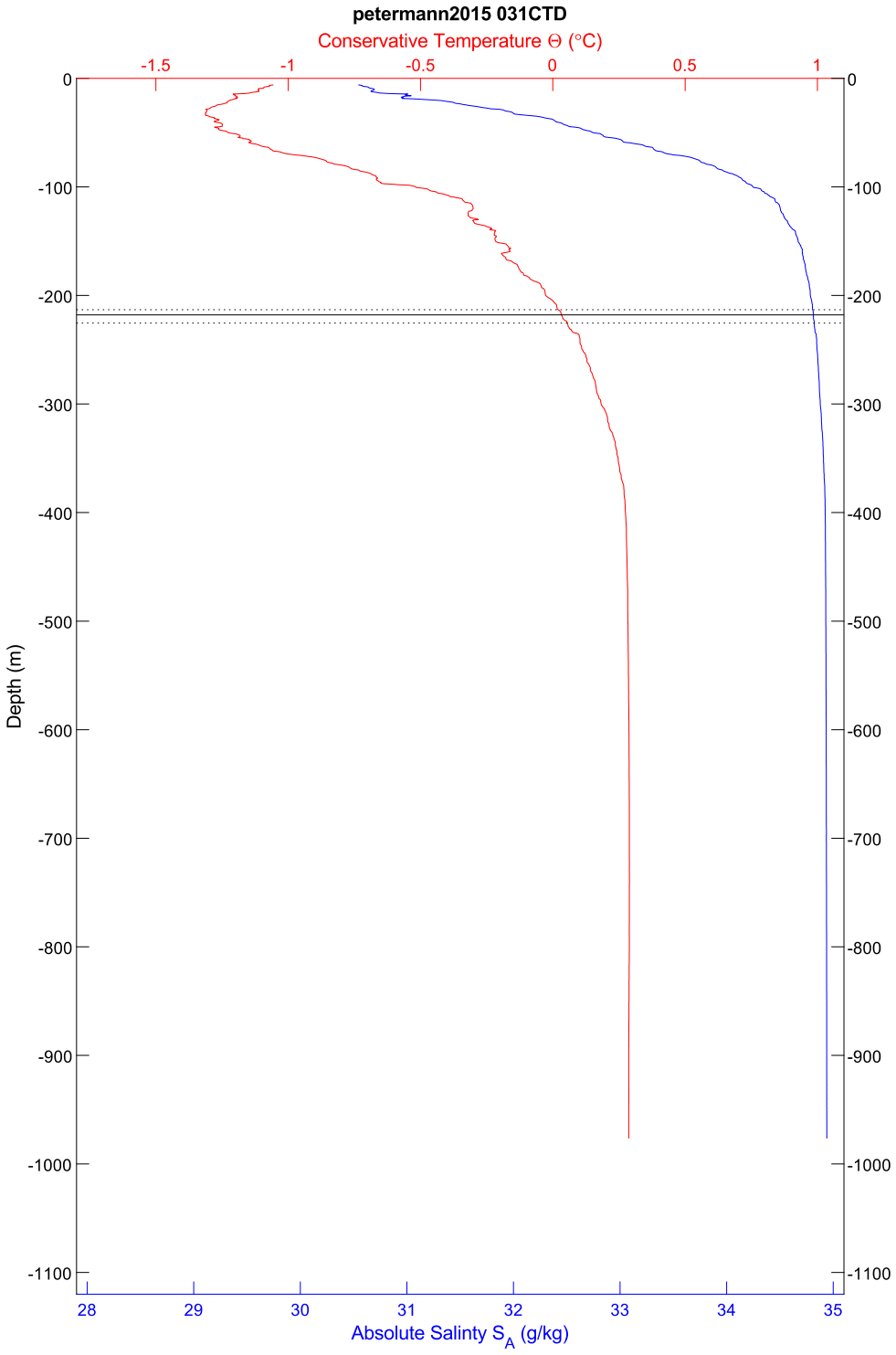

Figure 233: CTD 031, temperature and salinity plotted by depth. The scattering layer depth is indicated by horizontal lines; the solid line is the average depth, the dotted lines are the shallowest and deepest depths, in all cases for the top of the scattering layer.

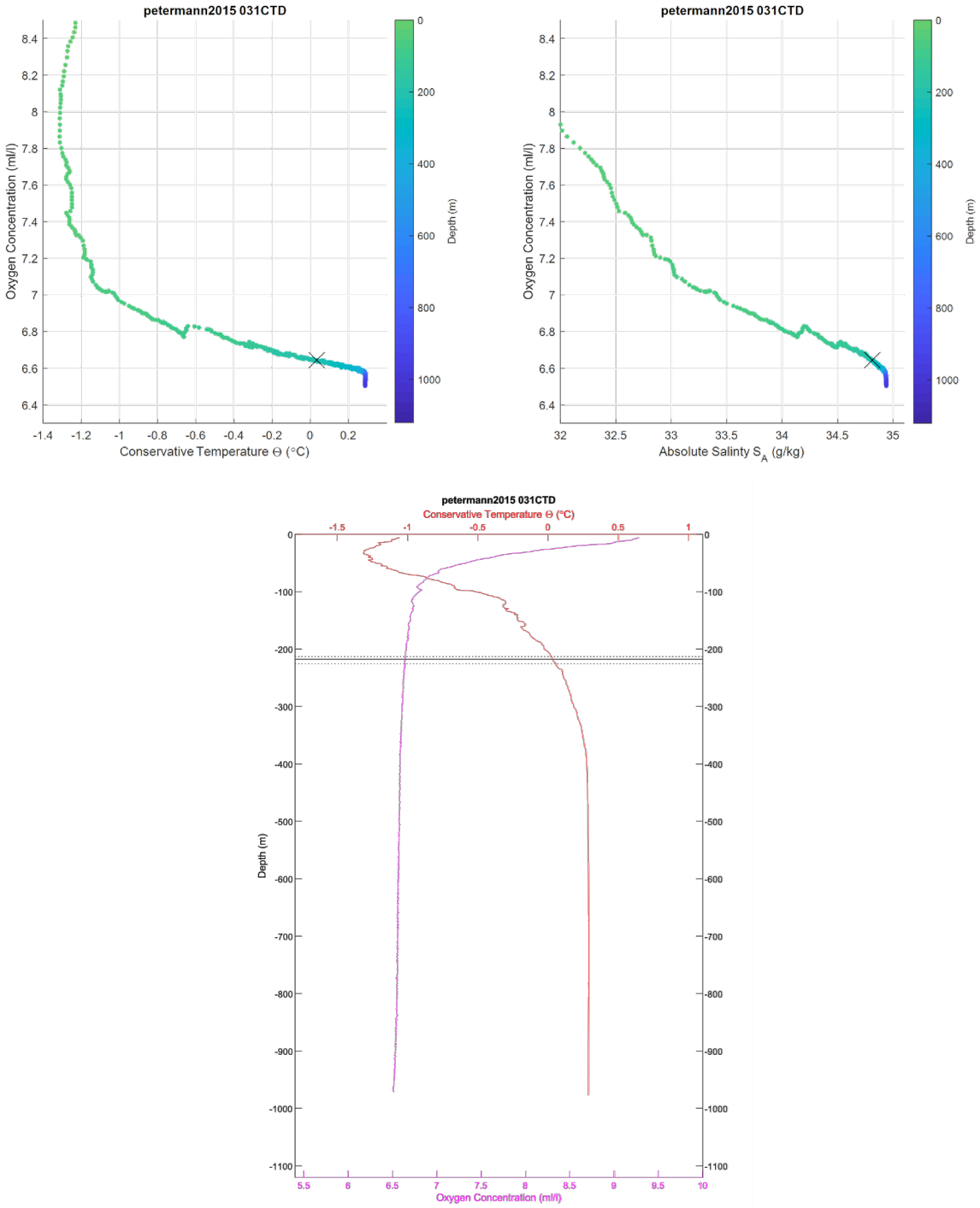

Figure 234: CTD 031. Top left, oxygen-temperature diagram, colored by depth. Top right, oxygen-salinity diagram, colored by depth. The black 'X' in the first two plots indicates the average depth for the top of the scattering layer in this location. Bottom center, temperature and oxygen plotted by depth. The scattering layer depth is indicated by horizontal lines; the solid line is the average depth, the dotted lines are the shallowest and deepest depths, in both cases for the top of the scattering layer.

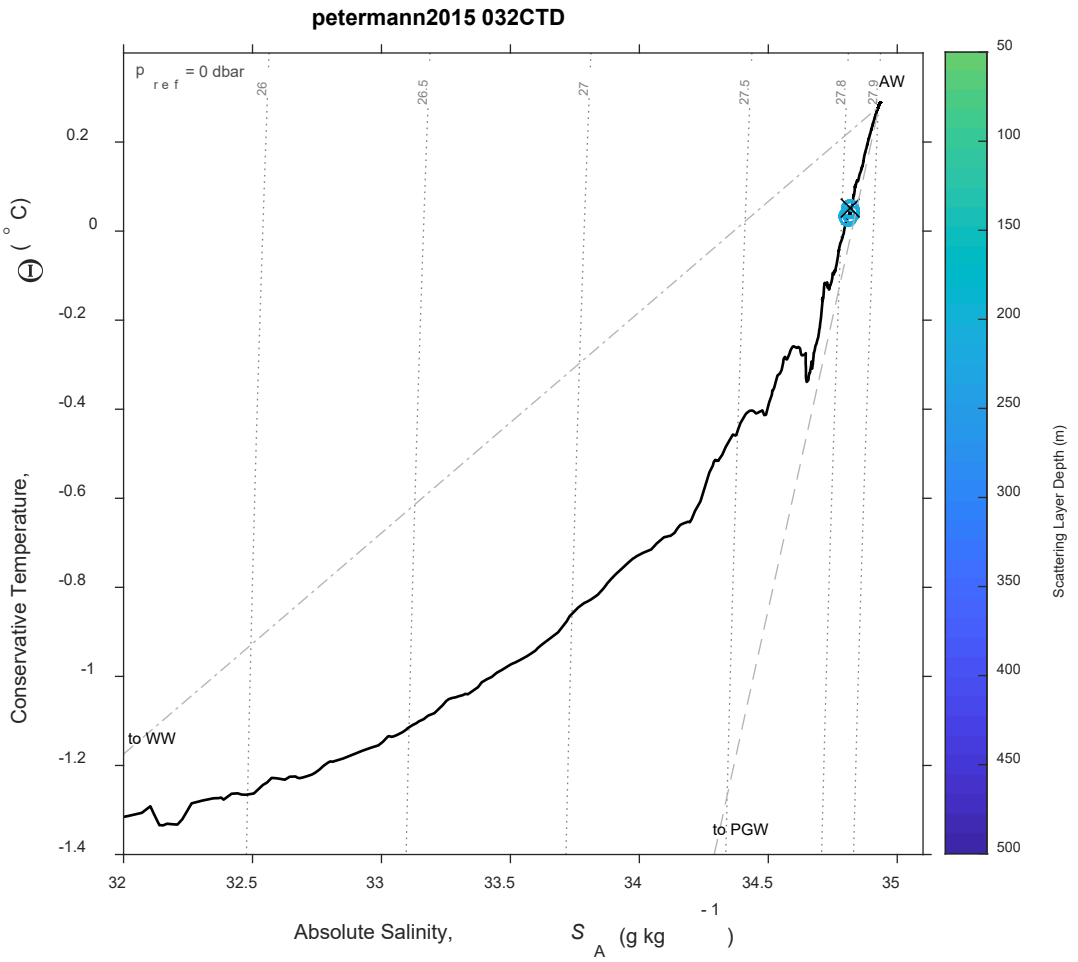

Figure 235: CTD 032, Temperature-Salinity (T-S) diagram. The scattering layer picks corresponding to this CTD are plotted as open circles colored by depth; a black 'X' indicates the average depth for the top of the scattering layer in this location. Isobars are shown as labeled grey dotted lines.

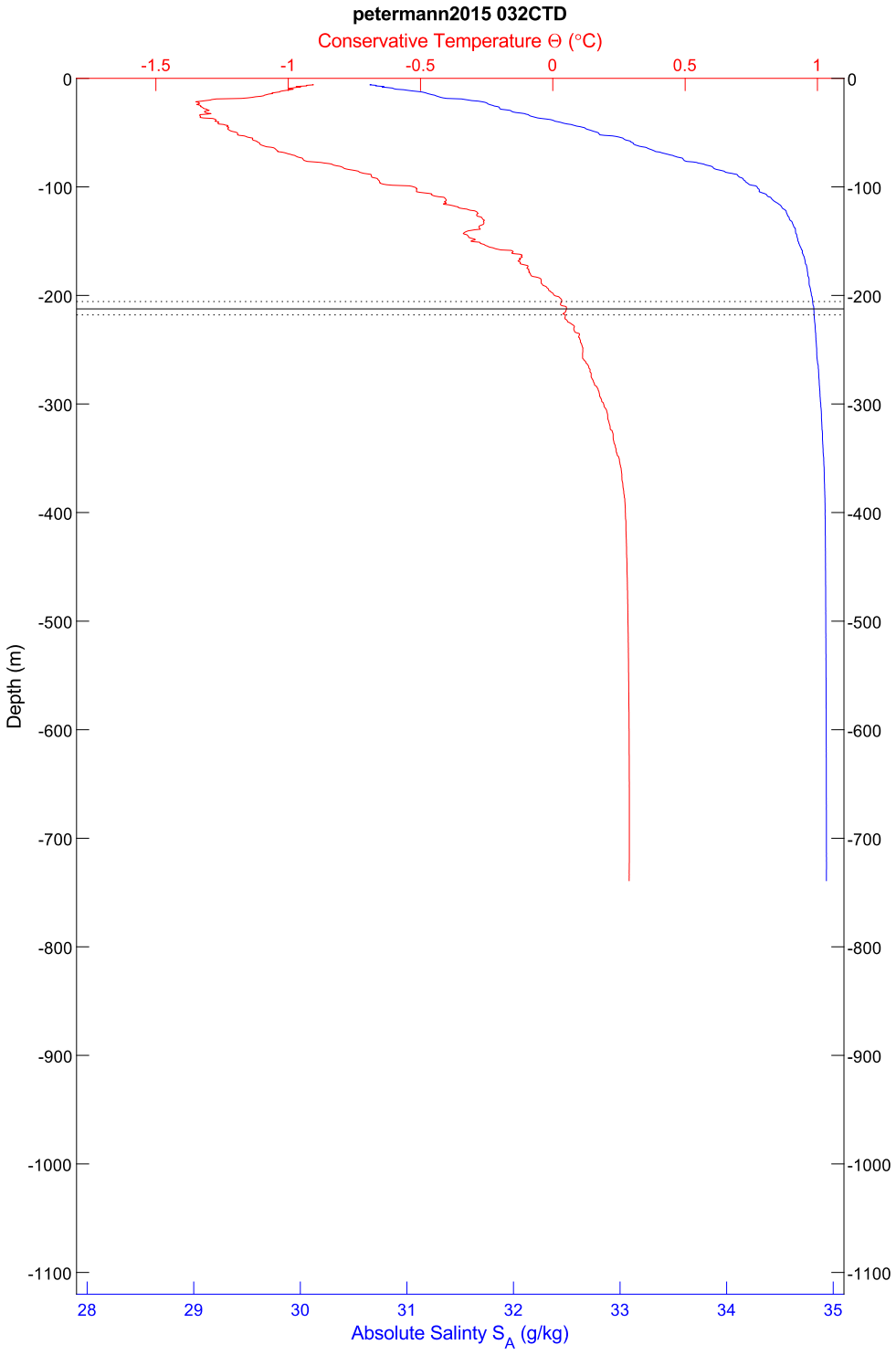

Figure 236: CTD 032, temperature and salinity plotted by depth. The scattering layer depth is indicated by horizontal lines; the solid line is the average depth, the dotted lines are the shallowest and deepest depths, in all cases for the top of the scattering layer.

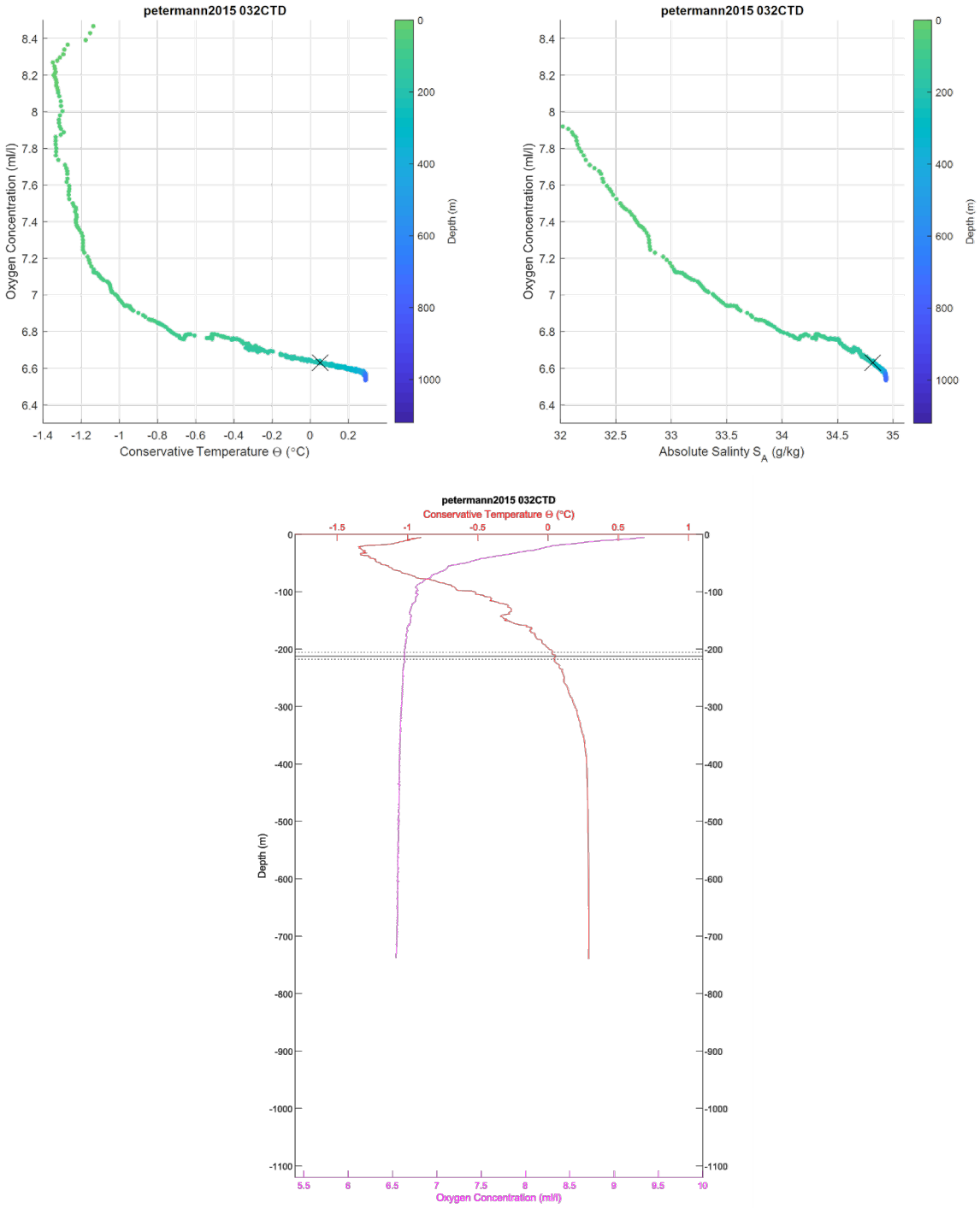

Figure 237: CTD 032. Top left, oxygen-temperature diagram, colored by depth. Top right, oxygen-salinity diagram, colored by depth. The black 'X' in the first two plots indicates the average depth for the top of the scattering layer in this location. Bottom center, temperature and oxygen plotted by depth. The scattering layer depth is indicated by horizontal lines; the solid line is the average depth, the dotted lines are the shallowest and deepest depths, in both cases for the top of the scattering layer.

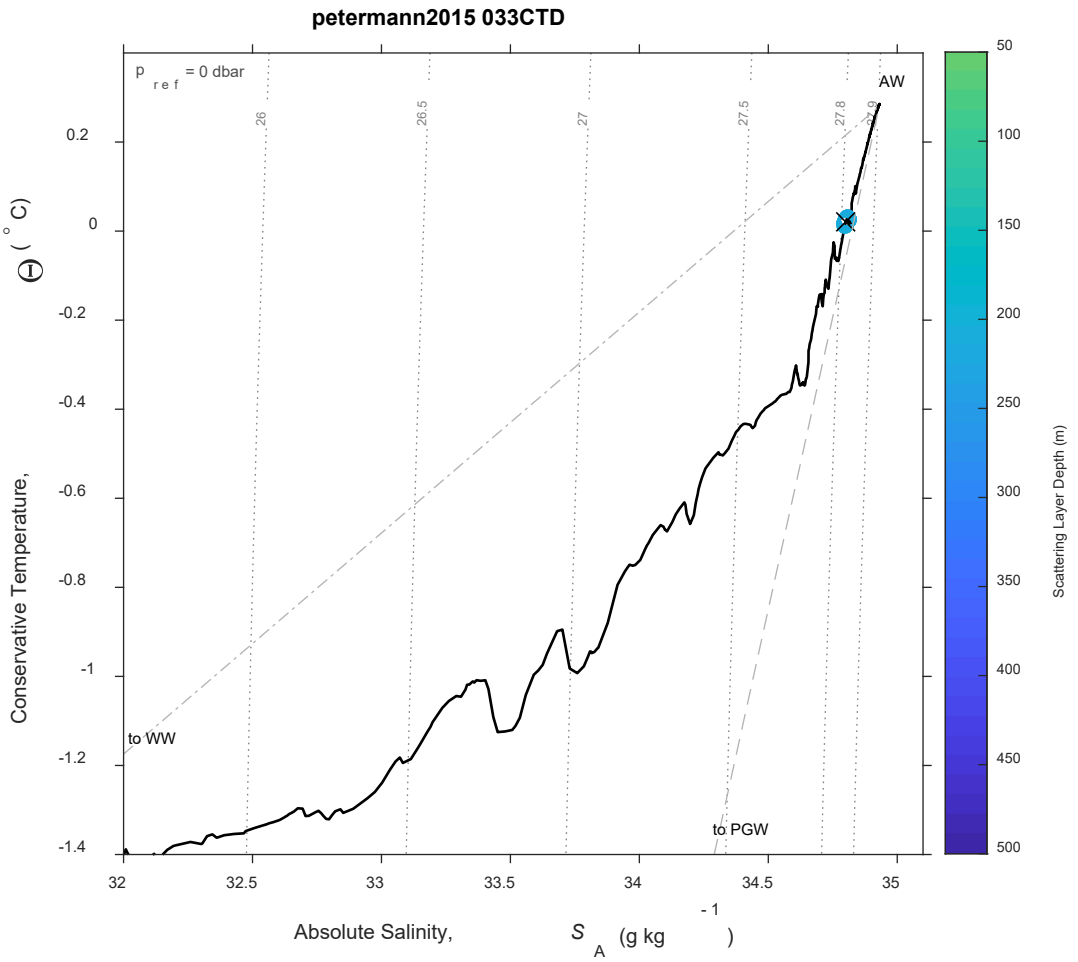

Figure 238: CTD 033, Temperature-Salinity (T-S) diagram. The scattering layer picks corresponding to this CTD are plotted as open circles colored by depth; a black 'X' indicates the average depth for the top of the scattering layer in this location. Isobars are shown as labeled grey dotted lines.

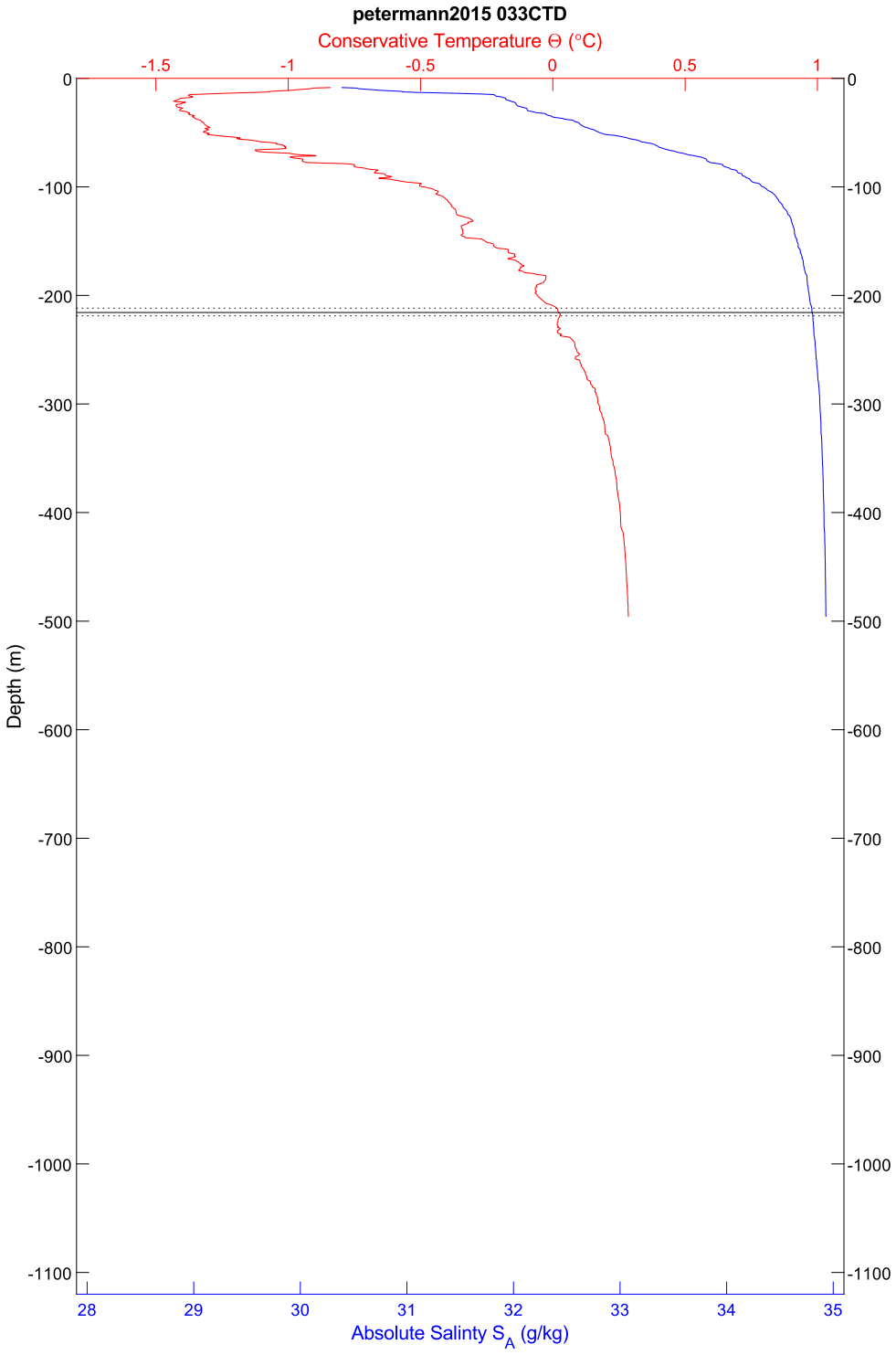

Figure 239: CTD 033, temperature and salinity plotted by depth. The scattering layer depth is indicated by horizontal lines; the solid line is the average depth, the dotted lines are the shallowest and deepest depths, in all cases for the top of the scattering layer.

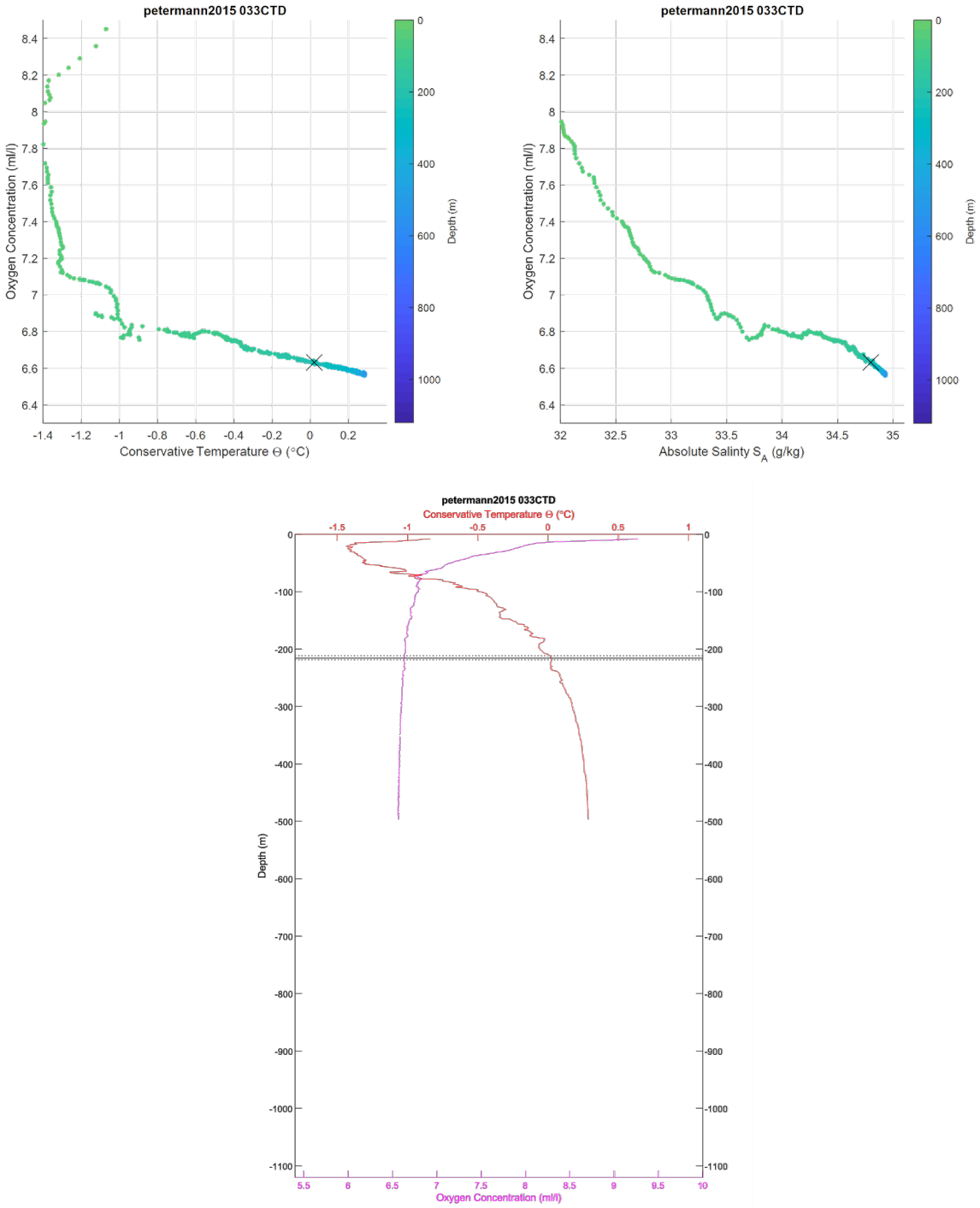

Figure 240: CTD 033. Top left, oxygen-temperature diagram, colored by depth. Top right, oxygen-salinity diagram, colored by depth. The black 'X' in the first two plots indicates the average depth for the top of the scattering layer in this location. Bottom center, temperature and oxygen plotted by depth. The scattering layer depth is indicated by horizontal lines; the solid line is the average depth, the dotted lines are the shallowest and deepest depths, in both cases for the top of the scattering layer.

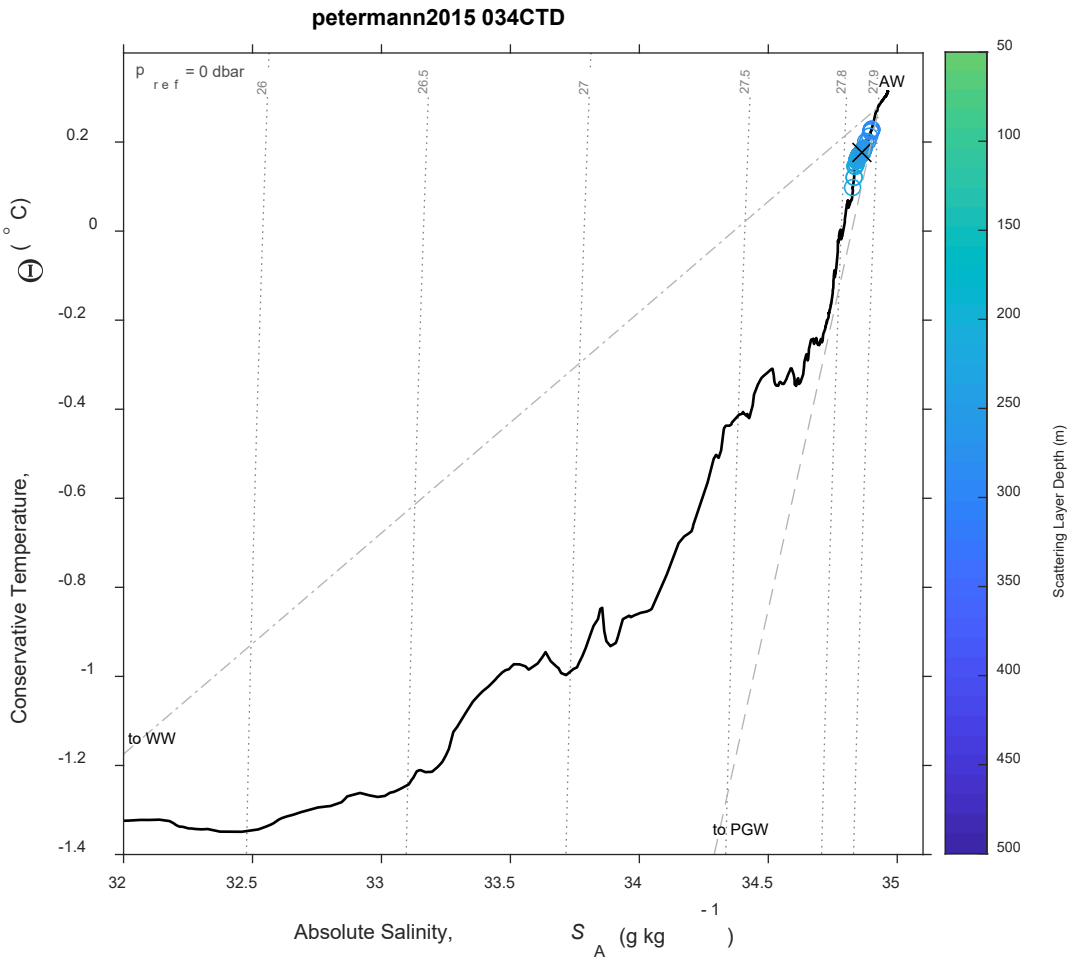

Figure 241: CTD 034, Temperature-Salinity (T-S) diagram. The scattering layer picks corresponding to this CTD are plotted as open circles colored by depth; a black 'X' indicates the average depth for the top of the scattering layer in this location. Isobars are shown as labeled grey dotted lines.

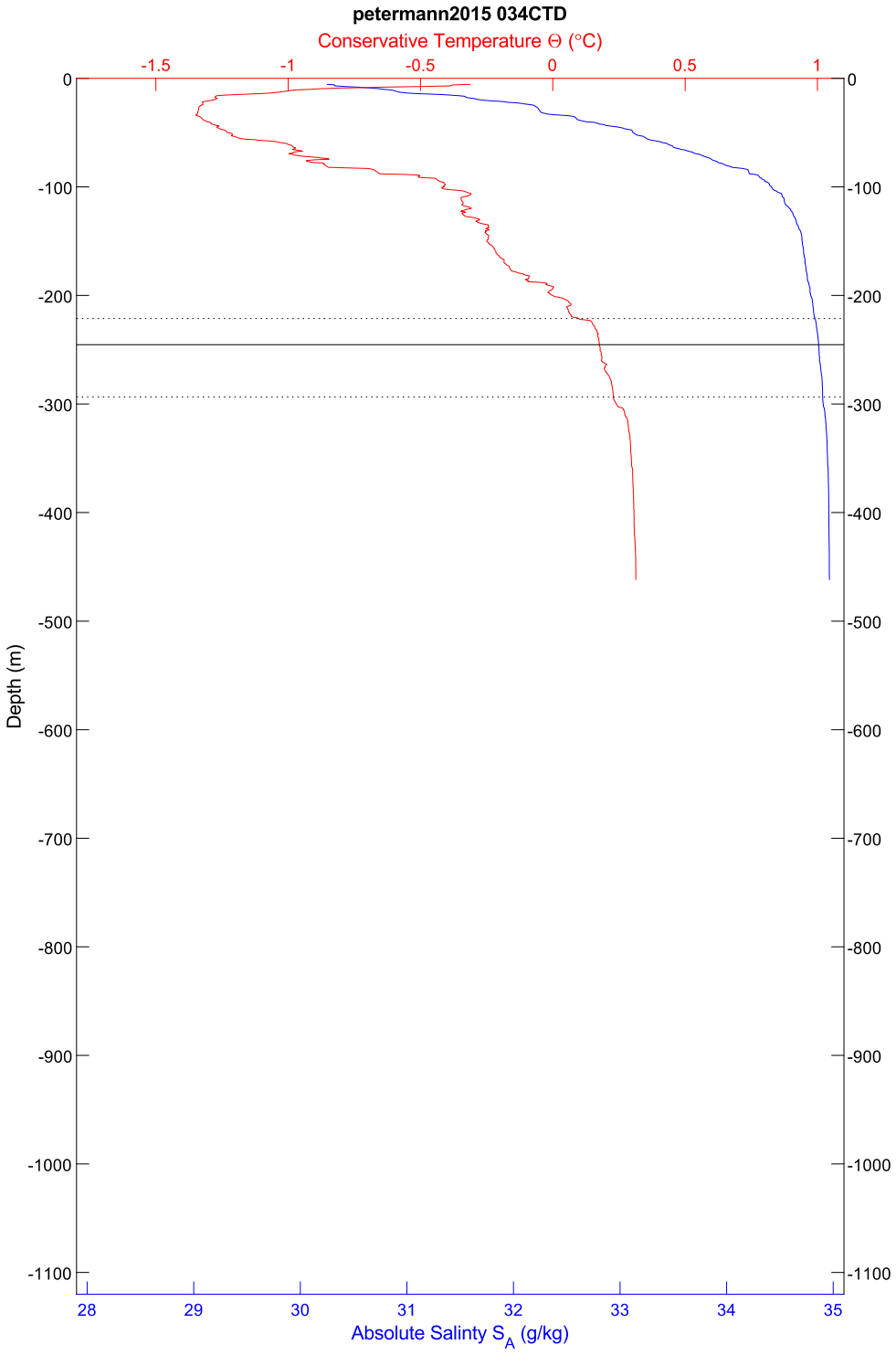

Figure 242: CTD 034, temperature and salinity plotted by depth. The scattering layer depth is indicated by horizontal lines; the solid line is the average depth, the dotted lines are the shallowest and deepest depths, in all cases for the top of the scattering layer.

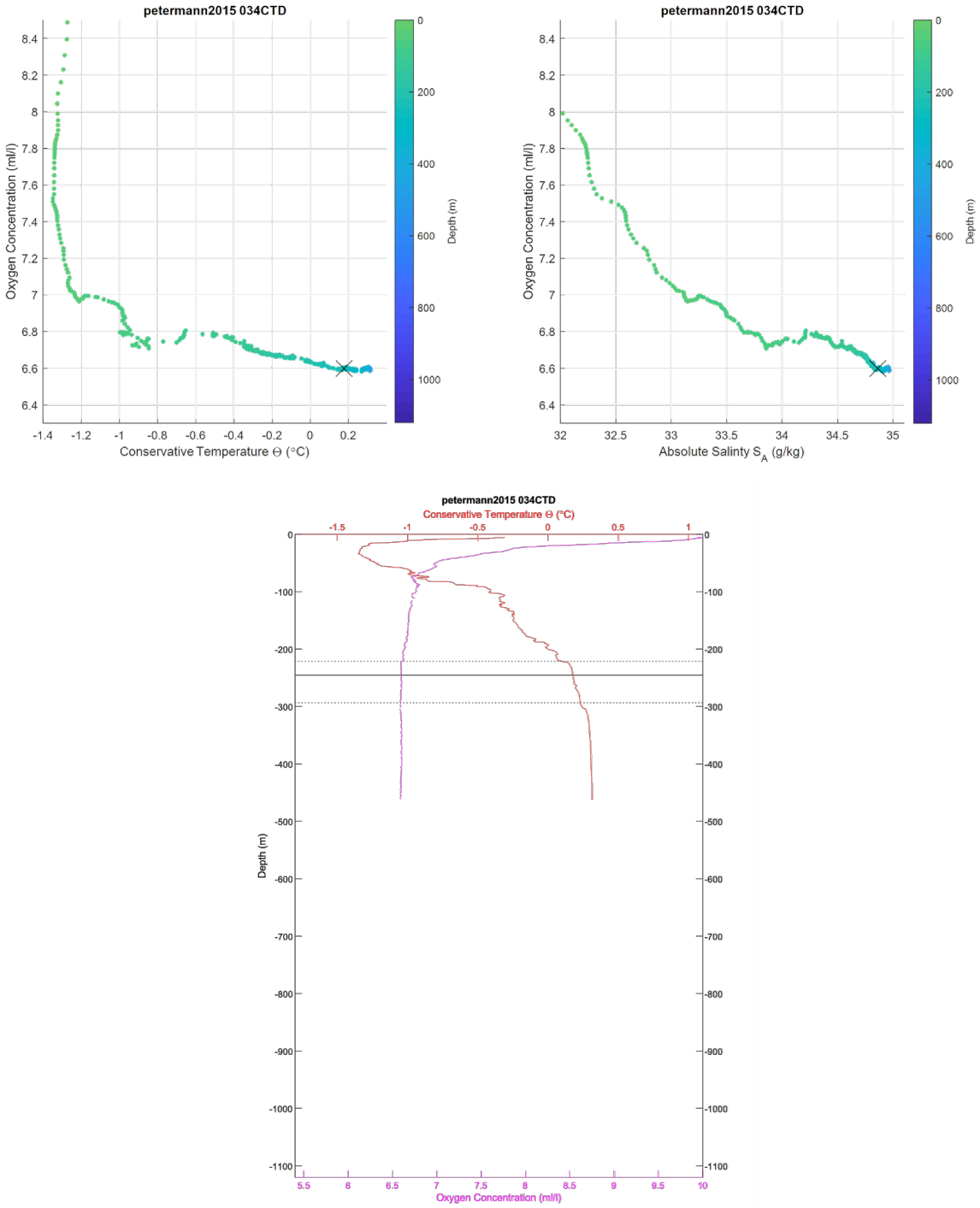

Figure 243: CTD 034. Top left, oxygen-temperature diagram, colored by depth. Top right, oxygen-salinity diagram, colored by depth. The black 'X' in the first two plots indicates the average depth for the top of the scattering layer in this location. Bottom center, temperature and oxygen plotted by depth. The scattering layer depth is indicated by horizontal lines; the solid line is the average depth, the dotted lines are the shallowest and deepest depths, in both cases for the top of the scattering layer.

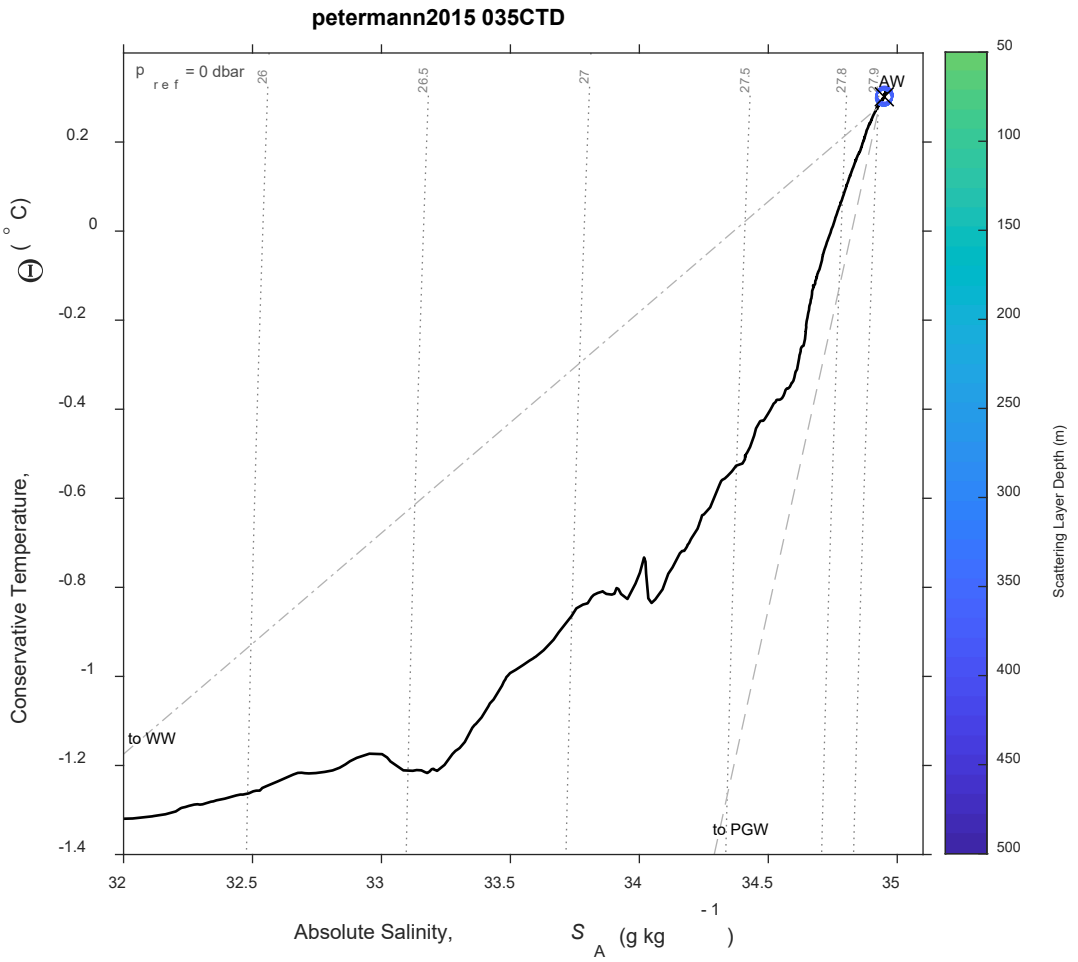

Figure 244: CTD 035, Temperature-Salinity (T-S) diagram. The scattering layer picks corresponding to this CTD are plotted as open circles colored by depth; a black 'X' indicates the average depth for the top of the scattering layer in this location. Isobars are shown as labeled grey dotted lines.

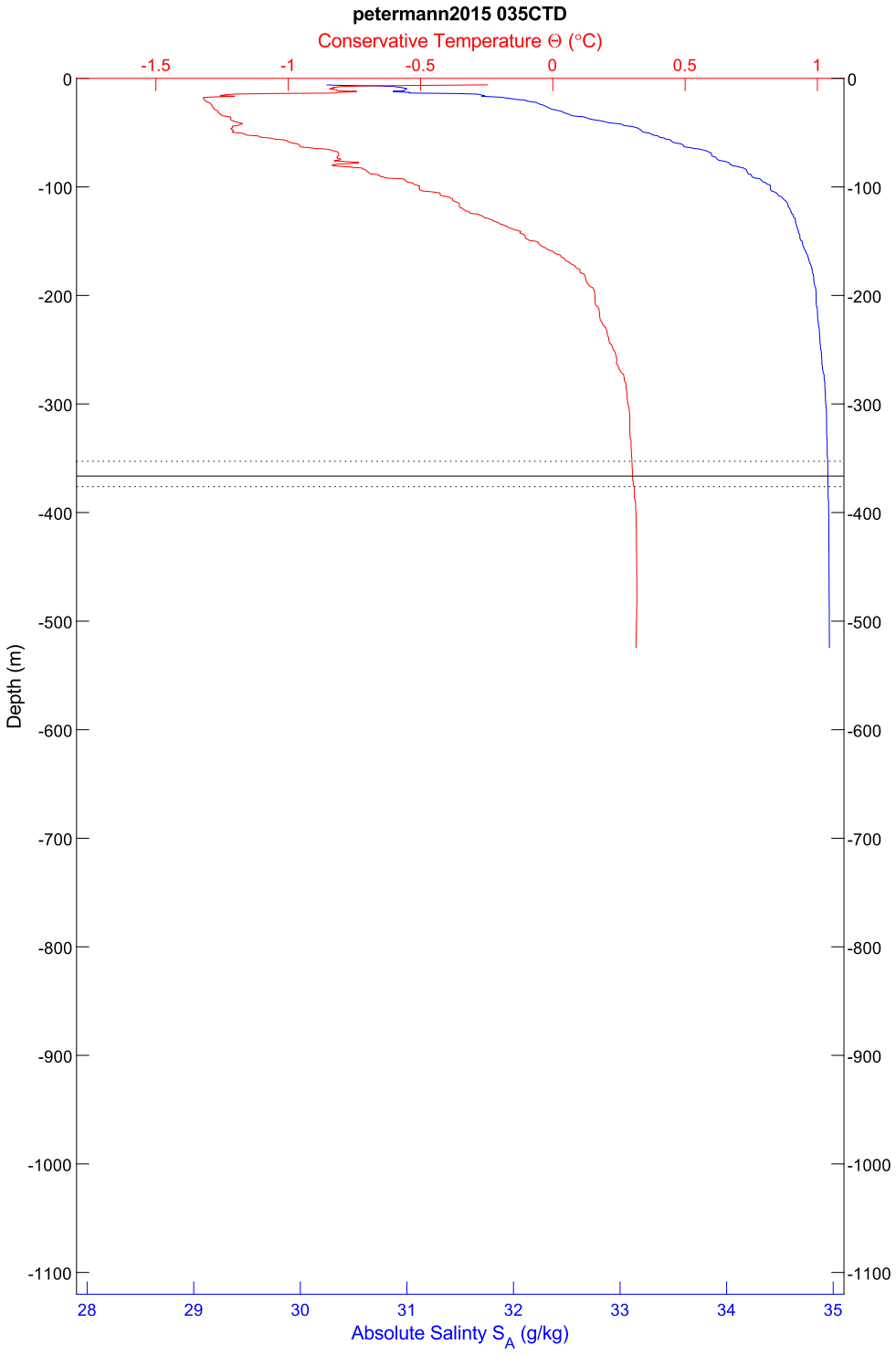

Figure 245: CTD 035, temperature and salinity plotted by depth. The scattering layer depth is indicated by horizontal lines; the solid line is the average depth, the dotted lines are the shallowest and deepest depths, in all cases for the top of the scattering layer.

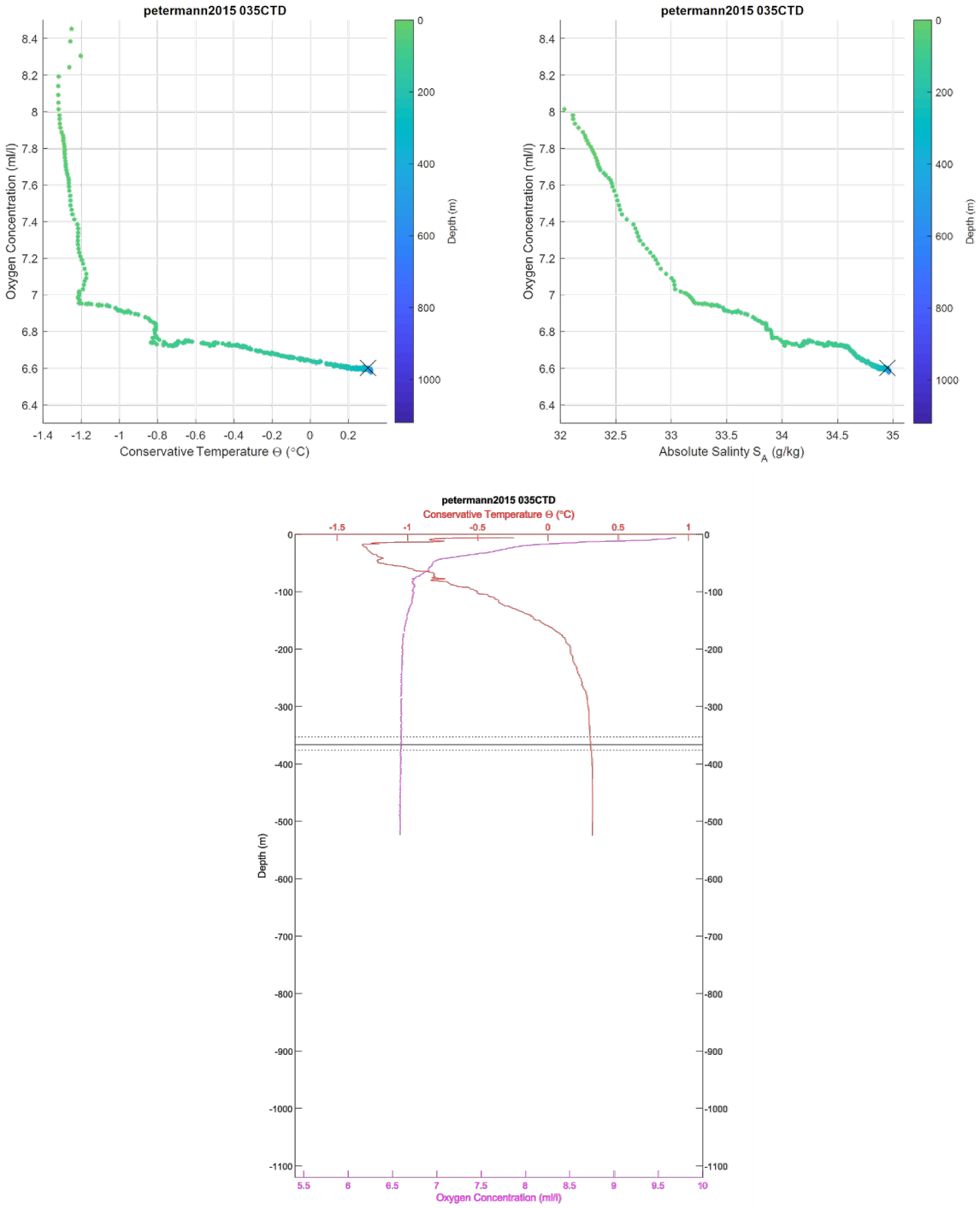

Figure 246: CTD 035. Top left, oxygen-temperature diagram, colored by depth. Top right, oxygen-salinity diagram, colored by depth. The black 'X' in the first two plots indicates the average depth for the top of the scattering layer in this location. Bottom center, temperature and oxygen plotted by depth. The scattering layer depth is indicated by horizontal lines; the solid line is the average depth, the dotted lines are the shallowest and deepest depths, in both cases for the top of the scattering layer.

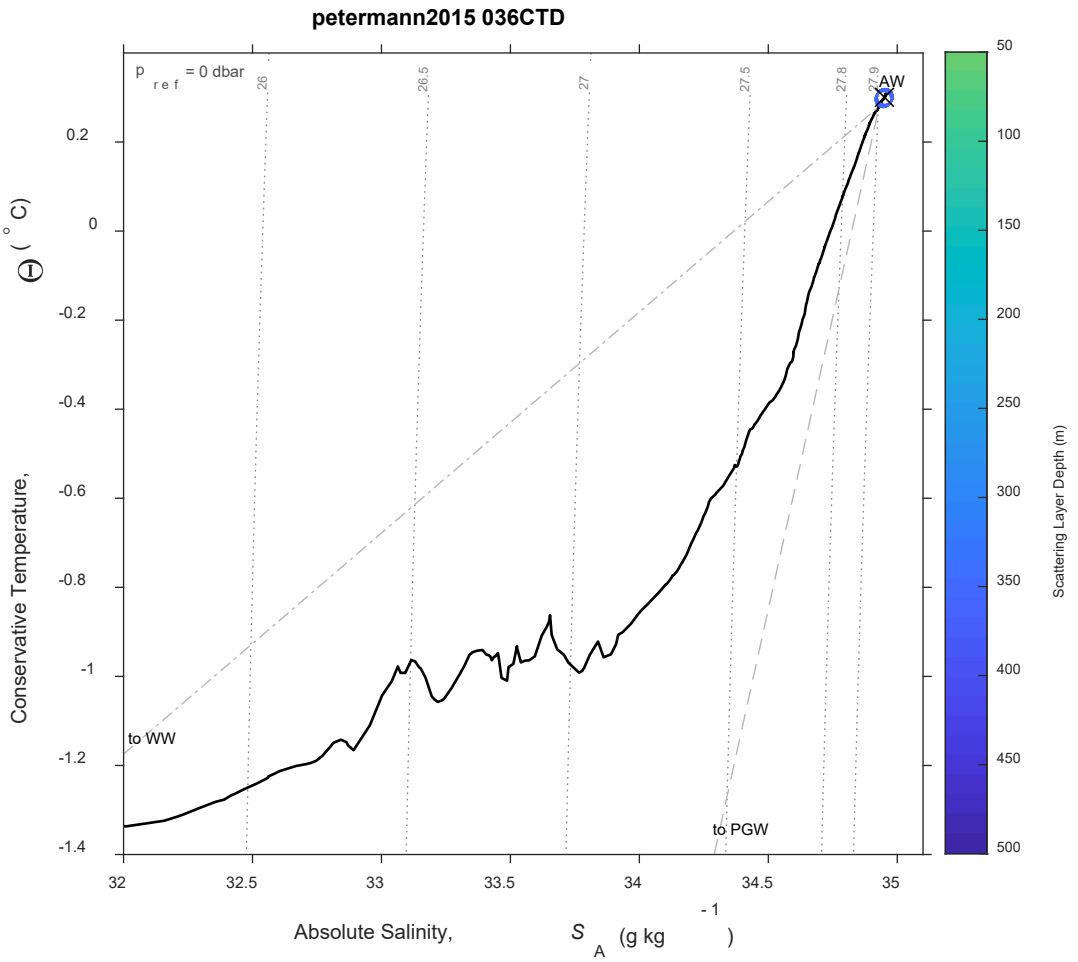

Figure 247: CTD 036, Temperature-Salinity (T-S) diagram. The scattering layer picks corresponding to this CTD are plotted as open circles colored by depth; a black 'X' indicates the average depth for the top of the scattering layer in this location. Isobars are shown as labeled grey dotted lines.

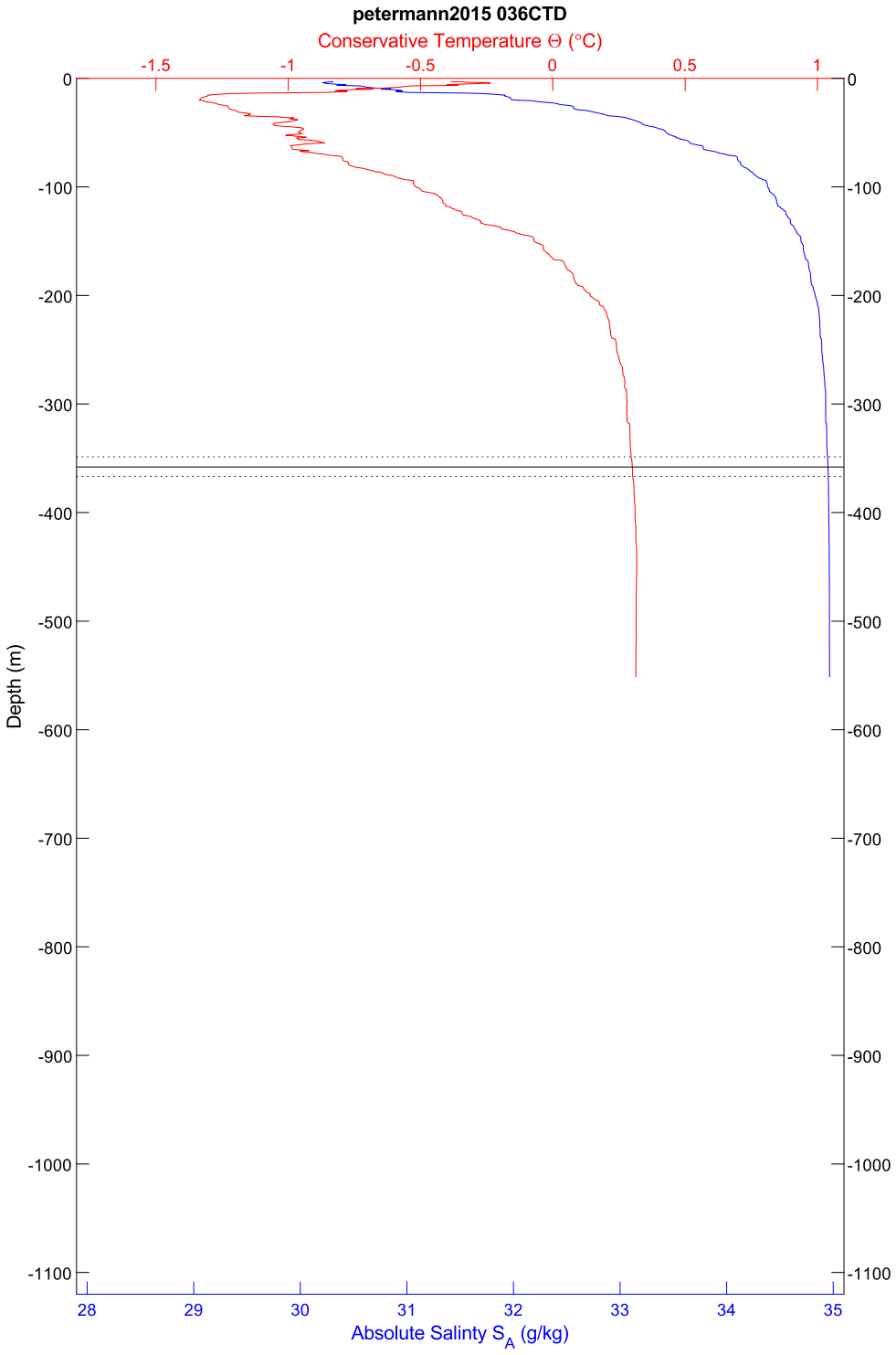

Figure 248: CTD 036, temperature and salinity plotted by depth. The scattering layer depth is indicated by horizontal lines; the solid line is the average depth, the dotted lines are the shallowest and deepest depths, in all cases for the top of the scattering layer.

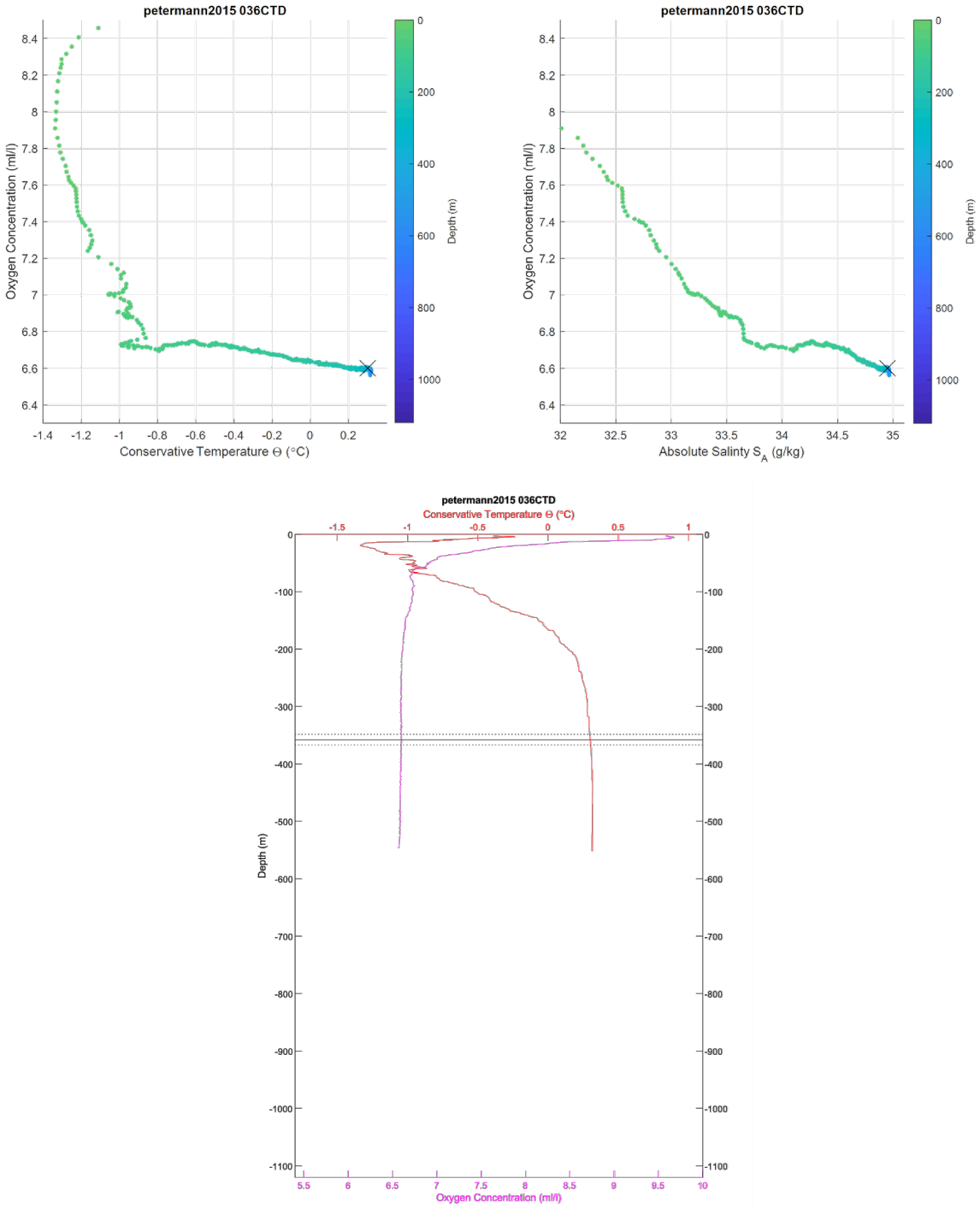

Figure 249: CTD 036. Top left, oxygen-temperature diagram, colored by depth. Top right, oxygen-salinity diagram, colored by depth. The black 'X' in the first two plots indicates the average depth for the top of the scattering layer in this location. Bottom center, temperature and oxygen plotted by depth. The scattering layer depth is indicated by horizontal lines; the solid line is the average depth, the dotted lines are the shallowest and deepest depths, in both cases for the top of the scattering layer.

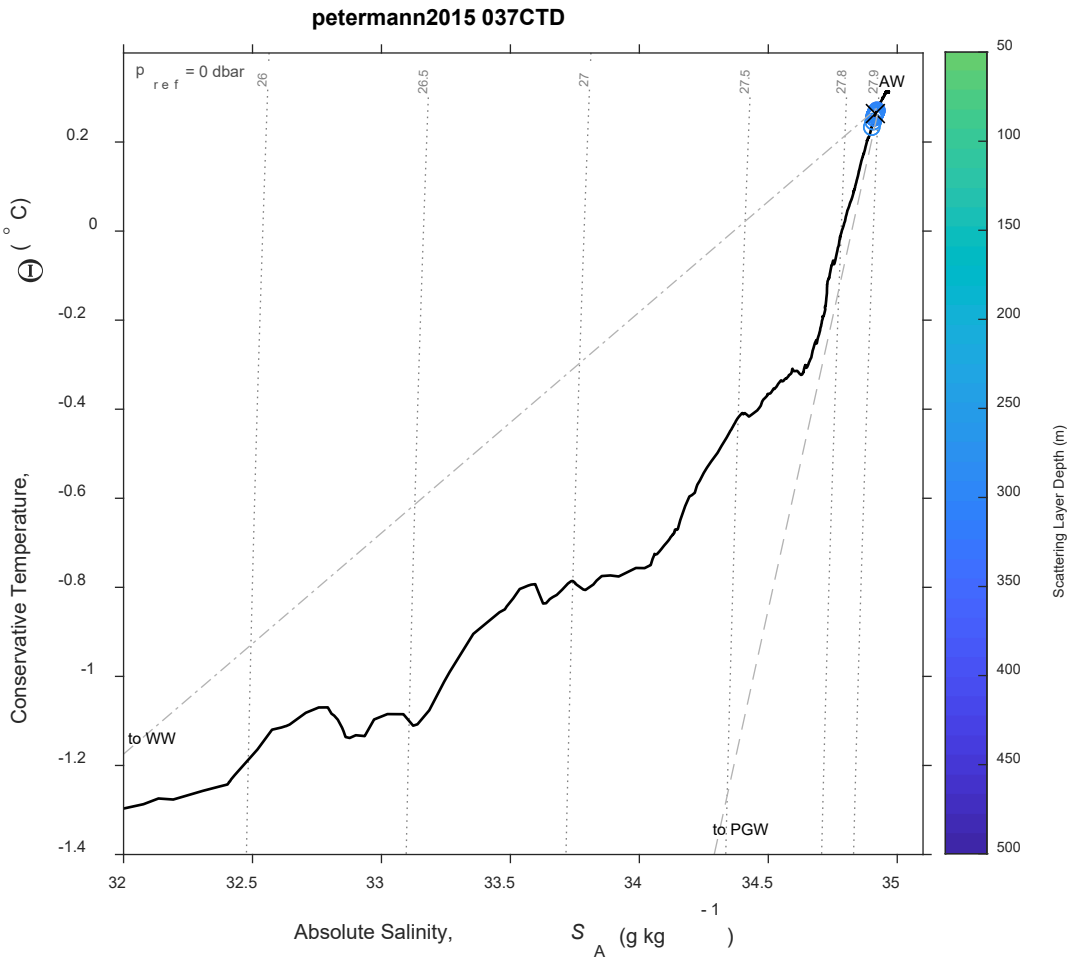

Figure 250: CTD 037, Temperature-Salinity (T-S) diagram. The scattering layer picks corresponding to this CTD are plotted as open circles colored by depth; a black 'X' indicates the average depth for the top of the scattering layer in this location. Isobars are shown as labeled grey dotted lines.

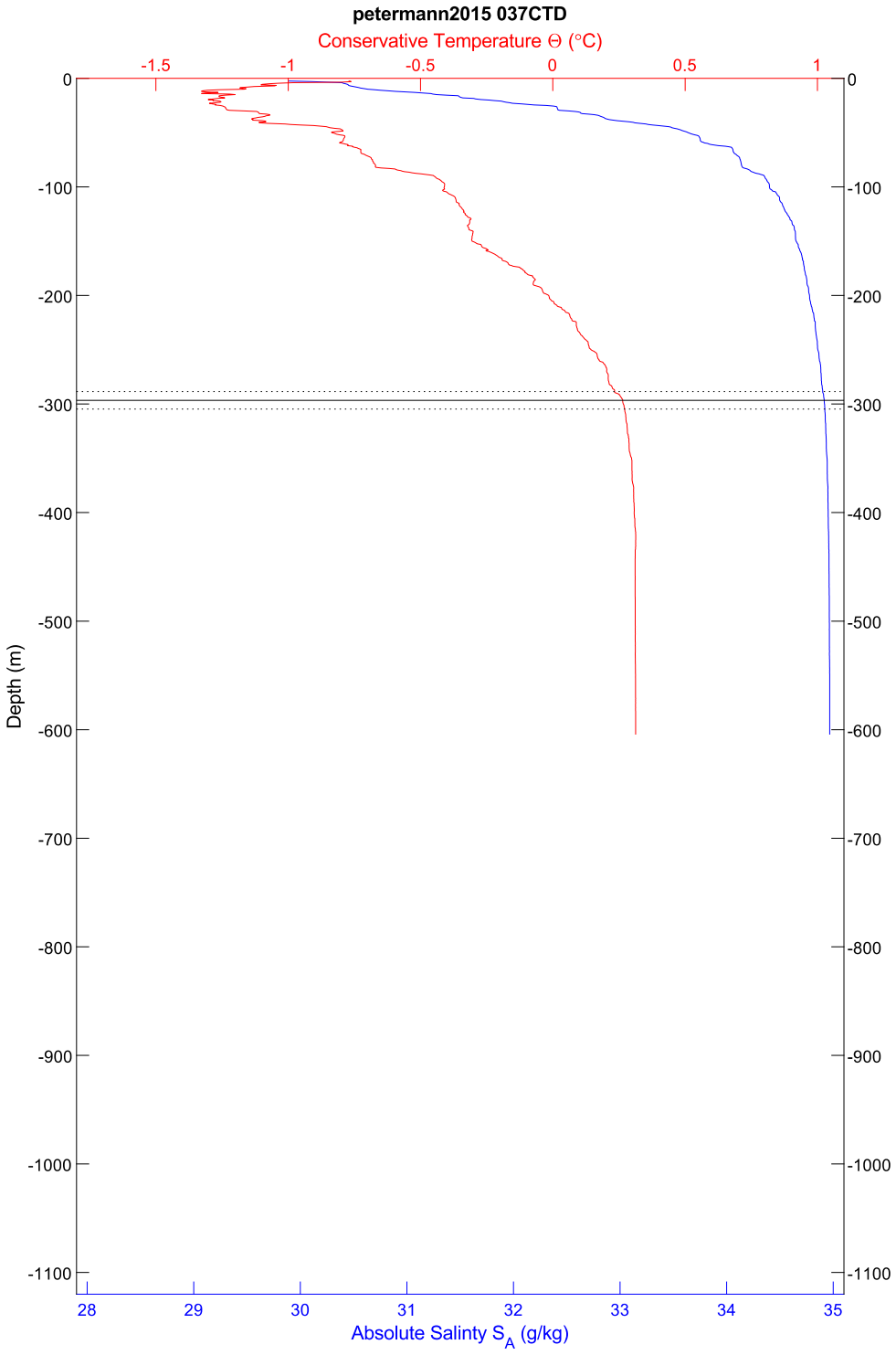

Figure 251: CTD 037, temperature and salinity plotted by depth. The scattering layer depth is indicated by horizontal lines; the solid line is the average depth, the dotted lines are the shallowest and deepest depths, in all cases for the top of the scattering layer.

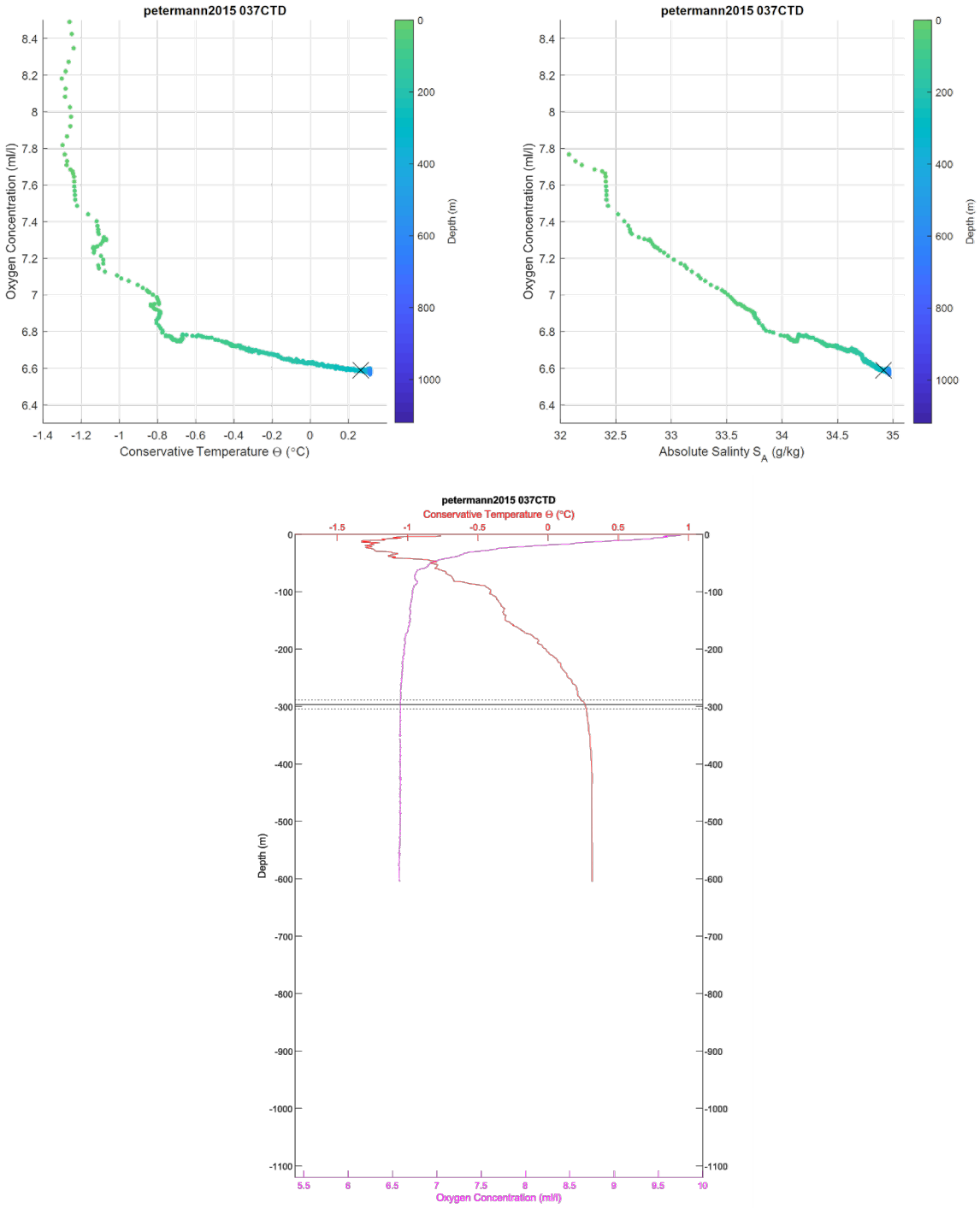

Figure 252: CTD 037. Top left, oxygen-temperature diagram, colored by depth. Top right, oxygen-salinity diagram, colored by depth. The black 'X' in the first two plots indicates the average depth for the top of the scattering layer in this location. Bottom center, temperature and oxygen plotted by depth. The scattering layer depth is indicated by horizontal lines; the solid line is the average depth, the dotted lines are the shallowest and deepest depths, in both cases for the top of the scattering layer.

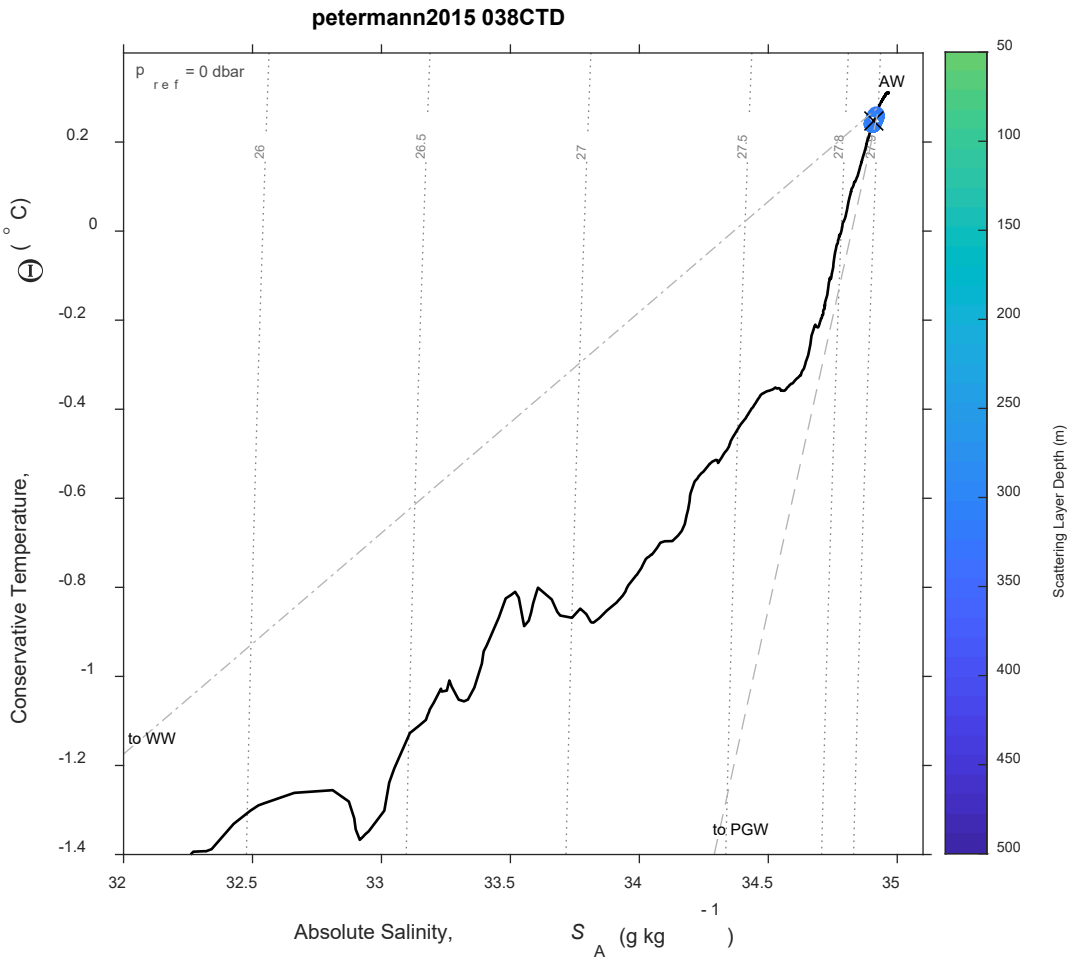

Figure 253: CTD 038, Temperature-Salinity (T-S) diagram. The scattering layer picks corresponding to this CTD are plotted as open circles colored by depth; a black 'X' indicates the average depth for the top of the scattering layer in this location. Isobars are shown as labeled grey dotted lines.

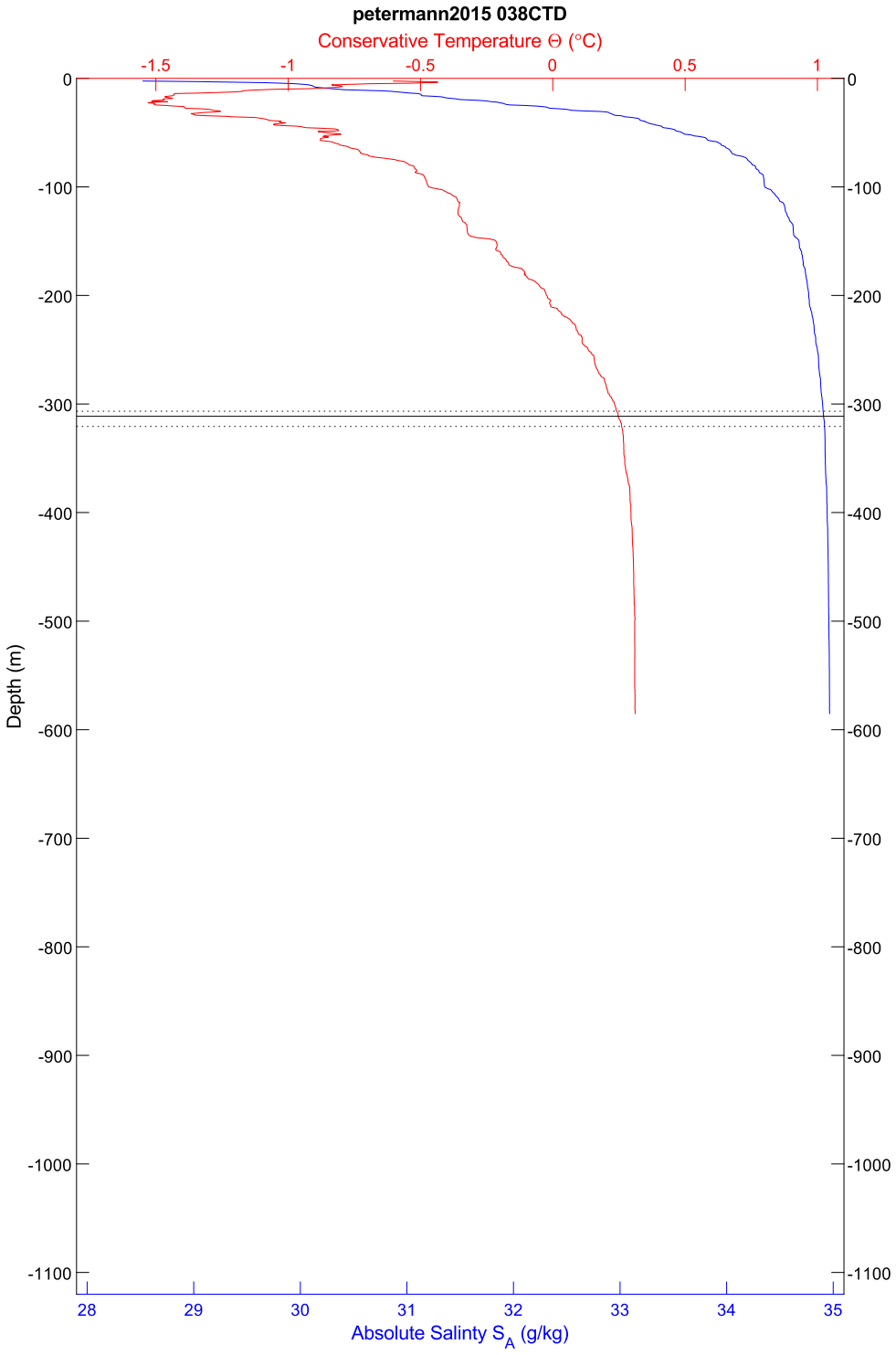

Figure 254: CTD 038, temperature and salinity plotted by depth. The scattering layer depth is indicated by horizontal lines; the solid line is the average depth, the dotted lines are the shallowest and deepest depths, in all cases for the top of the scattering layer.

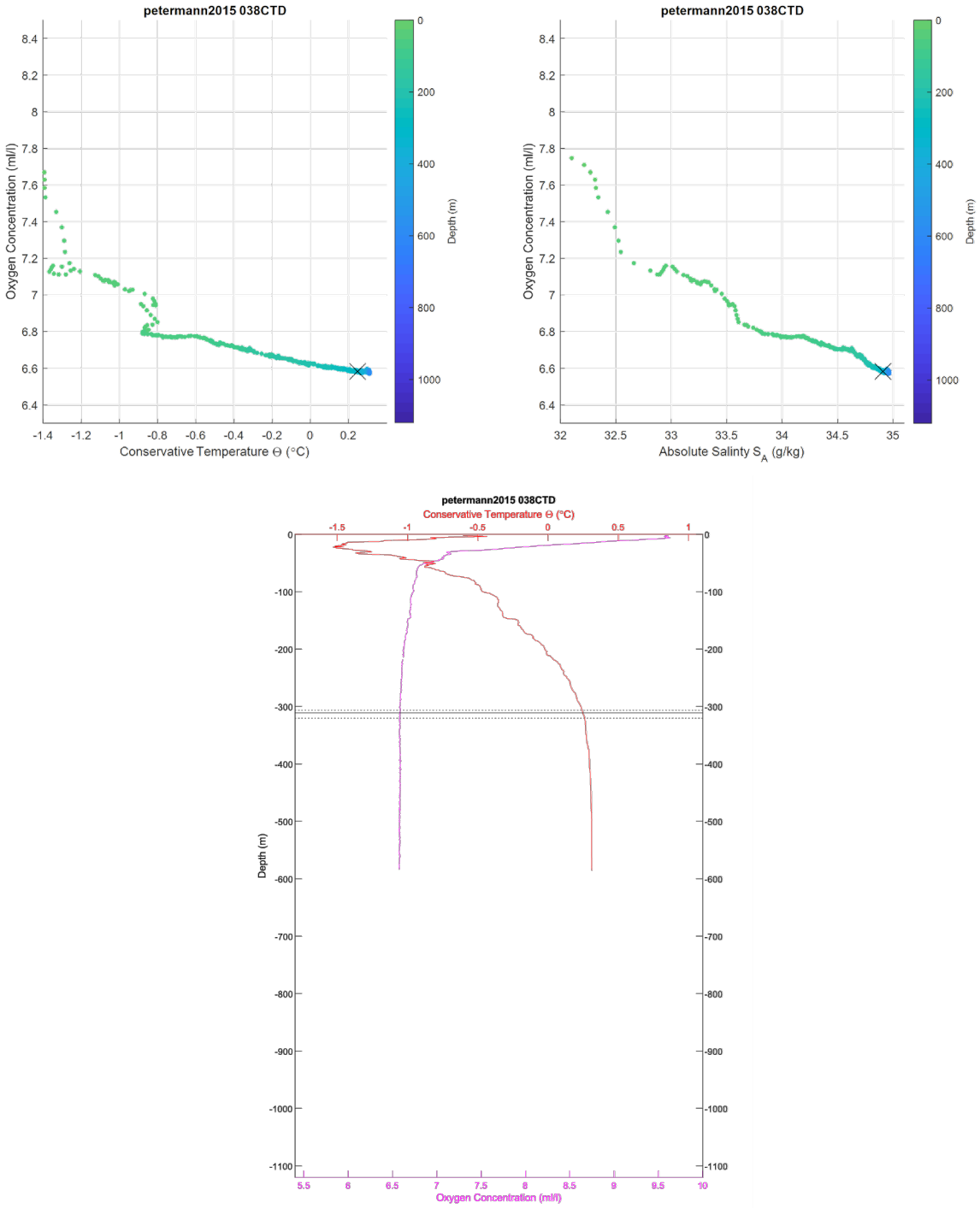

Figure 255: CTD 038. Top left, oxygen-temperature diagram, colored by depth. Top right, oxygen-salinity diagram, colored by depth. The black 'X' in the first two plots indicates the average depth for the top of the scattering layer in this location. Bottom center, temperature and oxygen plotted by depth. The scattering layer depth is indicated by horizontal lines; the solid line is the average depth, the dotted lines are the shallowest and deepest depths, in both cases for the top of the scattering layer.

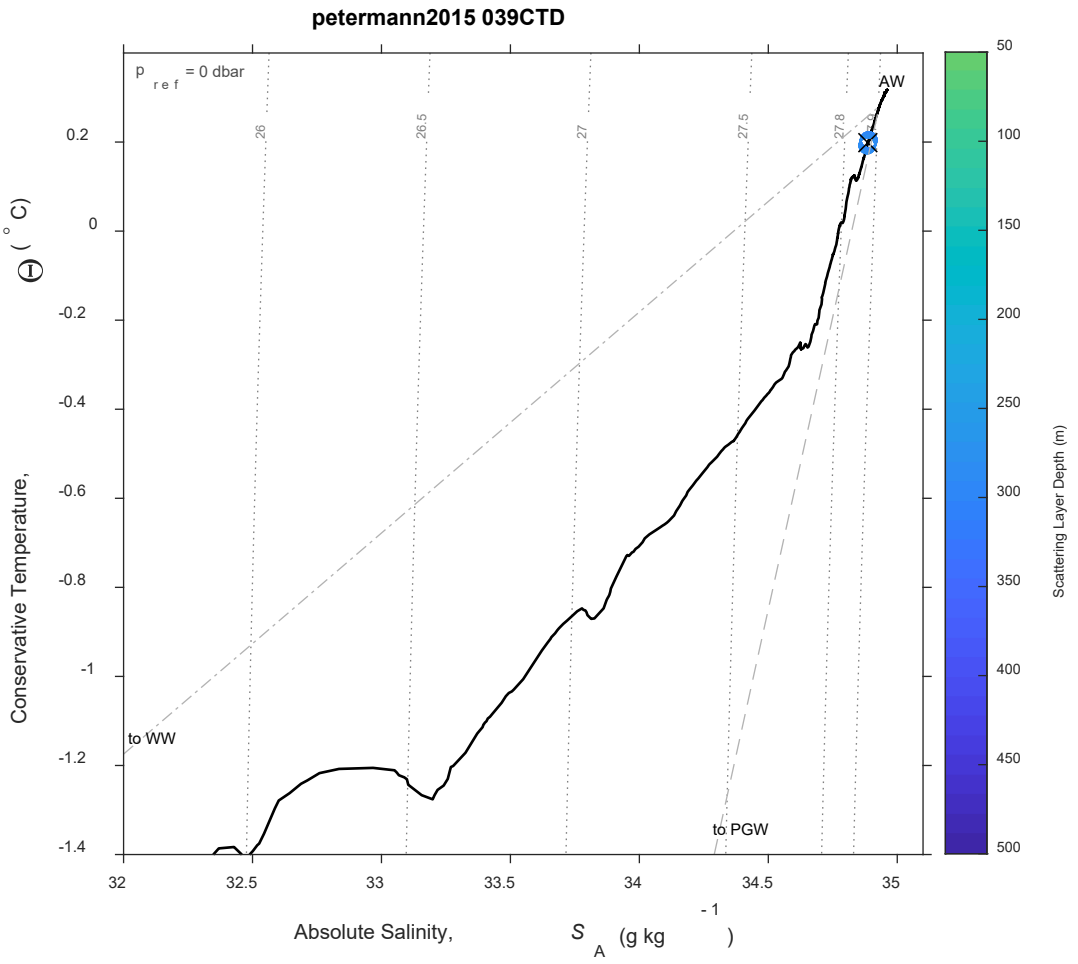

Figure 256: CTD 039, Temperature-Salinity (T-S) diagram. The scattering layer picks corresponding to this CTD are plotted as open circles colored by depth; a black 'X' indicates the average depth for the top of the scattering layer in this location. Isobars are shown as labeled grey dotted lines.

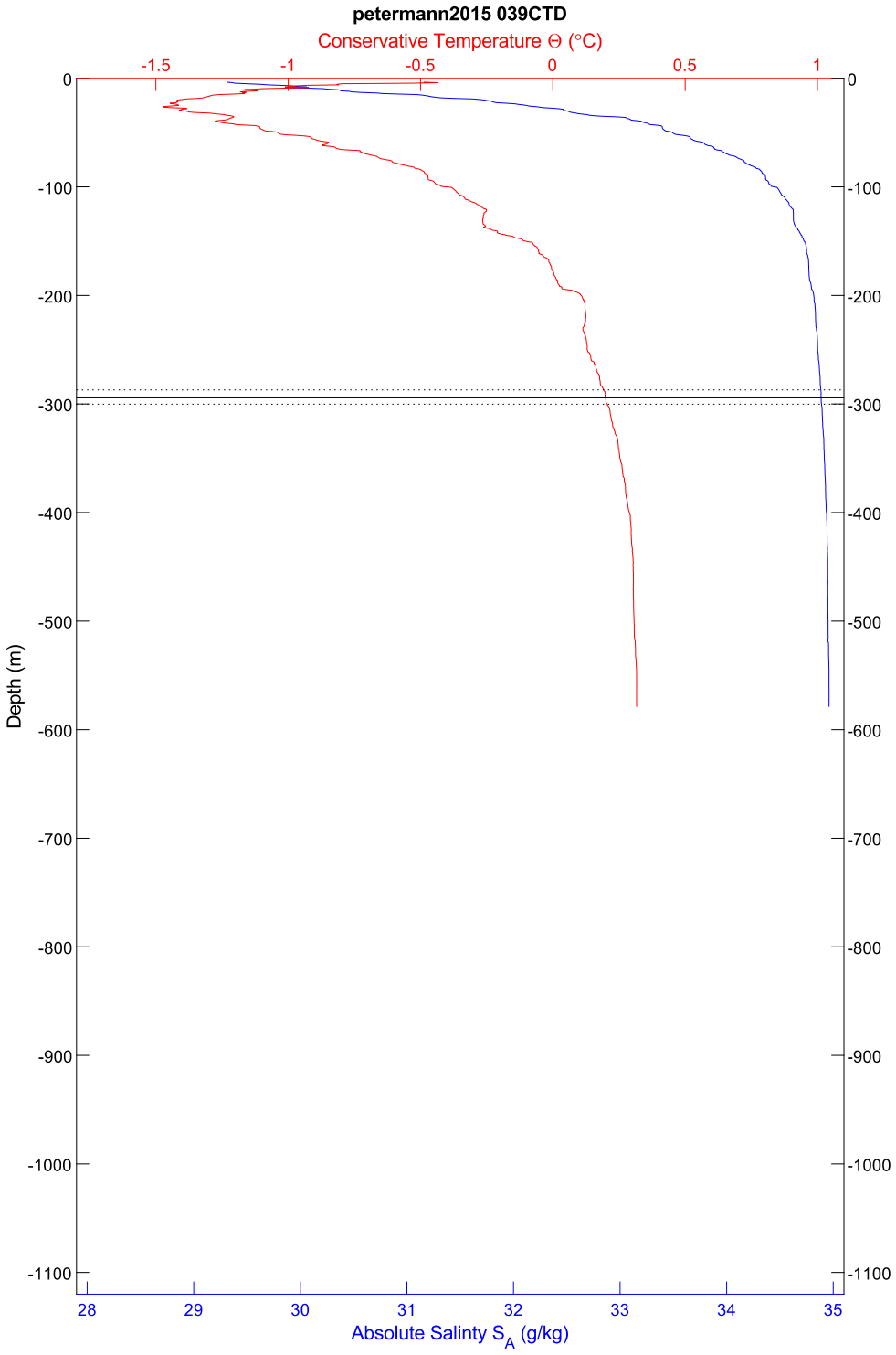

Figure 257: CTD 039, temperature and salinity plotted by depth. The scattering layer depth is indicated by horizontal lines; the solid line is the average depth, the dotted lines are the shallowest and deepest depths, in all cases for the top of the scattering layer.

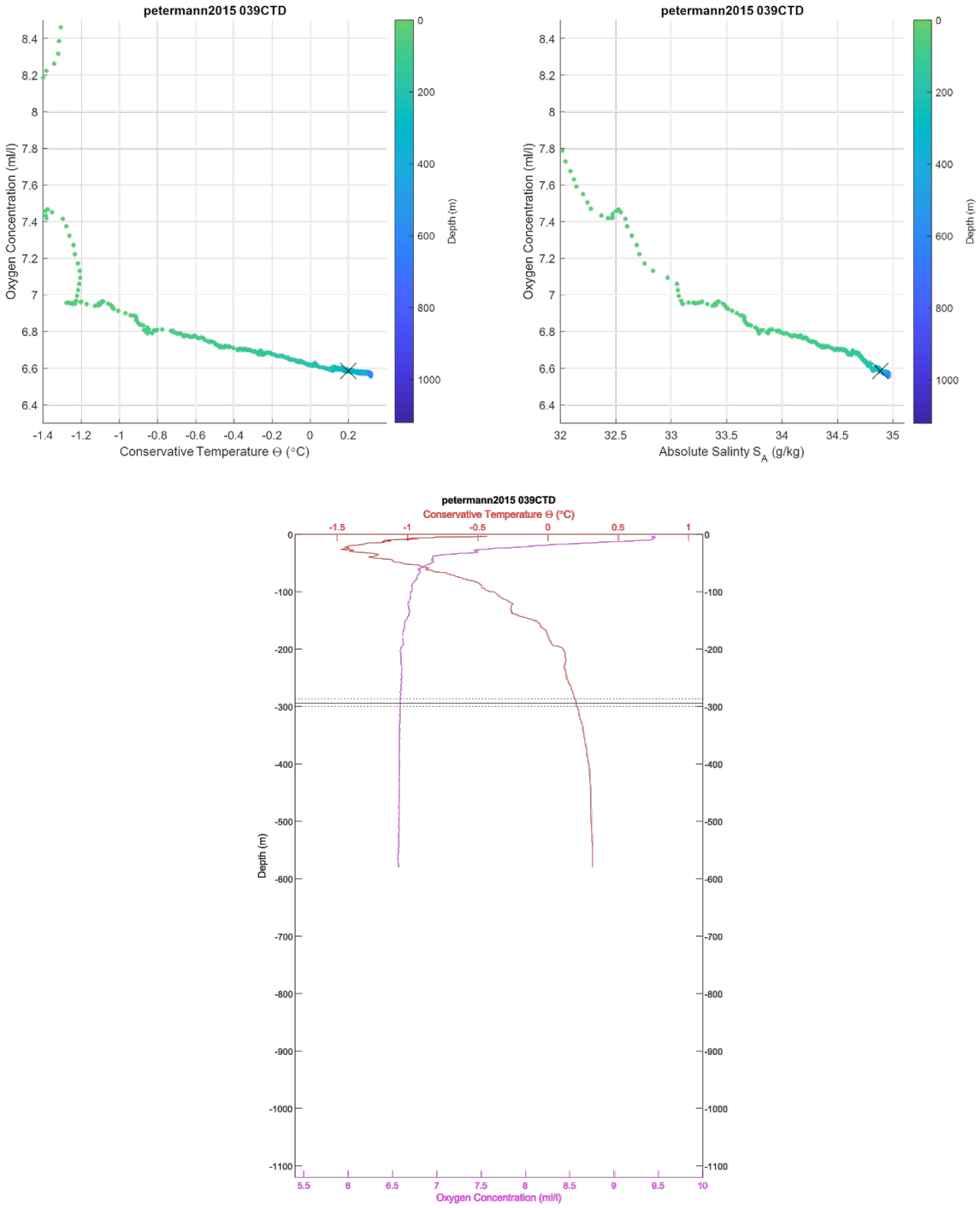

Figure 258: CTD 039. Top left, oxygen-temperature diagram, colored by depth. Top right, oxygen-salinity diagram, colored by depth. The black 'X' in the first two plots indicates the average depth for the top of the scattering layer in this location. Bottom center, temperature and oxygen plotted by depth. The scattering layer depth is indicated by horizontal lines; the solid line is the average depth, the dotted lines are the shallowest and deepest depths, in both cases for the top of the scattering layer.

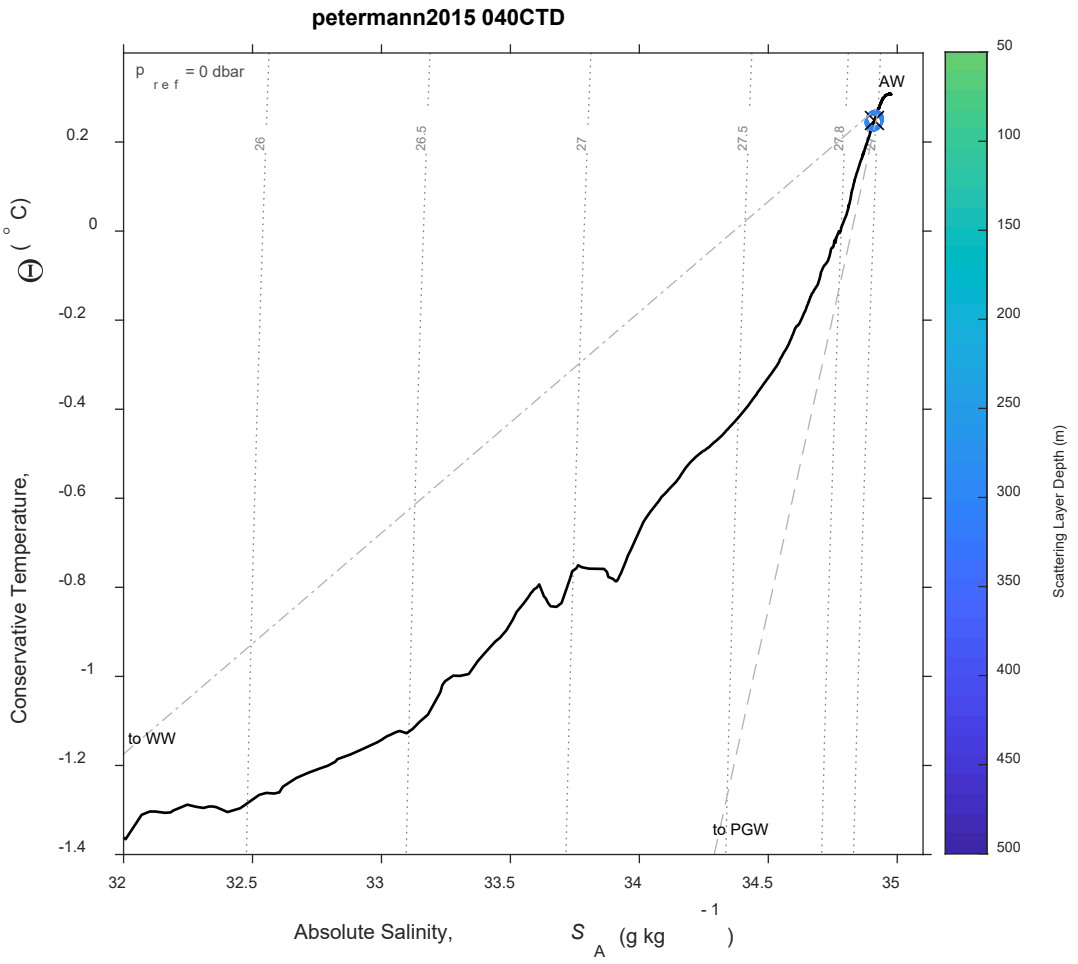

Figure 259: CTD 040, Temperature-Salinity (T-S) diagram. The scattering layer picks corresponding to this CTD are plotted as open circles colored by depth; a black 'X' indicates the average depth for the top of the scattering layer in this location. Isobars are shown as labeled grey dotted lines.

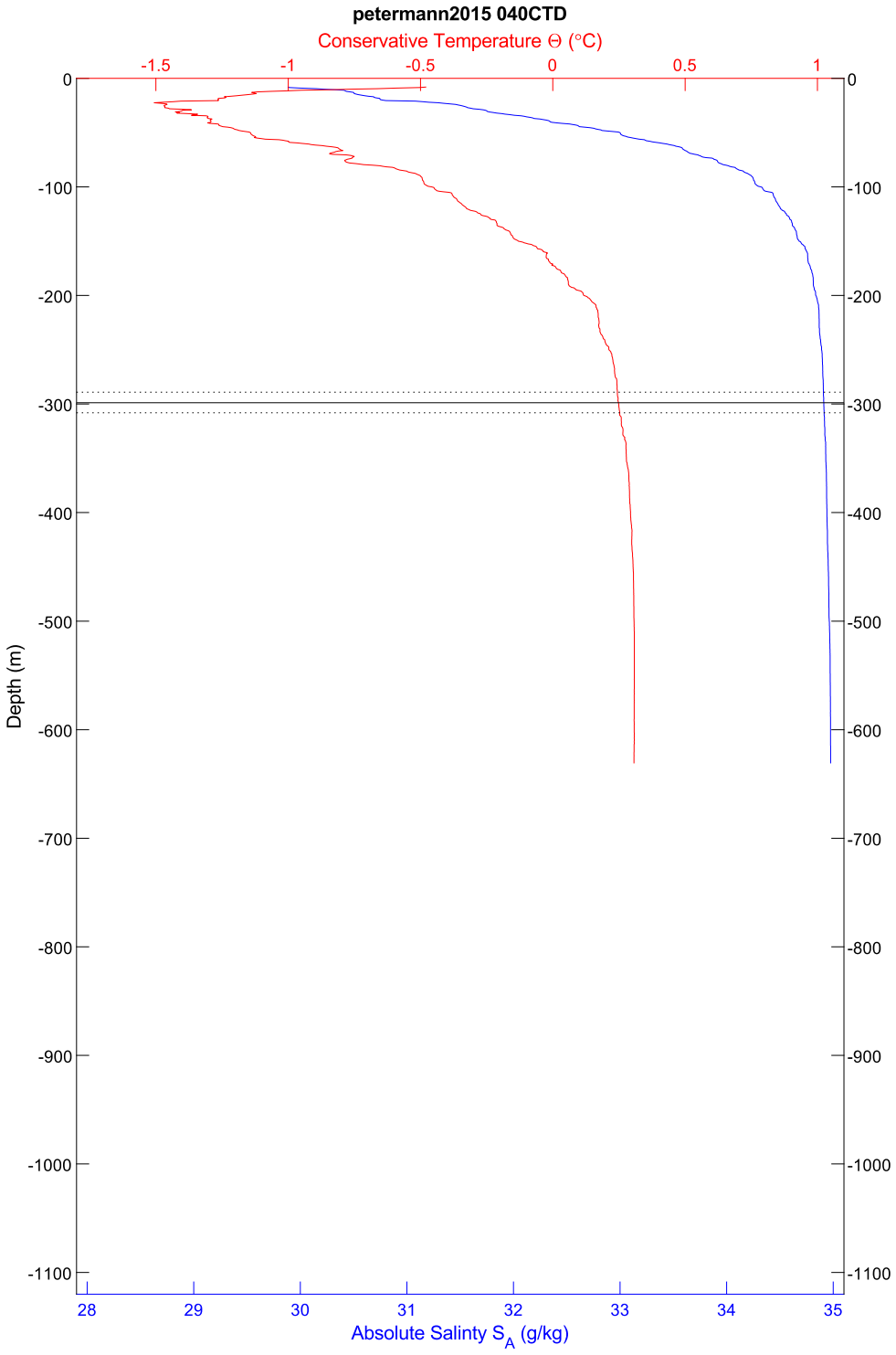

Figure 260: CTD 040, temperature and salinity plotted by depth. The scattering layer depth is indicated by horizontal lines; the solid line is the average depth, the dotted lines are the shallowest and deepest depths, in all cases for the top of the scattering layer.

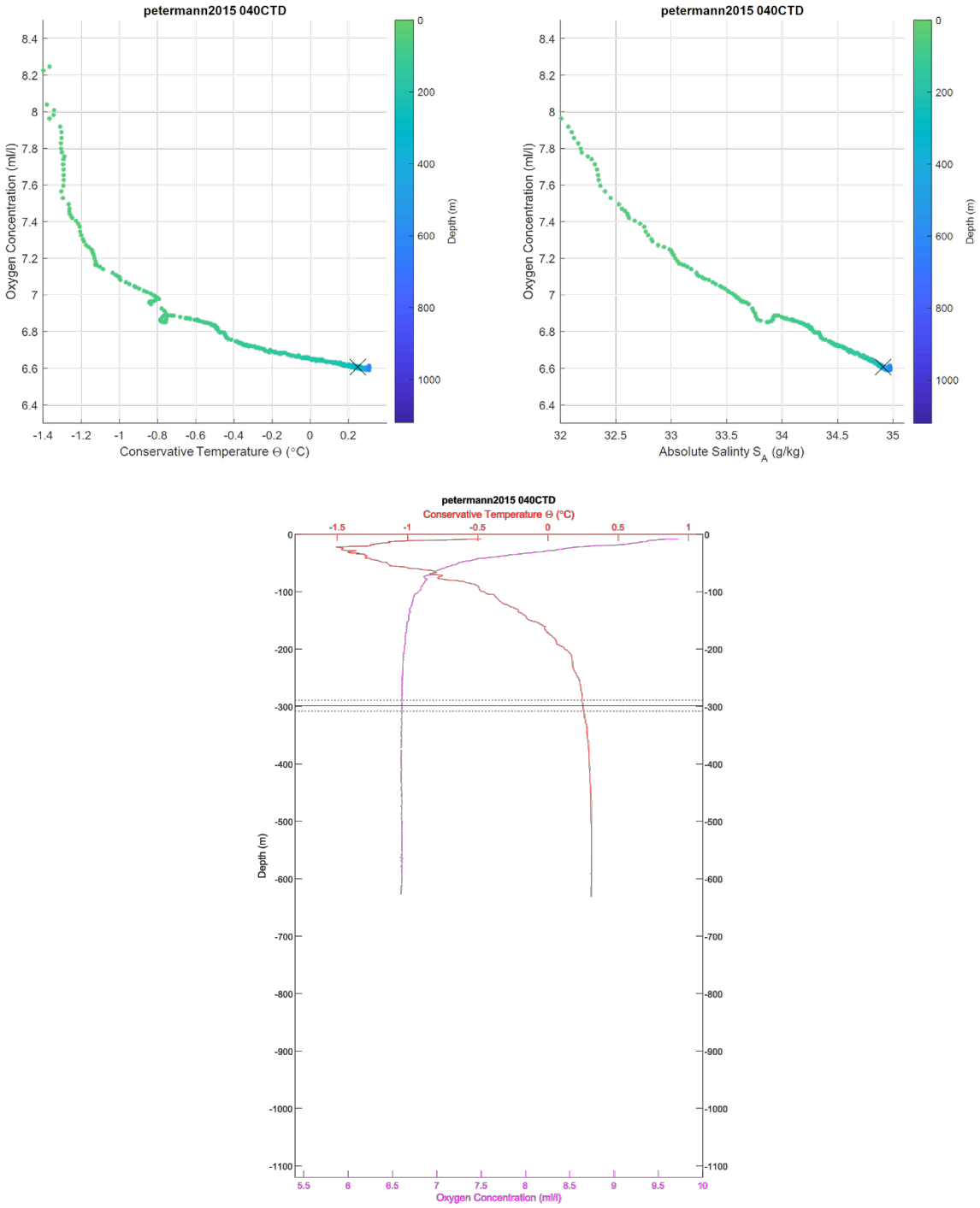

Figure 261: CTD 040. Top left, oxygen-temperature diagram, colored by depth. Top right, oxygen-salinity diagram, colored by depth. The black 'X' in the first two plots indicates the average depth for the top of the scattering layer in this location. Bottom center, temperature and oxygen plotted by depth. The scattering layer depth is indicated by horizontal lines; the solid line is the average depth, the dotted lines are the shallowest and deepest depths, in both cases for the top of the scattering layer.

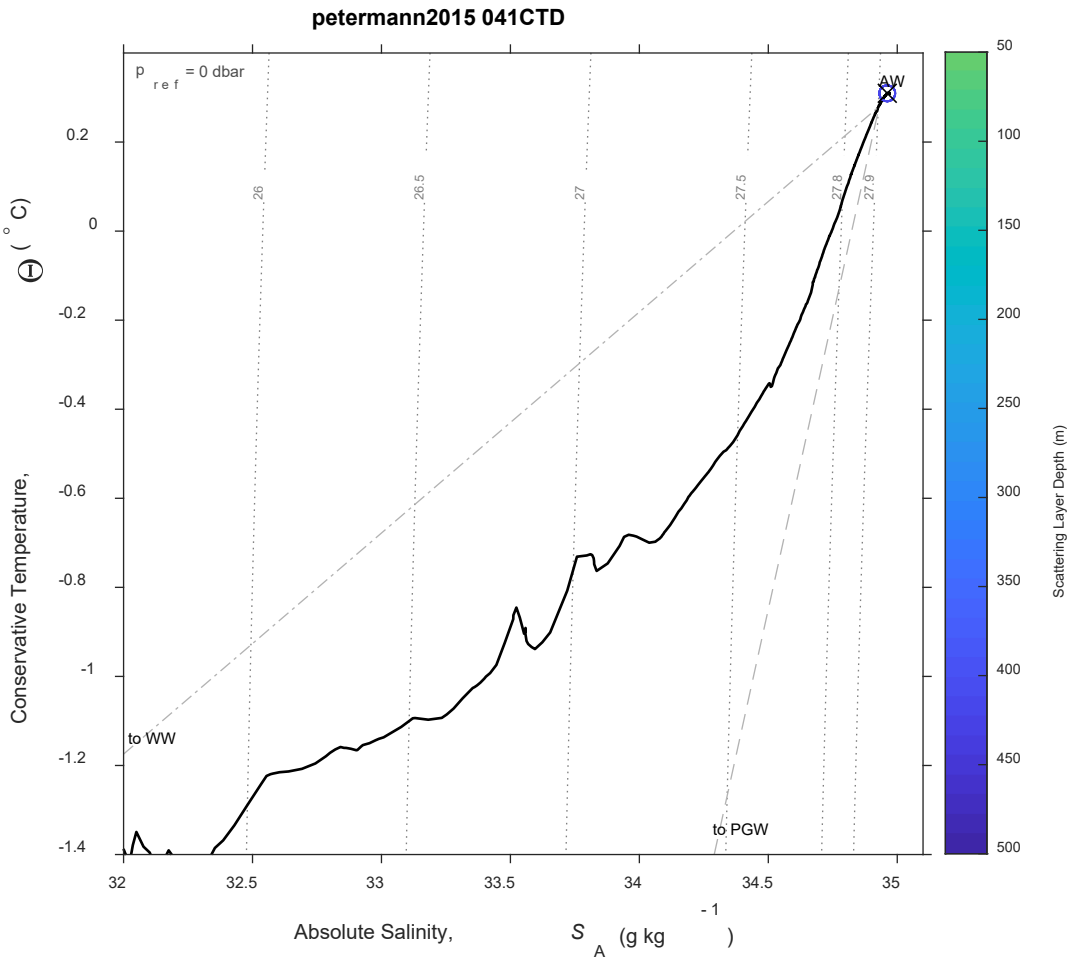

Figure 262: CTD 041, Temperature-Salinity (T-S) diagram. The scattering layer picks corresponding to this CTD are plotted as open circles colored by depth; a black 'X' indicates the average depth for the top of the scattering layer in this location. Isobars are shown as labeled grey dotted lines.

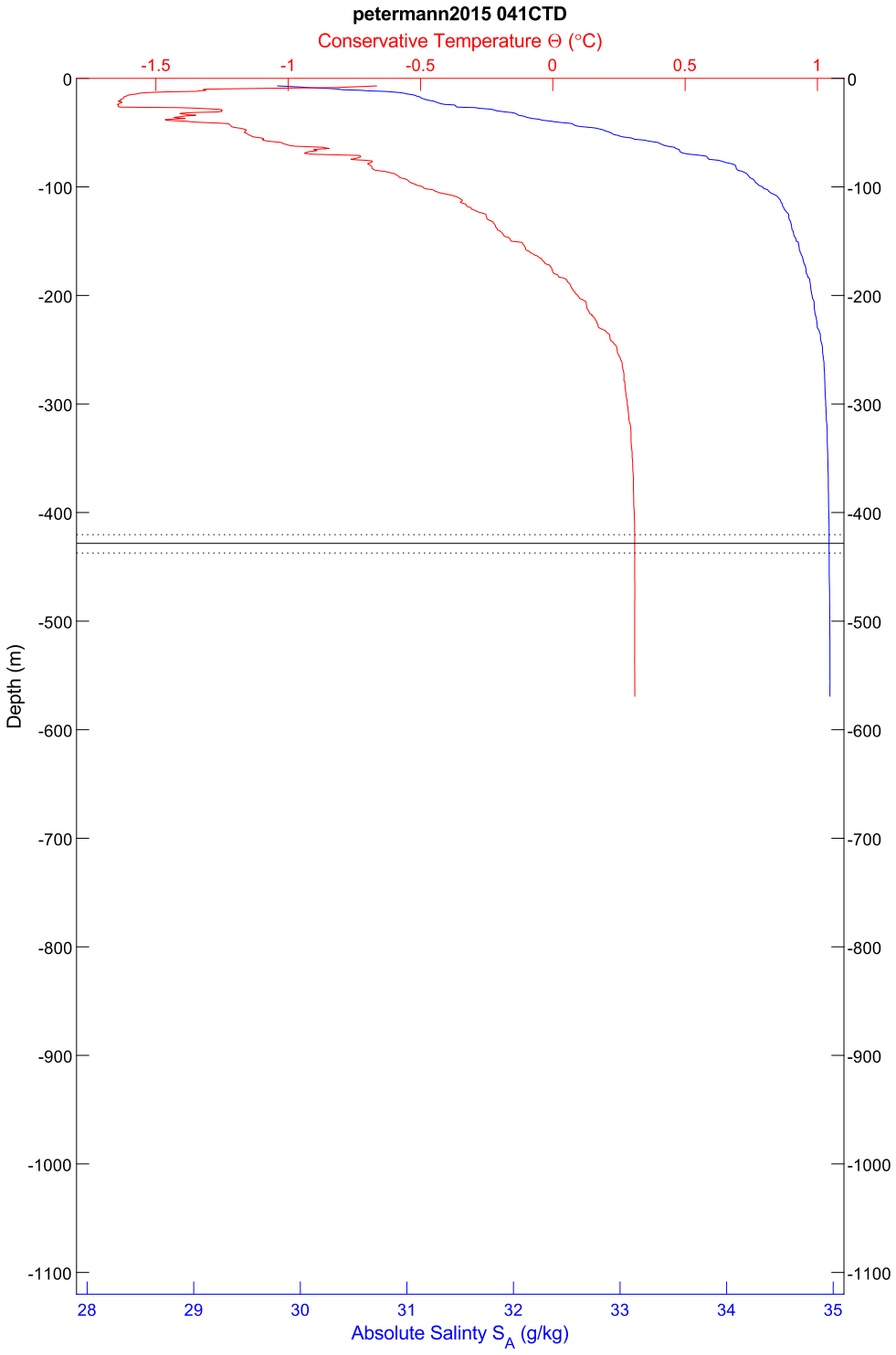

Figure 263: CTD 041, temperature and salinity plotted by depth. The scattering layer depth is indicated by horizontal lines; the solid line is the average depth, the dotted lines are the shallowest and deepest depths, in all cases for the top of the scattering layer.

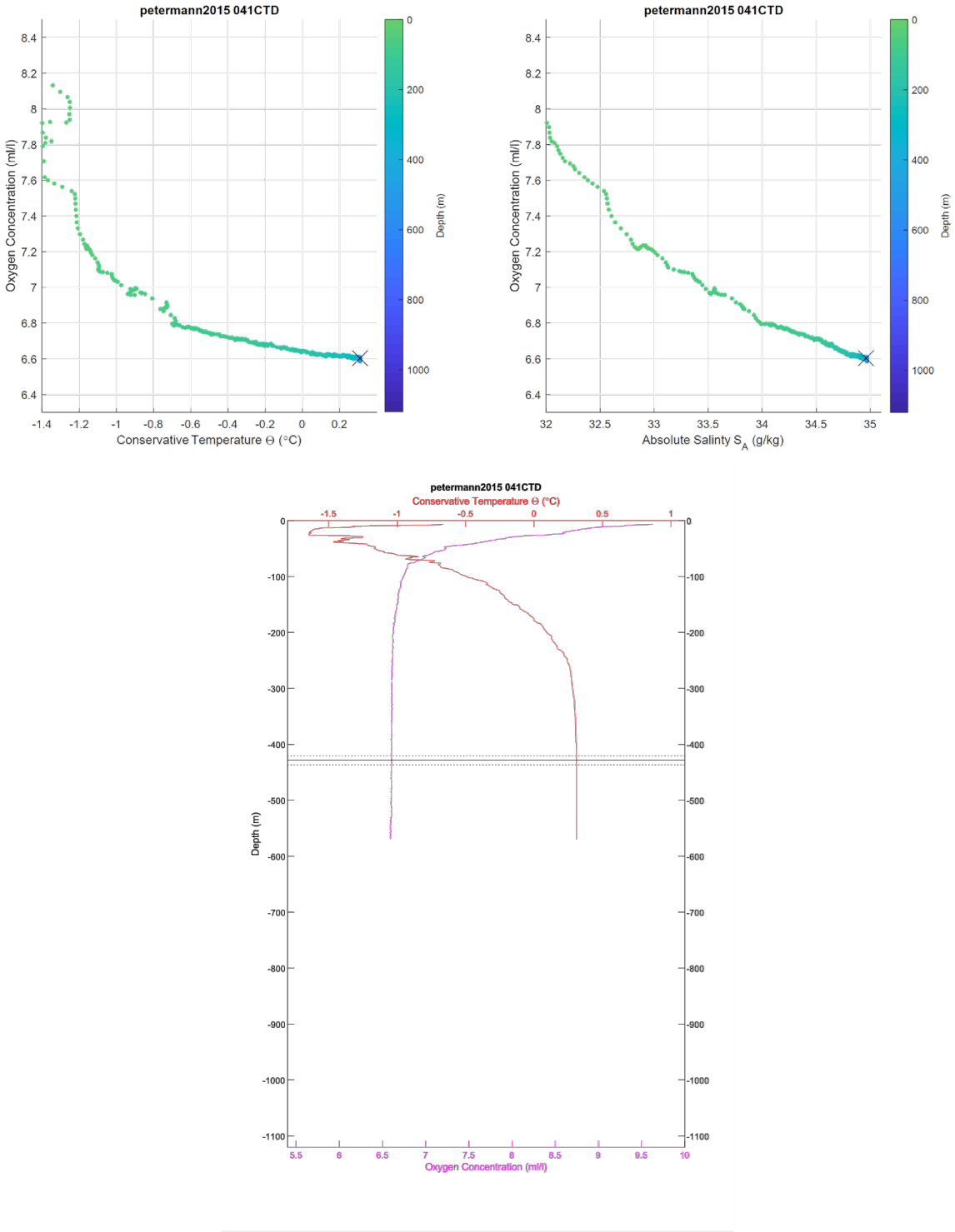

Figure 264: CTD 041. Top left, oxygen-temperature diagram, colored by depth. Top right, oxygen-salinity diagram, colored by depth. The black 'X' in the first two plots indicates the average depth for the top of the scattering layer in this location. Bottom center, temperature and oxygen plotted by depth. The scattering layer depth is indicated by horizontal lines; the solid line is the average depth, the dotted lines are the shallowest and deepest depths, in both cases for the top of the scattering layer.

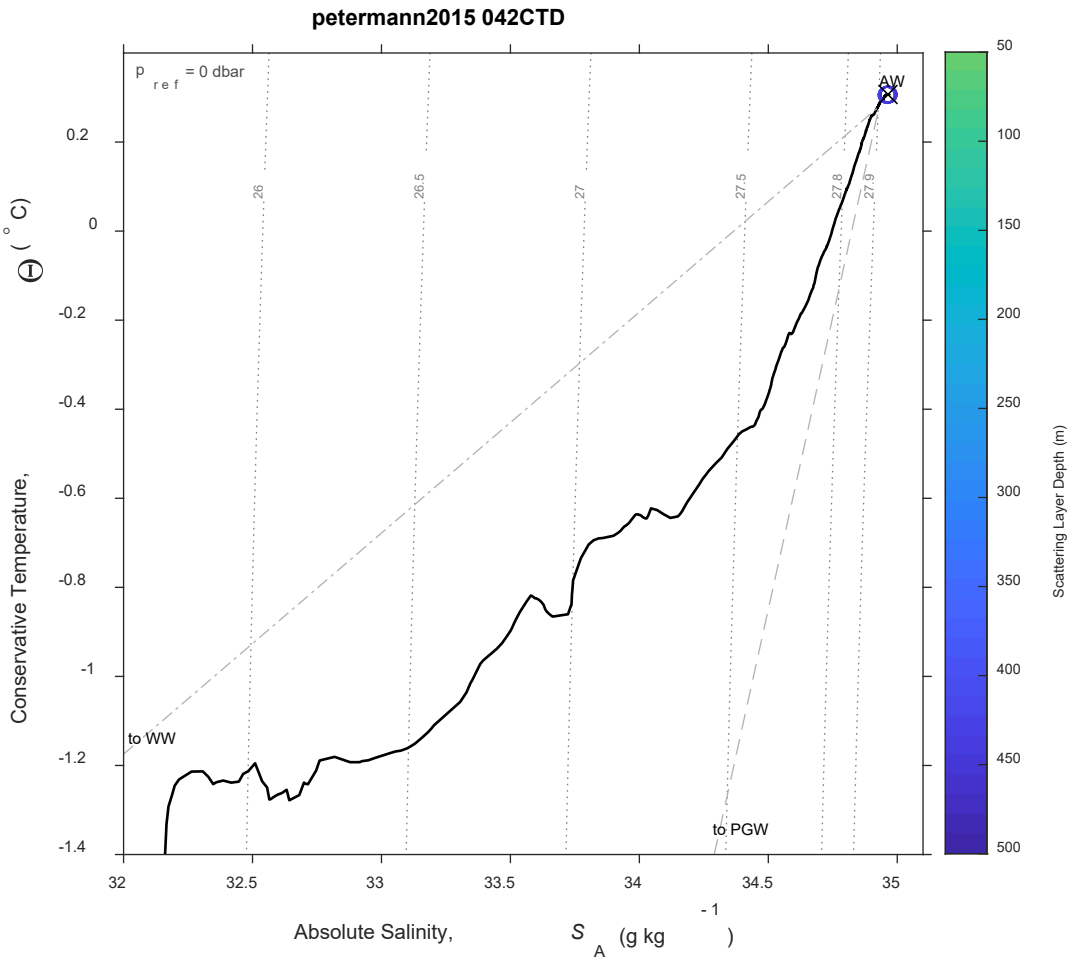

Figure 265: CTD 042, Temperature-Salinity (T-S) diagram. The scattering layer picks corresponding to this CTD are plotted as open circles colored by depth; a black 'X' indicates the average depth for the top of the scattering layer in this location. Isobars are shown as labeled grey dotted lines.

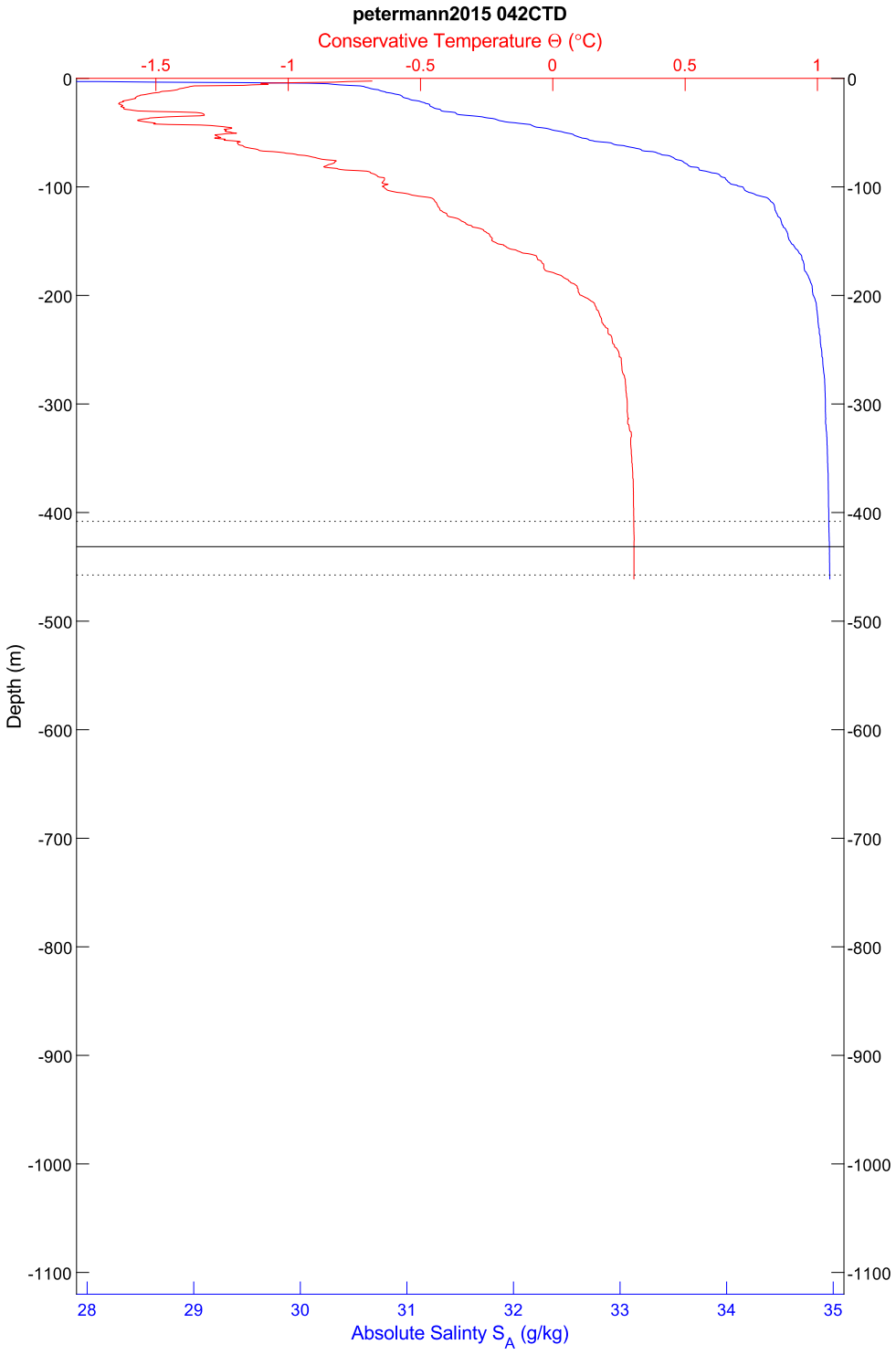

Figure 266: CTD 042, temperature and salinity plotted by depth. The scattering layer depth is indicated by horizontal lines; the solid line is the average depth, the dotted lines are the shallowest and deepest depths, in all cases for the top of the scattering layer.

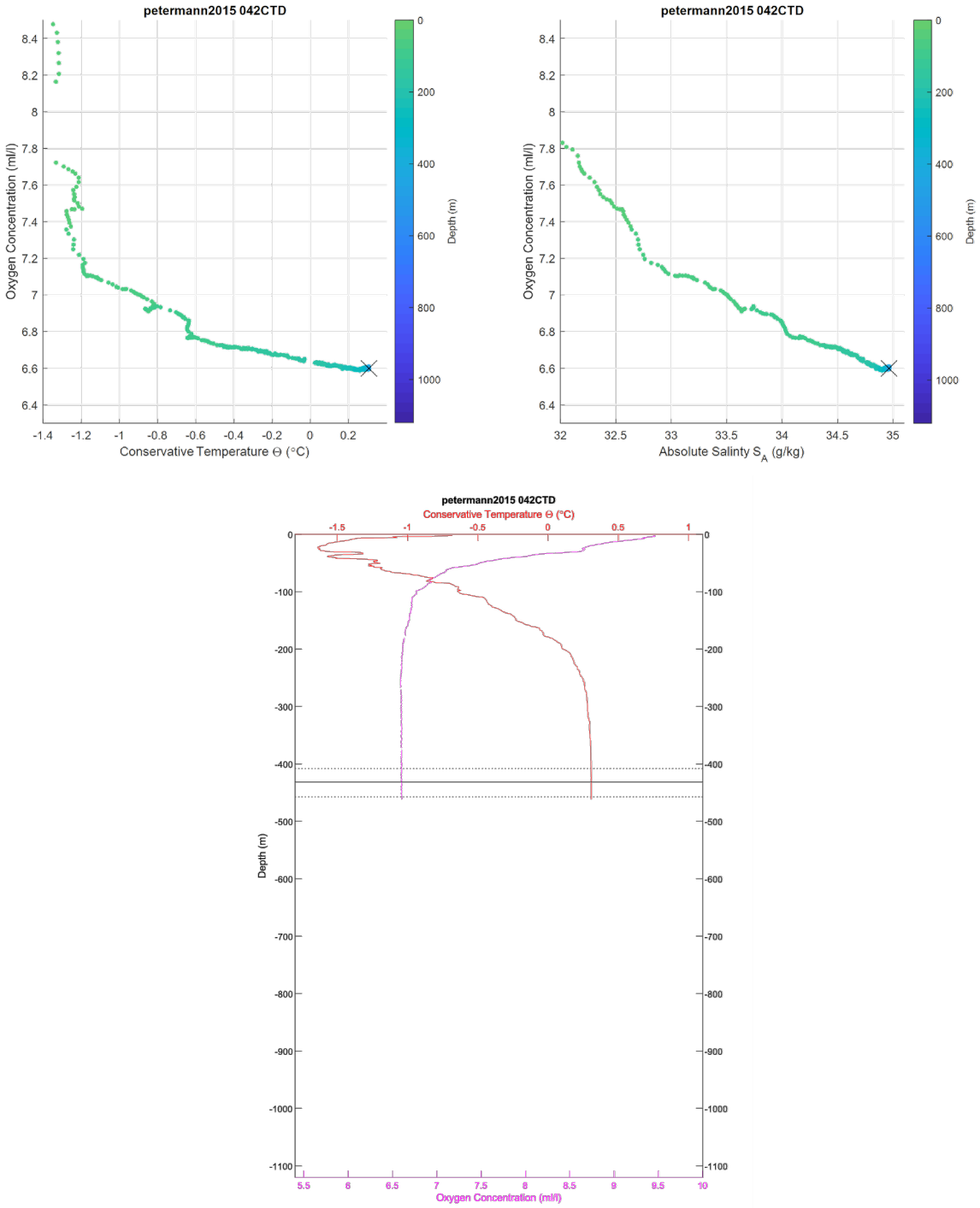

Figure 267: CTD 042. Top left, oxygen-temperature diagram, colored by depth. Top right, oxygen-salinity diagram, colored by depth. The black 'X' in the first two plots indicates the average depth for the top of the scattering layer in this location. Bottom center, temperature and oxygen plotted by depth. The scattering layer depth is indicated by horizontal lines; the solid line is the average depth, the dotted lines are the shallowest and deepest depths, in both cases for the top of the scattering layer.

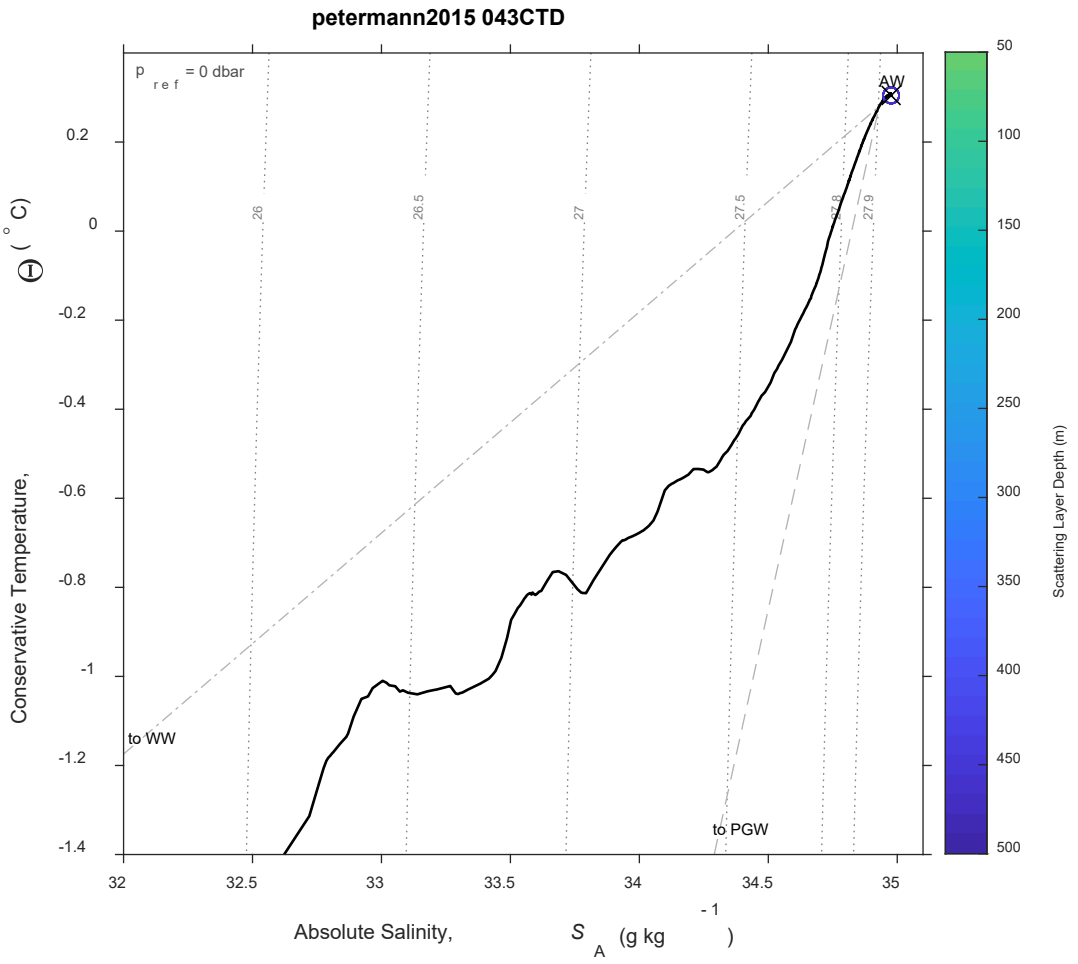

Figure 268: CTD 043, Temperature-Salinity (T-S) diagram. The scattering layer picks corresponding to this CTD are plotted as open circles colored by depth; a black 'X' indicates the average depth for the top of the scattering layer in this location. Isobars are shown as labeled grey dotted lines.

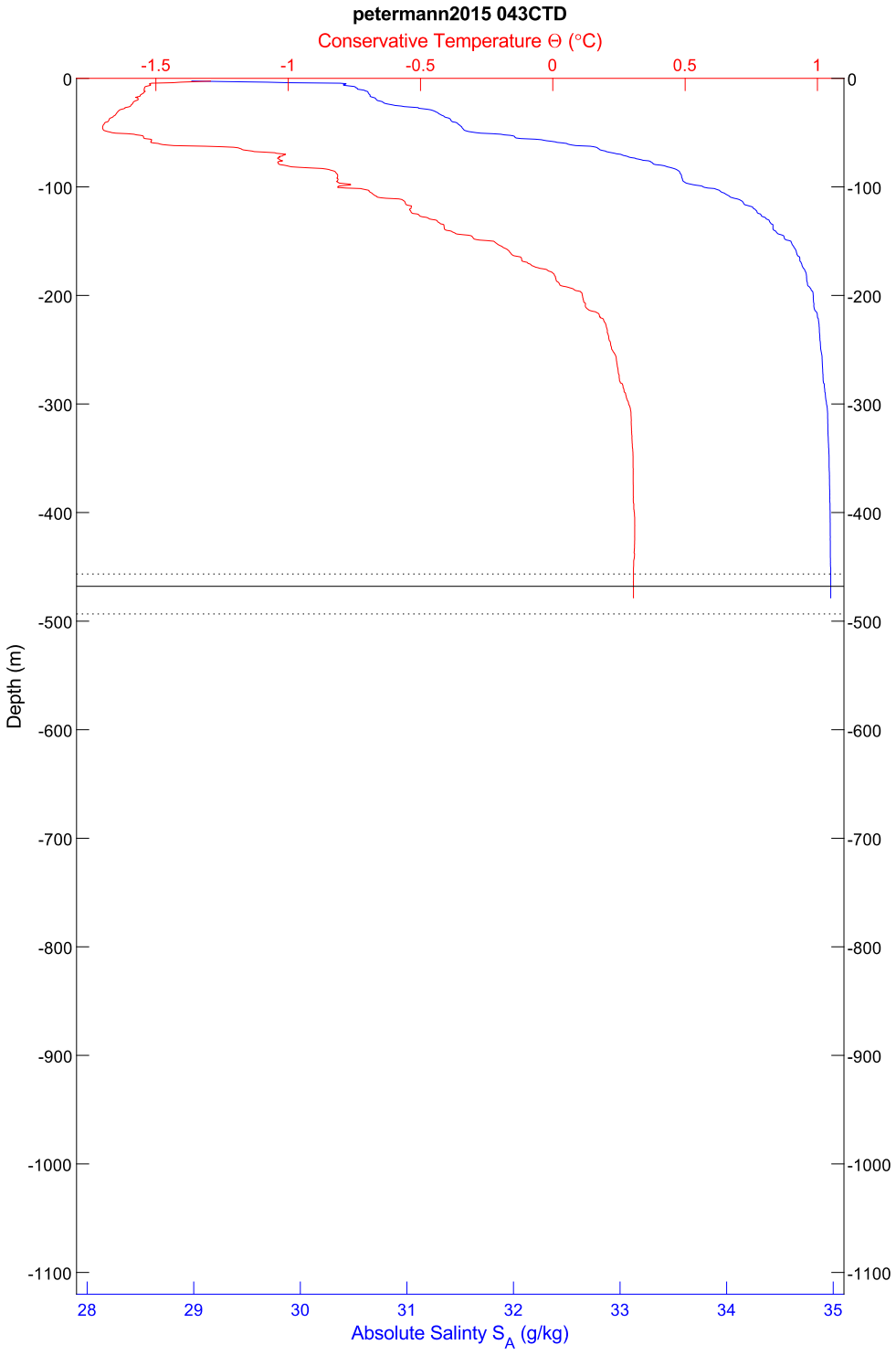

Figure 269: CTD 043, temperature and salinity plotted by depth. The scattering layer depth is indicated by horizontal lines; the solid line is the average depth, the dotted lines are the shallowest and deepest depths, in all cases for the top of the scattering layer.

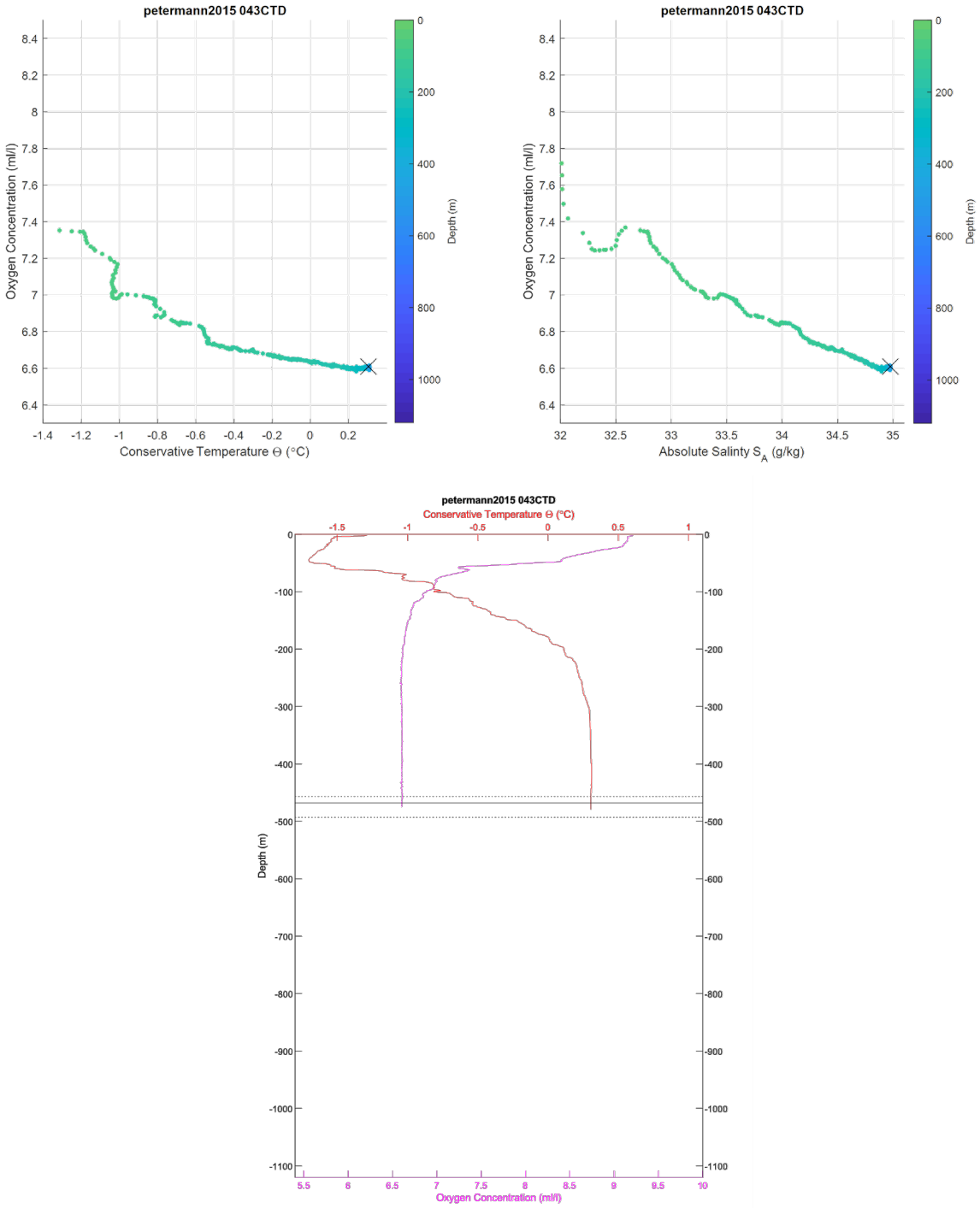

Figure 270: CTD 043. Top left, oxygen-temperature diagram, colored by depth. Top right, oxygen-salinity diagram, colored by depth. The black 'X' in the first two plots indicates the average depth for the top of the scattering layer in this location. Bottom center, temperature and oxygen plotted by depth. The scattering layer depth is indicated by horizontal lines; the solid line is the average depth, the dotted lines are the shallowest and deepest depths, in both cases for the top of the scattering layer.

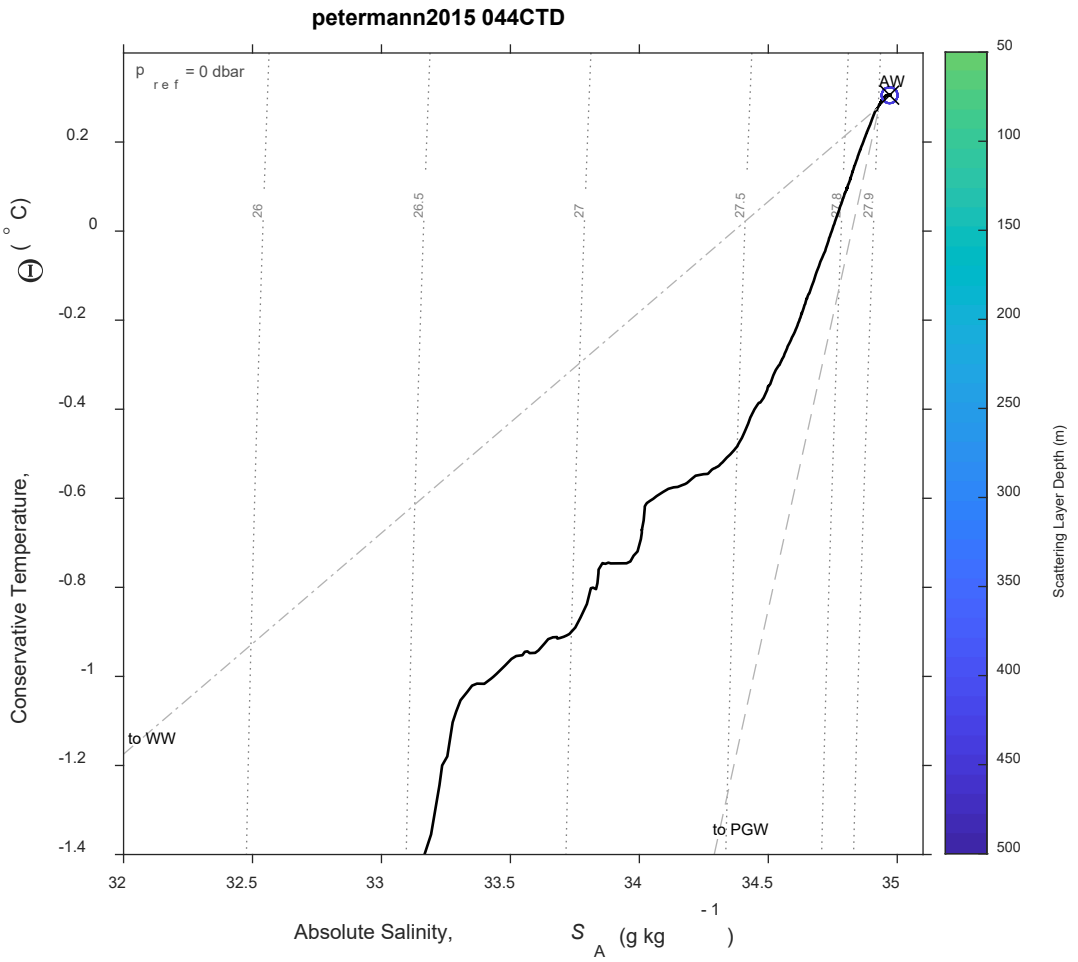

Figure 271: CTD 044, Temperature-Salinity (T-S) diagram. The scattering layer picks corresponding to this CTD are plotted as open circles colored by depth; a black 'X' indicates the average depth for the top of the scattering layer in this location. Isobars are shown as labeled grey dotted lines.

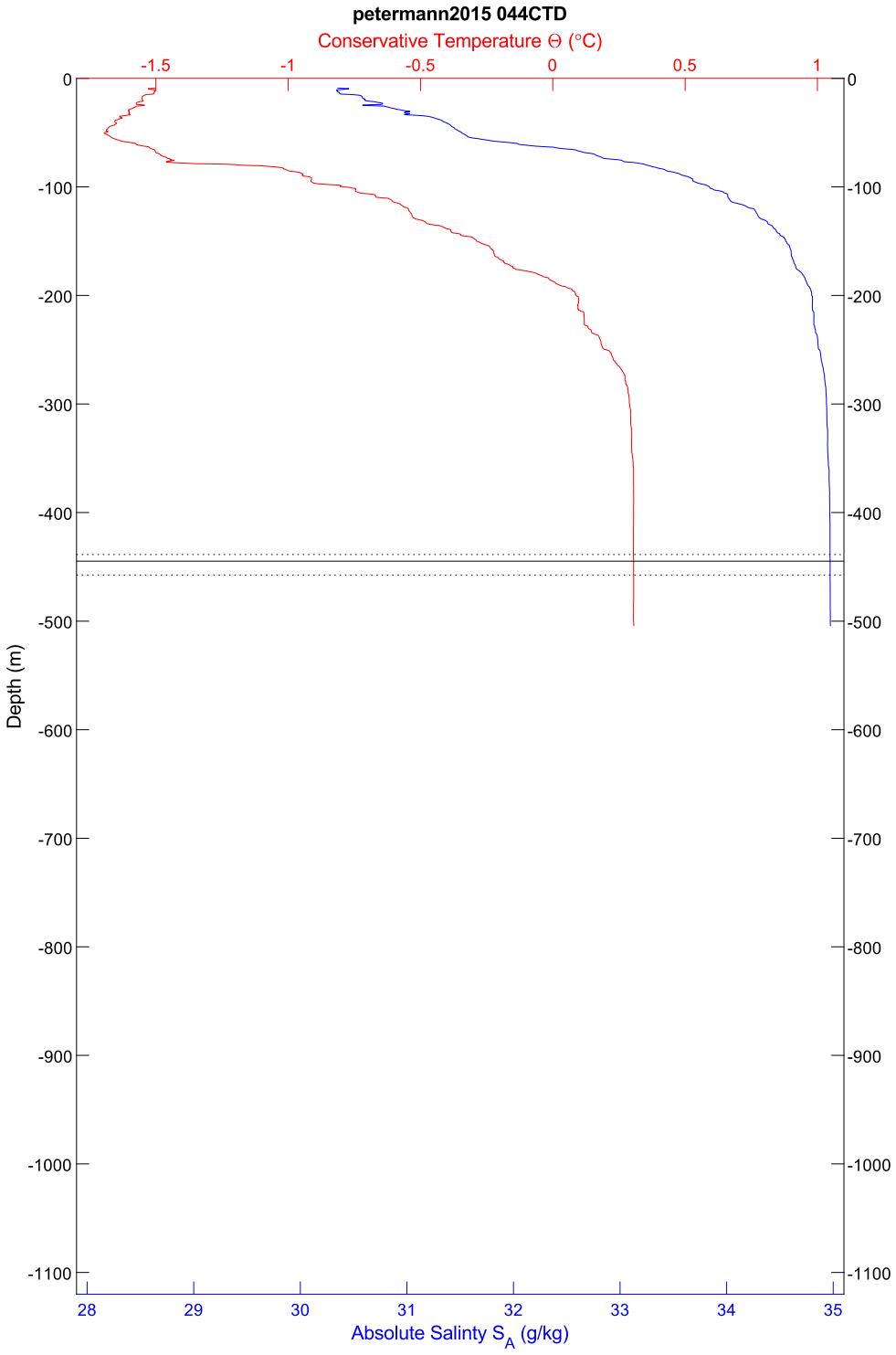

Figure 272: CTD 044, temperature and salinity plotted by depth. The scattering layer depth is indicated by horizontal lines; the solid line is the average depth, the dotted lines are the shallowest and deepest depths, in all cases for the top of the scattering layer.

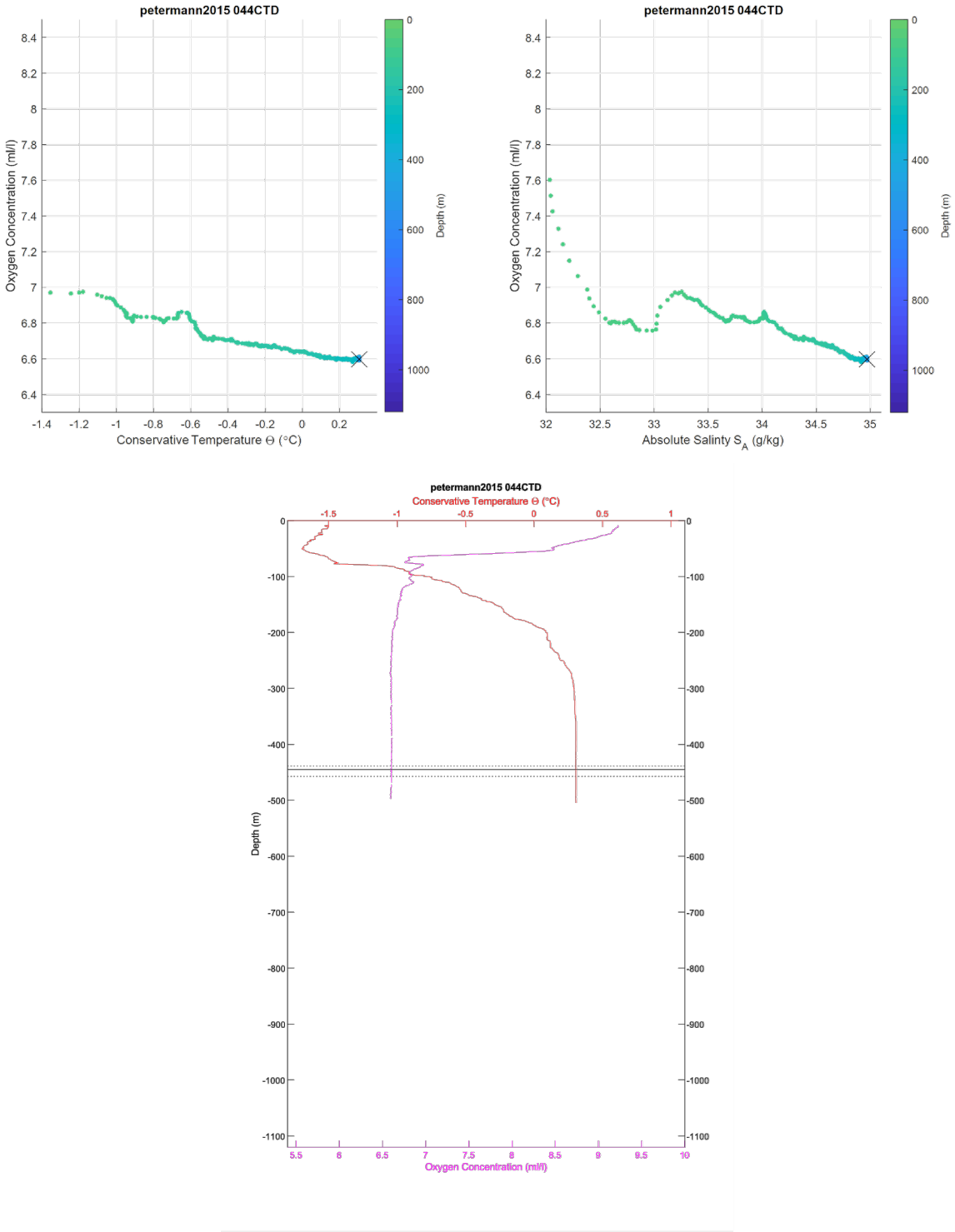

Figure 273: CTD 044. Top left, oxygen-temperature diagram, colored by depth. Top right, oxygen-salinity diagram, colored by depth. The black 'X' in the first two plots indicates the average depth for the top of the scattering layer in this location. Bottom center, temperature and oxygen plotted by depth. The scattering layer depth is indicated by horizontal lines; the solid line is the average depth, the dotted lines are the shallowest and deepest depths, in both cases for the top of the scattering layer.

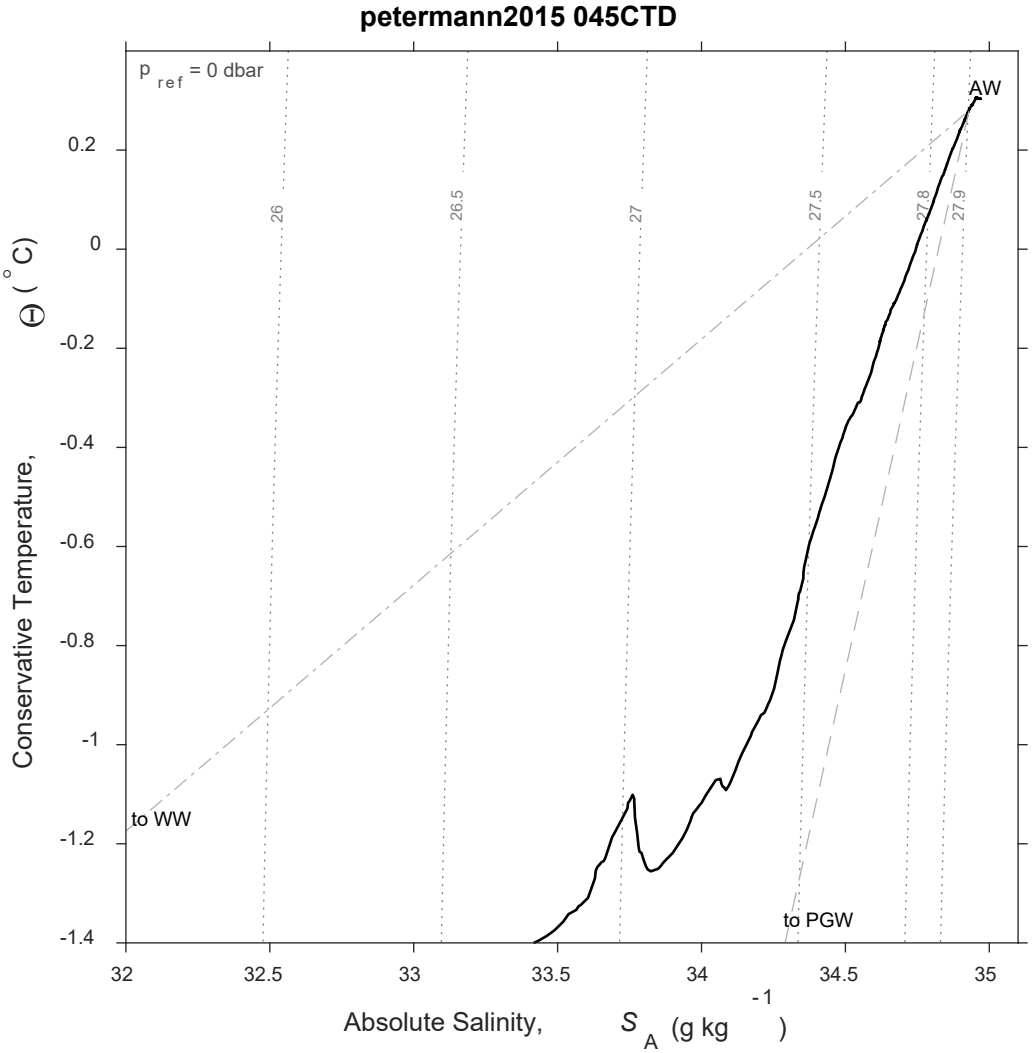

Figure 274: CTD 045, Temperature-Salinity (T-S) diagram. Isobars are shown as labeled grey dotted lines. There was no scattering layer associated with this CTD station.

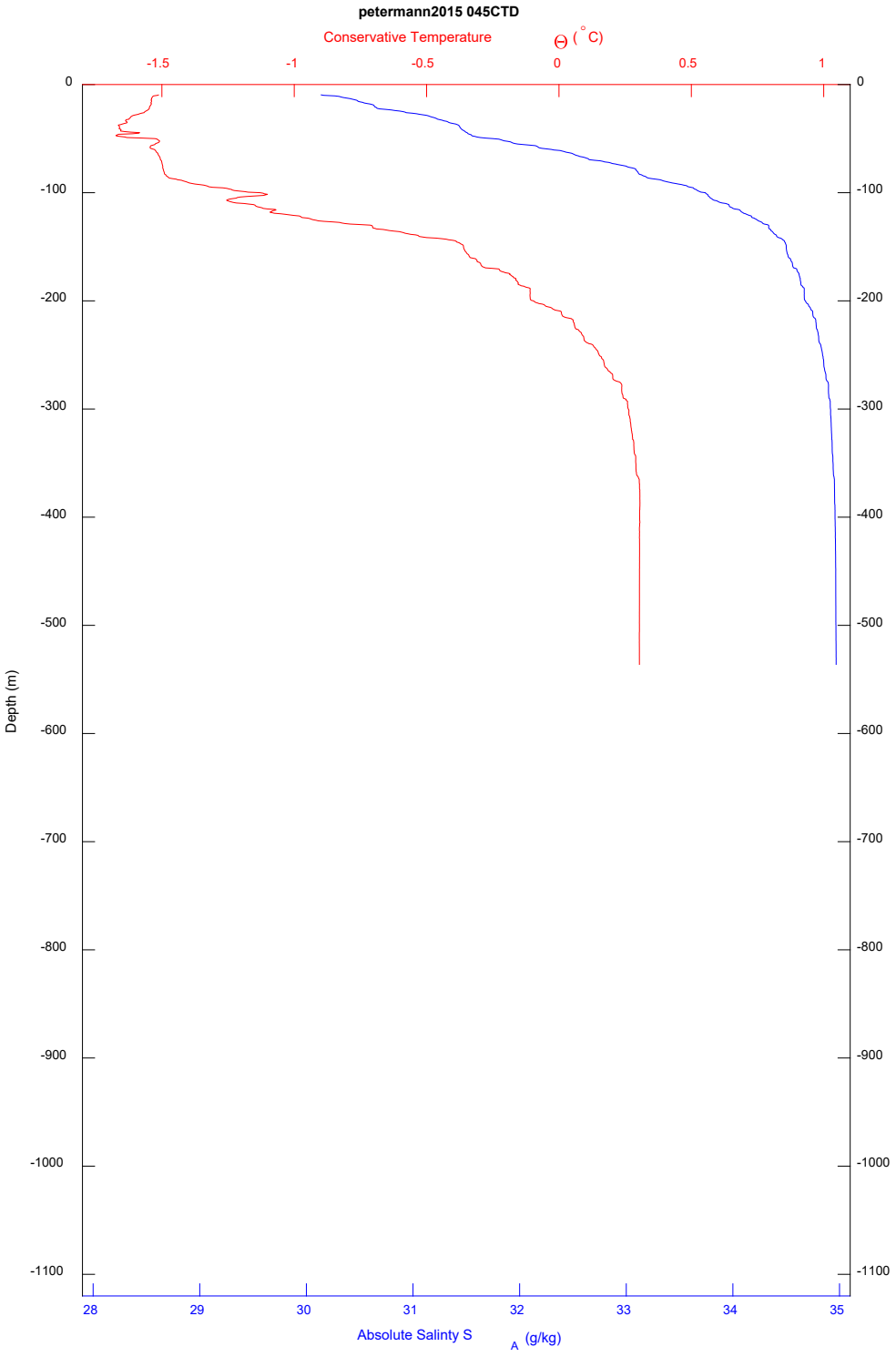

Figure 275: CTD 045, temperature and salinity plotted by depth. There was no scattering layer associated with this CTD station.

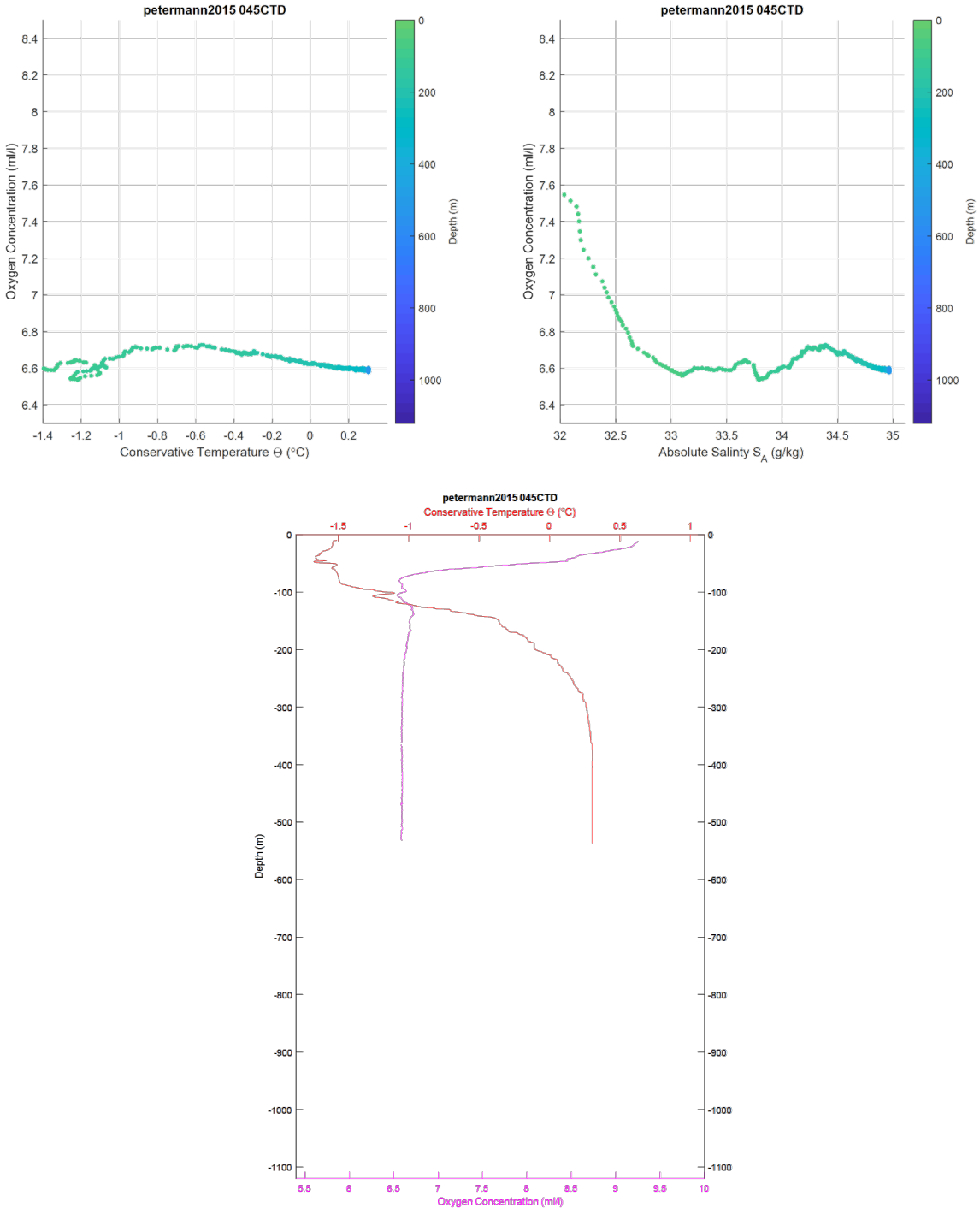

Figure 276: CTD 045. Top left, oxygen-temperature diagram, colored by depth. Top right, oxygen-salinity diagram, colored by depth. Bottom center, temperature and oxygen plotted by depth. There was no scattering layer associated with this CTD station.

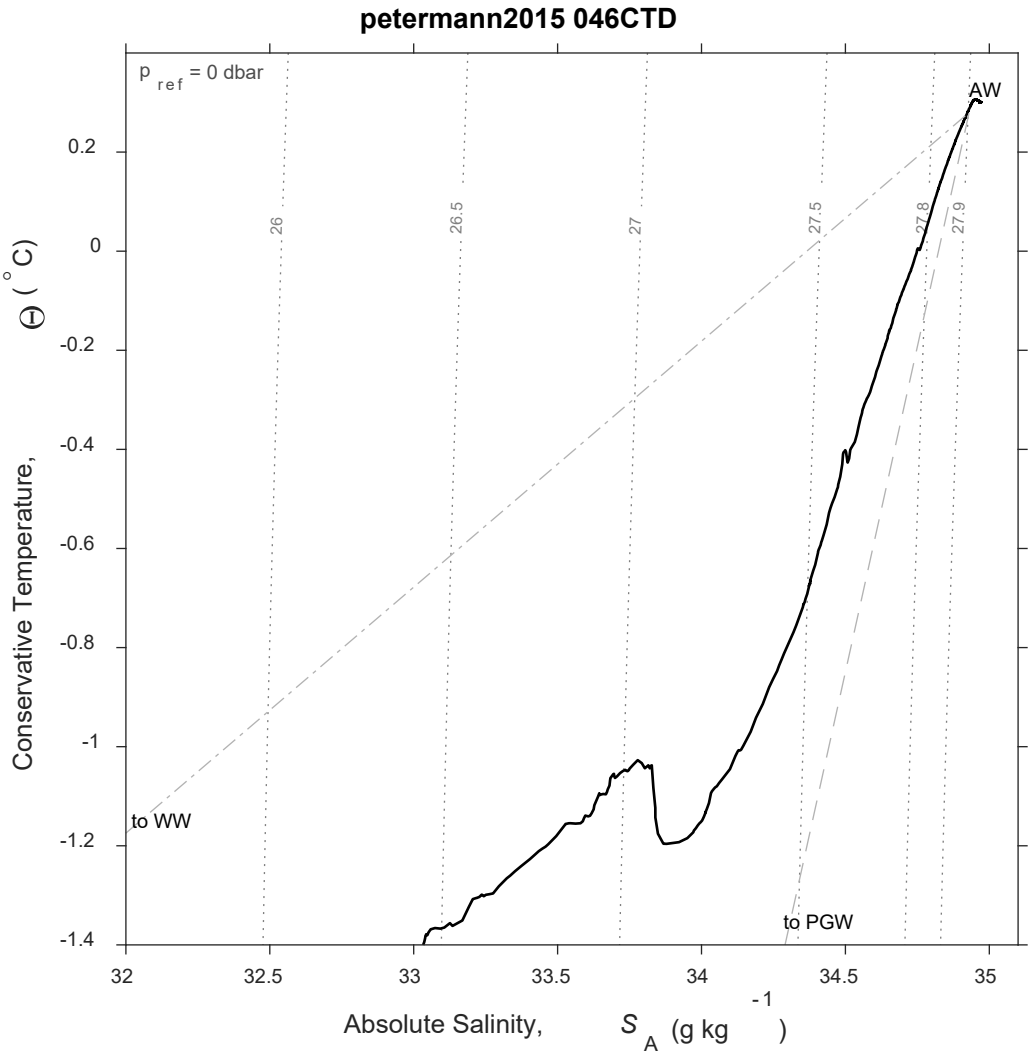

Figure 277: CTD 046, Temperature-Salinity (T-S) diagram. Isobars are shown as labeled grey dotted lines. There was no scattering layer associated with this CTD station.

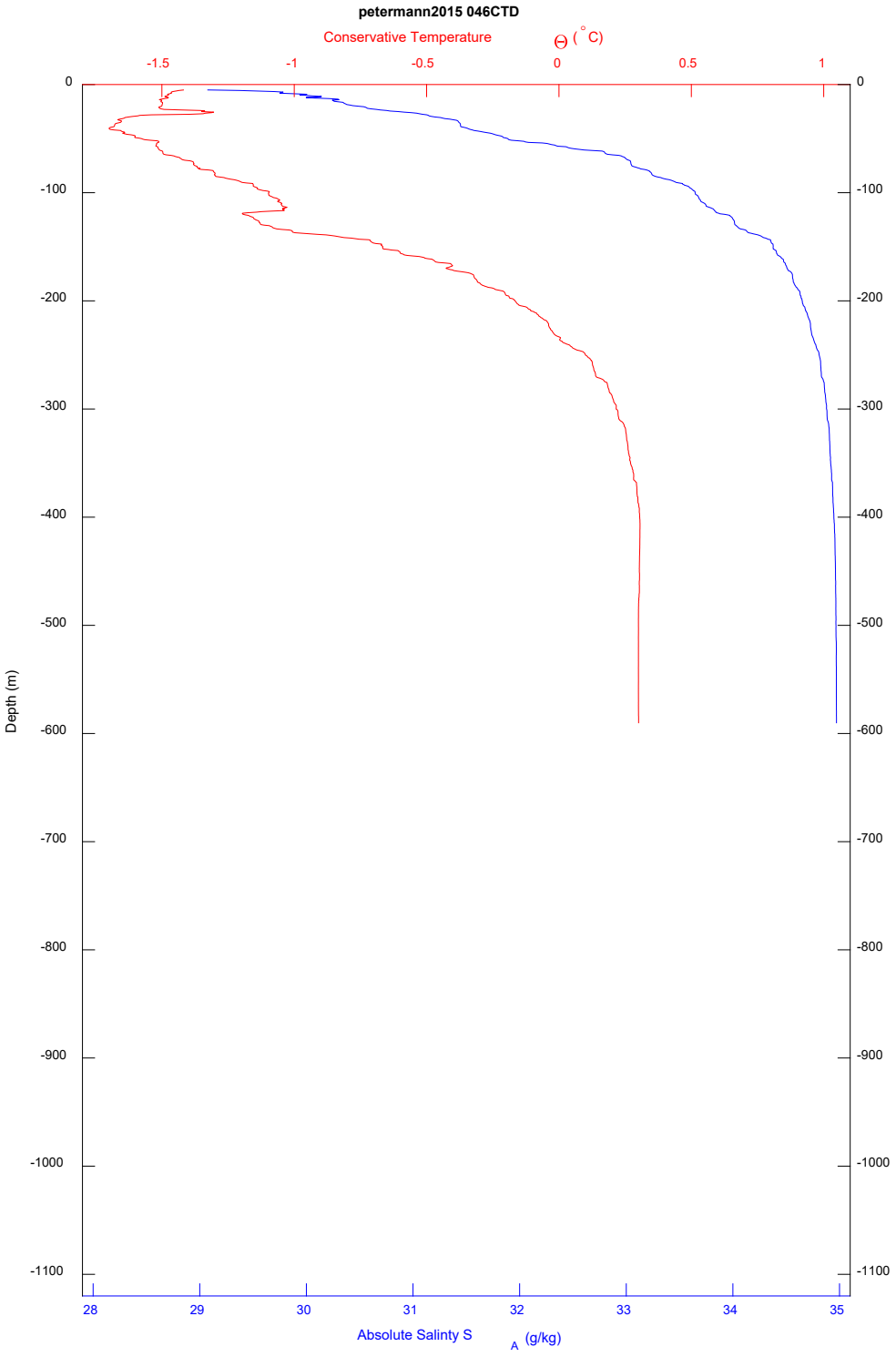

Figure 278: CTD 046, temperature and salinity plotted by depth. There was no scattering layer associated with this CTD station.

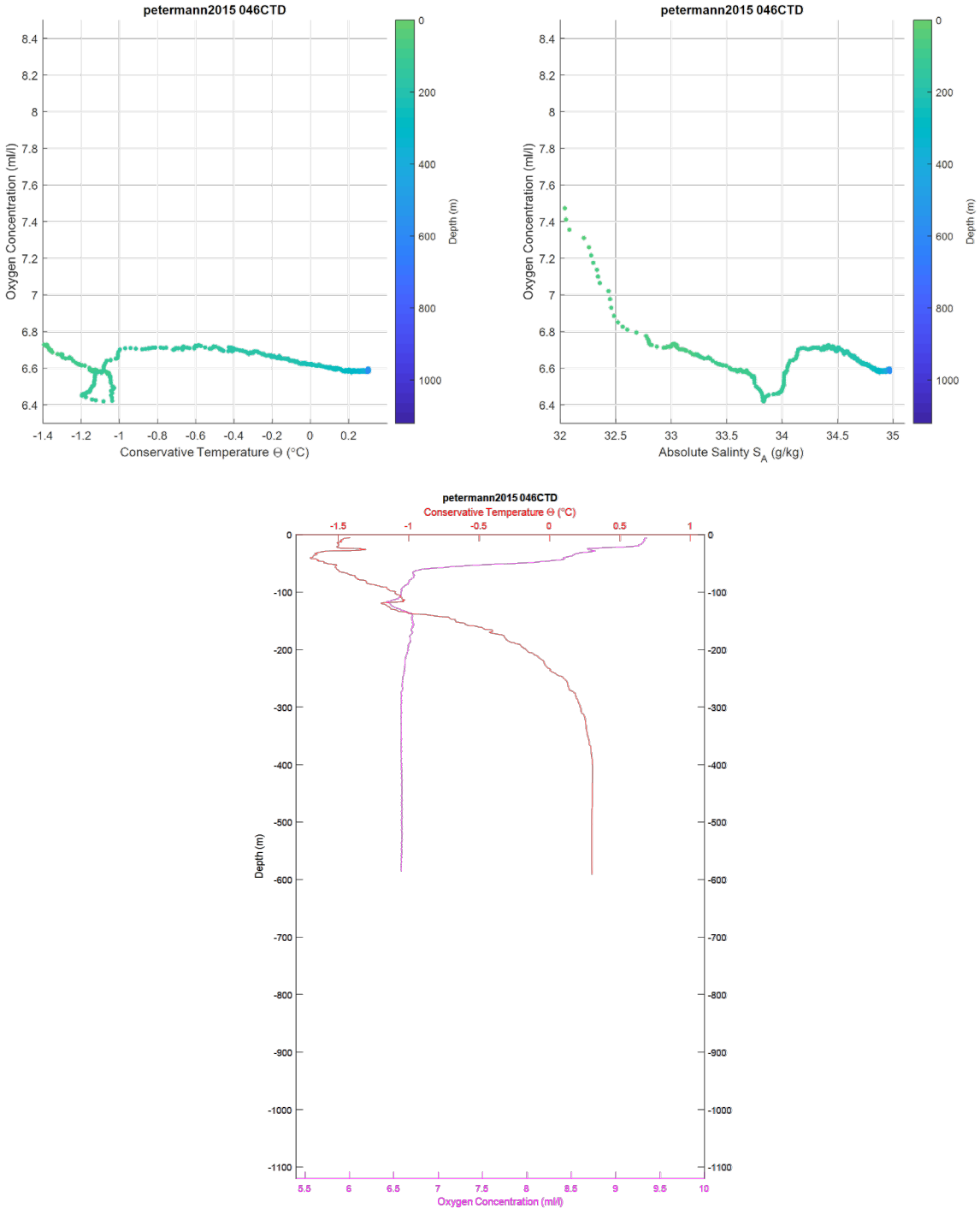

Figure 279: CTD 046. Top left, oxygen-temperature diagram, colored by depth. Top right, oxygen-salinity diagram, colored by depth. Bottom center, temperature and oxygen plotted by depth. There was no scattering layer associated with this CTD station.

APPENDIX E TARGET STRENGTH AND FREQUENCY RESPONSE

E.1 Evaluation of Probability Density Function (PDF) when setting thresholds

When considering what threshold to set for single target detection, the initial approach was to use a wide target strength (TS) threshold (-100 to 0 dB) over a broad portion of the water column to get an indication of TS values of potential single targets. In all cases, this resulted in a Probability Density Function (PDF) with a bimodal distribution (Figure 280). Applying the 'Target Tracking' algorithm to these two distributions showed that most tracked targets from the lower TS distribution were concentrated in the water column above the primary scattering layer. In the example below, the lower TS targets were concentrated in the 30 – 160 m depth range (Figure 281), above the main scattering layer (Figure 282). The higher TS targets were also found above the scattering layer, but were more importantly the primary tracked targets within the depth range of the scattering layer (Figure 281). This was typically the case for the deeper homogeneous preference scattering layers. The approximate limits of this higher TS distribution were used to threshold the 'Single Target' algorithm; the 'Target Tracking' algorithm was then run on this reduced set of single targets. These remaining tracked single targets were then used to generate TS frequency response curves and estimate average targets strength. The lower TS distribution in the upper water column may correspond to smaller or poorer scatterers, which may also

contribute to the scattering layer and may help explain the low S_v and low density values that were calculated based on the high TS distribution.

It is important to note that the TS values displayed in images of the PDFs that follow are uncalibrated TS values, unless otherwise specified. The calculated calibration curve is applied during the ‘Produce TS curves from tracks’ procedure, after single tracks are selected, and the exports from this step are used for the calculation of averages and densities. Using the uncalibrated parameters does not negatively affect the results of the single target algorithm, as the parameters are being applied to data that are not yet calibrated. In ESP3, a “rough” calibration can be applied to echograms and exports that don’t utilize the calibration curve by adjusting the gain applied during echogram generation to match the calculated calibration curve (Figure 283 and Figure 284, also discussed in Appendix A). The uncalibrated range for the higher TS distributions in the example below is approximately -46 to -20 dB. This corresponds to a roughly calibrated range of -65 to -37 dB (Figure 285).

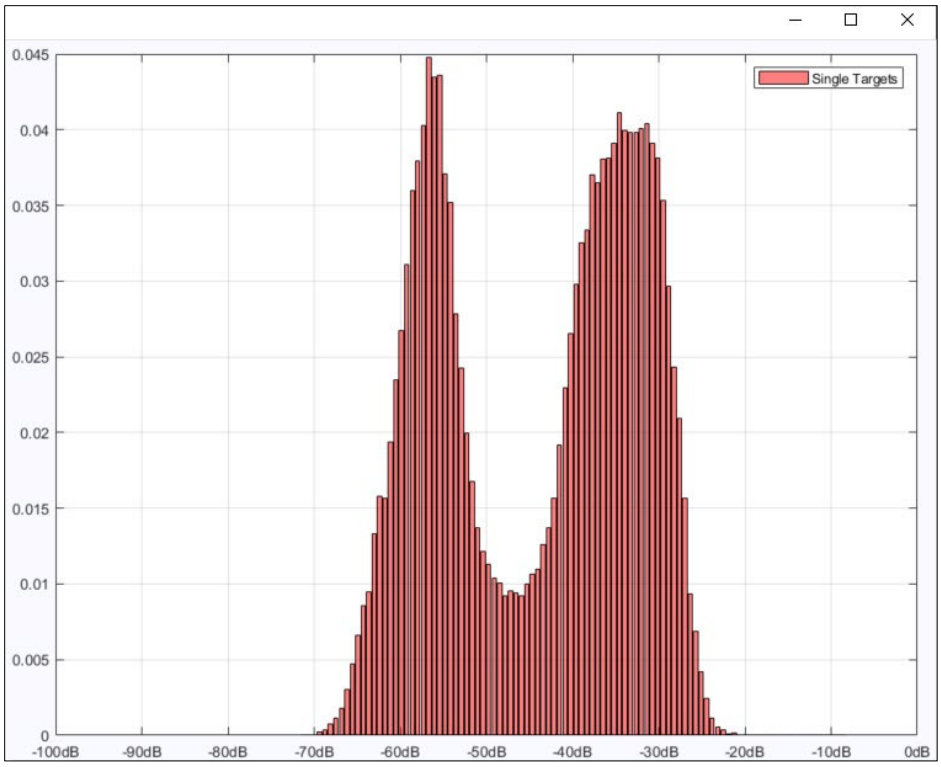

Figure 280: PDF of single targets for PETERMANN2015-D20150814-T134156.raw between 150 m and the seafloor.

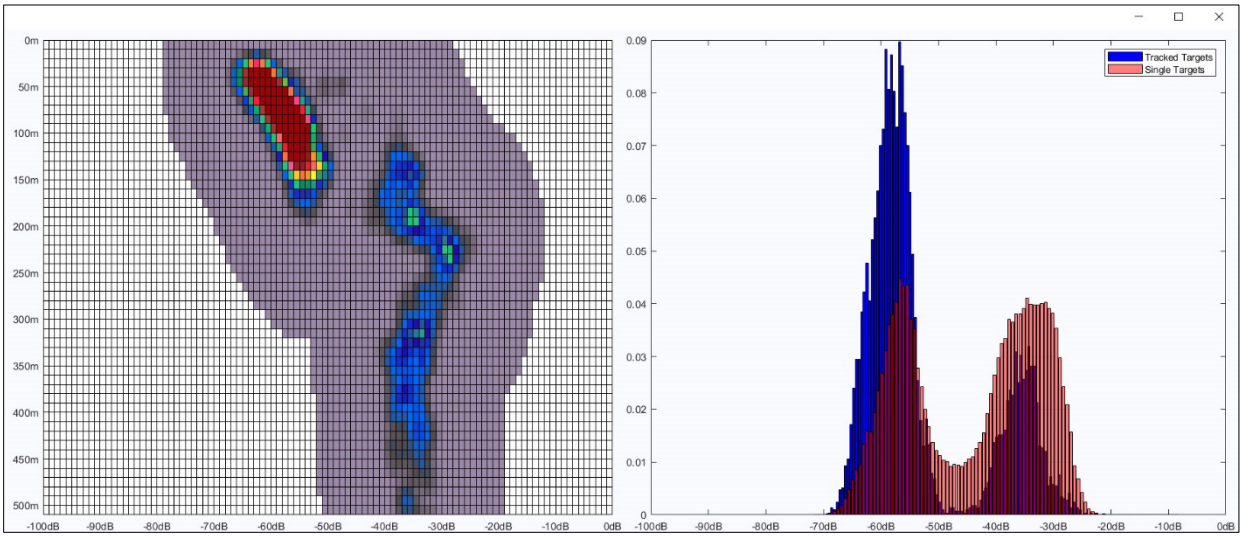

Figure 281: Distribution of tracked targets. The figure on the left shows the depth distribution for the tracked targets, colored by the number of tracked targets. The figure at the right shows the results of the single target algorithm in red and, of those targets, those that meet the target tracking algorithm parameters in blue.

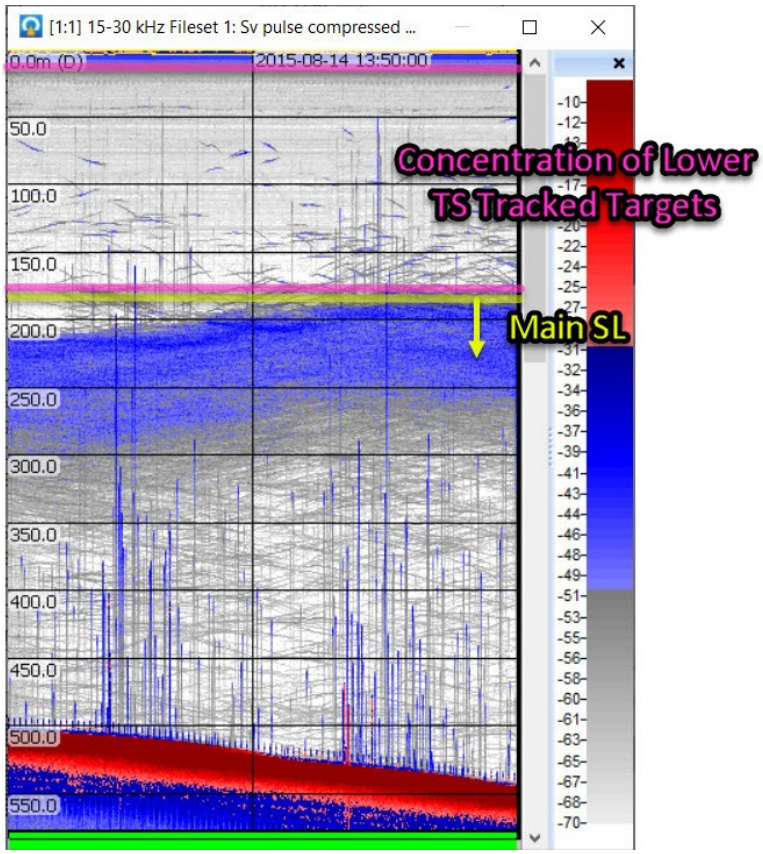

Figure 282: Echogram for PETERMANN2015-D20150814-T134156.raw showing location of main scattering layer compared to location of lower TS tracked targets.

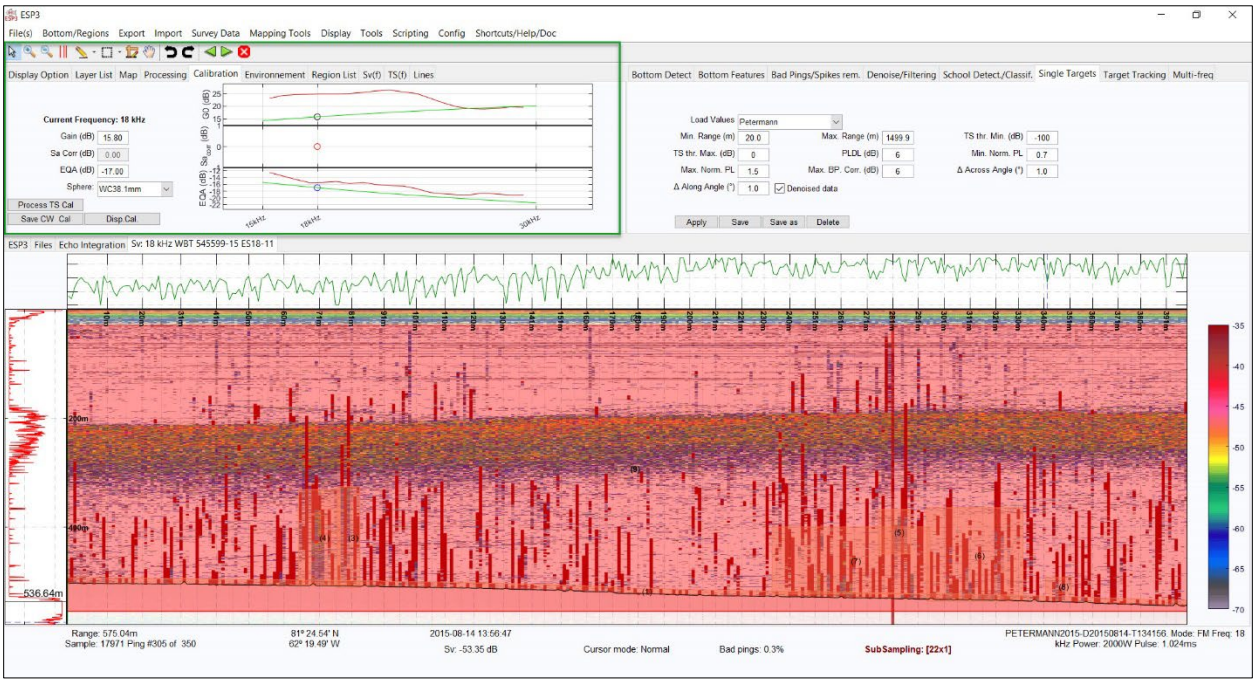

Figure 283: Echogram with default gain (gain values written into the file) applied. Note the separation between the green curve (default gain) and the red curve (gain based on calculated calibration curve) in the Calibration tab, highlighted by the green box.

Figure 284: Echogram with "rough" calibration applied. The gain has been adjusted to be closer to the calculated calibration value at the nominal frequency.

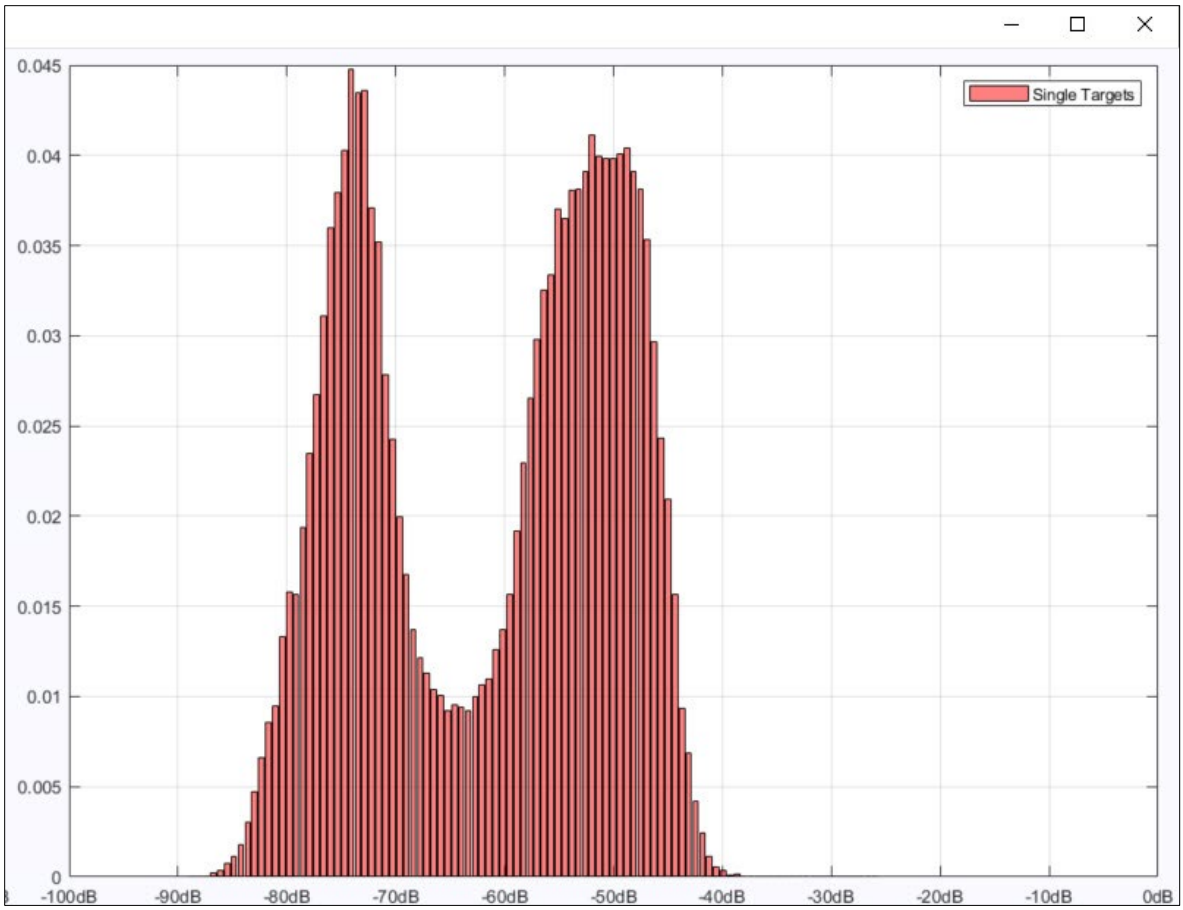

Figure 285: PDF of single targets for PETERMANN2015-D20150814-T134156.raw with a rough gain calibration applied in order to estimate calibrated TS thresholds.

The TS distributions found in transitional scattering layers were similar to homogeneous preference scattering layers, in that the tracked targets associated with the lower TS distribution were more prominent higher in the water column, above the scattering layer (Figure 286 and Figure 287). With the heterogeneous preference layers, however, the overlap in distributions corresponded with the top of the scattering layer (Figure 288 and Figure 289). Despite this, the separation between the higher and lower TS distributions was still used as the threshold for analyzed targets; the “rough” calibrated value of this separation was -64 to -75 dB. This may have left out some targets contributing to the scattering layer, but is in line with the value used by some

researchers as a lower threshold to remove the contribution of zooplankton (Geoffroy et al., 2011; Benoit et al., 2014).

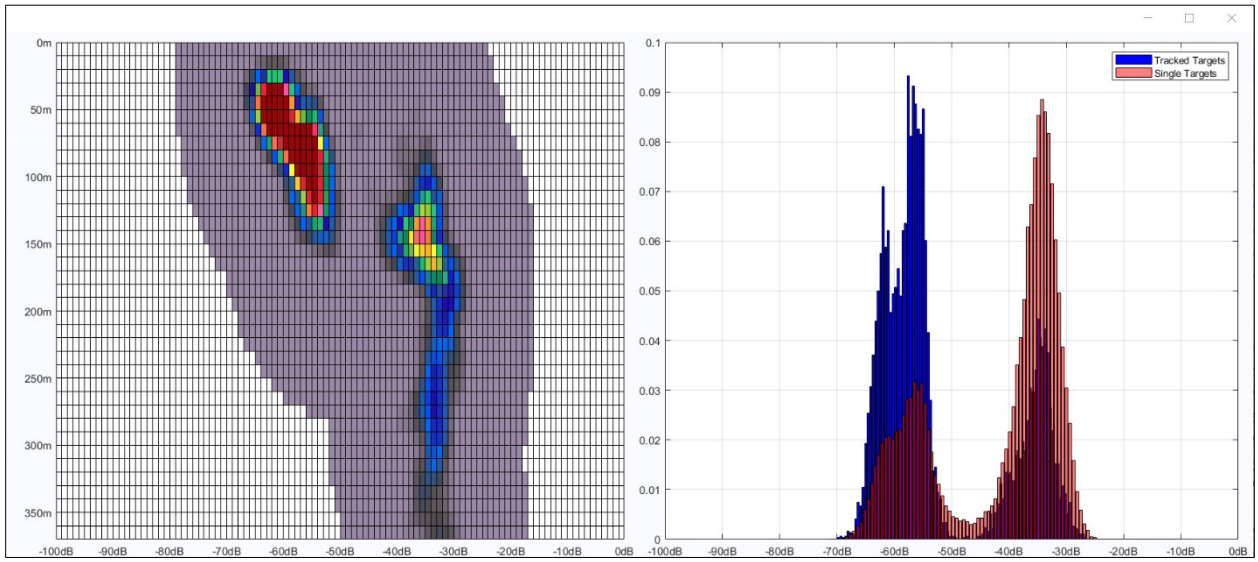

Figure 286: Distribution of tracked targets for PETERMANN-D20150815-T150617.raw, an example of a transitional scattering layer. Most of the low TS distribution is found above 150 m.

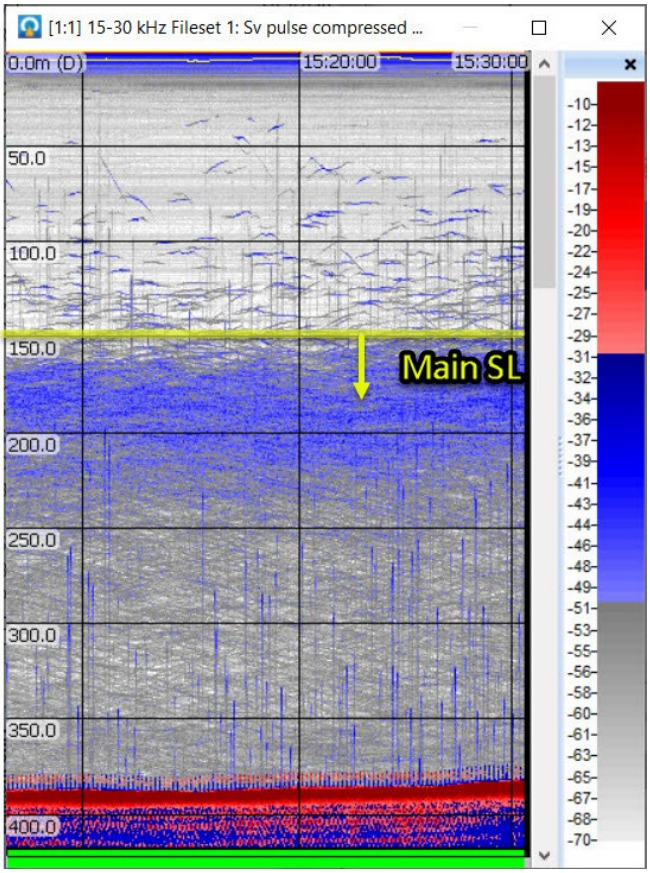

Figure 287: Echogram for PETERMANN-D20150815-T150617.raw. The primary scattering layer starts below 150 m.

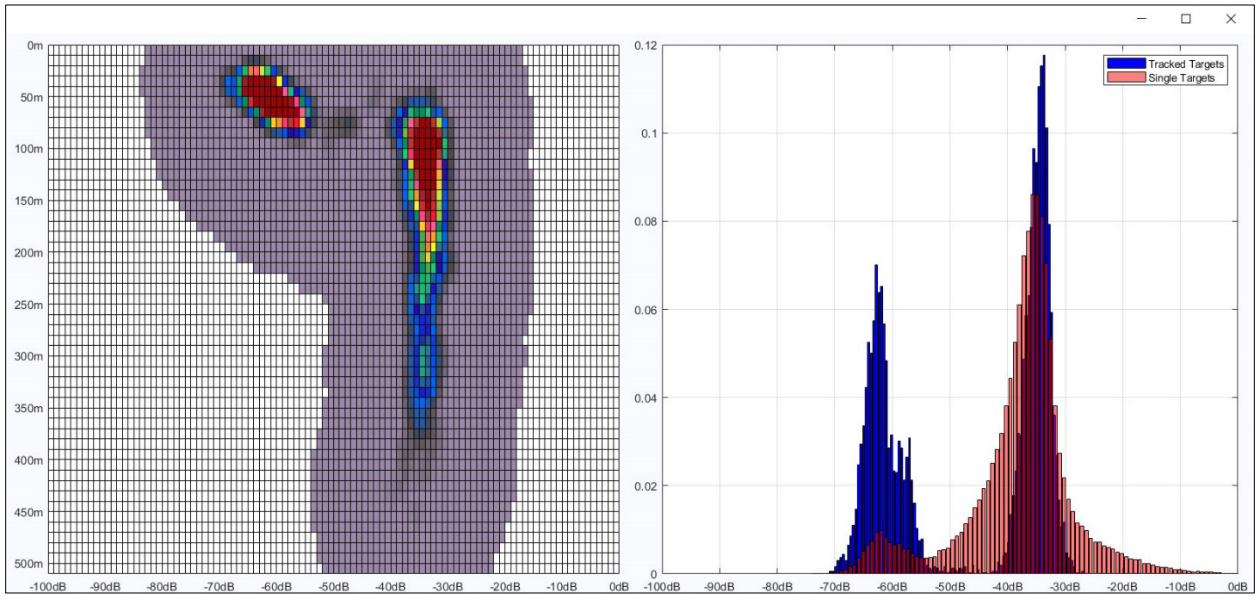

Figure 288: Distribution of tracked targets for PETERMANN-D20150807-T093944.raw, an example of a heterogeneous preference scattering layer. There is overlap in the distributions between 50 – 100 m.

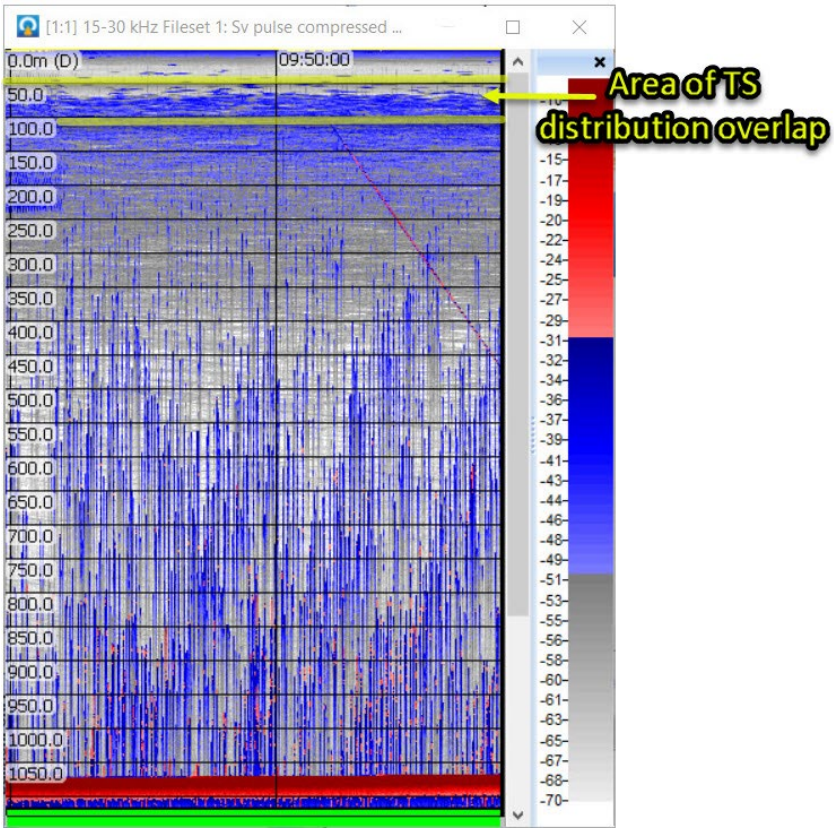

Figure 289: Echogram for PETERMANN-D20150807-T093944.raw. The scattering layer starts within the depth range where the TS distributions overlap.

E.2 Homogeneous Preference Scattering Layers

Scattering layers with a “homogenous preference” were observed at 23 CTD stations: 002, 015, 016, 020 – 023, and 030 – 044. Twenty-two of those stations were found in Hall Basin or along the western to central portion of the fjord entrance, the source area of inflow waters to the fjord (Johnson et al., 2011; Heuzé et al., 2017). A single station, 030, was found very near to the edge of the floating ice shelf. Here, eight lines corresponding to seven stations in that inflow area are examined (Figure 290). The station near the edge of the ice shelf, 030, was also examined and is found under the heading Outliers.

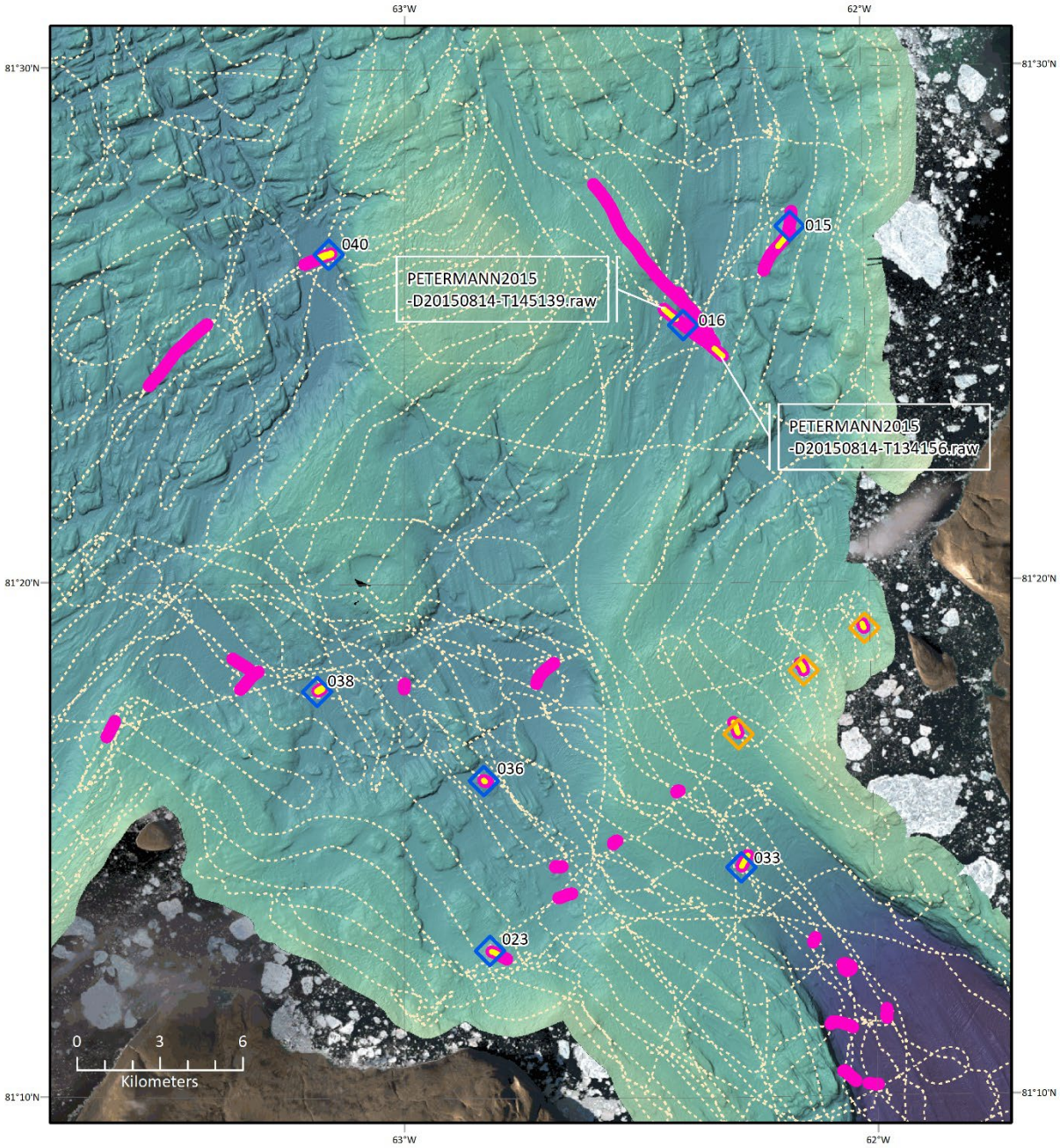

Figure 290: Location of reviewed homogenous preference scattering layers and associated CTD stations. The blue diamonds are CTD stations associated with homogenous preference scattering layers and are labeled with the CTD station number. All lines where the ship was moving at < 1.5 knots are shown in magenta; the reviewed lines are shown in yellow.

PETERMANN2015-D20150813-T215026.raw

Line PETERMANN2015-D20150813-T215026.raw (Figure 291) was located near CTD 015 (Figure 290). Based on the PDF (Figure 292), a lower threshold of -46 dB was

applied during single target detection. The minimum water column depth analyzed for single targets was restricted to 150 m due to a large number of targets higher in the water column that appeared significantly different from the targets in and around the scattering layer. The combined single target and target tracking algorithms resulted in 172 targets with a complete frequency response between 16.11 and 25.63 kHz (Figure 293 - Figure 294). Twenty-four selections were made for S_v analysis, twelve from dense areas and twelve from less dense areas (Figure 295). TS, S_v, and the calculated average density ($\hat{\rho}$) and the ensonified volume (V) are summarized for all reviewed lines in Table 7.

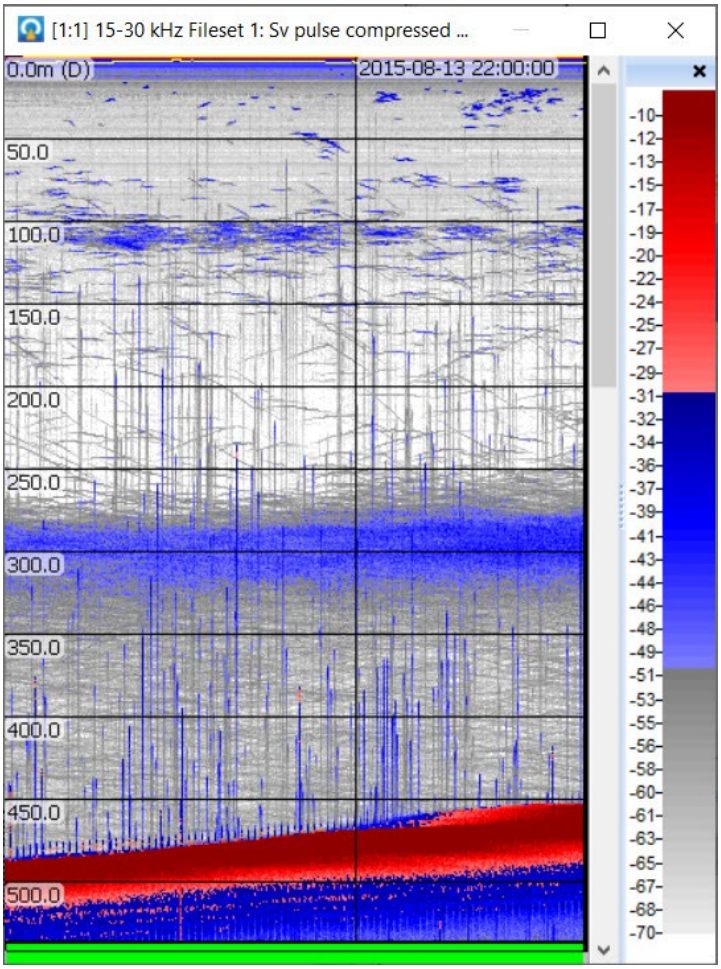

Figure 291: PETERMANN2015-D20150813-T215026.raw shown in Echoview.

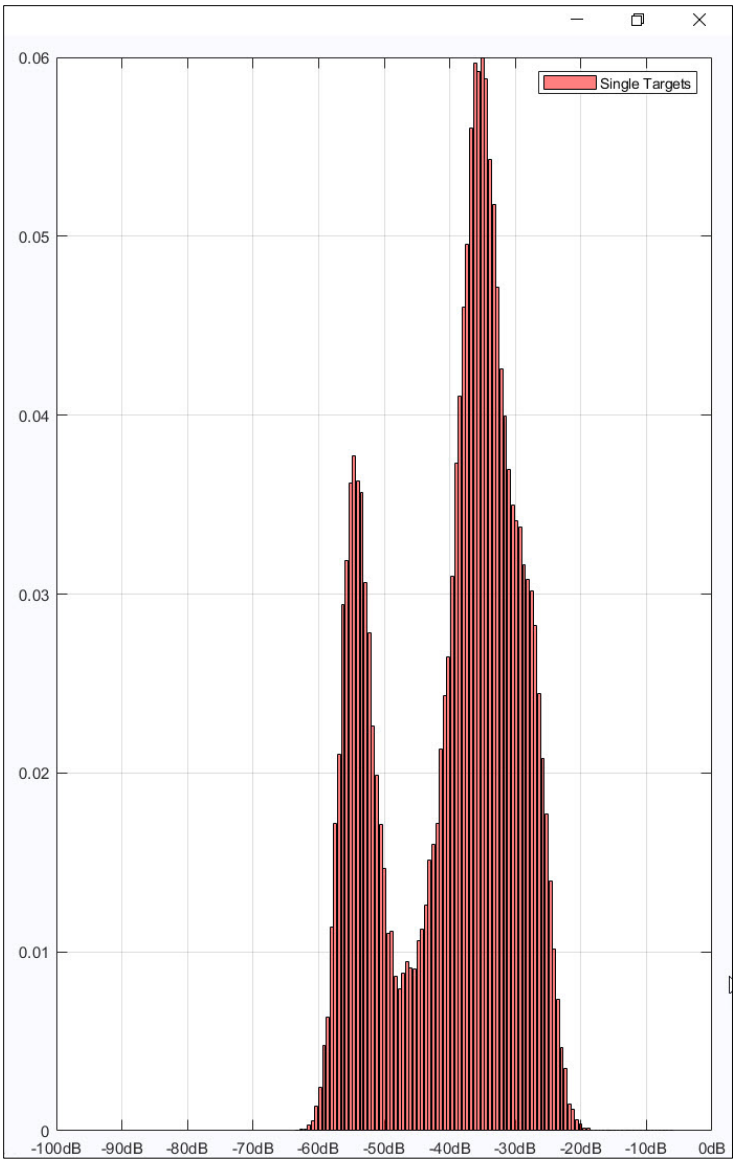

Figure 292: PDF for line PETERMANN2015-D20150813-T215026.raw. A lower threshold of -46 dB was used for single target detection.

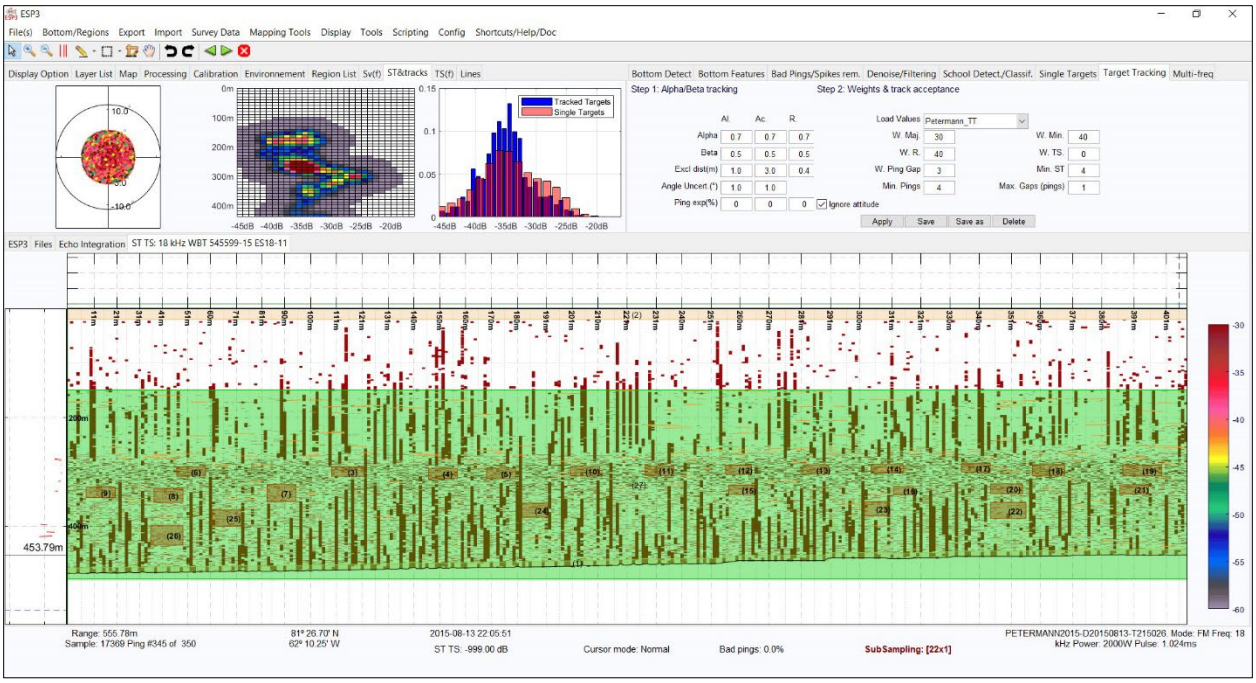

Figure 293: PETERMANN2015-D20150813-T215026.raw selected single targets and volume targets.

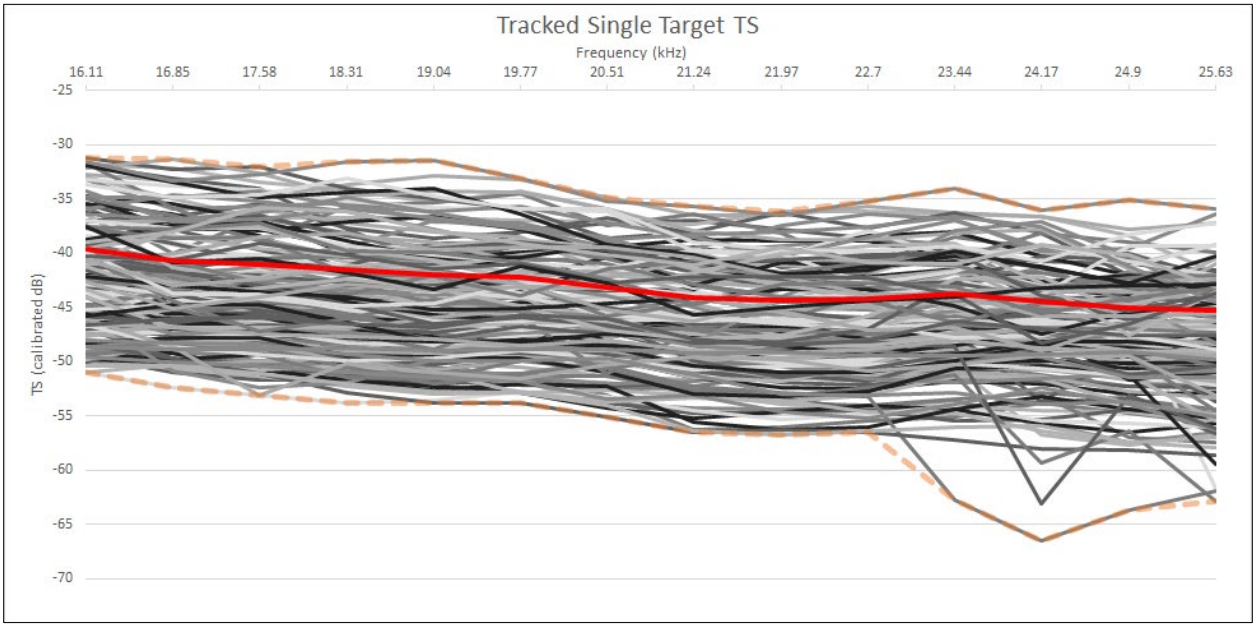

Figure 294: Frequency response for tracked single targets, PETERMANN2015-D20150813-T215026.raw. The solid red line is the average target strength across the frequency range and the orange dashed lines are the minimum and maximum target strengths across the frequency range. Colors of other lines are randomly assigned.

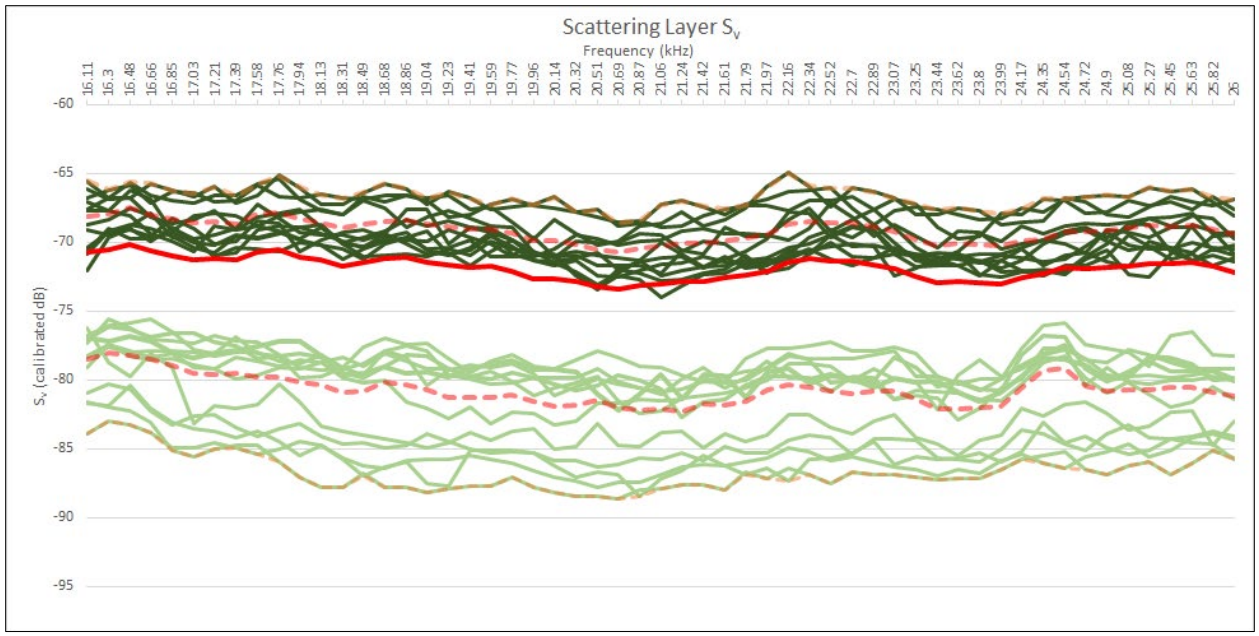

Figure 295: Frequency response for volume selections, PETERMANN2015-D20150813-T215026.raw. The solid red line is the average volume scattering across the frequency range and the orange dashed lines are the minimum and maximum volume scattering across the frequency range. The dark green lines are from dense portions of the scattering layer, the light green lines are from less dense areas. The dashed red lines are the averages for the dense and less dense layers.

PETERMANN2015-D20150814-T134156.raw

Line PETERMANN2015-D20150814-T134156.raw (Figure 296) was located near CTD 016 (Figure 290). Based on the PDF (Figure 297), a lower threshold of -44 dB was applied during single target detection. The combined single target and target tracking algorithms resulted in 299 targets with a complete frequency response between 16.11 and 25.63 kHz (Figure 298 - Figure 299). Thirteen selections were made for S_v analysis, seven from dense areas and five from less dense areas (Figure 300). TS, S_v, and the calculated average density ($\hat{\rho}$) and the ensonified volume (V) are summarized for all reviewed lines in Table 7.

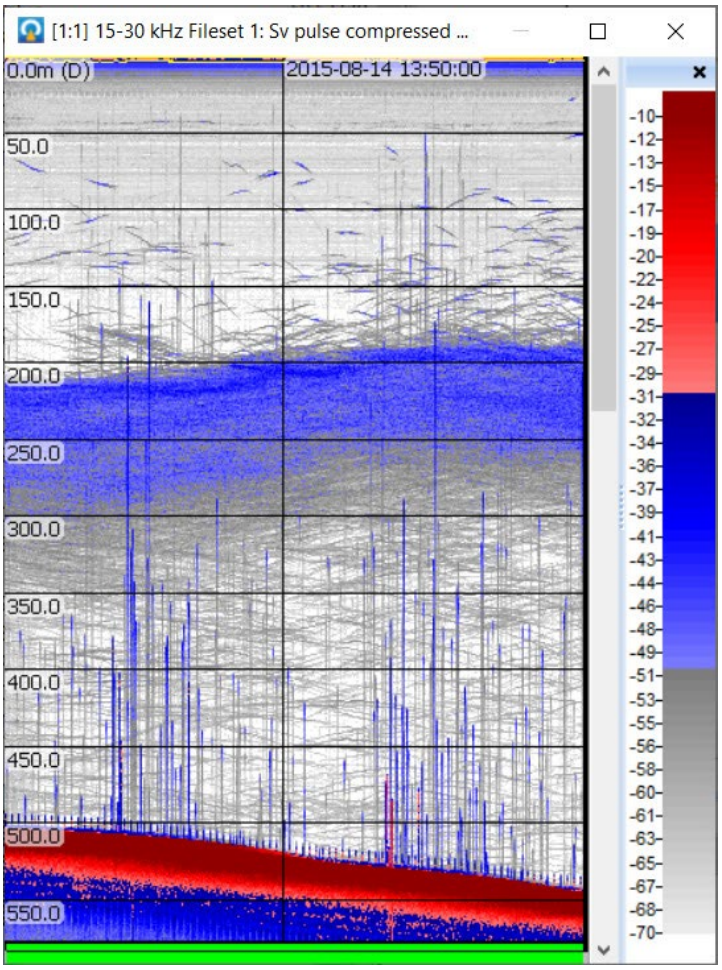

Figure 296: PETERMANN2015-D20150814-T134156.raw shown in Echoview.

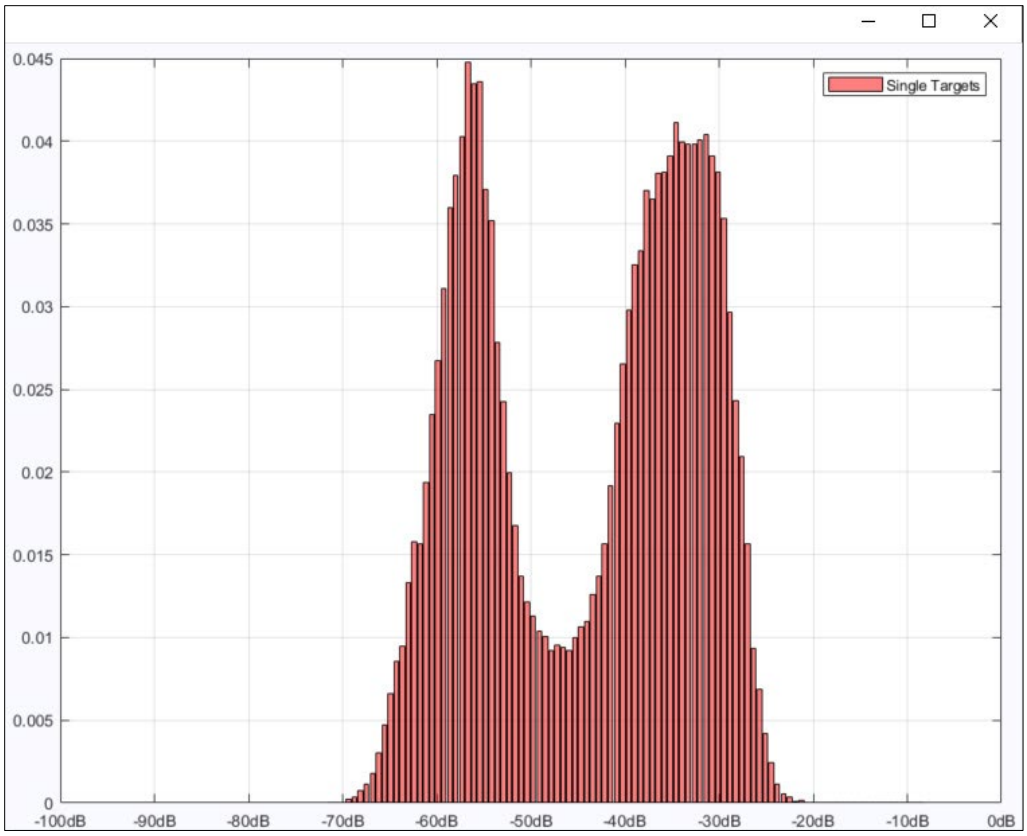

Figure 297: PDF for line PETERMANN2015-D20150814-T134156.raw. A lower threshold of -46 dB was used for single target detection.

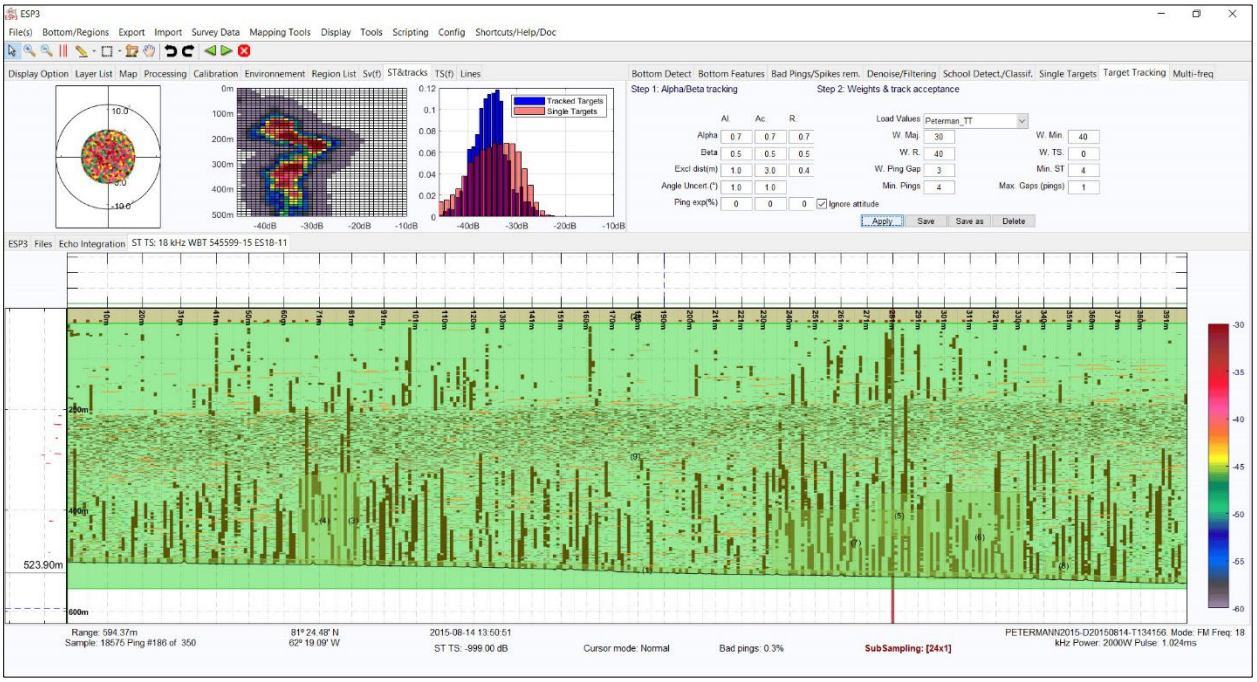

Figure 298: PETERMANN2015-D20150814-T134156.raw selected single targets.

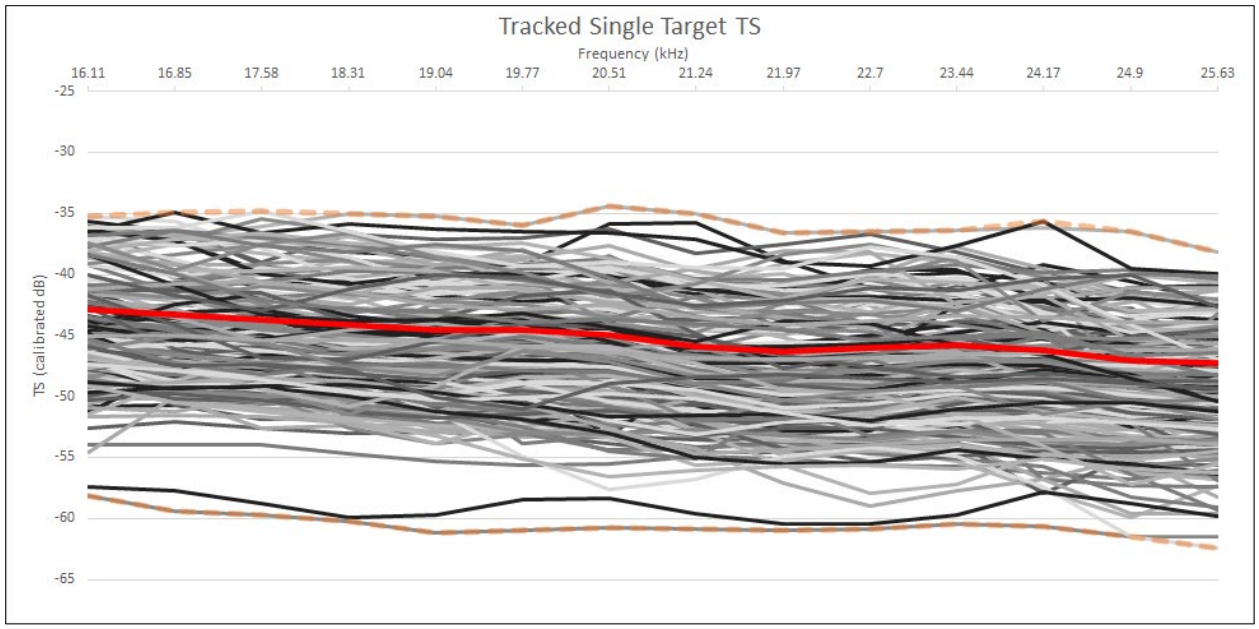

Figure 299: Frequency response for tracked single targets, PETERMANN2015-D20150814-T134156.raw. The solid red line is the average target strength across the frequency range and the orange dashed lines are the minimum and maximum target strengths across the frequency range. Colors of other lines are randomly assigned.

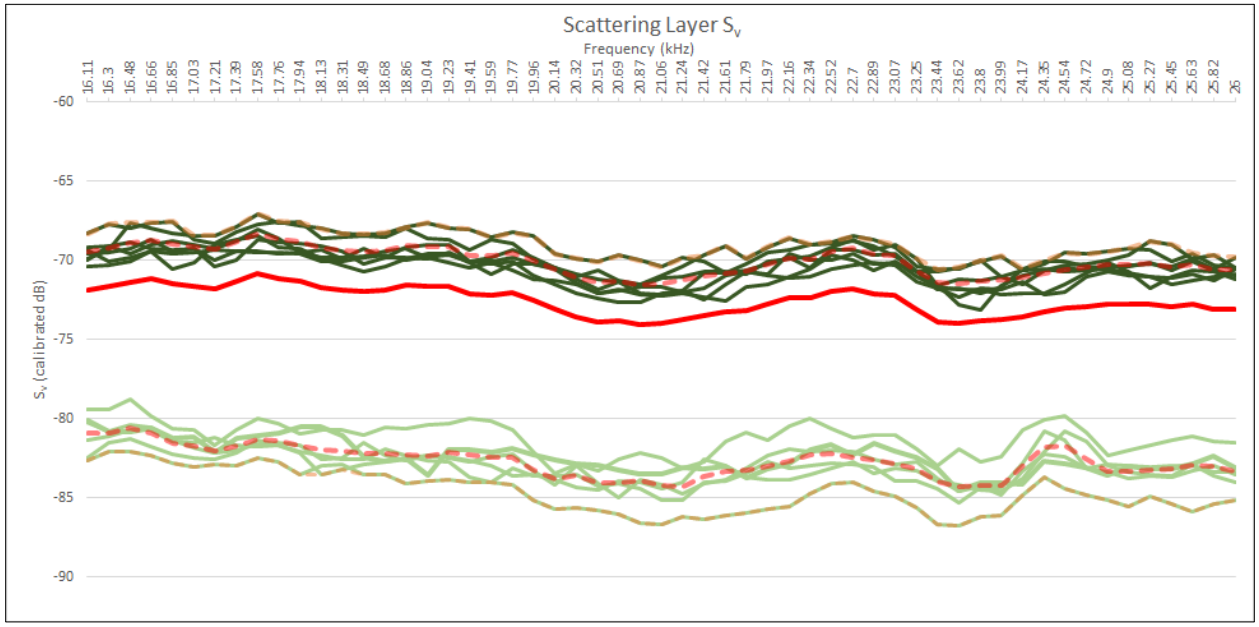

Figure 300: Frequency response for volume selections, PETERMANN2015-D20150814-T134156.raw. The solid red line is the average volume scattering across the frequency range and the orange dashed lines are the minimum and maximum volume scattering across the frequency range. The dark green lines are from dense portions of the scattering layer, the light green lines are from less dense areas. The dashed red lines are the averages for the dense and less dense layers.

PETERMANN2015-D20150814-T145139.raw

Line PETERMANN2015-D20150814-T145139.raw (Figure 301) was located near CTD 016 (Figure 290). Based on the PDF (Figure 302), a lower threshold of -43 dB was applied during single target detection. The combined single target and target tracking algorithms resulted in 228 targets with a complete frequency response between 16.11 and 25.63 kHz (Figure 303 - Figure 304). Twenty-three selections were made for S_v analysis, thirteen from dense areas and ten from less dense areas (Figure 305). TS, S_v, and the calculated average density ($\hat{\rho}$) and the ensonified volume (V) are summarized for all reviewed lines in Table 7.

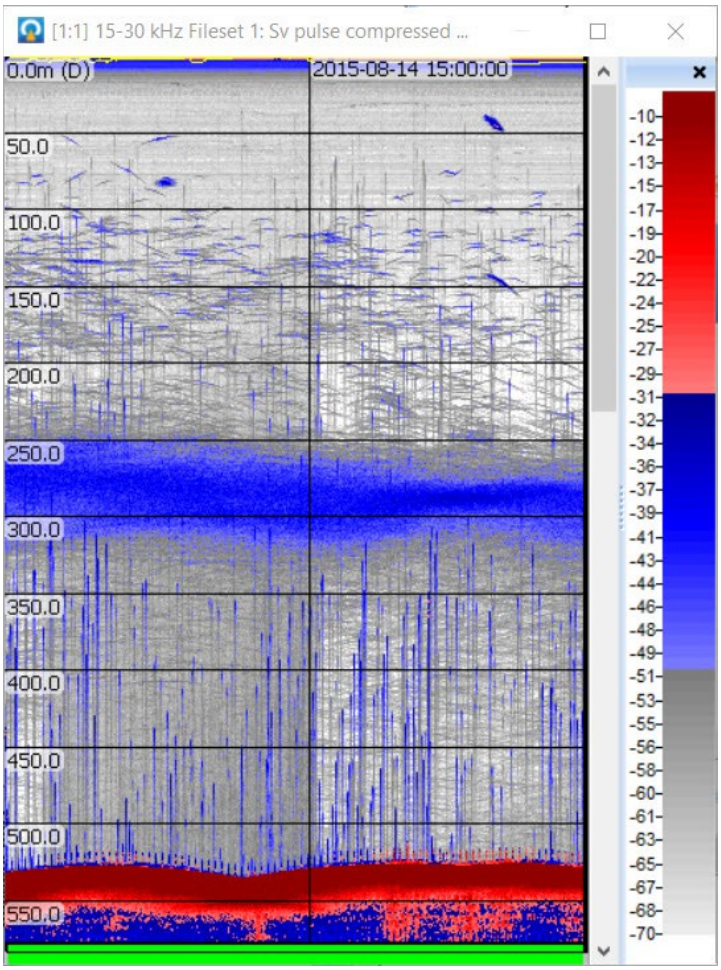

Figure 301: PETERMANN2015-D20150814-T145139.raw shown in Echoview.

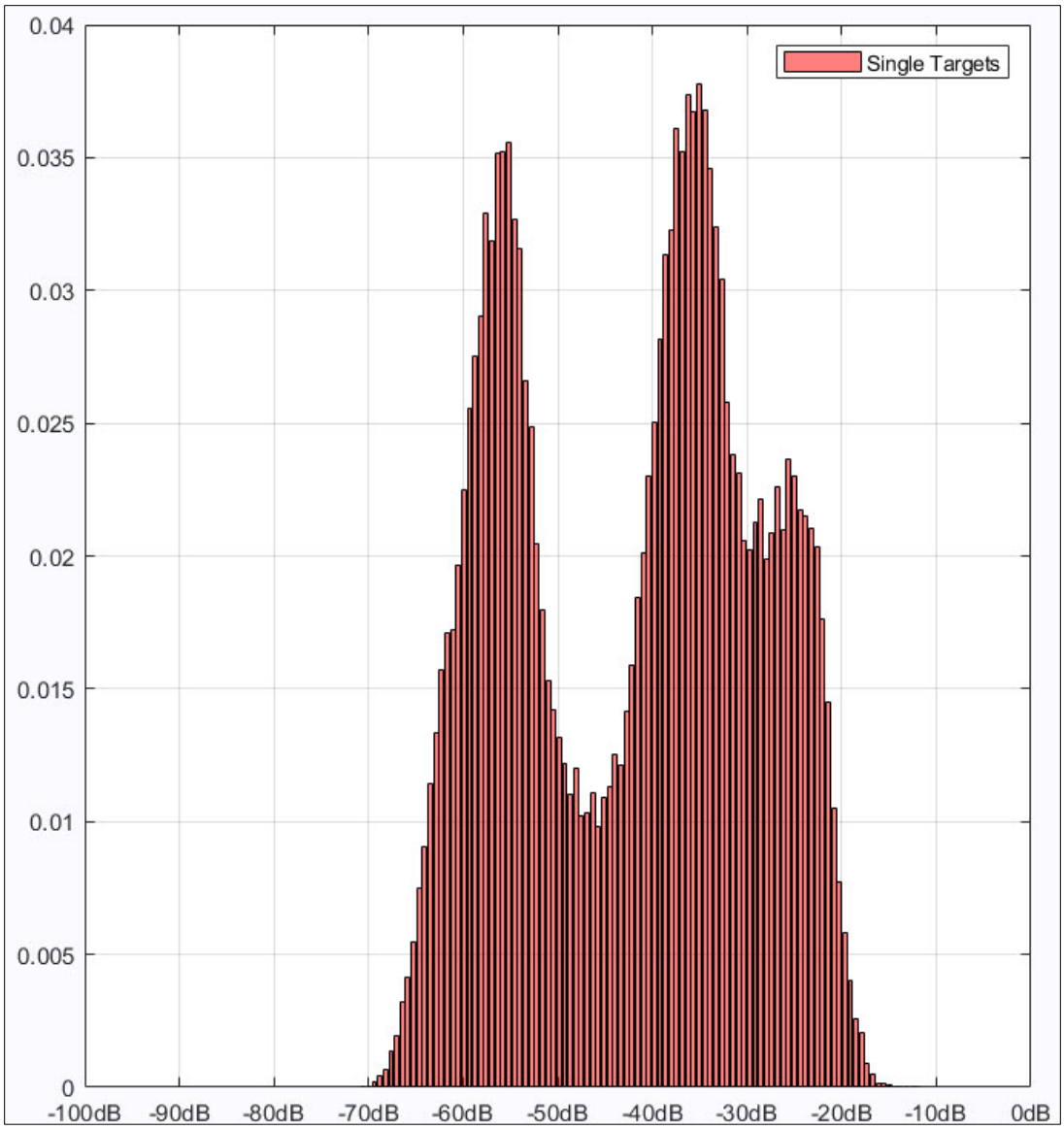

Figure 302: PDF for line PETERMANN2015-D20150814-T145139.raw. A lower threshold of -43 dB was used for single target detection.

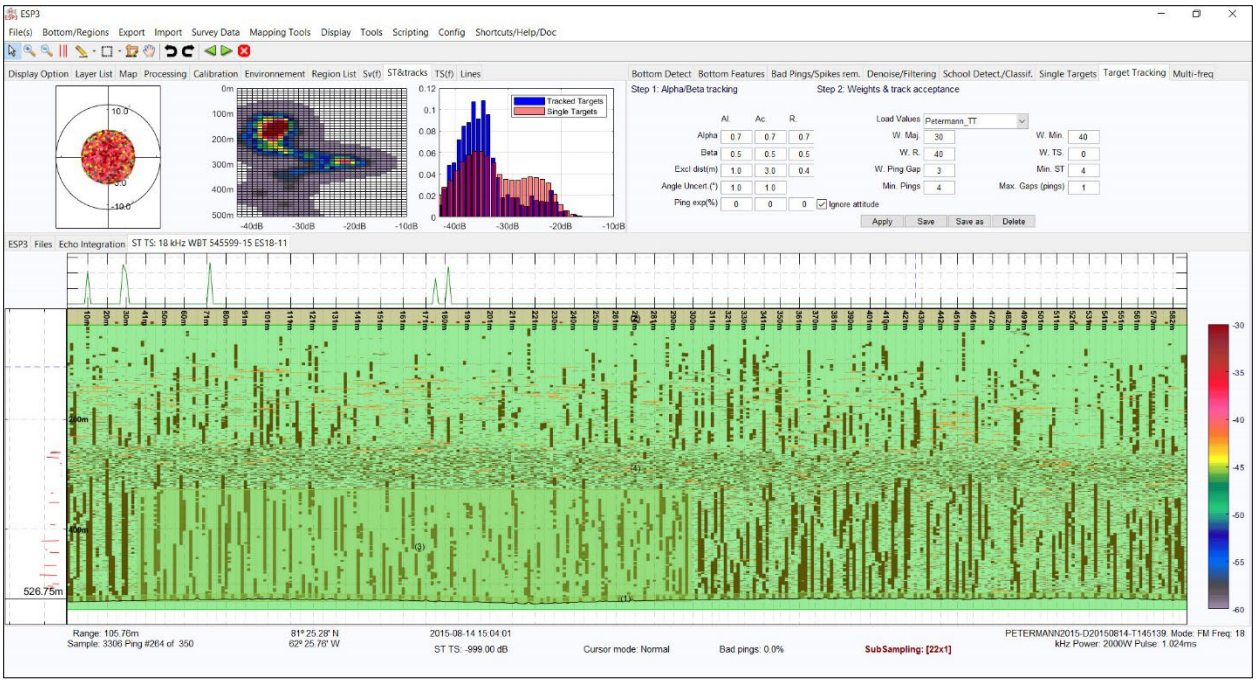

Figure 303: PETERMANN2015-D20150814-T145139.raw selected single targets.

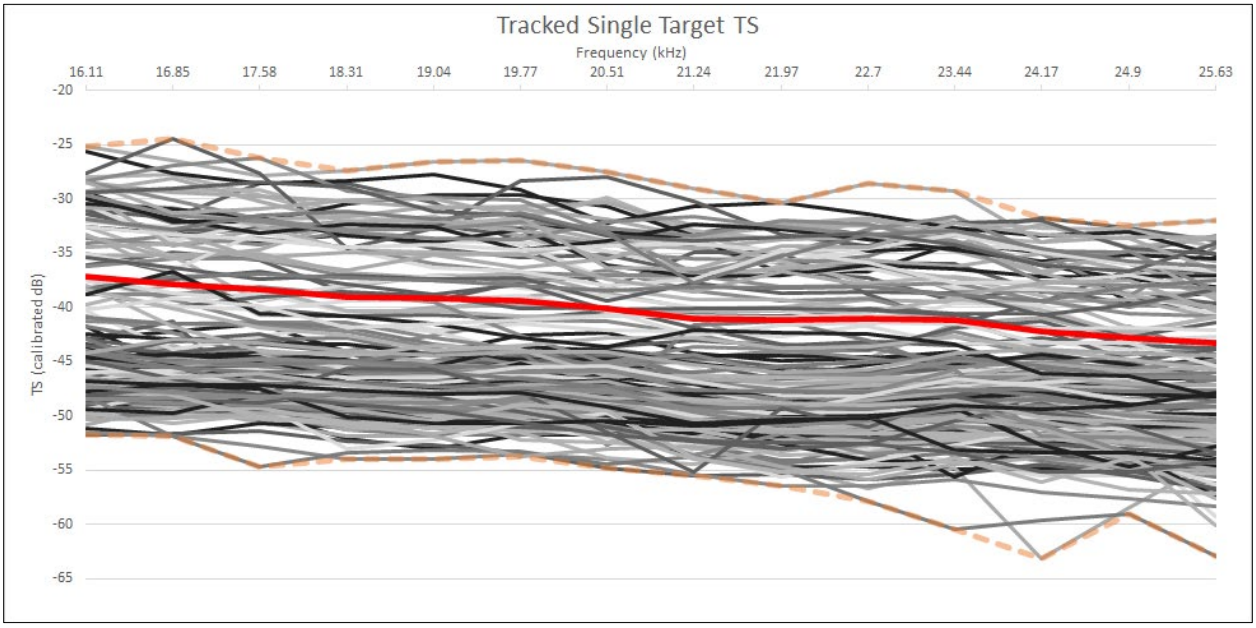

Figure 304: Frequency response for tracked single targets, PETERMANN2015-D20150814-T145139.raw. The solid red line is the average target strength across the frequency range and the orange dashed lines are the minimum and maximum target strengths across the frequency range. Colors of other lines are randomly assigned.

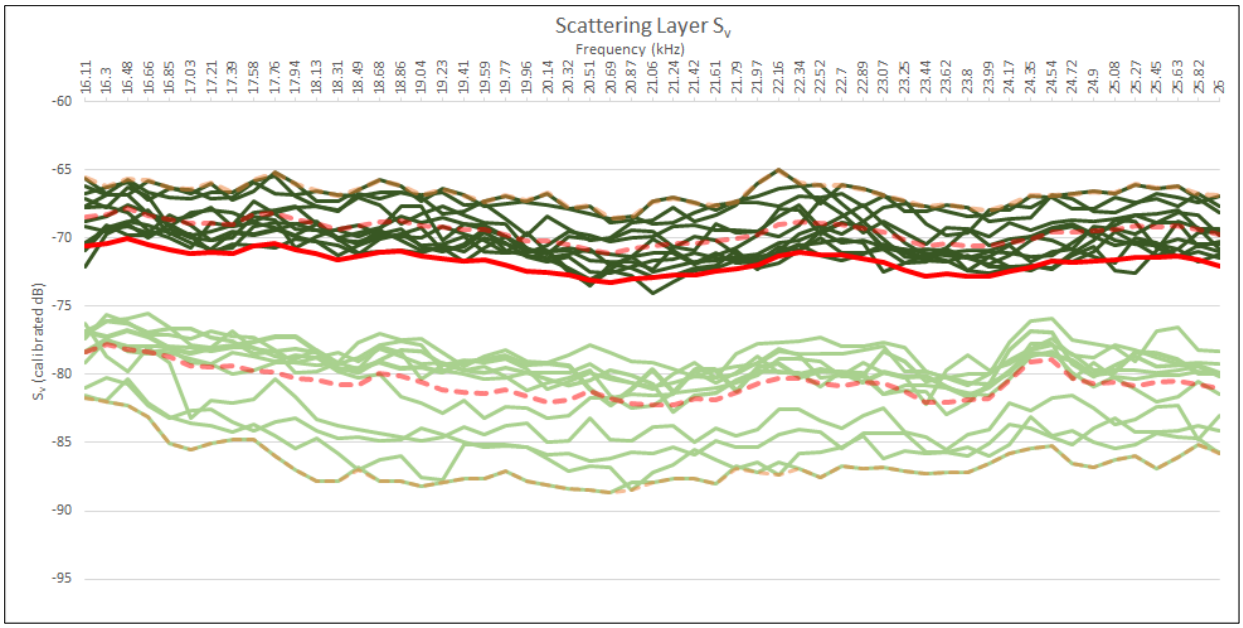

Figure 305: Frequency response for volume selections, PETERMANN2015-D20150814-T145139.raw. The solid red line is the average volume scattering across the frequency range and the orange dashed lines are the minimum and maximum volume scattering across the frequency range. The dark green lines are from dense portions of the scattering layer, the light green lines are from less dense areas. The dashed red lines are the averages for the dense and less dense layers.

PETERMANN2015-D20150815-T194637.raw

Line PETERMANN2015-D20150815-T194637.raw (Figure 306) was located near CTD 023 (Figure 290). Based on the PDF (Figure 307), a lower threshold of -45 dB was applied during single target detection. The combined single target and target tracking algorithms resulted in 134 targets with a complete frequency response between 16.11 and 25.63 kHz (Figure 308 - Figure 309). Fourteen selections were made for S_v analysis, six from dense areas and eight from less dense areas (Figure 310). TS, S_v, and the calculated average density ($\hat{\rho}$) and the ensonified volume (V) are summarized for all reviewed lines in Table 7.

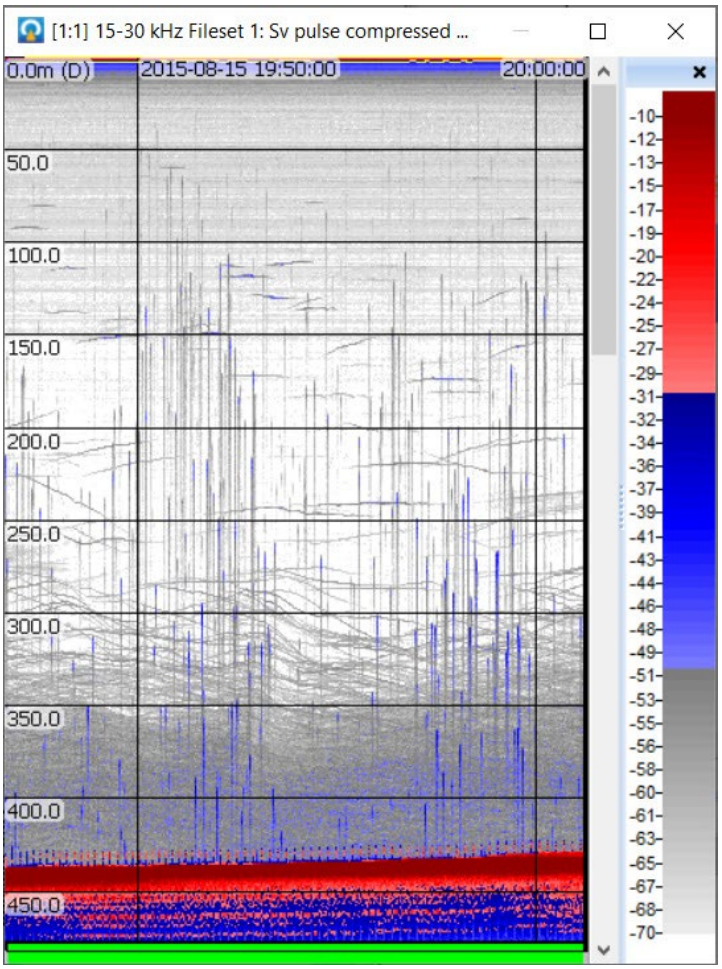

Figure 306: PETERMANN2015-D20150815-T194637.raw shown in Echoview.

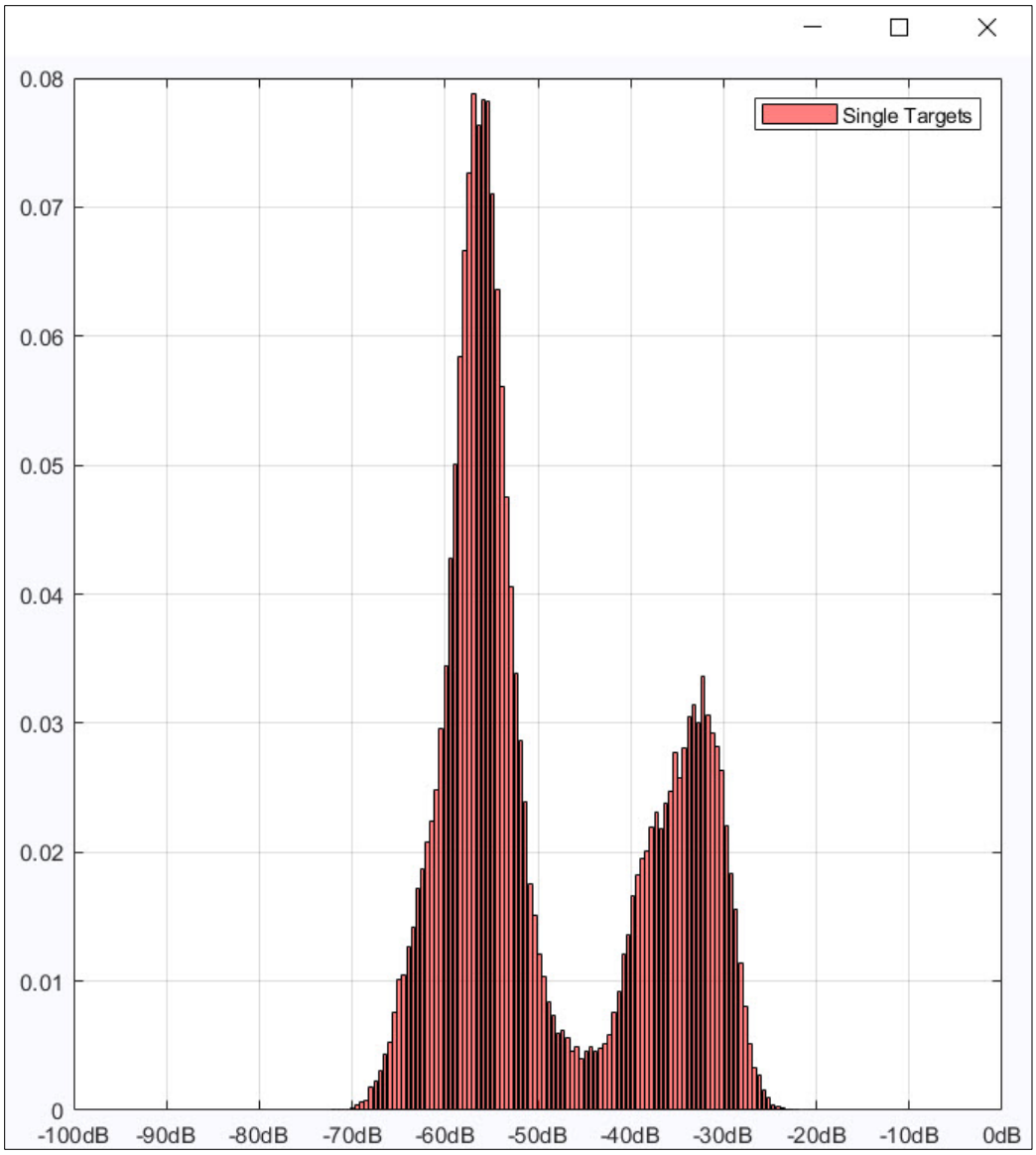

Figure 307: PDF for line PETERMANN2015-D20150815-T194637.raw. A lower threshold of -45 dB was used for single target detection.

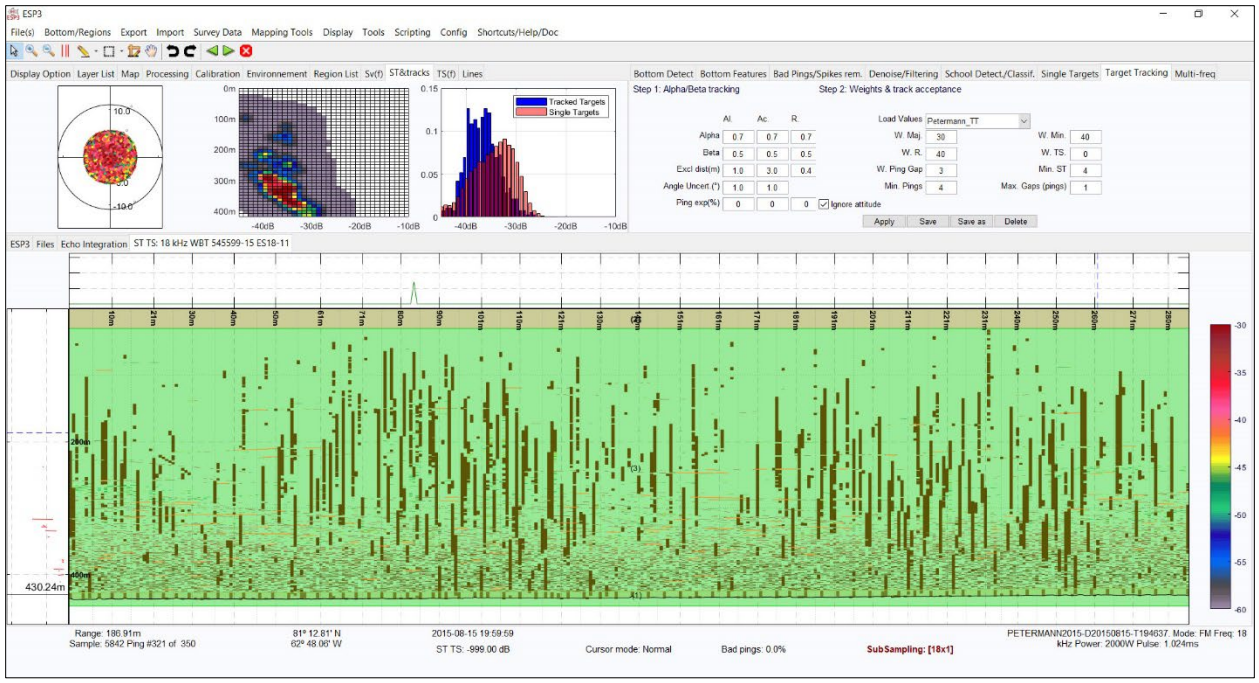

Figure 308: PETERMANN2015-D20150815-T194637.raw selected single targets.

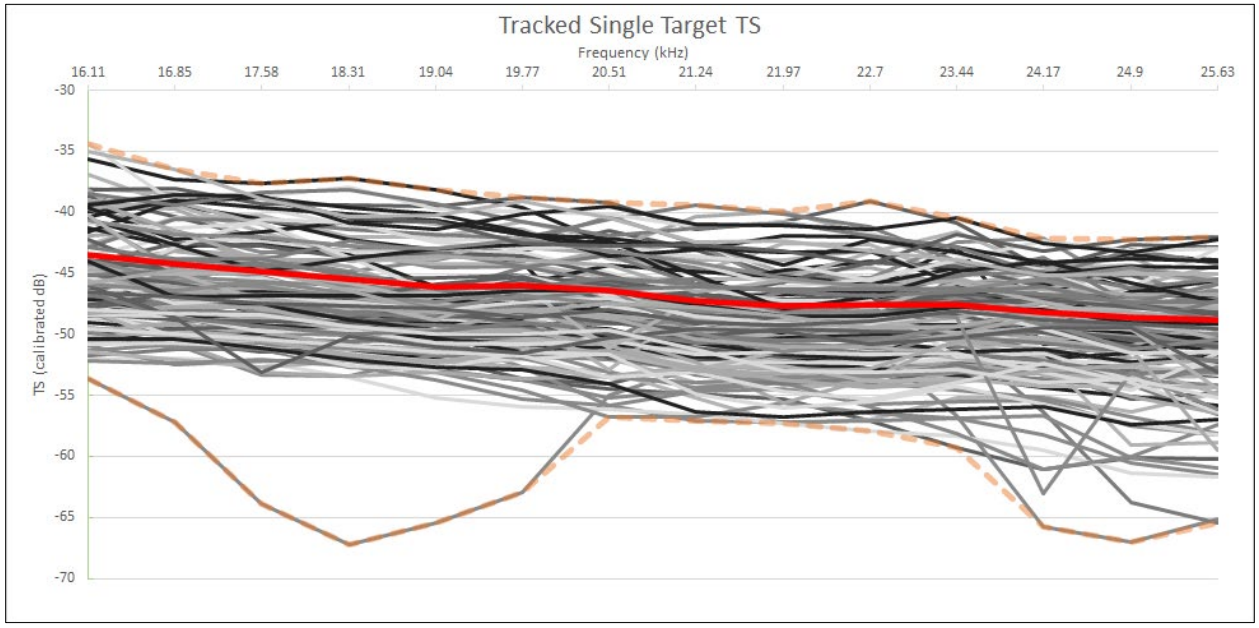

Figure 309: Frequency response for tracked single targets, PETERMANN2015-D20150815-T194637.raw. The solid red line is the average target strength across the frequency range and the orange dashed lines are the minimum and maximum target strengths across the frequency range. Colors of other lines are randomly assigned.

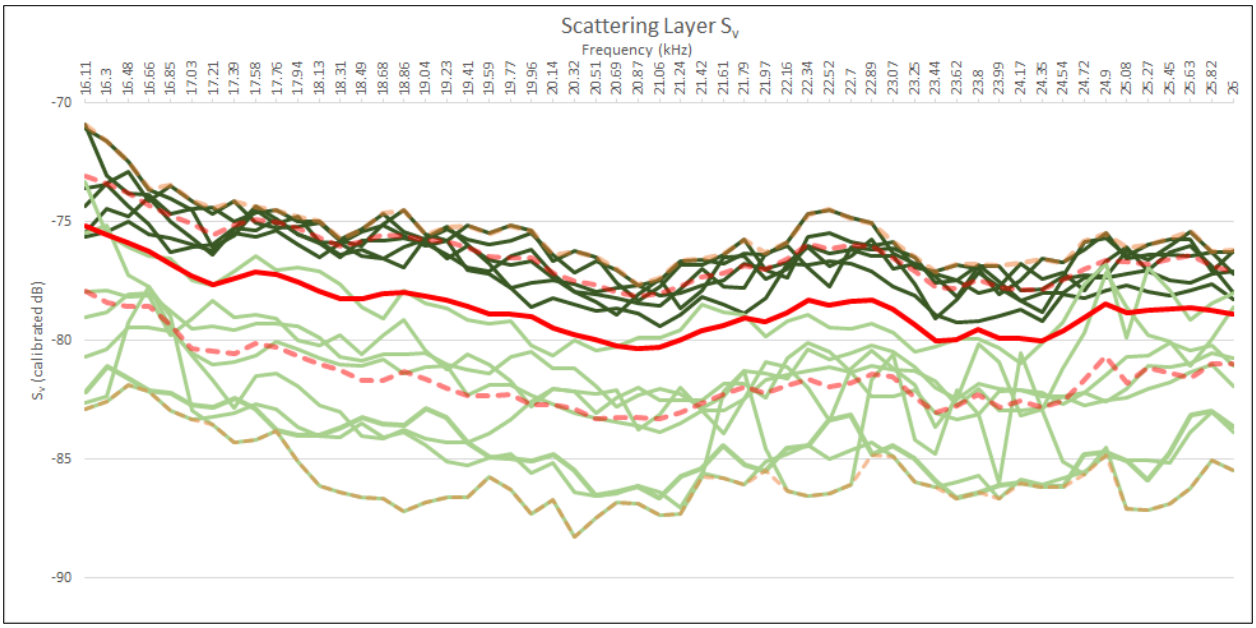

Figure 310: Frequency response for volume selections, PETERMANN2015-D20150815-T194637.raw. The solid red line is the average volume scattering across the frequency range and the orange dashed lines are the minimum and maximum volume scattering across the frequency range. The dark green lines are from dense portions of the scattering layer, the light green lines are from less dense areas. The dashed red lines are the averages for the dense and less dense layers.

PETERMANN2015-D20150823-T205547.raw

Line PETERMANN2015-D20150823-T205547.raw (Figure 311) was located near CTD 033 (Figure 290). Based on the PDF (Figure 312), a lower threshold of -47 dB was applied during single target detection. The combined single target and target tracking algorithms resulted in 378 targets with a complete frequency response between 16.11 and 25.63 kHz (Figure 313 - Figure 314). Twenty selections were made for S_v analysis, ten from dense areas and ten from less dense areas (Figure 315). TS, S_v, and the calculated average density ($\hat{\rho}$) and the ensonified volume (V) are summarized for all reviewed lines in Table 7.

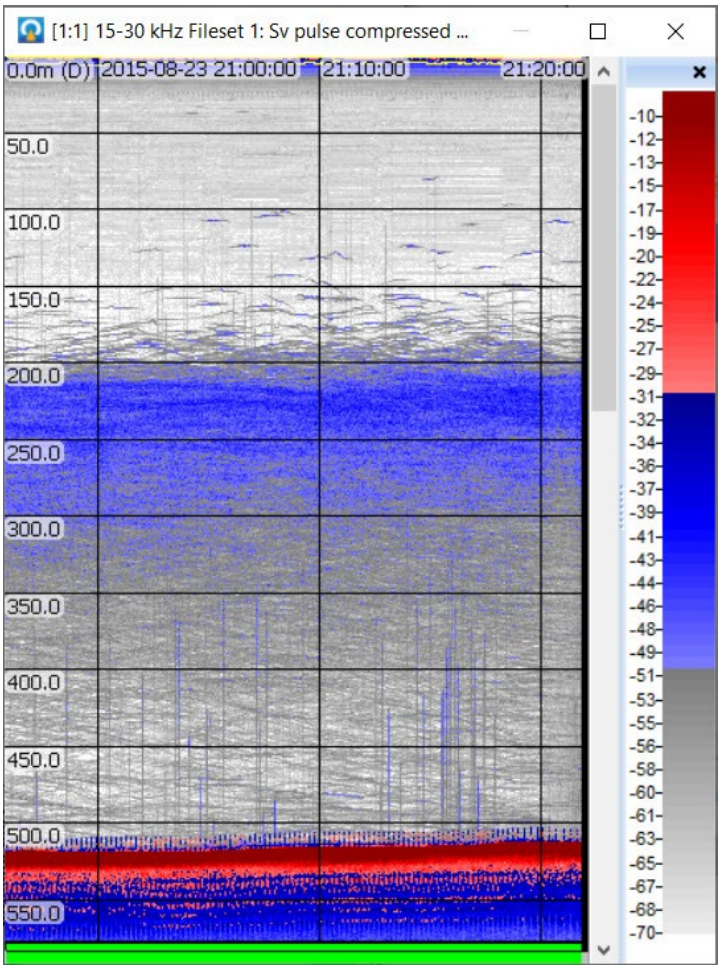

Figure 311: PETERMANN2015-D20150823-T205547.raw shown in Echoview.

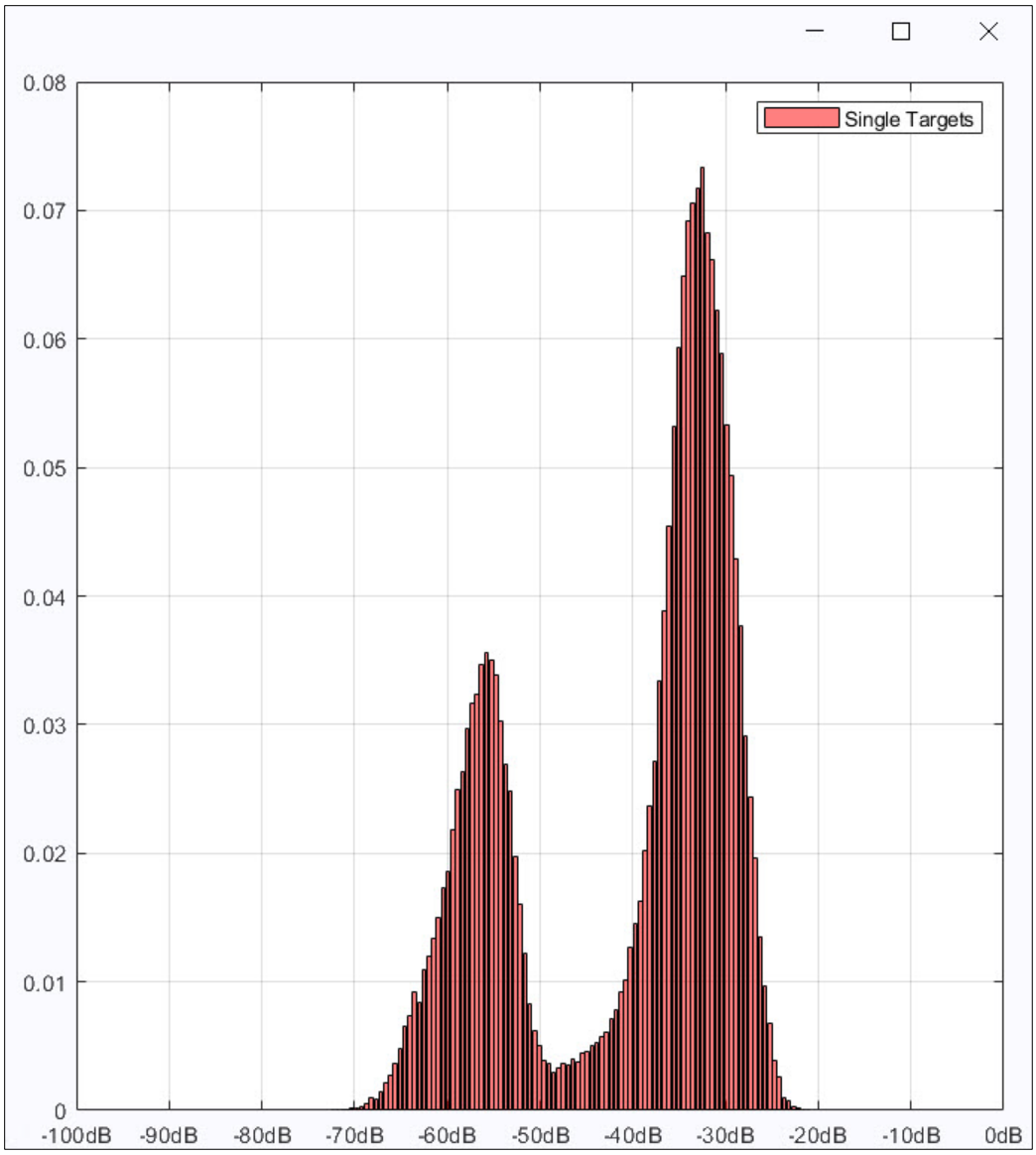

Figure 312: PDF for line PETERMANN2015-D20150823-T205547.raw. A lower threshold of -47 dB was used for single target detection.

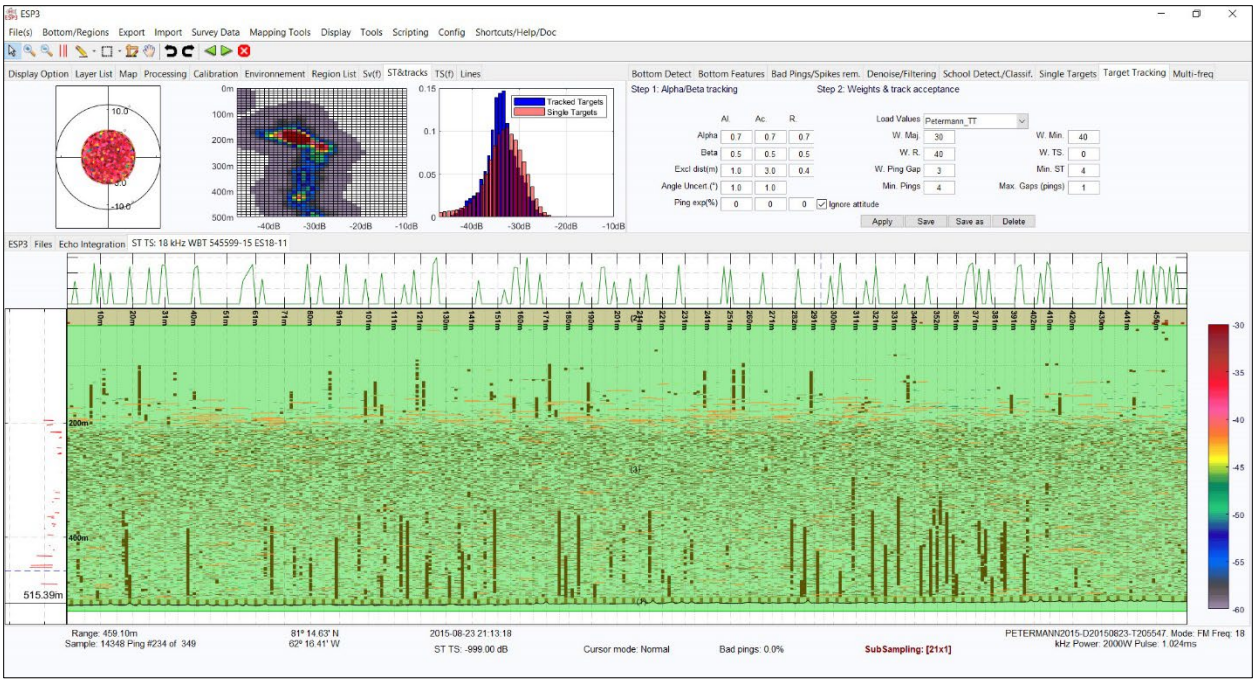

Figure 313: PETERMANN2015-D20150823-T205547.raw selected single targets.

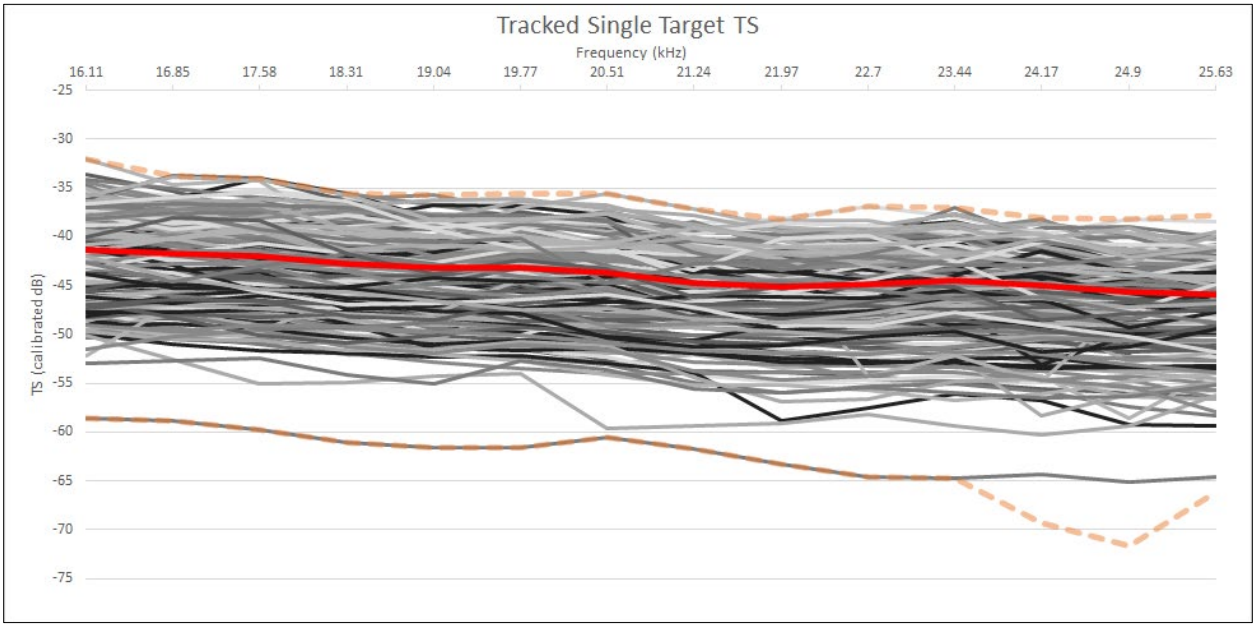

Figure 314: Frequency response for tracked single targets, PETERMANN2015-D20150823-T205547.raw. The solid red line is the average target strength across the frequency range and the orange dashed lines are the minimum and maximum target strengths across the frequency range. Colors of other lines are randomly assigned.

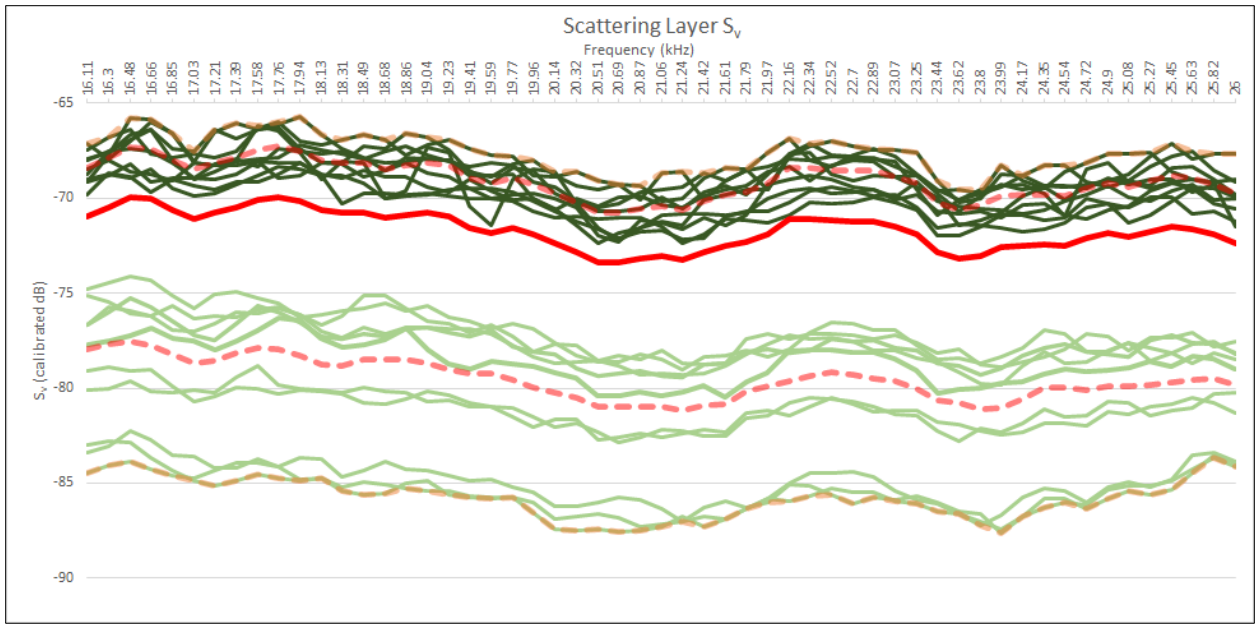

Figure 315: Frequency response for volume selections, PETERMANN2015-D20150823-T205547.raw. The solid red line is the average volume scattering across the frequency range and the orange dashed lines are the minimum and maximum volume scattering across the frequency.

PETERMANN2015-D20150824-T000615.raw

Line PETERMANN2015-D20150824-T000615.raw (Figure 316) was located near CTD 036 (Figure 290). Based on the PDF (Figure 317), a lower threshold of -45 dB was applied during single target detection. The combined single target and target tracking algorithms resulted in 87 targets with a complete frequency response between 16.11 and 25.63 kHz (Figure 318 - Figure 319). Twelve selections were made for S_v analysis, six from dense areas and six from less dense areas (Figure 320). TS, S_v, and the calculated average density ($\hat{\rho}$) and the ensonified volume (V) are summarized for all reviewed lines in Table 7.

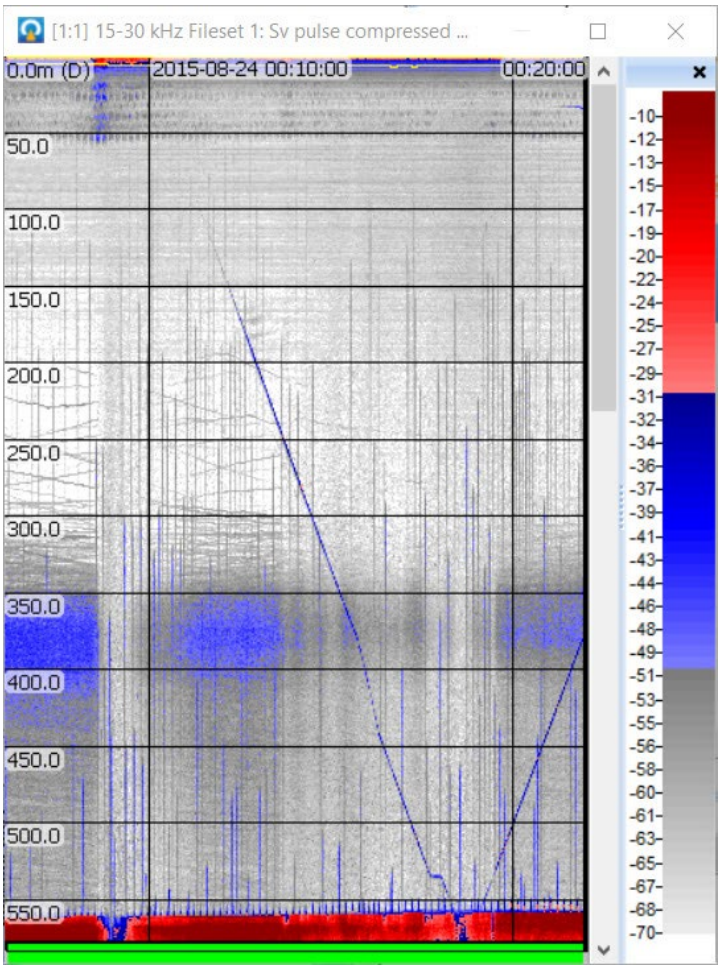

Figure 316: PETERMANN2015-D20150824-T000615.raw shown in Echoview.

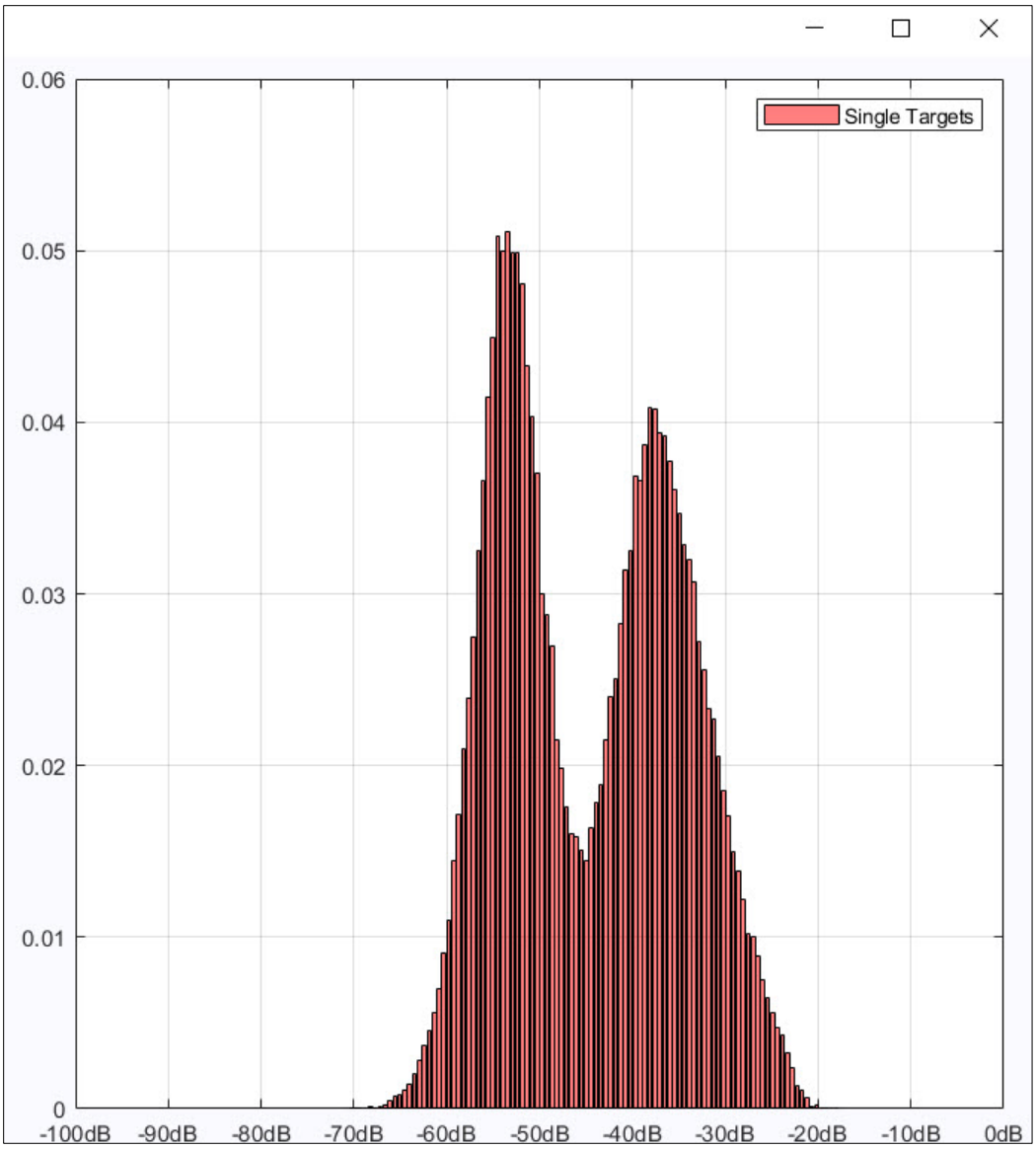

Figure 317: PDF for line PETERMANN2015-D20150824-T000615.raw. A lower threshold of -45 dB was used for single target detection.

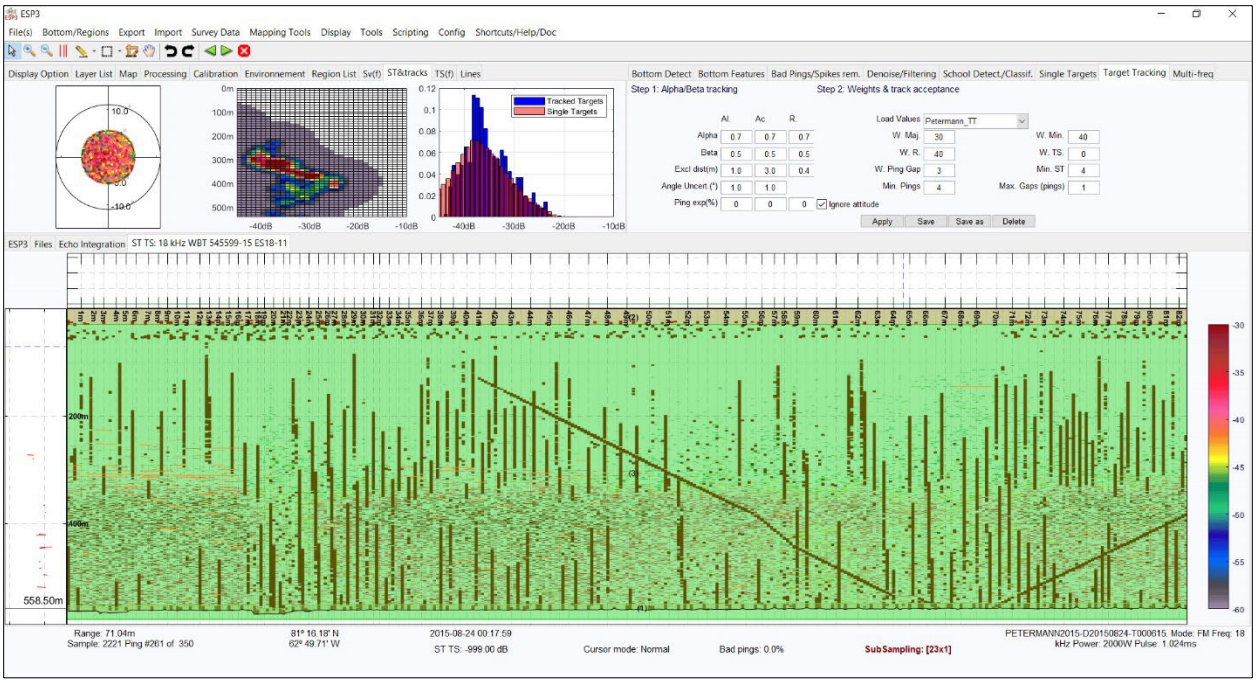

Figure 318: PETERMANN2015-D20150824-T000615.raw selected single targets.

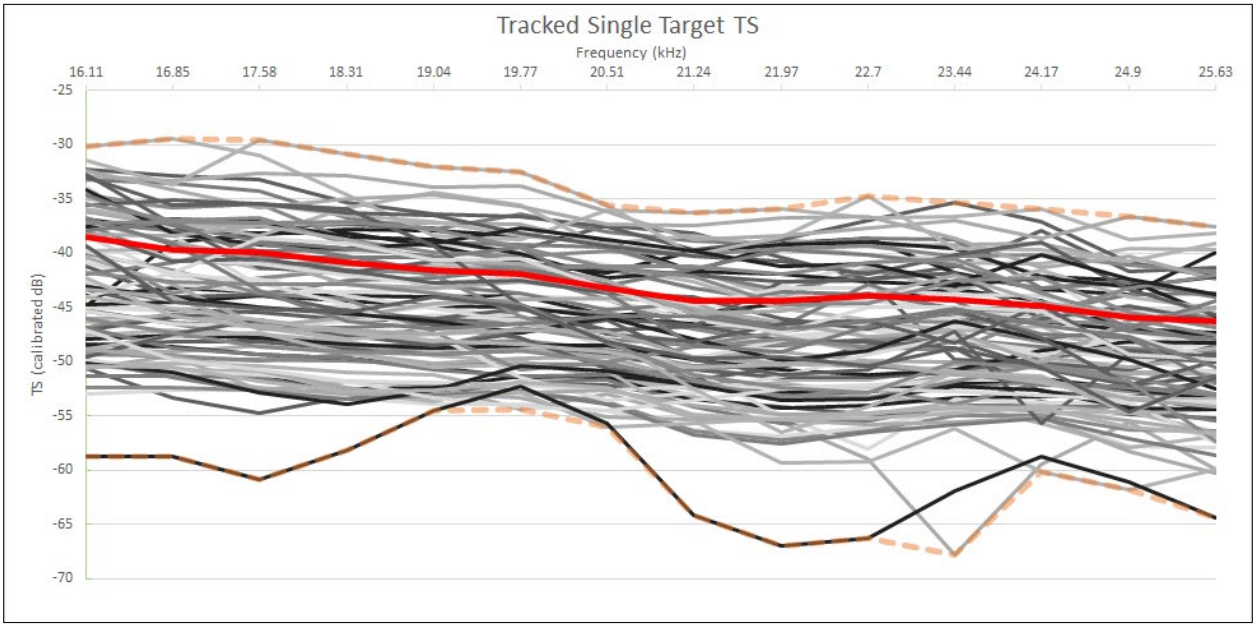

Figure 319: Frequency response for tracked single targets, PETERMANN2015-D20150824-T000615.raw. The solid red line is the average target strength across the frequency range and the orange dashed lines are the minimum and maximum target strengths across the frequency range. Colors of other lines are randomly assigned.

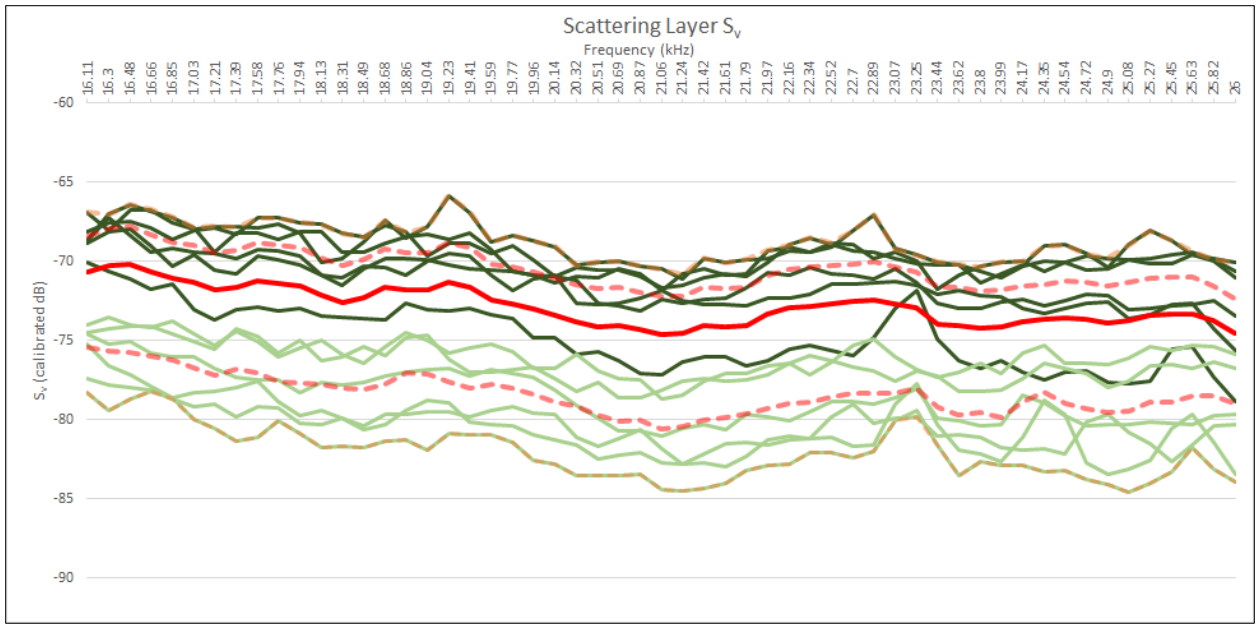

Figure 320: Frequency response for volume selections, PETERMANN2015-D20150824-T000615.raw. The solid red line is the average volume scattering across the frequency range and the orange dashed lines are the minimum and maximum volume scattering across the frequency.

PETERMANN2015-D20150824-T021509.raw

Line PETERMANN2015-D20150824-T021509.raw (Figure 321) was located near CTD 038 (Figure 290). Based on the PDF (Figure 322), a lower threshold of -44 dB was applied during single target detection. The combined single target and target tracking algorithms resulted in 324 targets with a complete frequency response between 16.11 and 25.63 kHz (Figure 323 - Figure 324). Twenty-one selections were made for S_v analysis, ten from dense areas and eleven from less dense areas (Figure 325). TS, S_v, and the calculated average density ($\hat{\rho}$) and the ensonified volume (V) are summarized for all reviewed lines in Table 7.

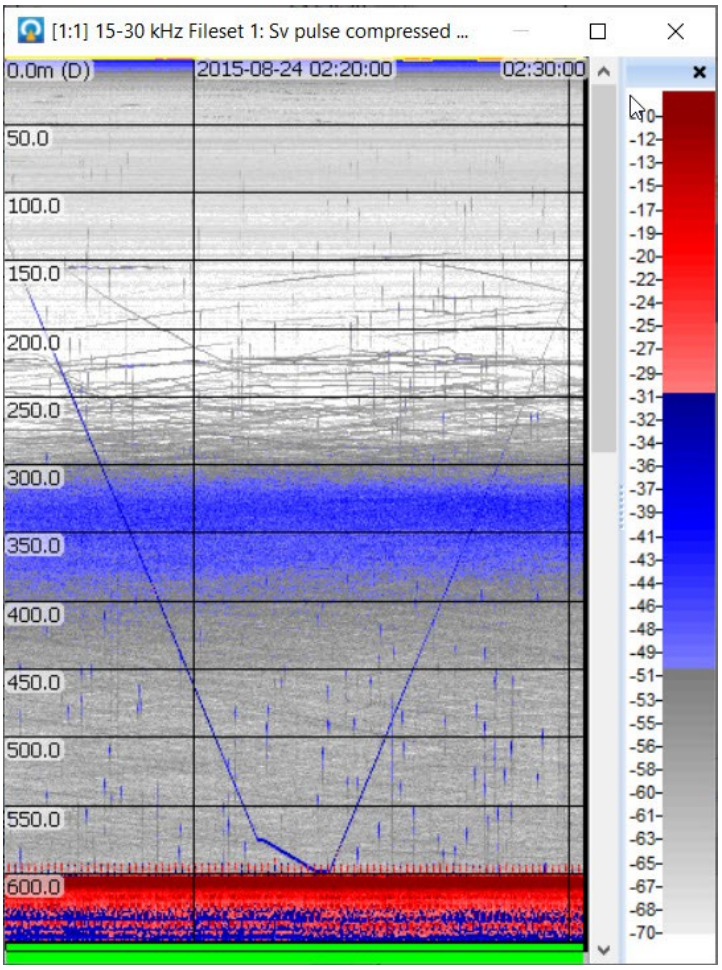

Figure 321: PETERMANN2015-D20150824-T021509.raw shown in Echoview.

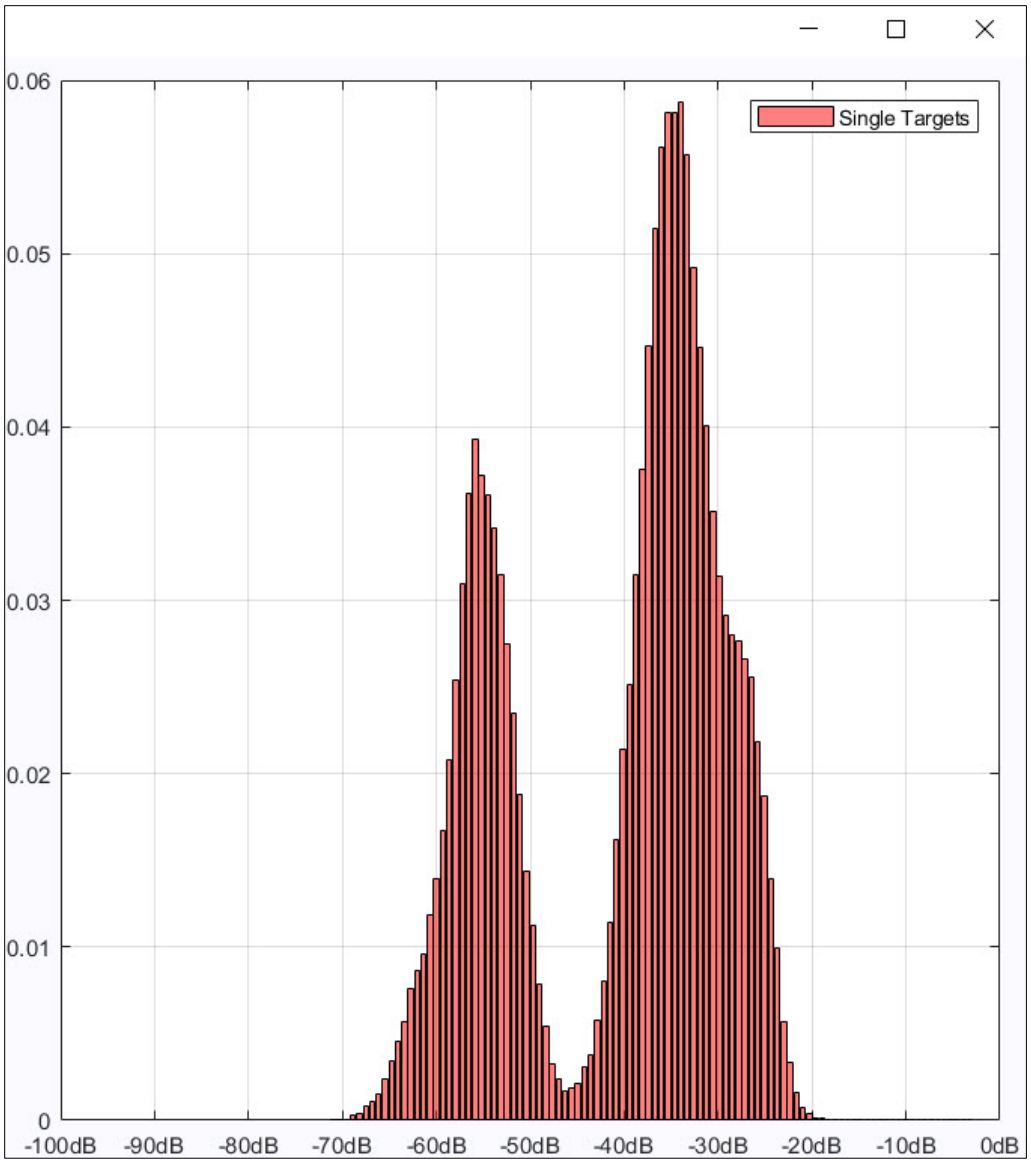

Figure 322: PDF for line PETERMANN2015-D20150824-T021509.raw. A lower threshold of -44 dB was used for single target detection.

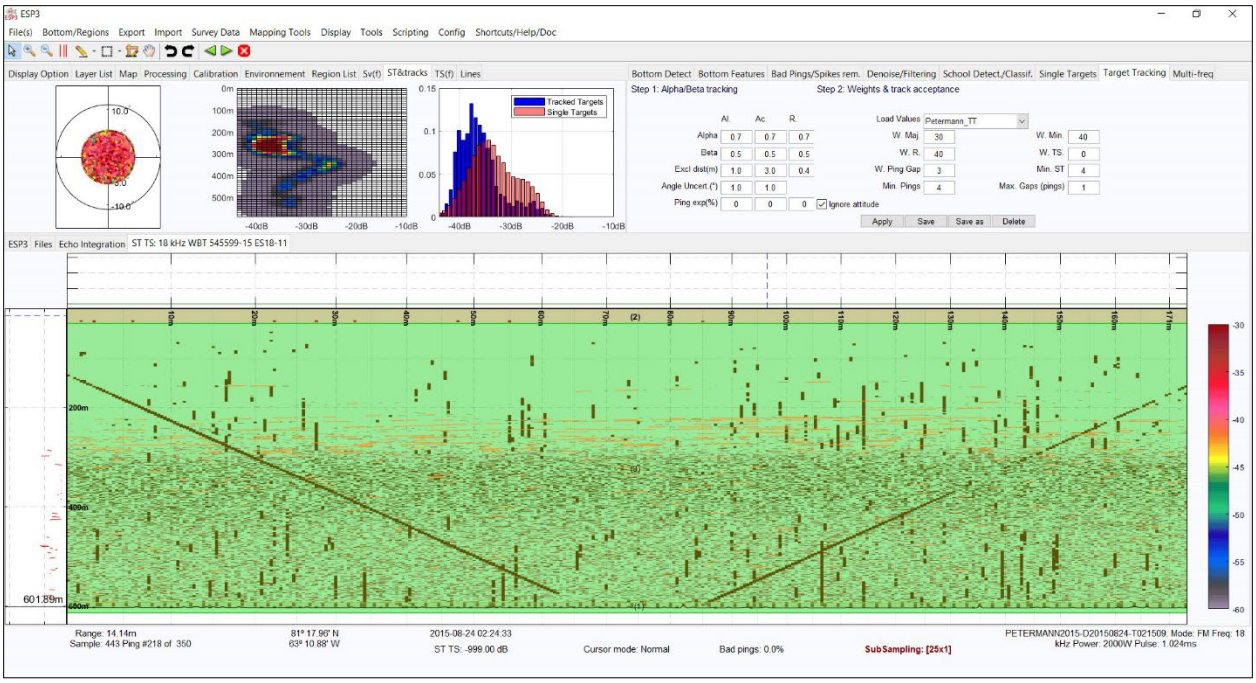

Figure 323: PETERMANN2015-D20150824-T021509.raw selected single targets.

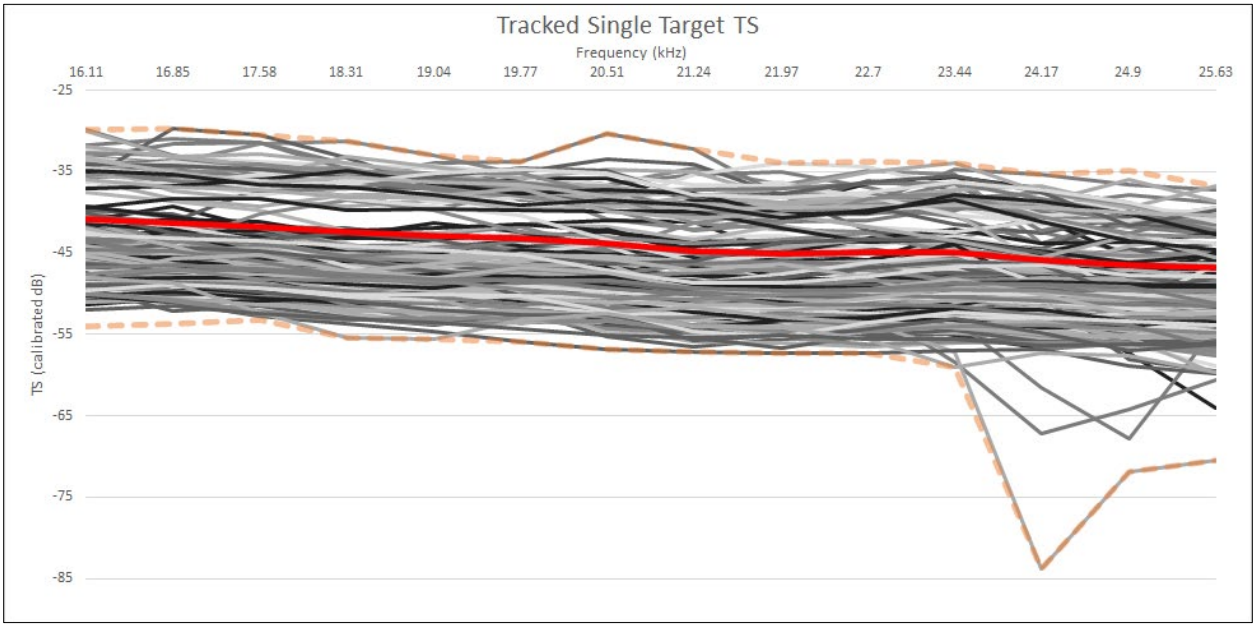

Figure 324: Frequency response for tracked single targets, PETERMANN2015-D20150824-T021509.raw. The solid red line is the average target strength across the frequency range and the orange dashed lines are the minimum and maximum target strengths across the frequency range. Colors of other lines are randomly assigned.

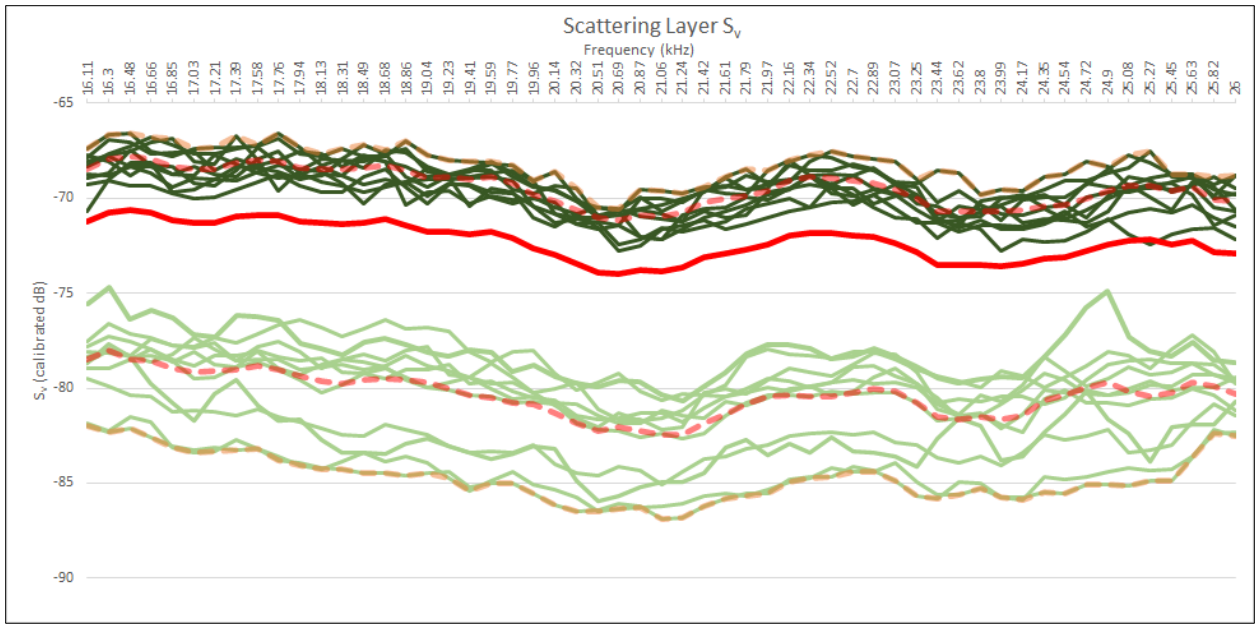

Figure 325: Frequency response for volume selections, PETERMANN2015-D20150824-T021509.raw. The solid red line is the average volume scattering across the frequency range and the orange dashed lines are the minimum and maximum volume scattering across the frequency.

PETERMANN2015-D20150824-T162333.raw

Line PETERMANN2015-D20150824-T162333.raw (Figure 326) was located near CTD 040 (Figure 290). Based on the PDF (Figure 327), a lower threshold of -42 dB was applied during single target detection. The combined single target and target tracking algorithms resulted in 118 targets with a complete frequency response between 16.11 and 25.63 kHz (Figure 328 - Figure 329). Fourteen selections were made for S_v analysis, six from dense areas and eight from less dense areas (Figure 330). TS, S_v, and the calculated average density ($\hat{\rho}$) and the ensonified volume (V) are summarized for all reviewed lines in Table 7.

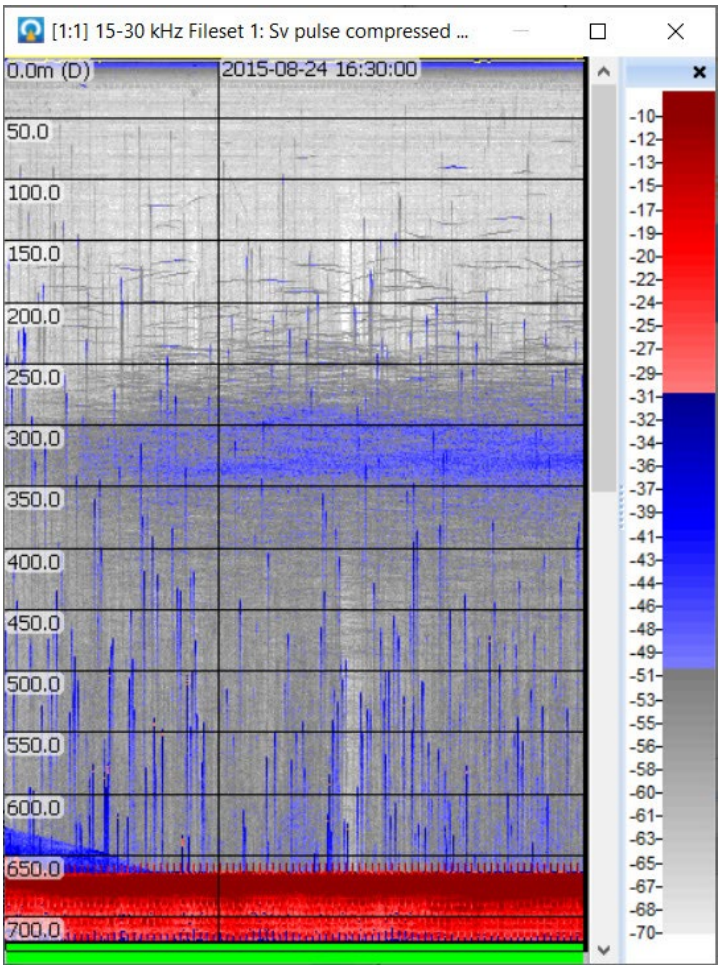

Figure 326: PETERMANN2015-D20150824-T162333.raw shown in Echoview.

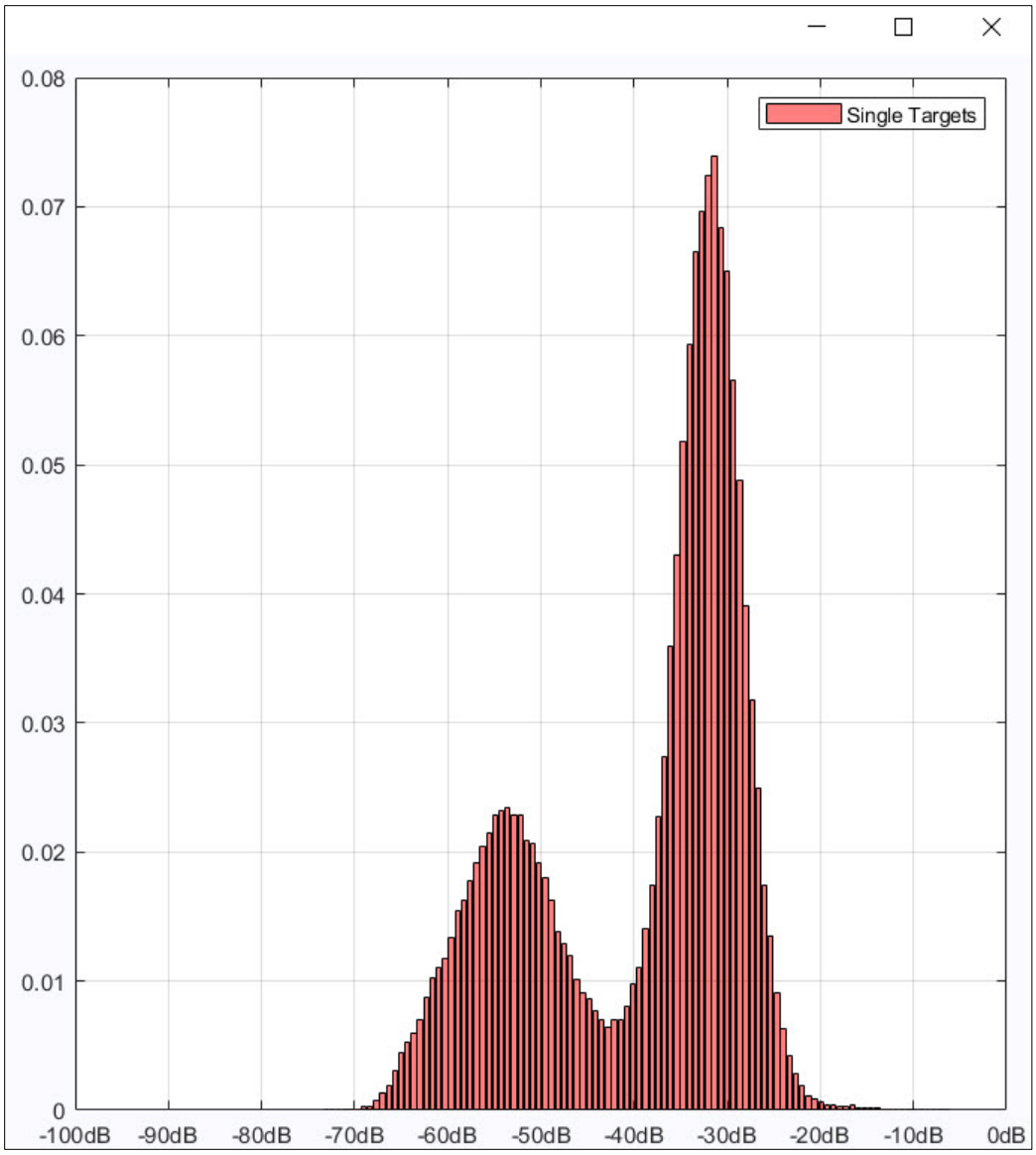

Figure 327: PDF for line PETERMANN2015-D20150824-T162333.raw. A lower threshold of -42 dB was used for single target detection.

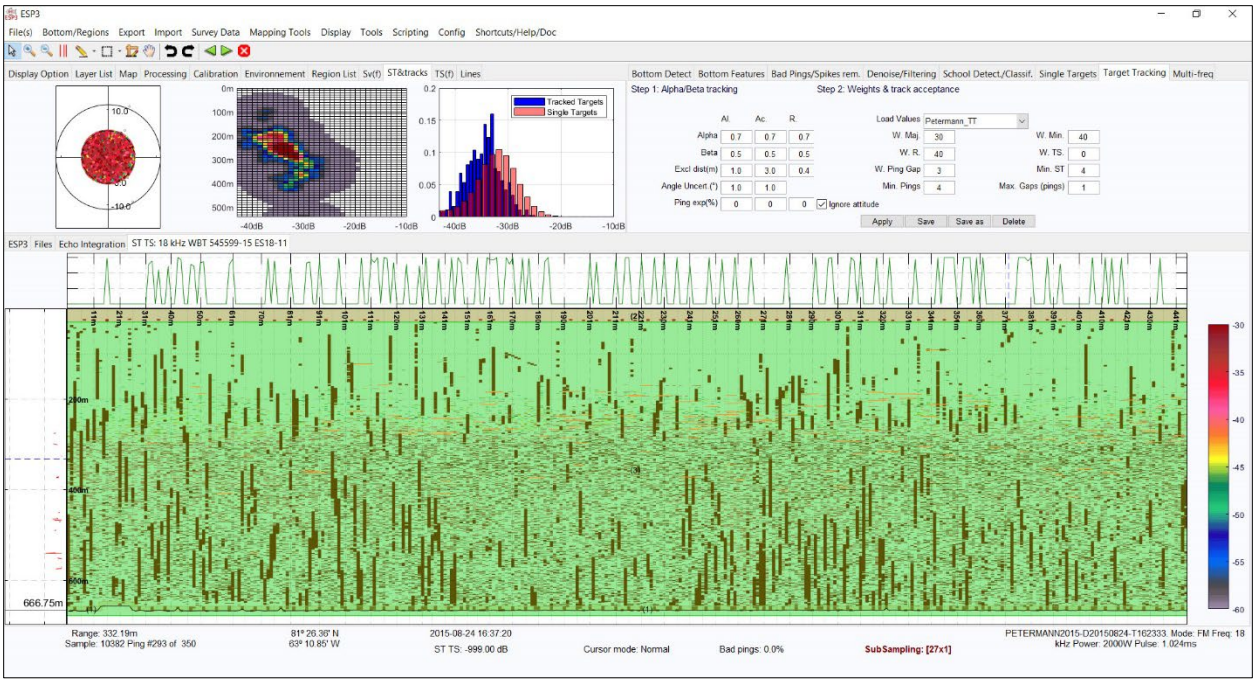

Figure 328: PETERMANN2015-D20150824-T162333.raw selected single targets.

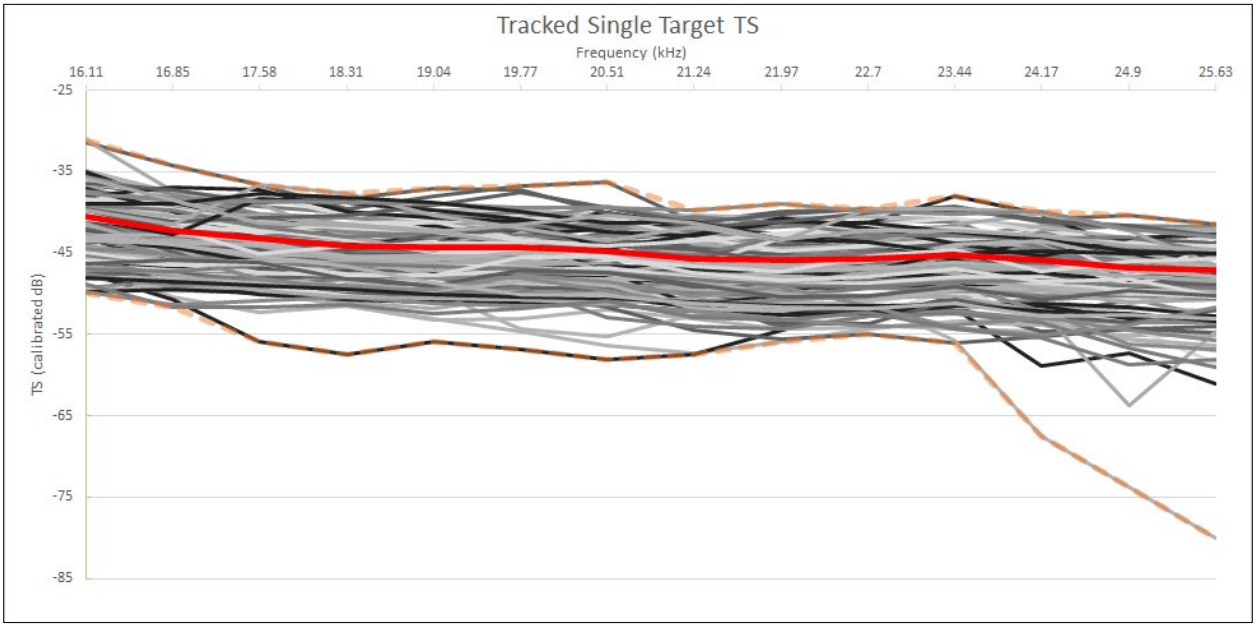

Figure 329: Frequency response for tracked single targets, PETERMANN2015-D20150824-T162333.raw. The solid red line is the average target strength across the frequency range and the orange dashed lines are the minimum and maximum target strengths across the frequency range. Colors of other lines are randomly assigned.

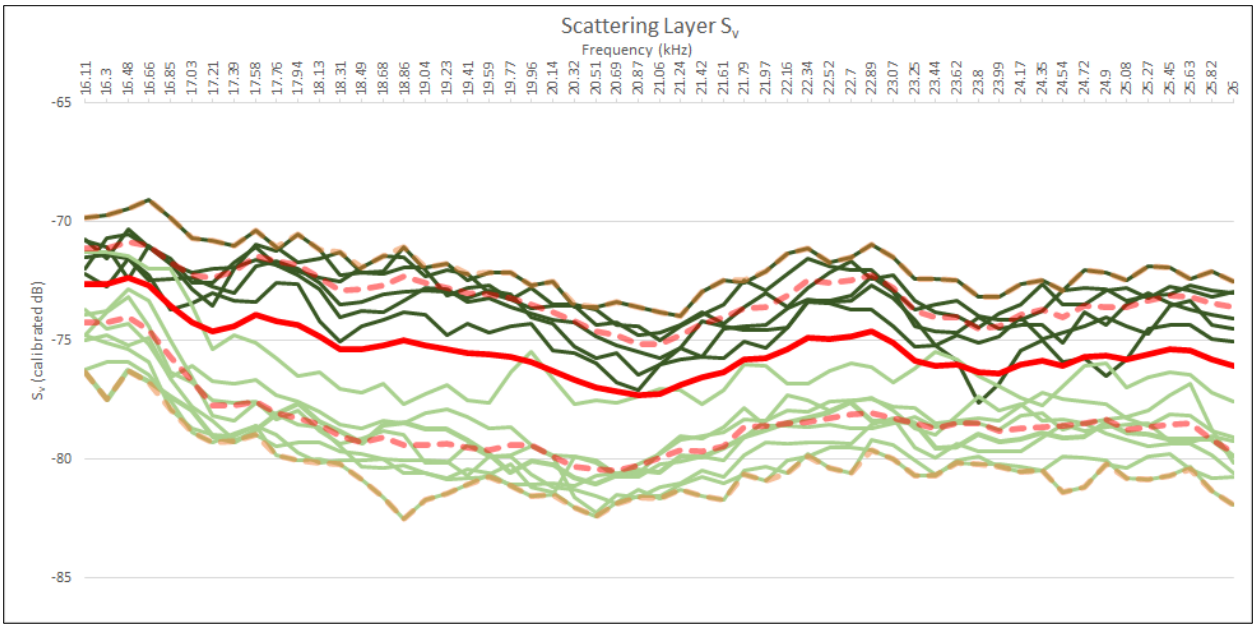

Figure 330: Frequency response for volume selections, PETERMANN2015-D20150824-T162333.raw. The solid red line is the average volume scattering across the frequency range and the orange dashed lines are the minimum and maximum volume scattering across the frequency.

E.3 Heterogeneous Preference Scattering Layers

Scattering layers with a “heterogeneous preference” were observed at 12 CTD stations, 003 – 014. All of those stations were found in Petermann Fjord, where high levels of meltwater from Petermann Glacier are present and contribute to the outflow from the fjord (Johnson et al., 2011; Heuzé et al., 2017). Here, five lines corresponding to five stations in that glacier outflow area are examined (Figure 331).

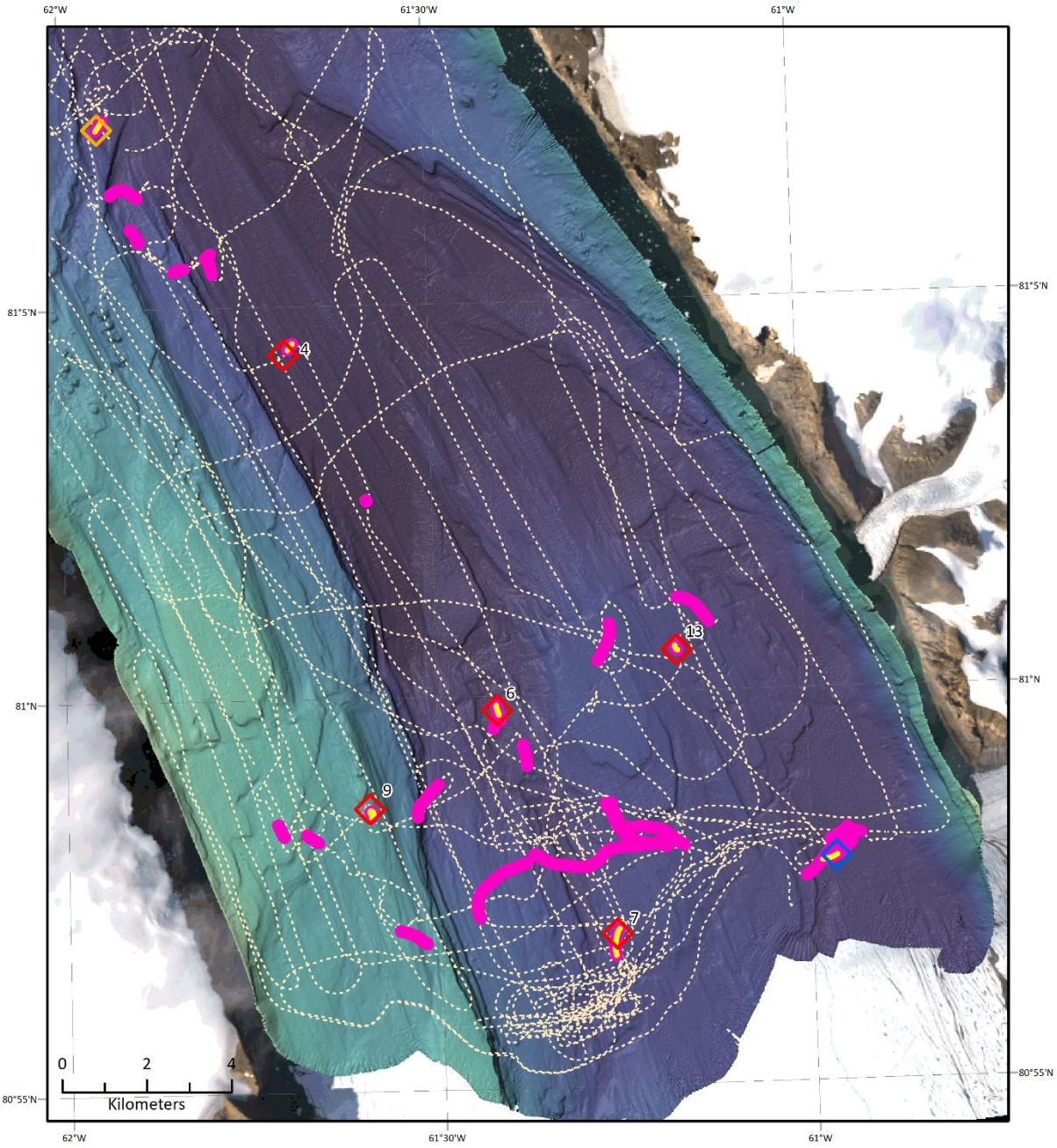

Figure 331: Location of reviewed heterogenous preference scattering layers and associated CTD stations. The red diamonds are CTD stations associated with heterogenous preference scattering layers and are labeled with the CTD station number. All lines where the ship was moving at < 1.5 knots are shown in magenta; the reviewed lines are shown in yellow.

PETERMANN2015-D20150807-T065201.raw

Line PETERMANN2015-D20150807-T065201.raw (Figure 332) was located near CTD 004 (Figure 290). Based on the PDF (Figure 333), a lower threshold of -48 dB was

applied during single target detection. The region analyzed for single targets was restricted to the water column between 30 and 400 m due high levels of noise as depth increased. There was interference present in the selected region of the water column, though at least part of it was removed by the spike filter (Figure 334). The combined single target and target tracking algorithms resulted in 179 targets with a complete frequency response between 16.11 and 25.63 kHz (Figure 334 - Figure 335). Sixteen selections were made for S_v analysis, ten from dense areas and six from less dense areas (Figure 336). TS, S_v, and the calculated average density ($\hat{\rho}$) and the ensonified volume (V) are summarized for all reviewed lines in Table 7.

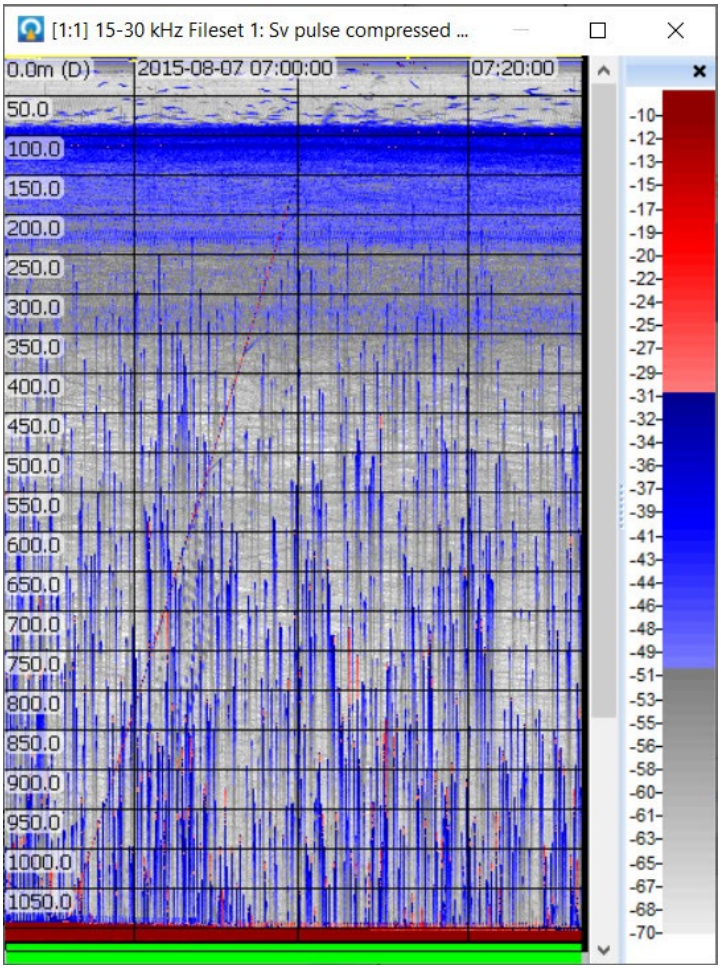

Figure 332: PETERMANN2015-D20150807-T065201.raw shown in Echoview.

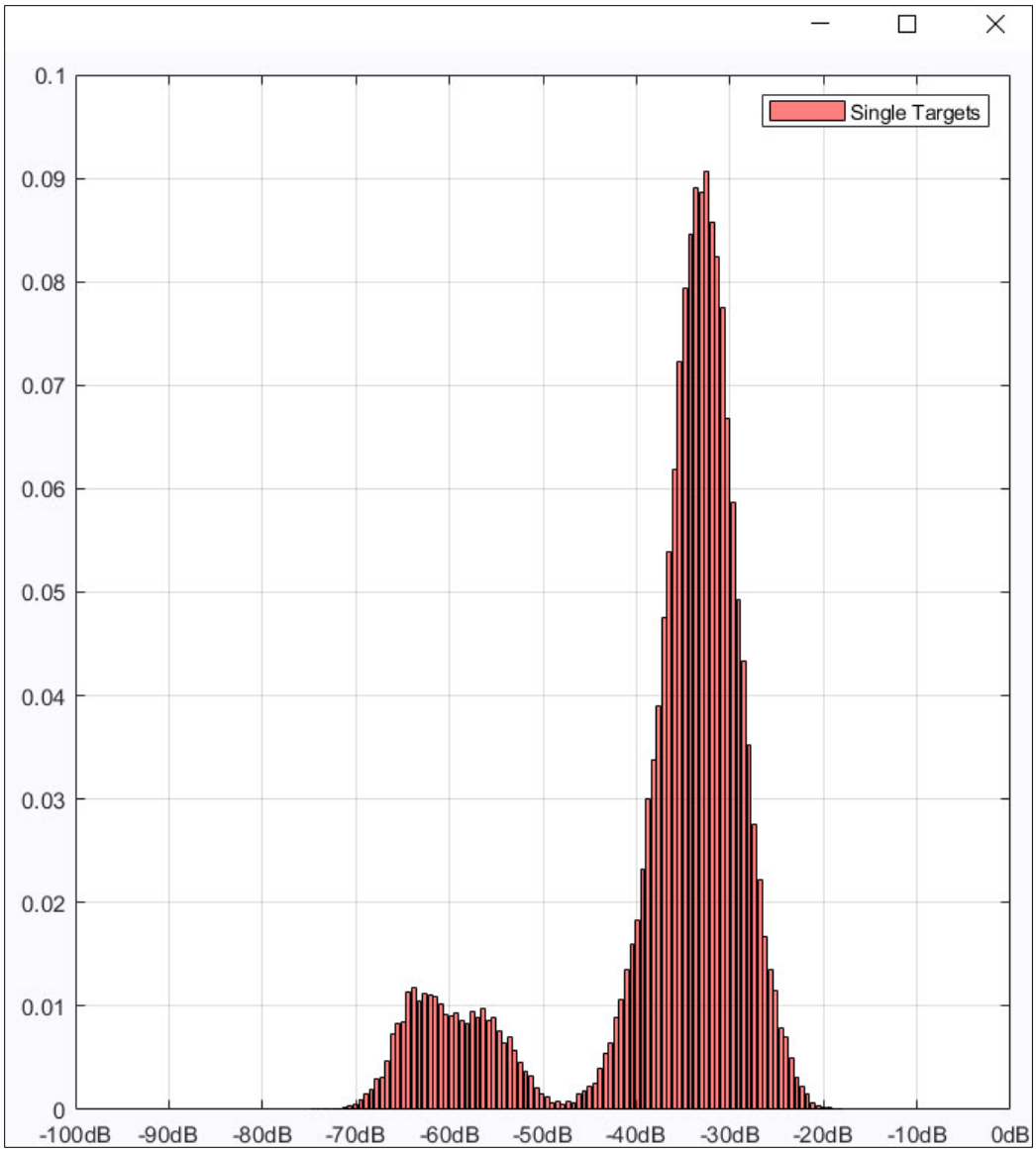

Figure 333: PDF for line PETERMANN2015-D20150807-T065201.raw. A lower threshold of -48 dB was used for single target detection.

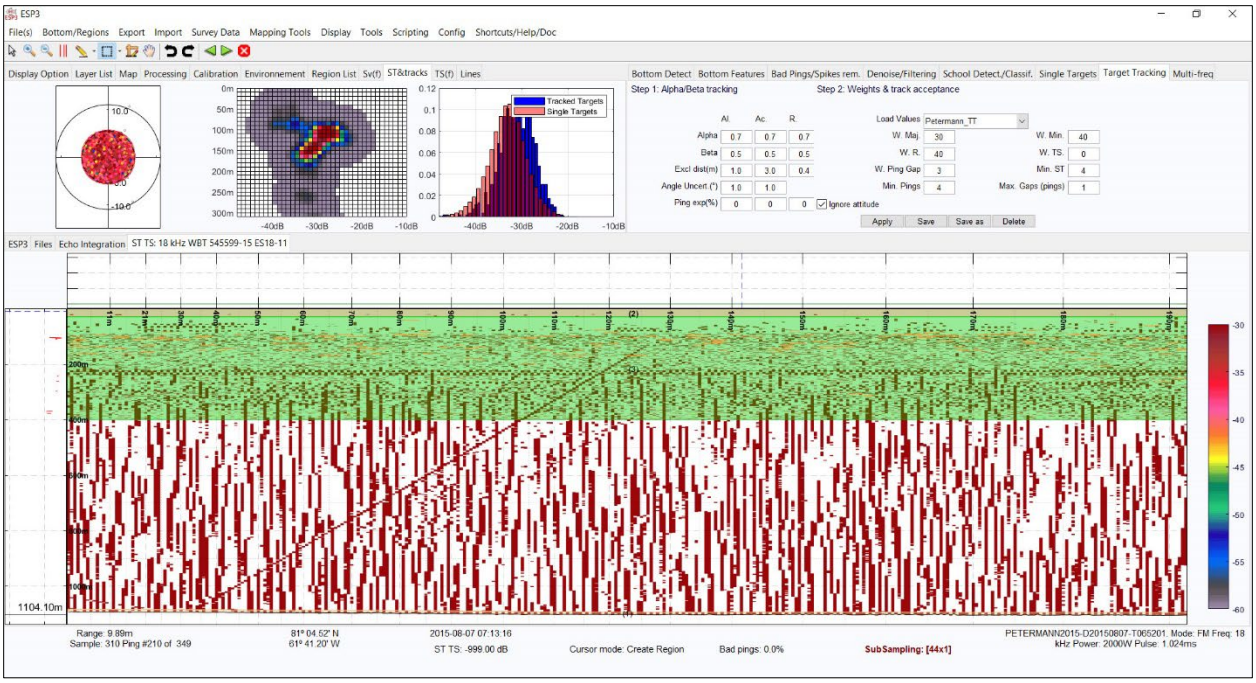

Figure 334: PETERMANN2015-D20150807-T065201.raw selected single targets. Note the strong band of interference just below 200 m that was partially removed by the spike filter.

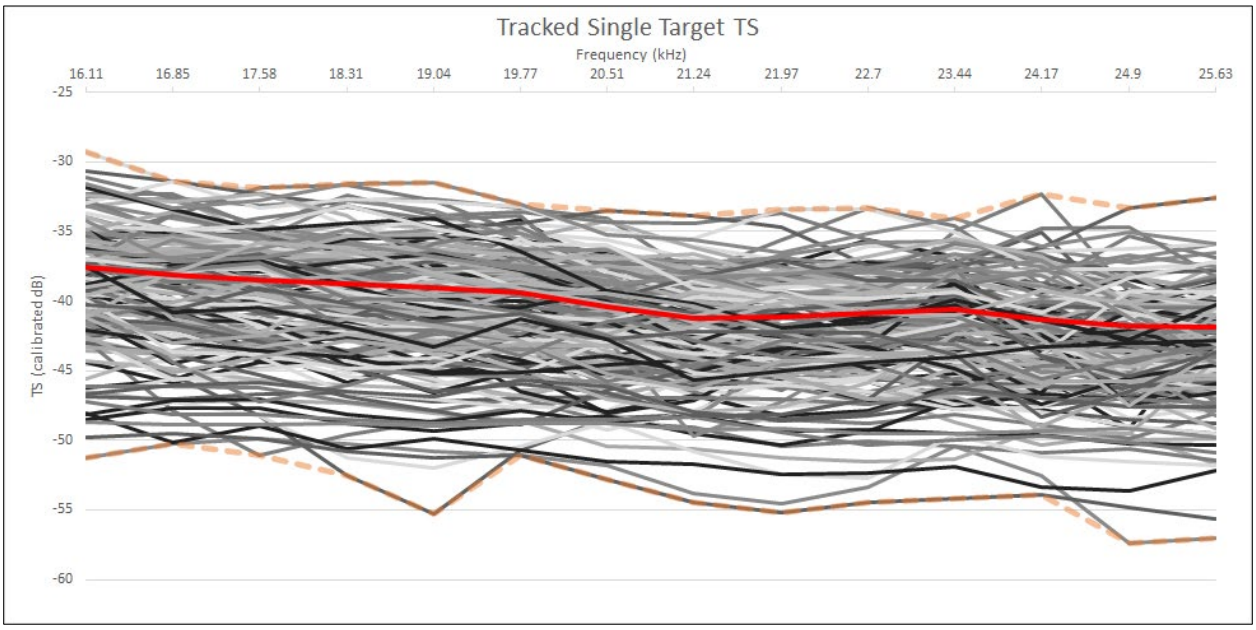

Figure 335: Frequency response for tracked single targets, PETERMANN2015-D20150807-T065201.raw. The solid red line is the average target strength across the frequency range and the orange dashed lines are the minimum and maximum target strengths across the frequency range. Colors of other lines are randomly assigned.

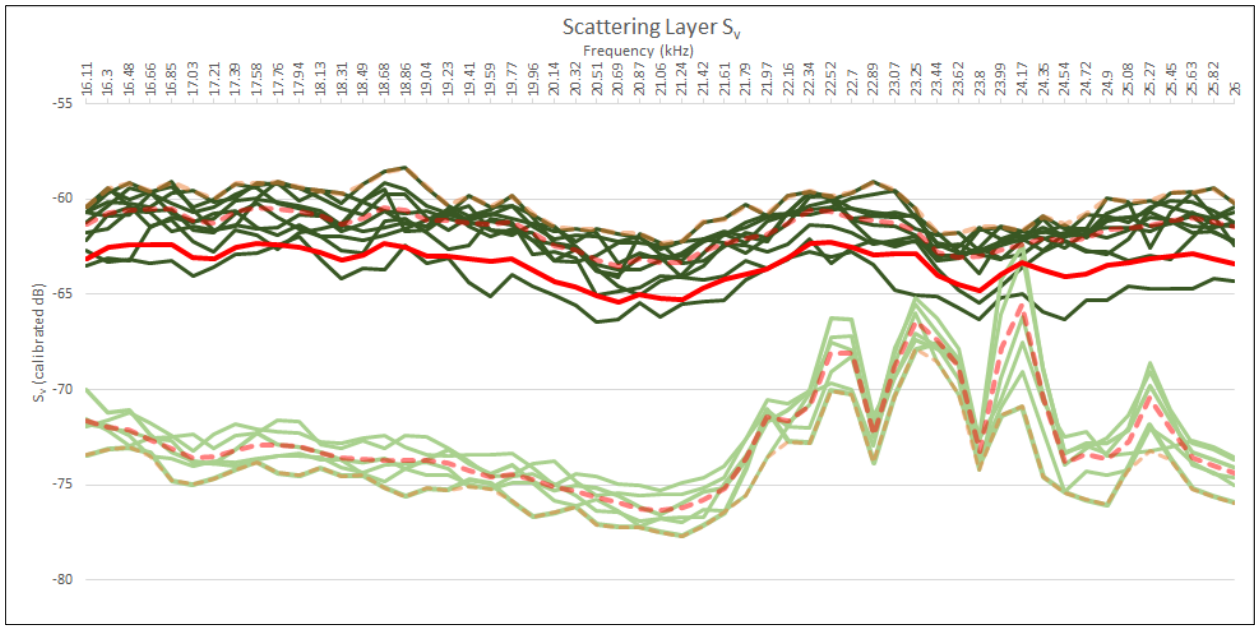

Figure 336: Frequency response for volume selections, PETERMANN2015-D20150807-T065201.raw. The solid red line is the average volume scattering across the frequency range and the orange dashed lines are the minimum and maximum volume scattering across the frequency. The less dense scattering layers have consistent frequency spikes above 21 kHz which may be related to the interference visible in the echogram (Figure 332).

PETERMANN2015-D20150807-T093944.raw

Line PETERMANN2015-D20150807-T093944.raw (Figure 337) was located near CTD 006 (Figure 331). Based on the PDF (Figure 338), a lower threshold of -52 dB was applied during single target detection. The region analyzed for single targets was restricted to the water column between 30 and 400 m due high levels of noise as depth increased. The combined single target and target tracking algorithms resulted in 687 targets with a complete frequency response between 16.11 and 25.63 kHz (Figure 339 - Figure 340). Fifteen selections were made for S_v analysis, eight from dense areas and seven from less dense areas (Figure 341). TS, S_v, and the calculated average density ($\hat{\rho}$) and the ensonified volume (V) are summarized for all reviewed lines in Table 7.

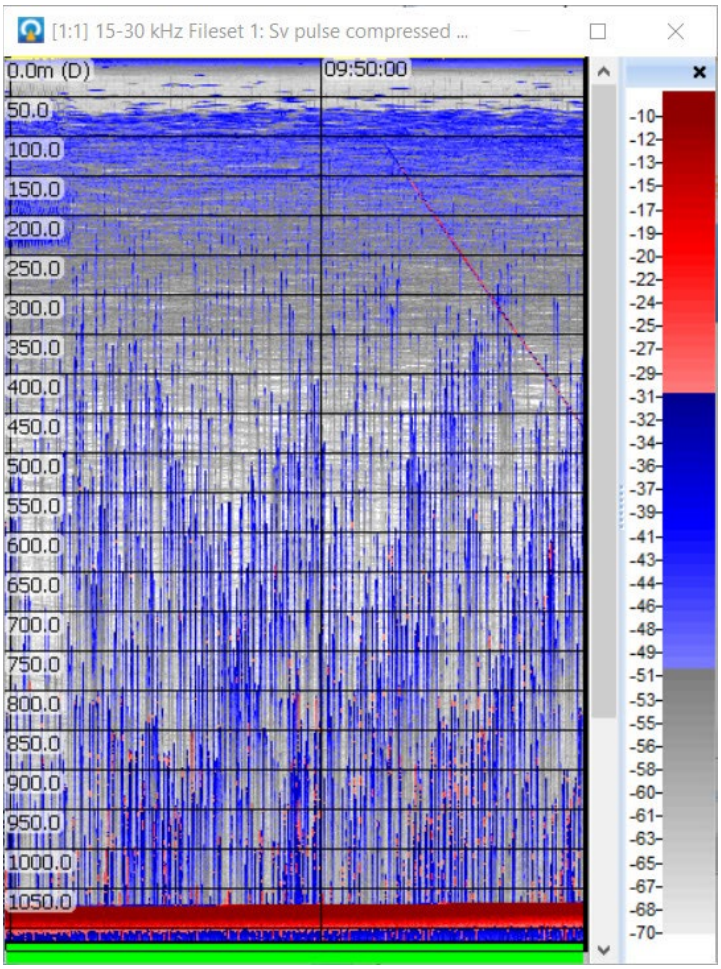

Figure 337: PETERMANN2015-D20150807-T093944.raw shown in Echoview.

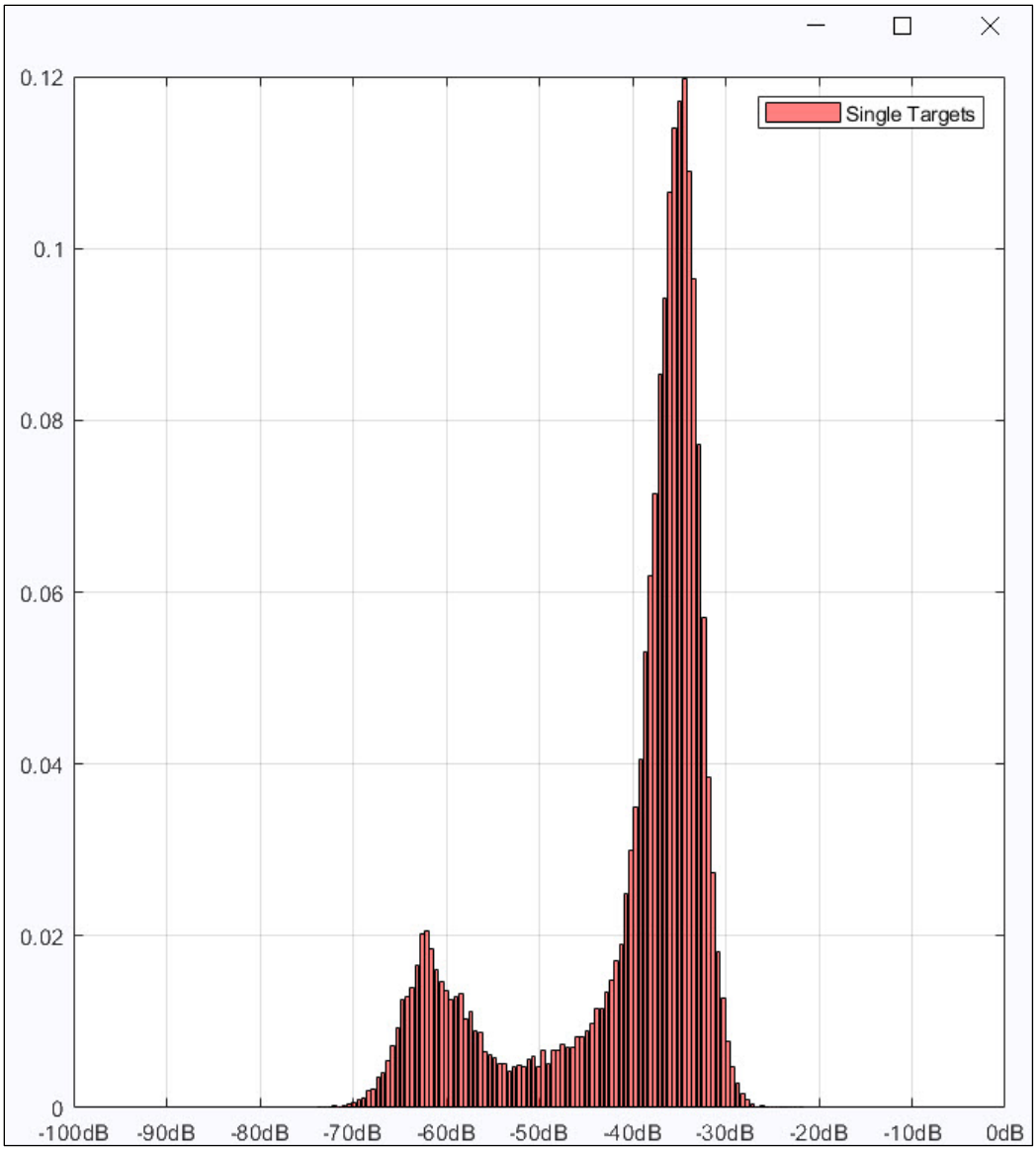

Figure 338: PDF for line PETERMANN2015-D20150807-T093944.raw. A lower threshold of -52 dB was used for single target detection.

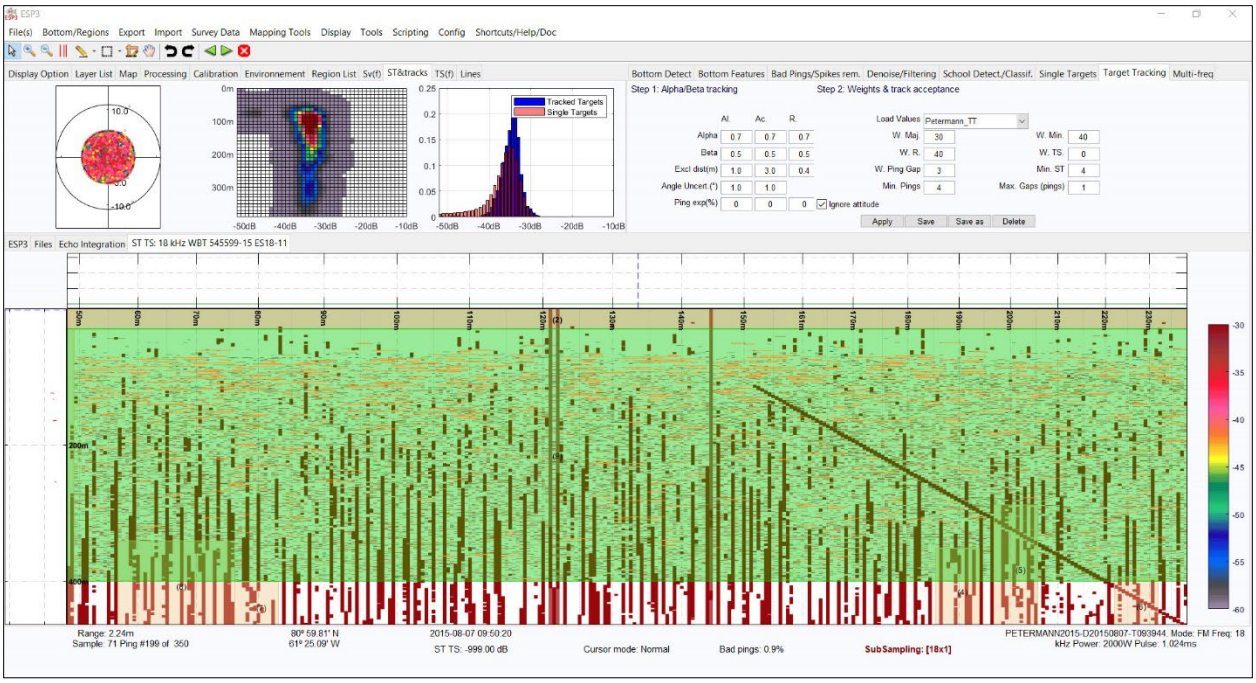

Figure 339: PETERMANN2015-D20150807-T093944.raw selected single targets.

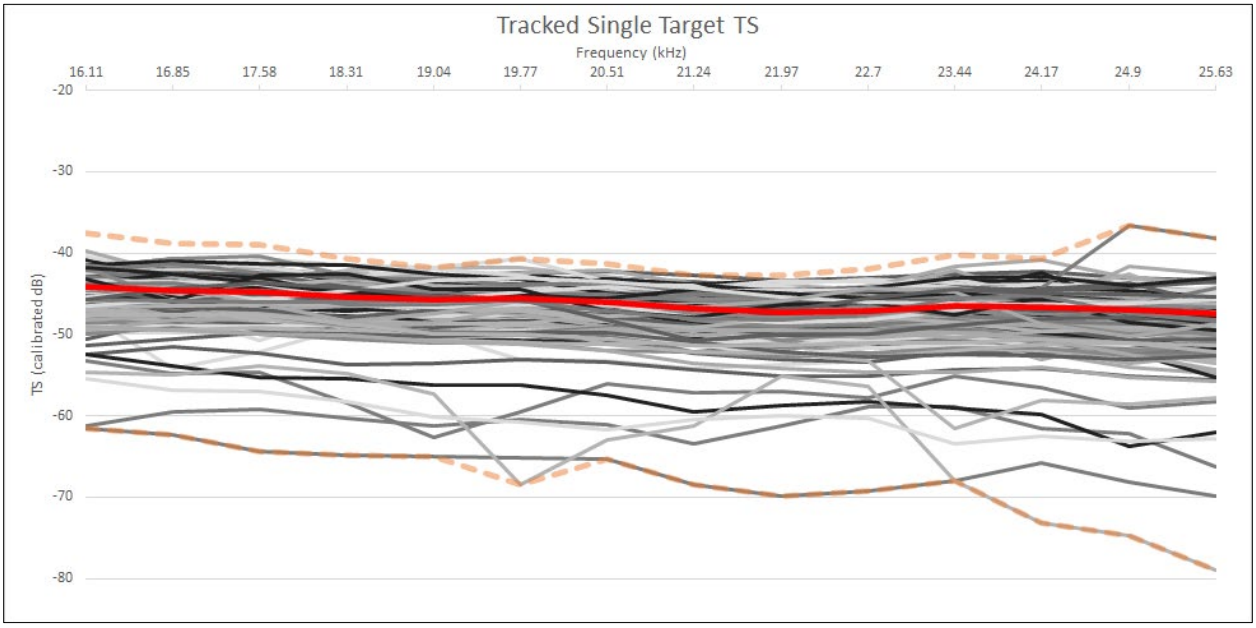

Figure 340: Frequency response for tracked single targets, PETERMANN2015-D20150807-T093944.raw. The solid red line is the average target strength across the frequency range and the orange dashed lines are the minimum and maximum target strengths across the frequency range. Colors of other lines are randomly assigned.

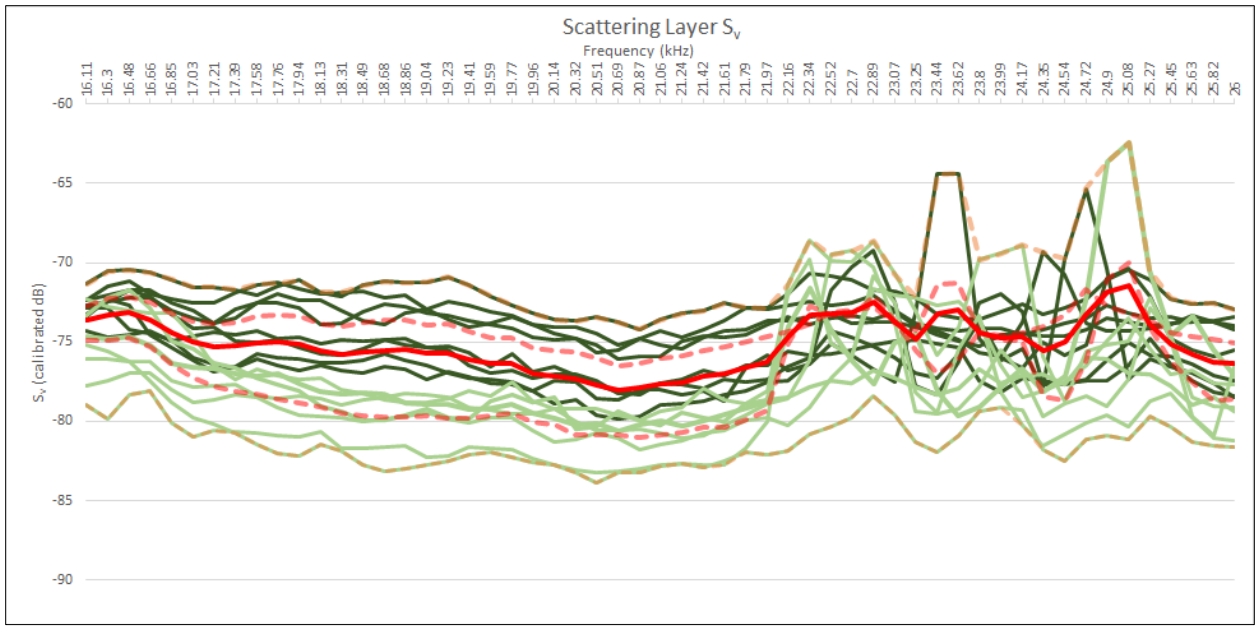

Figure 341: Frequency response for volume selections, PETERMANN2015-D20150807-T093944.raw. The solid red line is the average volume scattering across the frequency range and the orange dashed lines are the minimum and maximum volume scattering across the frequency.

PETERMANN2015-D20150807-T113408.raw

Line PETERMANN2015-D20150807-T113408.raw (Figure 342) was located near CTD 007 (Figure 331). Based on the PDF (Figure 343, a lower threshold of -49 dB was applied during single target detection. The region analyzed for single targets was restricted to the water column between 30 and 400 m due heavy noise as depth increased. The combined single target and target tracking algorithms resulted in 353 targets with a complete frequency response between 16.11 and 25.63 kHz (Figure 344-Figure 345). Sixteen selections were made for S_v analysis, eight from dense areas and eight from less dense areas (Figure 346). TS, S_v, and the calculated average density ($\hat{\rho}$) and the ensonified volume (V) are summarized for all reviewed lines in Table 7.

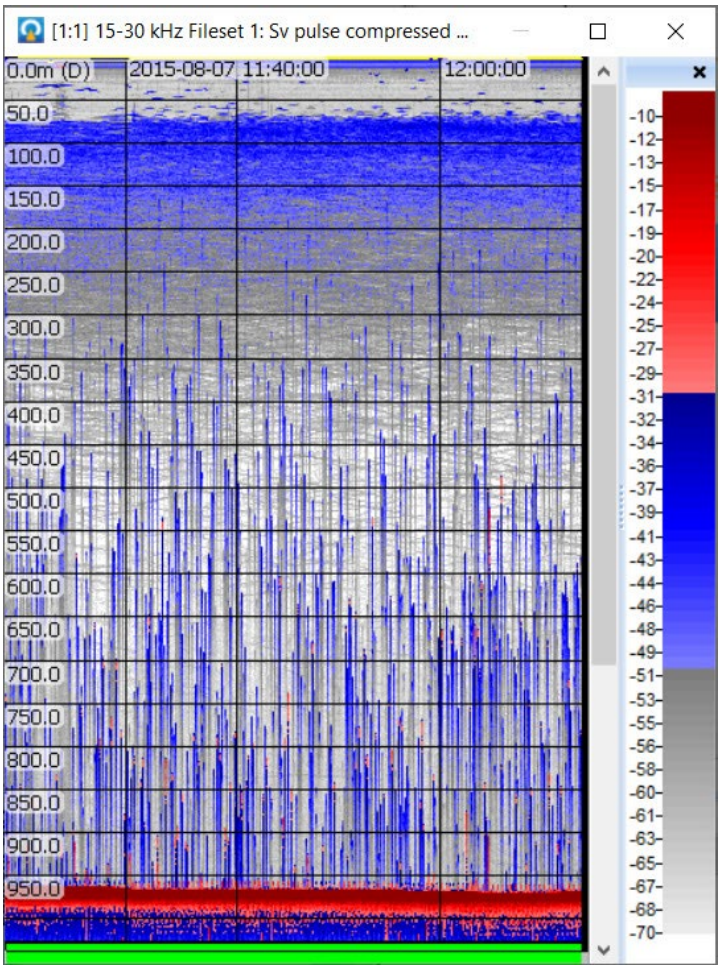

Figure 342: PETERMANN2015-D20150807-T0113408.raw shown in Echoview.

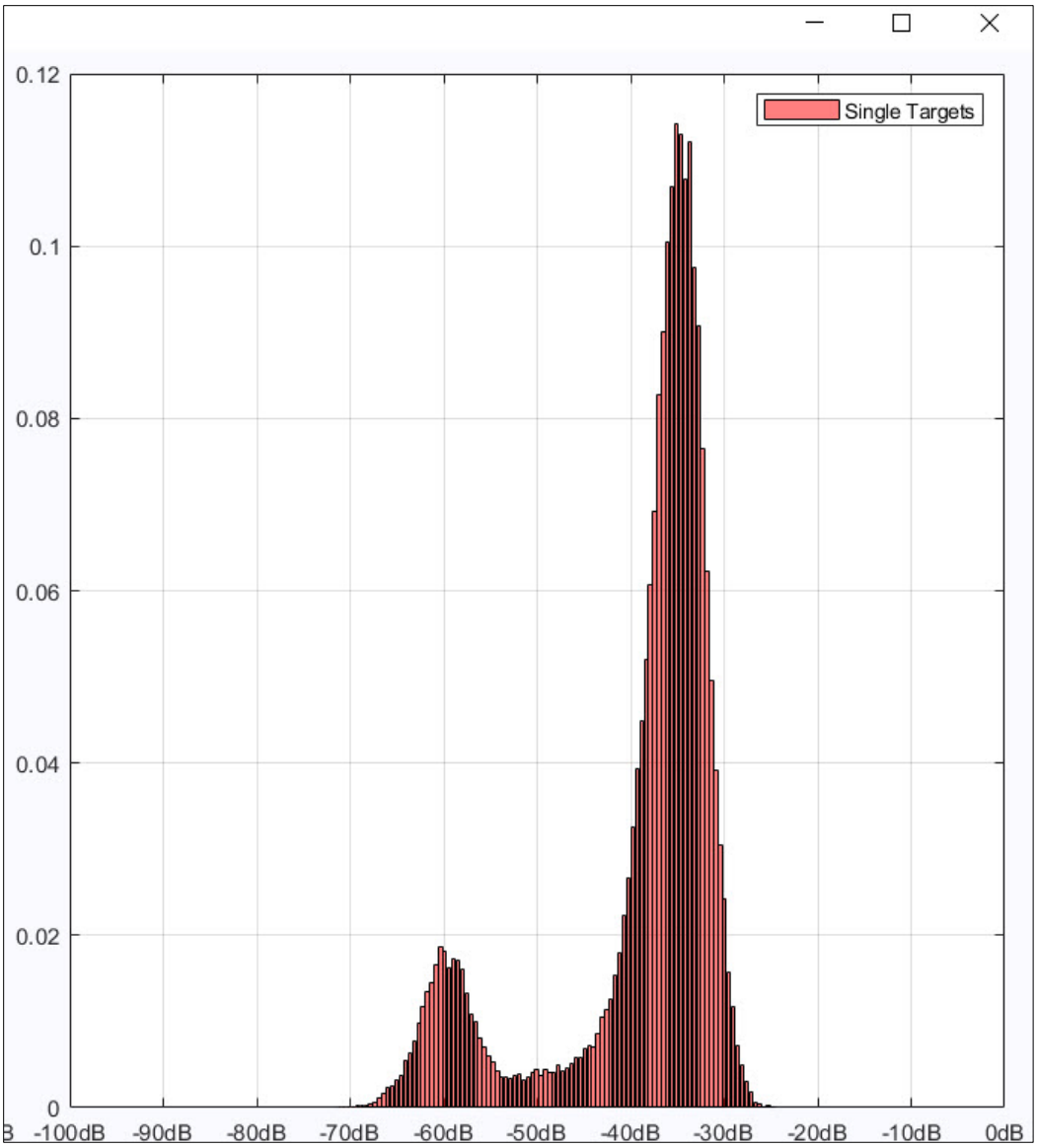

Figure 343: PDF for line PETERMANN2015-D20150807-T113408.raw. A lower threshold of -49 dB was used for single target detection.

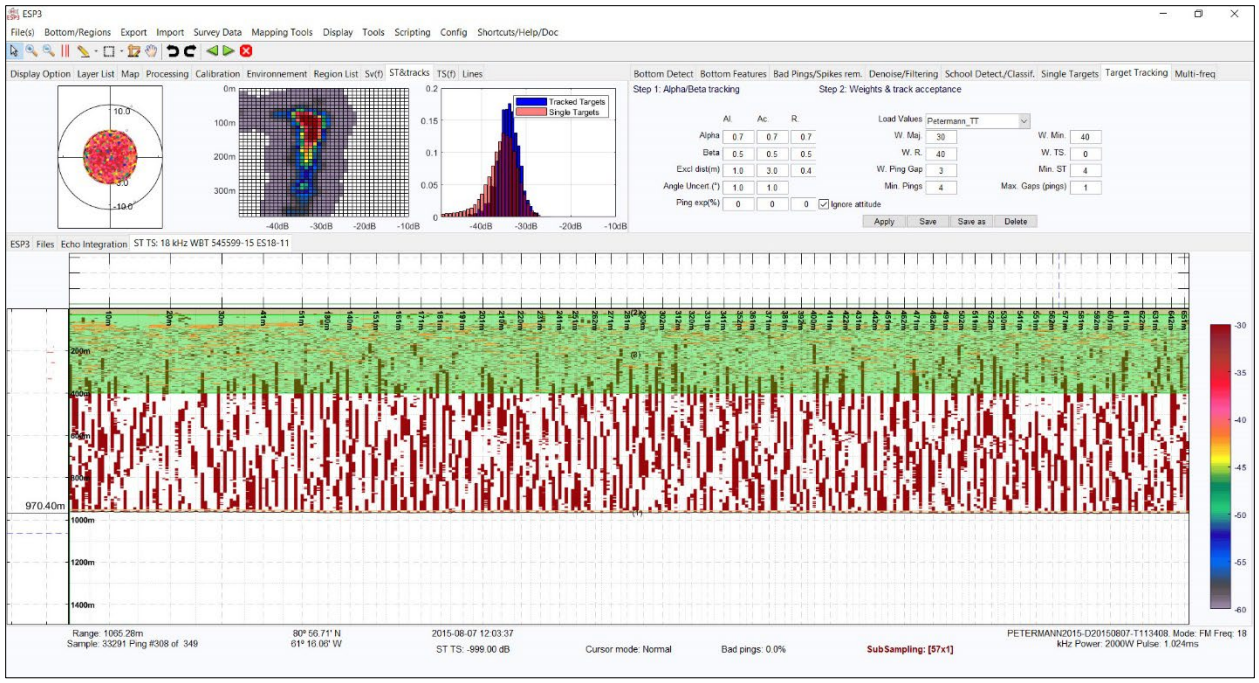

Figure 344: PETERMANN2015-D20150807-T113408.raw selected single targets.

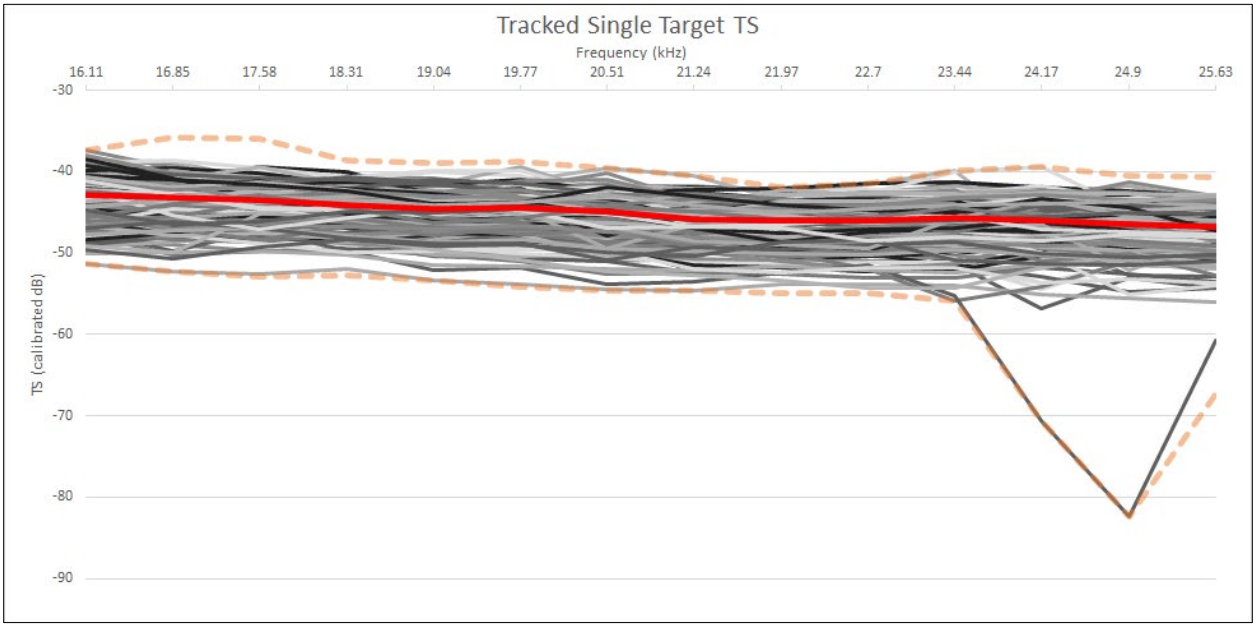

Figure 345: Frequency response for tracked single targets, PETERMANN2015-D20150807-T113408.raw. The solid red line is the average target strength across the frequency range and the orange dashed lines are the minimum and maximum target strengths across the frequency range. Colors of other lines are randomly assigned.

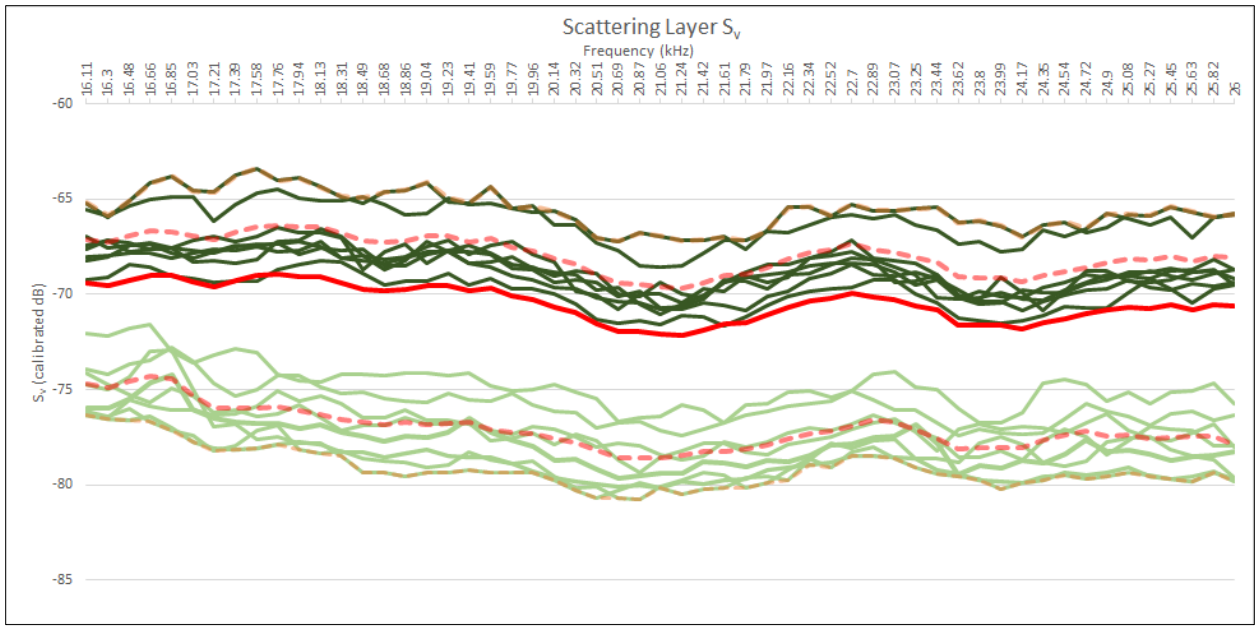

Figure 346: Frequency response for volume selections, PETERMANN2015-D20150807-T113408.raw. The solid red line is the average volume scattering across the frequency range and the orange dashed lines are the minimum and maximum volume scattering across the frequency.

PETERMANN2015-D20150807-T232746.raw

Line PETERMANN2015-D20150807-T232746.raw (Figure 347) was located near CTD 009 (Figure 331). Based on the PDF (Figure 348), a lower threshold of -52 dB was applied during single target detection. The entire water column depth range between 30 m and the seafloor was used, but several regions were selectively excluded where there were gaps or anomalously low signal levels related to gaps. The combined single target and target tracking algorithms resulted in 566 targets with a complete frequency response between 16.11 and 25.63 kHz (Figure 349- Figure 350). Fifteen selections were made for S_v analysis, eleven from dense areas and four from less dense areas (Figure 351). TS, S_v, and the calculated average density ($\hat{\rho}$) and the ensonified volume (V) are summarized for all reviewed lines in Table 7.

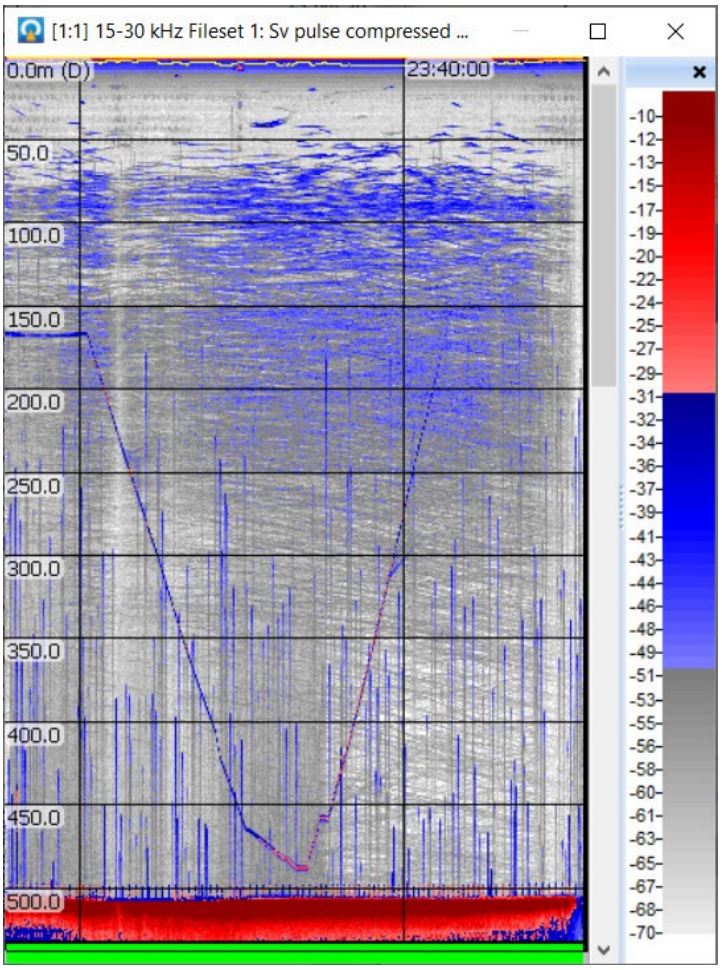

Figure 347: PETERMANN2015-D20150807-T232746.raw shown in Echoview.

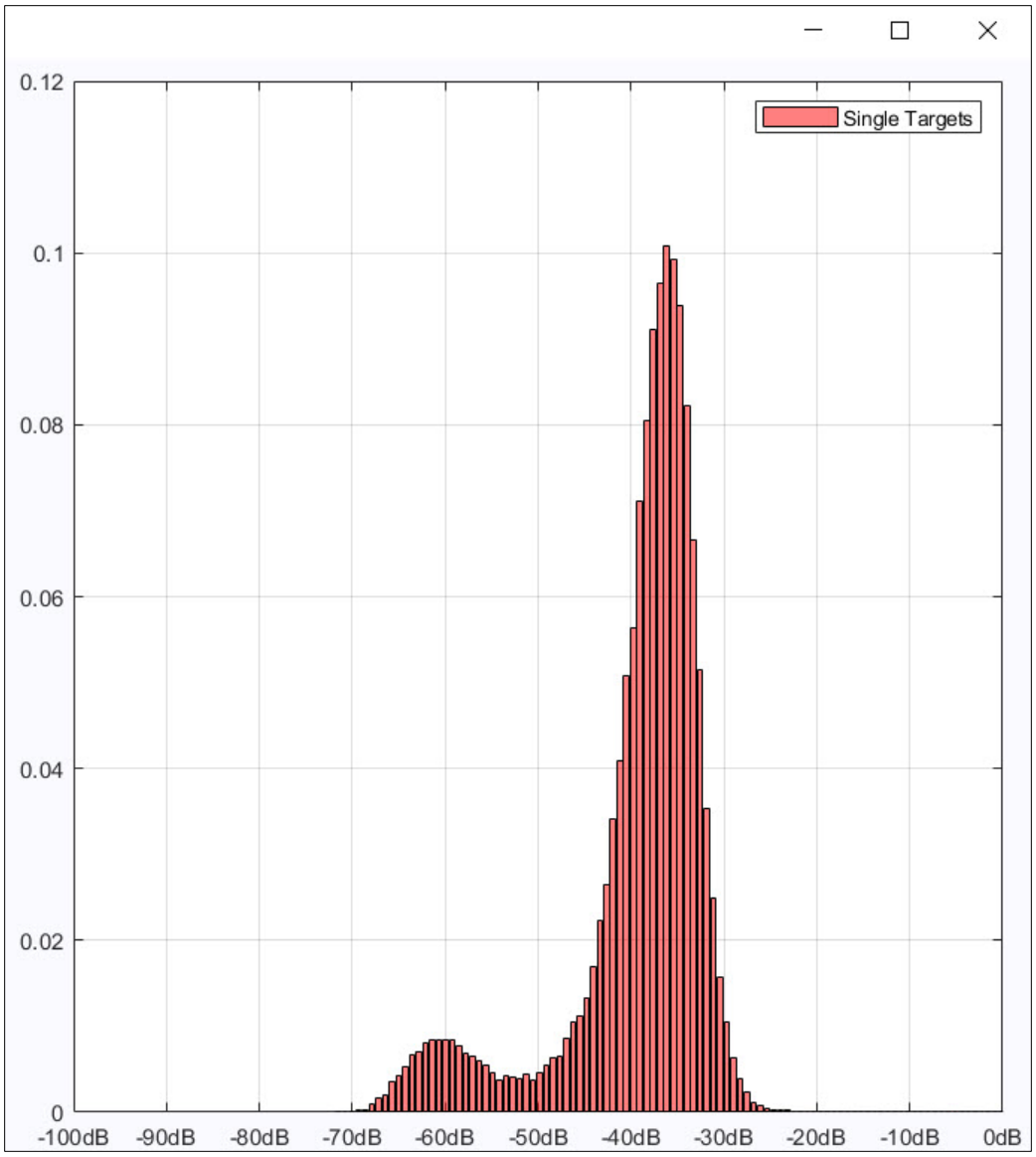

Figure 348: PDF for line PETERMANN2015-D20150807-T232746.raw. A lower threshold of -52 dB was used for single target detection.

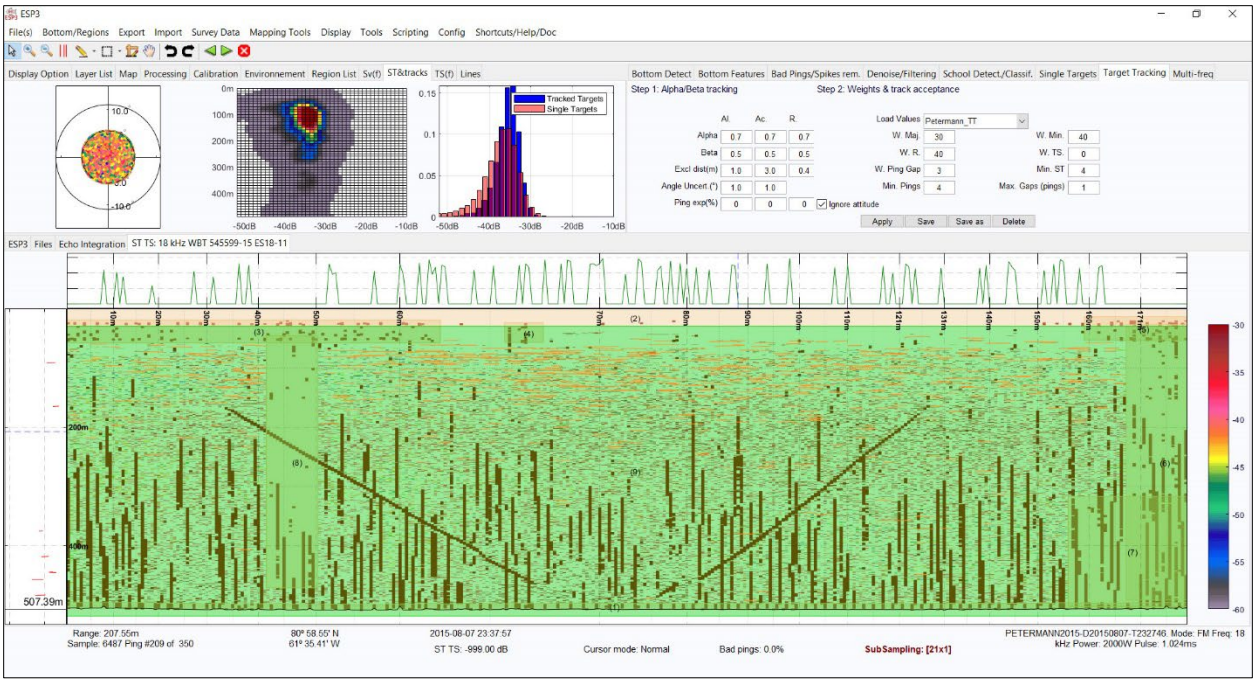

Figure 349: PETERMANN2015-D20150807-T232746.raw selected single targets.

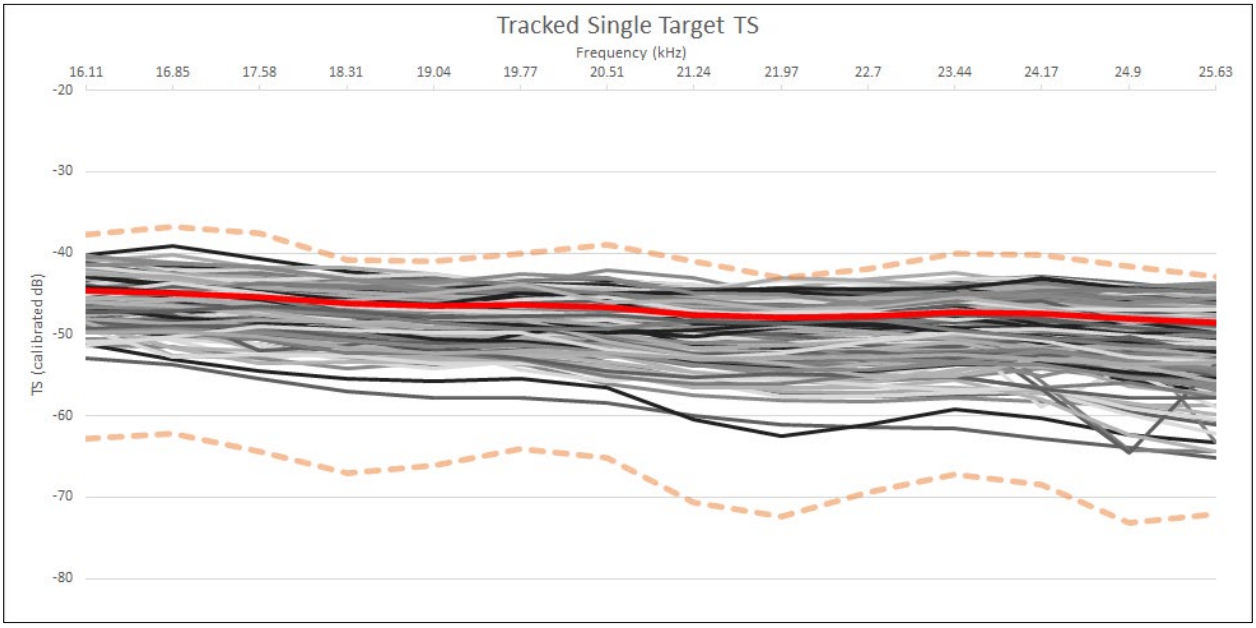

Figure 350: Frequency response for tracked single targets, PETERMANN2015-D20150807-T232746.raw. The solid red line is the average target strength across the frequency range and the orange dashed lines are the minimum and maximum target strengths across the frequency range. Colors of other lines are randomly assigned. This graph was produced from a reduced number of TS curves due to graphing limitations in Excel. The minimum, maximum and averages, however, are based on the full set of TS curves.

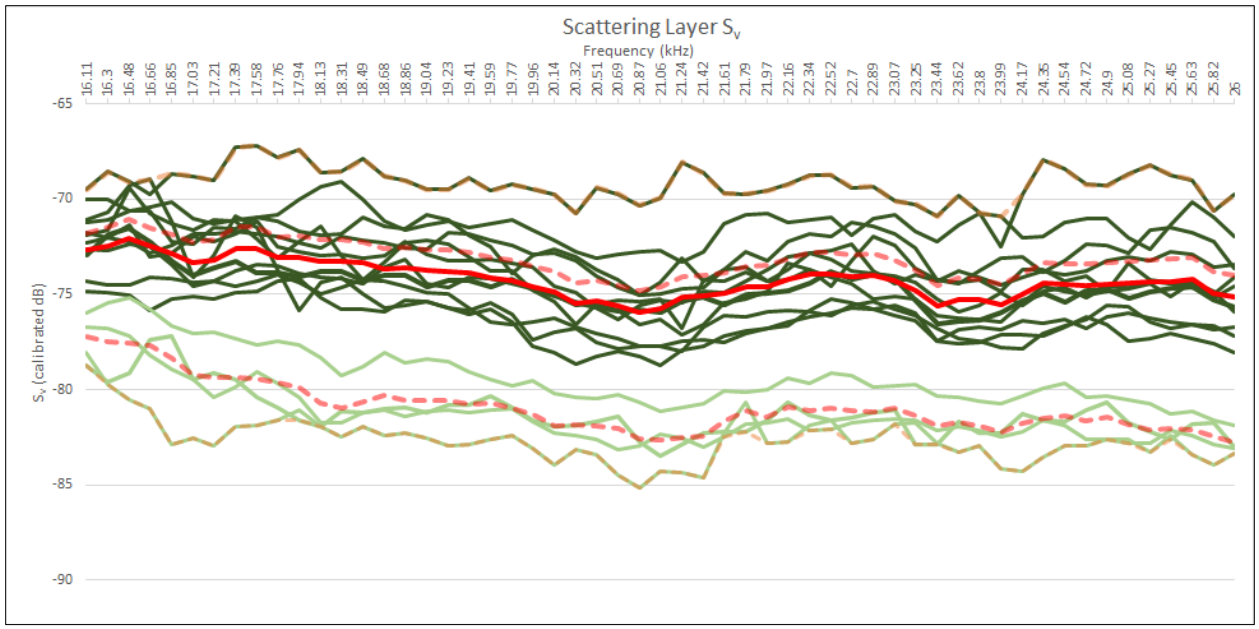

Figure 351: Frequency response for volume selections, PETERMANN2015-D20150807-T232746.raw. The solid red line is the average volume scattering across the frequency range and the orange dashed lines are the minimum and maximum volume scattering across the frequency.

PETERMANN2015-D20150808-T042810.raw

Line PETERMANN2015-D20150808-T042810.raw (Figure 352) was located near CTD 013 (Figure 331). Based on the PDF (Figure 353), a lower threshold of -55 dB was applied during single target detection. Water column depths between 30 and 400 m were analyzed due to high noise levels at depth, and several regions were selectively excluded where there were gaps or anomalously low signal levels related to gaps. The combined single target and target tracking algorithms resulted in 388 targets with a complete frequency response between 16.11 and 25.63 kHz (Figure 354 - Figure 355). Fifteen selections were made for S_v analysis, eleven from dense areas and four from less dense areas (Figure 356). TS, S_v, and the calculated average density ($\hat{\rho}$) and the ensonified volume (V) are summarized for all reviewed lines in Table 7.

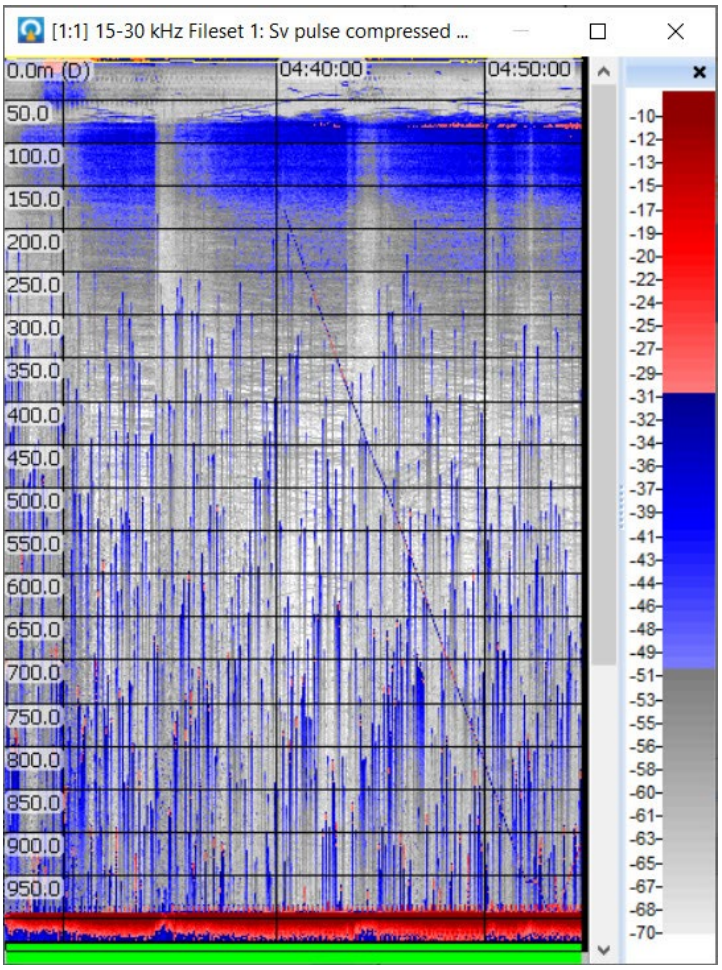

Figure 352: PETERMANN2015-D20150808-T042810.raw shown in Echoview.

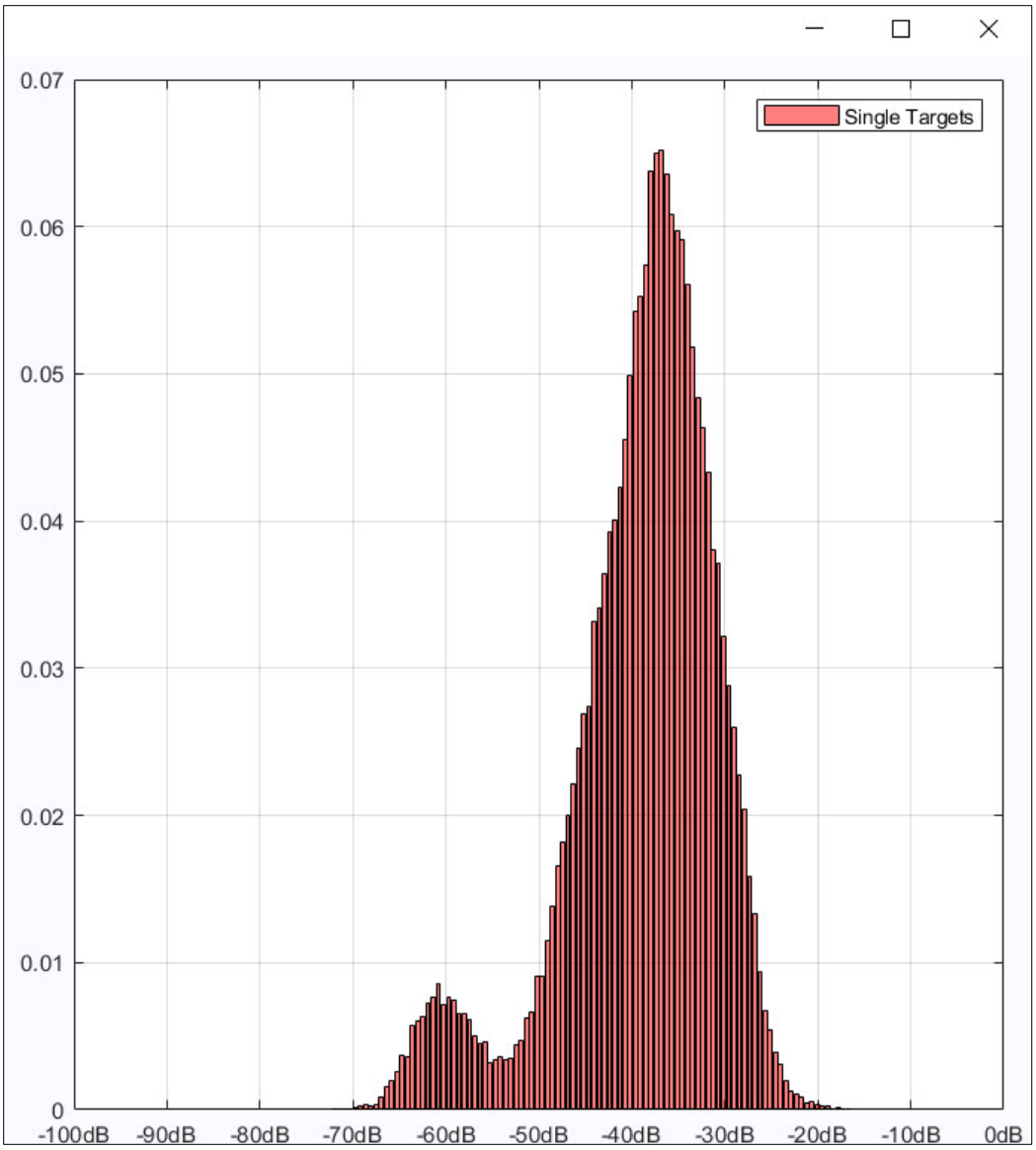

Figure 353: PDF for line PETERMANN2015-D20150807-T042810.raw. A lower threshold of -55 dB was used for single target detection.

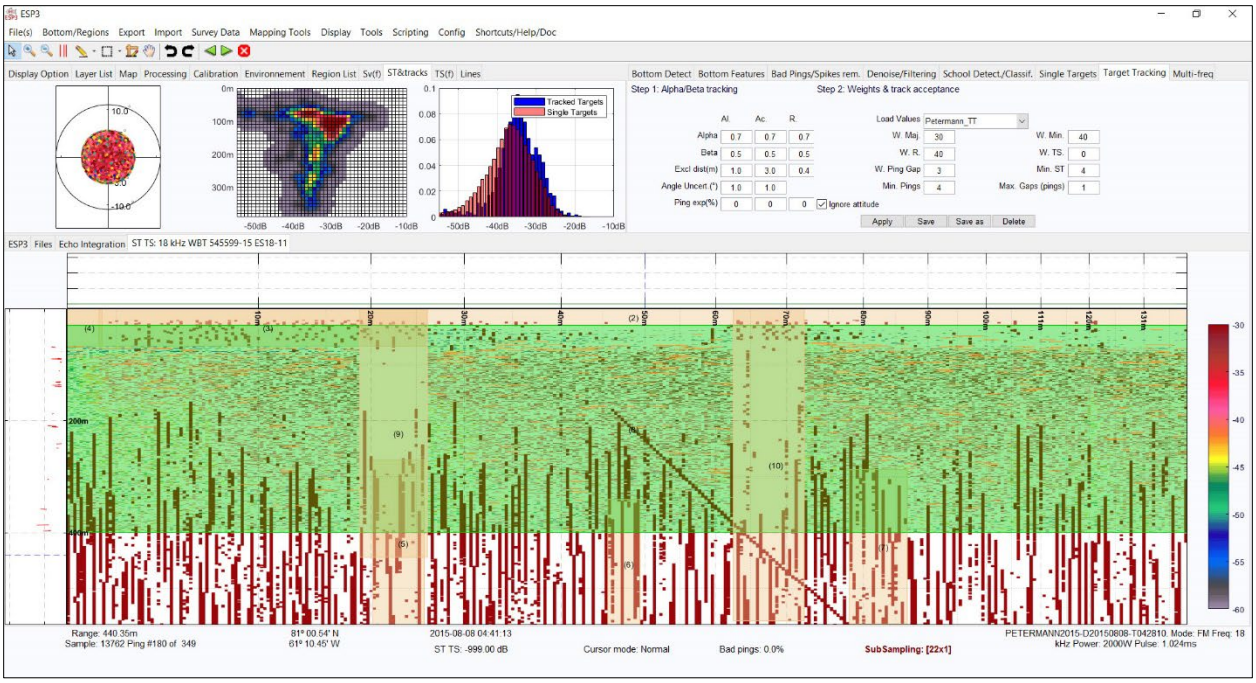

Figure 354: PETERMANN2015-D20150808-T042810.raw selected single targets.

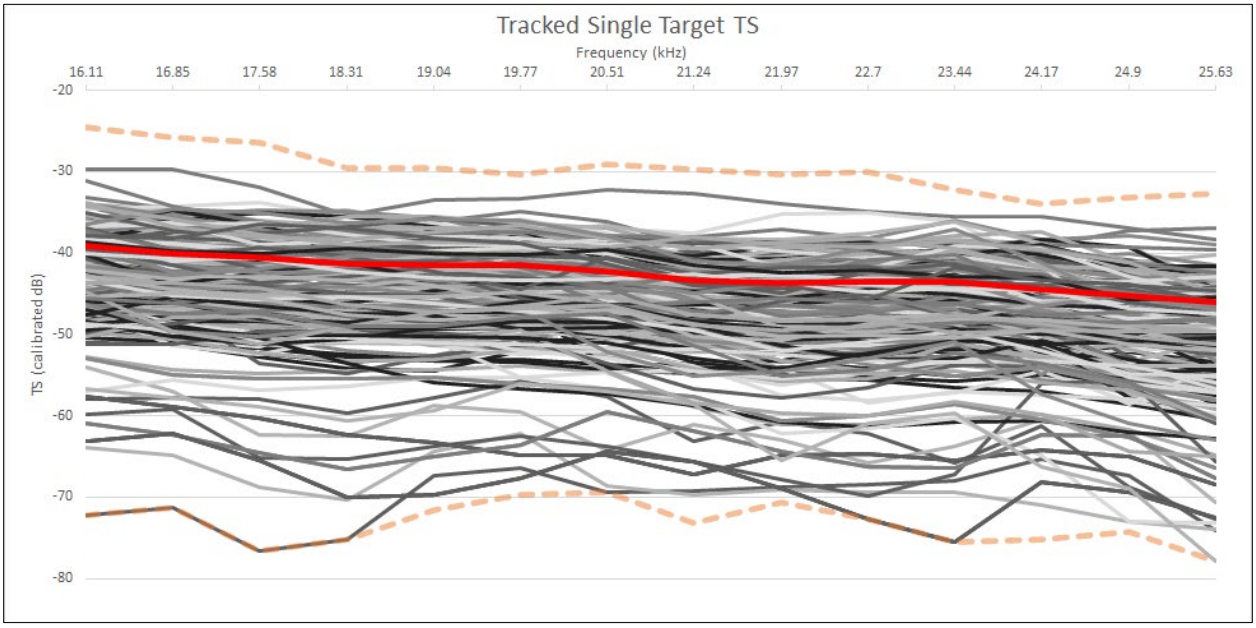

Figure 355: Frequency response for tracked single targets, PETERMANN2015-D20150808-042810.raw. The solid red line is the average target strength across the frequency range and the orange dashed lines are the minimum and maximum target strengths across the frequency range. Colors of other lines are randomly assigned. This graph was produced from a reduced number of TS curves due to graphing limitations in Excel. The minimum, maximum and averages, however, are based on the full set of TS curves.

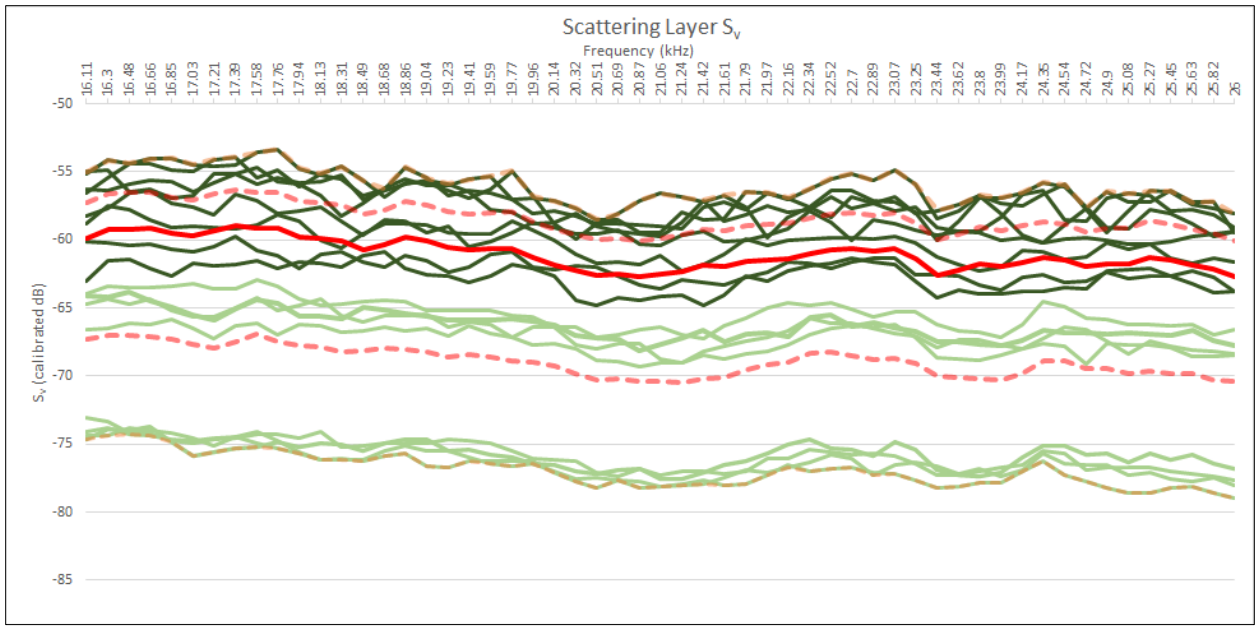

Figure 356: Frequency response for volume selections, PETERMANN2015-D20150808-T042810.raw. The solid red line is the average volume scattering across the frequency range and the orange dashed lines are the minimum and maximum volume scattering across the frequency.

E.4 Transitional Scattering Layers

"Transitional" scattering layers were observed at four CTD stations, 017 – 019 and 024. Three of those stations were found just outside the fjord on the eastern side, close to the Greenland coast. Outflow waters from the fjord are concentrated along this coast (Johnson et al., 2011; Heuzé et al., 2017). Three lines from these three stations are reviewed (Figure 357). The fourth station, 024, was found along the western wall of the deep fjord channel. Data from this station was also reviewed and is found under the heading Outliers.

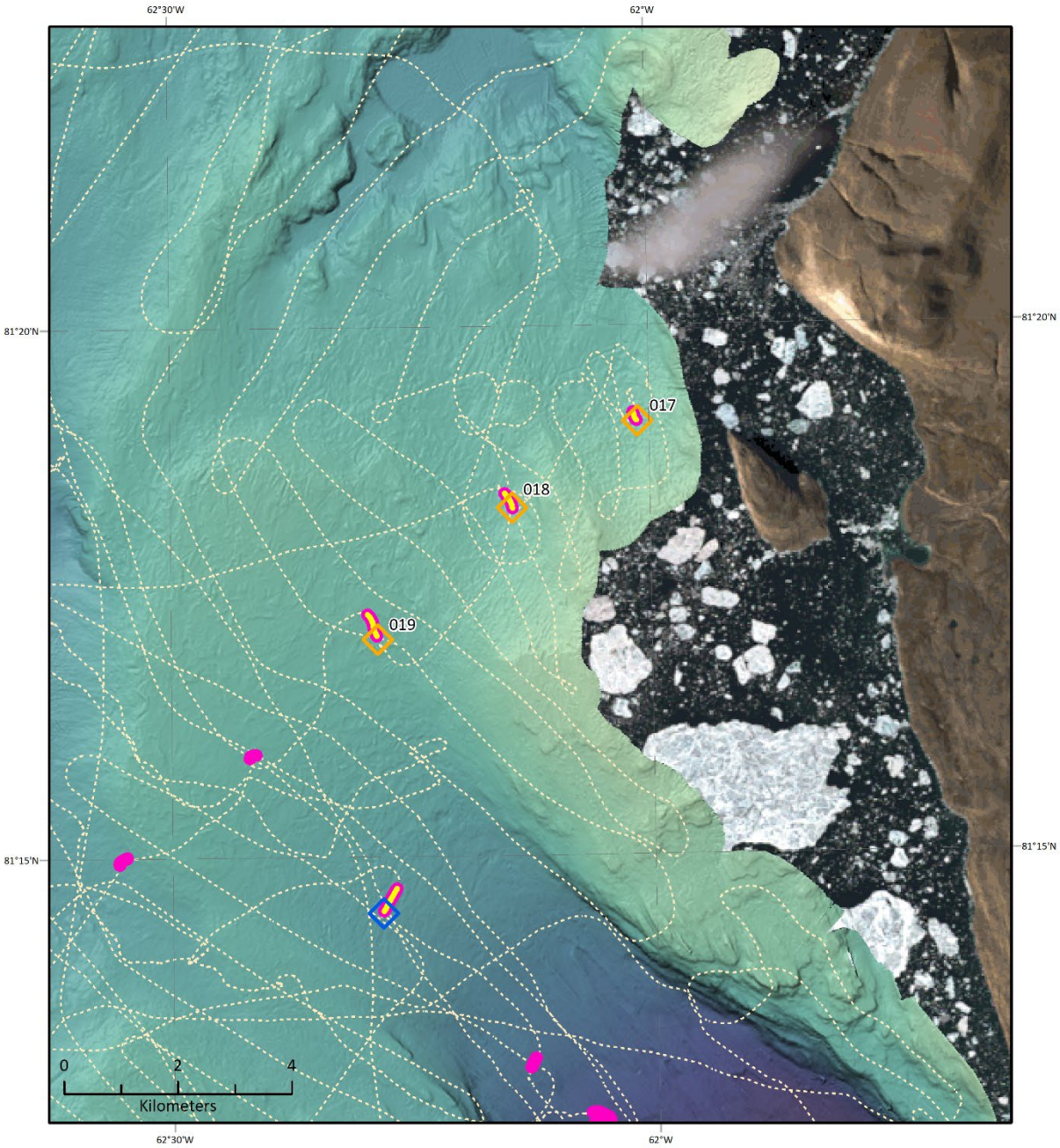

Figure 357: Location of reviewed transitional preference scattering layers and associated CTD stations. The orange diamonds are CTD stations associated with transitional preference scattering layers and are labeled with the CTD station number. All lines where the ship was moving at < 1.5 knots are shown in magenta; the reviewed lines are shown in yellow.

PETERMANN2015-D20150815-T125226.raw

Line PETERMANN2015-D20150815-T125226.raw (Figure 358) was located near CTD 017 (Figure 357). Based on the PDF (Figure 359), a lower threshold of -48 dB was

applied during single target detection. The combined single target and target tracking algorithms resulted in 379 targets with a complete frequency response between 16.11 and 25.63 kHz (Figure 360 - Figure 361). Seventeen selections were made for S_v analysis, eight from dense areas and nine from less dense areas (Figure 362). TS, S_v, and the calculated average density ($\hat{\rho}$) and the ensonified volume (V) are summarized for all reviewed lines in Table 8.

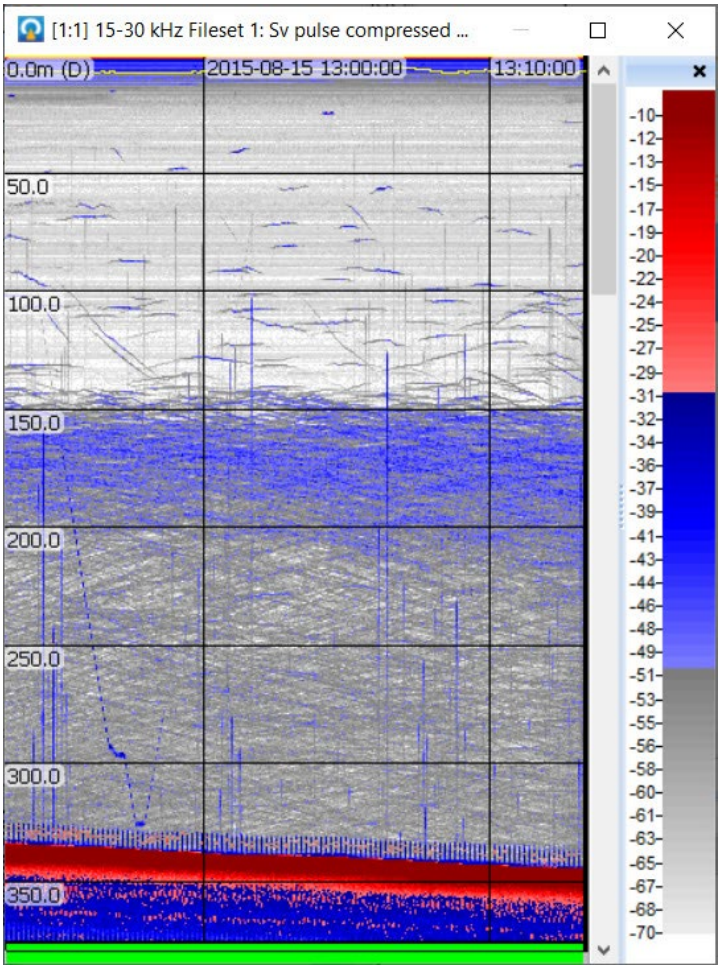

Figure 358: PETERMANN2015-D20150815-T125226.raw shown in Echoview.

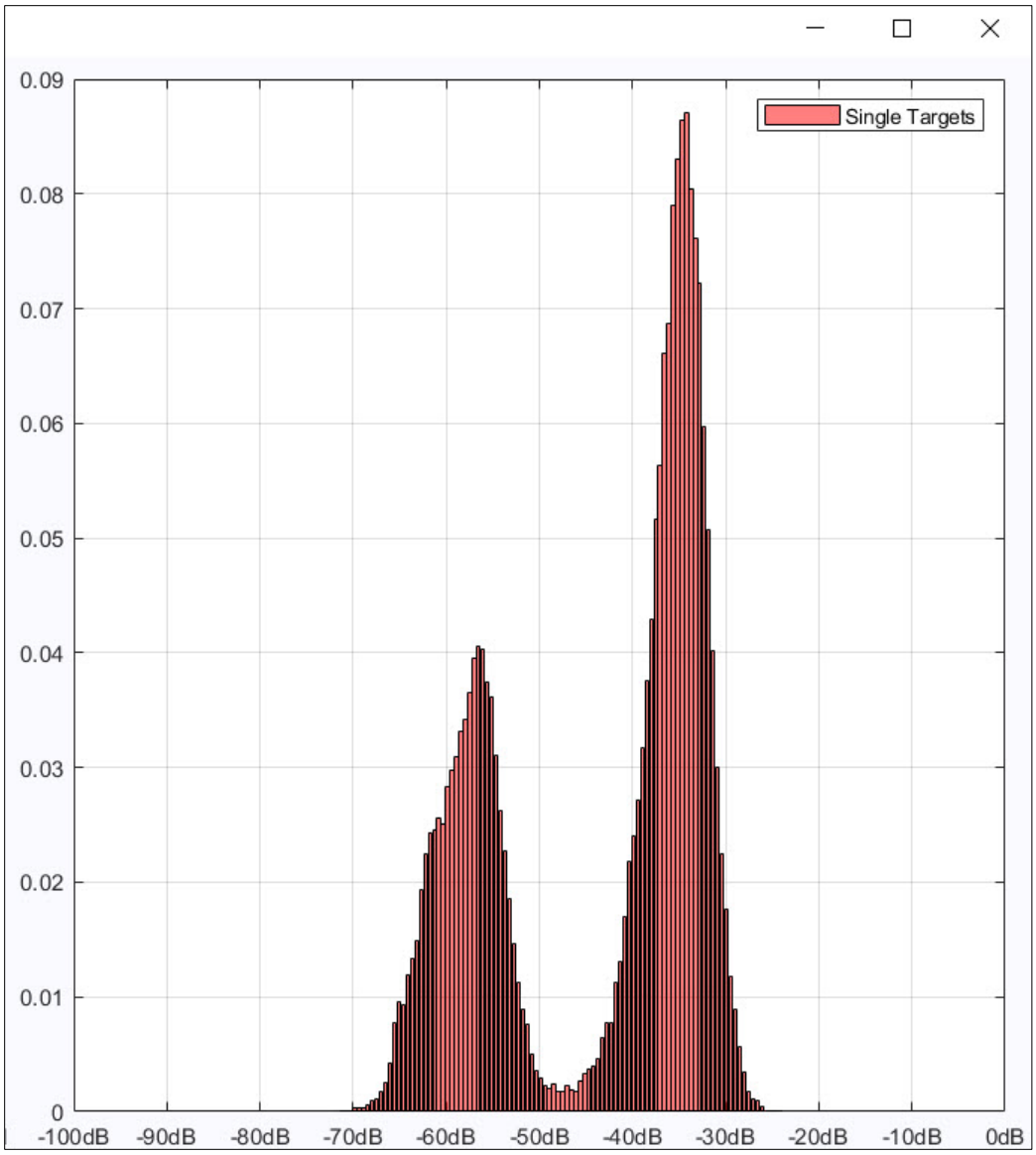

Figure 359: PDF for line PETERMANN2015-D20150815-T125226.raw. A lower threshold of -48 dB was used for single target detection.

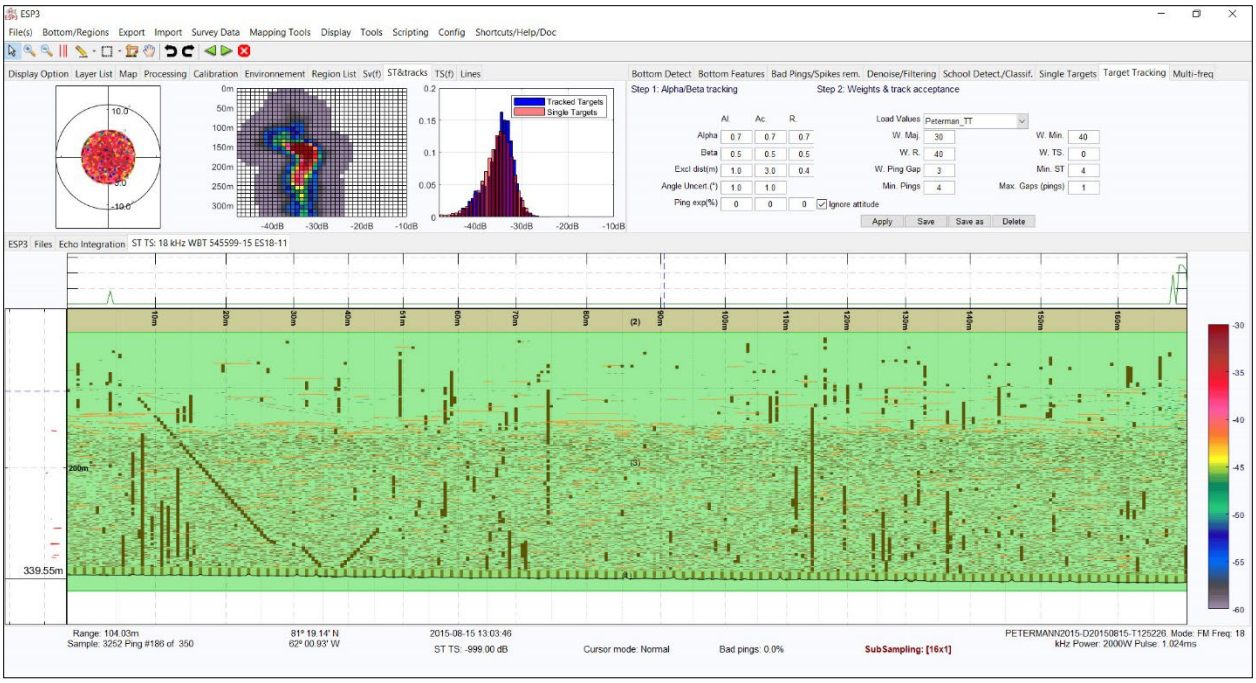

Figure 360: PETERMANN2015-D20150815-T125226.raw selected single targets.

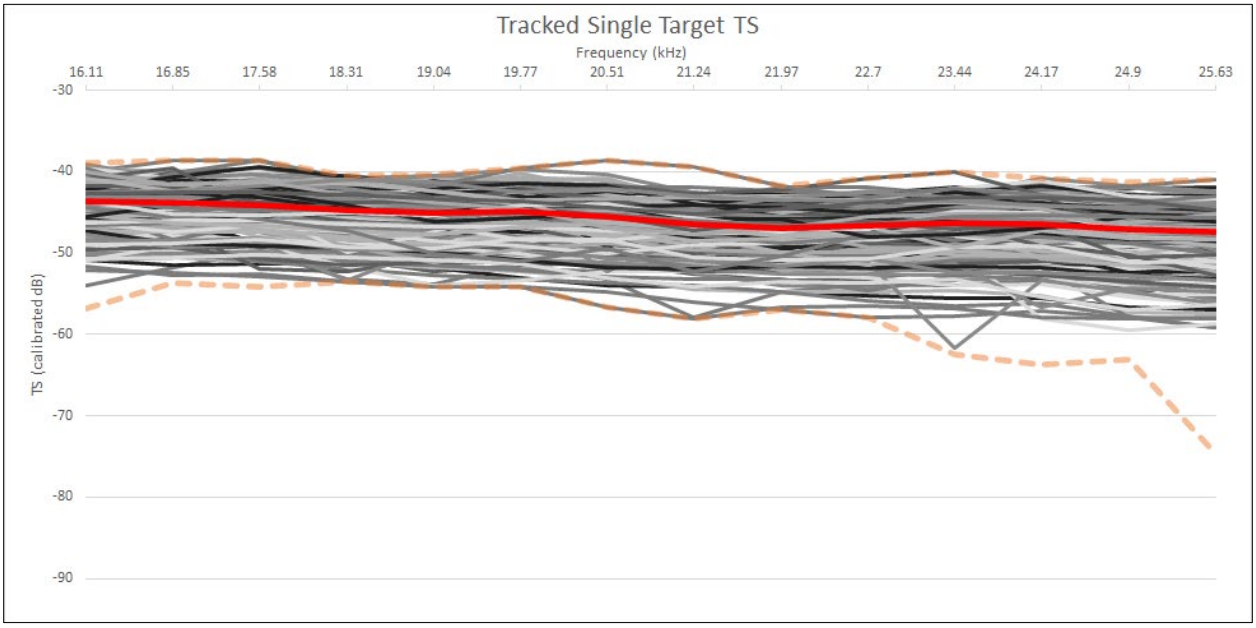

Figure 361: Frequency response for tracked single targets, PETERMANN2015-D20150815-125226.raw. The solid red line is the average target strength across the frequency range and the orange dashed lines are the minimum and maximum target strengths across the frequency range. Colors of other lines are randomly assigned. This graph was produced from a reduced number of TS curves due to graphing limitations in Excel. The minimum, maximum and averages, however, are based on the full set of TS curves.

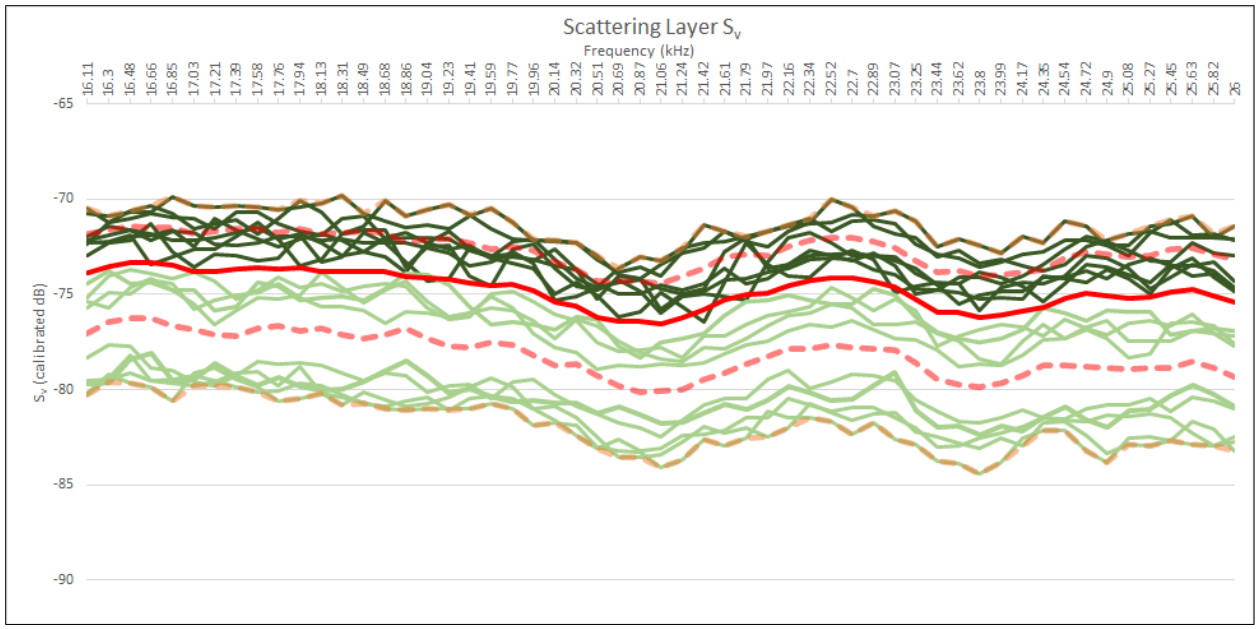

Figure 362: Frequency response for volume selections, PETERMANN2015-D20150815-T125226.raw. The solid red line is the average volume scattering across the frequency range and the orange dashed lines are the minimum and maximum volume scattering across the frequency.

PETERMANN2015-D20150815-T135816.raw

Line PETERMANN2015-D20150815-T135816.raw (Figure 363) was located near CTD 018 (Figure 357). Based on the PDF (Figure 364), a lower threshold of -48 dB was applied during single target detection. The combined single target and target tracking algorithms resulted in 346 targets with a complete frequency response between 16.11 and 25.63 kHz (Figure 365 - Figure 366). Twelve selections were made for S_v analysis, six from dense areas and six from less dense areas (Figure 367). TS, S_v, and the calculated average density ($\hat{\rho}$) and the ensonified volume (V) are summarized for all reviewed lines in Table 8.

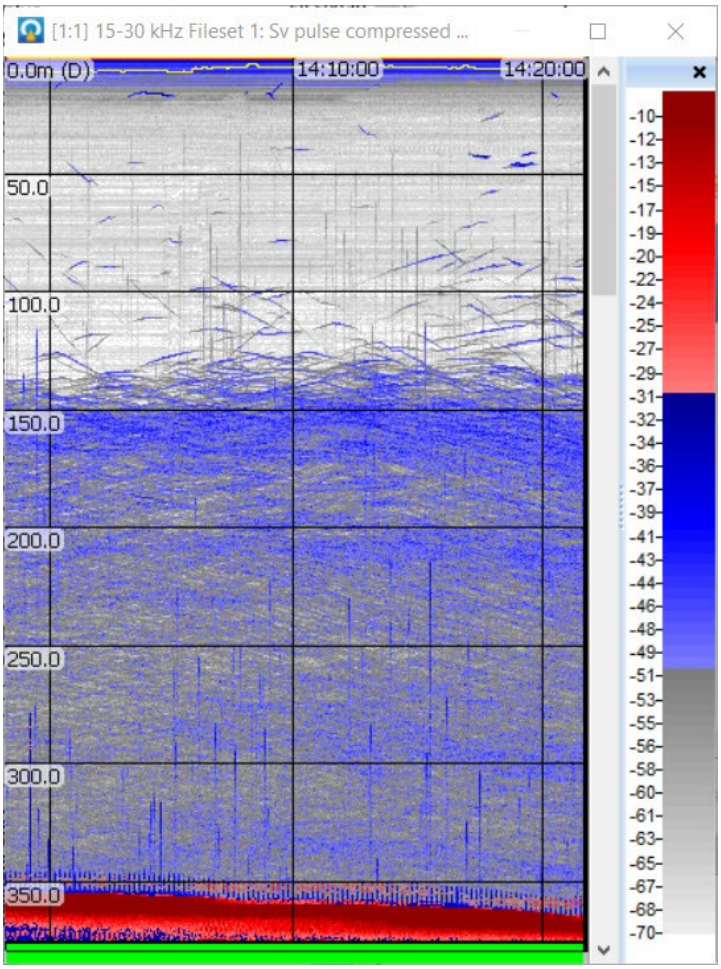

Figure 363: PETERMANN2015-D20150815-T135816.raw shown in Echoview.

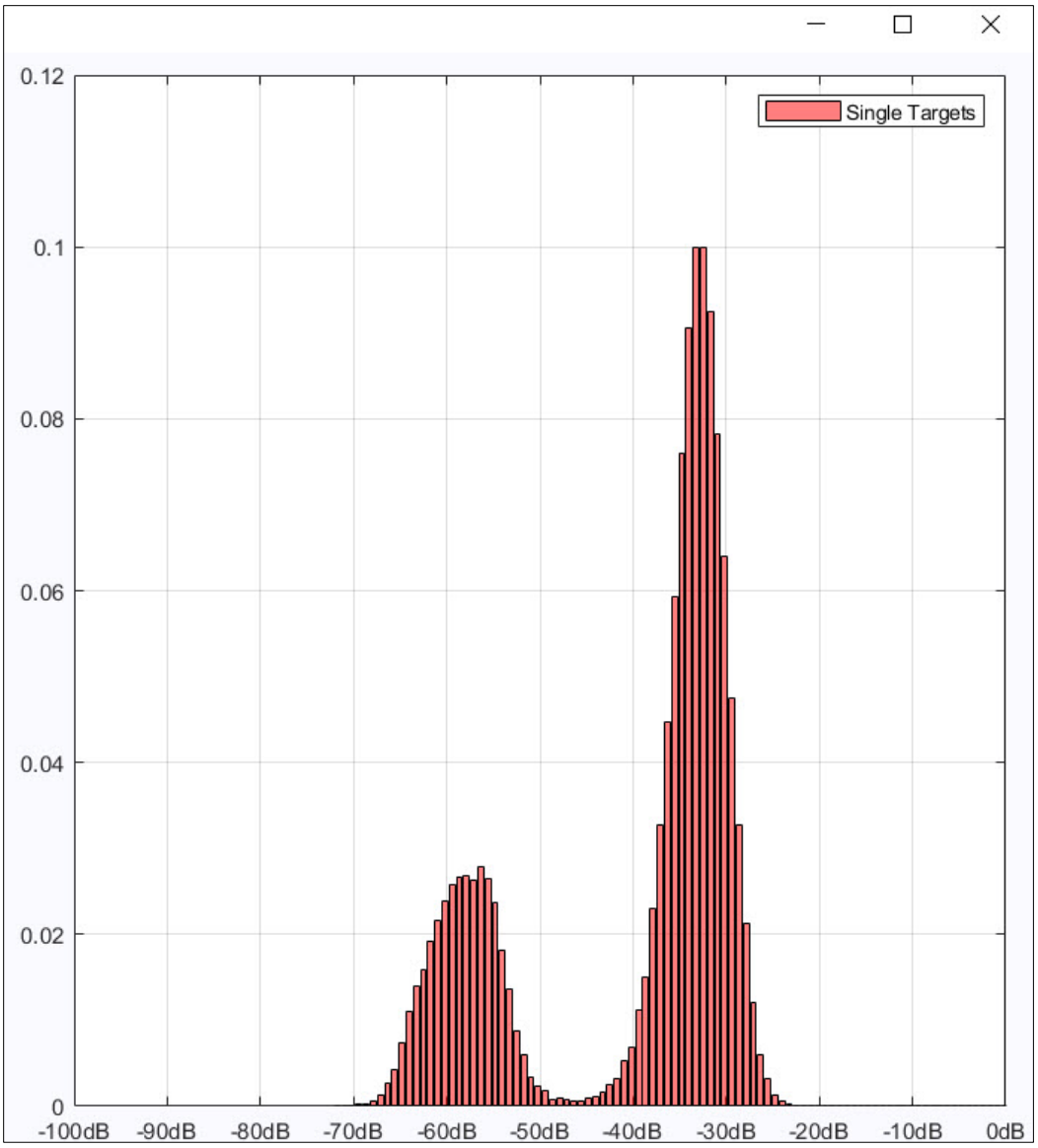

Figure 364: PDF for line PETERMANN2015-D20150815-T135816.raw. A lower threshold of -48 dB was used for single target detection.

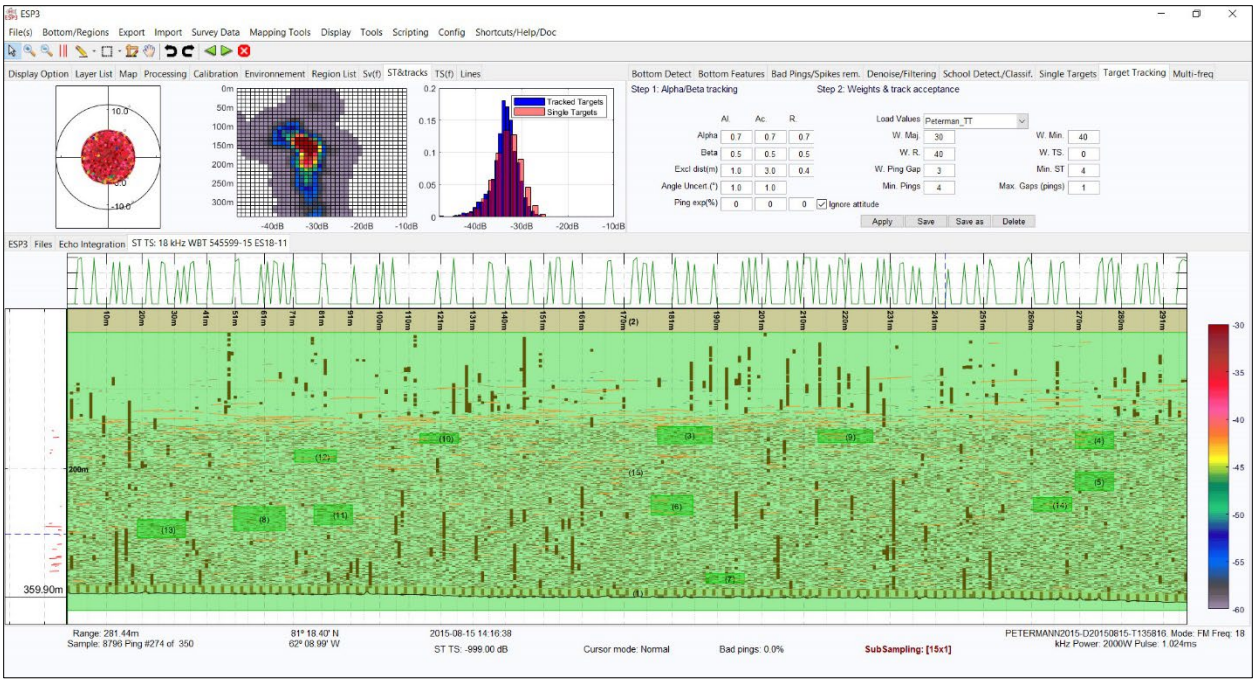

Figure 365: PETERMANN2015-D20150815-T135816.raw selected single targets.

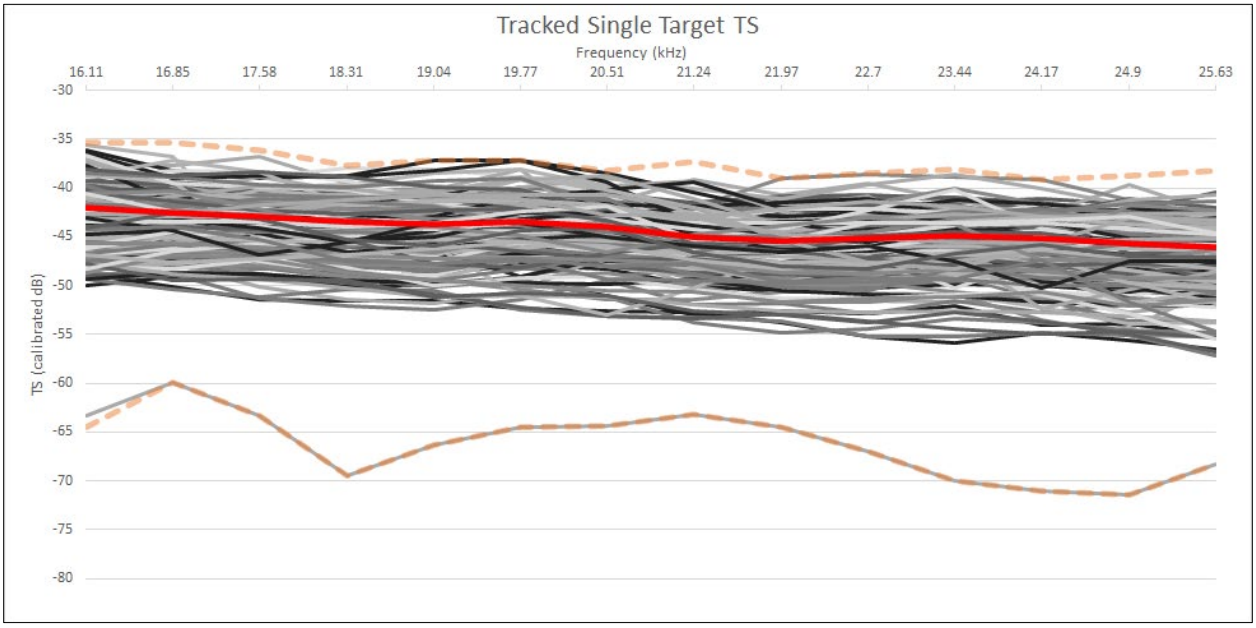

Figure 366: Frequency response for tracked single targets, PETERMANN2015-D20150815-135816.raw. The solid red line is the average target strength across the frequency range and the orange dashed lines are the minimum and maximum target strengths across the frequency range. Colors of other lines are randomly assigned. This graph was produced from a reduced number of TS curves due to graphing limitations in Excel. The minimum, maximum and averages, however, are based on the full set of TS curves.

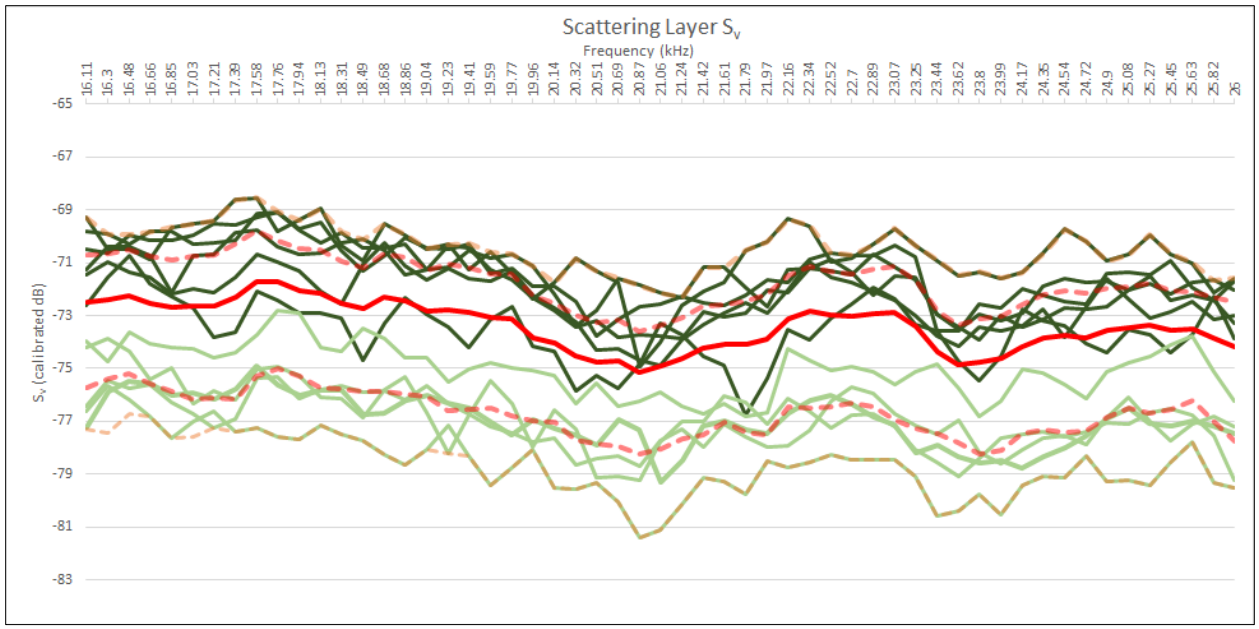

Figure 367: Frequency response for volume selections, PETERMANN2015-D20150815-T135816.raw. The solid red line is the average volume scattering across the frequency range and the orange dashed lines are the minimum and maximum volume scattering across the frequency.

PETERMANN2015-D20150815-T150617.raw

Line PETERMANN2015-D20150815-T150617.raw (Figure 368) was located near CTD 018 (Figure 357). Based on the PDF (Figure 369), a lower threshold of -46 dB was applied during single target detection. The combined single target and target tracking algorithms resulted in 329 targets with a complete frequency response between 16.11 and 25.63 kHz (Figure 370 - Figure 371). Fourteen selections were made for S_v analysis, seven from dense areas and eight from less dense areas (Figure 372). TS, S_v, and the calculated average density ($\hat{\rho}$) and the ensonified volume (V) are summarized for all reviewed lines in Table 8.

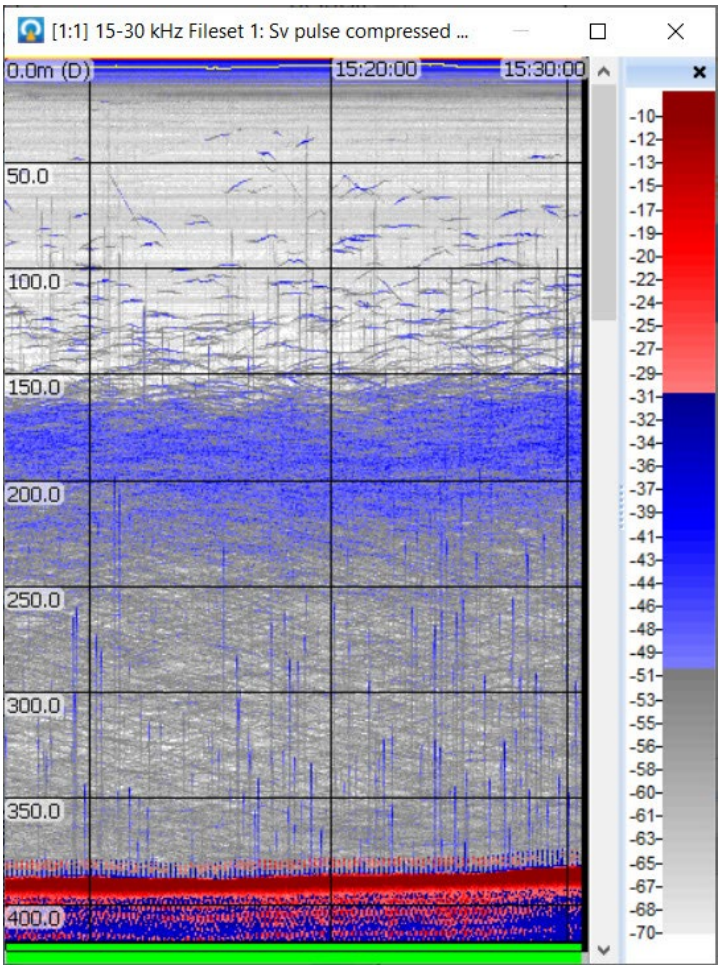

Figure 368: PETERMANN2015-D20150815-T150617.raw shown in Echoview.

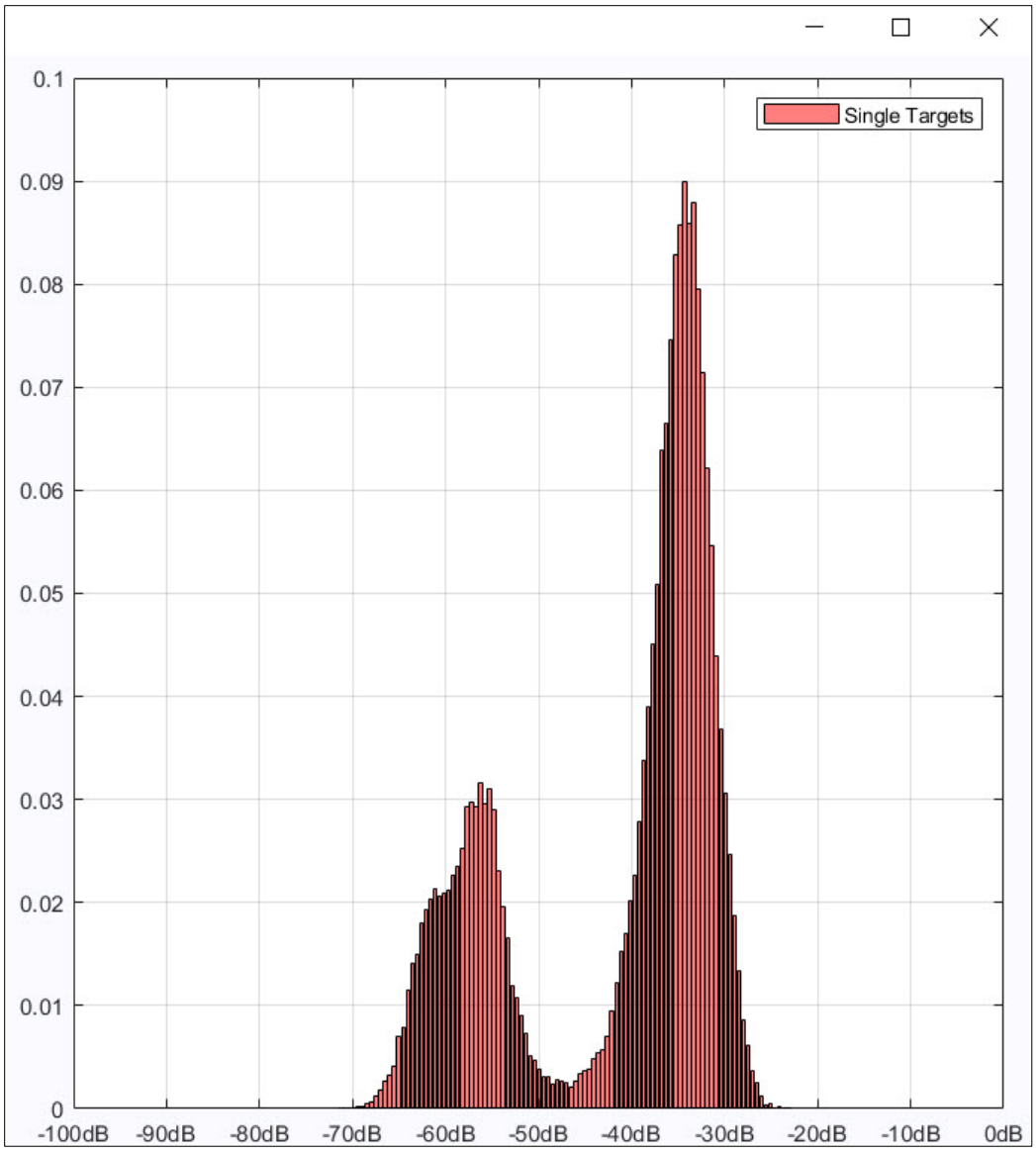

Figure 369: PDF for line PETERMANN2015-D20150815-T150617.raw. A lower threshold of -46 dB was used for single target detection.

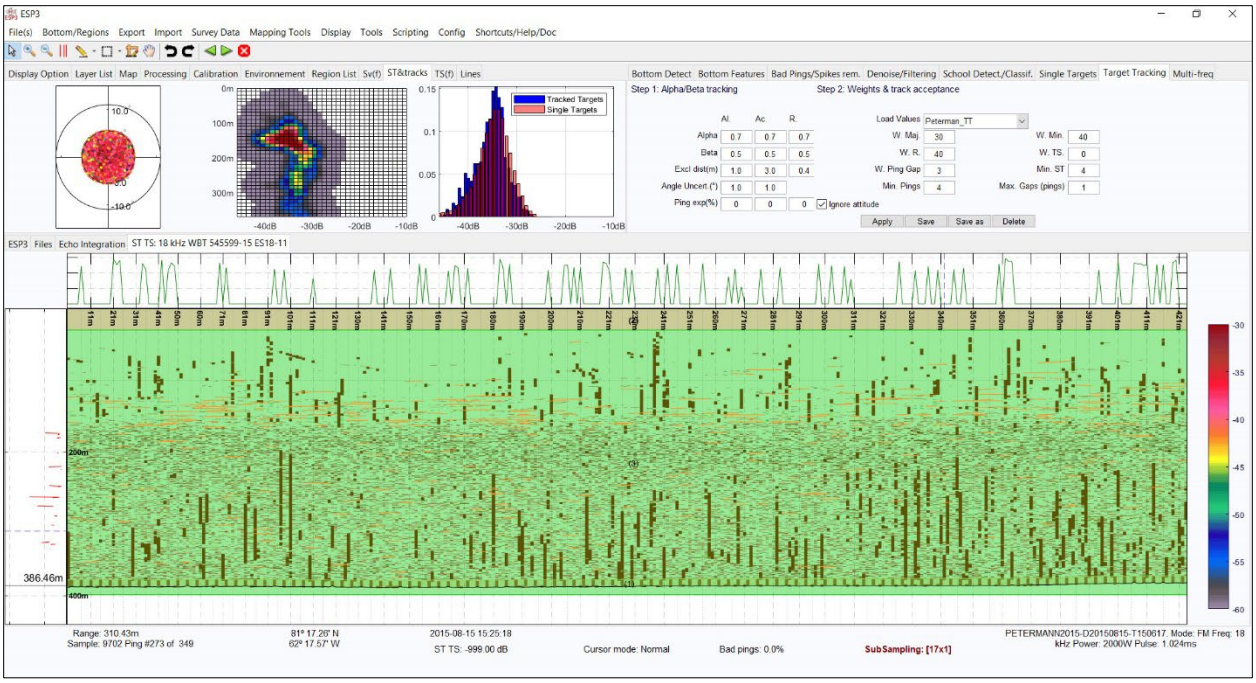

Figure 370: PETERMANN2015-D20150815-T150617.raw selected single targets.

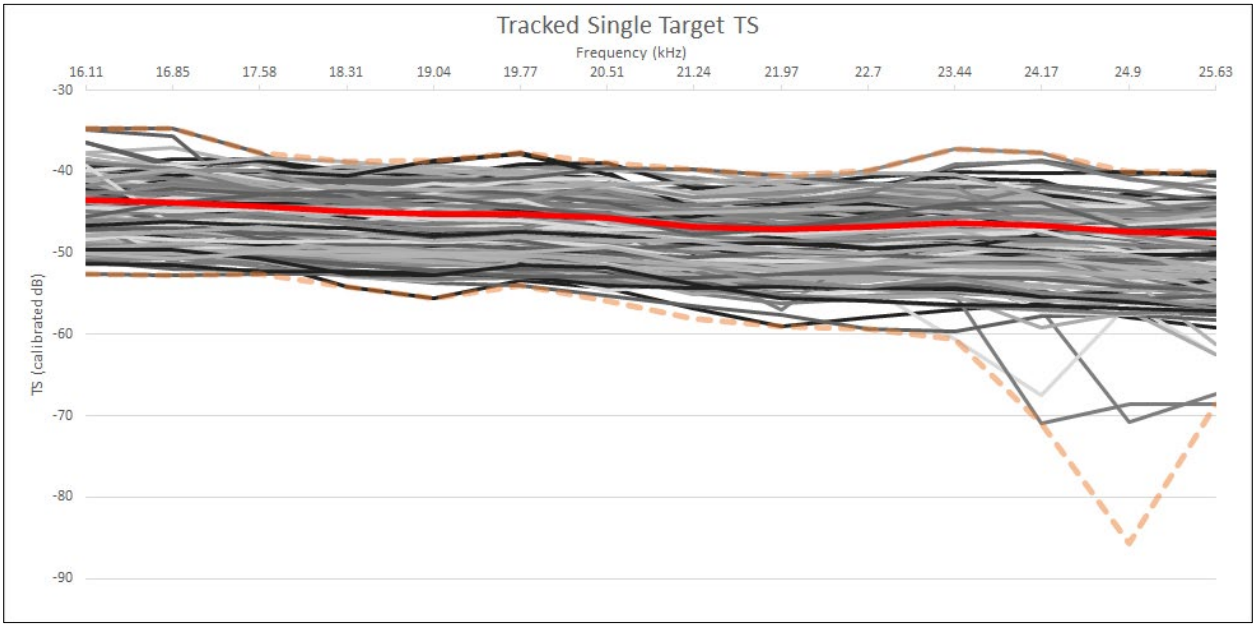

Figure 371: Frequency response for tracked single targets, PETERMANN2015-D20150815-150617.raw. The solid red line is the average target strength across the frequency range and the orange dashed lines are the minimum and maximum target strengths across the frequency range. Colors of other lines are randomly assigned. This graph was produced from a reduced number of TS curves due to graphing limitations in Excel. The minimum, maximum and averages, however, are based on the full set of TS curves.

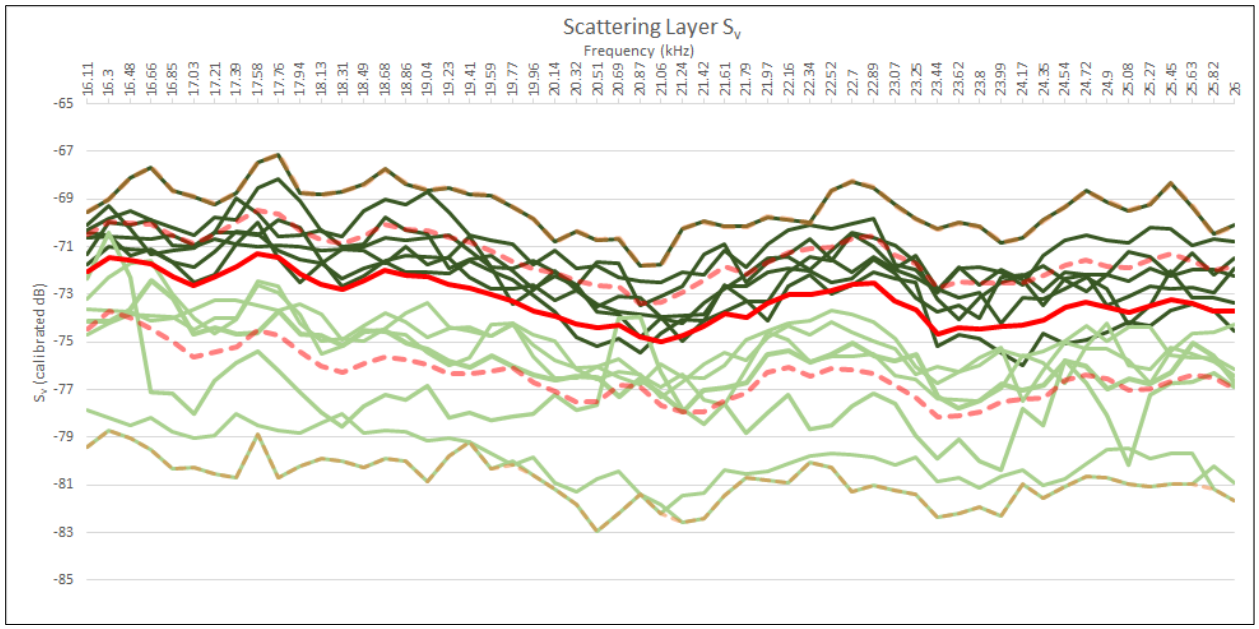

Figure 372: Frequency response for volume selections, PETERMANN2015-D20150815-T150617.raw. The solid red line is the average volume scattering across the frequency range and the orange dashed lines are the minimum and maximum volume scattering across the frequency.

E.5 Outliers

For the most part, CTD stations associated with homogeneous preference scattering layers were found in Hall Basin and the western to central fjord entrance and appear to be related to inflow waters, CTD stations associated with heterogenous preference scattering layers were in the central and eastern fjord and appear to be related to outflow waters, and transitional scattering layers were found near to the Greenland coast just outside the fjord. Two CTD stations, 024 and 030, did not fit this pattern (Figure 373).

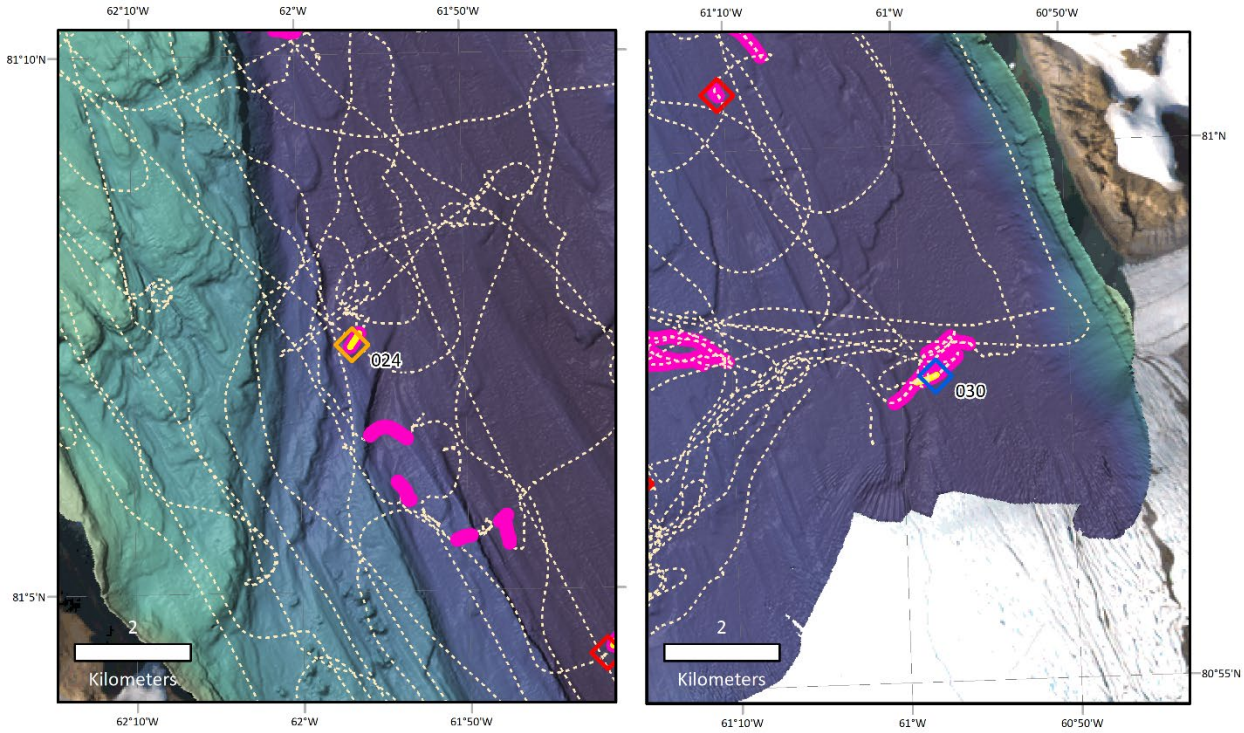

Figure 373: Location of CTD 024, left, and 030, right.

PETERMANN2015-D20150818-T095013.raw

Line PETERMANN2015-D20150818-T095013.raw (Figure 374) was located near CTD 024 (Figure 373). Based on the PDF (Figure 375), a lower threshold of -48 dB was applied during single target detection. The combined single target and target tracking algorithms resulted in 341 targets with a complete frequency response between 16.11 and 25.63 kHz (Figure 376 - Figure 377). Twenty-two selections were made for S_v analysis, ten from dense areas and twelve from less dense areas (Figure 378). TS, S_v, and the calculated average density ($\hat{\rho}$) and the ensonified volume (V) are summarized for all reviewed lines in Table 8.

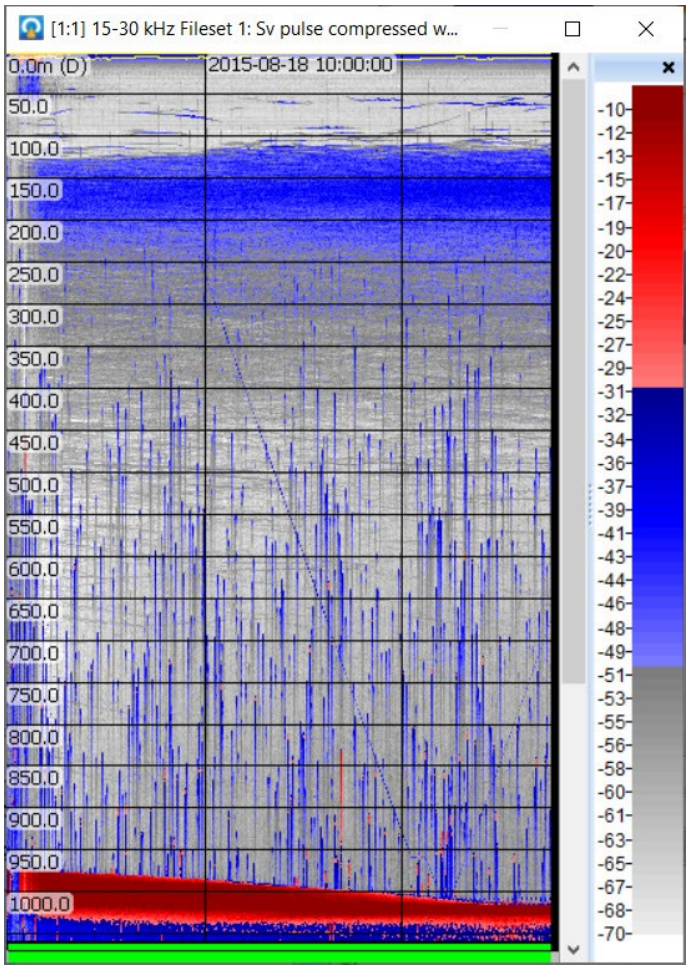

Figure 374: PETERMANN2015-D20150818-T095013.raw shown in Echoview.

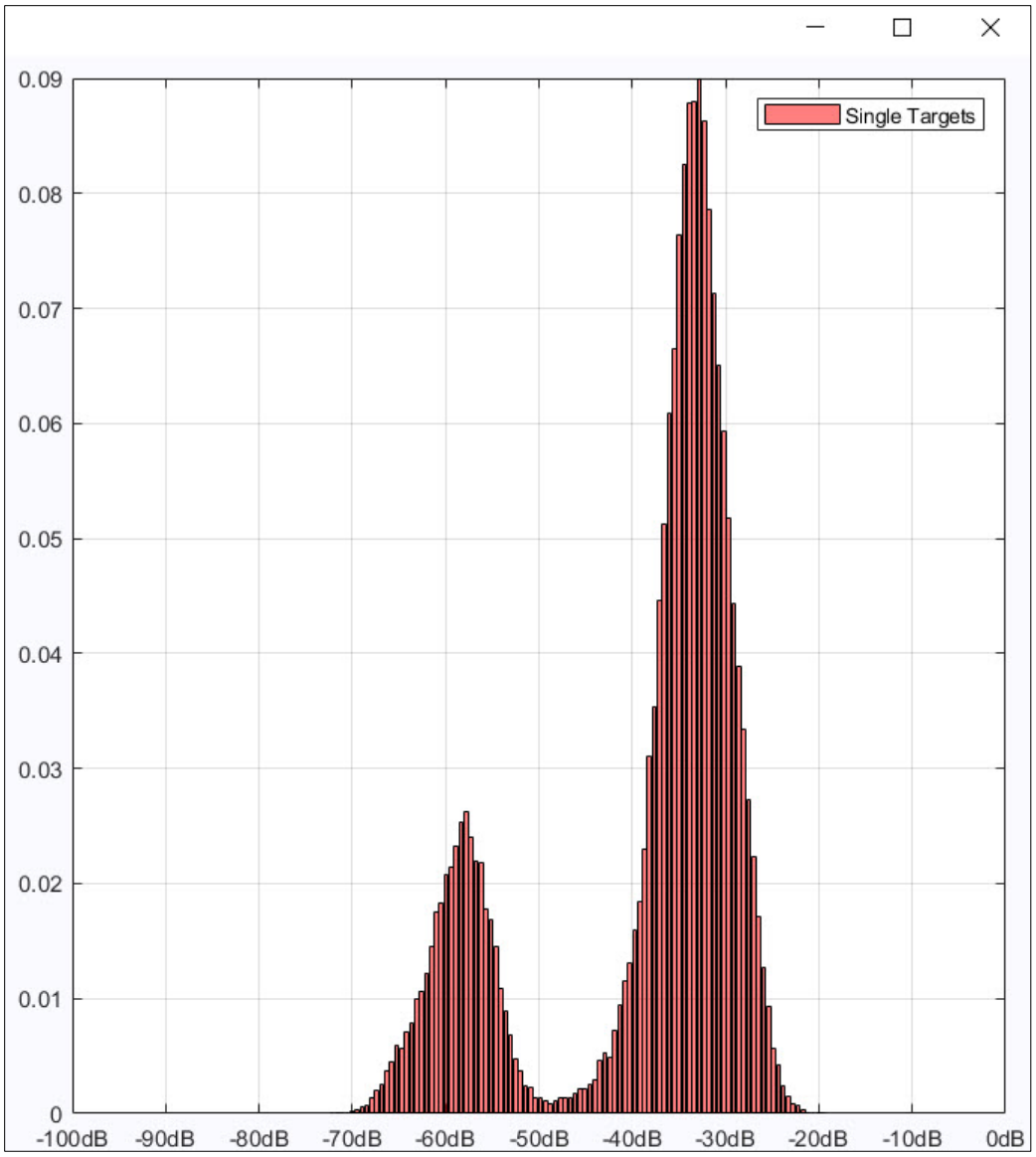

Figure 375: PDF for line PETERMANN2015-D20150818-T095013.raw. A lower threshold of -48 dB was used for single target detection.

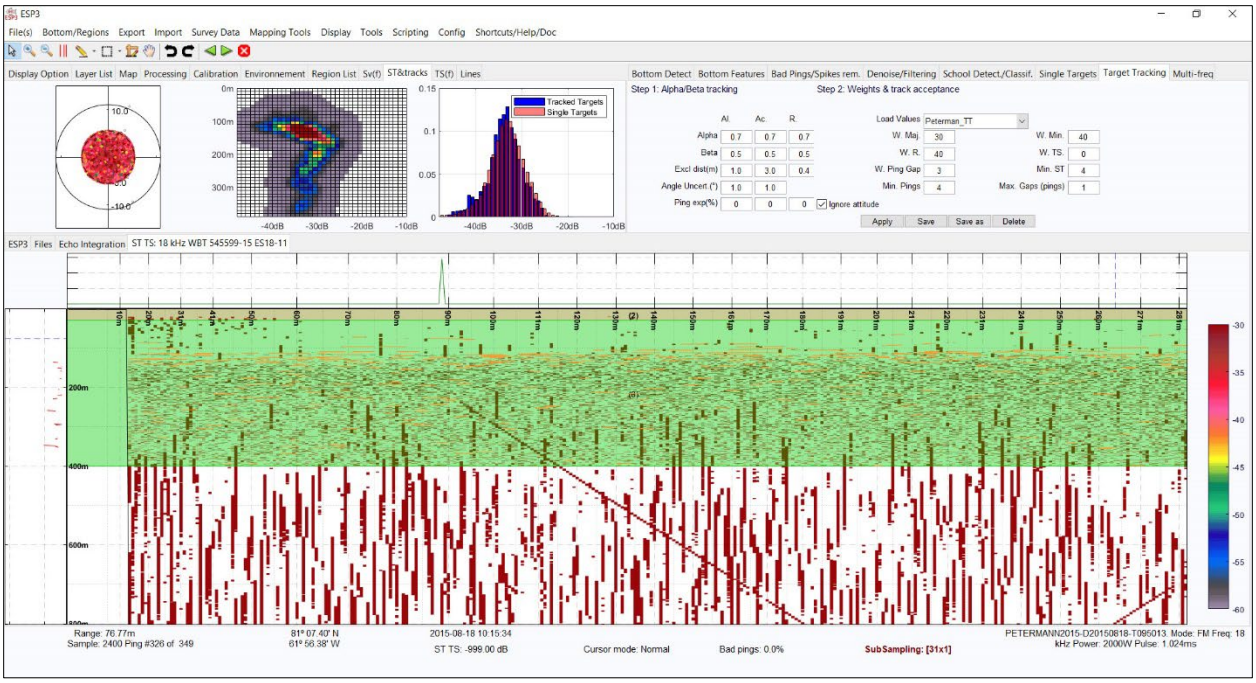

Figure 376: PETERMANN2015-D20150818-T095013.raw selected single targets.

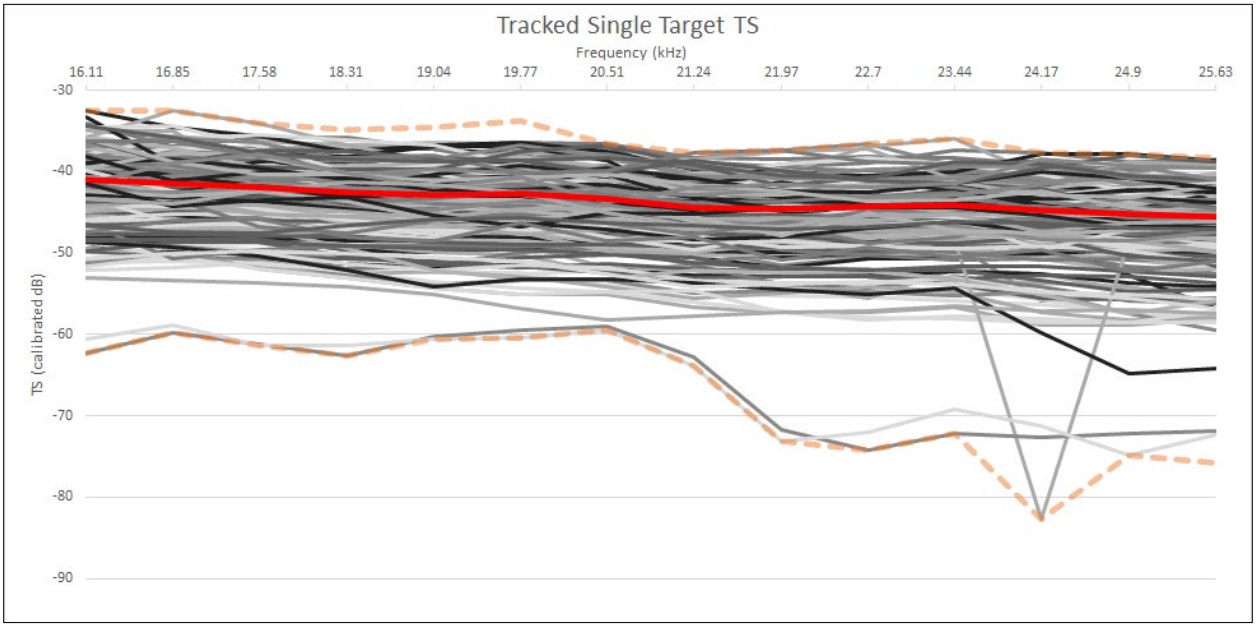

Figure 377: Frequency response for tracked single targets, PETERMANN2015-D20150818-095013.raw. The solid red line is the average target strength across the frequency range and the orange dashed lines are the minimum and maximum target strengths across the frequency range. Colors of other lines are randomly assigned. This graph was produced from a reduced number of TS curves due to graphing limitations in Excel. The minimum, maximum and averages, however, are based on the full set of TS curves.

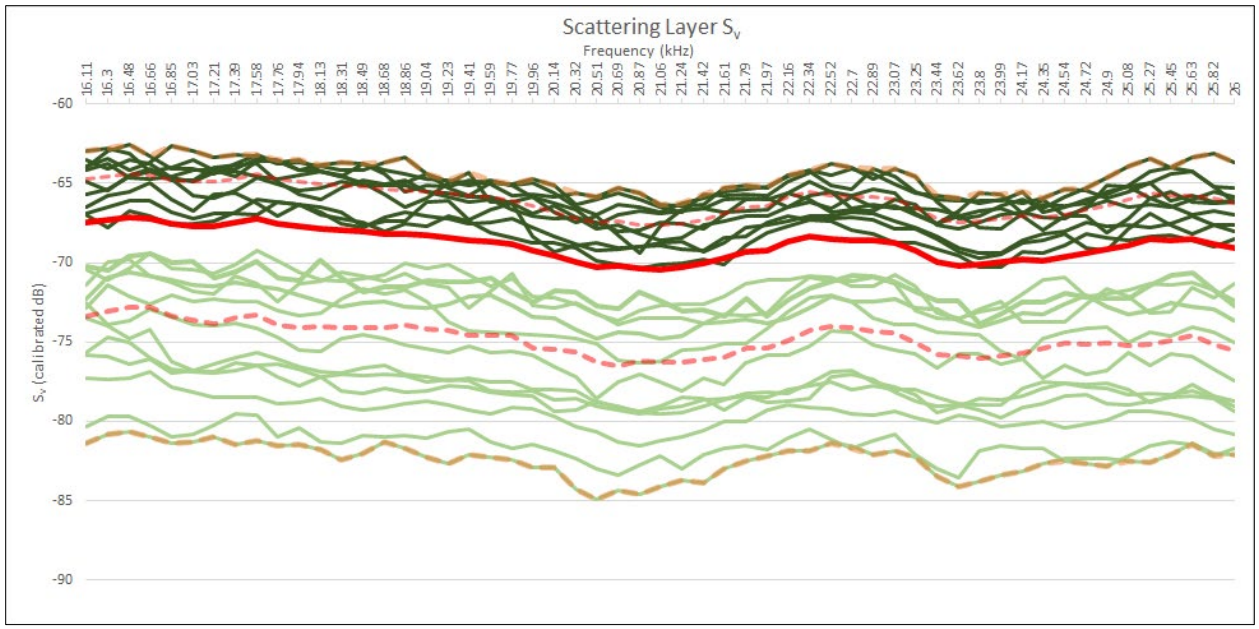

Figure 378: Frequency response for volume selections, PETERMANN2015-D20150818-T095013.raw. The solid red line is the average volume scattering across the frequency range and the orange dashed lines are the minimum and maximum volume scattering across the frequency.

PETERMANN2015-D20150822-T173712.raw

Line PETERMANN2015-D20150822-T73712.raw (Figure 379) was located near CTD 030 (Figure 373). Based on the PDF (Figure 380), a lower threshold of -53 dB was applied during single target detection. The analysis region was restricted to depths between 250 and 500m due to strong interference between 200 and 250 m that was not completely removed by the spike filter, even though it appears that the scattering layer has a component starting well above 250 m (see Figure 379, noting scatterers present around the interference band). Additionally, a large portion of the line was removed due to signal related to the deployment of equipment that caused bubbles, dropped sediment, or disturbed the scattering layer (see the top 200 m of the water column near the start of the line, Figure 379). The combined single target and target tracking algorithms resulted in 20 targets with a complete frequency response between 16.11 and 25.63 kHz (Figure 381 - Figure 382). Fifteen selections were made for S_v analysis,

six from dense areas and nine from less dense areas (Figure 383). TS, S_v, and the calculated average density ($\hat{\rho}$) and the ensonified volume (V) are summarized for all reviewed lines in Table 8.

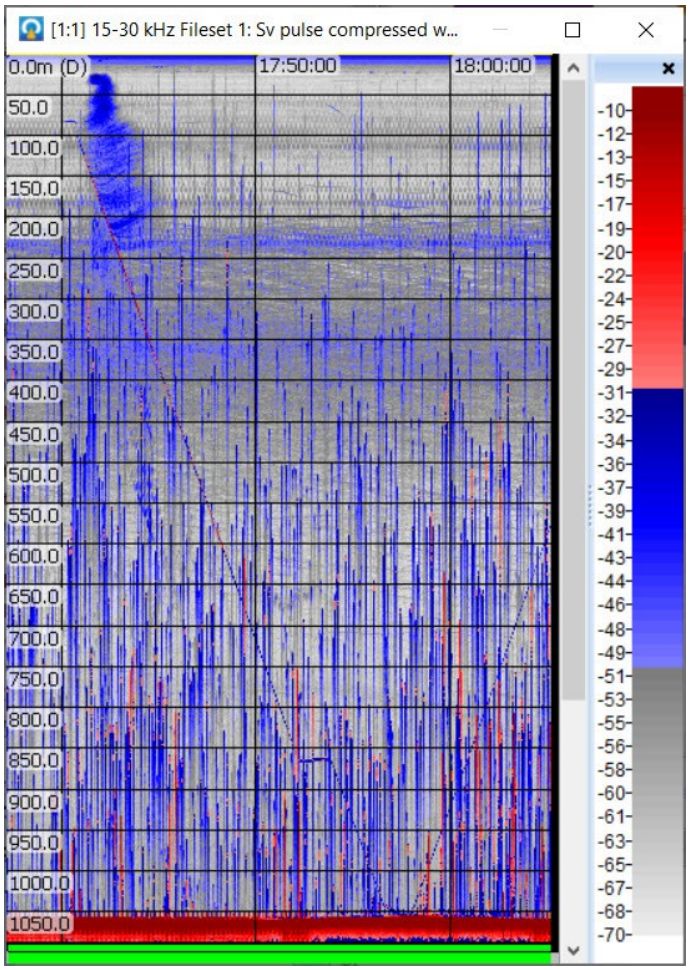

Figure 379: PETERMANN2015-D20150822-T173712.raw shown in Echoview.

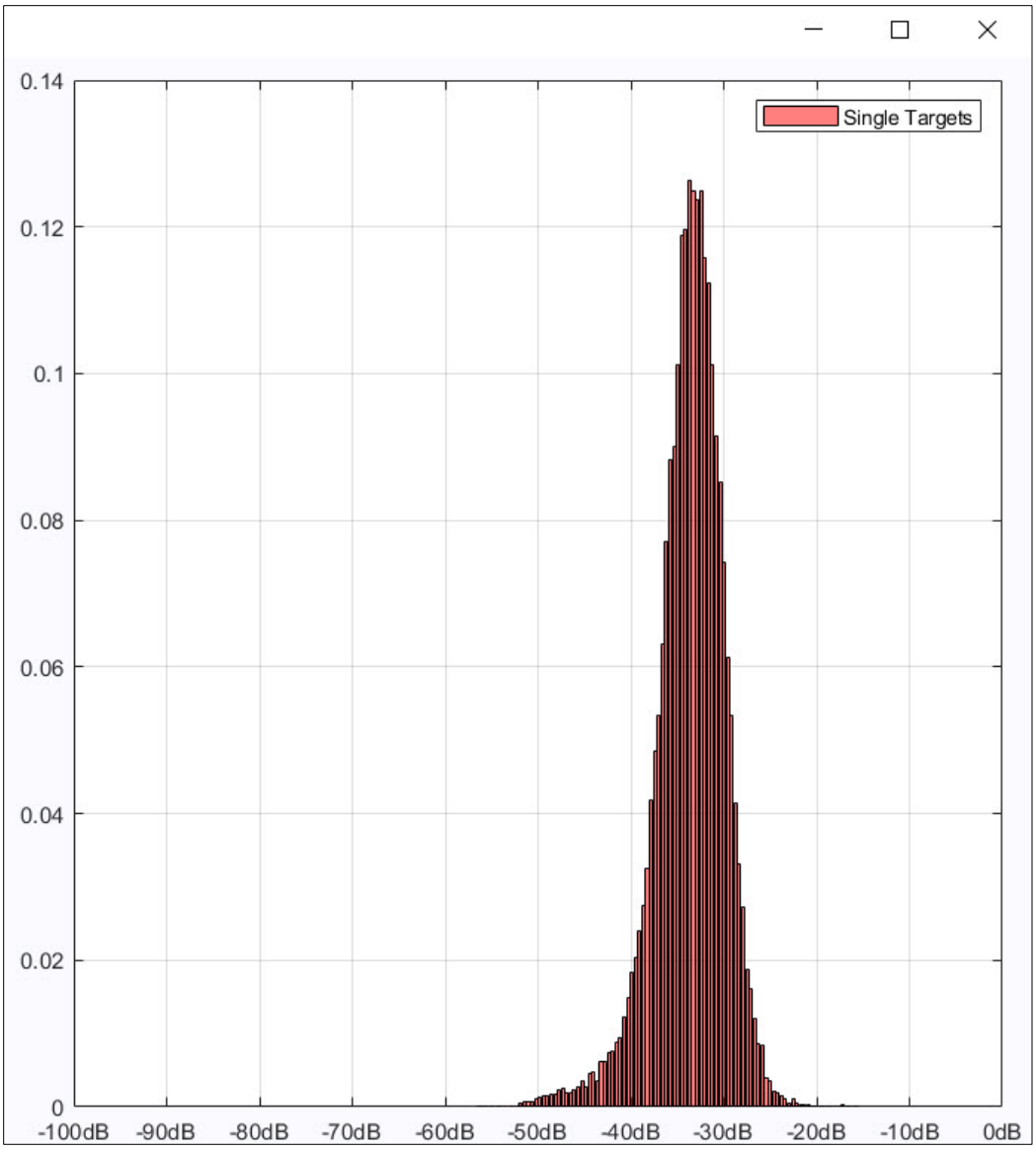

Figure 380: PDF for line PETERMANN2015-D20150822-T173712.raw. A lower threshold of -53 dB was used for single target detection.

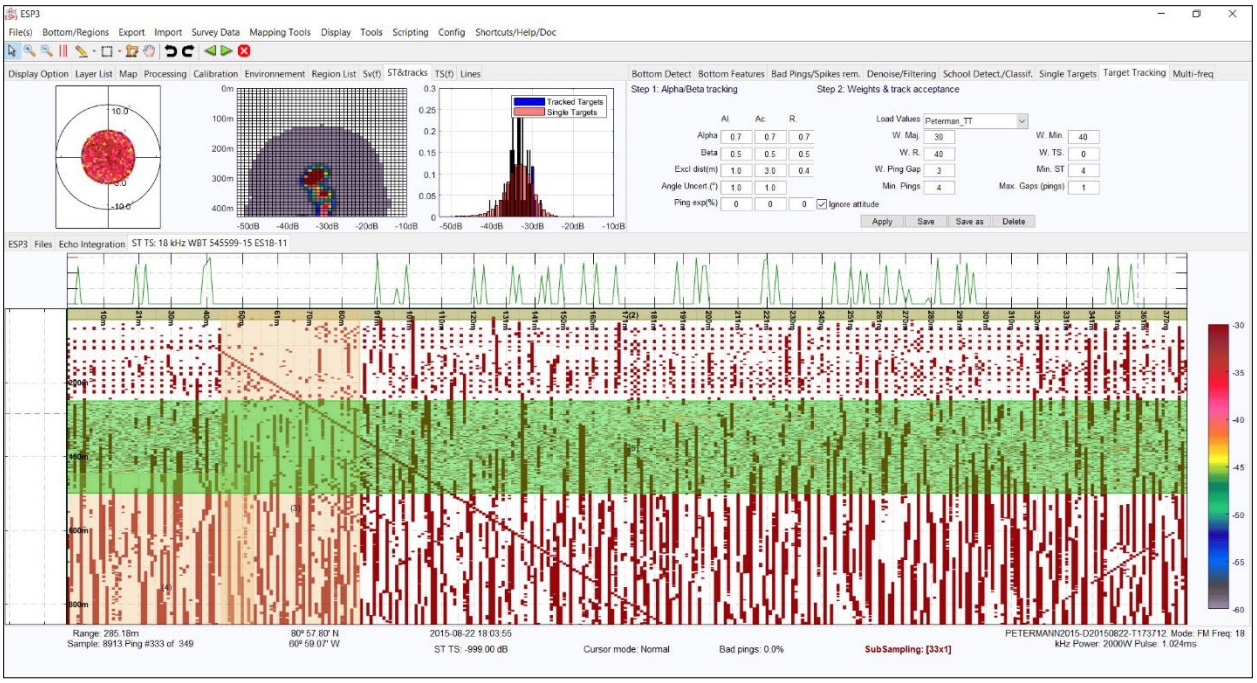

Figure 381: PETERMANN2015-D20150822-T173712.raw selected single targets.

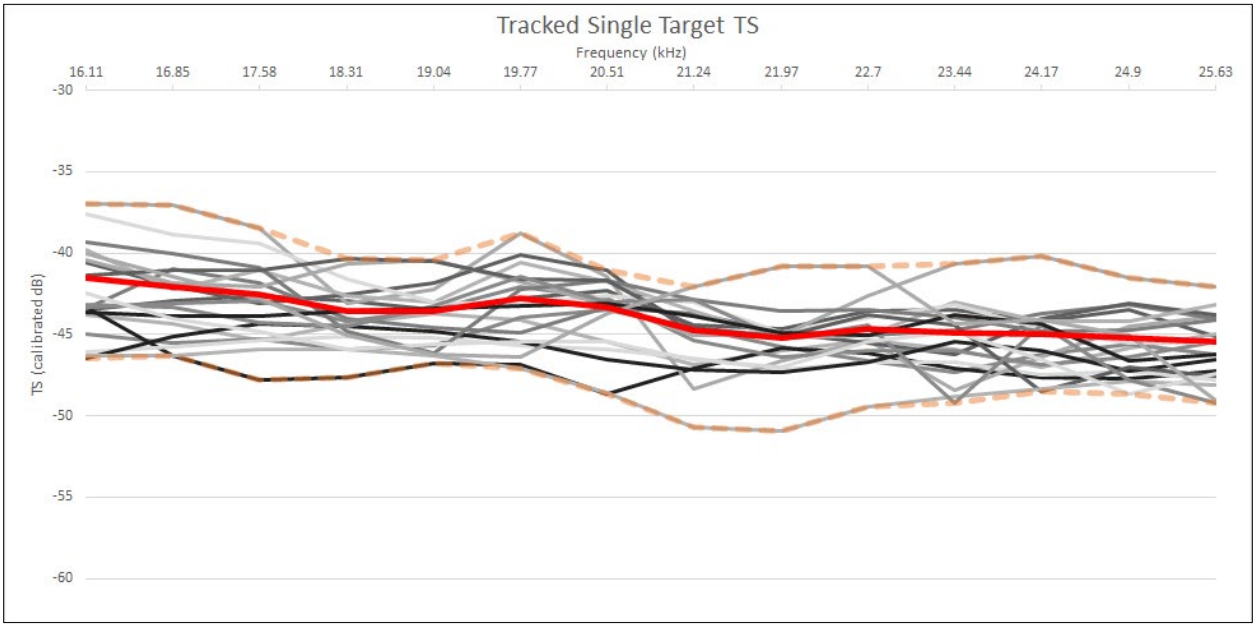

Figure 382: Frequency response for tracked single targets, PETERMANN2015-D20150822-173712.raw. The solid red line is the average target strength across the frequency range and the orange dashed lines are the minimum and maximum target strengths across the frequency range. Colors of other lines are randomly assigned.

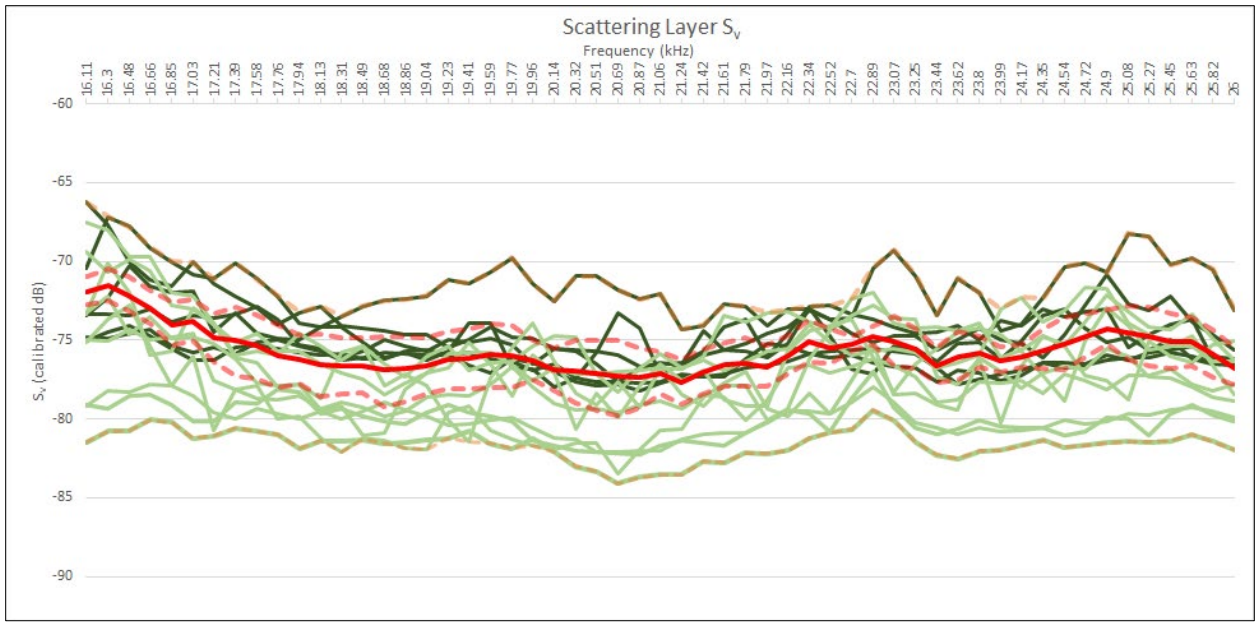

Figure 383: Frequency response for volume selections, PETERMANN2015-D20150822-T173712.raw. The solid red line is the average volume scattering across the frequency range and the orange dashed lines are the minimum and maximum volume scattering across the frequency.

Table 7: Summary of TS, S_v, average density ($\hat{\rho}$) and the acoustic sampling volume (V) as calculated for each line with a homogeneous (blue shading) and heterogeneous preference (red shading) scattering layer.

Line (.RAW file)	CTD station	TS (dB)	Less Dense S_v (dB)	Dense S_v (dB)	Density (targets m^{-3})	Acoustic Sampling Volume (m^3)
PETERMANN2015-D20150813-T215026	015	-42.29	-80.13	-68.32	0.0001 – 0.002	158.4
PETERMANN2015-D20150814-T134156	016	-43.90	-81.70	-68.80	0.0002 – 0.003	105.3
PETERMANN2015-D20150814-T145139	016	-38.70	-80.27	-68.63	0.00007 – 0.001	130.5
PETERMANN2015-D20150815-T194637	023	-45.15	-80.65	-75.30	0.0003 – 0.001	210.9
PETERMANN2015-D20150823-T205547	033	-42.37	-78.30	-67.51	0.0003 – 0.003	130.5
PETERMANN2015-D20150824-T000615	036	-40.40	-77.65	-69.10	0.0002 – 0.001	228.2
PETERMANN2015-D20150824-T021509	038	-42.13	-79.37	-68.38	0.0002 – 0.002	216.6
PETERMANN2015-D20150824-T162333	040	-43.64	-78.26	-71.80	0.0003 – 0.002	173.4
PETERMANN2015-D20150807-T065201	004	-38.63	-72.95	-60.64	0.0004 – 0.006	27.3
PETERMANN2015-D20150807-T093944	006	-45.08	-78.86	-73.41	0.0004 – 0.001	57.0
PETERMANN2015-D20150807-T113408	007	-43.74	-76.12	-66.49	0.0006 – 0.005	36.0
PETERMANN2015-D20150807-T232746	009	-45.72	-79.89	-71.95	0.0001 – 0.0008	40.8
PETERMANN2015-D20150808-T042810.raw	013	-40.87	-67.77	-57.17	0.002 – 0.02	23.3

Table 8: Summary of TS, S_v, average density ($\hat{\rho}$) and the acoustic sampling volume (V) as calculated for each line with a transitional preference (orange shading) or outlier (grey shading) scattering layer.

Line (.RAW file)	CTD station	TS (dB)	Less Dense S_v (dB)	Dense S_v (dB)	Density (targets m^{-3})	Acoustic Sampling Volume (m^3)
PETERMANN2015-D20150815-T125226	017	-44.43	-76.92	-71.57	0.0006 – 0.002	60.0
PETERMANN2015-D20150815-T135816.	018	-43.18	-75.56	-70.48	0.0006 – 0.002	72.6
PETERMANN2015-D20150815-T150617	019	-44.63	-75.42	-70.34	0.0008 – 0.003	66.2
PETERMANN2015-D20150818-T095013	024	-42.19	-74.12	-64.89	0.0006 – 0.005	60.0
PETERMANN2015-D20150822-T173712	030	-43.04	-77.74	-74.67	0.0003 – 0.0007	216.6